entropy

Finite-Time Thermodynamics

Edited by
R. Stephen Berry, Peter Salamon and Bjarne Andresen

Printed Edition of the Special Issue Published in *Entropy*

www.mdpi.com/journal/entropy

MDPI

Finite-Time Thermodynamics

Finite-Time Thermodynamics

Editors

R. Stephen Berry
Peter Salamon
Bjarne Andresen

MDPI • Basel • Beijing • Wuhan • Barcelona • Belgrade • Manchester • Tokyo • Cluj • Tianjin

Editors

R. Stephen Berry (deceased)
The University of Chicago
USA

Peter Salamon
San Diego State University
USA

Bjarne Andresen
University of Copenhagen
Denmark

Editorial Office
MDPI
St. Alban-Anlage 66
4052 Basel, Switzerland

This is a reprint of articles from the Special Issue published online in the open access journal *Entropy* (ISSN 1099-4300) (available at: https://www.mdpi.com/journal/entropy/special_issues/FTT).

For citation purposes, cite each article independently as indicated on the article page online and as indicated below:

LastName, A.A.; LastName, B.B.; LastName, C.C. Article Title. *Journal Name* **Year**, *Volume Number*, Page Range.

ISBN 978-3-0365-4949-1 (Hbk)
ISBN 978-3-0365-4950-7 (PDF)

Cover image courtesy of Bjarne Andresen based on a sketch by Lena Pedersen

Contents

About the Editors

R. Stephen Berry

R. Stephen Berry was professor of chemical physics at the University of Chicago since 1964 where he made major contributions in an exceptionally wide range of subjects, both experimentally and theoretically. Early in his career, he conceived of the idea that operating any process at a non-vanishing speed necessarily has a cost. The energy crisis of 1973 combined with a seminal paper in 1975 focused the effort, in collaboration with the other two editors of this volume, into what we named finite-time thermodynamics. In this effort, Steve always generously shared his insight and related the new findings to a wide range of other topics such as shock tube experiments and economics. At the same time, Steve contributed to atomic collision theory and experiments, photoelectron spectroscopy, thermodynamics of shock tubes, and the theory of clusters, just to mention a few examples. Early on, he studied the energy budget of the entire chain from the extraction of raw materials to the production of a finished car, and further to its disposal, a procedure which today is called life cycle analysis. Steve was a member of the academies of sciences in the USA and Denmark and home secretary of the National Academy of Sciences (USA) from 1999 until 2003. In addition, he served on many committees related to inclusion of scientific information into public policy and decision making. Science education for all students was also high on his agenda. Sadly, Steve passed away in 2020 as we were editing this volume.

Peter Salamon

Peter Salamon (contact at: psalamon@sdsu.edu) received his PhD in chemical physics from the University of Chicago during his collaboration with the other two editors of this volume, a collaboration that started finite-time thermodynamics. He has been a professor in the Mathematics Department at San Diego State University from 1980 to the present, with visiting positions at the Hebrew University, the University of Heidelberg, and the University of Copenhagen, among others. His research has always revolved around thermodynamics very broadly interpreted. This let him stray as far as machine learning, global optimization, and microbial ecology. His numerous collaborations earned him an Erdös number of one and the designation as a hub in the Collaborative Distance Graph linking collaborators from numerous far-flung fields to Paul Erdös. He co-founded Telluride Science Research Center, which gave early finite-time thermodynamics and other fledgling fields an important venue.

Bjarne Andresen

Bjarne Andresen (contact at: andresen@nbi.ku.dk) was a professor at the Niels Bohr Institute, University of Copenhagen 1978–2020 and is currently affiliated with the NBI as emeritus. Along with the other two editors of this Special Issue, he started the field of finite-time thermodynamics (FTT) in 1975 and has participated in spreading the idea of limiting the duration of a process to a fixed time, thus causing unavoidable losses. A key element of FTT is optimizing the path of the process. Prof. Bjarne Andresen has contributed to applying FTT to as diverse fields as chemistry, physics, engineering, optimization theory, economics, biology, a.o. Lately, he has worked with Professor Christopher Essex on extending thermodynamics to extremely long time and size scales. Early in his career, he contributed to atomic collision theory. In 1984, the three co-editors started The Telluride Science Research Center as a secluded retreat for developing new wild ideas in science. At the periphery of science, prof. Bjarne Andresen has been the president of the Section for Theoretical

Chemistry of the Danish Chemical Society, chairman of the committee on research and education of the Danish Confederation of Professional Associations, chairman of the Danish Forum for University Policy and Planning, and is currently treasurer of the Danish Academy of Natural Sciences.

Preface to "Finite-Time Thermodynamics"

Finite-time thermodynamics, as a field of theory as well as an application, was initiated 45 years ago. As is often the case when new concepts crystalize, stray ideas about "what if" had appeared earlier (e.g., Chambadal in 1957, Novikov in 1958, Curzon and Ahlborn in 1975, and Weinhold in 1975), but it was only in 1976 that a more comprehensive net of theory started to evolve. At the same time, it became clear that the restriction of finite time, or in general finite resources, is pervasive for all real processes. The "finite-time" idea spread to chemistry, physics, economics, engineering (under a different name and with preciously few references to its origin), and, in more recent years, to biology. It is now a solidly established field with an exceptionally wide range of applications.

In the present Special Issue of *Entropy*, we have collected 19 papers which provide a wide range of current topics for which finite time is a crucial element, some very abstract, some very applied, and some in unexpected directions. To wrap up the package, one paper provides a personal view of the beginnings, and one paper is our look into the crystal ball for the future. A lot more FTT and FTT-inspired research is on its way. Happy reading.

R. Stephen Berry, Peter Salamon, and Bjarne Andresen
Editors

entropy

MDPI

Creative

How It All Began

R. Stephen Berry [1], Peter Salamon [2] and Bjarne Andresen [3,*]

[1] Department of Chemistry, The University of Chicago, 5735 S. Ellis Ave, Chicago, IL 60637, USA
[2] Department of Mathematics and Statistics, San Diego State University, 5500 Campanile Drive, San Diego, CA 92182-7720, USA; salamon@sdsu.edu
[3] Niels Bohr Institute, University of Copenhagen, Blegdamsvej 17, DK-2100 Copenhagen Ø, Denmark
* Correspondence: andresen@nbi.ku.dk

Received: 5 August 2020; Accepted: 13 August 2020; Published: 18 August 2020

The first paper published as *Finite-Time Thermodynamics* is from 1977 [1]. It was preceded by the 1975 article by Curzon and Ahlborn entitled "Efficiency of a Carnot engine at maximum power output" [2]. But of course the climate for such a development had to be ripe. Below we each give our personal recollections about how we got started on this endeavor. This is not intended solely as a historical note, but also as a reminder to younger enthusiastic people that the road for new ideas that disturb the traditional lines of thought often is bumpy, if not outright hostile. But there is light at the end of the tunnel!

Shortly before the deadline, Steve Berry passed away. We have kept his recollections below exactly as he originally wrote them, except for correcting a single dating. We dedicate this special Finite-Time Thermodynamics issue to Prof. R. Stephen Berry for his vision, contributions, and perpetual assistance.

1. R. Stephen Berry

The topic—or field—of finite time thermodynamics has an interesting history. Its stimulus was a far cry from a motivation to do basic science. Its real origins began when I moved to The University of Chicago in 1964. I had thought I was prepared to adapt to the Chicago environment, but it turned out otherwise. At that time, Chicago was a very smoky, dirty, even smelly city. Each morning, windowsills had new layers of fine grit that had drifted in from the outside during the night. I found myself angry that my new city could have such terrible air pollution. I was sufficiently troubled that I wrote a letter to then-Mayor Richard Daley, which began, "Dear Mayor Daley, You live like a pig!" I went on to say that I had heard that the City of Chicago did have some activity to address air pollution, but I could see no sign of it. I received a reply with an invitation to visit the City's Air Pollution Laboratory. The visit left me with a sense that nothing substantive was happening to address the problem. I wrote an article [3], "Perspectives on Polluted Air", which pointed out the untoward consequences of severe air pollution, such as the human death rate in incidents of high levels of air pollution. I also became involved in some of the public anti-air pollution activities that were stirring at the time, activities that, nationwide, led to a "tipping point" that resulted in a national transformation, with the passing in 1967 of the Federal Air Quality Act and then the Clean Air Act, and the creation of the Environmental Protection Agency.

In that period of transformation, I came to believe that one necessary transformation to improve air quality would be to use energy more efficiently than we had been doing. Much of the pollution came from energy production and much from its end use. I was not alone by any means in my concern with the problem [4]. I was sufficiently concerned that, with my student Peter Lehman, we wrote a review article on the chemistry of air pollution [5]. But the "big step" for me came when Margaret Fels and I did a detailed study to show a way to identify likely targets for improving efficiency of energy use [6,7]. We chose the manufacture and disposal of automobiles as the subject and examined each step, from recovery of ore in the ground to final disposal of a used-up hulk, determining the actual

energy and free energy at each step, and comparing those values with theoretical ideal thermodynamic limits. Of course we supposed that where the differences were largest, would be the best opportunities for improving the efficiency. This kind of approach was just beginning and has become what is now called "life cycle analysis".

We thought this was rather a ground-breaking approach and applied the method to other systems, such as packaging, transporting and marketing consumer goods [8], and to polymers [9]. However, one person who had read the article said to me, "Why did you compare the actual energy and free energy use with the ideal thermodynamic limits? After all, those limits are based on reversible, infinitely slow processes. Who would wait for delivery of a car from a manufacturer who claimed to make his cars reversibly?" That challenge turned out to be the trigger!

In 1975 we began exploring these questions: "Is it possible to create, construct and evaluate the analogues of thermodynamic potentials for processes constrained to operate in finite times?" The first venture, carried out with postdoctoral associates Abraham Nitzan and Bjarne Andresen and graduate student Peter Salamon, made use of a model, a variant of the Carnot cycle in which the system moves around in a series of stepwise small pressure changes, relaxing at a finite rate to each new pressure [2]. Thus the system goes around its cycle in a finite number of steps, relaxing to each new pressure in a small, finite time. Very artificial, yes, but a model that lends itself to modeling a thermodynamic system that evolves in finite time, the relaxation times following each sudden stepwise change in pressure.

Very soon after that initial venture, we moved forward in more substantive ways. Within months of that first paper, we made what I feel was a major step, showing how one could create the analogues of traditional thermodynamic potentials for systems constrained to carry out their cycles in fixed, finite times [10], and then how to determine extremal values for finite-time processes [11]. That led naturally to a general method for optimization [12]. A slight pause and a new flow of publications began. When Mary Ondrechen joined the group, we began applying finite-time thermodynamics to chemical processes [13,14].

Our investigations broadened at that time, first to relate our work to a geometric concept from Frank Weinhold [15] and then to explicit optimization. First minimize entropy production [16] and then to improving performance of piston engines by controlling the piston's path in time [17]. We soon pursued that direction for both Otto and Diesel cycles but never found a practical way to achieve those optimal time paths.

At that time, finite-time thermodynamics had become a topic of investigation for enough people that we began holding Summer Conferences. The first two were at the Aspen Center for Physics, in 1981 and 1983. That second one was so popular that the participants didn't want to skip a year. However, the Aspen Physics Center's schedule was already full so we couldn't hold a meeting there in 1984. Peter Salamon and I were discussing this problem when he said, 'We both know Telluride; why don't we see if we can hold the meeting there?" I thought that was a brilliant idea, so we went ahead with it and, in the summer of 1984, held the first Telluride scientific conference. It was at least as popular as the Aspen meetings had been, and they have continued and stimulated many other kinds of meetings in Telluride. They mostly fall in a general category of "molecular science" so they are complementary, rather than competitive, with the Aspen Physics Center's meetings.

So we can see how anger at an unpleasant, even dangerous environment can have amazing and totally unexpected consequences.

"Acknowledgement—I would like to thank all the collaborators who have worked with me in creating, developing and applying finite-time thermodynamics, perhaps most notably Peter Salamon and Bjarne Andresen, with whom I am collaborating to create this volume."

2. Peter Salamon

As a freshman graduate student looking for an advisor to work with, I was looking for one to underwrite a project exploring the differential geometry of thermodynamics. When I approached Steve

Berry, he responded with a question, "While you're at it, can you put time in?" It was spring of 1973 and I had found my mentor.

The notion seemed intriguing. Having been raised in the deeply structuralist traditions prevailing in mathematics departments in the 1970s, it seemed likely to me that understanding the mathematical structure of thermodynamics would enable us to see how this structure might accommodate time. I had studied the differential geometrical framework of classical mechanics and knew how time dependence changes the symplectic structure on the manifold of configurations into a contact structure. I thought there was a good chance of finding something similar for thermodynamics.

Steve however did not conceive of the "add time" dictum in terms of the mathematical structure it would require. Rather he asked the much more physical question of what the constraint of a given time implied for a thermodynamic process. He also pointed us toward heat engines and drafted Abraham Nitzan who was doing a postdoc across town and Bjarne Andresen who joined in the summer of 1975. We learned of Curzon and Ahlborn's result from one of the more encouraging early referees, who rejected our work as legitimate new physics but suggested that we should consider it as physics education. What Steve's account of "How it began" did not mention about this nascent stage in the life of the subject was the initial hostility to the idea of finite-time thermodynamics on the part of referees and by extension the community. I feel this is an important historic detail for early career scientists to take heart from. I know I would likely not have survived the onslaught of rejections without Steve's staunch support.

Due to our years of abuse at the hands of referees, the subject did not seem fully legitimate to me until I could see the broader responses from the community. For this, the Aspen workshops in 1981 and 1983 were crucial. As I was driving home from the 1983 workshop, I came up with a proof of the horse–carrot theorem [18] and wanted to organize a workshop in 1984 on the many directions the result could lead. Alas, Steve told me Aspen was full. Bjarne was spending his sabbatical with me in San Diego, and with his help we organized the first Telluride workshop.

3. Bjarne Andresen

In 1975 I came to Chicago to work with Steve, financed by a grant from the Danish Science Foundation to study atomic collision theory, my previous specialty. Within a week, discussions with Steve and Peter had gotten me hooked on the idea that developing a more realistic form of thermodynamics than the standard reversible theory was a brilliant idea. After all, we had just had the oil crisis of 1973 with oil rationing and car-free Sundays in Europe. That started a year of enthusiastic search for consequences of adding that small detail of a finite time horizon for processes, "the cost of haste". At the end of the year I had to report to the Foundation that, sorry, I did not do anything of what you paid me for but I started this new project instead. No comment whatsoever, just "Thank you for the report". I am sure that wouldn't have worked today, but they did the right thing.

Our first four publications on Finite-Time Thermodynamics [1,10–12] carry the year 1977 even though all the work was done during this first year. The problem, as Peter also mentions above, was solid resistance from the established community. Extreme doubt at the first conference we presented the ideas [12] could be interpreted positively as "inspirational". But I had never imagined the solid opposition we met from the editors of several major journals. Later I have observed that such resistance to modifying established ideas is ubiquitous. The main point of telling youngsters about our trials and tribulations is to help them understand exactly this human trait. What we did simply could not be true because it was not within the standard teachings of thermodynamics. It took two years of fighting referees and editors to get those initial papers out. Some colleagues were so adamant in their efforts to eradicate these new thoughts that they wrote to editors of several journals trying to use their standing to convince the editors to reject anything with the words finite-time thermodynamics in the title outright, content unseen. However, that did not prevent some of those colleagues from taking our general proofs, restricting their coverage, and then publishing them as their own original discoveries, under a new name of course. At another incident in 1981, at a luncheon with a Nobel

laureate, he characterized the finite-time results as "either useless or something that I have already published". It was not until Physics Today in 1984 ran a news article [19] on the finite-time concept that recognition began. So, young scientists with all your bright and unorthodox ideas, beware. You have an uphill battle ahead of you, but don't give up.

During a subsequent stay in Chicago in 1977, we had started determining the process paths which would yield the optimal performance. As an enthusiastic young man I had invited myself to the General Motors Research Laboratories in Detroit, a short flight from Chicago, to offer them the great news that the ordinary gasoline engine could be made 15% more fuel efficient and at the same time cut the cooling requirement in half simply by moving the piston a little differently in each stroke [17]. I was well received and a group of engine design engineers listened patiently to my presentation. At the end the head of the department thanked me for coming over, but he did not want to get further into such a scheme because, as he said, "people are happily buying our current cars, so why should we change them"? This is just another version of the publication resistance to novel ideas mentioned above.

From the beginning we wanted to investigate the effects of requiring a finite time horizon for any process as widely as possible. Some efforts resulted in completely general principles involving duration dependent chemical potentials [10,20]. Others lead to the definition of a thermodynamic length [15,18] which ties dissipation, and thus the finite time, to a geometric formulation. The new concepts have been applied not just to thermodynamics but also to engineering [21], statistical mechanics [22], optimization theory, [23] chemical reactions [24], quantum mechanics [25], biology [26], and economics [27], just to mention some that we have been involved in ourselves. A major conceptual discovery, not related to the dissipation itself, is that it is possible to accurately measure changes in free energies, i.e., equilibrium properties of substances, through non-equilibrium measurements using, e.g., the Jarzynski equation [28] and the Crooks theorem [29]. A book [30] and two review articles [31,32] have summarized the FTT results so far.

It has been a pleasure to be along for this long and inspiring ride and I thank all the wonderful people I have encountered along the way. Let this be an encouragement to all young people to believe in their grand ideas and explore them in the face of opposition. Future paradigms must all pass through a heresy stage.

Author Contributions: All the three authors contribute equally to the paper.

Funding: This research received no external funding.

Conflicts of Interest: The authors declare no conflict of interest.

References

1. Andresen, B.; Berry, R.S.; Nitzan, A.; Salamon, P. Thermodynamics in finite time. I. The step-Carnot cycle. *Phys. Rev. A* **1977**, *15*, 2086–2093. [CrossRef]
2. Curzon, F.L.; Ahlborn, B. Efficiency of a Carnot engine at maximum power output. *Am. J. Phys.* **1975**, *43*, 22–24. [CrossRef]
3. Berry, R.S. Perspectives on Polluted Air. *Bull. At. Sci.* **1970**, *26*, 2–41. [CrossRef]
4. Anastaplo, G.; Berry, R.S.; Coase, R.H.; Demsetz, H.; Friedman, M. *The Legal and Economic Aspects of Pollution*; The University of Chicago Center for Policy Study: Chicago, IL, USA, 1970.
5. Berry, R.S.; Lehman, P.A. Aerochemistry of air pollution. *Annu. Rev. Phys. Chem.* **1971**, *22*, 47–84. [CrossRef]
6. Berry, R.S.; Fels, M.F. *The Production and Consumption of Automobiles, and Energy Analysis of the Manufacture, Discard and Reuse of the Automobile and Its Component Materials. Report to the Illinois Institute for Environmental Quality*; 1972; pp. 1–74. Available online: https://www.osti.gov/biblio/7364527 (accessed on 1 January 2020).
7. Berry, R.S.; Fels, M.F. The energy cost of automobiles. *Bull. At. Sci.* **1973**, *29*, 11–60. [CrossRef]
8. Berry, R.S.; Makino, H. Energy Thrift in Packaging and Marketing. *Technol. Rev.* **1974**, *76*, 32–43.
9. Berry, R.S.; Long, T.V.; Makino, H. Energy Budgets 5. An international comparison of polymers and their alternatives. *Energy Policy* **1975**, *3*, 144–155. [CrossRef]
10. Salamon, P.; Andresen, B.; Berry, R.S. Thermodynamics in finite time. II. Potentials for finite-time processes. *Phys. Rev. A* **1977**, *15*, 2094–2102. [CrossRef]

11. Andresen, B.; Salamon, P.; Berry, R.S. Thermodynamics in finite time. Extremals for imperfect heat engines. *J. Chem. Phys.* **1977**, *66*, 1571–1577. [CrossRef]
12. Andresen, B.; Berry, R.S.; Salamon, P. Optimization of processes with finite-time thermodynamics. In *International Conference on Energy Use Management*; Fazzolare, R., Smith, C.B., Eds.; Pergamon Press: New York, NY, USA, 1977; Volume II, pp. 1–9.
13. Ondrechen, M.J.; Berry, R.S.; Andresen, B. Thermodynamic in finite time: A chemically driven engine. *J. Chem. Phys.* **1980**, *72*, 5118–5124. [CrossRef]
14. Ondrechen, M.J.; Andresen, B.; Berry, R.S. Thermodynamics in finite time: Processes with temperature-dependent chemical reactions. *J. Chem. Phys.* **1980**, *73*, 5838–5843. [CrossRef]
15. Salamon, P.; Andresen, B.; Gait, P.D.; Berry, R.S. The significance of Weinhold's length. *J. Chem. Phys.* **1980**, *73*, 1001–1002. [CrossRef]
16. Salamon, P.; Nitzan, A.; Andresen, B.; Berry, R.S. Minimum entropy production and the optimization of heat engines. *Phys. Rev. A* **1980**, *21*, 2115–2129. [CrossRef]
17. Mozurkewich, M.; Berry, R.S. Finite time thermodynamics: Engine performance improved by optimized piston motion. *Proc. Nat. Acad. Sci. USA* **1981**, *78*, 1986–1988. [CrossRef] [PubMed]
18. Salamon, P.; Berry, R.S. Thermodynamic length and dissipated availability. *Phys. Rev. Lett.* **1983**, *51*, 1127. [CrossRef]
19. Andresen, B.; Salamon, P.; Berry, R.S. Thermodynamics in finite time. *Phys. Today* **1984**, *37*, 62. [CrossRef]
20. Andresen, B.; Rubin, M.H.; Berry, R.S. Availability for finite-time processes. General theory and a model. *J. Phys. Chem.* **1983**, *87*, 2704–2713. [CrossRef]
21. Schaller, M.; Hoffmann, K.H.; Rivero, R.; Andresen, B.; Salamon, P. The influence of heat transfer irreversibilities on the optimal performance of diabatic distillation columns. *J. Non Equilib. Thermod.* **2002**, *27*, 257–269. [CrossRef]
22. Salamon, P.; Nulton, J.D.; Berry, R.S. Length in Statistical Thermodynamics. *J. Chem. Phys.* **1985**, *82*, 2433–2436. [CrossRef]
23. Salamon, P.; Nulton, J.; Robinson, J.; Pedersen, J.; Ruppeiner, G.; Liao, L. Simulated Annealing with Constant Thermodynamic Speed. *Comput. Phys. Commun.* **1988**, *49*, 423. [CrossRef]
24. Bak, T.A.; Salamon, P.; Andresen, B. Optimal behavior of consecutive chemical reactions A<=>B<=>C. *J. Phys. Chem. A* **2002**, *106*, 10961–10964. [CrossRef]
25. Insinga, A.; Andresen, B.; Salamon, P.; Kosloff, R. Quantum heat engines: Limit cycles and exceptional points. *Phys. Rev. E* **2018**, *97*, 062153. [CrossRef] [PubMed]
26. Roach, T.N.F.; Salamon, P.; Nulton, J.; Andresen, B.; Felts, B.; Haas, A.; Calhoun, S.; Robinett, N.; Rohwer, F. Application of finite-time and control thermodynamics to biological processes at multiple scales. *J. Non-Equil. Thermod.* **2018**, *43*, 193–210. [CrossRef]
27. Tsirlin, A.; Gagarina, L. Finite-Time Thermodynamics in Economics. *Entropy* **2020**, *22*. [CrossRef]
28. Jarzynski, C. Nonequilibrium Equality for Free Energy Differences. *Phys. Rev. Lett.* **1997**, *78*, 2690–2693. [CrossRef]
29. Crooks, G.E. Nonequilibrium Measurements of Free Energy Differences for Microscopically Reversible Markovian Systems. *J. Stat. Phys.* **1998**, *90*, 1481–1487. [CrossRef]
30. Berry, R.S.; Kazakov, V.; Sieniutycz, S.; Szwast, Z.; Tsirlin, A.M. *Thermodynamic Optimization of Finite-Time Processes*; Wiley: Hoboken, NJ, USA, 2000.
31. Hoffmann, K.H.; Burzler, J.M.; Schubert, S. Endoreversible Thermodynamics. *J. Non Equilib. Thermodyn.* **1997**, *22*, 311–355.
32. Andresen, B. Current Trends in Finite-Time Thermodynamics. *Angew. Chem. Int. Ed.* **2011**, *50*, 2690–2704. [CrossRef]

entropy

MDPI

Article

Geometric Optimisation of Quantum Thermodynamic Processes

Paolo Abiuso [1], Harry J. D. Miller [2], Martí Perarnau-Llobet [3,*] and Matteo Scandi [1]

[1] ICFO—Institut de Ciències Fotòniques, The Barcelona Institute of Science and Technology, 08860 Castelldefels, Barcelona, Spain; paolo.abiuso@icfo.eu (P.A.); matteo.scandi@icfo.es (M.S.)
[2] Department of Physics and Astronomy, The University of Manchester, Manchester M13 9PL, UK; harry.miller@manchester.ac.uk
[3] Département de Physique Appliquée, Université de Genève, 1206 Genève, Switzerland
* Correspondence: marti.perarnaullobet@unige.ch

Received: 31 August 2020; Accepted:19 September 2020; Published: 24 September 2020

Abstract: Differential geometry offers a powerful framework for optimising and characterising finite-time thermodynamic processes, both classical and quantum. Here, we start by a pedagogical introduction to the notion of thermodynamic length. We review and connect different frameworks where it emerges in the quantum regime: adiabatically driven closed systems, time-dependent Lindblad master equations, and discrete processes. A geometric lower bound on entropy production in finite-time is then presented, which represents a quantum generalisation of the original classical bound. Following this, we review and develop some general principles for the optimisation of thermodynamic processes in the linear-response regime. These include constant speed of control variation according to the thermodynamic metric, absence of quantum coherence, and optimality of small cycles around the point of maximal ratio between heat capacity and relaxation time for Carnot engines.

Keywords: quantum thermodynamics; finite-time thermodynamics; thermodynamic length; heat engines; cooling

1. Introduction

Quasistatic processes can be successfully characterised by a few simple and universal results: work is given by the equilibrium free energy difference between the endpoints of a transformation, the efficiency of a Carnot engine depends only on the temperatures of the thermal baths, and in general all quantities of interest become state functions [1]. These results are extremely strong, but their applicability to real life situations is hindered by the necessity of performing all protocols in infinite time in order to ensure that the system remains in thermal equilibrium along the process. On the other hand, finite-time thermodynamic processes can become incredibly complex and strongly depend on the particular protocol and system. For this reason, universal results or simple characterisations are rare. A remarkable exception are fluctuation theorems, which are universal results that apply to arbitrary out-of-equilibrium processes under very mild assumptions [2]; however, they provide a few constraints on the statistics, which are far from sufficient for a full characterisation of the out-of-equilibrium process.

Noticeably, the middle ground between the two situations above, i.e., the case in which the protocol is performed in long but finite time, can be characterised by few geometrical quantities. The main ideas were introduced for classical systems in a series of seminal papers in the 80 s by Weinhold and Andresen, Berry and Salamon, among others [3–14]. More recently, the field saw a revival following a series of papers initiated by Crooks in 2007 [15–17], leading to several applications in, e.g., molecular motors [18], small-scale information processing [19], nonequilibrium

steady states [20,21], and many-body systems [22,23]. The same ideas have been generalised to the quantum regime for unitary dynamics using linear response [24–28], and to open system dynamics for Lindbladian systems [29,30]. Recent applications of thermodynamic geometry in quantum systems can be found in quantum heat engines [31–34], equilibration processes [35,36], phase transitions [37], quantum work and heat fluctuations [38–40], thermodynamic uncertainty relations [41,42], and shortcuts to adiabaticity [43]; see also Ref. [44] for a recent perspective on the subject.

The goal of this paper is two-fold: First, we aim to provide a pedagogic introduction to the notion of (quantum) *thermodynamic length*. This is done in Section 2, where we explicitly connect different frameworks where this concept can be derived: adiabatic linear response theory in closed quantum systems [26–28], adiabatic Lindblad master equations [29,30], and discrete processes [7]. Additionally, in Section 3, we use the concept of thermodynamic length to lower bound the dissipation in a finite-time process, generalising to quantum systems the so-called *Horse–Carrot* theorem [6,7]. Notably, the bound is process-independent, being a function of the endpoints and the (smallest) relaxation timescale. Thus, it can be seen as a geometric refinement of the second law of thermodynamics. Second, in Section 4, we apply these ideas to the optimisation of thermodynamic processes, with emphasis on heat engines in the low-dissipation regime [6,45–53]. Building upon previous works, we show how general conclusions can be drawn with analytical tools for a class of thermal machines, and a few principles of common application can be stated for optimal processes, with some examples. Finally, these results are illustrated in detail for the paradigmatic case of a finite-time Carnot engine with a driven two-level system as a working substance in Section 5.

2. Overview of Thermodynamic Length in Quantum Systems

Let us consider a system whose Hamiltonian H_t can be externally driven and which is weakly coupled to a thermal bath. Without loss of generality, we will decompose the system Hamiltonian as $H_t = \sum_i \lambda_t^i X_i$, where $\{\lambda_t^i\}$ is a family of time dependent external parameters, and $\{X_i\}$ are the corresponding observables. Moreover, in the following we will assume summation over repeated indexes. In this context the average work performed on the system is given by:

$$w = \int_\gamma dt\ \mathrm{Tr}\left[\dot{H}_t \rho_t\right] = \int_\gamma dt\ \dot{\lambda}_t^i\, \mathrm{Tr}\left[X_i \rho_t\right], \tag{1}$$

where γ is the path in the parameters space, and ρ_t is the evolved system density matrix at time $t \in (0, \tau)$. We know from equilibrium thermodynamics that if the process is infinitely slow the system is always at equilibrium. Consequently, the work is given by the difference of free energy at the endpoints of the transformation. Indeed, in this formalism we regain this result:

$$w_{\mathrm{eq}} = \int_\gamma dt\ \mathrm{Tr}\left[\dot{H}_t \pi_t\right] = \int_\gamma dt\ \frac{d}{dt}\left(-\beta^{-1} \log \mathcal{Z}_t\right) = \Delta F, \tag{2}$$

where we used the notation $\mathcal{Z}_t = \mathrm{Tr}\left[e^{-\beta H_t}\right]$ for the partition function, we denote the thermal state by $\pi_t := e^{-\beta H_t}/\mathcal{Z}_t$, and we used the definition of the free energy $F_t := -\beta^{-1} \log \mathcal{Z}_t$, as well as $\Delta F = F_\tau - F_0$. Given this result, it is then natural to define the dissipated work as $w_{\mathrm{diss}} := (w - w_{\mathrm{eq}}) = (w - \Delta F)$, in order to isolate the role of the dissipation arising from finite time effects.

A consequence of the second law is that $w_{\mathrm{diss}} \geq 0$ with equality only in the infinite time limit. Moreover, if the dynamics is divisible (e.g., Markovian) the rate of dissipation is also positive definite, and zero only in the infinite time limit [54]. This suggests that we can expand $\dot{w}_{\mathrm{diss}}$ in terms of $\{\dot{\lambda}_t^i\}$ around the quasistatic limit ($\dot{\lambda}_t^i \equiv 0$), and obtain:

$$\dot{w}_{\mathrm{diss}} = \dot{\lambda}_t^i \cancel{\partial_i\, \dot{w}_{\mathrm{diss}}\big|_{\dot{\lambda}_t \equiv 0}} + \dot{\lambda}_t^i \left(\partial_i \partial_j\, \dot{w}_{\mathrm{diss}}\big|_{\dot{\lambda}_t \equiv 0}\right) \dot{\lambda}_t^j + \mathcal{O}\left(||\dot{\lambda}||^3\right), \tag{3}$$

where the first derivative cancels since we are expanding around a minimum. For the same reason, we know that the Hessian $g_{i,j} = \beta\partial_i\partial_j \, \dot{w}_{\text{diss}}\big|_{\dot{\lambda}_t=0}$ is positive definite. From these considerations we see that the dissipated work can be written as:

$$w_{\text{diss}} = \frac{1}{\beta}\int_\gamma dt \; \dot{\lambda}_t^i \, (g_{i,j})_t \dot{\lambda}_t^j, \tag{4}$$

up to higher order corrections. Linear response theory tells us that the matrix g_t depends smoothly on the thermal state π_t. Moreover, we can deduce that it is positive definite and symmetric, being the Hessian of a function around its minimum. These are the defining properties of a metric. In fact, we can interpret Equation (4) as the energy functional or the action of the curve γ with respect to the metric g. This name comes from the formal analogy between Equation (4) and the action of a system of free particles with mass tensor given by g.

This interpretation is particularly useful thanks to the following fact. If one defines the length of γ as:

$$l_\gamma = \int_\gamma dt \; \sqrt{\dot{\lambda}_t^i \, (g_{i,j})_t \dot{\lambda}_t^j}, \tag{5}$$

we have the Cauchy–Schwarz like expression

$$\beta w_{\text{diss}} \geq l_\gamma^2/\tau, \tag{6}$$

which takes the name of "thermodynamic length inequality" [6]. Among the curves connecting two endpoints, $\{\lambda_0^i\}$ and $\{\lambda_\tau^i\}$, we call γ geodesic if it minimises the distance between the two points as measured by Equation (5). A geodesic is also characterised by the property that it keeps the product $\dot{\lambda}_t^i \, (g_{i,j})_t \dot{\lambda}_t^j$ constant along its path, implying that the Cauchy–Schwarz inequality in Equation (6) is saturated if γ is a geodesic. Physically, this means that in order to design minimal dissipating protocols in the slow driving regime, it is sufficient to solve a system of differential equations, i.e., the geodesic equations:

$$\ddot{\lambda}_t^i + \Gamma^i_{j,k}\big|_{\lambda_t} \dot{\lambda}_t^j \dot{\lambda}_t^k = 0, \tag{7}$$

where Γ denotes the Christoffel symbols, which are given by:

$$\Gamma^i_{j,k}|_{\lambda_t} = \frac{1}{2} g^{i,l} \left(\partial_j g_{l,k} + \partial_k g_{j,l} - \partial_l g_{j,k}\right)|_{\lambda_t}. \tag{8}$$

Here, $g^{i,l}$ is the inverse of the metric, and we use the shorthand notation $\partial_i g_{j,k}|_{\lambda_t} \equiv (\partial g_{j,k}/\partial\lambda_i)|_{\lambda=\lambda_t}$. Moreover, the dissipative properties of a driven system can be directly inferred from the spectral properties of g_t alone. In particular, starting from very general considerations on the nature of the metric tensor, this will allow us to give lower bounds on the rate of dissipation (Section 3) and to conclude that the creation of coherence is always detrimental to the efficiency (Section 3).

Another strength of the formalism presented is that g can be explicitly computed in many frameworks. For example, comparing Equations (1) and (2) it can be seen that the metric tensor can be computed from the slow driving approximation of the expectation value of the observables $\{X_i\}$s. This was explicitly carried out in the context of linear response of an adiabatically driven unitary dynamics in [28] (see also [26,27]), leading to the expansion:

$$\text{Tr}\left[X_i\rho_t\right] = \text{Tr}\left[X_i\pi_t\right] + \chi_t^{\text{ad}}[X_i, X_j]\dot{\lambda}_t^j + \mathcal{O}\left(||\dot{\lambda}||^2\right), \tag{9}$$

where χ_t^{ad} is the adiabatic response function given by:

$$\chi_t^{\mathrm{ad}}[A,B] = -i\int_0^\infty d\nu\ \left(\nu\,\mathrm{Tr}\left[[A(\nu),B]\pi_t\right]\right). \tag{10}$$

Here, we set $\hbar = 1$, and the Heisenberg picture $A(s)$ is defined with respect to the frozen Hamiltonian at time t, i.e., $A(s) = e^{iH_t s}Ae^{-iH_t s}$. Notice that the upper bound of the integral can be extended to ∞ thanks to the exponential decay of the correlation function $\mathrm{Tr}\left[[A(\nu),B]\pi_t\right]$. Now, if we plug the expansion just obtained in Equation (1) and we recall that the definition of the dissipated work is $w_{\mathrm{diss}} := (w - w_{\mathrm{eq}})$, we have the expression:

$$w_{\mathrm{diss}} = \frac{1}{\beta}\int_\gamma dt\ \dot\lambda_t^i\,(\beta\,\chi_t^{\mathrm{ad}}[X_i,X_j])\dot\lambda_t^j, \tag{11}$$

up to higher order in $\{\dot\lambda_i\}$. Comparing this equation with Equation (4), we see that in the context of adiabatic linear response the metric tensor is given by $g^{\mathrm{u}}_{i,j} = \frac{\beta}{2}(\chi_t^{\mathrm{ad}}[X_i,X_j] + \chi_t^{\mathrm{ad}}[X_j,X_i])$ (notice that even if χ_t^{ad} is not in general symmetric in its arguments it can always be symmetrised without affecting the result, since the velocities $\{\dot\lambda_t^i\}$ enter the integral in a symmetric way). This formalism was recently used to geometrically characterise thermal machines close to Carnot efficiency [33].

Another relevant framework where a thermodynamic length can be derived is open quantum systems [30] (see also [29]). In particular, consider the Lindbladian dynamics:

$$\dot\rho_t = \mathscr{L}_t[\rho_t], \tag{12}$$

with the property that each $\mathscr{L}_t$ has the real part of all the eigenvalues negative and that there exist a unique instantaneous steady state π_t. These two conditions ensure that the dynamics asymptotically equilibrates irrespective of the initial conditions:

$$\lim_{\nu\to\infty} e^{\nu\mathscr{L}_t}\rho = \pi_t. \tag{13}$$

In this case, it is possible to expand the state in the slow driving limit as $\rho_t \approx \pi_t + \delta\rho_t$ [55], where $\delta\rho_t$ can be expressed up to higher order corrections as [30]:

$$\rho_t = \pi_t + \mathscr{L}_t^+[\dot\pi_t] + \mathcal{O}(||\dot\lambda||^2), \tag{14}$$

where $\mathscr{L}_t^+$ is the Drazin inverse of the Lindbladian given by:

$$\mathscr{L}_t^+[A] = \int_0^\infty d\nu\, e^{\nu\mathscr{L}_t}\left(\pi_t\mathrm{Tr}\left[A\right] - A\right). \tag{15}$$

As it will be shown explicitly in the following, the eigenvalues of $\mathscr{L}_t^+$ encode the information about the thermalisation timescales. Moreover, we introduce the shorthand notation to indicate the derivative of the state:

$$\dot\pi_t = -\beta\,\dot\lambda_t^i\int_0^1 dx\ \pi_t^{1-x}\,\bar X_i\pi_t^x = -\beta\,\dot\lambda_t^i\mathbb{J}_t[\bar X_i], \tag{16}$$

where we denote by $\bar X_i := X_i - \mathrm{Tr}\left[X_i\pi_t\right]$. Hence, if we plug in this expansion into the expression of the work, we obtain that the dissipation takes the form:

$$w_{\mathrm{diss}} = -\frac{1}{\beta}\int_\gamma dt\ \dot\lambda_t^i\,(\beta^2\,\mathrm{Tr}\left[\bar X_i\mathscr{L}_t^+\mathbb{J}_t[\bar X_j]\right])\dot\lambda_t^j. \tag{17}$$

Again, it should be noticed that the quadratic form $q_{i,j} = -\beta^2\,\mathrm{Tr}\left[\bar X_i\mathscr{L}_t^+\mathbb{J}_t[\bar X_j]\right]$ is in general not symmetric, so that in the definition of the metric we need to explicitly symmetrise the expression:

$g^d_{i,j} := \frac{1}{2}(q_{i,j} + q_{j,i})$. The matrix g^d so defined can be then interpreted as the metric tensor for open quantum systems [30].

It is interesting to notice that the metric g^u obtained in the unitary setting can be cast in a form resembling the dissipative one g^d. In fact, explicitly carrying out the integral in the definition of the adiabatic response function χ^{ad}_t, we see that the metric can be recast in the form:

$$\chi^{\mathrm{ad}}_t[X_i, X_j] = -i\int_0^\infty d\nu\ \left(\nu\,\mathrm{Tr}\left[[X_i(\nu), X_j]\pi_t\right]\right) = -\frac{i}{\mathcal{Z}_t}\int_0^\infty d\nu\ \left(\nu\, e^{i(\varepsilon_m-\varepsilon_n)\nu}\right)(e^{-\beta\varepsilon_m} - e^{-\beta\varepsilon_n})(X_i)_{m,n}(X_j)_{n,m} \tag{18}$$

$$= -\frac{1}{\mathcal{Z}_t}\frac{(e^{-\beta\varepsilon_m} - e^{-\beta\varepsilon_n})}{(\varepsilon_m - \varepsilon_n)^2}(X_i)_{m,n}(X_j)_{n,m} = -i\beta\int_0^\infty d\nu\int_0^1 dx\ \mathrm{Tr}\left[\pi_t^{1-x}e^{iH_t\nu}X_i\, e^{-iH_t\nu}\pi_t^x X_j\right] \tag{19}$$

$$= -\beta\,\mathrm{Tr}\left[X_i\,\mathcal{U}_t^+[\mathbb{J}_t[X_j]]\right], \tag{20}$$

where we denoted by $\{\varepsilon_i\}$ the eigenvalues of H_t, and we defined the operator:

$$\mathcal{U}_t^+[A] := -i\int_0^\infty d\nu\ \mathrm{Tr}_B[e^{-iH_t\nu}Ae^{iH_t\nu}]. \tag{21}$$

We see that the role of $\mathscr{L}_t^+$ is taken in this case by the map $\mathcal{U}_t^+$, so that the dissipation in the unitary case is given in complete analogy to Equation (17).

One last example that one can consider is the case in which the Hamiltonian is changed in a sequence of quenches, followed by a perfect thermalisation of the system [7]. The total duration of the protocol is given by $\tau = N\tau_{\mathrm{eq}}$, where N is the number of quenches in which the protocol is realised and τ_{eq} is a fixed equilibration time. When the number of steps is large the state at each time $t = m\tau_{\mathrm{eq}}$ ($m = 0, \ldots, N-1$) is approximately given by: $\rho_m \simeq \pi_m - \Delta_m\pi$, where $\Delta_m\pi$ is the difference between the thermal states at two subsequent steps $\Delta_m\pi := \pi_{m+1} - \pi_m$. This term in the limit $N \gg 1$ is well approximated by $\tau_{\mathrm{eq}}\dot{\pi}_t$. We can interpret this contribution as an indication of how much the system lags behind the thermal state. Proceeding as before, the dissipation can be rewritten up to first order in $1/N = \tau_{\mathrm{eq}}/\tau$ as:

$$w_{\mathrm{diss}} = \frac{1}{2\beta}\int_\gamma dt\ \dot{\lambda}^i_t\,(\tau_{\mathrm{eq}}\beta^2\,\mathrm{Tr}\left[\bar{X}_i\mathbb{J}_t[\bar{X}_j]\right])\dot{\lambda}^j_t. \tag{22}$$

The metric tensor $g^q_{i,j}$ can be directly identified with the trace inside the integral, since $\mathbb{J}_t$ is self-adjoint, making the whole expression symmetric in (i,j). The metric so obtained can be rewritten as: $g^q_{i,j} = \tau_{\mathrm{eq}}\,\mathbf{g}^{BKM}_{i,j}$, where we implicitly defined $\mathbf{g}^{BKM}_{i,j} = \partial^2 \ln \mathcal{Z}/\partial\lambda_i\partial\lambda_j$. This last quantity is known as the Bogoliubov–Kubo–Mori (BKM) statistical distance, which encodes the geometry of the manifold of Gibbs states and has been thoroughly studied in the literature [56–60]. Due to the formal similarity between (22) and (17), it is insightful to study the relation between both metrics. In [30], it was shown that in the particular case in which the observables of interest $\{Y_\alpha\}$ are the left eigenoperators of the Lindbladian, meaning that they evolve according to the equation:

$$\frac{d}{dt}\mathrm{Tr}\left[Y_\alpha\rho_t\right] = \tau_\alpha^{-1}\left(\mathrm{Tr}\left[Y_\alpha\pi_t\right] - \mathrm{Tr}\left[Y_\alpha\rho_t\right]\right), \tag{23}$$

where $\{\tau_\alpha\}$ are the different timescales of the system, the expression of the metric for the Lindbladian dynamics takes the simple form:

$$g^d_{\alpha,\beta} = \frac{\tau_\alpha + \tau_\beta}{2}\,\mathbf{g}^{BKM}_{\alpha,\beta}, \tag{24}$$

in analogy with the classical result [17]. Since, at least for Lindbladians satisfying detailed balance, $\{Y_\alpha\}$ is a complete basis of operators, it is possible to rewrite in this case any observable X_i as $X_i = u_{i,\alpha} Y_\alpha$. That is, the Lindbladian metric for a general family of observables $\{X_i\}$ is given by:

$$g^d_{i,j} = u_{i,\alpha} u_{j,\beta} \frac{\tau_\alpha + \tau_\beta}{2} \mathbf{g}^{BKM}_{\alpha,\beta}. \tag{25}$$

This shows that the role of $\mathscr{L}_t^+$ is to encode the thermalisation timescales of the system, while the main geometrical properties are contained in $\mathbf{g}^{BKM}$. Finally, it should be noticed that in the case of a uniformly thermalising dynamics, i.e., $\tau_\alpha = \tau_{\text{eq}}\ \forall \alpha$, the thermodynamic metric is proportional to the BKM one.

3. Bounding Dissipation with Thermodynamic Length

In a wider context, the BKM metric plays a role within quantum information geometry [61], and can be interpreted as a form of quantum Fisher information [62]. Moreover, it belongs to the family of contractive Riemann metrics over the manifold of normalised density operators $\varrho_t = \varrho_t(\{\lambda^i_t\})$. A theorem by Petz gives a general characterisation of length between neighbouring quantum states [63]:

$$d\ell^2 = \mathbf{g}^f_{ij} d\lambda^i d\lambda^j \Longrightarrow \mathbf{g}^f_{ij} = \text{Tr}\left[\frac{\partial \varrho_t}{\partial \lambda^i} c^f(R_{\varrho_t}, L_{\varrho_t}) \frac{\partial \varrho_t}{\partial \lambda^j}\right], \tag{26}$$

where $c^f(x,y) = (yf(x/y))^{-1}$ and $f(t)$ is a so-called Morozova–Cencov function which is operator monotone, normalised such that $f(1) = 1$ and fulfils $f(t) = tf(1/t)$. Furthermore L_ϱ, R_ϱ represent the left and right multiplication operators defined according to $L_\varrho[A] = \varrho A$ and $R_\varrho[A] = A\varrho$ respectively [63]. For each different metric we have a different notion of distance between density matrices over a path γ:

$$\ell^f(\gamma) := \int_\gamma d\ell = \int_\gamma dt \sqrt{\mathbf{g}^f_{ij} \dot{\lambda}^i \dot{\lambda}^j}. \tag{27}$$

For the particular choice $f(x) = (x-1)/\log x$ one obtains the BKM metric $\mathbf{g}^f_{ij} = \mathbf{g}^{BKM}_{ij}$, namely

$$\mathbf{g}^{BKM}_{ij} = \int_0^1 dx\ \text{Tr}\left[\left(\frac{\partial \log \varrho_t}{\partial \lambda^i}\right) \varrho_t^x \left(\frac{\partial \log \varrho_t}{\partial \lambda^j}\right) \varrho_t^{1-x}\right]. \tag{28}$$

Restricting to the manifold of thermal states $\varrho_t = \pi_t$ we indeed recover the thermodynamic metric in (22). In general, any length of the form (27) is lower bounded by a geodesic path. Notably, analytical expressions for the shortest curves on the density operator manifold for each choice of metric are not known, aside from a couple of examples [64,65] excluding the BKM metric. However, for the BKM statistical length a lower bound is known (Corollary 5.1 of [66]) which depends only on the boundary conditions $\{\lambda^i_0\} \to \{\lambda^i_\tau\}$:

$$\ell^{BKM}(\gamma) \geq \mathcal{L}(\varrho_0, \varrho_\tau), \tag{29}$$

where

$$\mathcal{L}(\rho, \sigma) = 2 \arccos(\text{Tr}\left[\sqrt{\rho}\sqrt{\sigma}\right]), \tag{30}$$

is the quantum Hellinger angle. We stress that while this bound can always be saturated when the initial and final states commute, transitions between non-commuting states cannot typically saturate (29). Note that in the classical commutative regime, all monotone metrics (26) reduce to the classical Fisher–Rao metric, and a unique geodesic length is singled out by the Hellinger angle between

the initial and final probability distribution [65]. For a pair of discrete classical probability distributions p_n and q_n, the Hellinger angle is given by

$$\mathcal{L}(p,q) := 2\arccos\Big(\sum_n \sqrt{p_n\, q_n}\Big). \tag{31}$$

The geodesic bound (29) has an immediate consequence for thermodynamics. For step-equilibration processes, the work dissipation (22) is subsequently lower bounded via the Cauchy–Schwartz inequality (6) combined with (29):

$$w_{\text{diss}} \geq \frac{k_B T}{2N}\mathcal{L}^2(\pi_0, \pi_\tau). \tag{32}$$

One may interpret this as a geometric refinement to the second law of thermodynamics. Clearly, the bound depends only on the angle between the initial and final equilibrium state rather than the full path γ. For open systems undergoing Markovian dynamics, the corresponding dissipation (17) can be bounded in a similar fashion. Consider first the eigendecomposition of the Lindbladian (23) with associated relaxation timescales $\{\tau_\alpha\}$, which can be achieved for open systems satisfying detailed balance. Denoting τ_{min} as the shortest timescale along the curve γ and τ the total duration, work dissipation is bounded by

$$w_{\text{diss}} \geq k_B T\left(\frac{\tau_{\text{min}}}{\tau}\right)\mathcal{L}^2(\pi_0, \pi_\tau). \tag{33}$$

Note that, while (32) can always be saturated by following a geodesic, in general (33) is not tight whenever more than one relaxation timescale is present. The bounds (32) and (33) represent quantum generalisations of the so-called *Horse–Carrot* theorem in finite-time thermodynamics [6,7].

Considerations on Coherence Creation

Now we want to investigate the role of coherence in a a thermodynamic transformation whose dissipation can be described by Equation (17), see also Refs. [39,67]. We start by rewriting the expression for the dissipated work assuming full control on the system Hamiltonian

$$\dot{w}_{\text{diss}} = -\beta\,\text{Tr}\left[\dot{H}_t \mathscr{L}_t^+ \mathbb{J}_{\pi_t}\dot{H}_t\right] \equiv \langle \dot{H}_t, \dot{H}_t\rangle_t\,. \tag{34}$$

For notation simplicity we omit the explicit time dependence in this section. We split $\dot{H}$ in its diagonal and coherence parts, with respect the Hamiltonian basis of $\pi \propto e^{-\beta H}$, $|i\rangle$

$$\dot{H} = \dot{H}^{(d)} + \dot{H}^{(c)} \qquad \dot{H}^{(d)} = \sum_i |i\rangle\langle i|\,\dot{H}\,|i\rangle\langle i|\,. \tag{35}$$

Given that for any operator A we have $\text{Tr}\left[A^{(d)}A^{(c)}\right] = 0$, if we are able to prove that $\mathbb{J}_\pi$ and $\mathscr{L}^+$ do not mix the diagonal and coherent subspaces, then we would have

$$\langle \dot{H}, \dot{H}\rangle = \langle \dot{H}^{(d)}, \dot{H}^{(d)}\rangle + \langle \dot{H}^{(c)}, \dot{H}^{(c)}\rangle\,. \tag{36}$$

Now, this is always true for $\mathbb{J}_\pi$ as

$$\mathbb{J}_\pi[|i\rangle\langle j|] = \int_0^1 dx \pi^x\,|i\rangle\langle j|\,\pi^{1-x} \propto |i\rangle\langle j| \tag{37}$$

meaning that if $|i\rangle\langle j|$ is diagonal (i.e., $i = j$), it will stay diagonal, and vice versa (i.e., if $i \neq j$).

Is the same true for $\mathscr{L}^+$? This question can be answered affirmatively, by noting that $\mathscr{L}^+$ can be written as an exponentiation of $\mathscr{L}$ (cf. (17)), and that any $\mathscr{L}$ satisfying detailed balance does not mix

the diagonal and coherent subspaces [68]. More explicitly, standard Markovian thermal Lindbladians (satisfying detailed balance [68,69]) take the form $\mathscr{L}[\rho] = -i[H_{LS}, \rho] + \sum_\alpha \gamma_\alpha A_\alpha \rho A_\alpha^\dagger - \frac{1}{2}\{A_\alpha^\dagger A_\alpha, \rho\}$, the A_α being jump operators $A_\alpha = |i_\alpha\rangle\langle j_\alpha|$, and H_{LS} a general Lamb-Shift Hamiltonian $[H_{LS}, H] = 0$. This commutation property guarantees that the Hamiltonian term does not mix populations with coherences, while for the dissipative part we note

$$A_\alpha |i\rangle\langle j| A_\alpha^\dagger - \frac{1}{2}\{A_\alpha^\dagger A_\alpha, |i\rangle\langle j|\} = |i_\alpha\rangle\langle i_\alpha| \delta_{j_\alpha i}\delta_{j_\alpha j} - \frac{1}{2}|i\rangle\langle j| (\delta_{j_\alpha i} + \delta_{j_\alpha j}) . \tag{38}$$

From the expression above, it is easy to see that if $i = j$ the result will be diagonal as well, while if $i \neq j$ the result will be only made of coherences. Equation (36) is thus valid for standard Markovian master equations and

$$w_{\text{diss}} = w_{\text{diss}}^{(d)} + w_{\text{diss}}^{(c)} \tag{39}$$

where $w_{\text{diss}}^{(d)}$ is the term due to the modification of the spectrum of H, while $w_{\text{diss}}^{(c)}$ is due only to the rotation of the basis. Given that both $w_{\text{diss}}^{(d)}$ and $w_{\text{diss}}^{(c)}$ are positive, this property immediately implies that $w_{\text{diss}} \geq w_{\text{diss}}^{(d)}$, and hence we conclude that the creation of coherence is always detrimental when operating a thermal machine in the low-dissipation regime, as we explain more in detail in Section 4.2, and in agreement with recent results [42,67,70]. A similar separation of losses generated by diagonal and coherent parts of the Hamiltonian variation is presented in [32].

4. Optimisation of Thermodynamic Processes in the Slow Driving Regime

In this section, we derive and review generic considerations on the optimisation of finite-time thermal machines in the low-dissipation regime [6,14,31,46]. That is, when the irreversible entropy production is proportional to the inverse time duration. This assumption can be taken as empiric if no information on the system–bath interaction is given, or it can be justified and derived dynamically using the tools examined in Section 2. Part of the results are in agreement with previous literature and we aim here to collect them in a unified exposition that shows the generality and simplicity hidden in earlier works.

More precisely, we consider a thermal machine made up of a working substance (or machine) and several thermal baths at different temperatures. The level of control consists of n experimental parameters of the machine that can be driven (typically Hamiltonian parameters), together with the possibility to put the machine in contact with one of the thermal baths. The n control parameters are parametrised as $\vec{\lambda}(s) \equiv \vec{\lambda}_{s\tau}$ with $s \in (0, 1)$—note that this notation decouples the duration τ of each process from its shape $\vec{\lambda}(s)$. We assume in very general terms that the low-dissipation condition holds and it is described by an underlying thermodynamic metric, as presented in Section 2. That is, for an isothermal transformation at temperature $T = \beta^{-1}$, we rewrite Equation (4) as

$$\Delta Q = T\left(\Delta S - \frac{\sigma}{\tau}\right) \tag{40}$$

$$\sigma = \int_0^1 ds\, \vec{\lambda}'^T(s) g_{\vec{\lambda}} \vec{\lambda}'(s) \tag{41}$$

which follows from identifying $w_{\text{diss}} = w - \Delta F = T\Delta S - \Delta Q = T\sigma/\tau$ and by recalling $\vec{\lambda}(s) \equiv \vec{\lambda}_{s\tau}$, which has derivative $\vec{\lambda}' \equiv \frac{\partial}{\partial s}\vec{\lambda} = \tau\dot{\vec{\lambda}}$. Notice that in most of what follows, the exact form of $g_{\vec{\lambda}}$ does not significantly change the results. In this sense, most of the derivations are common to any system that has first-order losses described by some quadratic form, as in linear response theory.

We consider a machine performing M transformations close to equilibrium (in general with different baths), each described by some heat exchange and some dissipation in the low-dissipation regime, with an output

$$\Delta W_{out} = \sum_{i}^{M} \Delta Q_i = \sum_{i=1}^{M} T_i \Delta S_i - \frac{T_i \sigma_i}{\tau_i} \,. \tag{42}$$

The output being a sum of heat exchanges is guaranteed when considering cycling machines, or when the output of interest is the heat extraction from a subset of the sources. This framework thus includes a variety of tasks: cooling, work extraction, Landauer erasure, Carnot cycles, and generalised Carnot engines with multiple baths or finite size baths (see examples below). In any such a process, three main features can be optimised, corresponding to different levels of control over the machine:

1. **The speed of the trajectory**: that is, the duration τ, which characterises the average speed of the process, plus any rescaling of the instantaneous velocity along the trajectory. This can be formalised as a change of coordinates $\vec{\lambda}(s) \to \vec{\lambda}(\mathfrak{s}(s))$ with $\mathfrak{s}$ smooth monotonous and $\mathfrak{s}(0) = 0$, $\mathfrak{s}(1) = 1$.
2. **The path of the trajectory**: i.e., the (ordered) set of points swept by $\vec{\lambda}$, for fixed $\vec{\lambda}(0)$ and $\vec{\lambda}(1)$. This identifies a curve γ in $\mathbb{R}^n$.
3. **The extremal points** of γ, or the "location" of the process in the control space.

In the following, we elaborate on the above features and show how to optimise them, which can be done independently or sequentially. In particular, following the above order in Section 4.1 we optimize the time duration of each transformation τ_i and show a principle of constant dissipation rate optimality; in Section 4.2 we discuss consequences of the considerations presented in Section 3 when the experimental control is such to allow variations of the curve γ defined by $\vec{\lambda}(s)$; and in Section 4.3 we discuss the cases in which a full optimisation can be carried out, so that all the degrees of freedom listed above can be optimised.

4.1. Tuning the Speed: Optimality of Constant Dissipation Rate

Here, we suppose initially that the only control available on the machine (42) is the time tuning of each step τ_i. We wish to maximise the power output $P = \Delta W_{out} / \sum_j \tau_j$ for a given loss, or equivalently we fix the (maximum) amount of dissipated work,

$$\sum_i \frac{T_i \sigma_i}{\tau_i} \equiv w_{\text{diss}} \tag{43}$$

and maximize P. The power can be written as

$$P = \frac{(\sum_i T_i \Delta S_i) - w_{\text{diss}}}{\sum_j \tau_j} \,, \tag{44}$$

hence, maximising it is equivalent to minimising $\sum_j \tau_j$ with the constraint (43). This can be stated as

Principle 1. *Maximising the power at fixed dissipation is equivalent to minimising the dissipation at given duration.*

This remark is important as the main result of this subsection (the optimality of constant thermodynamic speed, or dissipation rate) will thus be valid for all machines performing tasks that are limited by the above trade-off. Examples are: maximising the power, minimising the dissipation (or entropy production) with fixed total time, or hybrid figures of merit combinations, such as maximising the power with a fixed amount of total loss. For a discussion of what machines maximise their outputs when the irreversible entropy production is minimised see [71].

The maximisation of (44) can be done differentiating w.r.t τ_i and using Lagrange multipliers, or directly with a Cauchy–Schwarz inequality

$$w_{\text{diss}} \sum_i \tau_i = \left(\sum_j \frac{T_j \sigma_j}{\tau_j} \right) \left(\sum_i \tau_i \right) \geq \left(\sum_j \sqrt{T_j \sigma_j} \right)^2 \tag{45}$$

which is saturated when all $T_j \sigma_j / \tau_j^2$ are equal, that is

$$\tau_j = \frac{\sqrt{T_j \sigma_j} (\sum_i \sqrt{T_i \sigma_i})}{w_{\text{diss}}} \tag{46}$$

$$P_{w_{\text{diss}}} = \frac{w_{\text{diss}} (\sum_i T_i \Delta S_i) - w_{\text{diss}}^2}{(\sum_j \sqrt{T_j \sigma_j})^2} \,. \tag{47}$$

Notice that the fact that $T_j \sigma_j / \tau_j^2$ is the same $\forall j$ means that the rate of dissipation is constant for each of the N steps of the protocol. In particular, when the dissipation is described by an underlying thermodynamic metric (41), this implies the optimality of constant thermodynamic velocity $T \vec{\lambda}'^T g_{\vec{\lambda}} \vec{\lambda}' = const.$, which can be seen by dividing each transformation into infinitesimal steps, i.e., expressing

$$T_i \Delta S_i - \frac{T_i \sigma_i}{\tau_i} = \int_{\gamma^{(i)}} T dS - \frac{T d\vec{\lambda}^T g_{\vec{\lambda}} d\vec{\lambda}}{d\tau} \tag{48}$$

and applying the above reasoning, which concludes that each of the infinitesimal $\frac{T d\vec{\lambda}^T g_{\vec{\lambda}} d\vec{\lambda}}{d\tau^2}$ must be equal. The "thermodynamic length inequality" inequality (6) ([6,72]) is indeed saturated when its integrand is constant, and coincides with the continuous version of (45). These considerations can be summed up saying that for the class of machines considered here

Principle 2. *In optimal protocols, the speed of the control variation is constant (as measured from the underlying thermodynamic metric), leading to a constant entropy production rate.*

The optimality of constant entropy production rate was noted already in the first seminal papers [73] in the context of endoreversible engines, and appeared in many works thereafter (for an historical perspective, see also [74,75]). The above formulation manifests the universality of this principle whenever a trade-off between output rate and losses is present in the regime where losses are linear in the average speed of the process.

The power (46) can be further maximised choosing $w_{\text{diss}} = \frac{1}{2} \sum_i T_i \Delta S_i$ to obtain the durations leading to the maximum power, in this case

$$P_{\max} = \frac{(\sum_i T_i \Delta S_i)^2}{4 (\sum_j \sqrt{\sigma_j})^2} \,. \tag{49}$$

At maximum power the losses thus correspond to half of the quasistatic output: this corresponds to the "7th principle of control thermodynamics" pointed out by Salamon et al. in [74], whose general validity was unknown: we can state it holds (at least) for all machines described by (42).

We give here an example of application of the time tuning optimisation just described.

Multi-Bath Carnot Engine

A generalised Carnot engine consists of a sequence of isotherms in contact with different thermal baths, alternated with adiabats as in the standard Carnot cycle. The total work output can be expressed as the sum of the heat exchanges due to cycling conditions, as in Equation (42), with $\sum_i \Delta S_i = 0$. All the

results described above apply and the maximum power obtainable by tuning the time durations of the isotherms is thus as in Equation (49). Moreover, in Appendix A we further analyze this result assuming that all the baths have the same spectral density $\propto \omega^{\alpha}$, described by the ohmicity α. Under this hypothesis and the assumption that all the isotherms are small enough (see details in Appendix A), we show how this can be translated in the maximum power being expressed by

$$P_{\max}^{\text{multi}-\text{Carnot}} = \frac{(\sum_i T_i dS_i)^2}{4\kappa_0 T_0 \left(\sum_i (\frac{T_i}{T_0})^{\frac{1-\alpha}{2}} |dS_i|\right)^2} \tag{50}$$

where κ_0 represents the local ratio between σ_0 and $(\Delta S_0)^2$ at some reference temperature T_0, and satisfies $\kappa_i/\kappa_j = (T_i/T_j)^{-\alpha}$. In the Appendix A, we show how in this case, the power is upper bounded by the same power when it is obtained by the use of the highest and lowest temperature only, which leads to the maximum power of a standard Carnot Engine (cf. Section 4.3 or [31])

$$P_{\max}^{\text{multi}-\text{Carnot}} \leq P_{\max}^{\text{Carnot}} = \frac{(\Delta S)^2}{\sigma_h} \frac{(T_h - T_c)^2}{4T_h \left(1 + (\frac{T_c}{T_h})^{\frac{1-\alpha}{2}}\right)^2} . \tag{51}$$

4.2. Path Optimisation: Geodesics and Coherences

When the control over the working fluid allows not only to vary the speed of the transformation, but includes possible modifications of the path γ of the trajectory $\vec{\lambda}(s)$, the machine can be substantially improved. The optimisation over γ is independent from the time tuning considered in the previous section. It consists of finding the shortest path $\sigma = \int_\gamma \vec{\lambda}'^T g_{\vec{\lambda}} \vec{\lambda}'$ between two fixed points for each isotherm (41) considered in the cycle. Indeed, when the extremal points of a trajectory are fixed, the quasistatic output is fixed and minimizing σ always improves both power and the efficiency.

More precisely, with the tools described in Section 2, each of the σ_i in Equation (42) will be described as in (5) by some metric $g^{(i)}$ and some trajectory $\vec{\lambda}_{(i)}$, in the form $\sigma_i = \int_{\gamma^{(i)}} \vec{\lambda}'^T_{(i)} g^{(i)}_{\vec{\lambda}} \vec{\lambda}'_{(i)}$. As mentioned earlier (see Section 2 or Section 4.1), by choosing the speed to be constant the above expression can be minimised to the thermodynamic length of the path $\gamma^{(i)}$

$$\sigma_i = \left(\int_{\gamma^{(i)}} ds \sqrt{\vec{\lambda}'^T_{(i)} g^{(i)}_{\vec{\lambda}} \vec{\lambda}'_{(i)}} \right)^2 \equiv l^2_{\gamma^{(i)}} . \tag{52}$$

This quantity depends only on the path $\gamma^{(i)}$ of the trajectory and not on its parametrisation $\vec{\lambda}(s)$, but it can be further minimised by considering its minimum among all the possible paths linking the extremal points, which then defines the geodesics distance between the extremal points

$$d_{\vec{\lambda}(0),\vec{\lambda}(1)} = \min_{\substack{\gamma \text{ with extremals} \\ \{\vec{\lambda}(0),\vec{\lambda}(1)\}}} l_\gamma \tag{53}$$

These considerations can be stated as follows:

Principle 3. *In optimal protocols, the driving minimises the entropy production, i.e., it follows a geodesic on the thermodynamic manifold.*

In the quantum case, as showed in Section 3, the irreversible entropy production can be split in two independent parts, one due to the variation of the spectrum $\dot{H}_t^{(d)}$ and one due to the rotation of the eigenvectors $\dot{H}_t^{(c)}$ of the Hamiltonian, i.e., $\dot{H}_t = \dot{H}_t^{(d)} + \dot{H}_t^{(c)}$ and

$$w_{\text{diss}} = w_{\text{diss}}^{(d)} + w_{\text{diss}}^{(c)} , \tag{54}$$

where $w^{(X)}_{\rm diss} = -\beta \int dt \ {\rm Tr}\left[\dot{H}^{(X)}_t \mathscr{L}^{+}_t \mathbb{J}_{\pi_t} \dot{H}^{(X)}_t\right]$, with $X = d, c$. Now, notice that the quasistatic (lossless) output of a thermal machine is given by the integral of the heat exchange, or the work exchange, computed on the equilibrium state π_t, for example

$$w_{\rm eq} = \int dt \ {\rm Tr}\left[\pi_t \dot{H}_t\right] = \int dt \ {\rm Tr}\left[\pi_t \dot{H}^{(d)}_t\right] \ , \tag{55}$$

which shows how the work exchange only depends on the diagonal variation of H, that is the spectrum variation. This easily follows from the fact that for thermal states at temperature T one has $\Delta U = w + \Delta Q = w + T\Delta S$, where all the quantities depend uniquely on the spectrum of the final and initial control H_0, H_τ (which define as well the spectrum of π_0, π_τ). This means that given the most general control $H_t = U_t H^{(d)}_t U^{\dagger}_t$, where $H^{(d)}_t$ is diagonal in a time-independent basis, all the lossless heat and work exchanges are the same for the protocol in which only the spectrum is varied, $H^{(d)}_t$. At the same time given $w^{(c)}_{\rm diss} \geq 0$, losses are clearly reduced using $H^{(d)}_t$. From this we learn that, for standard Markovian dissipators,

Principle 4. *Quantum coherences are not created in optimal protocols, i.e., non-commutativity* $[H_t, H_{t'}] \neq 0$ *is avoided.*

The effect of coherences inducing losses in the power was noted already in [67] in the context of linear response theory of slowly driven engines with slowly driven temperature, and more recently in [42]. A different approach to quantum dynamics, namely quantum jump trajectories, shows again the detrimental effects of coherence creation [70]. Moreover, notice that if the degree of control on the thermal machine allows to eliminate any coherence creation, using commutative controls all the metrics defined in Equation (26) collapse into the classical one and the geodesics distance between states is given by (31), and the bound (33) can be saturated.

We show here an example of application for a cooling process.

Cooling/Work Extraction

Suppose we are interested only in a subset of the heat currents that are part protocol, meaning that relevant output is the heat extracted from one (or multiple) thermal sources, as in a generalised refrigerator model. To fix the ideas for a single bath to be cooled the cooling rate is

$$P^{\rm cooling} = \frac{T_c \Delta S_c - \frac{T_c \sigma_c}{\tau_c}}{\tau_{ex} + \tau_c} \equiv \frac{T_c \Delta S_c - w_{\rm diss}}{\tau_{ex} + \tau_c} \tag{56}$$

where now τ_{ex} is additional time spent on parts of the cycle that do not contribute to the cooling output. The optimisation for fixed loss $w_{\rm diss}$ applies as from (46) leading to $\tau_c = T_c \sigma_c / w_{\rm diss}$, and a power

$$P^{\rm cooling}_{w_{\rm diss}} = \frac{T_c \Delta S_c - w_{\rm diss}}{\tau_{ex} + T_c \sigma_c w^{-1}_{\rm diss}} \ , \tag{57}$$

which clearly increases as σ_c is minimised. The overall maximum of the cooling rate becomes for a suitable choice of $w_{\rm diss}$

$$P^{\rm cooling}_{\rm max} = T_c \sigma_c \frac{\left(\sqrt{\Delta S_c \tau_{ex}/\sigma_c + 1} - 1\right)^2}{\tau^2_{ex}} = T_c \frac{\Delta S^2_c}{4\sigma_c} - T_c \frac{\Delta S^3_c}{8\sigma^2_c} \tau_{ex} + \mathcal{O}(\tau^2_{ex}) \ . \tag{58}$$

The above expressions are all decreasing in the value of σ_c, which is minimal when obtained on the geodesics of the transformation, as from Equations (52) and (53). For example, let us assume that the cooling consists of a single transformation from π_x to π_y, with no additional time $\tau_{ex} = 0$, and full control on the Hamiltonian defining $\pi_{x,y} = e^{-H_{x,y}/T_c} / {\rm Tr}\left[e^{-H_{x,y}/T_c}\right]$.

Then, the maximum cooling power is obtained for a coherence-free protocol $[H_x, H_y] = 0$ that leads to $\sigma_{\min} = 2\tau_{\rm eq} \arccos(\mathrm{Tr}\left[\sqrt{\pi_x}\sqrt{\pi_y}\right])$ from (30), whereas the maximum cooling rate is obtained by substituting it into (58). If the control does not allow for coherence-less transformations, or the Lindbladian has several time-scales, upper bounds on the cooling rate can be obtained by the use of (33).

4.3. Choosing the Location: Total Optimisation

After optimizing the time duration and trajectory of the transformations, the resulting optimal output rates only depend on the end points of the transformations. The final maximisation of such expressions is in general non-trivial. However, we note how the maximum power obtained in (51) is proportional $(\Delta S)^2/\sigma$, which is maximal when σ takes the geodesics value described above (53). Thus, this last quantity

$$\frac{(\Delta S)^2}{\sigma} = \frac{\left(S_{\vec{\lambda}(0)} - S_{\vec{\lambda}(1)}\right)^2}{d^2_{\vec{\lambda}(0),\vec{\lambda}(1)}} \tag{59}$$

can be maximised by changing the extremal of the transformation. The same quantity appears as the leading term for the cooling rate in (58). We find this to be a strikingly general feature of all thermal machines whose dynamical information ultimately consists of just one simple isothermal transformation close to equilibrium. This is clearly the case for a single heat extraction from a bath as in (58), but it happens also, e.g., for Carnot engines, which, due to the trivial dynamics at the quenches, have all relevant quantities which can be expressed solely in terms of the two isotherms. For example, power and efficiency of a Carnot engine read:

$$P^{\rm Carnot} = \frac{\Delta S(T_h - T_c) - \left(\frac{T_c\sigma_c}{\tau_c} + \frac{T_h\sigma_h}{\tau_h}\right)}{\tau_c + \tau_h}, \qquad \eta = \frac{Q_h + Q_c}{Q_h} = 1 - \frac{T_c(\Delta S + \frac{\sigma_c}{\tau_c})}{T_h(\Delta S - \frac{\sigma_h}{\tau_h})}, \tag{60}$$

where ΔS is the variation of entropy during the hot isotherm, and the irreversible entropy productions are proportional to each other on optimal protocols $\sigma_h/\sigma_c = (T_c/T_h)^{-\alpha}$, according to the spectral density of the baths [31,55] (cf. Appendix A). The two isotherms are thus *symmetric*, in the sense that by construction they have an opposite entropy variation $\Delta S_h = -\Delta S_c$, and the trajectories follow the same geodesics to link the endpoints [31,55]. After time optimisation on τ_c, τ_h in such a case it is clear from dimensional analysis that the resulting power can only be proportional to $(\Delta S)^2/\sigma_h$ (or equivalently $(\Delta S)^2/\sigma_c$ due to proportionality) multiplied by a function with the dimension of temperature.

In more detail, it has been shown recently [31] that is possible to express the maximum power at any given efficiency $\eta = (1-\delta)\eta_C = (1-\delta)(1 - T_c/T_h)$ for a Carnot engine (see also [51,52]). We report here for simplicity only on the case where $\alpha = 0$, thus $\sigma_c = \sigma_h = \sigma$, as

$$P^{\rm Carnot}_{\delta} = \frac{(\Delta S)^2}{4\sigma}\frac{(T_h - T_c)^2\delta(1-\delta)}{(1-\delta)T_c + \delta T_h} \tag{61}$$

The importance of the term $(\Delta S)^2/\sigma$ was noted already in [49] as a natural unit of entropy over time, defining the performance of thermal machines in the low-dissipation regime for any trade-off between power and efficiency. The equivalent optimisation for a refrigerator has been conducted in [76], where one has a cooling power and COP coefficient (this time ΔS is defined to be positive on the cold isotherm)

$$P^{\rm Refrigerator} = \frac{\Delta S T_c - \frac{T_c\sigma_c}{\tau_c}}{\tau_c + \tau_h}, \qquad \varepsilon = \frac{Q_c}{|Q_h| - Q_c} = \frac{T_c\left(\Delta S - \frac{\sigma_c}{\tau_c}\right)}{T_h\left(\Delta S + \frac{\sigma_h}{\tau_h}\right) - T_c\left(\Delta S - \frac{\sigma_c}{\tau_c}\right)}, \tag{62}$$

which leads to a maximum cooling power at given COP (again we report it for flat spectral density $\sigma_c = \sigma_h$, see [76] for generalisations) $\varepsilon = (1-\delta)\varepsilon_C = (1-\delta)T_c/(T_h - T_c)$

$$P_\delta^{\text{Refrigerator}} = \frac{(\Delta S)^2}{4\sigma}\frac{T_c(T_h - T_c)\delta}{T_h - \delta T_c}\,. \tag{63}$$

Crucially, the maximisation of the $(\Delta S)^2/\sigma$ term can always be obtained by the use of a Cauchy–Schwarz inequality [31], that is noticing that

$$\frac{(\int dS)^2}{\int ds\vec{\lambda}'^T g_{\vec{\lambda}}\vec{\lambda}'} = \frac{\left(\int ds\,\vec{\partial}S_{\vec{\lambda}}\cdot\vec{\lambda}'\right)^2}{\int ds\vec{\lambda}'^T g_{\vec{\lambda}}\vec{\lambda}'} \leq \int ds\,\vec{\partial}S_{\vec{\lambda}}^T g_{\vec{\lambda}}^{-1}\vec{\partial}S_{\vec{\lambda}} \leq \max_{\vec{\lambda}}\,\vec{\partial}S_{\vec{\lambda}}^T g_{\vec{\lambda}}^{-1}\vec{\partial}S_{\vec{\lambda}} \equiv \max_{\vec{\lambda}}\,C(\vec{\lambda}) \tag{64}$$

The upper bound in (64) can be saturated by performing an infinitesimal cycles around the point where $C(\vec{\lambda})$ is maximised. In the meaningful case in which the observables X_i decay with a well defined timescale τ_{eq}, the dissipation is described by the Kubo-Mori metric (see Section 3), and $C(\vec{\lambda})$ is exactly the heat capacity of the system divided by the equilibration time, leading to [31]:

$$\frac{(\Delta S)^2}{\sigma} \leq \max_G \frac{\mathcal{C}(G)}{\tau_{\text{eq}}}. \tag{65}$$

Here, $G = \beta H$ is the adimensional Hamiltonian, and the thermal state and the heat capacity can be expressed as $\pi = e^{-G}/\text{Tr}\left[e^{-G}\right]$ and $\mathcal{C}(G) = \text{Tr}\left[G^2\pi\right] - \text{Tr}\left[G\pi\right]^2$. In other words,

Principle 5. *In order to optimise the power-efficiency trade-off, perform the finite-time Carnot cycle around the point where the ratio between heat capacity and relaxation time of the working medium is maximised.*

This general principle is illustrated in the next section for a two-level Carnot engine.

5. Case Study: Finite-Time Qubit Carnot Engine

In what follows, we analyse the exactly solvable case of a heat engine where the engine consists of a driven two-level system:

$$H(t) = E(t)\sigma_z. \tag{66}$$

We consider a finite-time Carnot cycle where the working substance is sequentially connected with two thermal baths at different temperatures (see details of the cycle in [31]), and focus on the low-dissipation regime where the results of Section 4 naturally apply. We model the relaxation with any of the two baths by an exponential decay to equilibrium with timescale τ_{eq}, $\text{Tr}\left[H\dot{\rho}\right] = \tau_{\text{eq}}^{-1}\text{Tr}\left[H(\pi-\rho)\right]$, which corresponds to the so-called reset master equation. In this case, the thermodynamic metric is given by the KMB metric.

Let us define $g \equiv \beta E$ (with β being the inverse temperature of the bath the working substance is connected to), and let g_x and g_y be the two endpoints of the isotherms, with $g_x > g_y$. Let us also introduce the corresponding probabilities of the excited state:

$$\begin{aligned} p_x &= \frac{e^{-g_x}}{1+e^{-g_x}}, \\ p_y &= \frac{e^{-g_y}}{1+e^{-g_y}}, \end{aligned} \tag{67}$$

with $p_x < p_y$. Then, we easily obtain:

$$\Delta S = -p_y \ln p_y - (1-p_y)\ln(1-p_y) + p_x \ln p_x + (1-p_x)\ln(1-p_x). \tag{68}$$

On the other hand, we can use (33) to lower bound the entropy production in the isothermal processes as:

$$\sigma \geq \tau_{\rm eq} \left(2 \arccos\left[\sqrt{p_x p_y} + \sqrt{(1-p_x)(1-p_y)}\right]\right)^2 . \tag{69}$$

This bound can be saturated by following a geodesic, i.e., a protocol satisfying (7). Putting everything together, we can upper bound the relevant figure of merit $(\Delta S)^2/\sigma$ for the power-efficiency optimisation as:

$$\frac{(\Delta S)^2}{\sigma} \leq \frac{(-p_y \ln p_y - (1-p_y)\ln(1-p_y) + p_x \ln p_x + (1-p_x)\ln(1-p_x))^2}{\tau_{\rm eq}\left(2 \arccos\left[\sqrt{p_x p_y} + \sqrt{(1-p_x)(1-p_y)}\right]\right)^2} . \tag{70}$$

Importantly, this expression is protocol-independent and can be saturated. Indeed, the maximal power of a finite-time Carnot engine (for a given efficiency $\eta = (1-\delta)\eta_C$) given a two-level system can then be written as (see (61)):

$$\max_\gamma P_\delta^{\rm Carnot} = \frac{1}{4} \frac{(-p_y \ln p_y - (1-p_y)\ln(1-p_y) + p_x \ln p_x + (1-p_x)\ln(1-p_x))^2}{\tau_{\rm eq}\left(2 \arccos\left[\sqrt{p_x p_y} + \sqrt{(1-p_x)(1-p_y)}\right]\right)^2} \frac{(T_h - T_c)^2 \delta (1-\delta)}{(1-\delta)T_c + \delta T_h}, \tag{71}$$

where the maximisation is meant over all possible protocols in the slow driving regime. We show the upper bound (70) as a function of g_x in Figure 1 for various values of g_y, including the optimal one, $g_y \approx 2.4$. It can be seen that the maximum of $(\Delta S)^2/\sigma$ over $\{g_x, g_y\}$ is bounded by the maximum of $\mathcal{C}/\tau_{\rm eq}$, where $\mathcal{C}$ is the heat capacity,

$$\mathcal{C} = g^2 p(1-p), \tag{72}$$

where p is the excited state probability $p = e^{-g}/(1+e^{-g})$. This is in full agreement with (65) and [77], and is a particular illustration that the power of finite-time Carnot engines at any efficiency can be bounded by substituting the maximum value of $\mathcal{C}/\tau_{\rm eq}$ to $(\Delta S)^2/\sigma$ inside expression (61), as discussed in detail in Ref. [31].

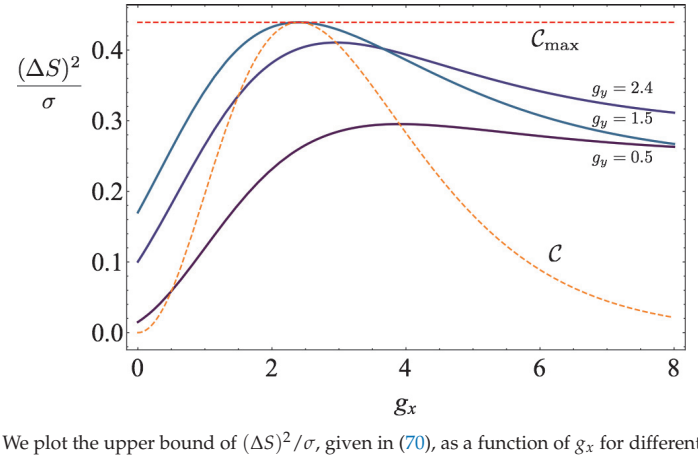

Figure 1. We plot the upper bound of $(\Delta S)^2/\sigma$, given in (70), as a function of g_x for different values of $g_y = \{0.5, 1.5, 2.4\}$. The point where $g_x = g_y \approx 2.4$ is the point where $(\Delta S)^2/\sigma$ is maximised (this can be easily checked numerically), which is also the point of maximum heat capacity C. The heat capacity and its maximum are also plotted in dashed lines. We take $\tau_{\rm eq} = 1$.

Summarising, here we have provided a tight upper bound on the relevant figure of merit $(\Delta S)^2/\sigma$ for power (and efficiency) of a finite-time Carnot engine, for the particular case of a two-level driven system. We note that such optimisation for a low-dissipation Carnot cycle or an Otto cycle has been performed in [77], while exact total optimisation for a two-level system performing an arbitrary cycle was solved in Refs. [78,79], with both bosonic and fermionic baths. While our results apply in the high efficiency or low-dissipation regime, their strength lies in its simplicity: indeed, Equation (70) can be easily computed for larger working substances, and extensions to more complex relaxation processes with multiple timescales can also be relatively straightforwardly built (see Equation (64) and Ref. [31]). This contrasts with exact results in finite-time thermodynamics [78,80], which rely on non-trivial optimisation procedures that can become quickly unfeasible as the size of the working substance increases.

6. Conclusions and Outlook

While originally developed for macroscopic systems, the geometric approach to finite-time thermodynamics is now finding renewed applications within the emerging fields of stochastic and quantum thermodynamics. In this paper, we have highlighted its utility for minimising dissipation in small scale systems operating close to equilibrium. We have derived lower bounds on thermodynamic length that provide a geometric refinement to the second law of thermodynamics and allow one to benchmark the attainable efficiency of quantum thermal machines. Alongside this, we summarised a set of key principles needed to optimise finite-time quantum low-dissipation engines in terms of efficiency and power, based on the computation of the thermodynamic metric tensor and length. Taken together, these principles provide a straightforward method for determining optimal thermodynamic processes. Indeed, we have seen that optimality is achieved by ensuring that the cycle follows a geodesic in the parameter space at constant velocity, while minimising the generation of quantum coherence and maximising the heat capacity relative to the relaxation time of the working system.

Interesting future directions for thermodynamic geometry in the quantum regime include the extension beyond the slow driving regime [81], the minimisation and characterisation of work and heat fluctuations [38–40,82], connections with strong coupling and speed-ups to isothermality [83], application to cooling processes and relations with the third law of thermodynamics [84–86], many-body systems and criticality [22,23,37].

Author Contributions: Conceptualization, P.A.; H.J.D.M.; M.P.-L. and M.S.; Investigation, P. A.; H.J.D.M.; M.P.-L. and M.S.; Writing—original draft, P.A.; H.J.D.M.; M.P.-L. and M.S.; Writing—review & editing, P.A.; H.J.D.M.; M.P.-L. and M.S. All authors have read and agreed to the published version of the manuscript.

Funding: P.A. is supported by "la Caixa" Foundation (ID 100010434, fellowship code LCF/BQ/DI19/11730023). M.P.-L. acknowledges funding from Swiss National Science Foundation (Ambizione PZ00P2-186067). H.J.D.M. acknowledges support from the EPSRC through a Doctoral Prize. M.S. acknowledges funding from the European Union's Horizon 2020 research and innovation programme under the Marie Sklodowska-Curie grant agreement No 713729. Both P.A. and M.S. also acknowledge funding from Spanish MINECO (QIBEQI FIS2016-80773-P, Severo Ochoa SEV-2015-0522), Fundacio Cellex, Generalitat de Catalunya (SGR 1381 and CERCA Programme).

Conflicts of Interest: The authors declare no conflict of interest.

Appendix A. Optimality of Lowest-Highest Temperature Use in Multi-Bath Carnot Engines

A generalised, finite-time Carnot engine between multiple thermal sources can be described as in Equation (42) (where the adiabatic steps between the isotherms are assumed to happen on a much shorter timescale and thus neglected when compared to the τ_is),

$$\Delta W_{out} = \sum_{i}^{N} \Delta Q_i = \sum_{i=1}^{N} T_i \Delta S_i - \frac{T_i \sigma_i}{\tau_i} \,, \tag{A1}$$

with $\Delta W \geq 0$ and where the index i runs over multiple thermal baths, possibly with infinitesimal steps, including as a possibility the case in which the reservoirs have finite size and change temperature

during the process (notice that in the case of finite size baths the total dissipation $\sum_i \frac{T_i \sigma_i}{\tau_i}$ is the natural measure of efficiency, as the total work extractable from the machine sources is finite and obtainable in the quasistatic regime). All the results of Section 4.1 apply, and the maximum power obtainable after tuning the τ_is can be written

$$P_{\max} = \frac{(\sum_i T_i dS_i)^2}{4(\sum_j \sqrt{T_j \sigma_j})^2}. \tag{A2}$$

To analyze further this result, we consider here the following property that holds for simple models where all the baths have the same spectral density

$$\sigma_i = \kappa_0 \left(\frac{T_i}{T_0}\right)^{-\alpha} dS_i^2 \tag{A3}$$

where α represents the spectral density exponent of the baths (their ohmicity), T_0 is a reference temperature that can be chosen at will, and κ_0 a constant that depends on the local thermal state. This property holds if the steps of the transformation are performed "parallel" to each other and are small enough for the state to be almost always the same. More precisely, baths with the same spectral density satisfy the property

$$g^{(T_1)}_{H_1} = \left(\frac{T_1}{T_2}\right)^{-\alpha} g^{(T_2)}_{H_2} \quad \text{when} \quad \frac{H_1}{T_1} = \frac{H_2}{T_2}\,. \tag{A4}$$

Here, g is the metric that defines the dissipation in terms of the variation of $dG \equiv dH/T$ (cf. Equation (17)), and the property $H_1/T_1 = H_2/T_2$ means that the thermal state is the same $\pi_1 = \pi_2$. The absolute value of the variation of entropy is instead the same if $dG_1 = \pm dG_2$, as in such a case

$$|dS_1| = |\mathrm{Tr}\,[d\pi_1 G_1]\,| = |\mathrm{Tr}\,[d\pi_2 G_2]\,| = |dS_2|\,. \tag{A5}$$

Combining the above two equations, we obtain (A3). For more details see [55] or the supplementary material of [31]. For such a case we obtain substituting (A3)

$$\bar{P} = \frac{(\sum_i T_i dS_i)^2}{4\kappa_0 T_0 \left(\sum_i (\frac{T_i}{T_0})^{\frac{1-\alpha}{2}} |dS_i|\right)^2}\,. \tag{A6}$$

Moreover, for a cycle we have $\sum_i dS_i = 0$ and we can divide the N steps into those having $dS_{k^+} > 0$ (which we will indicate with the index k^+ and those having $dS_{k^-} < 0$ (with index k^-). We have thus $\sum_{k^+} dS_{k^+} = -\sum_{k^-} dS_{k^-} \equiv \mathcal{S}$. The power (A12) can then be expressed in terms of the "weights" associated to each step for the positive and negative entropy variations. That is, we define

$$p_{k^+} = \frac{dS_{k^+}}{\mathcal{S}} \qquad p_{k^-} = -\frac{dS_{k^-}}{\mathcal{S}} \tag{A7}$$

The vectors p_{k^+} and p_{k^-} are normalised probability vectors and the power (A12) can be written as

$$4\kappa_0 T_0 \bar{P} = \frac{(\sum_{k^+} T_{k^+} p_{k^+} - \sum_{k^-} T_{k^-} p_{k^-})^2}{\left(\sum_{k^+} (\frac{T_{k^+}}{T_0})^{\frac{1-\alpha}{2}} p_{k^+} + \sum_{k^-} (\frac{T_{k^-}}{T_0})^{\frac{1-\alpha}{2}} p_{k^-}\right)^2} = \left(\frac{\vec{T}_+ \cdot \vec{p}_+ - \vec{T}_- \cdot \vec{p}_-}{\vec{T}'_+ \cdot \vec{p}_+ + \vec{T}'_- \cdot \vec{p}_-}\right)^2 \tag{A8}$$

where we defined 4 positive vectors $\vec{T}_+, \vec{T}_-, \vec{T}'_+, \vec{T}'_- > 0$. Being allowed to modify separately we positive and negative weight (essentially by tuning the size of the entropy variations (A7)) it is possible

to maximize the above quantity by noting that for any probability vector $\vec{p}$, positive vectors $\vec{B} > 0$, vector $\vec{C}$, positive constant $b > 0$, and constant c, it holds

$$\frac{c + \vec{C} \cdot \vec{p}}{b + \vec{B} \cdot \vec{p}} \leq \max_i \frac{c + C_i}{b + B_i} \tag{A9}$$

which is saturated by choosing $p_i = \delta_{i\bar{i}}$, where $\bar{i}$ is the index saturating the maximum of (A9). Applying twice the above inequality to $\sqrt{4\kappa_0 T_0 \bar{P}}$ of Equation (A8) we obtain

$$\sqrt{4\kappa_0 T_0 \bar{P}} \leq \max_{ij} \frac{T_{+i} - T_{-j}}{T'_{+i} + T'_{-j}} \,. \tag{A10}$$

Given that $T'_{\pm i} = T_{\pm i}^{\frac{1-\alpha}{2}}$, we study the function

$$f(x, y) = \frac{x - y}{x^\beta + y^\beta} \qquad x \geq y \geq 0 \tag{A11}$$

and find that it is always decreasing in y. Also, it increases always in x provided that $\beta \leq 1$. We thus conclude that for $\alpha \geq -1$ the maximisation on the right-hand side of (A10) is obtained by using the highest and lowest temperature available, that we will call T_h and T_c respectively. We thus find that

$$\bar{P} \leq \frac{(T_h - T_c)^2}{4\kappa_0 T_0 \left(\left(\frac{T_h}{T_0}\right)^{\frac{1-\alpha}{2}} + \left(\frac{T_c}{T_0}\right)^{\frac{1-\alpha}{2}} \right)^2} \tag{A12}$$

which is saturated when $dS_c = -dS_h$ and all the rest are null. This shows that under the assumption of equal spectral density the power is bounded by the power obtainable by using only the extremal baths.

References

1. Landau, L.D.; Lifshitz, E.M. *Statistical Physics*; Elsevier Science: Amsterdam, The Netherlands, 1980.
2. Jarzynski, C. Equalities and Inequalities: Irreversibility and the Second Law of Thermodynamics at the Nanoscale. *Annu. Rev. Condens. Matter Phys.* **2011**, *2*, 329–351. [CrossRef]
3. Weinhold, F. Metric geometry of equilibrium thermodynamics. *J. Chem. Phys.* **1975**, *63*, 2479. [CrossRef]
4. Weinhold, F. Metric Geometry of Equilibrium Thermodynamics. III. Elementary Formal Structure of a Vector-algebraic Representation of Equilibrium Thermodynamics. *J. Chem. Phys.* **1975**, *63*, 2488–2495. [CrossRef]
5. Salamon, P.; Andresen, B.; Gait, P.D.; Berry, R.S. The significance of Weinhold's length. *J. Chem. Phys.* **1980**, *73*, 1001–1002. [CrossRef]
6. Salamon, P.; Berry, R.S. Thermodynamic length and dissipated availability. *Phys. Rev. Lett.* **1983**, *51*, 1127–1130. [CrossRef]
7. Nulton, J.; Salamon, P.; Andresen, B.; Anmin, Q. Quasistatic processes as step equilibrations. *J. Chem. Phys.* **1985**, *83*, 334–338. [CrossRef]
8. Schlögl, F. Thermodynamic metric and stochastic measures. *Zeitschrift für Physik B Condensed Matter* **1985**, *59*, 449–454. [CrossRef]
9. Andresen, B.; Berry, R.S.; Gilmore, R.; Ihrig, E.; Salamon, P. Thermodynamic geometry and the metrics of Weinhold and Gilmore. *Phys. Rev. A* **1988**, *37*, 845–848. [CrossRef]
10. Ruppeiner, G. Riemannian geometry in thermodynamic fluctuation theory. *Rev. Mod. Phys.* **1995**, *67*, 605–659. [CrossRef]
11. Hoffmann, K.H.; Andresen, B.; Salamon, P. Measures of dissipation. *Phys. Rev. A* **1989**, *39*, 3618–3621. [CrossRef]
12. Diosi, L.; Kulacsy, K.; Lukacs, B.; Racz, A. Thermodynamic length, time, speed, and optimum path to minimize entropy production. *J. Chem. Phys.* **1996**, *105*, 11220–11225. [CrossRef]

13. Andresen, B. Finite-time thermodynamics and thermodynamic length. *Revue Générale Thermique* **1996**, *35*, 647–650. [CrossRef]
14. Sekimoto, K.; Sasa, S.I. Complementarity relation for irreversible process derived from stochastic energetics. *J. Phys. Soc. Jpn.* **1997**, *66*, 3326–3328. [CrossRef]
15. Crooks, G.E. Measuring thermodynamic length. *Phys. Rev. Lett.* **2007**, *99*, 100602. [CrossRef]
16. Zulkowski, P.R.; Sivak, D.A.; Crooks, G.E.; DeWeese, M.R. Geometry of thermodynamic control. *Phys. Rev. E* **2012**, *86*, 041148. [CrossRef] [PubMed]
17. Sivak, D.A.; Crooks, G.E. Thermodynamic metrics and optimal paths. *Phys. Rev. L* **2012**, *108*, 190602. [CrossRef]
18. Sivak, D.A.; Crooks, G.E. Thermodynamic geometry of minimum-dissipation driven barrier crossing. *Phys. Rev. E* **2016**, *94*, 052106. [CrossRef]
19. Zulkowski, P.R.; DeWeese, M.R. Optimal control of overdamped systems. *Phys. Rev. E* **2015**, *92*, 032117. [CrossRef]
20. Zulkowski, P.R.; Sivak, D.A.; DeWeese, M.R. Optimal Control of Transitions between Nonequilibrium Steady States. *PLoS ONE* **2013**, *8*, e82754. [CrossRef] [PubMed]
21. Mandal, D.; Jarzynski, C. Analysis of slow transitions between nonequilibrium steady states. *J. Stat. Mech.* **2016**, *2016*, 063204. [CrossRef]
22. Rotskoff, G.M.; Crooks, G.E. Optimal control in nonequilibrium systems: Dynamic Riemannian geometry of the Ising model. *Phys. Rev. E* **2015**, *92*, 060102. [CrossRef]
23. Rotskoff, G.M.; Crooks, G.E.; Vanden-Eijnden, E. Geometric approach to optimal nonequilibrium control: Minimizing dissipation in nanomagnetic spin systems. *Phys. Rev. E* **2017**, *95*, 012148. [CrossRef] [PubMed]
24. Deffner, S.; Lutz, E. Generalized Clausius inequality for nonequilibrium quantum processes. *Phys. Rev. Lett.* **2010**, *105*, 170402. [CrossRef] [PubMed]
25. Deffner, S.; Lutz, E. Thermodynamic length for far-from-equilibrium quantum systems. *Phys. Rev. E* **2013**, *87*, 022143. [CrossRef]
26. Campisi, M.; Denisov, S.; Hänggi, P. Geometric magnetism in open quantum systems. *Phys. Rev. A* **2012**, *86*, 032114. [CrossRef]
27. Bonança, M.V.S.; Deffner, S. Optimal driving of isothermal processes close to equilibrium. *J. Chem. Phys.* **2014**, *140*, 244119. [CrossRef]
28. Ludovico, M.F.; Battista, F.; von Oppen, F.; Arrachea, L. Adiabatic response and quantum thermoelectrics for ac-driven quantum systems. *Phys. Rev. B* **2016**, *93*, 075136. [CrossRef]
29. Zulkowski, P.R.; DeWeese, M.R. Optimal protocols for slowly driven quantum systems. *Phys. Rev. E* **2015**, *92*, 032113. [CrossRef]
30. Scandi, M.; Perarnau-Llobet, M. Thermodynamic length in open quantum systems. *Quantum* **2019**, *3*, 197. [CrossRef]
31. Abiuso, P.; Perarnau-Llobet, M. Optimal cycles for low-dissipation heat engines. *Phys. Rev. Lett.* **2020**, *124*, 110606. [PubMed]
32. Brandner, K.; Saito, K. Thermodynamic Geometry of Microscopic Heat Engines. *Phys. Rev. Lett.* **2020**, *124*, 040602. [CrossRef]
33. Bhandari, B.; Alonso, P.T.; Taddei, F.; von Oppen, F.; Fazio, R.; Arrachea, L. Geometric properties of adiabatic quantum thermal machines. *arXiv* **2020**, arXiv:2002.02225.
34. Hino, Y.; Hayakawa, H. Geometrical Formulation of Adiabatic Pumping as a Heat Engine. *arXiv* **2020**, arXiv:2003.05567.
35. Mancino, L.; Cavina, V.; De Pasquale, A.; Sbroscia, M.; Booth, R.I.; Roccia, E.; Gianani, I.; Giovannetti, V.; Barbieri, M. Geometrical Bounds on Irreversibility in Open Quantum Systems. *Phys. Rev. Lett.* **2018**, *121*, 160602. [CrossRef] [PubMed]
36. Shiraishi, N.; Saito, K. Information-Theoretical Bound of the Irreversibility in Thermal Relaxation Processes. *Phys. Rev. Lett.* **2019**, *123*, 110603. [CrossRef] [PubMed]
37. Deffner, S. Kibble-Zurek scaling of the irreversible entropy production. *Phys. Rev. E* **2017**, *96*, 052125. [CrossRef] [PubMed]
38. Miller, H.J.D.; Scandi, M.; Anders, J.; Perarnau-Llobet, M. Work Fluctuations in Slow Processes: Quantum Signatures and Optimal Control. *Phys. Rev. Lett.* **2019**, *123*, 230603. [CrossRef]

39. Scandi, M.; Miller, H.J.D.; Anders, J.; Perarnau-Llobet, M. Quantum work statistics close to equilibrium. *Phys. Rev. Res.* **2020**, *2*, 023377. [CrossRef]
40. Miller, H.J.; Guarnieri, G.; Mitchison, M.T.; Goold, J. Quantum fluctuations hinder finite-time information erasure near the Landauer limit. *arXiv* **2020**, arXiv:2007.01882.
41. Guarnieri, G.; Landi, G.T.; Clark, S.R.; Goold, J. Thermodynamics of precision in quantum nonequilibrium steady states. *Phys. Rev. Res.* **2019**, *1*, 033021. [CrossRef]
42. Miller, H.J.; Mohammady, M.H.; Perarnau-Llobet, M.; Guarnieri, G. Thermodynamic uncertainty relation in slowly driven quantum heat engines. *arXiv* **2020**, arXiv:2006.07316.
43. Acconcia, T.V.; Bonança, M.V.S.; Deffner, S. Shortcuts to adiabaticity from linear response theory. *Phys. Rev. E* **2015**, *92*, 042148. [CrossRef]
44. Deffner, S.; Bonança, M.V.S. Thermodynamic control—An old paradigm with new applications. *EPL Europhys. Lett.* **2020**, *131*, 20001. [CrossRef]
45. Schmiedl, T.; Seifert, U. Efficiency at maximum power: An analytically solvable model for stochastic heat engines. *EPL Europhys. Lett.* **2007**, *81*, 20003.[CrossRef]
46. Esposito, M.; Kawai, R.; Lindenberg, K.; Van den Broeck, C. Efficiency at maximum power of low-dissipation Carnot engines. *Phys. Rev. Lett.* **2010**, *105*, 150603. [CrossRef]
47. Guo, J.; Wang, J.; Wang, Y.; Chen, J. Efficiencies of two-level weak dissipation quantum Carnot engines at the maximum power output. *J. Appl. Phys.* **2013**, *113*, 143510. [CrossRef]
48. Den Broeck, C.V. Efficiency at maximum power in the low-dissipation limit. *EPL Europhys. Lett.* **2013**, *101*, 10006. [CrossRef]
49. Hernández, A.C.; Medina, A.; Roco, J.M.M. Time, entropy generation, and optimization in low-dissipation heat devices. *New J. Phys.* **2015**, *17*, 075011. [CrossRef]
50. Holubec, V.; Ryabov, A. Efficiency at and near maximum power of low-dissipation heat engines. *Phys. Rev. E* **2015**, *92*, 052125. [CrossRef]
51. Holubec, V.; Ryabov, A. Maximum efficiency of low-dissipation heat engines at arbitrary power. *J. Stat. Mech. Theory Exp.* **2016**, *2016*, 073204. [CrossRef]
52. Ma, Y.H.; Xu, D.; Dong, H.; Sun, C.P. Universal constraint for efficiency and power of a low-dissipation heat engine. *Phys. Rev. E* **2018**, *98*, 042112. [CrossRef]
53. De Tomás, C.; Hernández, A.C.; Roco, J. Optimal low symmetric dissipation Carnot engines and refrigerators. *Phys. Rev. E* **2012**, *85*, 010104. [CrossRef]
54. Spohn, H. Entropy production for quantum dynamical semigroups. *J. Math. Phys.* **1978**, *19*, 1227–1230. [CrossRef]
55. Cavina, V.; Mari, A.; Giovannetti, V. Slow dynamics and thermodynamics of open quantum systems. *Phys. Rev. Lett.* **2017**, *119*, 050601. [CrossRef] [PubMed]
56. Petz, D.; Toth, G. The Bogoliubov inner product in quantum statistics. *Lett. Math. Phys.* **1993**, *27*, 205–216. [CrossRef]
57. Michor, P.W.; Petz, D.; Andai, A. On the curvature of a certain Riemannian space of matrices. *Infin. Dimens. Anal. Quantum Probab. Relat. Top.* **2000**, *3*, 199–212. [CrossRef]
58. Petz, D. Covariance and Fisher information in quantum mechanics. *J. Phys. A Math. Gen.* **2002**, *35*, 929. [CrossRef]
59. Petz, D.; Ghinea, C. Introduction to quantum Fisher information. In *Quantum Probability and Related Topics*; World Scientific: Singapore, 2011; pp. 261–281. [CrossRef]
60. Balian, R. The entropy-based quantum metric. *Entropy* **2014**, *16*, 3878–3888. [CrossRef]
61. Hayashi, M. *Quantum Information Theory: Mathematical Foundation*; Springer: Berlin/Heidelberg, Germany, 2017.
62. Hayashi, M. Two quantum analogues of Fisher information from a large deviation viewpoint of quantum estimation. *J. Phys. A* **2002**, *35*, 7689. [CrossRef]
63. Petz, D. Monotone metrics on matrix spaces. *Linear Algebra Appl.* **1996**, *244*, 81–96. [CrossRef]
64. Uhlmann, A. Density operators as an arena for differential geometry. *Rep. Math. Phys.* **1993**, *33*, 253–263. [CrossRef]
65. Gibilisco, P.; Isola, T. Wigner—Yanase information on quantum state space: The geometric approach. *J. Math. Phys.* **2003**, *44*, 3752–3762. [CrossRef]
66. Jenčová, A. Geodesic distances on density matrices. *J. Math. Phys.* **2004**, *45*, 1787–1794. [CrossRef]

67. Brandner, K.; Bauer, M.; Seifert, U. Universal Coherence-Induced Power Losses of Quantum Heat Engines in Linear Response. *Phys. Rev. Lett.* **2017**, *119*, 170602. [CrossRef]
68. Breuer, H.P.; Petruccione, F. *The Theory of Open Quantum Systems*; Oxford University Press: Oxford, UK, 2002.
69. Alicki, R. On the Detailed Balance Condition for Non-Hamiltonian Systems. *Rep. Math. Phys.* **1976**, *10*, 249–258. [CrossRef]
70. Menczel, P.; Flindt, C.; Brandner, K. Quantum jump approach to microscopic heat engines. *arXiv* **2020**, arXiv:2005.12231.
71. Salamon, P.; Hoffmann, K.H.; Schubert, S.; Berry, R.S.; Andresen, B. What conditions make minimum entropy production equivalent to maximum power production? *J. Non-Equilib. Thermodyn.* **2001**, *26*, 73–83. [CrossRef]
72. Andresen, B.; Gordon, J.M. Constant thermodynamic speed for minimizing entropy production in thermodynamic processes and simulated annealing. *Phys. Rev. E* **1994**, *50*, 4346–4351. [CrossRef]
73. Salamon, P.; Nitzan, A.; Andresen, B.; Berry, R.S. Minimum entropy production and the optimization of heat engines. *Phys. Rev. A* **1980**, *21*, 2115–2129. [CrossRef]
74. Salamon, P.; Nulton, J.; Siragusa, G.; Andersen, T.; Limon, A. Principles of control thermodynamics. *Energy* **2001**, *26*, 307–319. [CrossRef]
75. Andresen, B. Current Trends in Finite-Time Thermodynamics. *Angew. Chem. Int. Ed.* **2011**, *50*, 2690–2704. [CrossRef] [PubMed]
76. Holubec, V.; Ye, Z. Maximum efficiency of low-dissipation refrigerators at arbitrary cooling power. *Phys. Rev. E* **2020**, *101*, 052124. [CrossRef]
77. Abiuso, P.; Giovannetti, V. Non-Markov enhancement of maximum power for quantum thermal machines. *Phys. Rev. A* **2019**, *99*, 052106. [CrossRef]
78. Cavina, V.; Mari, A.; Carlini, A.; Giovannetti, V. Optimal thermodynamic control in open quantum systems. *Phys. Rev. A* **2018**, *98*, 012139. [CrossRef]
79. Erdman, P.A.; Cavina, V.; Fazio, R.; Taddei, F.; Giovannetti, V. Maximum power and corresponding efficiency for two-level heat engines and refrigerators: Optimality of fast cycles. *New J. Phys.* **2019**, *21*, 103049. [CrossRef]
80. Menczel, P.; Pyhäranta, T.; Flindt, C.; Brandner, K. Two-stroke optimization scheme for mesoscopic refrigerators. *Phys. Rev. B* **2019**, *99*, 224306.[CrossRef]
81. Van Vu, T.; Hasegawa, Y. Geometrical bounds of the irreversibility in classical and open quantum systems. *arXiv* **2020**, arXiv:2005.02871.
82. Denzler, T.; Lutz, E. Power fluctuations in a finite-time quantum Carnot engine. *arXiv* **2020**, arXiv:2007.01034.
83. Pancotti, N.; Scandi, M.; Mitchison, M.T.; Perarnau-Llobet, M. Speed-Ups to Isothermality: Enhanced Quantum Thermal Machines through Control of the System-Bath Coupling. *Phys. Rev. X* **2020**, *10*, 031015. [CrossRef]
84. Clivaz, F.; Silva, R.; Haack, G.; Brask, J.B.; Brunner, N.; Huber, M. Unifying Paradigms of Quantum Refrigeration: A Universal and Attainable Bound on Cooling. *Phys. Rev. Lett.* **2019**, *123*, 170605. [CrossRef]
85. Clivaz, F.; Silva, R.; Haack, G.; Brask, J.B.; Brunner, N.; Huber, M. Unifying paradigms of quantum refrigeration: Fundamental limits of cooling and associated work costs. *Phys. Rev. E* **2019**, *100*, 042130. [CrossRef] [PubMed]
86. Guryanova, Y.; Friis, N.; Huber, M. Ideal Projective Measurements Have Infinite Resource Costs. *Quantum* **2020**, *4*, 222. [CrossRef]

entropy

MDPI

Article

Quantum Finite-Time Thermodynamics: Insight from a Single Qubit Engine

Roie Dann [1,*], Ronnie Kosloff [1] and Peter Salamon [2]

[1] The Institute of Chemistry, The Hebrew University of Jerusalem, Jerusalem 9190401, Israel; ronnie@fh.huji.ac.il

[2] Department of Mathematics and Statistics, San Diego State University, 5500 Campanile Drive, San Diego, CA 92182-7720, USA; salamon@sdsu.edu

* Correspondence: roie.dann@mail.huji.ac.il

Received: 6 September 2020; Accepted: 1 November 2020; Published: 4 November 2020

Abstract: Incorporating time into thermodynamics allows for addressing the tradeoff between efficiency and power. A qubit engine serves as a toy model in order to study this tradeoff from first principles, based on the quantum theory of open systems. We study the quantum origin of irreversibility, originating from heat transport, quantum friction, and thermalization in the presence of external driving. We construct various finite-time engine cycles that are based on the Otto and Carnot templates. Our analysis highlights the role of coherence and the quantum origin of entropy production.

Keywords: finite-time thermodynamics; quantum thermodynamics; quantum heat engine; carnot cycle; otto cycle

1. Introduction

The tradeoff between power and efficiency is well embedded in our everyday experience. It is witnessed in the performance of any realistic engine or refrigerator, from the operation of large nuclear plants, through the internal combustion engines of our automobiles, and all the way to microscopic biological engines and the quantum regime. Despite the intuitive notion, a theoretical analysis is quite involved, as it requires a theoretical construction that encompasses both thermodynamics and transient dynamics.

The limiting case was first treated by Carnot, who linked an engine's maximum attainable work production to reversible thermodynamic transformations, thereby obtaining the thermodynamic temperature scale and the universal optimal efficiency that only depends on the hot and cold bath temperatures [1]. Unlike efficiency, power requires knowledge of the transient dynamics, which is outside the realm of classical thermodynamics. Finite-time thermodynamics (FTT) was developed in order to include the limitations the process duration places on the performance of an engine [2–6]. Originally, the pioneers of FTT incorporated empirical kinetic laws to introduce an intrinsic timescale in the analysis of engine cycles [7,8]. Some results from these efforts are recapped in Section 2.1. In this paper, we address the need for kinetic laws by following a different approach: building upon a complete quantum description of the engine and baths.

However, such complete quantum description is not as straightforward as it sounds. Quantum mechanics is a dynamical theory that can supply equations of motion for thermodynamic processes. The well established portion of this theory has predominantly dealt with closed systems that conserve entropy and, thus, cannot deal with dissipation phenomena at the heart of thermodynamic analyses. This forces us to turn to open quantum systems, whose description from first principles relies on a reduction from a closed composite system. The reduced description is achieved by tracing over the degrees of freedom of the surroundings, interacting with our system of interest. This description does

not conserve entropy and allows for the exploration of thermodynamic processes in the quantum regime. Notably, the approach is based on the completely positive trace preserving (CPTP) dynamical map [9] and the Markovian Gorini–Kossakowski–Lindblad–Sudarshan (GKLS) master equation [10,11]. A thermodynamically consistent dynamical framework [12] is obtained by a first principle derivation based on weak interaction of an open system with a heat bath. The derivation is commonly termed the 'Davies construction' [13].

The quantum open system approach resulted in a number of surprises, initially reported as claimed contradictions to the second law [14–19]. These include reported claims of breakdown of the Carnot bound in such engines [20–22]. In turn, these results led to resolutions, explained by unexpected work that is available from quantum resources, including coherence [23], squeezed bath [24], entanglement [25], and information [26,27].

Another set of surprises came from attempts to use a naive GKLS formalism with a time-dependent driving, which possibly violates the second law [28–31]. This led to the realization that the inconsistency arises from the derivation of the reduced dynamics of the system. For periodic driving, a thermodynamically consistent GKLS equation was derived in Ref. [32]. In the case of a general (non-periodic) driving, only the adiabatic master equation was available [33]. This fact did not limit the analysis of the Otto cycle model, which could be studied up to the limit of vanishing cycle times. On the contrary, the analysis of the Carnot cycle model was limited to the linear response regime. Only recently has a derivation of the GKLS master equation for rapid non-adiabatic driving become available [34], and it is this discovery whose implications we explore in the present paper.

We adopt the dogma that thermodynamics and quantum mechanics address the same subject matter, therefore have to be consistent [35]. In this framework, quantum mechanics provides the tools for describing the dynamics, while the strict laws of thermodynamics must be obeyed. In addition, recent progress in the theory of quantum speed limits can illuminate fundamental bounds on the process timescale [36–41].

Engines have been an intrinsic part in the development of classical thermodynamics. Their analysis still serves as an integral part of current research in finite-time and quantum thermodynamics. These theories allow for describing engines more realistically including non-ideal performance. Any practical engine operates in a non-ideal irreversible mode. Typically, there are four sources of irreversible phenomena in engines:

1. Finite heat transport.
2. Friction.
3. Heat leaks.
4. Cost of switching contacts between subsystems.

Following the thermodynamic tradition of learning from example, we employ the most elementary working medium, a spin one half system to explore a quantum version of finite-time thermodynamics. A decade ago, such an example would have been criticized as a theoretician's toy with no connection to the world of real engines. The finite-time Otto type cycle, which our cars operate by, do not seem to be related to a single spin quantum engine. Nevertheless, recent experimental progress has enabled a realization of an Otto cycle engine constructed from a single spin of an atom in an ion trap [42], a single qubit in an impurity electron spin [43], or a working medium of ultracold hyperfine structure of Cs in a Rb bath [44].

The present paper begins by laying the quantum thermodynamic foundations for the qubit, giving the quantum definitions for energy, entropy, and temperature, Section 2.2. We continue by discussing sources of irreversibility: heat transport, Section 3, the quantum origin of friction, Section 4, and thermalization processes which combine heat transport and external work, Section 5. The quantum version of finite-time thermodynamics is studied by constructing two basic engine platforms: Carnot and Otto. These models illuminate different aspects of the tradeoff between power and efficiency and the role of coherence on the engines performance, Sections 6–8.

2. Some Preliminaries

The unfortunate collision of the different usages of the word adiabatic in thermodynamics and quantum mechanics have been sidestepped by using the term "unitary dynamics" for dynamics along what thermodynamics would call an adiabat leaving the use of adiabatic for the quantum meaning.

2.1. Classical Engines Operating in Finite-Time

Classical textbook treatments of heat engines define various kinds of engine cycles. These cycles are mostly four-stroke and consist of two unitary strokes and two open strokes in contact with a heat bath—one hot and one cold. Finite-time thermodynamic analyses of these cycles has given us the simplifying model of endoreversible processes—processes in which the participating systems are at each instant in equilibrium states and all irreversibility resides in the interactions between such systems. Endoreversible cycles play an important role by edging closer towards real cycles, being relatively easy to analyze and providing checks along the way for more ambitious treatments. They also provide an accurate picture of reality when the slow timescale is the interaction. The simplifying condition of instantaneous lossless adiabatic jumps, made possible for quantum systems using shortcuts to adiabaticity (cf. Section 4.3), is a hallmark simplifying feature that we inherit from these studies.

Additionally, important for these analyses is a much older result known as the Gouy—Stodola theorem [45–48] which established a connection between dissipated work and entropy production, cf.

$$\Delta \mathcal{A}^{U} = -T_0 \Delta \mathcal{S}^{U} \tag{1}$$

where the superscript U refers to the universe (all participating systems), $\mathcal{S}$ is the entropy, $\mathcal{A}$ is the available work, and T_0 is the temperature at which heat is freely available which means it carries no available work. The environment temperature T_0 is also used in the availability (also called exergy) state function $\mathcal{A} = \mathcal{E} - T_0\mathcal{S}$, where $\mathcal{E}$ is the internal energy. As a consequence, Equation (1) is valid with any constant temperature choice for T_0. In engineering treatments it is always the atmospheric temperature, but any temperature will do. In the physics literature T_0 is almost always taken to be the system's temperature making $\mathcal{A} = \mathcal{F}$, where $\mathcal{F}$ is the Helmholtz free energy. Note that $\mathcal{A} = \mathcal{F}$ can hold at only one temperature.

For our purposes, the importance of Equation (1) arises from the fact that it shows that dissipation can equivalently be measured in energetic or entropic terms, even when the system does not have a temperature or when this temperature is changing during the process of interest.

2.2. Qubit Engine Model

The engine model is constructed from a hot and cold bath and a controllable two-level-system shuttling between them. The Hamiltonian of the working medium, a qubit, is

$$\hat{H} = \omega(t)\hat{S}_z + \epsilon(t)\hat{S}_x \tag{2}$$

where $\hat{S}_j$ are the spin operators with the commutation relation of the $SU(2)$ algebra $[\hat{S}_i, \hat{S}_j] = i\hbar\epsilon_{ijk}\hat{S}_k$, see Appendix A. The time-dependent driving parameters $\omega(t)$ and $\epsilon(t)$, define a typical energy scale

$$\hbar\Omega(t) = \hbar\sqrt{\omega^2 + \epsilon^2} \quad , \tag{3}$$

where Ω is the Rabi frequency.

The state of the qubit working medium $\hat{\rho}$ can be expanded while using any orthonormal set of operators satisfying $\mathrm{tr}\{\hat{A}_i^\dagger \hat{A}_j\} = \delta_{ij}$. Choosing the polarizations $\hat{S}_j$ as basis operators, the state $\hat{\rho}$ is completely determined by the expectation value of the three polarizations

$$\hat{\rho} = \frac{1}{2}\hat{I} + \frac{2}{\hbar^2}\left(\langle\hat{S}_x\rangle\hat{S}_x + \langle\hat{S}_y\rangle\hat{S}_y + \langle\hat{S}_z\rangle\hat{S}_z\right) \quad . \tag{4}$$

It elucidates the analysis to represent the polarization vector as a geometric object $\vec{S} = \{\langle \hat{S}_x \rangle, \langle \hat{S}_y \rangle, \langle \hat{S}_z \rangle\}^T$, which resides inside the Bloch sphere (see Figure 1 and Appendix A). The polarization value is defined as

$$\bar{S} \equiv -|\vec{S}| = -\sqrt{\langle \hat{S}_x \rangle^2 + \langle \hat{S}_y \rangle^2 + \langle \hat{S}_z \rangle^2} \ . \tag{5}$$

It is related to the purity of the state, where $0 \geq \bar{S} \geq -\hbar/2$ where $|\bar{S}| = \hbar/2$ for a pure state. The sign convention of the polarization is motivated by the fact that we consider only positive temperatures, see Equation (6). The polarization value is invariant under unitary transformations that are generated by the $SU(2)$ group, which represents rotations of the polarization vector. It is related to the expectation value of the energy by $\mathcal{E} = \langle \hat{H} \rangle = \hbar\Omega \bar{S}_H$, where $\bar{S}_H$ is the projection of the polarization vector on the direction representing the Hamiltonian. In thermal equilibrium at temperature T, the polarization becomes

$$\langle \vec{S} \rangle = \bar{S}_H = \bar{S}_{eq} = -\frac{\hbar}{2} \tanh\left(\frac{\hbar\Omega}{2k_B T}\right) \ , \tag{6}$$

where k_B is the Boltzmann constant and T is the bath temperature.

The engines that are to be analyzed are discrete four stroke cycle models. Specifically, we will compare the Carnot cycle with the Otto cycle. Both of the cycles are constructed from the following sequence of strokes:

(A) $1 \to 2$ Hot bath thermalization.
(B) $2 \to 3$ Unitary expansion from hot to cold
(C) $3 \to 4$ Cold bath thermalization
(D) $4 \to 1$ Unitary compression from cold to hot

The two cycles differ by the nature of the thermalization strokes, $1 \to 2$ and $3 \to 4$. The reversible Carnot cycle includes isothermal strokes during the thermalization processes, while the Otto cycle utilizes isochores, see Figure 2. In the following study, we sometimes refer to the thermalization strokes as open-strokes, alluding to the fact that the working medium constitutes an open quantum system during these strokes.

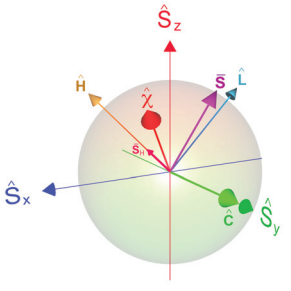

Figure 1. The state of the system, Equation (4), is represented by the polarization vector $\bar{S}$ in the Bloch sphere (purple). Alternatively, the state can be represented in a rotated frame Equation (33), defined by the set of coordinates $\langle \hat{H} \rangle, \langle \hat{L} \rangle, \langle \hat{C} \rangle$ in Equation (32). These coordinates are rotated about the $\langle \hat{S}_y \rangle$ axis relative to the static direction. The projection of the polarization on the energy direction $\bar{S}_H$, Equation (13), is shown in light red. The invariant of the free propagator $\langle \hat{\chi} \rangle$ in Equation (52) is shown in red. The direction of $\langle \hat{\chi} \rangle$ is rotated around the $\langle \hat{L} \rangle$ axis with respect to the $\langle \hat{H} \rangle$ direction (cf. Appendix A). The Bloch sphere representation can represent either the expectation values of the operators or the operators themselves. The latter constitute orthogonal vectors in Liouville space.

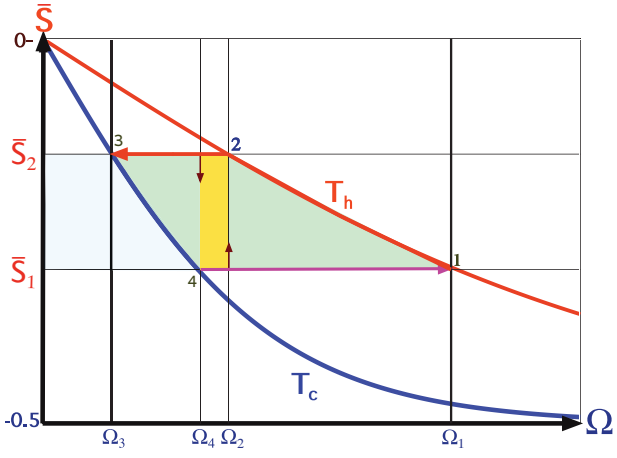

Figure 2. Carnot and Otto cycles: polarization $\bar{S}$ as a function of frequency Ω is shown along the hot (red) and cold (blue) isotherms. The four switching points between the strokes are indicated by numbers 1–4. The various strokes are represented by lines. Carnot cycle: Hot isotherm $(\Omega_1, \bar{S}_1) \rightarrow (\Omega_2, \bar{S}_2)$, unitary expansion $(\Omega_2, \bar{S}_2) \rightarrow (\Omega_3, \bar{S}_2)$, cold isotherm $(\Omega_3, \bar{S}_2) \rightarrow (\Omega_4, \bar{S}_1)$, and unitary compression $(\Omega_4, \bar{S}_1) \rightarrow (\Omega_1, \bar{S}_1)$. The filled area in light green represents the work output, while the area in light blue represents the heat that is absorbed by the cold bath. The sum of the two areas equals the heat exchange with the hot bath. This implies a nice geometric representation of the efficiency, as the ratio between the light green area and the combined area. Otto cycle embedded in the Carnot cycle (orange area); hot isochore $(\Omega_2, \bar{S}_1) \rightarrow (\Omega_2, \bar{S}_2)$, unitary expansion $(\Omega_2, \bar{S}_2) \rightarrow (\Omega_4, \bar{S}_2)$, cold isochore $(\Omega_4, \bar{S}_2) \rightarrow (\Omega_4, \bar{S}_1)$, and unitary compression $(\Omega_4, \bar{S}_1) \rightarrow (\Omega_2, \bar{S}_1)$. The short arrows designate the thermalization isochores.

The four stroke cycles can be described by the corresponding cycle propagator Λ_{cyc}, which is a product of individual stroke propagators:

$$\Lambda_{cyc} = \Lambda_{c\rightarrow h}\Lambda_c\Lambda_{h\rightarrow c}\Lambda_h \tag{7}$$

These propagators are completely positive trace-preserving (CPTP) maps on the space of qubit states [9]. The properties of the engine are extracted from the fixed point of the cycle map, ρ_{fp}, which represents the limit cycle and satisfies $\Lambda_{cyc}\hat{\rho}_{fp} = \hat{\rho}_{fp}$ [49]. The fixed point $\hat{\rho}_{fp}$, along with the stroke propagators, fully determine the qubit state throughout the fixed cycle. The existence of a single invariant of CPTP map guarantees monotonic convergence to the fixed point [49,50]. The value of $\hat{\rho}_{fp}$ is associated with a particular state of the limit cycle, from which all other states along the cycle can be calculated by applying the propagators Λ. In turn, this allows for evaluating the thermodynamic variables, such as work, heat, and entropy.

Two important quantities for the finite-time thermodynamic analysis of these cycles are the von-Neumann and the energy entropies of the qubit

$$\mathcal{S}_{v.n} \equiv -\mathrm{tr}\left[\hat{\rho}\ln\hat{\rho}\right] = -\left(\frac{1}{2} - \frac{\bar{S}}{\hbar}\right)\log\left(\frac{1}{2} - \frac{\bar{S}}{\hbar}\right) - \left(\frac{1}{2} + \frac{\bar{S}}{\hbar}\right)\log\left(\frac{\bar{S}}{\hbar} + \frac{1}{2}\right) \ , \tag{8}$$

and

$$\mathcal{S}_H = -p_H\ln p_H - (1 - p_H)\ln\left(1 - p_H\right) \ , \tag{9}$$

where $p_H = \left(\frac{1}{2} - \frac{\bar{S}_H}{\hbar}\right)$. Generally, we have $\mathcal{S}_H \geq \mathcal{S}_{v.n}$ with equality when the state is diagonal in the energy representation. At equilibrium, both entropies reduce to $\mathcal{S}_{v.n}\left(\bar{S}_{eq}\right)$, where $\bar{S}_{eq}$ is given

in Equation (6). The difference between the energy entropy and the von-Neumann entropy is a quantifier [51–54] of coherence. It is commonly known as the divergence [55]

$$\mathcal{D}(\hat{\rho}|\hat{\rho}_d) = \mathrm{tr}\{\hat{\rho}\ln\hat{\rho} - \hat{\rho}\ln\hat{\rho}_d\} = \mathcal{S}_H - \mathcal{S}_{v.n} \ , \tag{10}$$

where $\hat{\rho}_d$ is diagonal in the energy representation and defined in Equation (13). During the cycle's operation, the unitary strokes $\Lambda_{c\to h}$ and $\Lambda_{h\to c}$ maintain a constant von-Neumann entropy, while the energy entropy may increase with the generation of coherence.

3. Frictionless Engines

A non-vanishing heat transport rate is a prime source of irreversibility. Such heat transfer occurs when there exists a temperature gap on the interface between the engine and the baths. The influence of a realistic heat transport on cycle performance was first addressed by the classical endoreversible model [7]. Such a cycle assumes an empirical Newtonian heat transport law in order to describe the heat rate. For the qubit engine, we can replace the empirical Newtonian heat transport law with a quantum first principle derivation. The starting point is the composite Hamiltonian:

$$\hat{H}_{tot} = \hat{H}(t) + \hat{H}_{h/c} + \hat{H}_{s-h/c} \ , \tag{11}$$

where $\hat{H}_{h/c}$ are the hot and cold bath Hamiltonians and $\hat{H}_{s-h/c}$ represent the system-bath interaction, correspondingly. Reduced equations of motion for the system are obtained in the framework of the theory of open quantum systems [56]. This theory constitutes a general setting from which the dynamics can be derived from first principles, by employing a number of idealizations. The main assumptions, which are included in the derivation, are weak system-bath coupling and a separation of timescales between a fast bath and a sluggish system [13]. These assumptions are justified on the basis of physical reasoning and the fact that the obtained dynamical equations are indisputably consistent with the laws of thermodynamics [12,35].

To concentrate only on heat transport we can assume $\epsilon(t) = 0$, therefore $\Omega(t) = \omega(t)$, which leads to

$$\hat{H}^{elem}(t) = \hat{H}(t)_{\epsilon=0} = \Omega(t)\hat{S}_z = \omega(t)\hat{S}_z \ . \tag{12}$$

We refer to Equation (12) as the elementary Hamiltonian. For such a case, the Hamiltonian satisfies $[\hat{H}^{elem}(t), \hat{H}^{elem}(t')] = 0$, which decouples the dynamics of the populations and the coherence. This means that when the qubit is initialized in a diagonal state in the energy basis, the dynamics that are generated by the elementary Hamiltonian remain on the energy shell and are equivalent to frictionless solutions (cf. Section 4) of stochastic dynamics. For such instant, the analysis has common features with quantum adiabatic dynamics [57]. The state of the system then becomes:

$$\hat{\rho}_d = \frac{1}{2}\hat{I} + \frac{2}{(\hbar\Omega)^2}\langle\hat{H}^{elem}\rangle\hat{H}^{elem} \ , \tag{13}$$

which is diagonal in the energy representation, implying that $[\hat{\rho}_d, \hat{H}^{elem}] = 0$, $\bar{S} = -|\langle\hat{S}_z\rangle|$ and $\mathcal{S}_{v.n} = \mathcal{S}_E$. When the initial state exhibits quantum coherence, Equation (4), under these operating conditions and after a sufficient time, any initial coherence decays to zero. We will refer to this model as the elementary qubit engine.

In this framework, the reduced dissipative dynamics of the qubit is of the following structure [34]

$$\frac{d}{dt}\hat{\rho} = -\frac{i}{\hbar}[\hat{H}^{elem}(t), \hat{\rho}] + \mathcal{L}_D(\hat{\rho}) \tag{14}$$

where the dissipator $\mathcal{L}_D$ has a Gorini–Kossakowski–Lindblad–Sudarshan form (GKLS) [10,11]

$$\mathcal{L}_D(\rho) = \frac{4}{\hbar^2}\left[k_\uparrow(t)\left(\hat{S}_+\hat{\rho}\hat{S}_- - \frac{1}{2}\{\hat{S}_-\hat{S}_+,\hat{\rho}\}\right) + k_\downarrow(t)\left(\hat{S}_-\hat{\rho}\hat{S}_+ - \frac{1}{2}\{\hat{S}_+\hat{S}_-,\hat{\rho}\}\right)\right] \tag{15}$$

where $\hat{S}_\pm = \hat{S}_x \pm i\hat{S}_y$ and $k_\uparrow$ and $k_\downarrow$ obey instantaneous detailed balance:

$$\frac{k_\uparrow(t)}{k_\downarrow(t)} = e^{-\frac{\hbar\Omega(t)}{k_B T}} \quad . \tag{16}$$

The kinetic coefficients typically have a power dependence on Ω: $k_\downarrow(t) \propto \Omega(t)^n$, where $n \in \mathbb{R}$ depends on the spectral properties of the bath [56]. An alternative representation of the dynamics utilizes the Heisenberg picture, in which the equations of motion are of the form

$$\frac{d}{dt}\hat{X} = \frac{i}{\hbar}[\hat{H}^{elem}(t),\hat{X}] + \mathcal{L}_D^*(\hat{X}) + \frac{\partial}{\partial t}\hat{X} \ ; \tag{17}$$

where $\mathcal{L}_D^*(\bullet)$ is the adjoint generator. The relation to thermodynamics is achieved by setting $\hat{X} = \hat{H}$ and identifying the rate of change of the average energy as the quantum dynamical version of the first law of thermodynamics [58,59]

$$\frac{d}{dt}E = \mathcal{P} + \dot{\mathcal{Q}} \ , \tag{18}$$

where: $\mathcal{P} = \langle \frac{\partial}{\partial t}\hat{H}\rangle$ is the power and $\dot{\mathcal{Q}} = \langle \mathcal{L}_D^*(\hat{H})\rangle$ is the heat flux. Power is associated with the unitary part of the dynamics, for which the von-Neumann entropy remains constant, and heat flux is identified as the average energy transfer that induces entropy change. For the elementary qubit system, the power becomes

$$\mathcal{P} = \bar{S}_H(t)\frac{\partial\omega(t)}{\partial t} \tag{19}$$

This result is analogous to the classical definition of power, where $\partial\omega/\partial t$ takes the role of the generalized force and the polarization is its conjugate variable. The expression for the heat flux reads

$$\dot{\mathcal{Q}} = -\Gamma(t)\left(\langle\hat{H}^{elem}(t)\rangle - \langle\hat{H}_{eq}(\Omega(t),T\rangle\right) \ , \tag{20}$$

where $\Gamma = k_\uparrow + k_\downarrow$. $\langle\hat{H}_{eq}\left(\Omega\left(t\right),T\right)\rangle = \Omega\left(t\right)\bar{S}_{eq}\left(\Omega\left(t\right)\right)$ and $\bar{S}_{eq}(\Omega(t))$ is the instantaneous attractor (cf. Equation (56)), which is defined by the changing frequency $\Omega(t)$, Equation (6). As expected, the heat flux is proportional to the deviation from equilibrium and the relaxation rate. Equation (20) is identical to that one employed in [60], replacing Γ by τ_{eq}^{-1}.

The equilibration of energy is accompanied by decay of coherence. The coherence dynamics are obtained by substituting $\hat{S}_x$ or $\hat{S}_y$ for $\hat{X}$ in Equation (17), leading to

$$\frac{d}{dt}\begin{bmatrix}\hat{S}_x\\ \hat{S}_y\end{bmatrix} = \begin{bmatrix}-\frac{1}{2}\Gamma\left(t\right) & -\Omega\left(t\right)\\ \Omega\left(t\right) & -\frac{1}{2}\Gamma\left(t\right)\end{bmatrix}\begin{bmatrix}\hat{S}_x\\ \hat{S}_y\end{bmatrix} \ . \tag{21}$$

This set of equations reflects the separation of the coherence dynamics from the population dynamics [12]. It implies that any initial coherence will decay to zero once the limit cycle is reached. This mode of operation is equivalent to stochastic thermodynamics where all thermodynamic observables are obtained in terms of the populations of the energy levels [61–63].

3.1. Elementary Cycles

Utilizing the quantum description of heat transport, introduced above, we can assemble a finite-time model of a heat engine. We construct a Carnot-type cycle and an Otto cycle whose working fluids are governed by elementary Hamiltonians, Equation (12) and then compare their finite-time

thermodynamic performance. We will compare the work produced per cycle $-\mathcal{W}$ and heat $\mathcal{Q}_{h/c}$, which define the efficiency: $\eta = -\frac{\mathcal{W}}{\mathcal{Q}_h}$.

3.2. Elementary Carnot-Type Cycle

Consider a quantum version of a finite-time Carnot-type cycle thta is shown in Figure 3. When in contact with the heat bath, the qubit of the endoreversible engine maintains a constant internal temperature T', generating a temperature gap with the bath. In this scenario, one can optimize the power by varying the temperature gap [64]. The efficiency then shows a monotonic decrease with the deviation from the ideal Carnot cycle: $\eta_C \geq \eta \geq 0$.

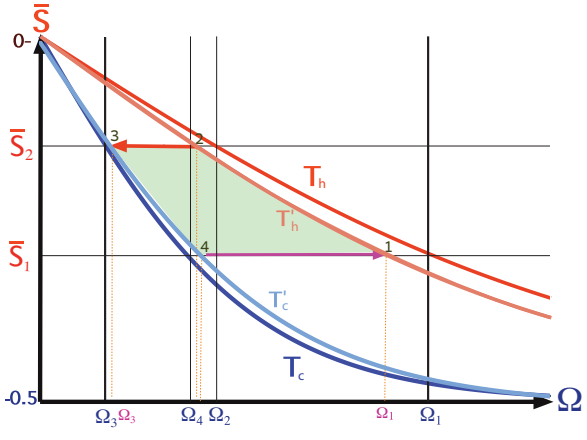

Figure 3. Endoreversible Carnot cycle: Polarization $\bar{S}$ as a function of frequency Ω. The hot and cold isotherms are designated in red and blue, correspondingly. Blue frequencies designate the corners of the reversible Carnot cycle and the small purple frequencies correspond to the corners of the endoreversible cycle. The endoreversible frequencies depend on the cycle time; in the quasi-static limit they converge to the frequencies of the reversible Carnot cycle. The finite-time engine follows internal hot $1 \to 2$ and cold $3 \to 4$ isotherms (light red and blue curved lines) with associated temperatures T'_h and T'_c, allowing for finite heat transport. The area in green equals the total work output.

At the high temperature limit the performance is very similar to the Curzon-Ahlborn empirical model [7,65] or low dissipation limit [66], where the heat conductance was modelled by the Newtonian heat transfer law. In this limit, the efficiency at maximum power converges to

$$\eta_{CA} = 1 - \sqrt{\frac{T_c}{T_h}} \ , \tag{22}$$

and the work per cycle becomes half the reversible work, Equation (26), $\mathcal{W}_{CA} = \frac{1}{2}\mathcal{W}_C$. The optimal power at high temperature can be approximated as [64]

$$\mathcal{P}^{Endo}_{Carnot} = \Gamma k_B \left(\sqrt{T_h} - \sqrt{T_c}\right)^2 \frac{2}{\hbar^2}\left(\bar{S}_2^2 - \bar{S}_1^2\right)\frac{1}{\ln(\bar{S}_2/\bar{S}_1)} \ . \tag{23}$$

This expression is reminiscent of the ideal work at the high temperature limit Equation (27), with a modified temperature gap. In this temperature regime, the optimum entropy production average rate per cycle obtains a similar form

$$\frac{\sigma^u_{cyc}}{\tau_{cyc}} = \Gamma\left(\frac{T_h - T_c}{\sqrt{T_c T_h}}\right)\frac{2}{\hbar^2}\left(\bar{S}_2^2 - \bar{S}_1^2\right)\frac{1}{\ln(\bar{S}_2/\bar{S}_1)} \ . \tag{24}$$

A similar structure to Equation (23) has been recently derived [67,68] based on a low dissipation limit.

The qubit Carnot-type cycle delivers finite power. In the limit of infinite cycle time, the cycle operates reversibly to obtain the Carnot efficiency

$$\eta_C = 1 - \frac{T_c}{T_h} \ . \tag{25}$$

The work per reversible cycle then becomes

$$\mathcal{W}_C = k_B \Delta T \Delta \mathcal{S}_{v.n} \ , \tag{26}$$

where $\Delta T = T_h - T_c$ is temperature gap and $\Delta \mathcal{S}_{v.n}$ is the change of the qubit's von-Neumann entropy on the cold or hot isotherms. For the elementary cycles, the von-Neumann and energy entropy S_E coincide, as the state remains on the energy shell. Another important characteristic of the engine is the compression ratio $\mathcal{C} = \Omega_{max}/\Omega_{min}$, for the ideal Carnot engine $\mathcal{C}_{Carnot} = \Omega_1/\Omega_3$, see Figure 3. The entropy of the qubit is bounded by ln2, giving a maximum possible work of $\max(\mathcal{W}_C) = k_B(T_h - T_c)\ln(2)$.

At the high temperature limit $\hbar\Omega \ll k_B T$ the energy entropy can be approximated as $\mathcal{S}_{v.n} \simeq -\ln 2 + 2\left(\frac{\bar{S}}{\hbar}\right)^2$ and the work becomes

$$\mathcal{W}_C \simeq k_B \Delta T \frac{2}{\hbar^2}(\bar{S}_2^2 - \bar{S}_1^2) \ . \tag{27}$$

This typical dependence is a general feature of any entropy dependent variable. The characteristic quadratic functionality of the polarization stems from the proximity to the maximum entropy point.

3.3. Elementary Otto Cycle

We consider an Otto cycle that is embedded within the same isotherms and frequency range of the elementary Carnot cycle and it is limited by the polarizations $\bar{S}_1$ and $\bar{S}_2$, see Figure 4 [63]. For an engine operation mode, the compression ratio of the Otto cycle is constrained by $\mathcal{C}_{Otto} = \Omega_c/\Omega_h \leq \mathcal{C}_{Carnot}$. The engine's work obtains the simple form

$$\mathcal{W}_{Otto} = \Delta\Omega \Delta\bar{S} \ , \tag{28}$$

where $\Delta\Omega = \Omega_h - \Omega_c = \Omega_2 - \Omega_4$ and $\Delta S = \bar{S}_2 - \bar{S}_1$. It is represented geometrically by the confined area between the frequencies and polarizations, colored as light green in Figure 4. Such an engine is characterized by a constant efficiency

$$\eta_{Otto} = 1 - \frac{\Omega_c}{\Omega_h} \ , \tag{29}$$

which leads to $\eta_{Otto} = 1 - \frac{\bar{S}_2 T_c}{\bar{S}_1 T_h} \leq \eta_C$ for the analyzed cycle. When $\bar{S}_2 \to \bar{S}_1$, the cycle operation becomes reversible and the Carnot bound is recovered $\eta_{Otto} \to \eta_C$. This limiting case is the transition point between the engine and refrigerator operation mode ($\mathcal{C}_{Otto} = \mathcal{C}_{Carnot}$).

The heat that is dissipated during the cycle operation leads to a rise in entropy. The entropy production per cycle obtains the form

$$\sigma^u_{cyc} = \frac{1}{k_B}\left(\frac{\Omega_h}{T_h} - \frac{\Omega_c}{T_c}\right)\Delta\bar{S} \ . \tag{30}$$

We obtain a linear dependence on the polarization difference, which contrasts with the endoreversible result at high temperature, Equation (24), characterized by a quadratic difference dependence.

We can compare between the geometric interpretation of the work output of the elementary Otto and Carnot cycles, Equations (26) and (28) . In the Otto cycle work is represented by the area that is enclosed by the cycle in the $(\Omega, \bar{S})$ plane, and in the $(T, \mathcal{S}_{v.n})$ plane for the Carnot cycle, see description in the caption of Figure 3.

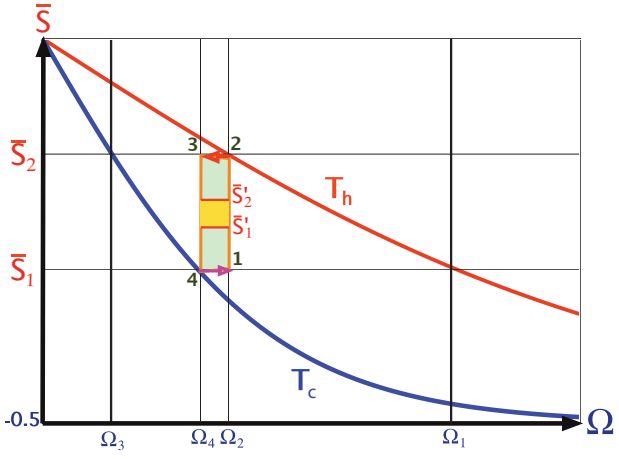

Figure 4. Otto cycle embedded within the Carnot cycle: Polarization $\bar{S}$ as a function of frequency Ω. The same extreme polarizations $\bar{S}_1$ and $\bar{S}_2$ are used. The area in light green is the work output. The area in orange represents a finite-time Otto engine operating between $\bar{S}'_2$ and $\bar{S}'_1$. The compression ratio $\mathcal{C}_{Otto}$ is reduced relative to $\mathcal{C}_{Carnot}$ as $\Omega_2 < \Omega_1$ and $\Omega_3 < \Omega_4$.

3.4. Optimization of the Elementary Otto Cycle

A modification of the present cycle includes optimizing the work per cycle with respect to the frequency Ω_2. At the high temperature limit $\hbar\Omega \ll k_B T$, this optimization procedure leads to $\mathcal{W}_{max} = \frac{\hbar^2\Omega_4^2}{k_B T_h}\left(1 - (\frac{T_c}{T_h})^2\right)$ with efficiency $\eta_{Otto} = 1 - \frac{2T_c}{T_h + T_c}$. Such an optimization is equivalent to a maximization of the area of a rectangular region embedded within the Carnot cycle.

Finite power is obtained when the working medium does not completely relax to thermal equilibrium during the open strokes. Power optimization is carried out with respect to the thermalization time. Surprisingly, the optimal cycle was found to be of the bang-bang type, with a vanishing cycle time. The optimal power becomes [63]

$$\mathcal{P}^{B.B}_{Otto} = \frac{1}{4}\Gamma\Delta\Omega\Delta\bar{S} \tag{31}$$

where $\Gamma_h = \Gamma_c = \Gamma$. This gives a simple relation to the maximum work $\mathcal{P}_{Otto} = \frac{\Gamma}{2}\mathcal{W}_{Otto}$, Equation (28). Such an engine operates at the polarization $\bar{S} = \frac{1}{2}(\bar{S}_2 + \bar{S}_1)$. We refer to cycles with vanishing cycle times as sudden cycles. A generalization of Equation (31) for different relaxation rates Γ on the hot and cold side can be found in [69]. A sudden type qubit refrigerator Otto cycle has also been investigated with similar conclusions [70,71].

The optimal power of the endoreversible Carnot cycle Equation (23) can be compared with the Otto cycle Equation (31) at the high temperature limit. The comparison shows that the optimal power of the Otto cycle may exceed the power of an endoreversible Carnot cycle with the same polarization and bath temperatures.

The counter intuitive result where the optimum power for the Otto cycle is obtained for vanishing cycle time can be understood by noting that the largest temperature gaps between the qubit and the reservoir is at the initial portion of each open stroke. Thus, the shorter the cycle time, the faster the heat

transfer, yielding an endpoint optimum (zero cycle time) for maximum power. If we put a restriction on the minimum time allocation of the unitary strokes, then the power becomes optimal for a finite cycle time [63]. This was the original motivation for adding friction phenomenologically [72]. An important outcome of the incorporation of phenomenological friction within the model is a minimum cycle time for an engine operation. The phenomenological friction is taken to be inversely proportional to the stroke time. Thus, rapid driving leads to enhanced friction, reducing the power. Below, a minimum cycle time the output power vanishes and the cycle operates as an accelerator or a dissipator, converting useful work to heat. In a dissipator, work is consumed ($\mathcal{W} > 0$), while heat is dissipated to both the hot and cold baths ($\mathcal{Q}_h, \mathcal{Q}_c < 0$). Using the efficiency definition, $\eta \equiv -\mathcal{W}/\mathcal{Q}_h$, the "efficiency" exceeds one. An accelerator operation mode includes positive work, accelerating the transfer of heat from the hot to the cold bath ($\mathcal{Q}_h > 0$ and $\mathcal{Q}_c < 0$). This leads to negative values of η.

4. The Quantum Origin of Friction

Quantum friction is associated with the consumption of energy in the generation of coherence, which thereafter dissipates to the bath. In a sense, coherence constitutes potential work [73], and the process of coherence generation can be viewed as a temporary storage of energy in the coherence degree(s) of freedom. When these modes decay, the associated potential work is lost. In terms of the work consumption, the dissipation of coherence is equivalent to dissipation of work and amounts to an additional cost. While such dissipation generally degrades the engines performance [51,74,75], it also speeds it up.

As in classical engines, quantum friction emerges naturally under rapid external driving. The driving generates coherence, which, in turn, leads to a higher work cost and friction, but a higher speed of operation. Generation of coherence is closely related to non-adiabatic quantum dynamics, which occurs whenever the system Hamiltonian does not self-commute at different times $[\hat{H}(t), \hat{H}(t')] \neq 0$ [76].

We employ the quantum qubit model to study the influence of quantum friction on the cycle performance. This model is simple enough to allow for an explicit solution and includes the sufficient condition for observing quantum friction. That is, the qubit working medium does not self commute if $\epsilon(t)$ and $\omega(t)$, in Equation (2), are not proportionate to each other. A natural time-dependent framework to describe the dynamics of the working medium employs the set of time-dependent quantum operators

$$\begin{aligned} \hat{H} &= \omega(t)\hat{S}_z + \epsilon(t)\hat{S}_x \\ \hat{L} &= \epsilon(t)\hat{S}_z - \omega(t)\hat{S}_x \\ \hat{C} &= \Omega(t)\hat{S}_y \ . \end{aligned} \tag{32}$$

This operator basis set $\vec{v} = \{\hat{H}, \hat{L}, \hat{C}\}^T$, completely defines the state of the working medium (cf. Appendix A)

$$\hat{\rho} = \frac{1}{2}\hat{I} + \frac{2}{(\hbar\Omega)^2}\left(\langle\hat{H}\rangle\hat{H} + \langle\hat{L}\rangle\hat{L} + \langle\hat{C}\rangle\hat{C}\right) \ , \tag{33}$$

which rotates with respect to the static polarization basis set Equation (4). The advantage of such a representation is the straightforward thermodynamic interpretation, where the energy, $\mathcal{E} = \langle\hat{H}\rangle$, and coherence

$$\mathfrak{C} = \frac{1}{\hbar\Omega}\sqrt{\langle\hat{L}\rangle^2 + \langle\hat{C}\rangle^2} \ , \tag{34}$$

have a simple geometric interpretation in the parameter space $\{\hat{H}, \hat{L}, \hat{C}\}$. The coherence measure $\mathfrak{C}$ can be viewed as the distance of the state from a dephased state, diagonal in the energy representation. $\mathfrak{C}$ serves as a quantifier of coherence similar to the divergence introduced in Equation (10) [54].

The cost of generating coherence can be evaluated by recalling two invariants of the unitary dynamics: the Casimir and the Casimir companion [77]. For the $SU(2)$ algebra in the $\vec{v}$ basis, the Casimir Companion obtains the simple form

$$\bar{X} = \frac{1}{(\hbar\Omega)^2}\left(\langle\hat{H}\rangle^2 + \langle\hat{L}\rangle^2 + \langle\hat{C}\rangle^2\right) \ , \tag{35}$$

and the Casimir is obtained by replacing the squares of expectation values by the expectation values of the squares, i.e., $\langle\hat{H}\rangle^2 \to \langle\hat{H}^2\rangle$, $\langle\hat{L}\rangle^2 \to \langle\hat{L}^2\rangle$, and $\langle\hat{C}\rangle^2 \to \langle\hat{C}^2\rangle$. One consequence of the invariance of $\bar{X}$ is the conservation of the polarization amplitude along a unitary (isolated) stroke. Thus, starting from an initial equilibrium state with polarization $\bar{S}_i$, the Casimir companion throughout the stroke becomes $\bar{X} = \bar{S}_i$ and the initial energy is $\langle\hat{H}\rangle_i = \Omega_i\bar{S}_i$. This implies that the final energy of the unitary stroke is of the form

$$\langle\hat{H}\rangle_f = \sqrt{\left(\frac{\Omega_f}{\Omega_i}\right)^2\langle\hat{H}_i\rangle^2 - \left(\hbar\Omega_f\mathfrak{C}_f\right)^2} \approx \frac{\Omega_f}{\Omega_i}\langle\hat{H}_i\rangle - \frac{\hbar^2\Omega_i\Omega_f}{2\langle\hat{H}_i\rangle}\mathfrak{C}_f^2 \ , \tag{36}$$

where the RHS is obtained in the limit of small coherence. This relation allows identifying the quantum adiabatic energy (first term on the RHS) corresponding to the optimal process, and an additional coherence $\mathcal{W}_{fric} \equiv |\mathcal{W} - \mathcal{W}_{ideal}| \approx \frac{\hbar^2\Omega_i\Omega_f}{2\langle\hat{H}_i\rangle}\mathfrak{C}_f^2$, which arises from the non-adiabatic dynamics. $\mathcal{W}_{fric}$ equals the extra work that is required to generate coherence.

We will now demonstrate that rapid unitary strokes lead to generation of coherence. Employing Equation (2), we can obtain the Heisenberg equation of motion for the unitary strokes:

$$\frac{1}{\Omega}\frac{d}{dt}\begin{pmatrix}\hat{H}(t)\\ \hat{L}(t)\\ \hat{C}(t)\end{pmatrix} = \left(\begin{pmatrix}0 & \mu & 0\\ -\mu & 0 & 1\\ 0 & -1 & 0\end{pmatrix} + \frac{\dot{\Omega}}{\Omega^2}\hat{I}\right)\begin{pmatrix}\hat{H}(t)\\ \hat{L}(t)\\ \hat{C}(t)\end{pmatrix} \ , \tag{37}$$

where

$$\mu = \frac{\dot{\omega}\epsilon - \omega\dot{\epsilon}}{\Omega^3} \tag{38}$$

is the adiabatic parameter.

Finite-time processes require $\mu \neq 0$, and, in the limit $\mu \to 0$, we recover the adiabatic solutions. The exact relation between the stroke duration τ_{uni} and μ depends on the protocol. Generally, it can be expressed as

$$\mu = \frac{K}{\tau_{uni}} \tag{39}$$

where $K = \left(\frac{d\omega}{ds}\epsilon - \omega\frac{d\epsilon}{ds}\right)/\Omega^3$, with $s = t/\tau_{uni}$. For constant ϵ, K simplifies to $K = \frac{1}{\epsilon}(\frac{\omega_i}{\Omega_i} - \frac{\omega_f}{\Omega_f})$.

For protocols that keep $\mu =$ constant, Equation (37) can be integrated in order to obtain the dynamical propagator Λ_{uni}. In general, a driven system's propagator depends explicitly on two reference times, $t_{initial}$ and t_{final}. We assume that $t_{initial} = 0$ and, therefore, index the propagator only in terms of the final time. The propagator of the unitary stroke of a product form: $\Lambda_{uni}(t) = \mathcal{U}_1(t)\,\mathcal{U}_2(t)$, where $\mathcal{U}_1(t)$ is a scaling by the compression ratio

$$\mathcal{U}_1(t) = \mathcal{C}\hat{I} = \frac{\Omega(t)}{\Omega(0)}\hat{I} \tag{40}$$

and $\mathcal{U}_2(t)$ represents the dynamical map of the polarization. In the $\{\hat{H}, \hat{L}, \hat{C}\}$ operator basis

$$\mathcal{U}_2(t) = \frac{1}{\kappa^2}\begin{pmatrix}1+\mu^2 c & \kappa\mu s & \mu(1-c)\\ -\kappa\mu s & \kappa^2 c & \kappa s\\ \mu(1-c) & -\kappa s & \mu^2 + c\end{pmatrix} \ , \tag{41}$$

where $\kappa = \sqrt{1+\mu^2}$ and $s = \sin(\kappa\theta)$, $c = \cos(\kappa\theta)$ and $\theta(t) = \int_0^t \Omega(t')dt'$.

Accelerating the driving increases μ, which, in turn, increases the coupling of the Hamiltonian $\hat{H}$ and coherence related operators $\hat{L}$ and $\hat{C}$. Therefore, rapid driving transforms energy to coherence. The constancy of the Casimir companion Equation (35) implies that, when the final state exhibits coherence, the work extraction relative to the equivalent adiabatic procedure is degraded.

4.1. Slow Driving Regime

We can use Equation (41) to estimate the additional fraction of work during the unitary strokes due to the finite-time operation. Assuming slow driving ($\mu \ll 1$ or long stroke duration), we expand $\mathcal{U}_2$ up to second order in the adiabatic parameter μ in order to obtain

$$\frac{\mathcal{W}_{fric}}{\mathcal{W}} \approx \mu^2 \ . \tag{42}$$

This expression relates the ratio of the additional work that is consumed due to friction, Equation (36), and the total work $\mathcal{W}$, to the adiabatic parameter. Hence, in the slow driving regime, speeding up the stroke requires additional work. The corresponding work cost for coherence generation is in accordance with the notion of geometric thermodynamic distance and the low dissipation limit [60,78]. When the dissipation becomes significant, the power loss can exceed the gain, which imposes a minimum stroke duration for engine operation.

4.2. Sudden Limit

In the opposite driving regime, including a sudden modulation of the driving parameters, the dynamical propagator is obtained by employing the sudden approximation [57]. The propagator in the sudden limit, $\tau_{uni} \to 0$, is given by

$$\Lambda_{i\to f}^{sudd} = \frac{\Omega_f}{\Omega_i}\begin{pmatrix} \cos(\Phi) & \sin(\Phi) & 0 \\ \sin(\Phi) & -\cos(\Phi) & 0 \\ 0 & 0 & 1 \end{pmatrix} \ , \tag{43}$$

where $\Phi = \Phi_f - \Phi_i$ is the angle of rotation between the initial and final polarizations and $\Phi = \arccos(\omega/\Omega)$. In the sudden limit, the work becomes

$$\mathcal{W} = \langle \hat{H}(0) \rangle \left(\frac{\Omega_f}{\Omega_i}\cos(\Phi) - 1 \right) \ , \tag{44}$$

and the ratio between the frictional and total work is

$$\left| \frac{\mathcal{W}_{fric}}{\mathcal{W}} \right| = \frac{1-\cos(\Phi)}{|\cos(\Phi) - \left(\Omega_i/\Omega_f\right)|} \ . \tag{45}$$

The frictional work dissipates during the open stroke (isotherm or isochore) that takes place after the unitary stroke. For a compression protocol ($\Omega_f > \Omega_i$), the ratio can diverge, since the work may vanish when $\cos(\Phi) = \Omega_i/\Omega_f$. In contrast, during an expansion process the ratio is bounded by $\frac{2\Omega_f}{\Omega_i+\Omega_f}$.

4.3. Shortcuts to Adiabaticity

The argument that fast dynamics on the adiabats generates coherence and leads to friction like phenomena [51,76] has a loophole. The unitary dynamics on the adiabats is in principle reversible. Because the dissipation of coherence, which seals the loss, does not take place until the thermalization stroke that follows the adiabatic stroke, protocols that null the coherence at the end of the adiabat will be frictionless.

Examining Equation (41), we find that solutions for which $\cos(\theta_f) = 1$ are frictionless. These solutions impose a quantization rule on μ:

$$\mu_l = \frac{1}{\sqrt{\left(\frac{2\pi l}{\Phi}\right)^2 - 1}} \quad , \; l = 1, 2, ... \tag{46}$$

where we used the identity $\theta = -\Phi/\mu$ (The identity is derived by substituting Equation (62) into the expression for μ, rearranging the equation and integrating). The relation between μ and the stroke duration leads to the minimum constant μ frictionless stroke duration

$$\tau_{uni}(l = 1) = K\sqrt{\left(\frac{2\pi}{\Phi}\right)^2 - 1} \; . \tag{47}$$

Adiabatic trajectories that begin and end with no coherence are frictionless (cf. Figure 5). In the limit of small and constant ϵ we get $\tau_{uni}(l = 1) \propto \epsilon(\frac{1}{\omega_f^2} - \frac{1}{\omega_i^2})$. These frictionless protocols are termed shortcuts to adiabaticity (STA) [79,80]. At intermediate times coherence is generated that requires extra work, but, if there is no dissipation in the drive, then this coherence is converted back by the working medium, arriving at the final target with no coherence. The associated speedup [79,80] may come with an accompanying cost if the control is prone to additional dissipation. Here, we consider the ideal case, assuming no dissipation and view the temporary investment of energy as a catalytic process since this energy can in principle be recouped [81]. An opposite viewpoint considers the average energy, stored during the shortcut, as wasted work [82–85].

Can the protocol duration be shortened further while keeping the frequency between its initial and final values? This is a problem in the framework of quantum control, a field which governs tasks related to manipulation of quantum systems by external fields under defined restrictions. The present control task is to transfer an initial thermal state $\hat{\rho}_i = \frac{1}{Z}e^{-\hat{H}_i/k_BT}$ to a final thermal state $\hat{\rho}_f = \frac{1}{Z}e^{-\hat{H}_f/k_BT'}$ as fast as possible on the unitary strokes of the cycle. Optimal control theory has been applied to address this task [86], obtaining the minimum time solution, a so-called Fastest Effectively Adiabatic Transition (FEAT) [87]. The task of minimizing the time can be reduced to minimize $\int \hat{S}_z d\hat{S}_x$ while following the dynamics generated by Equation (2), which here gives

$$\frac{d\hat{S}_z}{d\hat{S}_x} = -\frac{\omega}{\epsilon} \; . \tag{48}$$

For fixed ϵ and for ω in the range $\omega_i < \omega(t) < \omega_f$, the geometric solution is to keep the curve as close to the $\hat{S}_x$ axis as possible until the last moment to reach the final state, at which time the solution switches to the steepest curve possible [86]. Thus, the solution is of the bang-bang type, switching from the initial $\omega = \omega_i$ to the final $\omega = \omega_f$ to get the process started, keeping $\omega(t) = \omega_f$ for time $0 \leq t < \tau_1$, switching back to $\omega(t) = \omega_i$ for a time $\tau_1 \leq t < \tau_1 + \tau_2$, and finally switching to $\omega(\tau_1 + \tau_2) = \omega_f$ to reach the final state. The resulting two line segment trajectory is shown in Figure 5. The coherence that us generated during this protocol can be seen as the distance from the purple quarter-circle of zero coherence. The total FEAT time reads

$$\tau_{uni}(opt) = \tau_1 + \tau_2 = \left(\frac{1}{2\Omega_i} + \frac{1}{2\Omega_f}\right)\arccos(\zeta) \tag{49}$$

where $\zeta = \frac{\Omega_i\Omega_f(\epsilon^2+\omega_i\omega_f)-(\epsilon^2+\omega_i\omega_f)^2}{\epsilon^2(\omega_i-\omega_f)^2}$. While the FEAT time is much shorter than the time for a constant μ protocol, $\tau_{uni}(opt) < \tau_{uni}(l = 1)$, the FEAT solution does pay a significantly higher price in intermediate coherence.

Additional insight can be obtained by adding another control operator; a counter-diabatic term [85,88] with the control function $v(t)$ to the Hamiltonian Equation (2)

$$\hat{H}_{CA} = v(t)\hat{S}_y \ . \tag{50}$$

This term generates a rotation around the y axis in the z, x plane that can rotate the initial to the final Hamiltonian in a rate depending on the frequency $v(t)$. If $v(0) = v(t_f) = 0$ energy is only stored temporarily in the counter-diabatic drive, which classifies it as a catalyst.

The stroke duration τ_{uni} can be geometrically bound by the quantum speed limit [36–38,83]. The task is a rotation of the state by an angle Φ on the y axis. In the counter adiabatic case Equation (50) the angle Φ is related to the action $\int v(t)dt$, which can be related to the average stored energy $\bar{E}$ [83]; therefore, $\tau_{uni} > \Phi\hbar/\bar{E}$ which becomes $\tau_{uni} < \Phi/\bar{v}$. In other STA protocols where the Hamiltonian does not contain $\hat{S}_y$, the control action of rotation is obtained by the commutator $[\hat{S}_z, \hat{S}_x]$, which generates coherence. A bound can be obtained from (49), $\tau_{uni} > \Phi\hbar/\Delta E = \Phi/\Omega_{min}$, where $\hbar\Omega_{min}$ is the minimum energy gap.

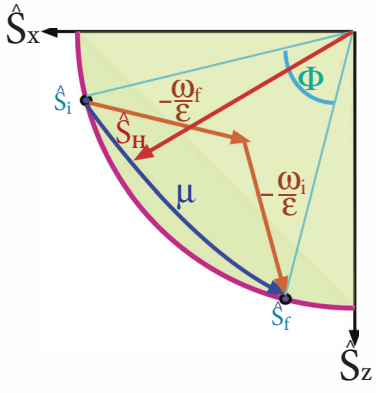

Figure 5. Optimal frictionless trajectories for the unitary stroke displayed on the polarization axis of $\langle\hat{S}_x\rangle$ and $\langle\hat{S}_z\rangle$. The radius of the semicircle is equivalent to the initial polarization $\bar{S}_i = \bar{S}_{H_i}$, which is on the energy axis. Because the unitary dynamics preserves the polarization and the chosen energy direction is on the x, z plane, the semicircle shows all the possible states on the energy axis. Any interior point possesses coherence. In orange is the optimal bang-bang protocol that is composed of two segments the first with a slope of $-\omega_f/\epsilon$ and the second $-\omega_i/\epsilon$. The blue arrow represents the constant μ protocol.

To summarize, fast frictionless protocols for the unitary strokes are possible provided the coherence is not transferred to the thermalization strokes. The price for acceleration of the stroke is the generation of intermediate coherence that requires a temporary investment of power. If no restrictions are imposed on the power invested, or analogously on the range of $\omega\,(t)$, the time period τ_{uni} can be shrunk to zero. Another scheme to achieve a vanishing time period includes adding an unrestricted counter-diabatic term, Equation (50), to the Hamiltonian [85]. For a more realistic description of the storage device, restriction on the control are introduced. One possible restriction is to limit the averaged stored energy. Another possibility is to restrict coherence. In principle, all of the temporary power can be retrieved in the external controller when the drive is completely isolated. However, in practice, this is an idealization, and any real storage device is sure to have some dissipation. Thus, one expects some dissipation from the controller [89].

5. Thermalization

Thermalization is the process of relaxing the system toward equilibrium with an external heat reservoir, e.g., the hot or cold baths. The relaxation is mediated by the system-bath interaction term $\hat{H}_{s-h/c}$ (Equation (11)), which generally depends on both the system and bath operators, as well as the coupling strength g. The question arises, can we actively influence the thermalization process? Three options for control are possible. The first, which we consider here, is to control the system Hamiltonian [90,91], the second is to vary the coupling strength [92,93], and the third is controlling the temperature of the bath.

5.1. Isochoric Thermalization

When compared to quantum Carnot-type cycles the analysis of the quantum Otto cycle is simplified, since the thermalization strokes are carried out at constant frequency Ω. For this reason, it is has been thoroughly studied, and originally constituted the main platform to investigate thermodynamics at the quantum level [94,95].

By definition, during an isochore the Hamiltonian is static. Consequently, the only adjustable control parameter of the thermalization is the contact time with the bath. This is equivalent to adjusting the system bath coupling. The dynamics along the stroke is described by Equations (14) and (15) with a constant Hamiltonian. These lead to transfer of energy and exponential decay of coherence, Equation (21), until the system reaches equilibrium.

5.2. Isothermal Thermalization

Here, we concentrate on the finite-time thermalization strokes, which transfer heat to and from the engine. Within the limits that are imposed by the isotherms of the working medium, we can find various choices for cycles with finite power [96–98].

Thermalization can be controlled by the varyingHamiltonian, while the system is simultaneously coupled to the bath. We now consider the general case, where the Hamiltonian does not commute with itself at different times, $[\hat{H}(t), \hat{H}(t')] \neq 0$. A prerequisite for obtaining control is to derive a dynamical description that is accurate and consistent with thermodynamics. Such a dynamical description has been formulated in Ref. [34], where a Non-Adiabatic Master Equation (NAME) was developed that incorporated the effect of the external driving.

Within this framework, we can address the issue of actively speeding up the thermalization. Typically, the rate of approaching equilibrium is proportional to deviation of the state from the fixed point of equilibrium. As we get closer to the target, the rate decreases. Broadly speaking, the strategy of speeding up the thermalization is to first generate coherence that moves the system away from the instantaneous attractor. Consequently, the relaxation is enhanced. At the final stage the system is rotated, converting the coherence to energy to reach the desired thermal state. The speedup comes with a price since, in contrast to the unitary strokes, during the open strokes we cannot separate the unitary drive from the dissipative loss.

5.3. Shortcut to Equilibrium Protocols

Shortcut to equilibrium protocols (STE) are active control protocols, generating a rapid transition between two equilibrium states with different Hamiltonians, while the system is coupled to a bath of a fixed temperature. This control task requires modifying the system entropy, in contrast to the common scheme of unitary control. The shortcut protocols fall within the framework of control of open quantum systems. The rules of the game that we consider restrict the active control to only the system Hamiltonian. The bath Hamiltonian is set and cannot be controlled, and the bath remains in a thermal state due to its enormous size and negligible influence of the qubit.

In the presence of non-adiabatic driving, the external field dresses the system, which consequently effectively modifies the system-bath interaction. As a result, the external driving enables indirect

coherent control of the system's dissipative dynamics. As previously stated, the control of the qubit state during the isothermal strokes requires prior knowledge of the open system dynamics. In turn, to describe the reduced dynamics of the open system, one first requires a closed form solution of the driven isolated system. To be specific, the derivation of the Non-Adiabatic Master Equation (NAME) requires, as an input, the free dynamics of the driven system [34]. The solution is non-trivial in the presence of non-adiabatic driving, when the Hamiltonian does not commute with itself at different times. For arbitrary driving, constructing an explicit solution of the dynamical propagator requires a time-ordering procedure [57].

We have developed an algebraic procedure in order to circumvent the time-ordering problem by employing a dynamical operator basis. This technique is closely related to the inertial theorem [99]. The theorem implies that, for a closed operator algebra, the dynamical propagator can be obtained for a family of non-adiabatic protocols, characterized by a slow 'acceleration' of the drive. The associated solutions and driving protocols are termed inertial solutions and protocols. These solutions are conveniently expressed as linear combinations of the eigenoperators of the propagator.

For the qubit working medium, as represented by Equation (2), the inertial protocol is characterized by a slowly varying adiabatic parameter, i.e., $\frac{1}{\Omega}\frac{d\mu}{dt} \ll 1$. Under this condition, the dynamics approximately follows the inertial solution. This solution is conveniently expressed in terms of the dynamics of the basis of operators $\vec{v}\left(t\right) = \{\hat{H}, \hat{L}, \hat{C}\}^T$ Equation (32)

$$\vec{v}\left(t\right) = \frac{\Omega\left(t\right)}{\Omega\left(0\right)} P\left(\mu\left(t\right)\right) e^{-i\int_0^t D(t')\Omega(t')dt'} P^{-1}\left(\mu\left(t\right)\right) \vec{v}\left(0\right) \quad , \tag{51}$$

where P is a 3 by 3 matrix that is dependent on the instantaneous adiabatic parameter $\mu\left(t\right)$, see Appendix B, and $D = \mathrm{diag}\left(0, \kappa, -\kappa\right)$ with $\kappa = \sqrt{1+\mu^2}$. The three operators obtained from $\left(\hbar\Omega\left(t\right)\right)^{-1} P^{-1}\vec{v}\left(t\right)$ are eigenoperators of the propagator. We introduce a scaled version of these operators $\vec{g} = \{\hat{\chi}, \hat{\sigma}, \hat{\sigma}^\dagger\}^T$, satisfying an eigenvalue type relation $\hat{\sigma}^H\left(t\right) = \hat{U}^\dagger\left(t\right)\hat{\sigma}\left(0\right)\hat{U}\left(t\right) = e^{-i\int_0^t dt'\kappa(t')\Omega(t')}\hat{\sigma}\left(0\right)$, where $\hat{U}\left(t\right)$ is the propagator and superscript H designates operators in the Heisenberg picture. The operator $\hat{\chi}^H\left(t\right) = \hat{\chi}\left(0\right)$ is the inertial invariant, i.e., the eigenoperator with a vanishing eigenvalue. Expressing the eigenoperators in terms of the $\{\hat{H}, \hat{L}, \hat{C}\}$ basis, we obtain

$$\begin{aligned} \hat{\chi}\left(t\right) &= \frac{\sqrt{2}}{\kappa\hbar\Omega}\left(\hat{H} + \mu\hat{C}\right) \\ \hat{\sigma}\left(t\right) &= \frac{1}{\kappa\hbar\Omega}\left(-\mu\hat{H} - i\kappa\hat{L} + \hat{C}\right) \quad , \end{aligned} \tag{52}$$

where all of the parameters may be time-dependent. The eigenoperators in $\vec{g}$ are orthonormal with respect to the inner product in Liouville space, $\left(\hat{A}, \hat{B}\right) = \mathrm{tr}\{\hat{A}^\dagger\hat{B}\}$, and satisfy the $SU(2)$ commutation relations of the form $\left[\hat{\sigma}, \hat{\sigma}^\dagger\right] = -\sqrt{2}\hat{\chi}$, $\left[\hat{\chi}, \hat{\sigma}\right] = -\sqrt{2}\hat{\sigma}$. Appendix A summarizes the relation between the various basis sets of expansion operators $\vec{s} = \{\hat{S}_x, \hat{S}_y, \hat{S}_z\}^T$, $\vec{v} = \{\hat{H}, \hat{L}, \hat{C}\}^T$ and $\vec{g} = \{\hat{\chi}, \hat{\sigma}, \hat{\sigma}^\dagger\}$, see also Figure 1 for a geometric representation.

Combining the inertial solution, Equation (51), for the isolated system dynamics with the NAME leads to a master equation for a broad range of driving protocols. The master equation is valid from the first principles under the following conditions: (i) the bath dynamics are rapid relative to the typical timescales of both the system and the driving, τ_s and τ_d, i.e., $\tau_b \ll \tau_s, \tau_d$, where τ_b is the typical timescale of the decay of correlations in the bath; (ii) the system-bath relaxation time τ_r is large relative to the system and bath timescales, i.e., $\tau_r \gg \tau_s, \tau_b$; and, (iii) the driving protocol satisfies the inertial condition, $\frac{1}{\Omega}\frac{d\mu}{dt} \ll 1$. Condition (i) is associated with Markovian dynamics and (ii) corresponds to a weak system-bath interaction, which is also known as the weak coupling limit [13,56].

In the interaction picture relative to the system-bath bare Hamiltonian, the qubit's open system dynamics obtains the familiar GKLS form [91]

$$\frac{d}{dt}\tilde{\rho} = \tilde{\mathcal{L}}(t)[\tilde{\rho}] = k_{\downarrow}(\alpha(t))\left(\hat{\sigma}\tilde{\rho}(t)\hat{\sigma}^{\dagger} - \frac{1}{2}\{\hat{\sigma}^{\dagger}\hat{\sigma}, \tilde{\rho}(t)\}\right) + k_{\uparrow}(\alpha(t))\left(\hat{\sigma}^{\dagger}\tilde{\rho}(t)\hat{\sigma} - \frac{1}{2}\{\hat{\sigma}\hat{\sigma}^{\dagger}, \tilde{\rho}(t)\}\right) \quad . \tag{53}$$

Here, $\hat{\sigma}$ and $\hat{\sigma}^{\dagger}$ designate operators at initial time and overscript tilde denotes operators in the interaction picture. The kinetic coefficients of Equation (53) depend on the spectral features of the bath and the effective time-dependent frequency α. This frequency serves as an effective generalized Rabi frequency of the driven system

$$\alpha(t) = \kappa(t)\,\Omega(t) \quad = \sqrt{1+\mu(t)^2}\;\Omega(t) \quad . \tag{54}$$

In the quantum adiabatic regime, $\mu \to 0$ and α converges to the instantaneous Rabi frequency, $\Omega(t)$. For $\mu > 0$, the effective frequency $\alpha(t) > \Omega(t)$. This is the outcome of an effective dressing of the system by the driving. As a consequence of the rapid driving, the bath interacts with the dressed system, which leads to deviations from the adiabatic dynamics. For the general case, there may be multiple effective frequencies $\{\alpha\}$. Their exact form depends on a particular system-bath interaction and the defined spectral density [34,91].

For the present analysis, we assume a bosonic bath with an Ohmic spectral density. The system-bath interaction is taken as $\hat{H}_{sb} = ig\sum_k \sqrt{\frac{2\pi\omega_k}{V\hbar}}\left(\hat{b}_k - \hat{b}_k^{\dagger}\right)\hat{S}_y$, where $\hat{b}_k^{\dagger}$ and $\hat{b}_k$ are the creation and annihilation operators of the k'th bath oscillator, and ω_k is the oscillator frequency. The coupling strength is represented by g and V is the reservoir size. For a large reservoir in equilibrium, the kinetic coefficients become

$$\begin{aligned} k_{\downarrow}(\alpha) &= \frac{g^2\alpha}{\hbar c\kappa}(1+N(\alpha)) \\ k_{\uparrow}(\alpha) &= \frac{g^2\alpha}{\hbar c\kappa}N(\alpha) \quad . \end{aligned} \tag{55}$$

where c is the speed of event propagation in the bath and $N(\alpha) = 1/(\exp(\hbar\alpha/k_BT) - 1)$ is the Bose–Einstein distribution, characterizing the correlations between bath modes at frequency α. It is simple to verify that these kinetic coefficients satisfy detailed balance with respect to α, Equation (16). This property is essential for a thermodynamically consistent dynamical description [12,35]. In the adiabatic limit, the kinetic coefficients converge to adiabatic rates and the Lindbald jump operators to the creation annihilation operators of the two-level system. As expected, Equation (53) then converges to the adiabatic master equation [33].

The NAME of the driven qubit, Equation (53) propagates the qubit state in the direction of the instantaneous attractor. The attractor is defined by the relation

$$\mathcal{L}(t)[\tilde{\rho}_{i.a}] = \tilde{\rho}_{i.a} \quad , \tag{56}$$

where $\tilde{\mathcal{L}}(t)$ is a superoperator that generates the dynamics in the interaction picture. For the qubit, the attractor is in the direction of $\hat{\chi}$, mixing energy, and coherence. The attractor is rotated by the angle $\xi = \arccos(1/\sqrt{1+\mu^2})$ from the energy axis. The attractor can be expressed in the Gibbs form:

$$\tilde{\rho}_{i.a}(t) = Z^{-1}e^{-\frac{\hbar\alpha\hat{\chi}}{\sqrt{2}k_BT}} \quad , \tag{57}$$

where $Z = \mathrm{tr}\left(e^{-\hbar\alpha\hat{\chi}/\sqrt{2}k_BT}\right)$ is the partition function. In the presence of driving, the attractor varies in time, and the system continuously aspires towards a changing target, but it does not manage to reach it. Only at the initial and final times, is the driving stationary and the qubit reaches the attractor. Remember that this analysis applies for the case when $\left[\hat{H}(t), \hat{H}(t')\right] \neq 0$. When the

Hamiltonian commutes with itself at different times, as in the elementary Hamiltonian Equation (12), the instantaneous attractor becomes a Gibbs state with the instantaneous Hamiltonian $\hat{H}(t)$ and temperature T. In the adiabatic limit, when $\mu \to 0$ Equations (52), (54) and (57) lead to the same result.

The qubit control is based on the master equation, Equation (53). Our present control target is to speed up the thermalization while changing the qubit Hamiltonian. This step will be employed in the open strokes of Carnot-type engines in Section 6. Specifically, we desire a control protocol that transfers an initial Gibbs state, defined by $\Omega(0) = \Omega_i$ and temperature T, to a final Gibbs state of the same temperature and final frequency $\Omega\left(t_f\right) = \Omega_f$. Moreover, we assume that the system at the initial and final times is stationary with no external driving. The control agents are the parameters of the free Hamiltonian $\omega(t)$ and $\varepsilon(t)$. Notice that these parameters only indirectly effect the master equation. To find a control, we opt to employ a reverse engineering approach, in which we propose a trajectory for the qubit state that forms a solution to the master equation. In turn, this solution determines the kinetic coefficients of the master equation, from which we can extract the direct control parameters.

Performing the analysis in the interaction representation relative to the bare system Hamiltonian simplifies the control scheme. In this frame, the Lindblad jump operators, $\hat{\sigma}$ and $\hat{\sigma}^{\dagger}$, vary slowly with μ.

The control trajectory, which is a dynamical solution of Equation (53), is obtained by representing the state $\tilde{\rho}$ in terms of the basis of eigenoperators $\vec{g}$ of the free dynamics, Appendix A:

$$\tilde{\rho} = \frac{1}{2}\hat{I} + c_{\sigma}\hat{\sigma} + c_{\sigma^{\dagger}}\hat{\sigma}^{\dagger} + c_{\chi}\hat{\chi} \ , \tag{58}$$

where $c_r = \mathrm{tr}\left(\hat{r}\tilde{\rho}\right)$, with $r = \sigma, \sigma^{\dagger}, \chi$, are time-dependent coefficients. Substituting Equation (58) into (53) and utilizing the orthogonality of the eigenoperators leads to an equivalent representation of the dynamics

$$\frac{d}{dt}c_{\chi} = -\left(k_{\downarrow}(t) + k_{\uparrow}(t)\right)c_{\chi} - \frac{1}{\sqrt{2}}\left(k_{\downarrow}(t) - k_{\uparrow}(t)\right) \tag{59}$$

$$\frac{d}{dt}c_{\sigma} = -\frac{1}{2}\left(k_{\downarrow}(t) + k_{\uparrow}(t)\right)c_{\sigma} \ . \tag{60}$$

and similarly for $c_{\sigma^{\dagger}}$. These equations completely determine the system dynamics and form the template for coherent control. What is missing are the boundary conditions. The choice of the initial and final Gibbs state along with the condition of stationarity at initial and final times imposes boundary conditions on Equation (60).

We can simplify the problem by eliminating Equation (60). For the boundary conditions (and any initial diagonal state in the energy representation), the coefficients $c_{\sigma}(0) = c_{\sigma^{\dagger}}(0) = 0$ and $\mu = 0$. These relations, together with Equation (60), imply that c_{σ} and $c_{\sigma^{\dagger}}$ vanish at all times.

We can now focus on a single equation, Equation (59), with boundary conditions: $c_{\chi}(0) = -\frac{1}{\sqrt{2}}\tanh\left(\frac{\hbar\Omega(0)}{2k_BT}\right)$, $c_{\chi}\left(t_f\right) = -\frac{1}{\sqrt{2}}\tanh\left(\frac{\hbar\Omega\left(t_f\right)}{2k_BT}\right)$, and $\mu(0) = \mu\left(t_f\right) = 0$. In addition, the initial and final states and Equation (59) imply that $\dot{c}_{\chi}(0) = \dot{c}_{\chi}\left(t_f\right) = 0$.

To proceed, we determine the trajectory solution through the coefficient c_{χ}. We choose the most simple polynomial solution that is compatible with the boundary conditions. In this case, a third order polynomial is sufficient. In terms of a dimensionless parameter $s = t/t_f$, the solution reads

$$c_{\chi}(s) = c_{\chi}(0) + 3\Delta s^2 - 2\Delta s^3 \ , \tag{61}$$

where $\Delta = c_{\chi}\left(t_f\right) - c_{\chi}(0)$. Next, we substitute the solution Equation (61) into Equation (59) and obtain the kinetic coefficients, from which we can extract $\alpha(t)$, Equation (55). These steps are achieved while utilizing a common numerical solver.

The control function $\Omega(t)$ is now evaluated by solving the master equation $\Omega = \alpha/\kappa$ for a set of defined controlled parameters $\omega(t)$ and $\epsilon(t)$. In practice, the master equation depends on the

generalized Rabi frequency $\Omega(t)$ and $\dot{\phi}$ (through μ); this means that we have an additional freedom in the control parameters of the Hamiltonian.

We chose to parameterize the control parameters in terms of the time-dependent frequency Ω and the phase ϕ:

$$\begin{aligned} \omega(t) &= \Omega\cos(\phi) \\ \epsilon(t) &= \Omega\sin(\phi) \quad . \end{aligned} \tag{62}$$

In this parametrization, the adiabatic parameter becomes $\mu = -\dot{\phi}/\Omega$ and the effective frequency can then be expressed as

$$\alpha = \sqrt{1+(\dot{\phi}/\Omega)^2}\Omega \ . \tag{63}$$

To set the angle ϕ, we study two protocols that differ by their boundary conditions. The first is a quadratic function of time $\phi(t) = a\left(t - 2t^2/3t_f\right)$, where is a a dimensionless free parameter taken to be equal to the numerical value of $1/t_f^2$ in the model units. This protocol leads to a final value for the angle that scales with the duration time $\phi\left(t_f\right) \propto t_f$. The second protocol starts at $\phi(0) = 0$ and ends at $\phi\left(t_f\right) = \pi/2$, where the direction of the final Hamiltonian is rotated by ninety degrees relative to the initial Hamiltonian. Introducing a polynomial that complies with the boundary conditions leads to $\phi(t) = \pi t^2\left(3t_f - 2t\right)/\left(6t_f^3\right)$. Both of the protocols satisfy the required condition of stationarity at initial and final times: $\dot{\phi}(0) = \dot{\phi}\left(t_f\right) = 0$. Finally, solving Equation (63) for $\Omega(t)$ leads to the control protocol.

Overall, the constructed shortcut to equilibration (STE) protocol rapidly modifies the system entropy, transferring an initial thermal state with a Rabi frequency Ω_i to a thermal state of a frequency Ω_f at the same temperature. In Ref. [91], a different STE protocol has been introduced, utilizing a product state consisting of exponentials, see Appendix A. In contrast, here we choose a linear combination of eigenoperators, Equation (58), which is the natural approach for a system that is described by a compact algebra. This choice has the advantage of leading to a simpler analysis.

5.4. Thermodynamic Cost of Finite-Time Thermalization

Fast driving moves the system away from equilibrium, leading to enhanced dissipation. The thermodynamic cost can be characterized by the entropy production rate

$$\Sigma^u \equiv -\frac{d}{dt}\mathcal{D}\left(\hat{\rho}|\hat{\rho}_{i.a}\right) = -k_B\mathrm{tr}\left(\tilde{\mathcal{L}}\left[\tilde{\rho}\right]\ln\tilde{\rho}\right) + k_B tr\left(\tilde{\mathcal{L}}\left[\tilde{\rho}\right]\ln\tilde{\rho}_{i.a}\right) = -k_B\mathrm{tr}\left(\tilde{\mathcal{L}}\left[\tilde{\rho}\right]\left(\ln\tilde{\rho} + \frac{\hbar\alpha}{\sqrt{2}T}\hat{\chi}\right)\right) \ . \tag{64}$$

In the infinitely long time limit, the state $\tilde{\rho}$ converges to $\tilde{\rho}_{i.a}$ and the entropy production rate vanishes. The entropy production in this limit has been studied recently [100] and is related to fluctuation theorems.

During the shortcut to equilibrium protocols $c_{\sigma,\sigma^\dagger} = 0$ and the state is completely characterized by the expectation value $c_\chi = \mathrm{tr}\left(\hat{\chi}\tilde{\rho}\right)$, $\tilde{\rho} = \frac{1}{2}I + c_\chi\hat{\chi}$. Alternatively, this state can be represented in a Gibbs form $\tilde{\rho} = Z^{-1}e^{-\beta\hat{\chi}}$. The role of β motivates introducing an effective temperature of the qubit in the interaction representation: $T' \equiv \hbar\alpha/\sqrt{2}k_B\beta$. Such a form allows for a straightforward interpretation of Equation (64); this is achieved by the following derivation. We begin by utilizing the Gibbs form of $\tilde{\rho}$ and insert Equation (57) into (64) to obtain

$$\Sigma_\chi^u = k_B\left(\frac{1}{T'} - \frac{1}{T}\right)\left(\frac{\hbar\alpha}{\sqrt{2}k_B}\right)tr\left(\dot{\tilde{\rho}}\chi\right) \quad . \tag{65}$$

This relation can be interpreted as the product of a thermodynamic force $\propto -\nabla\frac{1}{T}$ and heat current in units of the energy quanta $\hbar\alpha$. Next, we express $\tilde{\rho}$ in terms of β in order to obtain: $\dot{\tilde{\rho}} = -\left(\langle\hat{\chi}\rangle + 1\right)\dot{\beta}\tilde{\rho}$, with $\langle\hat{\chi}\rangle = -\frac{1}{\sqrt{2}}\tanh\left(\frac{\beta}{\sqrt{2}}\right)$, and

$$\dot{\beta} = \mathrm{tr}\left(\frac{d\tilde{\rho}}{dt}\tilde{\rho}^{-1}\hat{\chi}\right) = -\frac{1}{\sqrt{2}}\left[\left(1+e^{-\sqrt{2}\beta}\right)k_{\downarrow} - \left(1+e^{\sqrt{2}\beta}\right)k_{\uparrow}\right] \quad . \tag{66}$$

Substituting Equations (55), (66) into Equation (65) leads to the final expression

$$\Sigma^{u}_{\chi} = \left(\frac{1}{T'} - \frac{1}{T}\right)(\hbar\alpha)\,\frac{k_{\downarrow}(\alpha)\,\langle\hat{\chi}\rangle\left(\langle\hat{\chi}\rangle+1\right)}{2\left(1+e^{\hbar\alpha/k_BT'}\right)}\left(e^{-\hbar\alpha/k_BT'} - e^{-\hbar\alpha/k_BT}\right) \quad . \tag{67}$$

As expected, we obtain a positive entropy production. The first and last terms in the brackets have opposite signs while the expectation value of $\hat{\chi}$ satisfies $-1 < \langle\chi\rangle < 0$ for a positive temperature. This leads to a symmetric dependence on the temperature gap $\Delta T = T - T'$, i.e., the entropy production only depends on the magnitude of the gap and it is independent of whether the working medium effective temperature is hotter or colder relative to the bath temperature.

In the high temperature limit $\hbar\alpha/k_B \ll T, T'$, the relation can be further simplified, leading to entropy generation that scales as the square difference between inverse temperatures

$$\Sigma^{u}_{\chi} \approx -k_Bk_{\downarrow}\langle\chi\rangle\left(\frac{\hbar\alpha}{2k_B}\right)^2\left(\frac{1}{T'} - \frac{1}{T}\right)^2 \quad . \tag{68}$$

We next derive the entropy production rate for a general initial state that includes coherence, following the inertial solution, Equation (60). We begin by expressing the qubit state as a maximum entropy state $\tilde{\rho} = \bar{Z}^{-1}\exp\left(-\left(\bar{\beta}\hat{\chi} + \bar{\gamma}_x\hat{\sigma}_x + \bar{\gamma}_y\hat{\sigma}_y\right)\right)$, where $\sigma_x = \frac{1}{\sqrt{2}}\left(\sigma+\sigma^{\dagger}\right)$ and $\sigma_y = \frac{i}{\sqrt{2}}(\sigma-\sigma^{\dagger})$ see Appendix A for further details. The existence of such a form is guaranteed from the closure property of the operator algebra and the Baker–Campbell–Hausdorff formula [101]. Defining the effective thermodynamic forces $\mathcal{F}_l$ and effective "temperature": $\mathcal{F}_{\chi} = \frac{1}{T_{\chi}} - \frac{1}{T}$, where $T_{\chi} = \frac{\hbar\alpha}{\sqrt{2}k_B\bar{\beta}}$, $\mathcal{F}_{\sigma_x} = \frac{k_B\bar{\gamma}_x}{\hbar\alpha}$ and $\mathcal{F}_{\sigma_y} = \frac{k_B\bar{\gamma}_y}{\hbar\alpha}$ leads to the entropy production rate:

$$\Sigma^{u} = \sum_{l=\chi,\sigma_x,\sigma_y}\mathcal{F}_l\mathcal{J}_l \quad , \tag{69}$$

where $\mathcal{J}_l = \frac{\hbar\alpha}{\sqrt{2}}\mathrm{tr}\left(\dot{\tilde{\rho}}\hat{l}\right)$. We can further simplify the fluxes $\mathcal{J}_l$ by utilizing the linearity of the trace and the derivative operations and the dynamics of eigenoperators expectation values, as in Equation (60). This leads to

$$\mathcal{J}_{\chi} = -\frac{\hbar\alpha\Gamma}{\sqrt{2}}\left(\langle\hat{\chi}\rangle - \langle\hat{\chi}\rangle_{i.a}\right) \;\;;\;\; \mathcal{J}_{\sigma_x} = -\frac{\hbar\alpha\Gamma}{2}\langle\hat{\sigma}_x\rangle \;\;;\;\; \mathcal{J}_{\sigma_y} = -\frac{\hbar\alpha\Gamma}{2}\langle\hat{\sigma}_y\rangle \quad , \tag{70}$$

with $\Gamma = k_{\downarrow} + k_{\uparrow}$ and $\langle\hat{\chi}\rangle_{i.a} = -\frac{1}{\sqrt{2}}\tanh\left(\frac{\hbar\alpha}{2k_BT}\right)$. The form of the entropy production rate resembles the heat transfer entropy production law of classical non-equilibrium thermodynamics [102–104], but with a nonlinear relation between flux and force. The difference between the effective inverse temperature and bath temperature constitutes the thermodynamic forces, while $\mathcal{J}_l$ are the associated thermodynamic fluxes. The expression obtain a similar form, however, a fundamental difference between Equation (69) and the classical expression exists. In the classical expression the relations between the thermodynamic fluxes and forces is strictly phenomenological. Commonly, only the first order is considered and the fluxes are taken to be linear functions of the forces. For example, Fick's law for diffusion of matter relates the diffusion flux to the gradient in concentration, or Fourier's law for heat conduction relates the heat transport to the gradient of inverse temperature. In contrast,

the framework of open quantum systems, which we currently employ, allows for deriving the relation between thermodynamic fluxes and forces from a microscopic description.

In the high temperature limit when $\tilde{\beta}$ and $\tilde{\gamma}$ are small, we recover the linear response relation between fluxes and forces: $\mathcal{J}_\chi \approx L\mathcal{F}_\chi$, $\mathcal{J}_{\sigma_x} \approx L\mathcal{F}_{\sigma_x}$ and and $\mathcal{J}_{\sigma_y} \approx L\mathcal{F}_{\sigma_y}$, where $L = \frac{\Gamma}{k_B}\left(\frac{\hbar\alpha}{2}\right)^2$, see Appendix A for further details. As a result, the entropy production rate in the linear response region becomes

$$\Sigma^u = \sum_l L\mathcal{F}_l^2 \quad . \tag{71}$$

It should be noted that the diagonal Onsager matrix is a consequence of the fact that, in the interaction representation, the dynamics of the coherence are separated from χ. Once we rotate to the $\{\hat{H}, \hat{L}, \hat{C}\}$ basis we will get symmetric coupling elements between energy and coherence in the Onsager matrix. We stress that the current derivation, leading to the linear response result, is not based on the adiabatic assumption of a perturbation with respect to the Gibbs state [78].

Overall, in the general case, we observe three independent forces and fluxes that are responsible for entropy production, a heat flux, and two fluxes that are associated with loss of coherence.

6. Local Cycles

Closing the cycles requires concatenating the four strokes. We distinguish two families of cycles that differ by the coherence operation: global or local. In local cycles, the coherence vanishes on the four switching points between strokes. Global cycles, on the other hand, maintain coherence throughout the cycle and it will be treated in Section 7.

6.1. Local Otto Cycle

Local cycles are obtained by employing shortcuts to adiabaticity (STA) on the adiabats [105,106]. The chosen protocols are characterized by a minimum unitary stroke time $\tau_{uni}(l=1)$, which forces a finite optimum thermalization time. As a result, maximum power is obtained for a total finite cycle period [72], Figure 6 displays such a cycle.

Optimizing the thermalization period has been addressed in Ref. [63]. The main variable influencing the power output is the polarization difference $\bar{S}_2' - \bar{S}_1'$ (cf. Figure 4). Therefore, the gaps $|S_2 - S_2'|$ and $|S_1 - S_1'|$ are optimized in order to achieve finite heat transport. The described procedure leads to [63]

$$\bar{S}_2' - \bar{S}_1' = (\bar{S}_2 - \bar{S}_1)F(x,y) \ , \tag{72}$$

where $F(x,y) = \frac{(1-x)(1-y)}{1-xy}$, with $x = e^{-\Gamma_h \tau_h}$ and $y = e^{-\Gamma_c \tau_c}$. Here, τ_h and τ_c are the time allocation for thermalization. In addition, optimizing for $\Gamma_c = \Gamma_h$ leads to $\tau_h = \tau_c$. Optimizing for power under the constraint of a finite-time allocation during the unitary strokes, τ_{uni}, leads to [107]:

$$x + \Gamma\tau_{uni} = \sinh(x) \tag{73}$$

For small x, Equation (73) can be solved to obtain $\tau_h = \tau_c = \frac{1}{\Gamma}(\Gamma\tau_{uni}/3)^{1/3}$. In this limit, the optimal power of local Otto becomes

$$\mathcal{P}_{Otto}^{L.O} = \frac{1}{(\Gamma\tau_{uni}/3)^{1/3}}\frac{1}{4}\Gamma\Delta\Omega\Delta\bar{S} = \frac{1}{(\Gamma\tau_{uni}/3)^{1/3}}\mathcal{P}_{Otto}^{B.B} \ , \tag{74}$$

which is smaller than the bang-bang power $\mathcal{P}_{Otto}^{B.B}$ Equation (31).

The power of the local Otto cycle as a function of cycle time is shown in Figure 10 displaying the typical maximum power. The efficiency of the engine $\eta_{Otto}^{L.O}$ Equation (29) is independent of cycle period (cf. Figure 9). In practice, such a cycle can be analyzed by means of stochastic thermodynamics [61], since coherence has been eliminated from the analysis by employing shortcut protocols. A similar result employing a different derivation can be found in [68].

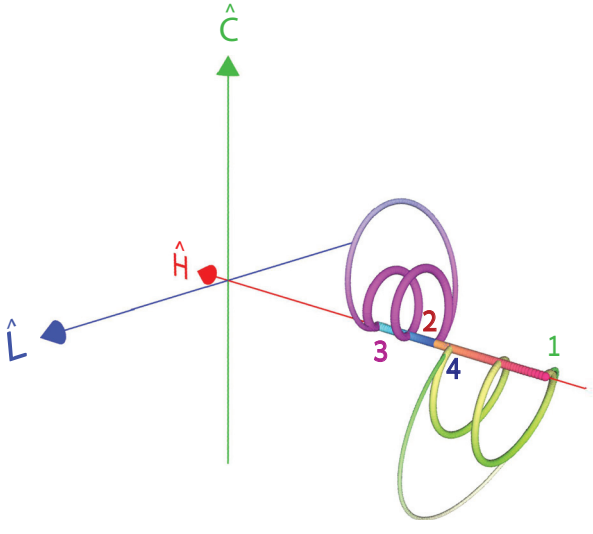

Figure 6. Frictionless shortcut (local) Otto cycle plotted in the $\{\langle\hat{H}\rangle, \langle\hat{L}\rangle, \langle\hat{C}\rangle\}$ space. The hot isochore $1 \to 2$ is represented by red thick line, and the cold isochore $3 \to 4$ is shown in blue. The expansion $2 \to 3$ and compression $4 \to 1$ unitary strokes begin and end on the energy axis, as the qubit exhibits no coherence between consecutive strokes. The fastest two solutions of shortcuts with constant μ are shown. The single large loop (thick line) corresponds to the fastest solution with $l = 1$ in Equation (46), which corresponds to τ_{min} and the second solution includes two small loops, $l = 2$.

6.2. Local Carnot Cycle

A local Carnot cycle, also called the 'Shortcut Carnot' cycle, is constructed by combining two shortcut to equilibrium protocols (open-strokes) and two shortcuts to adiabaticity protocols (unitary strokes), see Figure 7. It is characterized by the same cycle parameters as the Carnot cycle, while operating at finite speed, thus producing power. The increase in power does not come for free, as rapid driving increases dissipation, leading to a reduction in efficiency. Thus, the common tradeoff between efficiency and power is obtained from a first principle derivation, highlighting the quantum origins of the empirical phenomena associated with friction.

The shortcut cycle is constructed by setting the bath temperatures T_h and T_c, the minimum Rabi frequency $\Omega_{min} = \Omega_3$ and compression ratio $\mathcal{C} = \Omega_1/\Omega_3$. The remainder of the cycle parameters are then determined by the condition that the working medium is at equilibrium with the bath at the four corners of the cycle, see Figure 8a. This condition implies the relations $\Omega_4 T_h = \Omega_1 T_c$ and $\Omega_2 T_c = \Omega_3 T_h$; cycle parameters are given in Table 1. In contrast to the ideal Carnot cycle, the strokes, including exchange of energy with the bath, are denoted as open-expansion and open-compression. This change in nomenclature highlights the fact that, during these strokes, the qubit constitutes an open quantum system and at intermediate times along the strokes, the qubit is in a non-equilibrium state.

The adiabats (unitary strokes) are accelerated by employing shortcuts to adiabaticity (STA) protocols, characterized by a constant adiabatic parameter μ, see Section 4.3. The dynamics of these protocols are governed by the propagator $\Lambda_{uni} = \mathcal{U}_1\mathcal{U}_2$ given in Eqations (40) and (41). The shortcuts to adiabaticity protocols are then achieved by setting the stroke duration τ such that $\mathcal{U}_2$ is proportional to the identity. The net effect for an initial state with no coherence is a total scaling of the energy. This is achieved for τ, satisfying $\kappa\theta(\tau) = 2\pi l$, with $l \in \mathbb{N}$ Equation (41). In the following analysis, we choose $l = 1$, Equation (47).

Other STA protocols are possible; nevertheless, the specific choice of an STA protocol only slightly affects the qualitative thermodynamic cycle performance. Different STA protocols lead to the same state-to-state transformation, while generating different transient dynamics and having different stroke durations. In principle, if the energy of the driving is not bounded, then one can achieve the adiabats in vanishing time by utilizing the bang-bang protocols, Section 4.3. The net effect of different stroke duration is therefore just an additional constant to the cycle time. Overall, the qualitative thermodynamic performance is determined by the isothermal protocols. We present the description of the chosen STA protocol for the sake of completeness.

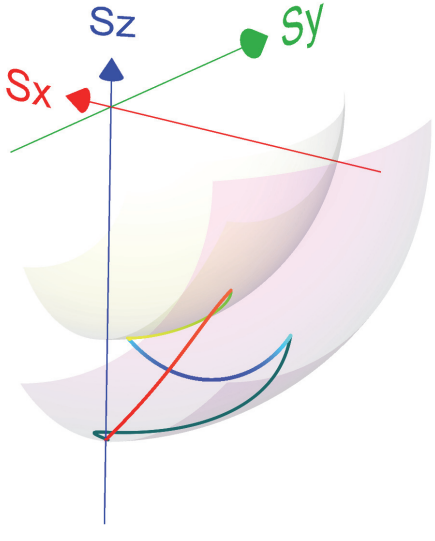

Figure 7. Shortcut Carnot cycle: Polarization change during the four strokes. The two hemispheres represent constant polarization for the two unitary strokes. The red part of the cycle trajectory is the hot isotherm connecting the two constant polarization hemispheres. The blue section is the cold isotherm. Green sections represent adiabats, where the the top curve corresponds to the expansion stroke and the bottom curve to the compression.

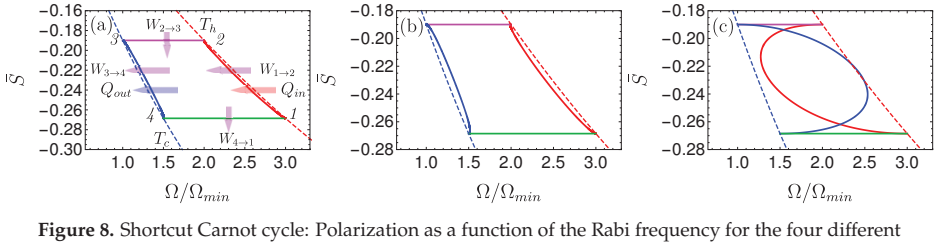

Figure 8. Shortcut Carnot cycle: Polarization as a function of the Rabi frequency for the four different cycle duration's: (**a**) $\tau_{cyc} = 192$ (**b**) $\tau_{cyc} = 108$ (**c**) $\tau_{cyc} = 9$, units of $(2\pi/\Omega_{min})$, with $\Omega_{min} = \Omega_3$ m.u. (model units $\hbar = k_B = c = 1$). The hot and cold isotherms are represented by dashed red and blue lines and the cycle points are denoted by numbers. Incoming (outgoing) arrows designate consumption (extraction) of work or transfer of heat to (from) the qubit. For slow driving, the cycle lies close to the reversible Carnot cycle, Panel (**a**). Increasing the driving speed leads to dissipation and deviations from reversible operation, Panel (**b**). Eventually, below a the transition cycle time $\tau_{trans} = 12.7\,(2\pi/\Omega_{min})$, the cycle transitions to a dissipator operation mode, Panel (**c**). Table 1 summarizes the cycle parameters.

The acceleration of the open-strokes is obtained by employing STE protocols, which are described in detail in Section 5.3. The speedup relies on non-adiabatic dynamics and the generation of coherence at intermediate times. The STE protocols are engineered in order to incorporate both the unitary effect, which leads to rise in coherence, and the dissipative interaction that induces decay of coherence. These two contributions are combined to induce conversion of all the coherence of the working medium to energy at the final stage of the protocol. When the driving is slow, only a small amount of coherence is generated and the evolution is close to an isothermal process. The close proximity of the polarization during the open-strokes is observed in Figure 8a (dashed lines).

Accelerating the driving generates larger coherence accompanied by a thermodynamic cost. This link between coherence and thermodynamic cost follows from the properties of the dynamical propagator at constant μ, Equation (41). During the open-strokes, the coupling to the bath leads to the decay of coherence. This decay increases with the amount of coherence present. As a result, rapid driving leads to enhanced dissipation, which reduces the cycle performance.

Figure 8 shows a visual representation of this phenomenon, which compares three Carnot-type cycles with varying cycle times. The amount of extracted work during a single cycle is related to the area enclosed by the $\bar{S}\left(\Omega\right)$ plot. As the cycle time decreases, the open-strokes deviate further from the isotherms (Panel **b**), consuming more work and dissipating larger amounts of energy and coherence. Figure 9 shows the entropy production rate on the open strokes for these cycles. At the beginning and the end of the stroke, the entropy production rate Equation (64) is zero, since the protocol is designed to reach equilibrium on the four corners of the cycle. The area under the lines is the total entropy production. As expected, the entropy production increases for decreasing stroke duration. Eventually, the cycle transitions to an accelerator operation mode, where work is consumed during both open-strokes (Figure 8c), which enhances the entropy production.

In the opposing limit of long cycle times, the dynamics are adiabatic and the efficiency approaches the Carnot efficiency η_C, Figure 10. The improved efficiency is obtained on account of a reduction in power, see Figure 11. Optimal power is obtained for relatively short cycle times $\tau_{cyc} \approx 24\ (2\pi/\Omega_{min})$ for the Carnot type cycle and a shorter time of $\tau_{cyc} \approx 11\ (2\pi/\Omega_{min})$ for the Otto cycle. Overall, the power of the shortcut Carnot cycle exceeds the local Otto cycle for almost all cycle times. Figure 12 shows the typical efficiency-power tradeoff for the shortcut Carnot cycle. The plot is compatible with the tradeoff bound in [108,109] (given by dashed purple and green lines), applicable to the low dissipation case. Two bounds are presented, the first, given by the expression: $\frac{\eta}{\eta_C} + \frac{(1-\eta_C)(\mathcal{P}/\mathcal{P}_{max})}{2\left(1+\sqrt{1-(\mathcal{P}/\mathcal{P}_{max})}\right)-\eta_C(\mathcal{P}/\mathcal{P}_{max})} \leq 1$, corresponds for efficiencies past the efficiency at maximum power (right bound—dashed green line), while the second line corresponds $2\left(\eta/\eta_C\right) + \sqrt{1-\left(\mathcal{P}/\mathcal{P}_{max}\right)} \geq 1$ (left bound—dashed orange line). Notice that the value of the normalized efficiency η/η_C for $\mathcal{P}/\mathcal{P}_{max} = 1$ is different for the right and left bounds. This emerges from the fact that the right bound depends explicitly on the Carnot efficiency, while the left bound only depends on the normalized ratio.

Surprisingly, when comparing the two different protocols for the angle ϕ (see below Equation (63)), the performance of the cycle is almost independent of the chosen protocol for ϕ. The primary difference between the two cycles concerns the amount of coherence that are generated during the open-strokes. As expected the protocol which includes a rotation of $\pi/2$ in ϕ exhibits much larger coherence along the stroke. We expect that, for higher values of μ, protocols that are characterized by a rotation of the Hamiltonian will generate more coherence. In turn, this will shift the point of transition from an engine to an accelerator to larger cycle times.

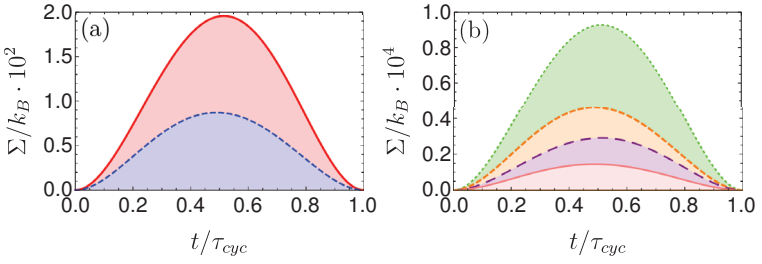

Figure 9. Entropy production rate for the open strokes of the shortcut Carnot cycle as a function of normalized time for various cycle times. Panel (**a**): Open-compression (red) and open-expansion (dashed blue) for a short cycle time $\tau_{cyc} = 9\,(2\pi/\Omega_{min})$. Panel (**b**): Open-compression (dotted green/dashed purple) and open-expansion (dashed orange/continuous pink) for a large cycle time $\tau_{cyc} = 108$ / $192\ (2\pi/\Omega_{min})$. The three cycle times correspond to the cycles that are plotted in Figure 8. Decreasing the cycle time increases the dissipation and results in a greater entropy production. The compression strokes include cooling the qubit, which requires greater amounts of entropy production relative to the open-expansion strokes for the same stroke times.

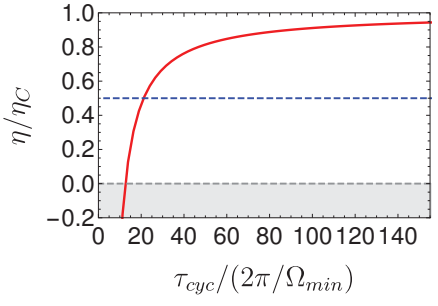

Figure 10. Normalized efficiency as a function of the cycle time for a local Carnot cycle (thick red) and local Otto cycle (blue dashed). In the local Carnot cycle long cycle times lead to close to reversible dynamics, optimizing the efficiency towards the Carnot bound η_C. For short cycle times dissipation of energy and coherence leads to a degradation of efficiency. Eventually, resulting in a transition from an engine operation mode ($\eta \equiv -\mathcal{W}/\mathcal{Q}_h > 0$) to an accelerator operation mode ($\eta < 0$). The two studied protocols for the angle $\phi\,(t)$ (below Equation (63)) cannot be distinguished in this graph. In the local Otto cycle, the efficiency $\eta_{Otto} = 1 - \Omega_c/\Omega_h$ is independent of the cycle time.

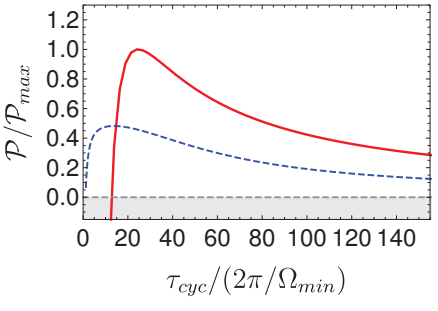

Figure 11. Power as a function of cycle time for a local Carnot cycle (red thick line) and local Otto cycle (blued dashed line). Slow driving leads to a reduction in power $\mathcal{P} \equiv -\mathcal{W}/\tau_{cyc}$. Moreover, under rapid driving dissipation reduces the net extracted work, leading to an optimal power of $\mathcal{P}_{max} = 5.19 \times 10^{-3}$ m.u. for $\tau_{cyc} \approx 24\ (2\pi/\Omega_{min})$ for the local Carnot and $\mathcal{P}_{max} = 2.5 \times 10^{-3}$ m.u. for $\tau_{cyc} \approx (2\pi/\Omega_{min})$ for the local Otto cycle.

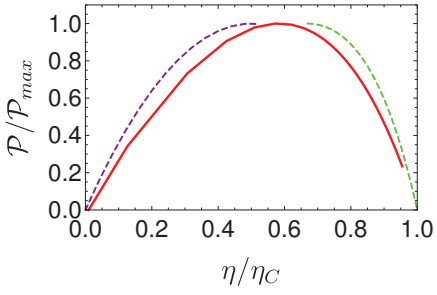

Figure 12. Power as a function of efficiency for the local Carnot cycle (red continuous line) and upper bounds (dashed purple and green lines) [108]. The typical behavior is a manifestation of the tradeoff between efficiency and power. The efficiency at maximum power $\eta_{\max\mathcal{P}} \approx 0.57$ exceeds the Curzon–Ahlborn efficiency $\eta_{CA} = 1 - \sqrt{T_c/T_h} \approx 0.3$. This result is not surprising, as the operation speed goes beyond the low dissipation regime [66].

7. Global Cycles

Closing globally coherent cycles requires more than just connecting the four strokes, since the four corners of our cycle are no longer required to be Gibbs states. In general, we prescribe a periodic driving protocol and the qubit is thereby driven to a limit cycle [76].

We will start by examining the Otto cycle which is easier to analyze. Figure 13 shows an example of a global Otto cycle. During the unitary strokes of the Otto cycle, $\Lambda_{h\to c}$ and $\Lambda_{c\to h}$, non-adiabatic dynamics generates coherence, which carries the system away from the energy direction [74,110,111]. This coherence subsequently decays during the isochoric strokes. Note that, if STA protocols are used on the unitary strokes, then no coherence ever dissipates, leading to no friction, and the discussion from the frictionless treatment in Sections 3.3 and 3.4 applies. Because our goal is to understand the behavior, including friction, we use constant μ protocols for the unitary strokes. These are only frictionless for quantized stroke durations. We present results for the power and the efficiency as a function of the cycle time. Because our STA protocols are only frictionless for quantized times, the behavior in Figures 15 and 16 shows oscillations for cycle times smaller than $\tau(l = 1)$. Interestingly, except for some wild oscillations for very small times, the power of the coherent Otto cycle is monotonically decreasing in the cycle time, reaching its maximum for the sudden cycle in the limit of $\tau \to 0$ for small Φ. Therefore, we begin with a closer look at this case.

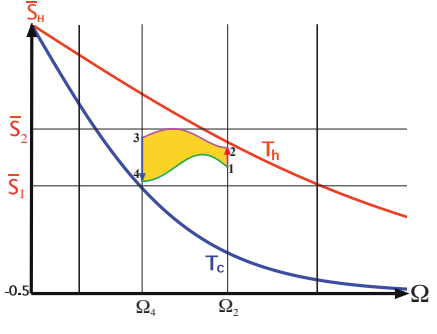

Figure 13. Global Otto cycle with friction. Projection of the polarization on the energy axis as a function of the generalized Rabi frequency. The coherence at the end of the adiabats dissipates during the isochores. Because of the decay of this coherence, the polarization along the adiabats always exceeds its initial value. In the presented cycle $\mu > \mu_{l=1}$.

7.1. Global Otto Cycle and the Sudden Limit

We now analyze the influence of coherence in the sudden limit. In general, the working medium Hamiltonian $\hat{H}(t)$, Equation (2), does not commute with itself at different times, generating substantial coherence under rapid driving. As will be demonstrated, this coherence has a direct effect on the thermodynamic performance and the cycle's operation mode.

The sudden operation is characterized by only two types of strokes: unitaries and isochores. When the Hamiltonian parameters are instantaneously varied, the working medium dynamics is dominated by the unitary part (adiabats). Any finite coupling with the bath (weak in our analysis) only negligibly affects the working medium state. During the isochores, the control parameters remain constant and a small amount of heat transfer occurs. Note that the initial portion of an isochore has the largest temperature difference between the bath and our qubit, so the sudden cycle only uses this fastest heat exchange, explaining how the power can be maximum in the zero time limit.

As in the general case, the evolution of the working medium during the sudden Otto cycle is constructed by combining the propagators of the adiabats $\Lambda^{sudd}_{i\to f}$, Equation (43), and the propagators for the isochores Λ^{iso}_{sudd}. The propagator for the isochores are obtained by substituting the basis operators $\{\hat{H}, \hat{L}, \hat{C}, \hat{I}\}$ into the Heisenberg form of the master equation, Equation (14), and expanding the solution up to first order in the stroke time τ. This leads to

$$\Lambda^{sudd}_{i} = \begin{bmatrix} 1-\Gamma_i\tau & 0 & 0 & \Gamma_i\tau\Omega_i\langle\bar{S}_{eq}(\Omega_i, T_i)\rangle \\ 0 & 1-\Gamma_i\tau/2 & -\Omega_i\tau & 0 \\ 0 & \Omega_i\tau & 1-\Gamma_i\tau/2 & 0 \\ 0 & 0 & 0 & 1 \end{bmatrix} , \tag{75}$$

where $i = h, c$ indicates the frequency of the hot and cold baths. In the studied sudden Otto cycle $\Omega_{h/c} = \Omega_{2/4}$ and the kinetic rates are taken to be equal $\Gamma_i = \Gamma_c = \Gamma_h$. Concatenating the stroke propagators in the suitable order generates the sudden cycle propagator

$$\Lambda^{sudd}_{cyc} = \Lambda^{sudd}_{c\to h}\Lambda^{sudd}_{c}\Lambda^{sudd}_{h\to c}\Lambda^{sudd}_{h} \quad . \tag{76}$$

Next, we solve for the invariant of the limit cycle $\Lambda^{sudd}_{cyc}\vec{v} = \vec{v}$, where the elements of $\vec{v}$ give the expectation values of the basis operators $\{\hat{H}, \hat{L}, \hat{C}\}$ at the beginning of the hot isochore. This information is sufficient for determining the qubits state throughout the cycle and, in turn, allow evaluating the thermodynamic quantities.

We find that in the sudden limit, the cycle's performance is highly sensitive to the coherence generation along the adiabats. The amount of accumulated coherence is determined by the relative phase Φ, see Equation (43). For $\Phi = 2\pi k$, $k \in \mathbb{Z}$, the Hamiltonian commutes with itself at different times and the state remains diagonal in the energy basis. In contrast, for intermediate values of Φ, coherence builds up along the adiabats and dissipates during the isochores. The dissipation leads to a reduction in power and efficiency. We find that, in the sudden limit, the extraction of power is only obtained for small amounts of coherence. This regime corresponds to phase values close to $\Phi = 2\pi k$, see Figure 14a. It is important to note that the generated coherence on a unitary stroke is employed to reduce the work against friction in the consecutive unitary stroke. Eliminating this coherence on the isochores will transform the engine into a dissipator.

It is convenient to characterize the cycle performance in terms of the standard expression of efficiency: $\eta = -\mathcal{W}/\mathcal{Q}_h$. Under an engine operation mode, the efficiency remains within the range $0 \leq \eta \leq \eta_C$. With increasing coherence generation (increasing Φ), the dissipated work exceeds the extracted work, leading to a net positive work. In this operation regime work is consumed ($\mathcal{W} > 0$), while heat keeps flowing from the hot bath to the cold bath ($\mathcal{Q}_h > 0, \mathcal{Q}_c < 0$). Thus, η becomes negative, see Figure 14b. When further increasing the coherence generation, the qubit starts dissipating energy to both baths ($\mathcal{Q}_c, \mathcal{Q}_h < 0$); this implies that η changes its sign abruptly and becomes positive.

The maximum coherence generation is achieved for $\Phi = \pi k$, which corresponds to an equal magnitude of the x and z components of the Hamiltonian (cf. Section 3.4).

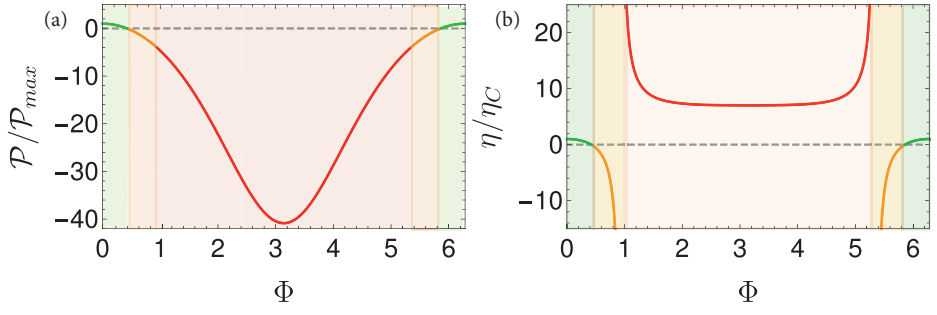

Figure 14. (**a**) Normalized power and (**b**) efficiency as a function of the relative phase Φ. When the phase values are near $2\pi k$, $k \in \mathbb{Z}$, only small amounts of coherence are generated and the cycle operates as an engine (green lines), which produces a positive power output. Once the phase deviates from the optimal values, the net work becomes positive and the cycle operates as an accelerator (orange lines, $\mathcal{W} > 0$, $\mathcal{Q}_h > 0$, $\mathcal{Q}_c < 0$), accelerating the flow from hot to cold. When the coherence generated during the adiabats dissipates to both baths on the isochores, the cycle transitions to a dissipator $\eta > 1$ (red line, $\mathcal{Q}_c$, $\mathcal{Q}_h < 0$, $\mathcal{W} > 0$). The model parameters are: $T_c = 5$, $T_h = 10$, $\Omega_c = 6$, $\Omega_h = 8$, $\Gamma_h \tau_h = \Gamma_c \tau_c = 0.01$, where τ_h and τ_c are the stroke durations of the hot and cold isochores.

The isochores include off-diagonal terms ($\propto \Omega_i \tau$), which couple the coherence operators $\hat{L}$ and $\hat{C}$. This coupling originates from the unitary contribution to the open-system dynamics, (the unitary term is of the form $\frac{i}{\hbar}\left[\hat{H}, \hat{X}\right]$ in the Heisenberg equation of motion for the operator $\hat{X}$), and tends to complicate the solution by coupling the dynamics of all three operators along a complete cycle. In practice, we find that this coupling only slightly affects the results, improving the power by a very small amount ($\sim 10^{-2}\mathcal{P}_{max}$). This typical behavior justifies discarding the coupling terms when evaluating the efficiency and power. Without these terms, their expressions in the sudden limit ($\tau_{cyc} \to 0$) read

$$\eta = \left(8c_\Phi \Omega_h \Omega_c \left(\bar{S}^c_{eq}\Omega_h + \bar{S}^h_{eq}\Omega_c\right) - \Omega_c \Omega_h \left(\Omega_h \bar{S}^h_{eq} + \Omega_c \bar{S}^c_{eq}\right)(c_{2\Phi} + 7)\right)/G \tag{77}$$

$$\mathcal{P} = \frac{\Gamma\left(8c_\Phi\left(\bar{S}^c_{eq}\Omega_h + \bar{S}^h_{eq}\Omega_c\right) - \left(\Omega_c \bar{S}^c_{eq} + \Omega_h \bar{S}^h_{eq}\right)(c_{2\Phi} + 7)\right)}{4\,(c_{2\Phi} - 17)}\,, \tag{78}$$

with $G \equiv \Omega_h\left(8\langle S^c_{eq}\rangle \Omega_c \Omega_h c_\Phi - \langle S^h_{eq}\rangle \Omega_h \Omega_c\,(c_{2\Phi} + 7)\right)$ and using the shorthand notation $c_x = \cos(x)$ and $s_x = \sin(x)$. In the evaluation of the power, we assumed equal stroke durations on all strokes.

7.2. Global Carnot-Type Constant Adiabatic Parameter Cycle

By definition, our Carnot-type cycles are constrained to be in equilibrium at switching points between two adjacent strokes. This requirement implies that coherence is only maintained "locally" within the strokes and it defines what we mean by local coherence operation of our engines. In the following analysis, we lift this restriction to study the properties of "global" coherence operation.

A globally coherent cycle is constructed from two open-strokes and two adiabats. For our implementation, the value of μ is kept constant for the entire protocol. We study the performance of the limit-cycle, which maintains coherence throughout the cycle. We reduce the compression ratio $\mathcal{C}$ of the cycle while maintaining the same bath temperatures in order to produce power. Two globally coherent Carnot cycles are studied, which differ by the inner frequencies of the cycle, Ω_2 and Ω_4. The frequencies are chosen to fit an endoreversible Carnot cycle with a constant temperature gap, in the

first cycle $\Delta T_h = \Delta T_c = 1$ m.u. and for the second cycle $\Delta T_h = \Delta T_c = 2$ m.u. Table 1 summarizes the cycle parameters. These cycles maintain a non-vanishing heat flow in the desired direction on the open-strokes.

The protocol choice of a constant adiabatic parameter allows for an additional degree of freedom in the choice of the Hamiltonian controls $\omega(t)$ and $\epsilon(t)$. We choose to set them, as in Equation (62). We then obtain a relation between the phase and Rabi frequency: $\Omega(t) = -\dot{\phi}/\mu$. For small $\dot{\phi}$, the protocols can be very rapidly achieved while keeping μ small, thus still maintaining quantum adiabatic evolution. However, in such regime a slow change in the phase implies that $\omega(t)$ and $\epsilon(t)$ are nearly proportionate to one another, resulting in a Hamiltonian that commutes with itself at different times. In order to study the influence of coherence on the thermodynamic performance, we require a substantial change in phase. For this reason, we determine the driving protocols by setting both initial and final Rabi frequencies, Ω_i and Ω_f and phases ϕ_i and ϕ_f. In the quantitative analysis, we choose $\Phi = \phi_f - \phi_i = \pi/2$, meaning that the Hamiltonian direction rotates from the z to the x axis during the open-expansion stroke ($-\pi/2$ on the open-compression stroke).

Global coherence operation allows for coherence, generated in one stroke, to be converted to energy and utilized during the adjacent strokes. Accelerating the driving enhances this phenomenon by generating greater coherence, which eventually dominates the cycle's performance. Using the coherence measure $\mathfrak{C}$, Equation (34), we observe that, when $\mathfrak{C} > 0.01$, relative to a maximum value of 0.5, strong interference takes place, which are manifested in oscillations in power and efficiency. The coherence value should also be compared to the typical value of $|\bar{S}_H|$, which is of the order $\approx$0.1. Figure 15 presents the scaled efficiency for varying cycle times. In the slow driving regime, coherence only degrades the extracted work and efficiency increases monotonically with the cycle time. In contrast, for sufficiently fast driving, the efficiency oscillates rapidly due to interference. If the generated coherence is utilized efficiently, the cycle extracts more work and the efficiency improves. Moreover, optimal power is obtained in the fast driving regime, as in Figure 16.

On the other hand, if generation and consumption of coherence is not coordinated with the stroke times (related to the cycle time), the dissipation increases, which decreases the efficiency. Overall, the oscillations in efficiency constitute a signature of a quantum operation mode [75], dominated by coherence.

Generally, the efficiency at long cycle durations surpasses the local optima seen at short cycle times. This is a consequence of strong dissipation of coherence under rapid driving. Even when the generation and consumption of coherence is fully coordinated with the stroke duration, a still greater amount of coherence leads to greater dissipation on the open strokes and a reduction in efficiency. Therefore, no quantum advantage is expected in this scenario.

The entropy production rate of these cycles is almost constant throughout the cycle, as in Figure 17. This is a confirmation that the cycle is always far from the instantaneous attractor. Shorter cycle periods lead to larger entropy production. The breakup of entropy production to an energy like term $\Sigma_\chi = \mathcal{F}_\chi \mathcal{J}_\chi$ and a coherent part $\Sigma_{\sigma_{x/y}} = \mathcal{F}_{\sigma_{x/y}} \mathcal{J}_{\sigma_{x/y}}$, Section 5.4, show similar values for large μ, which means that coherence dominates the cycle. For small μ (large cycle times), the entropy production is dominated by Σ_χ, which can be attributed to irreversible heat transport.

In the asymptotic limit (large τ_{cyc}), the working medium remains in the linear response regime during the open strokes. This regime is characterized by low dissipation and a typical $1/\tau_{cyc}$ scaling law of the dissipated energy. Similarly, one can introduce the dissipated power, defined as $\mathcal{P}_{diss} = \mathcal{P} - |\mathcal{W}_{ideal}|/\tau_{cycle}$, where the ideal work $\mathcal{W}_{ideal}$ is achieved in the large time limit. In the linear response regime the dissipated power is expected to scale asymptotically as $1/\tau_{cyc}^2$ [112]. Under small μ (slow driving), the globally coherent cycle exhibits such typical behavior, as showcased in the inset of Figure 15.

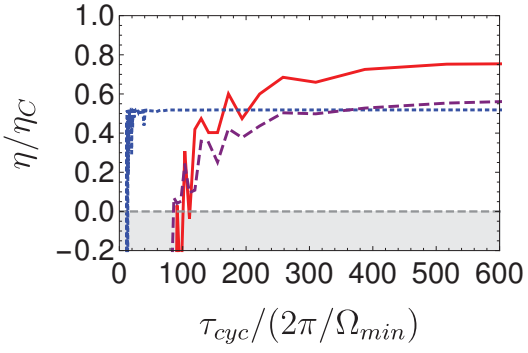

Figure 15. Normalized efficiency as a function of the cycle time for the Globally coherent Carnot (continuous red and dashed purple) and Otto cycles (dotted blue). In the slow driving regime, coherence only degrades the extracted work output and the efficiency. As the cycle time increases less coherence is generated and the efficiency increases monotonically. In the rapid driving regime, the cycle exhibits a quantum operation mode, where the cycle performance is dominated by coherence. In this driving regime, when coherence generation and consumption is coordinated with the stroke times, the cycle efficiently produces work. On the other hand, for stroke time leading to induced dissipation of coherence, the work extraction declines and the cycle may transfer to a dissipator operation mode ($\eta < 0$). This sensitivity to coherence leads to an oscillatory dependence for short cycle times. The efficiency of the Carnot-global cycle exceeds the efficiency of the global Otto cycle at long cycle times. This result stems from the reduced compression ratio of the global Otto cycle. This relative performance reverses for short cycle times. In this driving regime, the global Otto maintains a close to optimal efficiency where the Carnot cycle performance degrades and the cycle ceases to operate as an engine. For the chosen cycle parameters, the Carnot efficiency obtains a value of $\eta_C = 0.75$. The two Globally Carnot cycle differ by their Ω_2 and Ω_4 frequencies. As a result, the effective temperature gap of the purple cycle is larger compared to the red cycle. When comparing to the power plot (Figure 16), the cycle with lower efficiency exhibits a larger maximum power. The Globally coherent Carnot and global Otto cycles parameters are summarized in Tables 1 and 2.

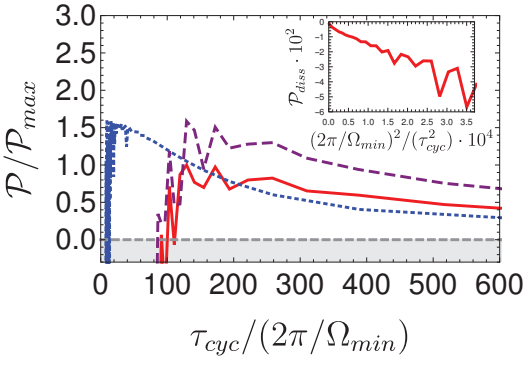

Figure 16. Power as a function of the cycle time for the Globally coherent Carnot (continuous red and dashed purple) and global Otto (dotted blue) cycles. The maximum power for the two Carnot cycles are $\mathcal{P}_{max} = 1.8 \cdot 10^{-3}$ m.u. for the purple $\mathcal{P}_{max} = 1.14 \cdot 10^{-3}$ m.u. for the red, and for the Otto $\mathcal{P}_{max} = 1.8 \cdot 10^{-3}$ m.u. Inset: Dissipated power $\mathcal{P}_{diss} = \mathcal{P} - |\mathcal{W}_{ideal}|/\tau_{cyc}$ as a function of a scaled $1/\tau_{cyc}^2$. For large cycle times, the dissipated work scales as $1/\tau_{cyc}$ and the dissipated power as $\mathcal{P}_{diss} \propto 1/\tau_{cyc}^2$. This result is in accordance with a linear response analysis. Cycle parameters are presented in Table 1.

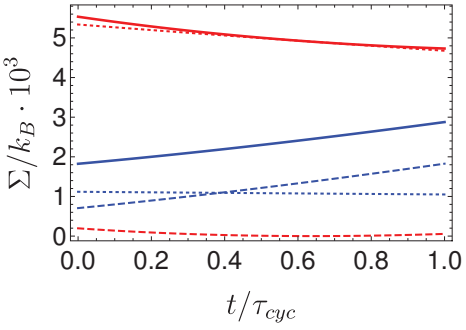

Figure 17. Entropy production rate as a function of normalized time for the Globally coherent Carnot cycle with $|\mu| = 0.3$. The total entropy production rate for the open-expansion and open-compression strokes are shown in thick red and blue lines, correspondingly. These are a sum of entropy production due to the flux of $\langle\hat{\chi}\rangle$, $\mathcal{F}_\chi\mathcal{J}_\chi$ (dashed lines), and coherence-like terms $\mathcal{F}_{\sigma_x}\mathcal{J}_{\sigma_x} + \mathcal{F}_{\sigma_y}\mathcal{J}_{\sigma_y}$ (dotted lines). The various contributions are, as expected, positive. With decreasing μ the coherence-like terms decrease and the term $\mathcal{F}_\chi\mathcal{J}_\chi$ is the dominant contribution to the entropy production. The breakup of the entropy production in the $\{\hat{H}, \hat{L}, \hat{C}\}$ basis will show a similar pattern.

We can compare the performance of the Globally coherent Carnot and Otto cycle. Both cycles maintain coherence throughout the cycle, where in the global Otto cycle coherence is generated only during the unitary strokes. The turnover to an operation mode that is strongly influenced by interference requires faster driving and larger value of coherence measure $\mathfrak{C} > 0.1$. As a result, the coherent affected operation mode at shorter cycle time. This characteristic behavior can be witnessed in Figure 15. The shorter cycle times allow for the global Otto cycle to posses comparable maximum power with respect to the Globally coherent Carnot cycle with higher efficiency.

Table 1. Shortcut (local) and Globally coherent cycle parameters are given in the model units (m.u.), satisfying $\hbar = k_B = c = 1$. The parameters for the Globally Carnot cycle correspond to the continuous red line in Figures 15 and 16, while the parameters in parentheses correspond to the purple dashed lines.

Parameters	Local Carnot	Globally Coherent Carnot	Local Otto	Globally Coherent Otto
Ω_1	12	10	8	9
Ω_2	8	9 (6.857)	8	9
Ω_3	4	6	6	$6\frac{2}{3}$
Ω_4	6	$6\frac{2}{3}$ (8.75)	6	$6\frac{2}{3}$
Hot bath temperature	$T_h = 10$	$T_h = 10$	$T_h = 10$	$T_h = 10$
Cold bath temperature	$T_c = 5$	$T_c = 5$	$T_c = 5$	$T_c = 5$

Table 2. Stroke parameters are given in the model units (m.u.), satisfying $\hbar = k_B = c = 1$.

Parameters	Value
Coupling constant $A \equiv g^2/2\hbar c$	0.01
Integration step size	10^{-3}

8. Quantum Signature: Constant Adiabatic Parameter Cycles Maintaining Global Coherence

A quantum signature is defined as a measurable quantity of the system which affirms non-classical behavior [23,113]. In the present scenario, we search for thermodynamic properties that are susceptible. Unlike classical features, quantum properties are sensitive to any measurement that extracts information on the system state. This feature allows validating the quantum signature by analyzing the affect of measurements on the cycle performance. Specifically, we compare the globally

coherent Carnot cycle efficiency to the efficiency in the presence of weak quantum measurements of energy in the instantaneous energy basis, which are performed on the unitary strokes.

The weak measurement back action effectively leads to a double commutator term $-k_d\left[\hat{H},\left[\hat{H},\hat{X}\right]\right]$ in the master equation for the system operator $\hat{X}$ [114]. Such a term leads to pure dephasing with a dephasing constant k_d. We compare the effect of dephasing for different cycle times for the global Carnot cycle. For a specific cycle time, the results shows a decrease in efficiency for small dephasing constant k_d, Figure 18. This regime corresponds to weak measurements that only slightly influence the system dynamics and decrease the coherence. When the system is weakly perturbed, the dephasing only increases the dissipation and, therefore, reduces the efficiency. Beyond a critical value, stronger measurements (increasing the value of k_d) lead to an opposite effect and improve the efficiency. This result is related to the Zeno effect [115,116] and quantum lubrication [117], as continuously measuring the qubit forces it to remain on the energy shell. In return, this leads to less coherence generation and, therefore, reduced dissipation. The measurement backaction and the present thermodynamic analysis, should be taken with certain care. Once the qubit state is being monitored, it ceases to be an isolated system and the measurement may be accompanied by an additional heat transfer [118,119]. In addition, the measurement itself requires resources of work and heat. In the limit of projective measurement, the resources required become infinite [120]. The additional heat that arises from the weak measurement and the resources required were not accounted for in the present analysis.

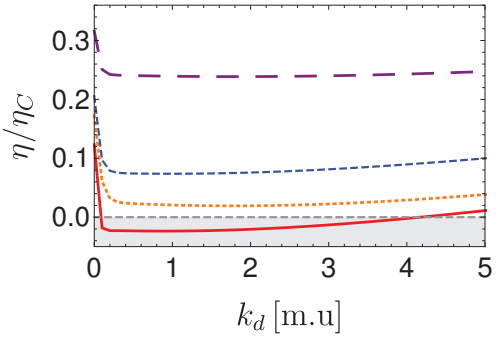

Figure 18. Efficiency as a function of dephasing constant k_d for varying cycle times for the globally coherent Carnot cycle: Red-continuous $\tau_{cyc}=102.5$, blue dashed $\tau_{cyc}=103$, orange dotted $\tau_{cyc}=105$, purple long dashed $\tau_{cyc}=129$, units of $(2\pi/\Omega_{min})$.

As expected, the influence of the measurement reduces with increasing cycle times, see Figure 18. Slower driving reduces the amount of coherence throughout the cycle, thus diminishing the affect of dephasing on the thermodynamic performance. In the quantum adiabatic limit, the system remains on the energy shell and the measurement does not disturb the system.

9. Discussion

9.1. What the Qubit Can and Cannot Do

The qubit QM model can generate expressions for thermodynamic quantities, based on first-principle derivations under the paradigm of open quantum systems. It incorporates all of the features that we expect from finite-time thermodynamics: tradeoff between efficiency and power, irreversible process, finite heat transport, friction, and heat leaks. A major advantage of the qubit model is its simplicity. Nevertheless, the model is able to elucidate the main issues of finite-time-thermodynamics, but not all types of effects. It is important to stress what phenomena we omitted from this paper, either since they deserve further study or because the model is restricted.

The present qubit model by construction is limited in describing many body effects on engine performance. For example, our model engines cannot include the entanglement in engines [121–123], engines based on many body localization as a working fluid [124], collective and critical quantum effects in engines [125–129], and synchronization [130].

In the introduction, we stated four possible sources of irreversibility; two sources that were not included in the present analysis are heat leaks and switching losses. In any realistic engine, there is always a residual system-bath coupling even during the unitary strokes [131]. As a result, additional heat currents from the hot to the cold reservoir occur. Moreover, such an interaction causes additional dephasing. These effects are not counted in our models. In addition, in all four stroke cycles presented, we ignored the energetic cost of switching the coupling to the bath, g, on and off [15,18,132,133]. Such switching occurs as the cycle transitions between unitary and open strokes. If one chooses, in Equation (11), a system bath interaction that satisfies $\left[\hat{H}_{s-h/c}, \hat{H}_s + \hat{H}_{h/c}\right] = 0$ the energetic cost of switching the coupling on vanishes. If correlations between the system and bath are generated, decoupling the system from the bath could result in an additional thermodynamic cost [132,133]. The miniaturization of engines emphasizes the role of fluctuations. Fluctuations add another twist to the tradeoff between power and efficiency [134–137]. It has recently been claimed that the possibility of heat engines to have finite power output, operate close to Carnot efficiency, and only exhibit small fluctuations is excluded [135]. For steady-state heat engines, driven by a constant temperature difference between the two heat baths, it has been claimed that, out of these three requirements, only two are compatible. The present qubit model could be a unique platform for testing these ideas [69,138].

9.2. Further Considerations

There are infinitely many thermal cycles that can operate between given hot and cold baths, and produce power. These cycles differ by the externally controlled protocols and the switching points between the strokes. Optimization can be applied to the control protocols in order to enhance power or to minimize entropy production.

In the present study, we only considered a restricted class of control strategies, and mostly emphasized control strategies that optimize individual strokes. Such control and optimization relies on the prior knowledge of the equations of motion of the working medium. The control of the qubit is based on the full $SU(2)$ algebra. This reflects the physical intuition that, in practice, the control operators do not commute in general with the system Hamiltonian. As a result, $[\hat{H}(t), \hat{H}(t')] \neq 0$.

In the unitary strokes, we explored shortcuts to adiabaticity (STA) protocols, as in Section 4.3. Without any restriction, employing STA protocols allows carrying out strokes with vanishing stroke duration. Restricting the energy or the coherence stored within the controller leads to a minimum stroke duration for frictionless operation. When analyzing the complete engine cycle, the time allocated to the unitary strokes was found to have no qualitative effect on the cycle performance.

The thermalization process during the open-strokes can be controlled as well. In the study of the Carnot-type cycles, we employed protocols that speedup the thermalization process, with the cost of additional dissipated work and concomitant entropy production. The utilized protocols achieve the target thermal state rapidly, but are by no means optimal. Thermalization strokes are a much newer development and what features might make them optimal is not yet clear. For example, it is not at all clear that our STE protocols, which cash in all of the coherence at the end of the stroke, are desirable. Cashing in this coherence before the end of the stroke may not be helpful as conversion during the following unitary stroke is easily handled. In fact, macroscopic optimizations of finite-time Carnot cycles [8] would lead to maximum energy exchange for a given entropy change of the working fluid and suggests that better use of the heat exchange time would be to utilize it fully by keeping the coherence for conversion during the following unitary stroke. Our expectation for an optimal implementation would be one that keeps the entropy production rate constant [139,140], and examining these rates in Figure 17 shows that our constant μ protocol comes reasonably close.

Besides serving as a comparison to Carnot-type cycles, our treatment of Otto cycles shows off some interesting new features. The fact that both the power and the entropy production of the cycle are proportionate to the change in polarization gives this cycle a unique character. In particular, it implies that the point of maximum power is the point of maximum entropy production, i.e., the two objectives are diametrically opposed for this engine. Some light can be shed on this situation by realizing that the thermal losses are set by the temperature gap between the qubit and the bath at their highest values at the beginning of the open strokes. After that, this gap decays, with the only control being the time spent on the stroke. This forces the heat exchange and entropy production to be the largest at the beginning of the stroke with rate decreasing with longer stroke duration.

This line of reasoning is also what led us to the closer examination of the sudden cycle for which only the very initial segment of the open branches are used. By the above line of reasoning, this initial segment is the fastest heat exchange. Using instantaneous counter-diabatic driving for the unitary strokes leads to overall frictionless operation of the sort discussed in reference [63]. The interesting feature of sudden cycles, without STAs for the unitary branches, is that instantaneous driving produces significant coherence, which is actually very useful for the cycles' performance. The unitary jumps are reversible; hence, there is no cost to going forwards and backwards and at the end we get all the invested work back [141]. The same coherence in the forward jump is used to power the backwards jump. The only difference between a forward and backward jump and sudden engine operation is the very brief stops in contact with the baths, during which some coherence decays. However, this cost in coherence is not enough to kill all the power and the sudden cycles give an important example of an engine in which coherence helps. This is contrary to conjectures in the literature that coherence is always an undesirable in heat engine operation [78]. Our findings show that this conjecture, while valid for slow operation, does not appear to be true of all types of operation; there exist valid benefits of coherence [142].

Increasing the driving increases coherence generation. On the open branches, this coherence results in rather significant frictional losses that quickly bring us to the turnover point where the friction dominates the cycle performance and the engine no longer produces work. This turnover point occurs in the Carnot cycle for much smaller values of the coherence than in the Otto cycle, presumably because, in the Carnot cycle, the open branches generate additional coherence. It is also the reason our graphs of the efficiency and the power for the Carnot cycle cannot reach lower cycle times, cf. Figures 10, 11, 15 and 16. The smooth behavior of both the efficiency and power as a function of the cycle time for local cycles gives way to oscillations at short times for global cycles (Figures 15 and 16). Coherence by nature oscillates, and these oscillations result in effectively constructive and destructive interference with the oscillation during the following stroke in our global cycles. Note that this feature also shows up for the global Otto, but at much faster cycle times. In general, the global Otto cycle is less sensitive to coherence (the coherence related operators and energy are on the same scale). While the sensitivity to coherence depends on the temperature gap between the system and bath during the open strokes; this lower sensitivity to coherence for the Otto cycle holds for any comparable gaps.

9.3. Comparing to the Harmonic Working Fluid

Engine models with the qubit and harmonic oscillator working medium have been the most popular quantum systems in the study of quantum heat devices [63,95,107,143–149]. These models share many common features, including the tradeoff between power and efficiency, and obtain the Carnot bound in the limit of large cycle time. Moreover, in the limit of low temperatures, the harmonic oscillator converges to the qubit model, and the thermodynamic performance should be equivalent. Despite the similarities, there are qualitative differences in the thermodynamic performance. The major differences between the two models can be traced to the dynamical algebra of the two, $SU(2)$ and the Heisenberg-Weyl group H_3. The former algebra is compact, while the latter is non-compact. A direct consequence is that the heat capacity of the harmonic oscillator increases with the temperature,

saturating for high temperatures. In contrast, the capacity of the qubit reaches a maximum value and then asymptotically decreases as T^{-2} in the high temperature regime.

The different algebra influences the dynamics as well. For example, for a constant adiabatic parameter protocol (non-adiabatic driving), the effective frequency of the qubit increases, while in the harmonic case the effective frequency decreases. In turn, the effective frequency determines the relaxation rate towards the instantaneous attractor. In both models, this rate increases monotonically with the effective frequency, and the relaxation rate will be influenced in an opposite manner. In addition, the detailed balance condition is also modified, which means the internal temperature of the qubit is reduced in the presence of non-adiabatic driving. When comparing the present global cycle to an analogous harmonic cycle [75], we find that the qubit cycle has a greater sensitivity to the presence of coherence (short cycle times). A possible explanation of this result is the shift to a lower internal temperature and higher relaxation rate, which destroys the coherence and nulls the extracted work.

In the operation of the engines, both working mediums allow for performing shortcut protocols [106] on the unitary and open strokes. For frictionless and shortcut cycles, the harmonic Otto cycle exhibits a maximum efficiency when optimizing the compression ratio, which corresponds to the classical endoreversible result η_{CA}, Equation (22) [95,107]. This result is independent of the power of the engine. In contrast, the qubit model reaches the Curzon–Ahlborn efficiency for an endoreversible cycle in the high temperature limit, Section 3.2 [64].

9.4. High Temperature Limit

With the motto of learning from example, we can employ the qubit model to elucidate the path from the quantum first principle derivation to the classical FTT results. The key is the high temperature limit. This means that the polarization $|\vec{S}|$ is small and it can be used to expand the thermodynamical expressions to first order. In the elementary Carnot-type cycle this expansion leads to the Curzon–Ahlborn efficiency at maximum power η_{CA}, Equation (50), without relying on the linear Newtonian heat transfer law or the low dissipation limit [67,68,78]. If we consider the cost of driving (Section 5.4), we find that the entropy production rate Σ^u at the high temperature limit can be cast into the template of the Onsager relations, Equation (71).

The qubit engine model operates in the low dissipation limit when the cycle period is very large. We observe the expected limit (insert of Figure 16), as the dissipated power scales inversely with the square of the cycle period $\mathcal{P}_{diss} \propto 1/\tau_{cyc}^2$. This is generically true, as discussed in the next subsection.

9.5. Dissipation

The problem of operating a heat engine while trying to minimize dissipation has a simple general answer: turn off the engine so nothing happens. This, of course, has a dissipation cost of zero; you cannot do better. In order to get an interesting answer to the minimum entropy production question, we have to require something to happen. For a heat engine, one natural choice is to carry entropy $\Delta\mathcal{S}$ from the hot bath at temperature T_h to the cold bath at temperature T_c. Once such a constraint is specified, the interesting optimizations for a finite-time heat engine range from minimum entropy production to maximum power, with maximum efficiency as merely an intermediate point [8].

The low dissipation limit has been recently employed to bound the dissipation in a heat engine while using the notion of thermodynamic distance [60,78,150]. This distance, defined on thermodynamic states using the second derivative of the entropy, bounds the finite-time cost of driving a system along a given trajectory in the linear response regime, i.e., the slow process limit. In fact the minimum cost of driving a system with relaxation time τ_R along a path of length $\mathcal{L}$ in time τ is $\tau_R\mathcal{L}^2/\tau$. Applied to our engine, when the qubit traces the cycle of length $\mathcal{L}$, the dissipated power for slow processes must be at least $\tau_R\mathcal{L}^2/\tau^2$ as matching our observations, cf. Figure 12. How to geometrically bound the dissipation in the context of our non-adiabatic master equation formalism for

faster driving is not clear. A major difference is the coupling of energy and coherence. This issue is left for future efforts.

9.6. Experimental Connections

Realization of engines with a working medium composed of an ensemble of spins is an expected development, such as in an NMR experiment [151]. The surprise is the ability to operate an engine with a single spin.

The experimental realization of single qubit engines and refrigerators is in the process of rapid development. In part, this progress is part of a larger effort in developing quantum technology. This breakthrough is due to the ability to cool the ambient environment to temperatures in the range, or colder than, the qubit energy gap [152]. Moreover, the rapid progress in manipulations, designed for quantum information processing, can be employed for the unitary strokes of quantum heat engines. Recently, experimental realizations of four-stroke cycles were demonstrated [42–44] as well as a two-stroke engine [153]. Another application for quantum engines is in quantum sensing and in particular, thermometry. Suggestions that are based on the transition point between a quantum engine cycle and a refrigerator have recently been proposed [154–157].

A more immediate goal is quantum refrigeration [152,158]. Because any quantum device operates in ultracold temperatures, the drive for miniaturization will require an on-the-chip quantum refrigerator replacing the cumbersome dilution refrigerators of today.

10. Conclusions

The qubit thermal engine has been a source of insight concerning finite-time thermodynamics for 30 years, with its origins dating back to a time when qubits were still two-level-systems. Among the lessons from the model was the role of coherence in friction, like phenomena, in the unitary strokes. Further analysis revealed that the generation of coherence occurs on the unitary strokes and is separated from its dissipation, which occurs when the qubit is in contact with the thermal bath. This insight led first to the notion of quantum friction and later to the exploration of shortcuts to adiabaticity (STA). The analysis of the qubit engine generated a unifying overview of these finite-time thermodynamic phenomena. We have tried to present such an overview alongside our new findings.

Our study explores a new chapter in the behavior of the qubit: the study of a driven isothermal process. Recent progress in open system dynamics allowed for the treatment of thermalization processes, driven processes with time dependent Hamiltonians in contact with a heat bath [34,91,99]. This allowed for the Carnot cycle to be analyzed for shorter times than the previous linear response treatments.

This breakthrough was achieved by using a basis of eigenvectors of the instantaneous propagator of the system dynamics in the interaction representation while exploiting the dynamical $SU(2)$ algebra of the qubit. The key to the breakthrough was the non-adiabatic master equation (NAME) [34] that could correctly describe the dynamics of thermalization in a thermodynamically consistent way and eliminate issues of time reordering [99]. In the qubit model, the instantaneous attractor is rotated from the energy direction by an amount that depends on the speed of the driving and it reveals the details of the coupling between energy and coherence.

In the present manuscript, we have analyzed local cycles where the coherence is required to vanish at the switching points between strokes as well as global cycles where coherence is set only by the driving protocols and it is carried from one stroke to the next. For local cycles we designed and implemented an STE protocol that mimics an isotherm. For the global cycles we used only constant adiabatic parameter μ trajectories. Both these types of cycles are analyzed and compared. As a result, for the qubit engine we are now able to assess the role of coherence along the isothermal strokes. The global cycles exhibit oscillations in their efficiency and power once we reach small cycle times (fast driving). These oscillations are due to the oscillations in coherence and how the timing of the switching between strokes happens to catch the coherence oscillation of the previous stroke.

The Carnot-like cycles show enhanced sensitivity to coherence. This coherence can be reduced by weak measurement of the energy causing pure dephasing. Dephasing is damaging for short cycles periods, but it can be beneficial for intermediate cycle times. Another coherence related finding concerns the global Otto cycle in the sudden limit near which the coherence of the engine acts as a useful flywheel.

Our analysis calculates the entropy production rate from first principles. Using inertial coordinates for the qubit, we generally find that this entropy production naturally takes a flux-times-force form. In the high temperature limit, we find a linear relation between these fluxes and forces and an associated Onsager relation.

The present manuscript managed to compare the known behavior of local and global Otto and Carnot-like cycles. That is a lot to compare. We tried to focus on the new emergent phenomena in a coherent Carnot-type cycle. We found that, to discuss these phenomena, we needed a backdrop of related results to compare to. The above attempted synthesis is the outcome.

Author Contributions: This study is a chapter in a 25 year collaboration between P.S. and R.K., initiated by the study of an Otto spin engine with Tova Feldmann and Eitan Geva [63]. The focus on the Carnot cycle was inspired by a comment by Peter during a visit to Jerusalem, pointing out a discrepancy in the quantum heat engine studies between the many studies of Otto cycles and the few studies of Carnot and other cycles. The reason was the lack of an adequate thermodynamically consistent master equation for the isothermal strokes. It took four years to address the issue. The first step is the development of the non adiabatic master equation by R.D. and Amikam Levy [34]. R.D. continued the development setting it on firm theoretical grounds with the inertial theorem. Returning to the original objective, a shortcut to equilibration was developed [91]. The present study incorporates a broad perspective as well as many new results on the role of coherence in entropy production in the Carnot and Otto cycles. All authors have read and agreed to the published version of the manuscript.

Funding: This research was supported by the Adams Fellowship Program of the Israel Academy of Sciences and Humanities and the Israel Science Foundation, grant number 2244/14.

Acknowledgments: We would like to thank our many contributors to this study: Tova Feldmann, Eitan Geva, Lajos Diosi, Jose P Palao, Yair Rezek, Karl Heinz Hoffmann, Amikam Levy, Raam Uzdin, James Nulton, Frank Boldt, Ander Tobalina, and Andrea Insinga.

Conflicts of Interest: The authors declare no conflict of interest.

Abbreviations

The following abbreviations are used in this manuscript:

GKLS	Gorini, Kossakowski, Linblad, Sudarshan; Master equation
CPTP	Completely Positive Trace Preserving map
NAME	Non-Adiabatic Master Equation
FEAT	Fastest Effectively Adiabatic transition
STA	Shortcut To Adiabticity
STE	Shortcut To Equilibrium

Appendix A. Representations of the Qubit State

The qubit state can be described in many alternative ways. Each representation highlights a certain aspect of the engine. We will now summarize the different approaches and the relation between them. The basic construction relies on a set of orthogonal operators that form a closed Lie Algebra $\{\hat{A}\}$

$$[\hat{A}_i, \hat{A}_j] = \sum_k C_k^{ij} \hat{A}_k \tag{A1}$$

where C_k^{ij} is the structure tensor of the algebra. The orthogonality relation:

$$\mathrm{tr}\{\hat{A}_i^\dagger \hat{A}_j\} = \delta_{ij} \ , \tag{A2}$$

where the identity $\hat{I}$ is part of the set and all other operators are therefore traceless. Under these conditions the state $\hat{\rho}$ can be expanded as a linear combination of the set $\{\hat{A}\}$

$$\hat{\rho} = \frac{1}{N}\hat{I} + \sum_j \alpha_j \hat{A}_j \ , \tag{A3}$$

where $\alpha_j = \langle \hat{A}_j \rangle$ and N is the size of Hilbert space. An alternative formulation includes representing the state in terms of a generalized Gibbs state [101]:

$$\hat{\rho} = \frac{1}{Z} \exp\left(\sum_j \lambda_j \hat{A}_j \right) \ . \tag{A4}$$

The generalized Gibbs state is the maximum entropy state subject to the constrains of the expectation value $\langle \hat{A}_j \rangle = \mathrm{tr}\{\hat{\rho}\hat{A}_j\}$, this leads to a set of non linear equations which determines the Lagrange multipliers λ_j. The forms (A3) and (A4) are unique once the expectation values $\langle \hat{A}_j \rangle$ are known.

It is convenient to express the generalized Gibbs state as a product form [159]

$$\hat{\rho} = \frac{1}{Z} \prod_k \exp(\gamma_j \hat{A}_j) \ . \tag{A5}$$

This form is not unique since it depends on the order of operators. Once the order is set the coefficients $\{\gamma_j\}$ are determined from the expectation values $\{\langle \hat{A}_j \rangle\}$.

Specifically, for the qubit we employ the $SU(2)$ algebra and three sets of orthogonal bases. The first basis set $\vec{s} = \{\hat{S}_x, \hat{S}_y, \hat{S}_z\}^T$ represents the static polarization, where $\hat{S}_j$ are the spin operators with the commutation relation of the $SU(2)$ algebra $[\hat{S}_i, \hat{S}_j] = i\hbar\epsilon_{ijk}\hat{S}_k$ and $\hat{\sigma}_j$. In terms of the Pauli operators $\hat{\sigma}_j$ they are expressed as $\hat{S}_j = \frac{\hbar}{2}\hat{\sigma}_j$. An arbitrary state is expressed as a linear combination of these operators in Equation (4). A geometric interpretation uses this set as a Cartesian basis in 3D Figure 1. A time-dependent rotation around the $\hat{S}_y$ axis leads, up to a scaling, to the dynamical basis set $\vec{v}\,(t) = \{\hat{H}, \hat{L}, \hat{C}\}^T$, Equation (32). The $SU(2)$ algebra in the polarization basis defines a rotation in Liouville space

$$\mathcal{R}_y(\phi) = \exp\left(\frac{i}{\hbar}[\hat{S}_y, \bullet]\phi \right) = e^{\frac{i}{\hbar}\hat{S}_y\phi} \bullet e^{-\frac{i}{\hbar}\hat{S}_y\phi} \ , \tag{A6}$$

and the relation between the two basis sets

$$\vec{v} = \Omega(t)\mathcal{R}_y(\phi(t))\vec{s} \tag{A7}$$

where $\phi = \arccos(\omega/\Omega)$. The explicit dependence of $\Omega(t)$ and $\phi(t)$ means that the dynamical basis set $\vec{v}$ is time-dependent.

In terms of the dynamical basis set, the linear form of the state Equation (33) is defined. Since the Hamiltonian $\hat{H}$ is part of $\vec{v}$, it is natural to define the generalized Gibbs state

$$\hat{\rho} = \frac{1}{Z} \exp\left(-(\beta\hat{H} + \lambda\hat{L} + \gamma\hat{C}) \right) \tag{A8}$$

The standard Gibbs state is obtained when $\gamma = \lambda = 0$ then $\beta = \frac{2}{\hbar\Omega}\tanh^{-1}\left(\frac{2\langle\hat{H}\rangle}{\hbar\Omega}\right)$.

The third basis set is obtained from the eigenoperators of the free propagator $\{\hat{\chi}, \hat{\sigma}, \hat{\sigma}^\dagger\}^T$, Equation (52). In terms of this set the linear form of the state in the interaction representation is given by Equation (58). In addition, the state can be expressed in a generalized Gibbs state form

$$\tilde{\rho} = \tilde{Z}^{-1} \exp\left(-\left(\tilde{\beta}\hat{\chi} + \tilde{\gamma}\hat{\sigma} + \tilde{\gamma}^*\hat{\sigma}^\dagger \right) \right) \ . \tag{A9}$$

An equivalent product form has been previously been employed in Ref. [91]

$$\tilde{\rho} = Z^{-1} e^{\tilde{\gamma}\hat{\sigma}} e^{\tilde{\beta}\hat{\chi}} e^{\tilde{\gamma}^{*}\hat{\sigma}^{\dagger}} \ , \tag{A10}$$

where $\tilde{Z} \equiv \tilde{Z}(t) = \mathrm{tr}\left(\tilde{\rho}_S(t)\right)$ is the partition function, with time-dependent parameters $\tilde{\gamma}(t)$ and $\tilde{\beta}$.

In Section 5.4 we modify the basis set $\vec{g} = \{\hat{\chi}, \hat{\sigma}, \hat{\sigma}^{\dagger}\}^{T}$ to a hemitian basis: $\vec{g}' = \{\hat{\chi}, \hat{\sigma}_x, \hat{\sigma}_y\}^{T}$ where $\hat{\sigma}_x = \frac{1}{\sqrt{2}}(\hat{\sigma} + \hat{\sigma}^{\dagger})$ and $\hat{\sigma}_y = \frac{i}{\sqrt{2}}(\hat{\sigma} - \hat{\sigma}^{\dagger})$. The new representation allows relating the basis $\vec{v}$ to $\vec{g}$ by a scaling and rotation around the $\hat{L}$ axis (cf. Figure 1)

$$\vec{g}' = \frac{\sqrt{2}}{\hbar\Omega} \mathcal{R}_L(\xi) \vec{v} \ , \tag{A11}$$

where $\xi = \arccos(1/\sqrt{1+\mu^2})$ and $\mathcal{R}_L(\xi) = \exp\left(\frac{i}{\hbar\Omega}[\hat{L}, \bullet]\xi\right)$.

When studying the entropy production rate in Section 5.4 we take advantage of the form

$$\tilde{\rho} = \tilde{Z}^{-1} \exp\left(-\left(\tilde{\beta}\hat{\chi} + \tilde{\gamma}_x\hat{\sigma}_x + \tilde{\gamma}_y\hat{\sigma}_y\right)\right) \ . \tag{A12}$$

The $\{\tilde{\beta}, \tilde{\gamma}_x, \tilde{\gamma}_y\}$ time-dependent parameters are defined by the eigenoperators expectation values. The relations are given by

$$\langle\hat{\chi}\rangle_{int} = f(r)\,\tilde{\beta} \ \ ; \ \ \langle\hat{\sigma}_x\rangle_{int} = f(r)\,\tilde{\gamma}_x \ \ ; \ \ \langle\hat{\sigma}_y\rangle_{int} = f(r)\,\tilde{\gamma}_y \ , \tag{A13}$$

where $\langle\bullet\rangle = \mathrm{tr}\left(\bullet\tilde{\rho}\right)$, $f(r) = -\frac{1}{\sqrt{2}r}\tanh\left(\frac{r}{\sqrt{2}}\right)$ with $r = \sqrt{\tilde{\beta}^2 + \tilde{\gamma}_x^2 + \tilde{\gamma}_y^2}$. In the large temperature limit $f(r) \approx -\frac{1}{2}$, which leads to simple relations between the thermodynamic fluxes and forces in the classical regime. Alternatively, the parameters can be expressed in terms of the expectation values

$$\tilde{\beta} = s(k)\,\langle\hat{\chi}\rangle_{int} \ \ ; \ \ \tilde{\gamma}_x = s(k)\,\langle\hat{\sigma}_x\rangle_{int} \ \ ; \ \ \tilde{\gamma}_y = s(k)\,\langle\hat{\sigma}_y\rangle_{int} \ , \tag{A14}$$

where $s(k) = \log\left(\frac{1-\sqrt{2}k}{\sqrt{2}k+1}\right) / \left(\sqrt{2}k\right)$ with $k = \sqrt{\langle\hat{\sigma}_x\rangle_{int}^2 + \langle\hat{\sigma}_y\rangle_{int}^2 + \langle\hat{\chi}\rangle_{int}^2}$

Appendix B. Explicit Expressions

The transition matrix from the basis operators $\vec{v}$ to the basis operators $\vec{g}$. The matrix appears in the inertial solution of the qubit, Equation (51):

$$P = \begin{bmatrix} 1 & -\mu & -\mu \\ 0 & i\kappa & -i\kappa \\ \mu & 1 & 1 \end{bmatrix} \ . \tag{A15}$$

Table A1. Definitions and notations summary.

Parameters	Description
$\{\hat{H}, \hat{L}, \hat{C}\}$; $\vec{v}$	dynamical operator basis; associated vector in Liouville space
$\{\hat{S}_x, \hat{S}_y, \hat{S}_z\}$; $\vec{s}$	polarization operator basis; vector in Liouville space
$\{\hat{\chi}, \hat{\sigma}, \hat{\sigma}^{\dagger}\}$; $\vec{g}$	eigenoperator basis; vector in Liouville space
$\{\hat{\chi}, \hat{\sigma}_x, \hat{\sigma}_y\}$; $\vec{g}'$	eigenoperator basis; vector in Liouville space
X^H	Heisenberg picture
$\tilde{X}$	interaction picture
ω and ϵ	control parameters
Ω	generalized Rabi frequency

Table A1. *Cont.*

Parameters	Description
$\vec{S}$	polarization vector
$\bar{S}$	polarization
$\bar{S}_H$	projection of the polarization vector on the energy axis
$\bar{S}_{eq}$	thermal polarization
T	bath temperature
$\{\Lambda\}$	dynamical propagators
$\mathcal{S}_{v.n}$	von-Neumann entropy
$\mathcal{S}_H$	energy entropy
σ^u_{cyc}	entropy production per cycle
Σ^u	entropy production rate
Γ	decay rate
η_C and $\mathcal{W}_C$	efficiency and work of the Carnot cycle
η_i, $\mathcal{W}_i$, $\mathcal{P}_i$ and $\mathcal{Q}_i$	efficiency, work, power and heat of the i'th cycle
μ	adiabatic parameter
κ	Inertial scaling factor
α	effective frequency
$\mathfrak{C}$	coherence
$\mathcal{W}_{fric}$	work to counter friction
ϕ	$\arccos(\omega/\Omega)$
Φ	$\phi_a - \phi_b$
P	transformation matrix between $\vec{v}$ and $\vec{g}$
D	eigenvalue matrix of the eigenoperators
T_i	effective temperatures
$\mathcal{J}_y$	thermodynamic fluxes
$\mathcal{F}_y$	thermodynamic force

References

1. Carnot, S. *Réflexions sur la Puissance Motrice du feu et sur les Machines Propres à Développer Cette Puissance*; Bachelier: Paris, France, 1824.
2. Salamon, P.; Nulton, J.; Siragusa, G.; Andersen, T.R.; Limon, A. Principles of control thermodynamics. *Energy* **2001**, *26*, 307–319. [CrossRef]
3. Andresen, B.; Berry, R.S.; Ondrechen, M.J.; Salamon, P. Thermodynamics for processes in finite time. *Acc. Chem. Res.* **1984**, *17*, 266–271. [CrossRef]
4. Andresen, B.; Salamon, P.; Berry, R.S. Thermodynamics in finite time: Extremals for imperfect heat engines. *J. Chem. Phys.* **1977**, *66*, 1571–1577. [CrossRef]
5. Hoffmann, K.H.; Burzler, J.M.; Schubert, S. Endoreversible Thermodynamics. *J. Non-Equilib. Thermodyn.* **1997**, *22* 311–355.
6. Andresen, B. Current trends in finite-time thermodynamics. *Angew. Chem. Int. Ed.* **2011**, *50*, 2690–2704. [CrossRef]
7. Curzon, F.; Ahlborn, B. Efficiency of a Carnot engine at maximum power output. *Am. J. Phys.* **1975**, *43*, 22–24. [CrossRef]
8. Salamon, P.; Nitzan, A. Finite time optimizations of a Newton's law Carnot cycle. *J. Chem. Phys.* **1981**, *74*, 3546–3560. [CrossRef]
9. Kraus, K. General state changes in quantum theory. *Ann. Phys.* **1971**, *64*, 311–335. [CrossRef]
10. Lindblad, G. On the generators of quantum dynamical semigroups. *Commun. Math. Phys.* **1976**, *48*, 119–130. [CrossRef]
11. Gorini, V.; Kossakowski, A.; Sudarshan, E.C.G. Completely positive dynamical semigroups of N-level systems. *J. Math. Phys.* **1976**, *17*, 821–825. [CrossRef]
12. Alicki, R.; Kosloff, R. Introduction to Quantum Thermodynamics: History and Prospects. In *Thermodynamics in the Quantum Regime*; Binder, F., Correa, L.A., Gogolin, C., Anders, J., Adesso, G., Eds.; Fundamental Theories of Physics; Springer: Berlin/Heidelberg, Germany, 2018. [CrossRef]
13. Davies, E.B. Markovian master equations. *Commun. Math. Phys.* **1974**, *39*, 91–110. [CrossRef]

14. Levy, A.; Kosloff, R. The local approach to quantum transport may violate the second law of thermodynamics. *EPL Europhys. Lett.* **2014**, *107*, 20004. [CrossRef]
15. Barra, F. The thermodynamic cost of driving quantum systems by their boundaries. *Sci. Rep.* **2015**, *5*, 14873. [CrossRef]
16. Hofer, P.P.; Perarnau-Llobet, M.; Miranda, L.D.M.; Haack, G.; Silva, R.; Brask, J.B.; Brunner, N. Markovian master equations for quantum thermal machines: Local versus global approach. *New J. Phys.* **2017**, *19*, 123037. [CrossRef]
17. González, J.O.; Correa, L.A.; Nocerino, G.; Palao, J.P.; Alonso, D.; Adesso, G. Testing the validity of the 'local'and 'global'GKLS master equations on an exactly solvable model. *Open Syst. Inf. Dyn.* **2017**, *24*, 1740010. [CrossRef]
18. De Chiara, G.; Landi, G.; Hewgill, A.; Reid, B.; Ferraro, A.; Roncaglia, A.J.; Antezza, M. Reconciliation of quantum local master equations with thermodynamics. *New J. Phys.* **2018**, *20*, 113024. [CrossRef]
19. Hewgill, A.; De Chiara, G.; Imparato, A. Quantum thermodynamically consistent local master equations. *arXiv* **2020**, arXiv:2008.04742.
20. Allahverdyan, A.; Nieuwenhuizen, T.M. Extraction of work from a single thermal bath in the quantum regime. *Phys. Rev. Lett.* **2000**, *85*, 1799. [CrossRef]
21. Hilt, S.; Shabbir, S.; Anders, J.; Lutz, E. Landauer's principle in the quantum regime. *Phys. Rev. E* **2011**, *83*, 030102. [CrossRef]
22. Boukobza, E.; Ritsch, H. Breaking the Carnot limit without violating the second law: A thermodynamic analysis of off-resonant quantum light generation. *Phys. Rev. A* **2013**, *87*, 063845. [CrossRef]
23. Uzdin, R.; Levy, A.; Kosloff, R. Equivalence of quantum heat machines, and quantum-thermodynamic signatures. *Phys. Rev. X* **2015**, *5*, 031044. [CrossRef]
24. Roßnagel, J.; Abah, O.; Schmidt-Kaler, F.; Singer, K.; Lutz, E. Nanoscale heat engine beyond the Carnot limit. *Phys. Rev. Lett.* **2014**, *112*, 030602. [CrossRef]
25. Alicki, R.; Fannes, M. Entanglement boost for extractable work from ensembles of quantum batteries. *Phys. Rev. E* **2013**, *87*, 042123. [CrossRef] [PubMed]
26. Mandal, D.; Jarzynski, C. Work and information processing in a solvable model of Maxwell's demon. *Proc. Natl. Acad. Sci. USA* **2012**, *109*, 11641–11645. [CrossRef]
27. Vidrighin, M.D.; Dahlsten, O.; Barbieri, M.; Kim, M.; Vedral, V.; Walmsley, I.A. Photonic Maxwell's demon. *Phys. Rev. Lett.* **2016**, *116*, 050401. [CrossRef]
28. Geva, E.; Kosloff, R.; Skinner, J. On the relaxation of a two-level system driven by a strong electromagnetic field. *J. Chem. Phys.* **1995**, *102*, 8541–8561. [CrossRef]
29. Geva, E.; Kosloff, R. The quantum heat engine and heat pump: An irreversible thermodynamic analysis of the three-level amplifier. *J. Chem. Phys.* **1996**, *104*, 7681–7699. [CrossRef]
30. Correa, L.A.; Palao, J.P.; Adesso, G.; Alonso, D. Performance bound for quantum absorption refrigerators. *Phys. Rev. E* **2013**, *87*, 042131. [CrossRef]
31. Correa, L.A.; Palao, J.P.; Alonso, D.; Adesso, G. Quantum-enhanced absorption refrigerators. *Sci. Rep.* **2014**, *4*, 3949. [CrossRef] [PubMed]
32. Alicki, R.; Gelbwaser-Klimovsky, D.; Kurizki, G. Periodically driven quantum open systems: Tutorial. *arXiv* **2012**, arXiv:1205.4552.
33. Albash, T.; Boixo, S.; Lidar, D.A.; Zanardi, P. Quantum adiabatic Markovian master equations. *New J. Phys.* **2012**, *14*, 123016. [CrossRef]
34. Dann, R.; Levy, A.; Kosloff, R. Time-dependent Markovian quantum master equation. *Phys. Rev. A* **2018**, *98*, 052129. [CrossRef]
35. Kosloff, R. Quantum thermodynamics: A dynamical viewpoint. *Entropy* **2013**, *15*, 2100–2128. [CrossRef]
36. Mandelstam, L.; Tamm, I. The energy–time uncertainty relation in non-relativistic quantum mechanics. *Izv. Akad. Nauk SSSR* **1945**, *9*, 122.
37. Jones, P.J.; Kok, P. Geometric derivation of the quantum speed limit. *Phys. Rev. A* **2010**, *82*, 022107. [CrossRef]
38. Giovannetti, V.; Lloyd, S.; Maccone, L. The speed limit of quantum unitary evolution. *J. Opt. B Quantum Semiclassical Opt.* **2004**, *6*, S807. [CrossRef]
39. Del Campo, A.; Egusquiza, I.; Plenio, M.B.; Huelga, S.F. Quantum speed limits in open system dynamics. *Phys. Rev. Lett.* **2013**, *110*, 050403. [CrossRef]

40. Uzdin, R.; Kosloff, R. Speed limits in Liouville space for open quantum systems. *EPL Europhys. Lett.* **2016**, *115*, 40003. [CrossRef]
41. Funo, K.; Shiraishi, N.; Saito, K. Speed limit for open quantum systems. *New J. Phys.* **2019**, *21*, 013006. [CrossRef]
42. von Lindenfels, D.; Gräb, O.; Schmiegelow, C.T.; Kaushal, V.; Schulz, J.; Mitchison, M.T.; Goold, J.; Schmidt-Kaler, F.; Poschinger, U.G. Spin Heat Engine Coupled to a Harmonic-Oscillator Flywheel. *Phys. Rev. Lett.* **2019**, *123*, 080602. [CrossRef]
43. Ono, K.; Shevchenko, S.; Mori, T.; Moriyama, S.; Nori, F. Analog of a quantum heat engine using a single-spin qubit. *Phys. Rev. Lett.* **2020**, *125*, 166802. [CrossRef]
44. Bouton, Q.; Nettersheim, J.; Burgardt, S.; Adam, D.; Lutz, E.; Widera, A. An endoreversible quantum heat engine driven by atomic collisions. *arXiv* **2020**, arXiv:2009.10946.
45. Bejan, A.; Kestin, J. Entropy Generation Through Heat and Fluid Flow. *J. Appl. Mech.* **1983**, *50*, 475. [CrossRef]
46. Szargut, J. International progress in second law analysis. *Energy* **1980**, *5*, 709–718. [CrossRef]
47. Gouy, M. Sur l'energie utilisable. *J. Phys.* **1889**, *8*, 501. [CrossRef]
48. Stodola, A. *Steam and Gas Turbines*; McGraw-Hill: New York, NY, USA, 1927.
49. Feldmann, T.; Kosloff, R. Characteristics of the limit cycle of a reciprocating quantum heat engine. *Phys. Rev. E* **2004**, *70*, 046110. [CrossRef]
50. Lindblad, G. Expectations and entropy inequalities for finite quantum systems. *Commun. Math. Phys.* **1974**, *39*, 111–119. [CrossRef]
51. Feldmann, T.; Kosloff, R. Quantum four-stroke heat engine: Thermodynamic observables in a model with intrinsic friction. *Phys. Rev. E* **2003**, *68*, 016101. [CrossRef]
52. Baumgratz, T.; Cramer, M.; Plenio, M.B. Quantifying coherence. *Phys. Rev. Lett.* **2014**, *113*, 140401. [CrossRef]
53. Girolami, D. Observable Measure of Quantum Coherence in Finite Dimensional Systems. *Phys. Rev. Lett.* **2014**, *113*, 170401. [CrossRef]
54. Feldmann, T.; Kosloff, R. Transitions between refrigeration regions in extremely short quantum cycles. *Phys. Rev. E* **2016**, *93*, 052150. [CrossRef] [PubMed]
55. Lin, J. Divergence measures based on the Shannon entropy. *IEEE Trans. Inf. Theory* **1991**, *37*, 145–151. [CrossRef]
56. Breuer, H.P.; Petruccione, F. *The Theory of Open Quantum Systems*; Oxford University Press: Oxford, UK, 2002.
57. Messiah, A. *Quantum Mechanics: Translated [from the French] by J. Potter*; North-Holland: Amsterdam, The Netherlands, 1962.
58. Spohn, H.; Lebowitz, J.L. Irreversible thermodynamics for quantum systems weakly coupled to thermal reservoirs. *Adv. Chem. Phys.* **1978**, *38*, 109–142.
59. Alicki, R. The quantum open system as a model of the heat engine. *J. Phys. A Math. Gen.* **1979**, *12*, L103. [CrossRef]
60. Abiuso, P.; Miller, H.J.; Perarnau-Llobet, M.; Scandi, M. Geometric optimisation of quantum thermodynamic processes. *Entropy* **2020**, *22*, 1076. [CrossRef]
61. Seifert, U. Stochastic thermodynamics, fluctuation theorems and molecular machines. *Rep. Prog. Phys.* **2012**, *75*, 126001. [CrossRef]
62. Sekimoto, K. *Stochastic Energetics*; Springer: Berlin/Heidelberg, Germany, 2010; Volume 799.
63. Feldmann, T.; Geva, E.; Kosloff, R.; Salamon, P. Heat engines in finite time governed by master equations. *Am. J. Phys.* **1996**, *64*, 485–492. [CrossRef]
64. Geva, E.; Kosloff, R. A quantum-mechanical heat engine operating in finite time. A model consisting of spin-1/2 systems as the working fluid. *J. Chem. Phys.* **1992**, *96*, 3054–3067. [CrossRef]
65. Novikov, I. The efficiency of atomic power stations (a review). *J. Nucl. Energy (1954)* **1958**, *7*, 125–128. [CrossRef]
66. Esposito, M.; Kawai, R.; Lindenberg, K.; Van den Broeck, C. Efficiency at maximum power of low-dissipation Carnot engines. *Phys. Rev. Lett.* **2010**, *105*, 150603. [CrossRef]
67. Abiuso, P.; Perarnau-Llobet, M. Optimal cycles for low-dissipation heat engines. *Phys. Rev. Lett.* **2020**, *124*, 110606. [CrossRef] [PubMed]
68. Abiuso, P.; Giovannetti, V. Non-Markov enhancement of maximum power for quantum thermal machines. *Phys. Rev. A* **2019**, *99*, 052106. [CrossRef]

69. Erdman, P.A.; Cavina, V.; Fazio, R.; Taddei, F.; Giovannetti, V. Maximum power and corresponding efficiency for two-level heat engines and refrigerators: Optimality of fast cycles. *New J. Phys.* **2019**, *21*, 103049. [CrossRef]
70. Karimi, B.; Pekola, J. Otto refrigerator based on a superconducting qubit: Classical and quantum performance. *Phys. Rev. B* **2016**, *94*, 184503. [CrossRef]
71. Pekola, J.P.; Karimi, B.; Thomas, G.; Averin, D.V. Supremacy of incoherent sudden cycles. *Phys. Rev. B* **2019**, *100*, 085405. [CrossRef]
72. Feldmann, T.; Kosloff, R. Performance of discrete heat engines and heat pumps in finite time. *Phys. Rev. E* **2000**, *61*, 4774. [CrossRef]
73. Scully, M.O.; Zubairy, M.S.; Agarwal, G.S.; Walther, H. Extracting work from a single heat bath via vanishing quantum coherence. *Science* **2003**, *299*, 862–864. [CrossRef]
74. Francica, G.; Goold, J.; Plastina, F. Role of coherence in the nonequilibrium thermodynamics of quantum systems. *Phys. Rev. E* **2019**, *99*, 042105. [CrossRef]
75. Dann, R.; Kosloff, R. Quantum signatures in the quantum Carnot cycle. *New J. Phys.* **2020**, *22*, 013055. [CrossRef]
76. Kosloff, R.; Feldmann, T. Discrete four-stroke quantum heat engine exploring the origin of friction. *Phys. Rev. E* **2002**, *65*, 055102. [CrossRef]
77. Boldt, F.; Nulton, J.D.; Andresen, B.; Salamon, P.; Hoffmann, K.H. Casimir companion: An invariant of motion for Hamiltonian systems. *Phys. Rev. A* **2013**, *87*, 022116. [CrossRef]
78. Brandner, K.; Saito, K. Thermodynamic geometry of microscopic heat engines. *Phys. Rev. Lett.* **2020**, *124*, 040602. [CrossRef]
79. Chen, X.; Ruschhaupt, A.; Schmidt, S.; del Campo, A.; Guéry-Odelin, D.; Muga, J.G. Fast optimal frictionless atom cooling in harmonic traps: Shortcut to adiabaticity. *Phys. Rev. Lett.* **2010**, *104*, 063002. [CrossRef]
80. Guéry-Odelin, D.; Ruschhaupt, A.; Kiely, A.; Torrontegui, E.; Martínez-Garaot, S.; Muga, J.G. Shortcuts to adiabaticity: Concepts, methods, and applications. *Rev. Mod. Phys.* **2019**, *91*, 045001. [CrossRef]
81. Torrontegui, E.; Lizuain, I.; González-Resines, S.; Tobalina, A.; Ruschhaupt, A.; Kosloff, R.; Muga, J.G. Energy consumption for shortcuts to adiabaticity. *Phys. Rev. A* **2017**, *96*, 022133. [CrossRef]
82. Zheng, Y.; Campbell, S.; De Chiara, G.; Poletti, D. Cost of counterdiabatic driving and work output. *Phys. Rev. A* **2016**, *94*, 042132. [CrossRef]
83. Campbell, S.; Deffner, S. Trade-off between speed and cost in shortcuts to adiabaticity. *Phys. Rev. Lett.* **2017**, *118*, 100601. [CrossRef]
84. Abah, O.; Lutz, E. Performance of shortcut-to-adiabaticity quantum engines. *Phys. Rev. E* **2018**, *98*, 032121. [CrossRef]
85. Çakmak, B.; Müstecaplıoğlu, Ö.E. Spin quantum heat engines with shortcuts to adiabaticity. *Phys. Rev. E* **2019**, *99*, 032108. [CrossRef]
86. Boldt, F.; Hoffmann, K.; Salamon, P.; Kosloff, R. Time-optimal processes for interacting spin systems. *EPL Europhys. Lett.* **2012**, *99*, 40002. [CrossRef]
87. Boldt, F.; Salamon, P.; Hoffmann, K.H. Fastest effectively adiabatic transitions for a collection of harmonic oscillators. *J. Phys. Chem. A* **2016**, *120*, 3218–3224. [CrossRef] [PubMed]
88. Funo, K.; Lambert, N.; Karimi, B.; Pekola, J.P.; Masuyama, Y.; Nori, F. Speeding up a quantum refrigerator via counterdiabatic driving. *Phys. Rev. B* **2019**, *100*, 035407. [CrossRef]
89. Tobalina, A.; Lizuain, I.; Muga, J. Vanishing efficiency of a speeded-up ion-in-Paul-trap Otto engine. *EPL Europhys. Lett.* **2019**, *127*, 20005. [CrossRef]
90. Dann, R.; Tobalina, A.; Kosloff, R. Shortcut to equilibration of an open quantum system. *Phys. Rev. Lett.* **2019**, *122*, 250402. [CrossRef]
91. Dann, R.; Tobalina, A.; Kosloff, R. Fast route to equilibration. *Phys. Rev. A* **2020**, *101*, 052102. [CrossRef]
92. Pancotti, N.; Scandi, M.; Mitchison, M.T.; Perarnau-Llobet, M. Speed-Ups to Isothermality: Enhanced Quantum Thermal Machines through Control of the System-Bath Coupling. *Phys. Rev. X* **2020**, *10*, 031015.
93. Villazon, T.; Polkovnikov, A.; Chandran, A. Swift heat transfer by fast-forward driving in open quantum systems. *Phys. Rev. A* **2019**, *100*, 012126. [CrossRef]
94. Henrich, M.J.; Rempp, F.; Mahler, G. Quantum thermodynamic Otto machines: A spin-system approach. *Eur. Phys. J. Spec. Top.* **2007**, *151*, 157–165. [CrossRef]
95. Kosloff, R.; Rezek, Y. The quantum harmonic Otto cycle. *Entropy* **2017**, *19*, 136. [CrossRef]

96. Wu, F.; Chen, L.; Sun, F.; Wu, C. Finite-time exergoeconomic performance bound for a quantum Stirling engine. *Int. J. Eng. Sci.* **2000**, *38*, 239–247. [CrossRef]
97. Yin, Y.; Chen, L.; Wu, F. Optimal power and efficiency of quantum Stirling heat engines. *Eur. Phys. J. Plus* **2017**, *132*, 1–10. [CrossRef]
98. Dong, C.; Lefkidis, G.; Hübner, W. Magnetic quantum diesel engine in Ni 2. *Phys. Rev. B* **2013**, *88*, 214421. [CrossRef]
99. Dann, R.; Kosloff, R. The Inertial Theorem. *arXiv* **2018**, arXiv:1810.12094.
100. Scandi, M.; Miller, H.J.; Anders, J.; Perarnau-Llobet, M. Quantum work statistics close to equilibrium. *Phys. Rev. Res.* **2020**, *2*, 023377. [CrossRef]
101. Alhassid, Y.; Levine, R. Connection between the maximal entropy and the scattering theoretic analyses of collision processes. *Phys. Rev. A* **1978**, *18*, 89. [CrossRef]
102. Onsager, L. Reciprocal relations in irreversible processes. I. *Phys. Rev.* **1931**, *37*, 405. [CrossRef]
103. Onsager, L. Reciprocal relations in irreversible processes. II. *Phys. Rev.* **1931**, *38*, 2265. [CrossRef]
104. De Groot, S.R.; Mazur, P. *Non-Equilibrium Thermodynamics*; North-Holland: Amsterdam, The Netherlands, 2013.
105. Hoffmann, K.; Salamon, P.; Rezek, Y.; Kosloff, R. Time-optimal controls for frictionless cooling in harmonic traps. *EPL Europhys. Lett.* **2011**, *96*, 60015. [CrossRef]
106. Del Campo, A.; Goold, J.; Paternostro, M. More bang for your buck: Super-adiabatic quantum engines. *Sci. Rep.* **2014**, *4*, 6208. [CrossRef] [PubMed]
107. Rezek, Y.; Kosloff, R. Irreversible performance of a quantum harmonic heat engine. *New J. Phys.* **2006**, *8*, 83. [CrossRef]
108. Ma, Y.H.; Xu, D.; Dong, H.; Sun, C.P. Universal constraint for efficiency and power of a low-dissipation heat engine. *Phys. Rev. E* **2018**, *98*, 042112. [CrossRef]
109. Ryabov, A.; Holubec, V. Maximum efficiency of steady-state heat engines at arbitrary power. *Phys. Rev. E* **2016**, *93*, 050101. [CrossRef]
110. Solfanelli, A.; Falsetti, M.; Campisi, M. Nonadiabatic single-qubit quantum Otto engine. *Phys. Rev. B* **2020**, *101*, 054513. [CrossRef]
111. Alecce, A.; Galve, F.; Gullo, N.L.; Dell'Anna, L.; Plastina, F.; Zambrini, R. Quantum Otto cycle with inner friction: Finite-time and disorder effects. *New J. Phys.* **2015**, *17*, 075007. [CrossRef]
112. Ma, Y.H.; Xu, D.; Dong, H.; Sun, C.P. Optimal operating protocol to achieve efficiency at maximum power of heat engines. *Phys. Rev. E* **2018**, *98*, 022133. [CrossRef]
113. Lostaglio, M. Certifying quantum signatures in thermodynamics and metrology via contextuality of quantum linear response. *arXiv* **2020**, arXiv:2004.01213.
114. Diosi, L. Weak measurements in quantum mechanics. *arXiv* **2005**, arXiv:quant-ph/0505075.
115. Facchi, P.; Gorini, V.; Marmo, G.; Pascazio, S.; Sudarshan, E. Quantum zeno dynamics. *Phys. Lett. A* **2000**, *275*, 12–19. [CrossRef]
116. Uzdin, R.; Gasparinetti, S.; Ozeri, R.; Kosloff, R. Markovian heat sources with the smallest heat capacity. *New J. Phys.* **2018**, *20*, 063030. [CrossRef]
117. Feldmann, T.; Kosloff, R. Quantum lubrication: Suppression of friction in a first-principles four-stroke heat engine. *Phys. Rev. E* **2006**, *73*, 025107. [CrossRef]
118. Elouard, C.; Herrera-Martí, D.A.; Clusel, M.; Auffèves, A. The role of quantum measurement in stochastic thermodynamics. *Npj Quantum Inf.* **2017**, *3*, 1–10. [CrossRef]
119. Elouard, C.; Jordan, A.N. Efficient quantum measurement engines. *Phys. Rev. Lett.* **2018**, *120*, 260601. [CrossRef]
120. Guryanova, Y.; Friis, N.; Huber, M. Ideal projective measurements have infinite resource costs. *Quantum* **2020**, *4*, 222. [CrossRef]
121. Zhang, T.; Liu, W.T.; Chen, P.X.; Li, C.Z. Four-level entangled quantum heat engines. *Phys. Rev. A* **2007**, *75*, 062102. [CrossRef]
122. Wang, H.; Liu, S.; He, J. Thermal entanglement in two-atom cavity QED and the entangled quantum Otto engine. *Phys. Rev. E* **2009**, *79*, 041113. [CrossRef]
123. He, J.-Z.; He, X.; Zheng, J. Entangled quantum heat engine based on two-qubit Heisenberg XY model. *Chin. Phys. B* **2012**, *21*, 050303. [CrossRef]
124. Halpern, N.Y.; White, C.D.; Gopalakrishnan, S.; Refael, G. Quantum engine based on many-body localization. *Phys. Rev. B* **2019**, *99*, 024203. [CrossRef]

125. Hardal, A.Ü.; Müstecaplıoğlu, Ö.E. Superradiant quantum heat engine. *Sci. Rep.* **2015**, *5*, 12953. [CrossRef]
126. Campisi, M.; Fazio, R. The power of a critical heat engine. *Nat. Commun.* **2016**, *7*, 11895. [CrossRef]
127. Niedenzu, W.; Kurizki, G. Cooperative many-body enhancement of quantum thermal machine power. *New J. Phys.* **2018**, *20*, 113038. [CrossRef]
128. Mukherjee, V.; Divakaran, U.; del Campo, A. Universal finite-time thermodynamics of many-body quantum machines from Kibble-Zurek scaling. *arXiv* **2020**, arXiv:2003.06607.
129. Jaramillo, J.; Beau, M.; del Campo, A. Quantum supremacy of many-particle thermal machines. *New J. Phys.* **2016**, *18*, 075019. [CrossRef]
130. Jaseem, N.; Hajdusek, M.; Vedral, V.; Fazio, R.; Kwek, L.C.; Vinjanampathy, S. Quantum synchronization in nanoscale heat engines. *Phys. Rev. E* **2020**, *101*, 020201. [CrossRef]
131. Correa, L.A.; Palao, J.P.; Alonso, D. Internal dissipation and heat leaks in quantum thermodynamic cycles. *Phys. Rev. E* **2015**, *92*, 032136. [CrossRef]
132. Newman, D.; Mintert, F.; Nazir, A. Performance of a quantum heat engine at strong reservoir coupling. *Phys. Rev. E* **2017**, *95*, 032139. [CrossRef]
133. Perarnau-Llobet, M.; Wilming, H.; Riera, A.; Gallego, R.; Eisert, J. Strong coupling corrections in quantum thermodynamics. *Phys. Rev. Lett.* **2018**, *120*, 120602. [CrossRef]
134. Shiraishi, N.; Saito, K.; Tasaki, H. Universal trade-off relation between power and efficiency for heat engines. *Phys. Rev. Lett.* **2016**, *117*, 190601. [CrossRef]
135. Pietzonka, P.; Seifert, U. Universal trade-off between power, efficiency, and constancy in steady-state heat engines. *Phys. Rev. Lett.* **2018**, *120*, 190602. [CrossRef]
136. Funo, K.; Ueda, M.; Sagawa, T. *Thermodynamics in the Quantum Regime*; Binder, F., Correa, L.A., Gogolin, C., Anders, J., Adesso, G., Eds.; Fundamental Theories of Physics; Springer: Berlin/Heidelberg, Germany, 2018; pp. 249–273. [CrossRef]
137. Denzler, T.; Lutz, E. Power fluctuations in a finite-time quantum Carnot engine. *arXiv* **2020**, arXiv:2007.01034.
138. Silaev, M.; Heikkilä, T.T.; Virtanen, P. Lindblad-equation approach for the full counting statistics of work and heat in driven quantum systems. *Phys. Rev. E* **2014**, *90*, 022103. [CrossRef]
139. Tsirlin, A.; Sukin, I. Averaged Optimization and Finite-Time Thermodynamics. *Entropy* **2020**, *22*, 912. [CrossRef]
140. Tondeur, D.; Kvaalen, E. Equipartition of entropy production. An optimality criterion for transfer and separation processes. *Ind. Eng. Chem. Res.* **1987**, *26*, 50–56. [CrossRef]
141. Korzekwa, K.; Lostaglio, M.; Oppenheim, J.; Jennings, D. The extraction of work from quantum coherence. *New J. Phys.* **2016**, *18*, 023045. [CrossRef]
142. Camati, P.A.; Santos, J.F.; Serra, R.M. Coherence effects in the performance of the quantum Otto heat engine. *Phys. Rev. A* **2019**, *99*, 062103. [CrossRef]
143. Geva, E.; Kosloff, R. On the classical limit of quantum thermodynamics in finite time. *J. Chem. Phys.* **1992**, *97*, 4398–4412. [CrossRef]
144. Abah, O.; Rossnagel, J.; Jacob, G.; Deffner, S.; Schmidt-Kaler, F.; Singer, K.; Lutz, E. Single-ion heat engine at maximum power. *Phys. Rev. Lett.* **2012**, *109*, 203006. [CrossRef]
145. Roßnagel, J.; Dawkins, S.T.; Tolazzi, K.N.; Abah, O.; Lutz, E.; Schmidt-Kaler, F.; Singer, K. A single-atom heat engine. *Science* **2016**, *352*, 325–329. [CrossRef]
146. Abah, O.; Paternostro, M. Shortcut-to-adiabaticity Otto engine: A twist to finite-time thermodynamics. *Phys. Rev. E* **2019**, *99*, 022110. [CrossRef] [PubMed]
147. Insinga, A.; Andresen, B.; Salamon, P. Thermodynamical analysis of a quantum heat engine based on harmonic oscillators. *Phys. Rev. E* **2016**, *94*, 012119. [CrossRef]
148. Insinga, A.; Andresen, B.; Salamon, P.; Kosloff, R. Quantum heat engines: Limit cycles and exceptional points. *Phys. Rev. E* **2018**, *97*, 062153. [CrossRef]
149. Deffner, S. Efficiency of harmonic quantum Otto engines at maximal power. *Entropy* **2018**, *20*, 875. [CrossRef]
150. Salamon, P.; Berry, R.S. Thermodynamic length and dissipated availability. *Phys. Rev. Lett.* **1983**, *51*, 1127. [CrossRef]
151. Peterson, J.P.; Batalhão, T.B.; Herrera, M.; Souza, A.M.; Sarthour, R.S.; Oliveira, I.S.; Serra, R.M. Experimental characterization of a spin quantum heat engine. *arXiv* **2018**, arXiv:1803.06021.
152. Pekola, J.P.; Khaymovich, I.M. Thermodynamics in single-electron circuits and superconducting qubits. *Annu. Rev. Condens. Matter Phys.* **2019**, *10*, 193–212. [CrossRef]

153. Klatzow, J.; Becker, J.N.; Ledingham, P.M.; Weinzetl, C.; Kaczmarek, K.T.; Saunders, D.J.; Nunn, J.; Walmsley, I.A.; Uzdin, R.; Poem, E. Experimental demonstration of quantum effects in the operation of microscopic heat engines. *Phys. Rev. Lett.* **2019**, *122*, 110601. [CrossRef]
154. Hofer, P.P.; Brask, J.B.; Perarnau-Llobet, M.; Brunner, N. Quantum thermal machine as a thermometer. *Phys. Rev. Lett.* **2017**, *119*, 090603. [CrossRef]
155. Bhattacharjee, S.; Bhattacharya, U.; Niedenzu, W.; Mukherjee, V.; Dutta, A. Quantum magnetometry using two-stroke thermal machines. *New J. Phys.* **2020**, *22*, 013024. [CrossRef]
156. Bhattacharjee, S.; Dutta, A. Quantum thermal machines and batteries. *arXiv* **2020**, arXiv:2008.07889.
157. Levy, A.; Göb, M.; Deng, B.; Singer, K.; Torrontegui, E.; Wang, D. Single-atom heat engine as a sensitive thermal probe. *New J. Phys.* **2020**, *22*, 093020. [CrossRef]
158. Ronzani, A.; Karimi, B.; Senior, J.; Chang, Y.C.; Peltonen, J.T.; Chen, C.; Pekola, J.P. Tunable photonic heat transport in a quantum heat valve. *Nat. Phys.* **2018**, *14*, 991–995. [CrossRef]
159. Wei, J.; Norman, E. On global representations of the solutions of linear differential equations as a product of exponentials. *Proc. Am. Math. Soc.* **1964**, *15*, 327–334. [CrossRef]

entropy

MDPI

Article

The Quantum Friction and Optimal Finite-Time Performance of the Quantum Otto Cycle

Andrea R. Insinga

DTU Energy Conversion and Storage, Technical University of Denmark Anker Engelundsvej, Building 301, 2800 Kgs. Lyngby, Denmark; aroin@dtu.dk

Received: 31 July 2020; Accepted: 18 September 2020; Published: 22 September 2020

Abstract: In this work we considered the quantum Otto cycle within an optimization framework. The goal was maximizing the power for a heat engine or maximizing the cooling power for a refrigerator. In the field of finite-time quantum thermodynamics it is common to consider frictionless trajectories since these have been shown to maximize the work extraction during the adiabatic processes. Furthermore, for frictionless cycles, the energy of the system decouples from the other degrees of freedom, thereby simplifying the mathematical treatment. Instead, we considered general limit cycles and we used analytical techniques to compute the derivative of the work production over the whole cycle with respect to the time allocated for each of the adiabatic processes. By doing so, we were able to directly show that the frictionless cycle maximizes the work production, implying that the optimal power production must necessarily allow for some friction generation so that the duration of the cycle is reduced.

Keywords: quantum thermodynamics; maximum power; shortcut to adiabaticity; quantum friction; Otto cycle; quantum engine; quantum refrigerator

1. Introduction

Quantum models of heat engines and refrigerators have been investigated extensively, especially because of the relevance of these models to the problem of cooling at extremely low temperatures, i.e., near absolute zero. The most well-studied case is the quantum analog of the Otto cycle [1–4] for which heat-exchange and work-exchange take place in different steps of the thermodynamic cycle, although the Carnot cycle has been investigated as well [5,6].

We consider the typical optimization perspective assumed in the field of finite-time thermodynamics: maximization of the average power extracted from a heat-engine [7–9] or the average cooling power provided by a refrigerator [3,10].

In the seminal works by Berry [11] and by Rezek et al. [12] it has been shown that finite-time cycles can be constructed such that quantum friction is entirely suppressed. This result is surprising since intuition would suggest that frictionless operation could only be achieved in the quasi-static regime, i.e., cycles of infinite duration. The attainability of frictionless finite-time quantum processes has been experimentally confirmed by Deng et al. [13].

Salamon et al. [14] showed that these frictionless adiabatic trajectories maximize the work exchanged with the system with respect to the compression/expansion time-law. This is due to the suppression of quantum friction which would otherwise cause part of the exchanged energy to be spent in increasing the coherence of the system. Similarly to other relevant studies, such as those by Abah et al. [15,16], frictionless trajectories have been shown to be the optimal finite-time processes that connect two different thermal states while guaranteeing maximal work extraction, i.e., equal to that obtained in the quasi-static limit.

These analyses are often very insightful [1,17,18], due to the fact that the resulting cycles are mathematically simpler to investigate, thereby admitting analytical computation of, e.g., power and

efficiency. Frequently, cycles for which the power is optimized with the constraint of frictionless adiabats are referred to as maximum-power cycles. The argument behind this statement is that the maximum realizable work can be obtained in finite time, but there is a lower bound to the minimum time required to achieve this effect. This observation would appear to suggest that the minimum-time frictionless cycle has to correspond to maximum power.

However, as we argue in the present work, the frictionless cycles are not truly maximizing the power with respect to the time allocated for the cycle. In fact, by relaxing the requirement of frictionless adiabats it is possible to reduce the time allocation for the adiabatic processes, thereby improving the power extraction, although the work extraction per cycle is slightly reduced as well. Evidence for this argument has already been presented by employing numerical methods [19]. Moreover, the experimental realization of a quantum engine demonstrated by Peterson et al. [2] also revealed that maximal power production is obtained by a time allocation that is shorter than that of a maximal-work cycle.

Here we consider general limit-cycle trajectories as functions of the time allocation for the adiabatic processes. By employing analytical calculations, we explicitly show for the first time that the special frictionless cycles provide maximum work extraction over the whole cycle. Since the average power is the work divided by the total duration of the cycle, maximum-work cycles cannot simultaneously be maximum-power cycles. It is convenient to allow for a small amount of friction production, which slightly reduces the work extraction, in order to reduce the total duration of the cycle and maximize the average power.

The case of a quantum heat engine based on harmonic oscillators is used here as a prototypical system and is analyzed in detail. Subsequently, we consider generalization of the results to other relevant cases. In particular, we also consider the case of maximum cooling power for a quantum refrigerator based on harmonic oscillators. We also consider quantum heat engines and refrigerators with different working fluids, namely, an ensemble of spin systems. All these other cases are shown to be analogous to the harmonic heat engine in that frictionless cycles are not providing maximal power with respect to the time allocation.

2. Framework

2.1. Notation and Units

In this paper, the calligraphic typeface (e.g., $\mathcal{W}$) is used for scalar quantities, underlined uppercase letters (e.g., $\underline{X}$) are used for column vectors, underlined lowercase letters (e.g., $\underline{w}$) are used for row vectors and bold letters (e.g., $\boldsymbol{U}$) are used for matrices.

Superscripts correspond to the row indexes and subscripts to the column indexes. For example $(\boldsymbol{AB})_3^2$ indicates the entry on the second row and third column of the product between the matrix $\boldsymbol{A}$ and the matrix $\boldsymbol{B}$. Operators are denoted with the $\hat{}$ symbol, as in $\hat{X}$. Super-operators are linear operators having operators as input and output arguments. The letter $\mathcal{L}$ in calligraphic font is used for super-operators. For example, $\mathcal{L}_H(\hat{X})$ denotes the super-operator $\mathcal{L}_H$ applied to the operator $\hat{X}$.

Moreover, in this work we assume that the mass m of the oscillators, the Boltzmann constant k and the reduced Planck constant $\hbar$ are all equal to 1.

2.2. Governing Equations

We briefly review here the mathematical formalism discussed in reference [12,19]. The working fluid of the engine is an ensemble of identical quantum harmonic oscillators. The corresponding Hamiltonian operator $\hat{H}$ is parameterized by the angular frequency ω and the mass m of each oscillator:

$$\hat{H}(t) = \frac{1}{2m}\hat{P}^2 + \frac{1}{2}m(\omega(t))^2\,\hat{Q}^2 \tag{1}$$

where $\hat{Q}$ and $\hat{P}$ are the position operator and momentum operator, respectively. In the Heisenberg formalism, the time-evolution of a Hermitian operator $\hat{X}$ is described by the following equation of motion:

$$\frac{d}{dt}\hat{X}(t) = \mathcal{L}_H^*(\hat{X}(t)) + \mathcal{L}_D^*(\hat{X}(t)) + \frac{\partial}{\partial t}\hat{X}(t), \tag{2}$$

where $\mathcal{L}_H^*$ and $\mathcal{L}_D^*$ denote the unitary and non-unitary Liouville super-operators, respectively [1]. The unitary super-operator $\mathcal{L}_H^*$ describes the evolution of a closed system, whose Hamiltonian may be explicitly time-dependent. The super-operator $\mathcal{L}_H^*$ is given by:

$$\mathcal{L}_H^*(\hat{X}(t)) = \frac{i}{\hbar}\left[\hat{H}, \hat{X}\right] \tag{3}$$

For an open system [20,21], i.e., coupled to a thermal reservoir, it is necessary to include the additional non-unitary super-operator $\mathcal{L}_D^*$. For the harmonic oscillator, the non-unitary super-operator is given by:

$$\mathcal{L}_D^*(\hat{X}(t)) = k_\downarrow\left(\hat{a}^\dagger\hat{X}\hat{a} - \frac{1}{2}\left\{\hat{a}^\dagger\hat{a}, \hat{X}\right\}\right) + k_\uparrow\left(\hat{a}\hat{X}\hat{a}^\dagger - \frac{1}{2}\left\{\hat{a}\hat{a}^\dagger, \hat{X}\right\}\right). \tag{4}$$

where $k_\downarrow$ and $k_\uparrow$ are the transition rates, $\hat{a} = 2^{-1/2}\left((m\omega/\hbar)^{1/2}\hat{Q} + i\left(1/(m\omega\hbar)\right)^{1/2}\hat{P}\right)$ is the annihilation operator, its Hermitian conjugate $\hat{a}^\dagger$ is the creation operator and the curly brackets denote the anti-commutator between two operators.

The form assumed by Equation (2) depends on which Lie algebra of Hermitian operators has been chosen [8,22]. In this work, we consider the set $\{\hat{H}, \hat{L}, \hat{C}, \hat{1}\}$, where $\hat{L}$ denotes the Lagrangian operator, $\hat{C} = (\omega/2)\left(\hat{Q}\hat{P} + \hat{P}\hat{Q}\right)$ denotes the position-momentum correlation operator and $\hat{1}$ denotes the identity operator. This set of operators, together with the Lie bracket consisting of taking the commutator between two operators, forms a Lie algebra. It can be shown that the algebra is closed with respect to the time-evolution described by Equation (2). Therefore, denoting by $\underline{X}$ the vector of expectation values $(\langle\hat{H}\rangle, \langle\hat{L}\rangle, \langle\hat{C}\rangle, \langle\hat{1}\rangle)^T$, the linear equation of motion (2) is expressed as:

$$\frac{d}{dt}\underline{X} = \boldsymbol{A}\underline{X} \tag{5}$$

The matrix $\boldsymbol{A}$ is obtained by plugging each of the operators $\{\hat{H}, \hat{L}, \hat{C}, \hat{1}\}$ in Equation (2) and applying the commutation rules derived from the canonical commutation relation $[\hat{Q}, \hat{P}] = i\hbar$.

During the adiabatic processes, i.e., when the ensemble of oscillators is decoupled from the thermal reservoir, the matrix $\boldsymbol{A}$ is given by:

$$\boldsymbol{A} = \omega(t)\begin{pmatrix} \mu & -\mu & 0 & 0 \\ -\mu & \mu & -2 & 0 \\ 0 & 2 & \mu & 0 \\ 0 & 0 & 0 & 0 \end{pmatrix} \tag{6}$$

where μ denotes the dimensionless non-adiabatic parameter; i.e., $\mu = \dot{\omega}/\omega^2$. In this work the parameter μ is assumed to be constant during each of the adiabatic processes, leading to the following time-evolution law [1]:

$$\omega(t) = \frac{\omega(0)}{1 - \mu\omega(0)t} \tag{7}$$

During the isochoric processes the frequency ω is constant, while heat is flowing between the ensemble of oscillators and one of the thermal reservoirs. The matrix $\boldsymbol{A}$ for these steps of the cycle is given by:

$$\boldsymbol{A} = \begin{pmatrix} -\Gamma & 0 & 0 & +\Gamma H_{\mathrm{eq}} \\ 0 & -\Gamma & -2\omega & 0 \\ 0 & +2\omega & -\Gamma & 0 \\ 0 & 0 & 0 & 0 \end{pmatrix} \tag{8}$$

where $\Gamma = k_{\downarrow} - k_{\uparrow}$ denotes the heat conductance and H_{eq} denotes the thermal equilibrium energy, which is a function of the temperature T of the heat reservoir. By inspecting Equation (8), we notice that the dynamic evolution of $\langle \hat{L} \rangle$ and $\langle \hat{C} \rangle$, which during the isochoric processes is decoupled from the evolution of $\langle \hat{H} \rangle$ and $\langle \hat{1} \rangle$, corresponds to a rotation with frequency 2ω accompanied by a decrease of the rotation amplitude. In the long-time limit the amplitude of the rotations approaches zero, thereby leading to a zero-coherence state for which $\langle \hat{L} \rangle = \langle \hat{C} \rangle = 0$, and $\langle \hat{H} \rangle = H_{\mathrm{eq}}$.

The formal solution of Equation (5) is given by the following time-evolution equation:

$$\underline{X}(t) = \boldsymbol{U}(t)\underline{X}(0) \tag{9}$$

where $\boldsymbol{U}$ is called time-evolution matrix, and $\underline{X}(0)$ is the vector defining the initial state at $t = 0$.

We consider the quantum Otto cycle, which consists of four processes. It is customary to employ the same terminology used for the classical Otto cycle. The rationale behind this analogy is that when the frequency ω is larger, the oscillators composing the working fluid are more tightly confined, which corresponds to a smaller available volume. Conversely, when the frequency is smaller the oscillators are less tightly confined, corresponding to a larger volume. Therefore, the two steps for which the frequency is held constant are called hot and cold isochoric processes, depending on which of the two thermal reservoirs is contact with the working medium, i.e., the hot or cold heat reservoir, respectively. In some works the term iso-frequency is used to refer to the isochoric processes. Following the analogy with the classical Otto cycle, the step for which the frequency is decreasing is called expansion adiabat, and the step for which the frequency is increasing is called compression adiabat.

Each of the four processes of the cycle is assigned a time-evolution matrix. In particular, we denote by $\boldsymbol{U}_H$, $\boldsymbol{U}_{HC}$, $\boldsymbol{U}_C$ and $\boldsymbol{U}_{CH}$, the time-evolution matrices for the hot isochore, the expansion adiabat, the cold isochore and the compression adiabat, respectively. The closed-form expression of each of the time-evolution matrices has previously been derived [1,12]. Therefore, the time-evolution matrix for one entire cycle, denoted simply by $\boldsymbol{U}$, is given by the ordered composition of the four individual matrices:

$$\boldsymbol{U} = \boldsymbol{U}_{CH}\boldsymbol{U}_C\boldsymbol{U}_{HC}\boldsymbol{U}_H \tag{10}$$

Analogous notation is also used for the time allocated for each of the four processes:

$$\tau = \tau_H + \tau_{HC} + \tau_C + \tau_{CH} \tag{11}$$

The temperatures for the hot and cold thermal reservoirs are denoted by T_H and T_C, respectively. The frequencies for the hot and cold isochoric processes are denoted by ω_H and ω_C, respectively.

It is important to stress that Equation (11) must not be interpreted as a constraint. In fact, the unconstrained optimization problem considered in this paper is the optimization of the average power with respect to the four times allocated for the four processes composing the Otto cycle. In other words, the total duration τ of the cycle is not predetermined. We are interested in the behavior of the heat machine at steady state, also called limit cycle, for which the state of the system is the same at the beginning and at the end of each cycle.

2.3. Frictionless Cycles

Among all the possible cyclic trajectories, we consider a special class, called frictionless cycles. For the time-dependence described by Equation (7) (i.e., constant μ), these special trajectories can be obtained by suitably selecting the times allocated for the adiabatic processes, i.e., τ_{HC} and τ_{CH}.

The details can be found in reference [12,14]. In brief, the dynamic of sufficiently slow, i.e., $\mu < 2$, adiabatic processes describe an oscillation overlapping a slower drift of the frame of reference. If the values of τ_{HC} and τ_{CH} are selected so that an integer number of such oscillations occurs, the process maps a zero-coherence initial state, i.e., one for which $\langle \hat{L} \rangle = \langle \hat{C} \rangle = 0$, into another zero-coherence final state with different energy. If this is true for both the adiabatic processes, the resulting limit-cycle will maintain the property $\langle \hat{L} \rangle = \langle \hat{C} \rangle = 0$ for the whole duration of each of the isochoric processes. The condition of having an integer number of oscillations limits the allowed values of adiabat times to a countable set. These times will be denoted by τ_n^*, where n is a positive integer.

It is worth mentioning that the strategy of selecting these special cycles is sometimes called shortcut to adiabaticity [16,23,24]. The reason is that the effect $\langle \hat{L} \rangle = \langle \hat{C} \rangle = 0$ can also be obtained in the quasi-static limit: i.e., when $\tau_H, \tau_{HC}, \tau_C, \tau_{CH} \to +\infty$. The adiabatic theorem predicts that in the quasi-static regime the occupation probability of each of the energy levels remains constant during the adiabatic processes. Consequently, the amount of energy lost to quantum friction is zero. However, it is somewhat surprising that the same effect can also be attained in finite-time by a suitable selection of the adiabat times, hence the term shortcut to adiabaticity.

Besides properly selecting τ_{HC} and τ_{CH} with ω time-dependence characterized by constant μ, frictionless adiabat processes can also be obtained by considering different protocols $\omega(t)$. Most notably, a bang–bang type solution [14] leads to frictionless cycles with the additional advantage of minimizing the time allocated for the adiabatic process. The minimum time bang–bang $\omega(t)$ evolution is composed of five steps: an initial sudden transition to the final frequency; a wait of duration τ_1; a sudden transition back to the initial frequency; a wait of duration τ_2; and finally, one more sudden transition to the final frequency. The waiting periods τ_1 and τ_2 are determined by the initial and final frequencies. The total duration of the adiabatic process is thus constrained to $\tau_1 + \tau_2$.

Figure 1 illustrates three different cycles by showing the time-evolution of the vector $(\langle \hat{H} \rangle, \langle \hat{L} \rangle, \langle \hat{C} \rangle)^T$, i.e., the first three components of the vector $\underline{X}$ introduced in Section 2.2. The cycle shown in Figure 1a corresponds to constant μ adiabatic processes for which the allocated times are not selected among the frictionless set $\{\tau_n^*\}$. Figure 1b shows a constant μ frictionless cycle and Figure 1c shows a minimum time bang–bang frictionless cycle. As can be noticed, for frictionless cycles the condition $\langle \hat{L} \rangle = \langle \hat{C} \rangle = 0$ is satisfied for the whole duration of the isochoric processes.

The search for frictionless solutions can also be seen from a different perspective, closely related to that of searching for the optimal control $\omega(t)$. In this framework, an additional driving Hamiltonian is added to the original Hamiltonian [25] to counteract the non-adiabatic effects that are normally present for a finite-time process. By doing so, the transitions between different eigenstates of the original Hamiltonian can be entirely suppressed. For this reason, this strategy is often called transitionless quantum driving [11,26].

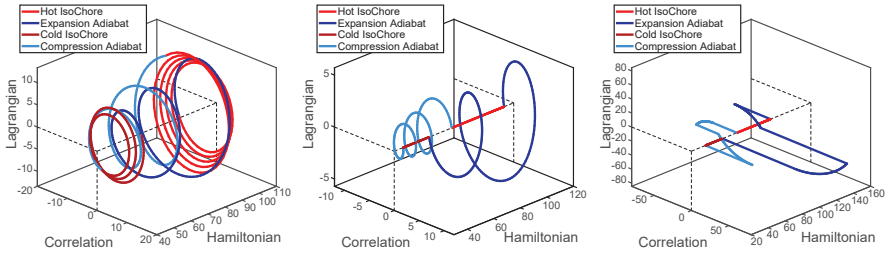

Figure 1. Three limit cycles corresponding to different adiabatic processes. For the cycles shown in (**a**,**b**) the $\omega(t)$ time dependence is characterized by constant μ. For the case of (**b**) the adiabat time allocations τ_{HC} and τ_{CH} are chosen among the frictionless set $\{\tau_n^*\}$, while for the case of (**a**) they are not. (**c**) A frictionless bang–bang cycle.

3. Analytical Results

In this work we consider the following optimization problem: maximize the average power extraction of the engine with respect to the four variables τ_H, τ_{HC}, τ_C and τ_{CH}, i.e., the time allocations for each of the four processes.

As mentioned in the introduction, we will show that the trajectories leading to maximum average power are not frictionless cycles. First, we will show in Section 3.1 that frictionless cycles are relative maxima of the total work extracted during a cycle with respect to the times τ_{HC} and τ_{CH} allocated during the adiabatic processes. Then in Section 3.2 we show that in order to maximize the average power it is convenient to reduce the durations of the adiabat times, thereby allowing for some quantum friction to be generated.

In Section 3.3 we show an analogous result for a quantum refrigerator, where the optimization objective is the maximization of the average cooling power. Finally, in Section 3.4 we argue why identical results are also applicable to heat engines and refrigeration having as working fluid an ensemble of spin systems.

3.1. Maximum Work

We want to show that for a constant μ frictionless trajectory the total work $\mathcal{W}_{\text{tot}}$ extracted from the system during one cycle is locally optimal with respect to the adiabat times:

$$\left(\frac{\partial \mathcal{W}_{\text{tot}}}{\partial \tau_{HC}}\right)_{\substack{\tau_{HC}=\tau_n^* \\ \tau_{CH}=\tau_m^*}} = \left(\frac{\partial \mathcal{W}_{\text{tot}}}{\partial \tau_{CH}}\right)_{\substack{\tau_{HC}=\tau_n^* \\ \tau_{CH}=\tau_m^*}} = 0 \quad \forall n, m, \tau_H, \tau_C \tag{12}$$

We start from the compression adiabat by showing that the derivative of $\mathcal{W}_{\text{tot}}$ with respect to τ_{CH} is zero when the trajectory is frictionless. We will then argue that the derivation is completely analogous for the expansion adiabat and τ_{HC}.

The amount of heat $\mathcal{Q}_H$ extracted during the hot isochore is a linear function of the initial state vector $\underline{X}_\infty$ of the limit cycle, and can thus be expressed as the scalar product between a row vector $\underline{q}_H$ and $\underline{X}_\infty$. The row vector $\underline{q}_H$ does not depend on the initial state of the system, but only on the process that the system undergoes during the hot isochoirc step. When $\underline{q}_H$ is applied to the initial state vector, the result is the amount of heat extracted during the hot isochore:

$$\mathcal{Q}_H = \underline{q}_H \underline{X}_\infty = \sum_k (\boldsymbol{U}_H)_k^1 (\underline{X}_\infty)^k - (\underline{X}_\infty)^1 \tag{13}$$

Denoting by $\mathbf{1}$ the identity matrix, the row vector $\underline{q}_H$ is defined as:

$$(\underline{q}_H)_k = (\boldsymbol{U}_H - \mathbf{1})_k^1 \tag{14}$$

Similarly, the amount of heat $\mathcal{Q}_C$ extracted during the cold isochore is obtained from the state vector $(\boldsymbol{U}_{HC}\boldsymbol{U}_H\underline{X}_\infty)$ at the beginning of the cold isochore:

$$\mathcal{Q}_C = \underline{q}_C \underline{X}_\infty = \sum_k (\boldsymbol{U}_C)_k^1 (\boldsymbol{U}_{HC}\boldsymbol{U}_H\underline{X}_\infty)^k - (\boldsymbol{U}_{HC}\boldsymbol{U}_H\underline{X}_\infty)^1 \tag{15}$$

The row vector $\underline{q}_C$ is defined as:

$$(\underline{q}_C)_k = (\boldsymbol{U}_C\boldsymbol{U}_{HC}\boldsymbol{U}_H - \boldsymbol{U}_{HC}\boldsymbol{U})_k^1 \tag{16}$$

At steady state the total work $\mathcal{W}_{\text{tot}}$ extracted from the system is equal to the total heat flowing into the system, and is thus given by the sum of the two contributions:

$$\mathcal{W}_{\text{tot}} = \underline{w}_{\text{tot}}\underline{X}_{\infty} = \underline{q}_{H}\underline{X}_{\infty} + \underline{q}_{C}\underline{X}_{\infty} \tag{17}$$

We can calculate the derivative of the work with respect to τ_{CH} as:

$$\partial_{\tau_{CH}}\mathcal{W}_{\text{tot}} = (\partial_{\tau_{CH}}\underline{w}_{\text{tot}})\underline{X}_{\infty} + \underline{w}_{\text{tot}}(\partial_{\tau_{CH}}\underline{X}_{\infty}) \tag{18}$$

As we can see from Equations (14) and (16), the total work vector $\underline{w}_{\text{tot}}$ is independent of $\boldsymbol{U}_{CH}$, and its derivative with respect to τ_{CH} is thus zero. The total work $\mathcal{W}_{\text{tot}}$ depends on τ_{CH} only through the limit cycle initial vector $\underline{X}_{\infty}$. In order for the work to be a stationary point with respect to τ_{CH}, the second term on the right-hand side of Equation (18) must be zero:

$$\partial_{\tau_{CH}}\mathcal{W}_{\text{tot}} = \underline{w}_{\text{tot}}(\partial_{\tau_{CH}}\underline{X}_{\infty}) = 0 \tag{19}$$

For now we only need to assume that $\tau_{HC} = \tau_n^*$. It can be shown that the second and third components of $\underline{w}_{\text{tot}}$ are zero for such a trajectory; i.e., the work only depends on $\langle\hat{H}\rangle$ and $\langle\hat{1}\rangle$. Denoting by $\star$ the non-zero matrix entries, we have:

$$\tau_{HC} = \tau_n^* \quad \Rightarrow \quad \underline{w}_{\text{tot}} = \begin{pmatrix} \star & 0 & 0 & \star \end{pmatrix} \tag{20}$$

Intuitively, it is not surprising that for a frictionless trajectory the work extraction does not depend on $\langle\hat{L}\rangle$ or $\langle\hat{C}\rangle$. In fact, the evolution during the icochoric processes decouples $\hat{H}$ from $\hat{L}$ and $\hat{C}$, and the time τ_{HC} allocated for the expansion adiabat is picked in such a way that an integer number of oscillations occurs and the state of the system returns to the same accumulated phase (i.e., $i\Omega\theta = n\pi$), with $\hat{H}$ and $\hat{L}$ rescaled by a factor ω_C/ω_H. During the first three steps of the cycle the Hamiltonian, which determine the heat exchange, evolution is thus completely decoupled from $\hat{L}$ and $\hat{C}$, and this explains why the work, when expressed as a functionn of the state of the system at the beginning of the cycle, does not depend on $\langle\hat{L}\rangle$ or $\langle\hat{C}\rangle$.

The fourth component of $\partial_{\tau_{CH}}\underline{X}_{\infty}$ is clearly zero since it corresponds to the expectation value $\langle\hat{1}\rangle$ which is always equal to 1. Therefore, we only need to show that its first component is also zero. It is convenient to start from the equation expressing the invariance, with respect to the whole cycle evolution matrix $\boldsymbol{U}$, of the limit cycle's initial state $\underline{X}_{\infty}$:

$$\boldsymbol{U}\underline{X}_{\infty} = \underline{X}_{\infty} \tag{21}$$

By taking the derivative with respect to τ_{CH} on both sides we get:

$$\partial_{\tau_{CH}}(\boldsymbol{U}\underline{X}_{\infty}) = (\partial_{\tau_{CH}}\boldsymbol{U})\underline{X}_{\infty} + \boldsymbol{U}(\partial_{\tau_{CH}}\underline{X}_{\infty}) = (\partial_{\tau_{CH}}\underline{X}_{\infty}) \tag{22}$$

Reordering, we get:

$$(\boldsymbol{U} - \mathbf{1})(\partial_{\tau_{CH}}\underline{X}_{\infty}) = -(\partial_{\tau_{CH}}\boldsymbol{U})\underline{X}_{\infty} \tag{23}$$

The τ_{CH} derivative of $\underline{X}_{\infty}$ can thus be obtained by solving the linear system of equations expressed by Equation (23). The derivative $(\partial_{\tau_{CH}}\boldsymbol{U})$ is obtained from $(\partial_{\tau_{CH}}\boldsymbol{U}_{CH})$:

$$(\partial_{\tau_{CH}}\boldsymbol{U}) = (\partial_{\tau_{CH}}\boldsymbol{U}_{CH})\boldsymbol{U}_{C}\boldsymbol{U}_{HC}\boldsymbol{U}_{H} \tag{24}$$

All the quantities appearing in Equation (23) can be easily evaluated for $\tau_{CH} = \tau_m^*$ and $\tau_{HC} = \tau_n^*$, before solving the linear system for $\partial_{\tau_{CH}}\underline{X}_{\infty}$. In fact, the operation of replacing the values of τ_{CH} and τ_{HC} and that of solving the system are interchangeable, but the calculation is easier if the substitution is performed before solving the system. In frictionless conditions we have the following matrix structure:

$$\boldsymbol{U} = \begin{pmatrix} \star & 0 & 0 & \star \\ 0 & \star & \star & 0 \\ 0 & \star & \star & 0 \\ 0 & 0 & 0 & \star \end{pmatrix} \; ; \quad (\partial_{\tau_{CH}} \boldsymbol{U}) = \begin{pmatrix} 0 & \star & \star & 0 \\ \star & \star & \star & \star \\ 0 & \star & \star & 0 \\ 0 & 0 & 0 & 0 \end{pmatrix} \; ; \quad \underline{X}_\infty = \begin{pmatrix} \star \\ 0 \\ 0 \\ 1 \end{pmatrix} \tag{25}$$

The second and third components of $\underline{X}_\infty$ are zero, and also the first and fourth components of the first row of $\partial_{\tau_{CH}} \boldsymbol{U}$ are zero. This implies that the first component of the vector $-(\partial_{\tau_{CH}} \boldsymbol{U})\underline{X}_\infty$ on the right-hand side of Equation (23) is zero:

$$-(\partial_{\tau_{CH}} \boldsymbol{U})\underline{X}_\infty = \begin{pmatrix} 0 & \star & 0 & 0 \end{pmatrix}^T \tag{26}$$

Since the matrix $(\boldsymbol{U} - \mathbf{1})$ decouples the first and fourth components, (i.e., $\hat{H}$ and $\hat{1}$), from the second and third components, (i.e., $\hat{L}$ and $\hat{C}$), solving the linear system shows that indeed the first component of $\partial_{\tau_{CH}} \underline{X}_\infty$ is zero:

$$\partial_{\tau_{CH}} \underline{X}_\infty = \begin{pmatrix} 0 & \star & \star & 0 \end{pmatrix}^T \tag{27}$$

Plugging Equations (20) and (27) into Equation (19) shows that:

$$\left(\frac{\partial \mathcal{W}_{\text{tot}}}{\partial \tau_{CH}} \right)_{\substack{\tau_{HC} = \tau_n^* \\ \tau_{CH} = \tau_m^*}} = 0 \quad \forall n, m, \tau_H, \tau_C \tag{28}$$

The same result can be shown for the expansion adiabat by considering a cycle in which the four steps are rearranged in such a way that the expansion adiabat is the last step (i.e., cold isochore, compression adiabat, hot isochore, expansion adiabat).

As discussed in [1], the total work for the case of frictionless trajectories can be computed analytically, and it assumes a particularly simple expression:

$$\mathcal{W}_{\text{tot}} = -G_W(T_C, \omega_C, T_H, \omega_H) F(\tau_C, \tau_H) \tag{29}$$

where the function G_W is entirely determine by the engine parameters

$$G_W(T_C, \omega_C, T_H, \omega_H) = \left(\frac{\omega_H - \omega_C}{e^{\omega_H / T_H} - 1} - \frac{\omega_H - \omega_C}{e^{\omega_C / T_C} - 1} \right) \tag{30}$$

and the function F is determined by the isochore times and the heat conductance Γ

$$F(\tau_C, \tau_H) = \frac{(e^{\Gamma \tau_H} - 1)(e^{\Gamma \tau_C} - 1)}{e^{\Gamma \tau_C + \Gamma \tau_H} - 1} \tag{31}$$

It is important to stress that the value of $\mathcal{W}_{\text{tot}}$ for frictionless cycles remains the same regardless of the particular choice of $\omega(t)$ time dependence, i.e., constant μ or bang–bang process.

3.2. Maximum Power

It is now easy to show that the power cannot be optimal for frictionless trajectories. The average power $\overline{\mathcal{P}}_{\text{tot}}$ is defined as the work $\mathcal{W}_{\text{tot}}$ extracted during a cycle divided by the duration τ of the cycle. It is convenient to express $\overline{\mathcal{P}}_{\text{tot}}$ as the following product:

$$\overline{\mathcal{P}}_{\text{tot}} = \mathcal{W}_{\text{tot}} f(\tau_{CH}) \tag{32}$$

where the scaling function $f(\tau_{CH})$ is given by:

$$f(\tau_{CH}) = \frac{1}{\tau_H + \tau_{HC} + \tau_C + \tau_{CH}} \tag{33}$$

Since the derivative of $f(\tau_{CH})$ is always negative, it is already apparent that the trajectories that are locally optimal for $\mathcal{W}_{\text{tot}}$ cannot be optimal for $\overline{\mathcal{P}}_{\text{tot}}$. From Equation (32), the derivative of $\overline{\mathcal{P}}_{\text{tot}}$ with respect to τ_{CH} is given by:

$$\partial_{\tau_{CH}}\overline{\mathcal{P}}_{\text{tot}} = (\partial_{\tau_{CH}}\mathcal{W}_{\text{tot}})(f(\tau_{CH})) + (\mathcal{W}_{\text{tot}})(\partial_{\tau_{CH}}f(\tau_{CH})) \tag{34}$$

As shown in the previous section, the derivative $\partial_{\tau_{CH}}\mathcal{W}_{\text{tot}}$ is zero when both the conditions $\tau_{CH} = \tau_m^*$ and $\tau_{HC} = \tau_n^*$ are satisfied. Therefore, the derivative of the average power $\overline{\mathcal{P}}_{\text{tot}}$ with respect to τ_{CH} is given by:

$$\partial_{\tau_{CH}}\overline{\mathcal{P}}_{\text{tot}} = (\mathcal{W}_{\text{tot}})(\partial_{\tau_{CH}}f(\tau_{CH})) \tag{35}$$

Since $\partial_{\tau_{CH}}f(\tau_{CH}) < 0$ and $\mathcal{W}_{\text{tot}} > 0$ the derivative is negative. It is thus convenient to reduce τ_{CH} from τ_m^* and allow for some friction generation in order to reduce the total cycle time and increase the average power $\overline{\mathcal{P}}_{\text{tot}}$. These arguments are illustrated in Figure 2. Work and average power are plotted as functions of the compression adiabat time. The expansion adiabat time is $\tau_{HC} = \tau_1^*$, thereby leading to a frictionless cycle when $\tau_{CH} \in \{\tau_n^*\}$. As can be seen from the graph, the work is maximized for these choices, always leading to the value expressed by Equation (29). On the other hand, the maximum power is obtained when τ_{CH} is slightly smaller than τ_1^*. The results shown in Figure 2 correspond to the following choice of parameters: $\omega_C = 15$, $\omega_H = 30$, $T_C = 100/3$, $T_H = 125$, $\Gamma = 0.7$.

So far it was implicitly assumed that around the point $\tau_{CH} = \tau_n^*$, $\tau_{HC} = \tau_m^*$ the work extraction $\mathcal{W}_{\text{tot}}$ is differentiable with respect to the time allocations τ_{HC} and τ_{CH} and that the derivative is continuous around that point. By considering the definitions [1] of the time evolution matrices $\{\boldsymbol{U}_H, \boldsymbol{U}_{HC}, \boldsymbol{U}_C, \boldsymbol{U}_{CH}\}$, it is easy to show that they are continuously differentiable functions of all the parameters, including the time allocations. Therefore, the same property is satisfied by the row vectors $\{\underline{w}_{\text{tot}}, \underline{q}_H, \underline{q}_C\}$, since these are defined from the evolution matrices (see Equations (14) and (16)). The only possible source of discontinuity is thus the limit-cycle state vector $\underline{X}_\infty$. The vector $\underline{X}_\infty$ could indeed be not continuously differentiable since it is defined as the solution of the linear system expressed by Equation (21). In other words, the calculation of $\underline{X}_\infty$ involves a matrix inversion, which can bring about a discontinuity. As discussed in reference [22], this happens in the presence of a bifurcation. However, as shown in reference [19,22], a bifurcation never occurs in a neighborhood of a frictionless cycle, thereby guaranteeing that $\mathcal{W}_{\text{tot}}$ is continuously differentiable around its maxima.

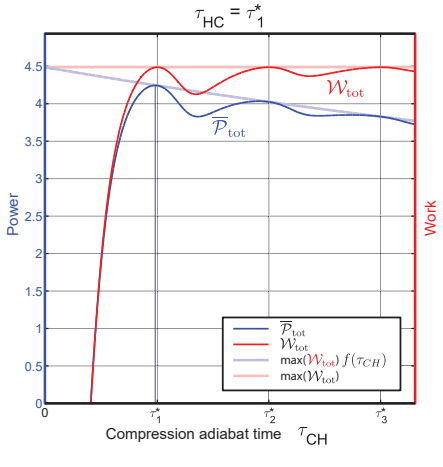

Figure 2. Shift of the power optimal point with respect to τ_{CH}. The vertical grid lines correspond to $\tau_{CH} = \tau_n^*$ for $n = 1, 2, 3$. The expansion adiabat time is $\tau_{HC} = \tau_1^*$. The isochore times are constant: $\tau_H = \tau_C = 1.24$.

3.3. Harmonic Refrigerator

We argue here that the same results apply to the optimization of the cooling power of a refrigerator.

The machine will behave as an engine or a refrigerator depending on the values of the compression ratio ω_H/ω_C and the temperature ratio T_H/T_C. In particular, as long as $\omega_H/\omega_C < T_H/T_C$ the machine will act as a heat engine, whereas when $\omega_H/\omega_C > T_H/T_C$ the machine behaves as a refrigerator.

The procedure of the previous section can be applied to a refrigerator by replacing the work vector $\underline{w}_{\rm tot}$ with the cold heat vector $\underline{q}_C$. Since the plus sign means that energy is flowing into the system from the cold heat reservoir, the objective is to maximize the cooling power (i.e., $\mathcal{Q}_C$ divided by the total duration of a cycle). Using the same notation adopted in the previous section, we write:

$$\overline{\mathcal{Q}}_C = \mathcal{Q}_C f(\tau_{CH}), \quad \text{with} \quad f(\tau_{CH}) = \frac{1}{\tau_H + \tau_{HC} + \tau_C + \tau_{CH}} \tag{36}$$

As in the previous case $\underline{q}_C$ is independent of $\boldsymbol{U}_{CH}$ and so $\partial_{\tau_{CH}} \underline{q}_C = 0$. Moreover, the second and third components of $\underline{q}_C$ are still zero, because of the same arguments presented in the previous section: for a frictionless steady-state trajectory the heat transfer does not depend on the initial values of $\langle \hat{L} \rangle$ or $\langle \hat{C} \rangle$.

The limit cycle is calculated in the same way as for a heat engine. The derivative with respect to τ_{CH} of the first component of $\underline{X}_\infty$ is zero for a frictionless cycle. This property remains true regardless of the choice of parameters (i.e., for $\omega_H/\omega_C < T_H/T_C$ corresponding to a heat engine, or for $\omega_H/\omega_C > T_H/T_C$ corresponding to a refrigerator).

In conclusion, frictionless trajectories correspond to the locally optimal cold heat transfer with respect to τ_{CH} and τ_{HC}, implying that they cannot also give the optimal cooling power $\overline{\mathcal{Q}}_C$.

3.4. Spin System

The same results apply also to heat machines and engines having the spin system as the working fluid. These systems have been extensively studied by Kosloff and Feldmann [27–29] .

It is still possible to select particular values of the time allocated during the adiabatic processes in order to eliminate the correlation between the Hamiltonian $\hat{H}$ and the operators $\hat{L}$ and $\hat{C}$. In this case the evolution matrices for the adiabats become diagonal. The operators are rescaled by factor that depends on the initial and final frequencies. The first 3×3 matrix block of the evolution matrix $\boldsymbol{U}_{CH}$ is proportional to the identity matrix:

$$\tilde{\boldsymbol{U}}_{CH} = \left(\frac{(J^2 + \omega_H^2)}{(J^2 + \omega_C^2)} \right)^{1/2} \tilde{\mathbf{1}} \equiv (\Omega_H/\Omega_C)\, \tilde{\mathbf{1}} \tag{37}$$

This similarity with the harmonic case already shows that for a frictionless steady-state cycle the work and heat transfer vectors are independent of the values of $\langle \hat{L} \rangle$ and $\langle \hat{C} \rangle$. Moreover, the same vectors $\underline{w}_{\rm tot}$ and $\underline{q}_C$ are independent of τ_{CH}.

We thus only have to show that the derivative with respect to τ_{CH} of the first component (i.e., $\langle \hat{H} \rangle$) of the initial state is zero for a frictionless cycle. The same procedure employed in the previous section can be used to show that this property holds also for the spin case.

4. Numerical Results

While the case of frictionless trajectories can be treated by employing analytical techniques, the general case involves complicated mathematical expressions which cannot be manipulated analytically for the purpose of obtaining the maximum power. Therefore, we resort to numerical methods to compute the performance improvement with respect to the frictionless case. We denote by $\overline{\mathcal{P}}_{\rm tot}(\tau_H, \tau_{HC}, \tau_C, \tau_{CH})$ the average power as a function of the time allocations for the four processes.

In order to reduce the computation time, we consider a simplified case as an example: We assume that the time allocated for the hot isochore is the same as the time allocated for the cold isochore, and it will be denoted by $\tau_{\text{is.}}$. Furthermore, we assume that the time allocated for the compression adiabat is the same as the time allocated for the expansion adiabat, and it will be denoted by $\tau_{\text{ad.}}$. We performed numerical optimization of the average power $\overline{\mathcal{P}}_{\text{tot}}$ as a function of these two parameters: $\tau_{\text{is.}}$ and $\tau_{\text{ad.}}$. Due to the analytical results presented in the previous sections, for the adiabats time we only consider the interval $[0, \tau_1^*]$.

Figure 3a shows an example of work landscape as a functionn of the two parameters and Figure 3b shows the corresponding power landscape. The optimal power among the frictionless trajectories with constant μ will be denoted by $\overline{\mathcal{P}}_{\text{tot}}^{\text{opt}(*)}$:

$$\overline{\mathcal{P}}_{\text{tot}}^{\text{opt}(*)} = \max_{\tau_{\text{is.}}} \left[\overline{\mathcal{P}}_{\text{tot}}(\tau_{\text{is.}}, \tau_1^*, \tau_{\text{is.}}, \tau_1^*) \right] \tag{38}$$

In Figure 3a,b the point corresponding to $\overline{\mathcal{P}}_{\text{tot}}^{\text{opt}(*)}$ is indicated by the white circle located on the right border of the graph (i.e., $\tau_{\text{ad.}} = \tau_1^*$).

The unconstrained optimal power is denoted by $\overline{\mathcal{P}}_{\text{tot}}^{\text{opt}}$:

$$\overline{\mathcal{P}}_{\text{tot}}^{\text{opt}} = \max_{\tau_{\text{is.}}, \tau_{\text{ad.}}} \left[\overline{\mathcal{P}}_{\text{tot}}(\tau_{\text{is.}}, \tau_{\text{ad.}}, \tau_{\text{is.}}, \tau_{\text{ad.}}) \right] \tag{39}$$

The point corresponding to $\overline{\mathcal{P}}_{\text{tot}}^{\text{opt}}$ is indicated by the white diamond located in the left border of the graph. In fact, for this choice of engine parameters the optimal power corresponds to a sudden-adiabats cycle, despite the fact the the optimal work is given by the frictionless trajectory. It is interesting to notice that, in contrast with Figure 2, the optimal power was not found in the vicinity of a frictionless trajectory. While this result might be counter-intuitive, it highlights the fact that maximizing the power and maximizing the work are indeed very different optimization problems. The results presented in Figure 3 correspond to the following choice f engine parameters: $\omega_C = 15$, $\omega_H = 16$, $T_C = 100/3$, $T_H = 125$, $\Gamma = 0.7$.

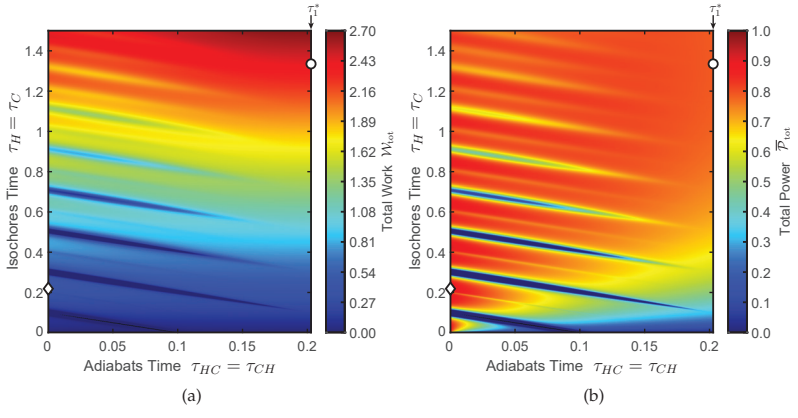

Figure 3. The work and power landscape as functions of adiabat and isochore times are shown in (**a**,**b**), respectively. The maximum power among frictionless cycles, $\overline{\mathcal{P}}_{\text{tot}}^{\text{opt}(*)}$, is indicated by the white circle. This cycle is located on the right border of each graph corresponding to $\tau_{\text{ad.}} = \tau_1^*$. The unconstrained maximum power cycle $\overline{\mathcal{P}}_{\text{tot}}^{\text{opt}}$ is indicated by the white diamond. For this case the unconstrained optimum is located on the left border of each graph since it corresponds to a sudden-adiabats cycle. Although the total work is significantly less than that of the frictionless cycle, the reduction of the cycle duration is even higher, thereby resulting in higher average power.

We now consider the dependence of $\overline{\mathcal{P}}_{\rm tot}^{\rm opt(*)}$ and $\overline{\mathcal{P}}_{\rm tot}^{\rm opt}$ on the engine parameters, i.e., the compression ratio ω_H/ω_C and the temperature ratio T_H/T_C, with $\Gamma = 0.7$. Since we are interested in the relative power improvement, we compute the unconstrained maximum power normalized by the maximum power among frictionless cycles with the same engine parameters, i.e.,

$$\hat{\mathscr{P}} = \frac{\overline{\mathcal{P}}_{\rm tot}^{\rm opt}(\omega_H/\omega_C, T_H/T_C)}{\overline{\mathcal{P}}_{\rm tot}^{\rm opt(*)}(\omega_H/\omega_C, T_H/T_C)} \tag{40}$$

The result is shown in Figure 4a for the $\omega(t)$ time dependence corresponding to constant μ. The black region on the bottom-right corner of the axis corresponds to the combinations of parameters for which $(\omega_H/\omega_C) > (T_H/T_C)$, i.e., leading to cooling cycles for which the working fluid behaves as a refrigerator.

As can be noticed, the maximum improvement is obtained in the limit $\omega_H \to \omega_C$ and $T_H \gg T_C$. The maximum improvement within the region shown in the figure is $\approx 21\%$, but an even greater improvement can be obtained for higher values of T_H/T_C.

The results shown in Figure 4b are analogous to those shown in Figure 4a except that the $\omega(t)$ time dependence is of the bang–bang type instead of constant μ. As explained in Section 2.3, the adiabat times for the frictionless cycles are determined by the engine parameters ω_H and ω_C according to the condition $\tau_{\rm ad.} = \tau_1 + \tau_2$. However, the time allocation for the adiabatic processes can be reduced by relaxing the frictionless requirement. There are many ways to do that. Ideally, one would apply the methods of optimal control theory to $\omega(t)$ for each of the adiabatic processes in order to optimize the average power over the whole cycle while satisfying the limit-cycle requirement expressed by Equation (21). However, this calculation would be very complex and it would not be possible to determine the solution of the optimal control problem by employing analytical methods. Therefore, this analysis goes beyond the scope of this work. Instead, here we consider the simplified case for which τ_1 and τ_2 are reduced by the same factor. As can be seen from Figure 4b this method leads to a maximum improvement of $\approx 9\%$ within the parameter region shown in the graph. As for Figure 4b, the improvement would be even greater for higher values of T_H/T_C.

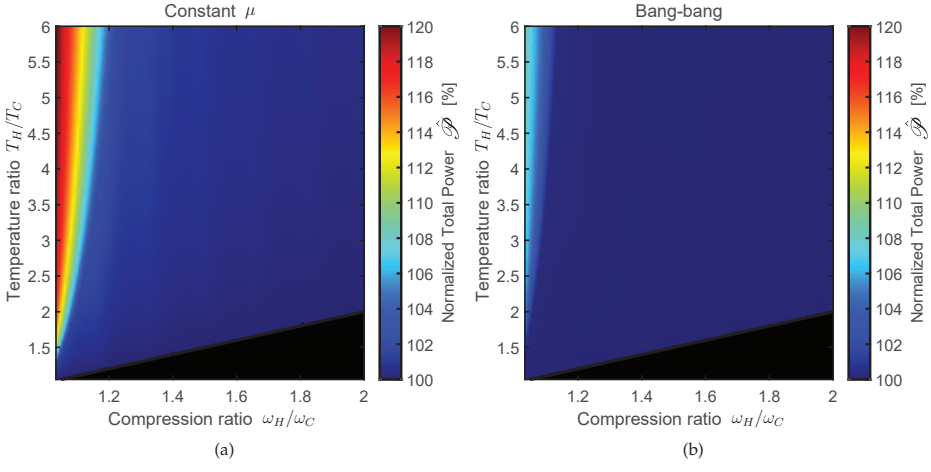

Figure 4. Maximum power as a function of the engine parameters ω_H/ω_C and T_H/T_C. The power $\overline{\mathcal{P}}_{\rm tot}^{\rm opt}$ of the unconstrained optimum is normalized by the maximum power $\overline{\mathcal{P}}_{\rm tot}^{\rm opt(*)}$ among frictionless cycles. The normalized power $\hat{\mathscr{P}}$ is expressed as a percentage. (**a**,**b**) Different $\omega(t)$ time dependence, i.e., constant μ and bang–bang, respectively.

5. Conclusions

We discussed the finite-time performance optimization of the quantum Otto cycle by considering two different well-known models for the working fluid: an ensemble of harmonic oscillators and an ensemble of spin systems. Moreover, we considered both the power optimization of the engine-cycle and the cooling power optimization of the refrigeration-cycle.

The optimization variables are the time allocations of the four processes composing the thermodynamic cycle. In contrast to the majority of studies within this field, we considered the unconstrained optimization problem. This means that the two adiabatic processes were not frictionless: we allowed for some friction generation in order to reduce the duration of the cycle and improve the average power production.

We used analytical techniques to compute the derivative of the work production for a limit-cycle trajectory with respect to the time allocation for the adiabatic processes. We explicitly show that for a frictionless cycle the derivative is zero: the work is a relative maximum. This result immediately implies that the power cannot be optimal for a frictionless cycle. In particular, the globally optimal point must be searched in the region of the configuration space for which the time allocation for the adiabatic processes is shorter than that of the minimum time frictionless process.

Numerical computations have been used to obtain the performance improvement with respect to the constrained optimal power. Depending on the engine parameters, the improvement can be quite significant. The next logical step would be to formulate this problem as a control problem and find the frequency time-dependence leading to maximum power.

Funding: This research received no external funding

Acknowledgments: I would like to thank Bjarne Andresen for introducing me to the field of quantum thermodynamics and optimization. Over the years my interest for this fascinating field has grown thanks to Bjarne's precious guidance and insightful perspective.

Conflicts of Interest: The author declares no conflict of interest.

References

1. Kosloff, R.; Rezek, Y. The Quantum Harmonic Otto Cycle. *Entropy* **2017**, *19*, 136. [CrossRef]
2. Peterson, J.P.; Batalhão, T.B.; Herrera, M.; Souza, A.M.; Sarthour, R.S.; Oliveira, I.S.; Serra, R.M. Experimental Characterization of a Spin Quantum Heat Engine. *Phys. Rev. Lett.* **2019**, *123*, 240601. [CrossRef] [PubMed]
3. Abah, O.; Lutz, E. Optimal performance of a quantum Otto refrigerator. *EPL* **2016**, *113*, 60002. [CrossRef]
4. Solfanelli, A.; Falsetti, M.; Campisi, M. Nonadiabatic single-qubit quantum Otto engine. *Phys. Rev. B* **2020**, *101*, 054513. [CrossRef]
5. Chen, L.; Liu, X.; Ge, Y.; Wu, F.; Feng, H.; Xia, S. Power and efficiency optimization of an irreversible quantum Carnot heat engine working with harmonic oscillators. *Phys. A Stat. Mech. Appl.* **2020**, *550*, 124140. [CrossRef]
6. Dann, R.; Kosloff, R. Quantum signatures in the quantum Carnot cycle. *New J. Phys.* **2020**, *22*, 013055. [CrossRef]
7. Curzon, F.; Ahlborn, B. Efficiency of a carnot engine at maximum power output. *Am. J. Phys.* **1975**, *43*, 22–24. [CrossRef]
8. Rezek, Y.; Kosloff, R. Irreversible performance of a quantum harmonic heat engine. *New J. Phys.* **2006**, *8*, 83. [CrossRef]
9. Deffner, S. Efficiency of harmonic quantum Otto engines at maximal power. *Entropy* **2018**, *20*, 875. [CrossRef]
10. Abah, O.; Paternostro, M.; Lutz, E. Shortcut-to-adiabaticity quantum Otto refrigerator. *Phys. Rev. Res.* **2020**, *2*, 023120. [CrossRef]
11. Berry, M.V. Transitionless quantum driving. *J. Phys. A Math. Theor.* **2009**, *42*, 365303. [CrossRef]
12. Rezek, Y.; Salamon, P.; Hoffmann, K.H.; Kosloff, R. The quantum refrigerator: The quest for absolute zero. *EPL* **2009**, *85*, 30008. [CrossRef]
13. Deng, S.; Chenu, A.; Diao, P.; Li, F.; Yu, S.; Coulamy, I.; Del Campo, A.; Wu, H. Superadiabatic quantum friction suppression in finite-time thermodynamics. *Sci. Adv.* **2018**, *4*, eaar5909. [CrossRef]

14. Salamon, P.; Hoffmann, K.H.; Rezek, Y.; Kosloff, R. Maximum work in minimum time from a conservative quantum system. *Phys. Chem. Chem. Phys.* **2009**, *11*, 1027–1032. [CrossRef] [PubMed]
15. Abah, O.; Lutz, E. Energy efficient quantum machines. *EPL (Europhys. Lett.)* **2017**, *118*, 40005. [CrossRef]
16. Abah, O.; Lutz, E. Performance of shortcut-to-adiabaticity quantum engines. *Phys. Rev. E* **2018**, *98*, 032121. [CrossRef]
17. del Campo, A.; Goold, J.; Paternostro, M. More bang for your buck: Super-adiabatic quantum engines. *Sci. Rep.* **2014**, *4*, 6208. [CrossRef]
18. Beau, M.; Jaramillo, J.; del Campo, A. Scaling-up quantum heat engines efficiently via shortcuts to adiabaticity. *Entropy* **2016**, *18*, 168. [CrossRef]
19. Insinga, A.; Andresen, B.; Salamon, P. Thermodynamical analysis of a quantum heat engine based on harmonic oscillators. *Phys. Rev. E* **2016**, *94*, 012119. [CrossRef]
20. Breuer, H.P.; Petruccione, F. *The Theory of Open Quantum Systems*; Vol. 9780199213900; Oxford University Press: Oxford, UK, 2007; pp. 1–656. [CrossRef]
21. Geva, E.; Kosloff, R. On the Classical Limit of Quantum Thermodynamics in Finite-Time. *J. Chem. Phys.* **1992**, *97*, 4398–4412. [CrossRef]
22. Insinga, A.; Andresen, B.; Salamon, P.; Kosloff, R. Quantum heat engines: Limit cycles and exceptional points. *Phys. Rev. E* **2018**, *97*, 062153. [CrossRef] [PubMed]
23. Torrontegui, E.; Ibáñez, S.; Martínez-Garaot, S.; Modugno, M.; del Campo, A.; Guéry-Odelin, D.; Ruschhaupt, A.; Chen, X.; Muga, J.G. Shortcuts to Adiabaticity. *Adv. Atomic Mol. Opt. Phys.* **2013**, *62*, 117–169. [CrossRef]
24. Deng, J.; Wang, Q.h.; Liu, Z.; Hänggi, P.; Gong, J. Boosting work characteristics and overall heat-engine performance via shortcuts to adiabaticity: Quantum and classical systems. *Phys. Rev. E* **2013**, *88*, 062122. [CrossRef] [PubMed]
25. Demirplak, M.; Rice, S.A. Adiabatic population transfer with control fields. *J. Phys. Chem. A* **2003**, *107*, 9937–9945. [CrossRef]
26. Muga, J.G.; Chen, X.; Ibáñez, S.; Lizuain, I.; Ruschhaupt, A. Transitionless quantum drivings for the harmonic oscillator. *J. Phys. B Atomic Mol. Opt. Phys.* **2010**, *43*, 085509. [CrossRef]
27. Kosloff, R.; Feldmann, T. Discrete four-stroke quantum heat engine exploring the origin of friction. *Phys. Rev. E Stat. Nonlinear Soft Matter Phys.* **2002**, *65*, 055102. [CrossRef]
28. Feldmann, T.; Kosloff, R. Quantum four-stroke heat engine: Thermodynamic observables in a model with intrinsic friction. *Phys. Rev. E Stat. Nonlinear Soft Matter Phys.* **2003**, *68*, 016101. [CrossRef]
29. Feldmann, T.; Kosloff, R. Quantum lubrication: Suppression of friction in a first-principles four-stroke heat engine. *Phys. Rev. E Stat. Nonlinear Soft Matter Phys.* **2006**, *73*, 025107. [CrossRef]

entropy

MDPI

Article

Optimal Control of Hydrogen Atom-Like Systems as Thermodynamic Engines in Finite Time

Johann Christian Schön

Max Planck Institute for Solid State Research, Heisenbergstr. 1, D-70569 Stuttgart, Germany; C.Schoen@fkf.mpg.de

Received: 27 August 2020; Accepted: 19 September 2020; Published: 23 September 2020

Abstract: Nano-size machines are moving from only being topics of basic research to becoming elements in the toolbox of engineers, and thus the issue of optimally controlling their work cycles becomes important. Here, we investigate hydrogen atom-like systems as working fluids in thermodynamic engines and their optimal control in minimizing entropy or excess heat production in finite-time processes. The electronic properties of the hydrogen atom-like system are controlled by a parameter κ reflecting changes in, e.g., the effective dielectric constant of the medium where the system is embedded. Several thermodynamic cycles consisting of combinations of iso-κ, isothermal, and adiabatic branches are studied, and a possible a-thermal cycle is discussed. Solving the optimal control problem, we show that the minimal thermodynamic length criterion of optimality for finite-time processes also applies to these cycles for general statistical mechanical systems that can be controlled by a parameter κ, and we derive an appropriate metric in probability distribution space. We show how the general formulas we have obtained for the thermodynamic length are simplified for the case of the hydrogen atom-like system, and compute the optimal distribution of process times for a two-state approximation of the hydrogen atom-like system.

Keywords: optimal control; thermodynamic cycles; finite-time thermodynamics; thermodynamic length; hydrogen atom; nano-size engines; a-thermal cycle

1. Introduction

Optimal control of physical and chemical systems, and of the processes taking place in such systems, has been a major goal since the beginning of scientific investigations [1,2]. Essentially any application of scientific insights to practical problems has constituted such an effort in optimal control of some kind—even if not formulated as a mathematical control problem—, with the objective ranging from minimizing the difference of the values of characteristic parameters and quantities between the ideal theory and the real experiment [3,4], to maximizing the amount or quality of the desired output for given material and technical constraints. One can distinguish between those controls that are based on practical limitations due to the availability of tools and materials or lack thereof, and those based on the laws of physics.

Perhaps the classical examples of optimal control based on laws of physics have been the analyses of thermodynamic cycles [5–7], where the famous formulas for maximal efficiencies of hypothetical engines are sometimes given a status nearly equal to the fundamental laws of thermodynamics [6]. Such formulas have typically been derived under the assumption of infinite time available for each step of the cycles, allowing us to move from equilibrium state to equilibrium state. About fifty years ago, engineers and scientists began to question this assumption and re-formulated the optimal control problem by demanding that the cycle should be performed in a given finite amount of time, leading to the development of the field of finite-time thermodynamics [8–11].

A second aspect of optimal control based on the laws of physics is to reduce the engine under consideration to the most elementary physical systems that are stripped of all weaknesses and

complications which are associated with the macroscopic aspects of the experimental apparatus employed in their realization, resulting in the creation and investigation of molecular machines [12]. Typically, this involves reducing the size of the system in the sense that we are dealing with a macroscopic system as a (non-interacting) ensemble of elementary but microscopic systems. Of course, in practice, isolating the individual elementary system often requires a very large experimental apparatus, but for the purpose of the analysis of the physics and the optimal control of the system, this counts as "environment" and "control tools", whose optimality in themselves are usually irrelevant to the issue of optimally controlling the (ensemble of) elementary system(s) as such. Many experiments have been performed where single atoms or ions in vacuum [13–15] or single defects in solids [16,17] have been studied and controlled in some fashion.

A third feature of achieving optimal control of systems on the level of physical laws is dealing with the quantum nature of these elementary systems, which is forced upon us when reducing the elementary systems to atomic dimensions. While the quantum aspects are unavoidable, one can nevertheless often separate them from the issue of optimal control one investigates, especially if the time resolution of the control is so large that many quantum aspects can be captured by, e.g., effective decay rates.

From the point of view of a theorist, such a reduction to elementary physical systems is often a desirable feature because it allows us to focus on the elementary system itself—which can, in many cases, be analyzed analytically to a certain point—while assigning all other aspects to a generic environment. Examples are the optimal control of harmonic oscillator systems, which have been studied both on the classical and on the quantum mechanical level [18–26], spin systems [26–28], particles in a box [26], and generic two-level systems [29].

In this study, we are going to analyze the basic concepts of optimal control at the example of a hydrogen atom-like system, which we employ as an engine, or more specifically, the working fluid of such an engine, to perform a thermodynamic cycle within finite time. On the technical mathematical level, the electronic Hamiltonian possesses a very high degree of symmetry allowing at least some analytical treatment. On the level of possible applications, there exist systems equivalent to hydrogen-like atoms, e.g., excitons inside a solid [30], that can be controlled by modifying the environment while the hydrogen atom-like system remains in its state. Controlling such a system might allow us to construct nano-size engines inside solids. Alternatively, we can consider isolated hydrogen atoms inside a cavity [31], where also the conditions can be controlled such that the hydrogen atom becomes a modified hydrogen atom.

We will analyze the stages of the thermodynamic control cycle on the general level of probability distributions, both for the ideal (infinite-time) cycle and the cycle at finite time, derive an optimality criterion for minimal waste of work/minimal excess production of heat (dissipation)/minimal production of entropy during finite-time processes for general statistical mechanical systems, and apply these formulas to the example of the hydrogen atom-like system. Note that we are dealing with an "electronic" states-based engine, not with a standard thermal atom movement-based engine as studied, e.g., in [13].

2. Background

2.1. Aspects of the Hydrogen Atom-Like System

Due to the high symmetry of the Coulomb potential, the electronic Schrödinger equation for the hydrogen atom can be solved analytically, and we get for the energy eigenvalues

$$E_n = -\frac{\alpha}{n^2} \tag{1}$$

where $\alpha = \frac{me^4}{2\hbar^2}$. The degeneracy of the n'th energy level is $g(n) = n^2$. In principle, we need to add a factor 2 for the spin degeneracy of the electron, but this factor is not relevant for this study and will be dropped.

If we consider hydrogen atom-like systems, the formula for the energy is modified by, e.g., changing the mass of the electron or quasi-particle $m \to m^*$, i.e., $\alpha \to \alpha^* = \frac{m^*}{m}\alpha$, by changing the effective charge that generates the Coulomb field $e \to {q_1}^*$ and/or the effective charge of the quasi-particle $e \to {q_2}^*$, i.e., $\alpha \to \alpha^* = \frac{m({q_2}^*)^2({q_1}^*)^2}{2\hbar^2}$ or by introducing a shielding dielectric constant $\varepsilon \neq 1$, such that $E_n = -\frac{\alpha}{n^2}$, or combinations thereof. Quite generally, we note that these modifications can be incorporated in a straightforward fashion by introducing a modification factor

$$\kappa = \frac{m^*({q_2}^*)^2({q_1}^*)^2}{me^4\varepsilon^2}, \tag{2}$$

such that

$$E_n(\kappa) = -\kappa\frac{\alpha}{n^2} = \kappa E_n(\kappa = 1). \tag{3}$$

If we can apply external forces or fields to the system such that κ (i.e., m^*, ${q_{1,2}}^*$ and/or ε) can be smoothly varied, then we can modify the energy levels in a controlled fashion. In that case, the hydrogen atom-like system is used as the working fluid of an engine, where the changing of the energy levels leads to a change in energy that may be extracted as work. A change of the statistical occupation of the various energy levels at given temperature T is associated with the entropy content and the heat exchanges of the system, and we can define work cycles in, e.g., (κ, T)-space. Examples for individual legs (or branches) of such a cycle would be adiabatic or isothermal changes in κ from some initial value κ_{in} to a final value κ_f, and iso-κ changes in temperature where we keep κ constant (see Figures 1–3 below).

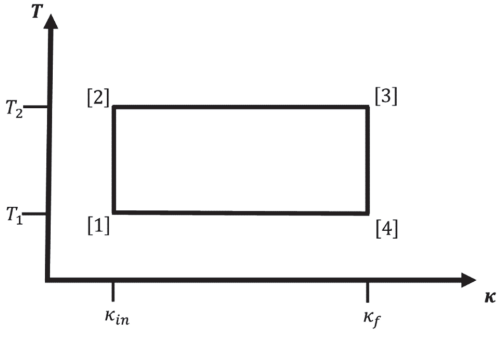

Figure 1. Sketch of an iso-κ-isothermal cycle for a hydrogen atom-like system. Branches [1] $\to$ [2] and [3] $\to$ [4] are iso-κ-legs and branches [2] $\to$ [3] and [4] $\to$ [1] are isothermal legs, respectively. The four corners of the cycle are the points [1] $= \left(\kappa^{[1]}, T^{[1]}\right) = (\kappa_{in}, T_1)$, [2] $= \left(\kappa^{[2]}, T^{[2]}\right) = (\kappa_{in}, T_2)$, [3] $= \left(\kappa^{[3]}, T^{[3]}\right) = \left(\kappa_f, T_2\right)$ and [4] $= \left(\kappa^{[4]}, T^{[4]}\right) = \left(\kappa_f, T_1\right)$ in the (κ, T) plane. Note that for given κ_{in}, $\kappa_f > \kappa_{in}$ and $T^{[1]} = T_1$, there remains only one variable, e.g., $T^{[2]} = T_2$, we are free to choose; all other variables are fixed by the choice of path types. All cycles for which $T_2 > T_1$ are feasible iso-κ-isothermal cycles.

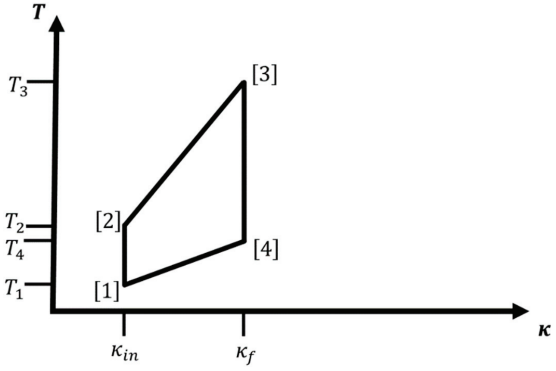

Figure 2. Sketch of an iso-κ-adiabatic cycle for a hydrogen atom-like system. Branches [1] → [2] and [3] → [4] are iso-κ-legs and branches [2] → [3] and [4] → [1] are (special) adiabatic legs, respectively. Note that the adiabatic legs run along straight lines through the origin. The four corners of the cycle are the points $[1] = \left(\kappa^{[1]}, T^{[1]}\right) = (\kappa_{in}, T_1)$, $[2] = \left(\kappa^{[2]}, T^{[2]}\right) = (\kappa_{in}, T_2)$, $[3] = \left(\kappa^{[3]}, T^{[3]}\right) = \left(\kappa_f, T_3\right)$, and $[4] = \left(\kappa^{[4]}, T^{[4]}\right) = \left(\kappa_f, T_4\right)$ in the (κ, T) plane. Note that for given κ_{in}, $\kappa_f > \kappa_{in}$, and $T^{[1]} = T_1$ there remains only one variable, e.g., $T^{[2]} = T_2$, we are free to choose; all other variables are fixed by the choice of path types. All cycles for which $T_2 > T_1$ are feasible iso-κ-adiabatic cycles.

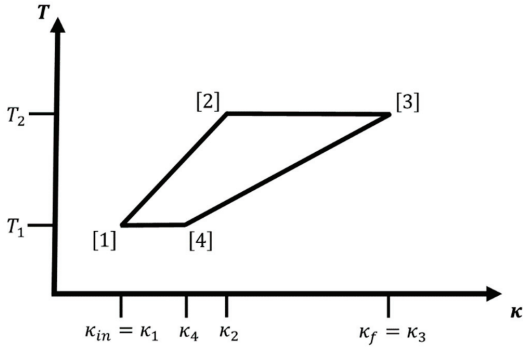

Figure 3. Sketch of an adiabatic-isothermal cycle for a hydrogen atom-like system. Branches [1] → [2] and [3] → [4] are (special) adiabatic legs and branches [2] → [3] and [4] → [1] are isothermal legs, respectively. Note that the adiabatic legs run along straight lines through the origin. The four corners of the cycle are the points $[1] = \left(\kappa^{[1]}, T^{[1]}\right) = (\kappa_{in}, T_1)$, $[2] = \left(\kappa^{[2]}, T^{[2]}\right) = (\kappa_2, T_2)$, $[3] = \left(\kappa^{[3]}, T^{[3]}\right) = \left(\kappa_f, T_2\right)$, and $[4] = \left(\kappa^{[4]}, T^{[4]}\right) = (\kappa_4, T_1)$ in the (κ, T) plane. Note that for given κ_{in}, $\kappa_f > \kappa_{in}$ and $T^{[1]} = T_1$, there remains only one variable, e.g., $T^{[2]} = T_2$, we are free to choose; all other variables are fixed by the choice of path types. However, only cycles for which $T_2^{max} > T_2 > T_1$, with $T_2^{max} = \frac{\kappa_f}{\kappa_{in}} T_1$, are feasible adiabatic-isothermal cycles for the hydrogen atom-like system.

In this context, one should note that, e.g., the dielectric constant $\varepsilon = \varepsilon(p, T)$ depends on both temperature and pressure, complicating the issue considerably; for small ranges of temperature and pressure, $\varepsilon(p, T)$ commonly changes with temperature and pressure in an approximately linear fashion in a solid [32,33], i.e., $\varepsilon(p, T) \approx \varepsilon\left(p_{ref}, T_{ref}\right) + \gamma_T\left(p_{ref}, T_{ref}\right)\left(T - T_{ref}\right) + \gamma_p\left(p_{ref}, T_{ref}\right)\left(p - p_{ref}\right)$. Depending on the type of system, we may have $\gamma_T\left(p_{ref}, T_{ref}\right) > 0$ and $\gamma_p\left(p_{ref}, T_{ref}\right) < 0$, respectively [32], or the opposite [33], or other combinations. Thus, e.g., we find that $\kappa \sim \frac{1}{\varepsilon^2}$ increases with pressure and decreases with temperature for CdF_2 [32], and we could translate our analysis from using (κ, T) to (p, T) as control variables, in principle.

Of course, all energy levels of the hydrogen atom-like system will exhibit nonzero occupancy in thermodynamic equilibrium in general—in principle, even including the continuous distribution of energy levels associated with modified plane–wave states beyond the ionization energy (although these will most likely be irrelevant due to the assumed localization or confinement of the electron). However, for practical calculations, one can often simplify the system by considering, e.g., only the two lowest energy levels E_1 and E_2. Frequently, such simplified models can yield some quantitative results and help to better understand the qualitative behavior of the full system [34]. Finally, we note that there are other ways to modify the electronic states of the hydrogen atom-like system, e.g., by breaking the spherical symmetry of the Hamiltonian, such that Equations (1)–(3) no longer apply. Since the corresponding changes in the eigenvalue spectrum of such a modified Hamiltonian are very specific to the way we break the symmetry and need to be treated on a case-by-case basis, we are not going to discuss such systems and only allow modifications of the hydrogen atom-like system that preserve the spherical symmetry and the $1/r$ dependence of the Coulomb potential.

2.2. Thermodynamic Cycles for the Hydrogen Atom-Like System

In general, we can distinguish two ways to change the occupation of the energy levels: directly via radiation with suitable frequencies corresponding to energy differences between specific energy levels, and stochastically by contact to heat baths at various temperatures. However, in the case of a radiation driven a-thermal cycle, we are not dealing with a system close to thermodynamic equilibrium, and the classical thermodynamic optimal control might not be suitable. Thus, in this study, we focus on the more familiar cycles involving interactions with heat reservoirs.

Regarding the notation, we write $X^{(j)}$ or $X_{j\to j+1}$ to indicate that the variable, parameter, or quantity X belongs to leg (j) which runs from corner $[j]$ to corner $[j+1]$ of the four-leg cycle (corner [5] = corner [1], of course). Furthermore, quantities associated with corner $[j]$ are referred to as $X^{[j]}$. This notation is introduced to keep the labeling of legs and corners distinct from the one for quantities such as the probability distribution $\vec{p}_i$ at step i along each branch when analyzing the effect of finite-time processes. Finally, the subscripts $\{\kappa;T\}$, $\{\kappa;S\}$, and $\{S;T\}$ indicate that the quantity is associated with an iso-κ-isothermal, iso-κ-adiabatic, or adiabatic-isothermal cycle, respectively.

If we allow interaction with a heat bath, we need to consider an ensemble of identical isolated localized hydrogen atom-like systems such that we can apply statistical mechanics to evaluate the (equilibrium) probabilities of occupation of the individual energy levels. From a statistical point of view, the microstates correspond to the eigenstates of the hydrogen-like atom. For concreteness, we always define (without loss of generality) κ_{in} and $\kappa_f > \kappa_{in}$ to denote the smallest and largest value of κ on the cycle, and $T^{[1]} = T_1$ as the lowest temperature in the cycle. Starting point of the cycle is always $\left(\kappa^{[1]}, T^{[1]}\right) = (\kappa_{in}, T_1)$. Together with the assignment of path types to the legs (adiabatic, isothermal, iso-κ), there is only one additional temperature, which we can choose, e.g., $T^{[2]} = T_2$ or $T^{[4]} = T_4$; all other temperatures and κ values of the cycle are then fixed. We always assume smooth changes in both κ and T along the legs of the cycle, i.e., for example, the system is exposed to an infinite number of heat baths with intermediary temperatures when changing T.

Note that we use the terms adiabatic and isentropic essentially interchangeably for thermodynamic equilibrium paths, since we assume that the system is in thermodynamic equilibrium both at the starting and at the end point of a leg. In the general case of such an adiabatic path, only the entropy remains constant along the path. However, for some physical systems, such as the hydrogen atom-like ones we are going to discuss, not only the entropy but also the equilibrium Boltzmann distribution remains unchanged along an adiabatic path, and we call such paths "special adiabatic".

For such a macroscopic system, Figures 1 and 2 show cycles combining two iso-κ legs with two isothermal or adiabatic legs, respectively. We excite the ensemble of atoms via change in temperature $T^{[1]} \to T^{[2]} = T_2 > T_1$, while we keep κ at the value κ_{in}: $\kappa^{[2]} = \kappa^{[1]} = \kappa_{in}$. Next, we perform/extract work while we increase κ from $\kappa^{[2]} = \kappa_{in}$ to $\kappa^{[3]} = \kappa_f > \kappa_{in}$. This can be done adiabatically, thus involving a concomitant change in temperature during the process ($T^{[2]} \to T^{[3]} = T_3 > T_2$),

or isothermally keeping the temperature constant at $T^{[2]} \to T^{[3]} = T_3 = T_2$. In leg 3, we de-excite the atom ensemble via change in temperature $T^{[3]} \to T^{[4]} = T_4 < T_3$, while we keep κ at the value $\kappa^{[3]} = \kappa^{[4]} = \kappa_f$, and finally, we decrease κ from $\kappa^{[4]} = \kappa_f$ back to $\kappa^{[1]} = \kappa_{in}$; again, this can be done either adiabatically ($T^{[4]} \to T^{[1]} = T_1 < T_4$) or isothermally at $T^{[4]} \to T^{[1]} = T_1 = T_4$. Note that for cycles containing two iso-κ branches, the only condition on T_2 is $T_2 > T_1$. In the literature, one sometimes calls the iso-κ-adiabatic cycle an Otto cycle, in analogy to the isochore-adiabatic cycle, which is the underlying cycle of an Otto engine [7], and similarly, we could call the iso-κ-isothermal cycle a Stirling cycle in analogy to the isochore-isothermal cycle belonging to the Stirling engine [7].

An alternative type of cycle shown in Figure 3 would include no legs with constant κ; instead, we combine two adiabatic and two isothermal legs to the analogue of a Carnot cycle [7]. We adiabatically increase κ from $\kappa^{[1]} = \kappa_{in}$ to $\kappa^{[2]} = \kappa_2$, $\kappa_{in} < \kappa_2 < \kappa_f$, appropriately changing the temperature during the process ($T^{[1]} \to T^{[2]} = T_2 > T_1$), followed by an isothermal leg where we increase κ from $\kappa^{[2]} = \kappa_2$ to $\kappa^{[3]} = \kappa_3 = \kappa_f$ while keeping the temperature constant at $T^{[2]} \to T^{[3]} = T_3 = T_2$. Next, we adiabatically decrease κ from $\kappa^{[3]} = \kappa_3$ to $\kappa^{[4]} = \kappa_4$, $\kappa_{in} < \kappa_4 < \kappa_f$, while appropriately changing the temperature ($T^{[3]} \to T^{[4]} = T_4 < T_3$), and finally, we decrease κ from $\kappa^{[4]} = \kappa_4$ back to $\kappa^{[1]} = \kappa_{in}$ while keeping the temperature constant $T^{[4]} \to T^{[1]} = T_1 = T_4$.

Note that a feasible isothermal-adiabatic cycle usually will have an additional condition on $T^{[2]}$. For the special adiabatic legs of a hydrogen atom-like system, feasibility requires that the temperature at the second corner fulfills the condition

$$T_1 < T_2 < T_2^{max}, \tag{4}$$

where

$$T_2^{max} = \frac{\kappa_f}{\kappa_{in}} T_1; \tag{5}$$

otherwise, leg 3 would have a larger slope than leg 1, violating the condition that $\kappa_{in} < \kappa_2, \kappa_4 < \kappa_f$.

When analyzing the work performed and the heat exchanged along the legs of the cycles, we do not include the work done on the environment of the hydrogen atom-like system (e.g., the solid or the cavity), which is needed to vary κ. Of course, we can take that into account, e.g., via replacing κ by the pressure p as control variable if $\kappa = \kappa(p)$ depends on pressure in a monotonic fashion, and then compute the work needed to establish such a pressure inside the solid. However, the focus is on the hydrogen-atom like system, and not on the whole solid or cavity where the system might be realized in the experiment. Thus, we will stay with using κ as the control variable, and only consider the change in the hydrogen atom-like system itself.

There are several general aspects that need to be considered regarding the equilibrium distributions, relaxation, and entropy/excess heat production along the cycles. How close are the instantaneous probability distributions over the states of the system to the (equilibrium) Boltzmann distributions at the various temperatures along its iso-κ legs? Similarly, for branches where κ is changed, how does the finite time available to vary κ affect our ability to keep the probability distribution close to the appropriate Boltzmann distribution for isothermal processes, and how close can the adiabatic path in (κ, T)-space which is realized in experiment, be to the ideal adiabatic path? All these questions directly lead to the issue of relaxation to the appropriate Boltzmann distributions in finite time, for which we can hope to derive general formulas as long as we can assume that the processes are slow enough for the system to always remain close to thermodynamic equilibrium throughout the cycle.

2.3. Statistical Mechanics and Thermodynamics of Cycles

Regarding the statistical mechanics and thermodynamics of cycles, the starting point of our analysis will be the first law of thermodynamics,

$$dE = \delta Q - \delta W \tag{6}$$

along a piece of path in thermodynamic space, which is equivalent to $\delta W = \delta Q - dE$. Here, $dE > 0$ means that the internal energy of the system is increased along the leg, and $\delta Q > 0$ means that heat is added to the atom from the reservoir(s) the atom is in contact with along the path, thus increasing the system's internal energy. $\delta W > 0$ means that the system does work on the apparatus, radiation field or the environment in general, along the leg, and reduces the system's internal energy in the process. To avoid confusion, we note that in the literature $\delta W(> 0)$ is frequently defined in an alternative fashion to refer to the amount of work done by the apparatus on the system increasing its internal energy; as a consequence, one then would write the first law as $dE = \delta Q + \delta W$ and $\delta W = dE - \delta Q$.

The connection to statistical mechanics appears via the information theoretic definition of the entropy

$$S = -k_B \sum_{j=1}^{N_S} p_j ln\big(p_j\big), \tag{7}$$

where p_j is the probability for the microstate j to be occupied, and the sum is over all N_S microstates [5]. In equilibrium at given temperature T, these probabilities π_j correspond to the equilibrium Boltzmann probability distribution,

$$\pi_j(T) = \frac{exp\Big(-\frac{E_j}{k_B T}\Big)}{Z(T)} \tag{8}$$

for the case of the canonical ensemble, where the sum over states $Z(T) = \sum_{k=1}^{N_S} exp\Big(-\frac{E_k}{k_B T}\Big)$ serves as the normalization of the probability distribution, and E_j is the energy of microstate j. Keep in mind that the equilibrium distribution maximizes the entropy, for a given set of boundary conditions that are, e.g., defining the ensemble.

If we consider the energy levels $E_n (= \widetilde{E}_n)$ of the states instead of the microstates themselves in the formula of the entropy, then we need to include the degeneracies g_n of the energies $\widetilde{E}_n$. As far as the equilibrium probabilities are concerned, we can assume that the probabilities of occupying two states i and j with the same energy $E_i = E_j = \widetilde{E}_n$ are equal; for convenience, we define $\rho_n = \pi_i = \pi_j$, and thus

$$\widetilde{\pi}_n = g_n \rho_n, \tag{9}$$

is the equilibrium probability to find the system with energy $\widetilde{E}_n$. In general, we can write the equilibrium entropy as

$$\begin{array}{c} S = -k_B \sum_{n=1}^{N_E} g_n \rho_n ln(\rho_n) = -k_B \sum_{n=1}^{N_E} \widetilde{\pi}_n ln(\rho_n) = -k_B \sum_{n=1}^{N_E} \widetilde{\pi}_n ln\Big(\frac{\widetilde{\pi}_n}{g_n}\Big) = \\ -k_B \sum_{n=1}^{N_E} \widetilde{\pi}_n [ln(\widetilde{\pi}_n) - ln(g_n)], \end{array} \tag{10}$$

where now the summation goes over the N_E energy levels and $\widetilde{\pi}_n$ are the equilibrium probabilities to find the system in a state with energy $\widetilde{E}_n$. Note that for non-degenerate states, i.e., $g_n = 1$, this expression reverts to the original microstate-based formula, and for the special case $\widetilde{\pi}_n = 1$ for $n = m$ while $\widetilde{\pi}_n = 0$ for $n \neq m$, we obtain the formula for the entropy in the microcanonical ensemble, $S = k_B ln(g_m)$.

Finally, for those probability distributions where we deviate from the equilibrium distribution but nevertheless can assume that the probabilities of being in a state with energy $E_i = E_j = \widetilde{E}_n$ are the same, we can define $r_n = p_i = p_j$, and thus $\widetilde{p}_n = g_n r_n$. Then, we get for the entropy the expression $S = -k_B \sum_{n=1}^{N_E} g_n r_n ln(r_n) = -k_B \sum_{n=1}^{N_E} \widetilde{p}_n ln\Big(\frac{\widetilde{p}_n}{g_n}\Big)$ and the normalization $\sum_{n=1}^{N_E} g_n r_n = \sum_{n=1}^{N_E} \widetilde{p}_n = \sum_{j=1}^{N_S} p_j = 1$. Note that this is a substantial restriction in the set of allowed probability distributions; thus, unless this assumption is valid, we need to employ the microstate formulation of the problem.

As a shorthand notation, we can represent the probability distributions by vectors $\vec{p} = \left(p_1, \ldots, p_{N_S}\right)$, and expressions like $\sum_{j=1}^{N_S} p_j ln\left(p_j\right)$ can be written as

$$\sum_{j=1}^{N_S} p_j ln\left(p_j\right) = \vec{p} \cdot ln\left(\vec{p}\right), \tag{11}$$

where $ln\left(\vec{p}\right) = \left(ln(p_1), \ldots, ln\left(p_{N_S}\right)\right)$. Similarly, $\vec{E} = \left(E_1, \ldots, E_{N_S}\right)$, and we can relate the equilibrium probabilities of the Boltzmann distribution to the energies via

$$\vec{E} = -k_B T ln\left(\vec{\pi}\right) + C\left(\vec{\pi}\right)\vec{1} = -k_B T ln\left(\vec{\pi}\right) - k_B T ln\left(g\left(\vec{\pi}\right)\right)\vec{1}, \tag{12}$$

where $g\left(\vec{\pi}\right)$ is a constant that can be related to an overall shift of the energy scale, and $\vec{1} = (1, \ldots, 1)$ [35]. The expectation value of the energy is then given by

$$\sum_{j=1}^{N_S} p_j E_j = \vec{E} \cdot \vec{p}, \tag{13}$$

or, for the case of the expectation value in equilibrium, $\sum_{j=1}^{N_S} \pi_j E_j = \vec{E} \cdot \vec{\pi}$. Note that some of these energies will appear many times in this vector if the energy level is degenerate. Another example is the expectation value of the square of the energy, $\sum_{j=1}^{N_S} \pi_j \left(E_j\right)^2 = \vec{E^2} \cdot \vec{\pi}$, where $\vec{E^2} = \left((E_1)^2, \ldots, \left(E_{N_S}\right)^2\right)$. If appropriate, we can replace the sums over the N_S microstates by sums over the N_E energies, i.e., $\sum_{j=1}^{N_S} \pi_j E_j = \sum_{j=1}^{N_E} \widetilde{\pi}_j \widetilde{E}_j = \vec{\widetilde{E}} \cdot \vec{\widetilde{\pi}}$, where $\vec{\widetilde{\pi}} = \left(\widetilde{\pi}_1, \ldots, \widetilde{\pi}_{N_E}\right)$ and $\vec{\widetilde{E}} = \left(\widetilde{E}_1, \ldots, \widetilde{E}_{N_E}\right)$, or for the entropy $S = -k_B \sum_{n=1}^{N_E} \widetilde{\pi}_n ln(\rho_n) = -k_B \vec{\widetilde{\pi}} \cdot ln\left(\vec{\rho}\right)$ where $ln\left(\vec{\rho}\right) = \left(ln(\rho_1), \ldots, ln\left(\rho_{N_E}\right)\right) = \left(ln\left(\frac{\widetilde{\pi}_1}{g_1}\right), \ldots, ln\left(\frac{\widetilde{\pi}_{N_E}}{g_{N_E}}\right)\right)$. In the case of the single atom-like system, the microstates correspond to the eigenfunctions of the Hamiltonian of an electron (or a quasi-particle) in a (shielded) Coulomb potential. Note that we are not considering the degeneracy due to the multiple copies of the atom-like system in the ensemble—the ensemble is only introduced to allow us to visualize the occupation probabilities of the single atom-like system with which we are dealing.

Since the energy is a state function, the change of its equilibrium expectation value

$$\langle E \rangle = \sum_{j=1}^{N_S} E_j \pi_j = \vec{E} \cdot \vec{\pi} \tag{14}$$

along a leg (j) of the path does not depend on the choice of path, i.e., the total change in energy can be computed directly from taking the difference between the two states,

$$\left(\Delta E\right)_{j \to j+1} = \langle E \rangle^{[j+1]} - \langle E \rangle^{[j]}. \tag{15}$$

For the heat delivered/absorbed by the atom along a leg (j) (parametrized by $\lambda \in \left[\lambda^{[j]}, \lambda^{[j+1]}\right]$), we can use the formula

$$\begin{aligned} Q_{\vec{\pi}}^{(j)} = \int_{S^{[j]}}^{S^{[j+1]}} T dS = -k_B \int_{\lambda^{[j]}}^{\lambda^{[j+1]}} T(\lambda) \frac{d}{d\lambda}\left[\vec{\pi} \cdot ln\left(\vec{\pi}\right)\right] d\lambda = -k_B \int_{\lambda^{[j]}}^{\lambda^{[j+1]}} T(\lambda)\left[ln\left(\vec{\pi}(\lambda)\right) + \vec{1}\right] \cdot \\ \frac{d\vec{\pi}}{d\lambda} d\lambda = -k_B \int_{\vec{\pi}^{[j]}}^{\vec{\pi}^{[j+1]}} T\left(\vec{\pi}\right)\left[ln\left(\vec{\pi}\right) + \vec{1}\right] \cdot d\vec{\pi}, \end{aligned} \tag{16}$$

if we stay at the equilibrium distribution along the path, and an analogous expression in $\vec{p}$ if we deviate from the equilibrium distribution because of, e.g., finite-time effects:

$$Q_{\vec{p}}^{(j)} = \int_{S^{[j]}}^{S^{[j+1]}} T dS = -k_B \int_{\lambda^{[j]}}^{\lambda^{[j+1]}} T(\lambda)\left[ln\left(\vec{p}\,(\lambda)\right) + \vec{1}\right] \cdot \frac{d\vec{p}}{d\lambda} d\lambda. \tag{17}$$

Finally, the work performed by the atom can be computed via the first law by taking the difference between δQ and dE along the path. Along the legs where κ is constant, both Q and ΔE will vary as they are both functions of the probability distribution, which in turn evolves as the temperature changes. To compute ΔE is no problem, but the expression for Q is nontrivial. We can switch coordinates to follow the change in temperature instead of the change in entropy,

$$Q_{j\to j+1} = \int_{S^{[j]}}^{S^{[j+1]}} T dS = \left[T^{[j+1]}S^{[j+1]} - T^{[j]}S^{[j]}\right] - \int_{T^{[j]}}^{T^{[j+1]}} S dT = \left[T^{[j+1]}S^{[j+1]} - T^{[j]}S^{[j]}\right] + k_B \int_{T^{[j]}}^{T^{[j+1]}} \vec{\pi}(T)\cdot ln\Big(\vec{\pi}(T)\Big) dT, \tag{18}$$

However, we note that this way of writing $Q^{(j)}$ does not necessarily make the integral easier to perform in general either, even though κ, and thus all the energy levels $E_n(\kappa)$, are constant along these legs of the cycle. However, since the work δW would usually be associated with changes in κ, we expect that $W = 0$ along thermodynamic equilibrium paths with fixed κ, and therefore, $Q = \Delta E$. Using Equations (16) and (12), we find:

$$\begin{aligned}
W^{(j)} &= Q^{(j)} - (\Delta E)^{(j)} = \int_{S^{[j]}}^{S^{[j+1]}} T dS - [\langle E\rangle^{[j+1]} - \langle E\rangle^{[j]}] \\
&= -\int_{\vec{\pi}(T^{[j]})}^{\vec{\pi}(T^{[j+1]})} k_B T[ln(\vec{\pi}) + \vec{1}]\cdot d\vec{\pi} - \vec{E}(\kappa_{in})\cdot(\vec{\pi}(\kappa_{in}, T^{[j+1]}) - \vec{\pi}(\kappa_{in}, T^{[j]})) \\
&= -\int_{\vec{\pi}(T^{[j]})}^{\vec{\pi}(T^{[j+1]})} k_B T[ln(\vec{\pi}) + \vec{1}]\cdot d\vec{\pi} - \int_{\vec{\pi}(T^{[j]})}^{\vec{\pi}(T^{[j+1]})} \vec{E}(\kappa_{in})\cdot d\vec{\pi} \\
&= -\int_{\vec{\pi}(T^{[j]})}^{\vec{\pi}(T^{[j+1]})} \{k_B T[ln(\vec{\pi}) + \vec{1}] + \vec{E}(\kappa_{in})\}\cdot d\vec{\pi} \\
&= -\int_{\vec{\pi}(T^{[j]})}^{\vec{\pi}(T^{[j+1]})} \{k_B T[ln(\vec{\pi}) + \vec{1}] - k_B T\Big[ln(\vec{\pi}) + ln(g(\vec{\pi}))\vec{1}\Big]\}\cdot d\vec{\pi} \\
&= -\int_{\vec{\pi}(T^{[j]})}^{\vec{\pi}(T^{[j+1]})} \{k_B T[ln(\vec{\pi}) + \vec{1} - ln(\vec{\pi}) - ln(g(\vec{\pi}))\vec{1}]\}\cdot d\vec{\pi} \\
&= -\int_{\vec{\pi}(T^{[j]})}^{\vec{\pi}(T^{[j+1]})} \{k_B T[1 - ln(g(\vec{\pi}))]\}\vec{1}\cdot d\vec{\pi} = 0\,,
\end{aligned} \tag{19}$$

since $\vec{1}\cdot d\vec{\pi} = 0$ along a thermodynamic equilibrium path because of probability conservation. Note that we have not exploited the fact that we are dealing with a hydrogen atom-like system, and thus this result is general for any statistical mechanical system along legs with κ = constant, even for the most general case of many control parameters $\kappa \hat{=} \vec{\kappa} = (\kappa_a, \kappa_b, \ldots)$.

If we consider the complete cycle, the changes in energy will sum to zero, and thus $W = Q$ over the whole cycle, i.e., the net heat added to the atom over the cycle must be converted into net work done by the atom on the apparatus. The discussion in this subsection is standard procedure from equilibrium thermodynamics [5,6], but has been included to establish the concepts and notation needed for analyzing the thermodynamics of the cycles of statistical mechanical systems in finite time in the next sections.

3. Optimal Control Criterion for Finite-Time Thermodynamic Cycles of General Statistical Mechanical Systems

3.1. Finite-Time Optimal Control along a General Path in (κ, T) Space

If thermodynamic processes are performed in finite time, one usually encounters deviations in the heat exchanged and work performed along the path from those values that one finds for the ideal quasi-static processes for which infinite times are available, because the system cannot maintain thermodynamic equilibrium over the whole cycle when the total time τ is finite. As a consequence, a net amount of entropy is produced over the whole cycle or excess heat/work is found while the system tries to move towards or stay close to the elusive thermal equilibrium along the path. Typically, one would attempt to minimize this entropy or excess heat production, leading to the formulation of the minimum

excess heat/work production optimal control problems discussed in finite-time thermodynamics. In this study, we will focus on minimum entropy production and minimum excess heat production; other possible optimal control objectives such as maximum power or maximum efficiency are not considered. In the following, the subscript Q will indicate minimization of excess heat, while the subscript S indicates minimization of entropy production.

In general, one would need to analyze each process in depth, in order to compute the excess heat or excess work associated with the given physical situation. However, we can perform an approximate analysis of the difference $I_Q = Q_{\vec{\pi}} - Q_{\vec{p}}$ between the heat $Q_{\vec{\pi}}$ we would obtain under the assumption that along the path the system is everywhere in thermodynamic equilibrium, i.e., $\vec{p}_i(T_i) = \vec{\pi}_i(T_i)$, and the corresponding expression $Q_{\vec{p}}$ along the path for the real probability distribution where $\vec{p}_i(T_i) \neq \vec{\pi}_i(T_i)$, yet $\vec{p}_i(T_i)$ is nevertheless close to $\vec{\pi}_i(T_i)$ and just a bit "behind", i.e., we can approximate $\vec{p}_i(T_i)$ as

$$\vec{p}_i(T_i) = \vec{\pi}_{i-1}(T_{i-1}), \tag{20}$$

For the remainder of this study, we will assume that Equation (20) is a suitable approximation; the issue of incomplete relaxation to equilibrium of $\vec{p}_i(T_i)$ to $\vec{\pi}_{i-1}(T_{i-1})$ is discussed in Refs. [35,36].

Using Equations (16) and (17) where λ now corresponds to time, we get

$$\begin{array}{l} I_Q = Q_{\vec{\pi}} - Q_{\vec{p}} = -k_B \int_0^\tau T(t)\left\{\dot{\vec{\pi}}\cdot\left[ln\left(\vec{\pi}(t)\right) + \vec{1}\right] - \dot{\vec{p}}\cdot\left[ln\left(\vec{p}(t)\right) + \vec{1}\right]\right\}dt \approx -k_B \int_0^\tau T(t)\dot{\vec{\pi}}\cdot \\ \left\{ln\left(\vec{\pi}(t)\right) - ln\left(\vec{p}(t)\right)\right\}dt \approx k_B \int_0^\tau T(t)\dot{\vec{\pi}}\cdot\left\{\frac{d}{d\vec{\pi}} ln\left(\vec{\pi}(t)\right)\cdot\left(\vec{\pi}(t) - \vec{p}(t)\right)\right\}dt \approx \\ \sum_{i=1}^{N_{st}}\left(\vec{\pi}_i - \vec{\pi}_{i-1}\right)\cdot\left\{\frac{k_B T_i}{\overleftrightarrow{\pi}_i}\right\}\left(\vec{\pi}_i - \vec{p}_i\right) \approx \sum_{i=1}^{N_{st}}\left(\vec{\pi}_i - \vec{\pi}_{i-1}\right)\cdot\left\{\frac{k_B T_i}{\overleftrightarrow{\pi}_i}\right\}\left(\vec{\pi}_i - \vec{\pi}_{i-1}\right). \end{array} \tag{21}$$

Here, N_{st} is the number of possible steps in (κ, T) space during the finite time τ assuming that each temperature-plus-κ change requires a "relaxation-to-equilibrium" time of $(\Delta t)_{st}$, i.e., $\tau = N_{st}(\Delta t)_{st}$. In the above derivation, several approximations were applied. First, we have employed the fact that $\vec{p}(t)$ essentially follows $\vec{\pi}(t)$, and thus $\dot{\vec{\pi}} = \dot{\vec{p}}$ to first order in $\left(\vec{\pi}(t) - \vec{p}(t)\right)$. Furthermore, we assumed that $\left(\vec{\pi}(t) - \vec{p}(t)\right)$ is very small, and thus we can make a Taylor expansion of $ln\left(\vec{p}(t)\right)$ about $\vec{\pi}(t)$. Next, we assumed that we can make a large number of changes in (κ, T) along the path, such that we can replace the integral by a sum over such discrete changes, resulting in $\dot{\vec{\pi}}dt \approx \dot{\vec{\pi}}(\Delta t)_{st} \approx \left(\vec{\pi}_i - \vec{\pi}_{i-1}\right)$, and finally we assumed that Equation (20) holds, i.e., $\vec{p}_i \approx \vec{\pi}_{i-1}$.

Analogously, we can derive an expression for the entropy production over the path as

$$\begin{array}{l} I_S = -k_B \int_0^\tau \left\{\dot{\vec{\pi}}\cdot\left[ln\left(\vec{\pi}(t)\right) + \vec{1}\right] - \dot{\vec{p}}\cdot\left[ln\left(\vec{p}(t)\right) + \vec{1}\right]\right\}dt \\ \approx \sum_{i=1}^{N_{st}}\left(\vec{\pi}_i - \vec{\pi}_{i-1}\right)\cdot\left\{\frac{k_B}{\overleftrightarrow{\pi}_i}\right\}\left(\vec{\pi}_i - \vec{\pi}_{i-1}\right). \end{array} \tag{22}$$

Looking at the expressions for the excess heat and the entropy production that are to be minimized, we see that $\overleftrightarrow{M}_Q = \left\{\frac{k_B T_i}{\overleftrightarrow{\pi}_i}\right\}$ and $\overleftrightarrow{M}_S = \left\{\frac{k_B}{\overleftrightarrow{\pi}_i}\right\}$, repectively, are positive definite diagonal matrices that can serve as metrics in the space of probability distributions with components

$$(\overleftrightarrow{M}_Q)_{kl} = \left\{\frac{k_B T_i}{\overleftrightarrow{\pi}_i}\right\}_{kl} = \frac{k_B T_i}{\pi_k(\kappa_i, T_i)}\delta_{kl} \text{ and } (\overleftrightarrow{M}_S)_{kl} = \left\{\frac{k_B}{\overleftrightarrow{\pi}_i}\right\}_{kl} = \frac{k_B}{\pi_k(\kappa_i, T_i)}\delta_{kl}, \tag{23}$$

which allows us to define distances in thermodynamic space, and thus yield the corresponding thermodynamic lengths of the path. Note that both the temperature T_i and $\vec{\pi}_i$ (which is a function

of (κ_i, T_i)) depend on i, and thus the metrics $\overleftrightarrow{M}_{Q/S}$ vary along the path. $I_{Q/S}$ is now minimized by picking the stopping points along the path such that the thermodynamic lengths

$$\left(\Delta L_Q\right)_i = \left[\left(\vec{\pi}_i - \vec{\pi}_{i-1}\right)\left\{\frac{k_B T_i}{\overleftrightarrow{\pi}_i}\right\}\left(\vec{\pi}_i - \vec{\pi}_{i-1}\right)\right]^{1/2} \text{ or } \left(\Delta L_S\right)_i = \left[\left(\vec{\pi}_i - \vec{\pi}_{i-1}\right)\left\{\frac{k_B}{\overleftrightarrow{\pi}_i}\right\}\left(\vec{\pi}_i - \vec{\pi}_{i-1}\right)\right]^{1/2}, \quad (24)$$

respectively, of all N_{st} pieces of the path are equal. This follows from the Cauchy–Schwarz inequality

$$I_{Q/S} = \sum_{i=1}^{N_{st}}\left[\left(\Delta L_{Q/S}\right)_i\right]^2 \geq \frac{1}{N_{st}}\left[\sum_{i=1}^{N_{st}}\left(\Delta L_{Q/S}\right)_i\right]^2 = \frac{\left[\left(\Delta L_{Q/S}\right)_{total}\right]^2}{N_{st}}, \quad (25)$$

implying that equality holds only if the lengths of all individual pieces $\left(\Delta L_{Q/S}\right)_i$ are equal,

$$\left(\Delta L_{Q/S}\right)_i = \frac{\left(\Delta L_{Q/S}\right)_{total}}{N_{st}}. \quad (26)$$

Note that this criterion of equal thermodynamic lengths of sub-pieces is equivalent to the constant thermodynamic speed criterion [37] employed, e.g., in the context of optimization of global optimization algorithms [38], where thermodynamic speed corresponds to thermodynamic distance per relaxation, i.e., time is measured in units of relaxation-to-equilibrium times.

Since $\overleftrightarrow{M}_Q = \left\{\frac{k_B T_i}{\overleftrightarrow{\pi}_i}\right\}$ is a diagonal matrix, we can rewrite each term in the sum as

$$\left(\vec{\pi}_i - \vec{\pi}_{i-1}\right)\cdot\left\{\frac{k_B T_i}{\overleftrightarrow{\pi}_i}\right\}\left(\vec{\pi}_i - \vec{\pi}_{i-1}\right) = k_B T_i \sum_{k=1}^{N_S}\frac{(d\pi_i)_k (d\pi_i)_k}{(\pi_i)_k}, \quad (27)$$

where $d\vec{\pi}_i = \left(\vec{\pi}_i - \vec{\pi}_{i-1}\right) = \left((d\pi_i)_1, \ldots (d\pi_i)_{N_S}\right)$ is the infinitesimal difference between the equilibrium probability distributions at steps $i-1$ and i. For the total length of the path along, e.g., leg (j) with $N^{(j)}$ steps, we thus get the expression

$$\begin{aligned} L_Q^{(j)} &= \sum_{i=1}^{N^{(j)}}\sqrt{\left(\vec{\pi}_i - \vec{\pi}_{i-1}\right)\cdot\left\{\frac{k_B T_i}{\overleftrightarrow{\pi}_i}\right\}\left(\vec{\pi}_i - \vec{\pi}_{i-1}\right)} = \sum_{i=1}^{N^{(j)}}\sqrt{\left[k_B T_i \sum_{k=1}^{N_S}\frac{(d\pi_i)_k (d\pi_i)_k}{(\pi_i)_k}\right]} \approx \\ &\left|\int_{leg\ (j)}\sqrt{\left[k_B T(\lambda)\sum_{k=1}^{N_S}\frac{(d\pi(\lambda))_k (d\pi(\lambda))_k}{(d\lambda)^2 (\pi(\lambda))_k}\right]}d\lambda\right| = \left|\int_{leg\ (j)}\sqrt{k_B T(\lambda)}\sqrt{\left[\sum_{k=1}^{N_S}\frac{1}{(\pi(\lambda))_k}\left(\frac{(d\pi(\lambda))_k}{d\lambda}\right)^2\right]}d\lambda\right|, \end{aligned} \quad (28)$$

where λ is the variable of integration along the branch (j). Note that we have taken the absolute value of the integral, since $L_Q^{(j)} \geq 0$ by definition, independent of whether λ increases or decreases along the path. Analogously, we obtain for $L_S^{(j)}$ the expression

$$L_S^{(j)} = \left|\int_{leg\ (j)}\sqrt{k_B}\sqrt{\left[\sum_{k=1}^{N_S}\frac{1}{(\pi(\lambda))_k}\left(\frac{(d\pi(\lambda))_k}{d\lambda}\right)^2\right]}d\lambda\right|. \quad (29)$$

Of course, we must first choose the path in (κ, T)-space between the starting and end point of the leg in such a way that its total length is minimal. For general statistical mechanical systems, where the Hamiltonian is controlled not only by one single parameter κ but by a whole set of such parameters $\vec{\kappa} = (\kappa_a, \kappa_b, \ldots)$, this task is usually very complex. However, for the individual legs of the cycles for the hydrogen atom-like system, this is trivial, as we have only one parameter which can be varied (either just κ with fixed T for the isothermal leg, or both κ and T but in a synchronized fashion along the adiabatic leg, or finally only T with fixed κ along the iso-κ leg), and thus the path itself is given, and we

can only vary the location of the steps i along the path. One additional aspect needs to be addressed: the optimization encompasses the whole cycle, and thus the available time τ needs to be distributed over the four legs, i.e., we have $\tau = \tau^{(1)} + \tau^{(2)} + \tau^{(3)} + \tau^{(4)}$. In principle, this poses no difficulty as long as the relaxation times per step are the same for all legs, $\Delta t^{(j)} = (\Delta t)_T = (\Delta t)_\kappa = (\Delta t)_a$, regardless of whether we are dealing with an isothermal, iso-κ, or adiabatic leg: knowing the thermodynamic lengths for the four legs $L^{(1)}$, $L^{(2)}$, $L^{(3)}$, and $L^{(4)}$, we use $L_{cycle} = L^{(1)} + L^{(2)} + L^{(3)} + L^{(4)}$ and the principle of constant thermodynamic speed [37] to assign the times as

$$\tau^{(j)} = \frac{L^{(j)}}{L_{cycle}}\tau. \tag{30}$$

Once $\tau^{(i)}$ is known, then the number of available steps along the leg is given by

$$N^{(j)} = \frac{\tau^{(j)}}{\Delta t^{(j)}}. \tag{31}$$

However, if the relaxation times vary between the legs—or more generally, vary along the legs as function of κ and T, i.e., $(\Delta t)_{st} = (\Delta t)_{st}(\kappa, T)$—, we need to be more circumspect. Assuming that $(\Delta t)_{st}(\kappa, T)$ is known, in a first step, we would evaluate the average relaxation time along the path, $(\Delta t)_{av}$, which allows us to compute an estimate of the number of discrete steps along the path $N_{st} = \tau/(\Delta t)_{av}$. With this information, we can use Equation (25) to compute the optimal length of each sub-piece i, $(\Delta L)_i = (\Delta L)_{opt} = \frac{L_{cycle}}{N_{st}} = \frac{L_{cycle}}{\tau}(\Delta t)_{av}$. By construction, the value of $(\Delta L)_{opt}$ is independent of the position (κ_i, T_i) of sub-piece i along the path. Since the relaxation time varies with position i, we now need to assign each sub-piece i its own time $\tau(\kappa_i, T_i) = \tau_i = (\Delta t)_{st}(\kappa_i, T_i)$. As long as the relaxation times do not vary much along the path, the sum of the assigned times $\sum_{i=1}^{N_{st}} \tau_i = \tau_{cycle}$ will nearly equal the total available time $\tau_{cycle} \approx \tau$, and the result is self-consistent. Otherwise, we need to set up a feedback loop and re-compute N_{st}, via, e.g., $N_{st}^{(k+1)} = N_{st}^{(k)} \frac{\tau}{\tau_{cycle}^{(k)}}$, and then assign τ_i, until self-consistency has been reached, i.e., $\sum_{i=1}^{N_{st}^{(k)}} \tau_i^{(k)} = \tau_{cycle}^{(k)} = \tau$. For further discussions concerning the influence of varying relaxation times in step optimal control processes, we refer to the literature [35,36].

Note that this derivation did not depend on the specific features of the hydrogen atom-like system. Thus, the minimal thermodynamic length criterion of optimality we have derived is valid for general statistical mechanical systems, whose Hamiltonian is controlled by a set of parameters $\vec{\kappa} = (\kappa_a, \kappa_b, \ldots)$. In this context, we note that the metric $\overleftrightarrow{M}_Q$ at each point i along the path is proportional to T_i, and thus we expect that the branches (j) (or parts thereof) that lie in a high temperature region, should exhibit larger thermodynamic lengths $L_Q^{(j)}$ than those at lower temperatures since the formulas for those lengths contain $\sqrt{T_i}$ as factors in each term or integral.

We now turn to the three special cases of iso-κ, isothermal, and isentropic (adiabatic and special adiabatic) paths.

3.2. Finite-Time Optimal Control along Isothermal Legs

For the legs with isothermal change in the parameter κ, Equation (21) yields for the excess heat $I_{Q;iso-T} \approx k_B T \sum_{i=1}^{N_\kappa} \left(\vec{\pi}_i - \vec{\pi}_{i-1}\right) \cdot \left\{\frac{1}{\overleftrightarrow{\pi}_i}\right\} \left(\vec{\pi}_i - \vec{\pi}_{i-1}\right)$ and similarly, Equation (22) for the entropy production $I_{S;iso-T} \approx k_B \sum_{i=1}^{N_\kappa} \left(\vec{\pi}_i - \vec{\pi}_{i-1}\right) \cdot \left\{\frac{1}{\overleftrightarrow{\pi}_i}\right\} \left(\vec{\pi}_i - \vec{\pi}_{i-1}\right) = I_{Q;iso-T}/T$, where N_κ is the number of changes in the value of κ along the branch, which are feasible during the finite time τ assuming that each κ change

takes at least a time of $(\Delta t)_\kappa$, i.e., $\tau = N_\kappa(\Delta t)_\kappa$. Again, $I_{Q/S}$ is minimized by picking the stopping points along the path such that the thermodynamic lengths

$$\left(\Delta L_Q\right)_i = \sqrt{k_B T}\left[\left(\vec{\pi}_i - \vec{\pi}_{i-1}\right)\left\{\frac{1}{\vec{\pi}_i}\right\}\left(\vec{\pi}_i - \vec{\pi}_{i-1}\right)\right]^{1/2} \text{ or } (\Delta L_S)_i = \sqrt{k_B}\left[\left(\vec{\pi}_i - \vec{\pi}_{i-1}\right)\left\{\frac{1}{\vec{\pi}_i}\right\}\left(\vec{\pi}_i - \vec{\pi}_{i-1}\right)\right]^{1/2}, \quad (32)$$

respectively, of all N_κ pieces of the path are equal,

$$\left(\Delta L_{Q/S}\right)_i = \frac{\left(\Delta L_{Q/S}\right)_{total}}{N_\kappa}. \quad (33)$$

We realize that the change in κ can be interpreted as the change in the Hamiltonian of the system. Thus, the isothermal branch of the cycle for a system with only one control parameter κ represents a special case of the general estimates of the difference between computational work and the free energy (at constant temperature)—which is computed via various thermodynamic integration methods [39–41] between two different Hamiltonians in finite time—, for which the optimal control problem has been analyzed in earlier work [35]. In this earlier study, it had been found that as long as we can stay close to the equilibrium distribution such that we can assume that the actual probability distribution $\vec{p}_i$ at step i equals the equilibrium probability distribution $\vec{\pi}_{i-1}$ at the previous step $i-1$, the amount of excess work along an isothermal leg is given by

$$\begin{array}{c} I_{iso-T} = W_{iso-T} - \Delta F_{iso-T} = \int_0^\tau \dot{\vec{E}}\left(\vec{p} - \vec{\pi}\right)dt = k_B T \int_0^\tau \dot{\vec{\pi}}\cdot\left\{\frac{1}{\vec{\pi}}\right\}\cdot\left(\vec{\pi} - \vec{p}\right)dt \approx \\ \sum_{i=1}^{N_\kappa}\left(\vec{\pi}_i - \vec{\pi}_{i-1}\right)\cdot\left\{\frac{k_B T}{\vec{\pi}_i}\right\}\left(\vec{\pi}_i - \vec{p}_i\right) \approx k_B T \sum_{i=1}^{N_\kappa}\left(\vec{\pi}_i - \vec{\pi}_{i-1}\right)\cdot\left\{\frac{1}{\vec{\pi}_i}\right\}\left(\vec{\pi}_i - \vec{\pi}_{i-1}\right). \end{array} \quad (34)$$

However, this is just the same expression as $I_{Q;iso-T}$, which we have obtained for the excess heat along an isothermal leg in (κ, T)-space, as one would have already expected from energy conservation. Since the temperature is constant along the path, we can pull T as a factor in front of the summation when computing the excess heat, and thus the thermodynamic length L_Q of an isothermal leg (j) is proportional to $\sqrt{T^{(j)}}$. Nevertheless, since the matrix $\left\{\frac{1}{\vec{\pi}_i}\right\}$ varies along the path, the computation of the thermodynamic length is not trivial in general.

Equations (28) and (29) can be specialized to an isothermal path by replacing λ by κ, and explicitly computing

$$\frac{\partial \pi_k}{\partial \kappa} = -\frac{1}{k_B T}\pi_k\left[\frac{\partial E_k}{\partial \kappa} - \sum_j \frac{\partial E_j}{\partial \kappa}\pi_j\right] = -\frac{1}{k_B T}\pi_k\left[\frac{\partial E_k}{\partial \kappa} - \left(\frac{\partial \vec{E}}{\partial \kappa}\right)\cdot\vec{\pi}\right] \quad (35)$$

and

$$\begin{array}{l} \sum_{k=1}^{N_S}\frac{1}{(\pi(\lambda))_k}\left(\frac{(d\pi(\lambda))_k}{d\lambda}\right)^2 = \sum_{k=1}^{N_S}\frac{1}{\pi_k}\left(-\frac{1}{k_B T}\pi_k\left[\frac{\partial E_k}{\partial \kappa} - \left(\frac{\partial \vec{E}}{\partial \kappa}\right)\cdot\vec{\pi}\right]\right)^2 \\ = \frac{1}{(k_B T)^2}\sum_{k=1}^{N_S}\left(\pi_k\left[\frac{\partial E_k}{\partial \kappa} - \left(\frac{\partial \vec{E}_j}{\partial \kappa}\right)\cdot\vec{\pi}\right]^2\right) \\ = \frac{1}{(k_B T)^2}\left(\vec{\pi}\cdot\left(\frac{\partial \vec{E}}{\partial \kappa}\right)^2 - \left(\left(\frac{\partial \vec{E}}{\partial \kappa}\right)\cdot\vec{\pi}\right)^2\right) = \frac{1}{(k_B T)^2}Var_{\vec{\pi}}\left(\frac{\partial E}{\partial \kappa}\right). \end{array} \quad (36)$$

Plugging this into Equations (28) and (29), we obtain

$$L^{(j)}_{Q;iso-T} = \left|\frac{1}{\sqrt{k_B T}}\int_{\kappa^{[j]}}^{\kappa^{[j+1]}}\sqrt{Var_{\vec{\pi}}\left(\frac{\partial E}{\partial \kappa}\right)}d\kappa\right| \text{ and } L^{(j)}_{S;iso-T} = \left|\frac{1}{\sqrt{k_B T^2}}\int_{\kappa^{[j]}}^{\kappa^{[j+1]}}\sqrt{Var_{\vec{\pi}}\left(\frac{\partial E}{\partial \kappa}\right)}d\kappa\right|, \quad (37)$$

respectively. Note that the term under the square root is the variance of $\frac{\partial E}{\partial \kappa}$ with respect to the equilibrium probability distribution $\vec{\pi}(\kappa, T)$, $Var_{\vec{\pi}}\left(\frac{\partial E}{\partial \kappa}\right)$, as function of T and κ.

3.3. Finite-Time Optimal Control along Iso-κ Legs

Next, we turn to the case of changing temperature while keeping κ constant. Along those branches, only the temperature varies, but we cannot directly profit from the fact that κ is constant when computing the excess heat. Equations (21) and (22) yield $I_{Q;iso-\kappa} \approx \sum_{i=1}^{N_T}\left(\vec{\pi}_i - \vec{\pi}_{i-1}\right)\cdot\left\{\frac{k_B T_i}{\overleftrightarrow{\pi}_i}\right\}\left(\vec{\pi}_i - \vec{\pi}_{i-1}\right)$ and $I_{S;iso-\kappa} \approx \sum_{i=1}^{N_T}\left(\vec{\pi}_i - \vec{\pi}_{i-1}\right)\cdot\left\{\frac{k_B}{\overleftrightarrow{\pi}_i}\right\}\left(\vec{\pi}_i - \vec{\pi}_{i-1}\right)$, respectively, where N_T is the number of changes in the value of the temperature T along the branch, which are feasible during the finite time τ, assuming that each temperature change takes at least a time of $(\Delta t)_T$, i.e., $\tau = N_T(\Delta t)_T$.

Again, we see that finding the optimal solution of distributing N_T temperature changes over the path corresponds to minimizing $I_{Q/S}$, where the thermodynamic length of each piece i of the path is

$$\left(\Delta L_Q\right)_i = \left[\left(\vec{\pi}_i - \vec{\pi}_{i-1}\right)\left\{\frac{k_B T_i}{\overleftrightarrow{\pi}_i}\right\}\left(\vec{\pi}_i - \vec{\pi}_{i-1}\right)\right]^{1/2} \text{ or } \left(\Delta L_S\right)_i = \left[\left(\vec{\pi}_i - \vec{\pi}_{i-1}\right)\left\{\frac{k_B}{\overleftrightarrow{\pi}_i}\right\}\left(\vec{\pi}_i - \vec{\pi}_{i-1}\right)\right]^{1/2}, \quad (38)$$

respectively. To do so, we first minimize the thermodynamic length of the complete path, $\left(\Delta L_{Q/S}\right)_{total} = \sum_{i=1}^{N_T}\left(\Delta L_{Q/S}\right)_i$, and then pick the size of each step such that they all have the same thermodynamic length

$$\left(\Delta L_{Q/S}\right)_i = \frac{\left(\Delta L_{Q/S}\right)_{total}}{N_T}. \quad (39)$$

Equations (28) and (29) can be specialized to an iso-κ path by replacing λ by T, switching variables to $\beta = \frac{1}{k_B T}$ and explicitly computing

$$\frac{\partial \pi_k}{\partial T} = \frac{\partial \beta}{\partial T}\frac{\partial \pi_k}{\partial \beta} = -\frac{1}{k_B T^2}\left(-\pi_k\left[E_k - \sum\nolimits_j E_j \pi_j\right]\right) = \frac{1}{k_B T^2}\pi_k\left[E_k - \vec{E}\cdot\vec{\pi}\right] \quad (40)$$

and

$$\sum\nolimits_{k=1}^{N_S}\frac{1}{(\pi(\lambda))_k}\left(\frac{(d\pi(\lambda))_k}{d\lambda}\right)^2 = \frac{1}{\left(k_B T^2\right)^2}\left(\vec{\pi}\cdot\vec{(E)}^2 - \left(\vec{E}\cdot\vec{\pi}\right)^2\right) = \frac{1}{\left(k_B T^2\right)^2}Var_{\vec{\pi}}(E), \quad (41)$$

where $Var_{\vec{\pi}}(E)$ is the variance in energy $E(\kappa)$ with respect to the probability distribution $\vec{\pi}$. Plugging this into Equation (28), we obtain

$$\begin{aligned} L^{(j)}_{Q;iso-\kappa} &= \left|\int_{T^{[j]}}^{T^{[j+1]}}\frac{\sqrt{k_B T}}{\sqrt{k_B T^2}}\sqrt{\frac{Var_{\vec{\pi}}(E)}{k_B T^2}}dT\right| = \left|\int_{T^{[j]}}^{T^{[j+1]}}\sqrt{\frac{C(\kappa,T)}{T}}dT\right| \text{ or } L^{(j)}_{S;iso-\kappa} \\ &= \left|\int_{T^{[j]}}^{T^{[j+1]}}\sqrt{\frac{C(\kappa,T)}{T^2}}dT\right|, \end{aligned} \quad (42)$$

respectively, where $C(\kappa, T) = \frac{1}{k_B T^2}Var_{\vec{\pi}}(E)$ is the specific heat at T and κ. Note that these expressions are reminiscent of optimal control results for the minimal entropy/excess heat production for paths where we change the temperature of a thermodynamic system in finite time [36,42]. Furthermore, for iso-κ legs along which the specific heat is approximately constant, we find $L^{(j)}_{Q;iso-\kappa} \sim \left(\sqrt{T^{[j+1]}} - \sqrt{T^{[j]}}\right)$.

3.4. Finite-Time Optimal Control for Adiabatic Legs

3.4.1. General Adiabatic Paths

Clearly, minimizing the excess heat along a general isentropic adiabatic path is just another special case of the finite-time optimal control along general paths in (κ, T)-space. Thus, we find

for the excess heat the expression $I_{Q;iso-S} \approx \sum_{i=1}^{N_a} \left(\vec{\pi}_i - \vec{\pi}_{i-1}\right) \cdot \left\{ \frac{k_B T_i}{\overleftrightarrow{\pi}_i} \right\} \left(\vec{\pi}_i - \vec{\pi}_{i-1}\right)$ and for the entropy production $I_{S;iso-S} \approx \sum_{i=1}^{N_a} \left(\vec{\pi}_i - \vec{\pi}_{i-1}\right) \cdot \left\{ \frac{k_B}{\overleftrightarrow{\pi}_i} \right\} \left(\vec{\pi}_i - \vec{\pi}_{i-1}\right)$, where N_a is the number of changes in the values of $(\kappa, T(\kappa))$, or equivalently $(\kappa(T), T)$ along the branch, which are feasible during the finite time τ assuming that each change in (κ, T) requires at least a time of $(\Delta t)_a$, i.e., $\tau = N_a (\Delta t)_a$. We keep in mind that any change in κ automatically determines a corresponding change in T such that the thermodynamic equilibrium entropy after the move has not changed, or conversely, changing the temperature enforces an appropriate change in κ.

Again, $I_{Q/S}$ is minimized by picking the stopping points along the path such that the thermodynamic lengths

$$\left(\Delta L_Q\right)_i = \left[\left(\vec{\pi}_i - \vec{\pi}_{i-1}\right) \left\{ \frac{k_B T_i}{\overleftrightarrow{\pi}_i} \right\} \left(\vec{\pi}_i - \vec{\pi}_{i-1}\right) \right]^{1/2} \text{ or } \left(\Delta L_S\right)_i = \left[\left(\vec{\pi}_i - \vec{\pi}_{i-1}\right) \left\{ \frac{k_B}{\overleftrightarrow{\pi}_i} \right\} \left(\vec{\pi}_i - \vec{\pi}_{i-1}\right) \right]^{1/2}, \quad (43)$$

respectively, of all N_a pieces of the path are equal:

$$\left(\Delta L_{Q/S}\right)_i = \frac{\left(\Delta L_{Q/S}\right)_{total}}{N_a}. \quad (44)$$

However, for a general adiabatic path, no system independent simplification of Equations (28) and (29) is possible, since both κ and T change along such a path and their relationship $T(\kappa)$ varies from system to system.

3.4.2. Special Adiabatic Paths

As mentioned above, there are physical systems where not only the equilibrium entropy but also the equilibrium probability distribution of the occupancy of the microstates does not change along an adiabatic isentropic path. For such special adiabatic paths, adiabaticity is equivalent to a constant equilibrium probability distribution along the path, i.e., $\vec{\pi}_i$ = constant. On the other hand, our assumption that $\vec{p}_i$ is close to $\vec{\pi}_i$ implied that $\vec{p}_i$ can be approximated by $\vec{p}_i \approx \vec{\pi}_{i-1}$, and thus, to first order in $\left(\vec{\pi}(t) - \vec{p}(t)\right)$, we find for a special adiabatic path,

$$I_{Q;iso-S} = Q_{iso-S;\vec{\pi}} - Q_{iso-S;\vec{p}} = 0, \quad (45)$$

i.e., along such a leg there is no excess heat being produced due to finite time effects. We can see this also directly from the general expression for the thermodynamic length of the general adiabatic path:

$$\begin{aligned} \left(\Delta L_Q\right)_{total} &= \sum_{i=1}^{N_a} (\Delta L)_i = \sum_{i=1}^{N_a} \sqrt{\left(\vec{\pi}_i - \vec{\pi}_{i-1}\right) \cdot \left\{ \frac{k_B T_i}{\overleftrightarrow{\pi}_i} \right\} \left(\vec{\pi}_i - \vec{\pi}_{i-1}\right)} = \\ &\sum_{i=1}^{N_a} \sqrt{\left(\vec{\pi}_i - \vec{\pi}_i\right) \cdot \left\{ \frac{k_B T_i}{\overleftrightarrow{\pi}_i} \right\} \left(\vec{\pi}_i - \vec{\pi}_i\right)} = 0, \end{aligned} \quad (46)$$

since $\vec{\pi}_i = \vec{\pi}_{i-1}$ along a special adiabatic path, and analogously $(\Delta L_S)_{total} = 0$. Here, N_a is the number of steps along the special adiabatic path. As a consequence, the work performed by the system on the apparatus equals the negative of the energy difference between the two end points of leg (j), $W_{j \to j+1} = -(\Delta E)_{j \to j+1} = -\left(\langle E \rangle^{[j+1]} - \langle E \rangle^{[j]}\right)$, regardless of whether we were restricted to finite time or not, and thus no excess work or heat is present, at least to first order under the assumptions we have made. Even when including higher orders, the fact that $\vec{\pi}_i$ is constant along the whole path together with $\vec{p}_{i=0} = \vec{\pi}_{i=0}$ ensures that all higher order terms vanish because no relaxation of $\vec{p}_i$ to $\vec{\pi}_i$ is ever needed, thus also eliminating the issue of incomplete relaxation to equilibrium discussed in refs. [35,36].

The way finite-time considerations can enter the estimates along a special adiabatic branch must therefore involve deviations of the control itself from the true adiabatic path. Note that we did not consider such deviations from the target curve of the control parameters for the isothermal or the iso-κ branches. Since, in general, any motion of the system along these two types of branches already involves substantial changes in the equilibrium probability distribution, $\vec{\pi}_i \neq \vec{\pi}_{i-1}$, one usually assumes that the additional effects related to being "off-target" can be ignored in the analysis, although the issue of keeping the control parameters "on target" might be quite relevant in practical applications!

However, since $\vec{\pi}_i \equiv \vec{\pi}_{i-1}$ along the ideal special adiabatic path, deviations in the control parameters now become the primary source of entropy or excess heat production; other possible sources such as equilibrium fluctuations in the probability distribution $\vec{p}_i$ about $\vec{\pi}_i$ will not be considered here. As we have no knowledge about the way the control would be established in practice (i.e., in the experiment), we make the reasonable assumption that trying to stay as close as possible to the ideal adiabatic values of the control requires us again to maximize the number of change steps. This is analogous to how we proceeded earlier, where we assumed that the optimal solution of minimizing excess heat or entropy production for the general adiabatic, the isothermal, and the iso-κ branches would be found using the maximal number of steps feasible between the two endpoints of the leg: if the optimal solution requires fewer than the maximally possible number of steps, then we can just "throw away" the superfluous steps by assigning zero time to them and/or placing them at one of the endpoints of the branch.

The maximal-number-of-steps assumption implies that we cannot perform an optimal control on the sub-step level, i.e., the deviation associated with the movement from one point $i-1$ with values (κ_{i-1}, T_{i-1}) along the ideal adiabatic curve to the next point i with values (κ_i, T_i) can only involve one "virtual stopping point" away from the curve "halfway" between the two curve points. In general, there exist an infinite number of choices for such "halfway points", but from the basic modeling point of view, only two of them make sense, i.e., are consistent with our deviation analysis: (κ_i, T_{i-1}) "below" the adiabatic curve or (κ_{i-1}, T_i) "above" the adiabatic curve for paths moving from low to high temperatures; conversely, if we move from high to low temperatures, the (κ_i, T_{i-1}) points are "above" and the (κ_{i-1}, T_i) "below" the adiabatic curve (see Figure 4 below). If we could be closer to the curve than these points, then we would appear to have the ability to access temperatures and κ values in-between those of the two consecutive points along the adiabatic curve, suggesting that we have not yet maxed out the number of steps. Of course, this is only a plausibility argument and not a proof that such closer points would not be possible, but for this analysis we will employ the two virtual points given above since no further information about the actual functioning of the experimental apparatus is available. In fact, we can interpret our choice of virtual points as providing a heuristic upper bound on the entropy/excess heat production along the special adiabatic path; we essentially assume that we are able to be perfectly on target in either κ or T, and the excess production is due to the adjustment in the lagging parameter T or κ, respectively. In the following discussion, we only employ the metric $\overleftrightarrow{M}_Q$; completely analogous results are obtained when using the metric $\overleftrightarrow{M}_S$.

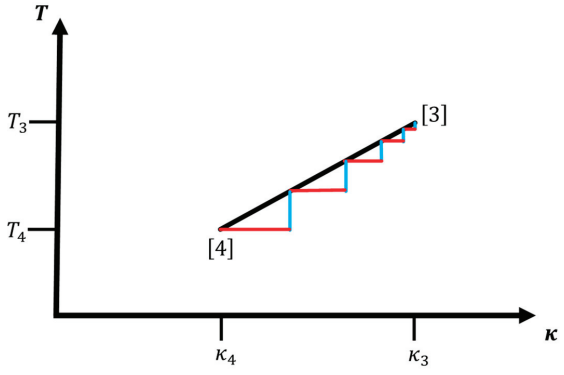

Figure 4. Sketch of an optimal setting of step points along a (special) adiabatic leg moving from corner [3] to corner [4], where the excess heat associated with being "off-target" with respect to the ideal adiabatic path is minimized. Note that the density of step points (κ_i, T_i) along the leg increases with temperature, approximately in a square-root fashion. Red lines are the isothermal and blue lines the iso-κ sub-pieces, respectively, which connect two points (κ_{i-1}, T_{i-1}) and (κ_i, T_i) along the perfect adiabatic path via the virtual intermediary off-target points (κ_{i-1}, T_i).

We note that reaching the point i via either of the virtual points requires an isothermal step and an iso-κ step. Since no sub-optimization along these steps is possible, we can directly write down the excess heat associated with each half-step and sum them. For the virtual point (κ_i, T_{i-1}), we have for the thermodynamic length to go from $i-1$ to i:

$$\begin{aligned}\left(\Delta L_Q\right)_i &= \sqrt{\begin{array}{c}\left(\vec{\pi}\left(\kappa_i, T_{i-1}\right) - \vec{\pi}_{i-1}\right)\cdot\left\{\frac{k_B T_{i-1}}{\overleftrightarrow{\pi}(\kappa_i, T_{i-1})}\right\}\left(\vec{\pi}\left(\kappa_i, T_{i-1}\right) - \vec{\pi}_{i-1}\right)+ \\ \left(\vec{\pi}_i - \vec{\pi}(\kappa_i, T_{i-1})\right)\cdot\left\{\frac{k_B T_i}{\overleftrightarrow{\pi}_i}\right\}\left(\vec{\pi}_i - \vec{\pi}(\kappa_i, T_{i-1})\right)\end{array}} \\ &= \sqrt{\begin{array}{c}\left(\vec{\pi}\left(\kappa_i, T_{i-1}\right) - \vec{\pi}_i\right)\cdot\left\{\frac{k_B T_{i-1}}{\overleftrightarrow{\pi}(\kappa_i, T_{i-1})}\right\}\left(\vec{\pi}\left(\kappa_i, T_{i-1}\right) - \vec{\pi}_i\right)+ \\ \left(\vec{\pi}_i - \vec{\pi}(\kappa_i, T_{i-1})\right)\cdot\left\{\frac{k_B T_i}{\overleftrightarrow{\pi}_i}\right\}\left(\vec{\pi}_i - \vec{\pi}(\kappa_i, T_{i-1})\right)\end{array}} \\ &= \sqrt{\left(\vec{\pi}_i - \vec{\pi}(\kappa_i, T_{i-1})\right)\cdot\left[\left\{\frac{k_B T_i}{\overleftrightarrow{\pi}_i}\right\} + \left\{\frac{k_B T_{i-1}}{\overleftrightarrow{\pi}(\kappa_i, T_{i-1})}\right\}\right]\left(\vec{\pi}_i - \vec{\pi}(\kappa_i, T_{i-1})\right)},\end{aligned} \tag{47}$$

where $\vec{\pi}_{i-1} = \vec{\pi}\left(\kappa_{i-1}, T_{i-1}\right)$ and $\vec{\pi}_i = \vec{\pi}\left(\kappa_i, T_i\right)$ are the two consecutive points on the adiabatic curve, and we have used the fact that $\vec{\pi}_i = \vec{\pi}_{i-1}$.

Similarly, for the virtual point (κ_{i-1}, T_i), we have

$$\left(\Delta L_Q\right)_i = \sqrt{\left(\vec{\pi}_i - \vec{\pi}(\kappa_{i-1}, T_i)\right)\cdot\left[\left\{\frac{k_B T_i}{\overleftrightarrow{\pi}_i}\right\} + \left\{\frac{k_B T_i}{\overleftrightarrow{\pi}(\kappa_{i-1}, T_i)}\right\}\right]\left(\vec{\pi}_i - \vec{\pi}(\kappa_{i-1}, T_i)\right)}. \tag{48}$$

Since it is not clear which of the two virtual points would be more suitable, one might suggest that a decent approximation for $\left(\Delta L_Q\right)_i$ would be the average of the two thermodynamic lengths for the two points:

$$\begin{aligned}\left(\Delta L_Q\right)_i \cong \tfrac{1}{2}\Bigg(&\sqrt{\left(\vec{\pi}_i - \vec{\pi}(\kappa_i, T_{i-1})\right)\cdot\left[\left\{\frac{k_B T_i}{\overleftrightarrow{\pi}_i}\right\} + \left\{\frac{k_B T_{i-1}}{\overleftrightarrow{\pi}(\kappa_i, T_{i-1})}\right\}\right]\left(\vec{\pi}_i - \vec{\pi}(\kappa_i, T_{i-1})\right)} \\ &+ \sqrt{\left(\vec{\pi}_i - \vec{\pi}(\kappa_{i-1}, T_i)\right)\cdot\left[\left\{\frac{k_B T_i}{\overleftrightarrow{\pi}_i}\right\} + \left\{\frac{k_B T_i}{\overleftrightarrow{\pi}(\kappa_{i-1}, T_i)}\right\}\right]\left(\vec{\pi}_i - \vec{\pi}(\kappa_{i-1}, T_i)\right)}\Bigg).\end{aligned} \tag{49}$$

However, from the point of view of optimal control, this average is not very helpful; in particular, the thermodynamic metric becomes a very complicated expression.

Instead it is more effective to systematically pick one of the two virtual points, e.g., (κ_i, T_{i-1}), because this allows us to write the excess heat production due to deviations in the control from the special adiabatic path as

$$I_{Q;iso-S} \;=\; \sum_{i\,=\,1}^{N_a}\left(\vec{\pi}_i - \vec{\pi}(\kappa_i, T_{i-1})\right)\cdot\left[\left\{\frac{k_B T_i}{\overleftrightarrow{\pi}_i}\right\} + \left\{\frac{k_B T_{i-1}}{\overleftrightarrow{\pi}(\kappa_i, T_{i-1})}\right\}\right]\left(\vec{\pi}_i - \vec{\pi}(\kappa_i, T_{i-1})\right) \;=\; \sum_{i\,=\,1}^{N_a}\left[\left(\Delta L_Q\right)_i\right]^2, \tag{50}$$

where each $\left(\Delta L_Q\right)_i$ is the thermodynamic distance between the points $i-1$ and i computed with the metric $\left[\left\{\frac{k_B T_i}{\overleftrightarrow{\pi}_i}\right\} + \left\{\frac{k_B T_{i-1}}{\overleftrightarrow{\pi}(\kappa_i, T_{i-1})}\right\}\right]$, with the virtual intermediary point fixed as (κ_i, T_{i-1}).

We note that the probability distribution $\vec{\pi}(\kappa_i, T_{i-1})$ at the virtual point, which enters the expression for $\left(\Delta L_Q\right)_i$, is completely determined from our information about the temperatures and κ-values of the two consecutive points along the ideal special adiabatic path which are "connected" via the virtual point. Thus, there is no internal degree of freedom left for the piece of path between the points $i-1$ and i, which could be adjusted as part of the optimal control analysis. As a consequence, the choice of the locations of the consecutive points along the special adiabatic path completely determines $\left(\Delta L_Q\right)_i$, although in a slightly more involved fashion than for the isothermal and the iso-κ legs. This allows us to conclude that choosing the step points (κ_i, T_i) such that the lengths of all the $\left(\Delta L_Q\right)_i$ have the same value, again yields the optimal solution for minimizing the excess heat.

While the general formula for the metric and thus the thermodynamic length of the path is more complicated than for the isothermal or iso-κ legs, we note that the metric is still essentially proportional to $k_B T_i$ at step i. Furthermore, due to the leg being special adiabatic, the term $\left[\left\{\frac{k_B T_i}{\overleftrightarrow{\pi}_i}\right\} + \left\{\frac{k_B T_{i-1}}{\overleftrightarrow{\pi}(\kappa_i, T_{i-1})}\right\}\right]$ does only weakly vary as function of the probability distribution $\vec{\pi}_i$ since the distribution is constant on the path, and should only differ slightly from $\vec{\pi}_i$ along the virtual points. Thus, we can conclude that the thermodynamic length of the virtual-point pieces between two points along the special adiabatic path mostly depends on the temperature, with

$$\left(\Delta L_Q\right)_i \;\sim\; \sqrt{T_i}. \tag{51}$$

As a consequence, the optimal distribution of points will be related to the square root of the temperature in the sense that the distance of step points along the leg (as function of temperature) will monotonically decrease as $1/\sqrt{T_i}$, leading to a higher density of step points at higher temperatures (c.f. Figure 4).

4. Application to the Hydrogen Atom-Like System

Regarding the hydrogen atom-like system, we first note that κ and T enter the formulas for the equilibrium probability distribution everywhere in the combination

$$A \;=\; \frac{\kappa}{T}, \tag{52}$$

such that

$$\pi_k(\kappa, T) \;=\; \pi_k\left(\frac{\kappa}{T}\right) \;=\; e^{-\left(\frac{\kappa}{T}\right)\frac{E_k(1)}{k_B}} \Big/ \sum_{j\,=\,1}^{N_S} e^{-\left(\frac{\kappa}{T}\right)\frac{E_j(1)}{k_B}} \;=\; e^{-A\frac{E_k(1)}{k_B}} \Big/ \sum_{j\,=\,1}^{N_S} e^{-A\frac{E_j(1)}{k_B}}. \tag{53}$$

In particular, this means that the ratio $\frac{\kappa}{T}$ remains constant along the adiabatic legs of the cycle, ensuring that $\vec{\pi}$ does not change along this branch. Thus, the adiabatic branches for cycles involving the hydrogen atom-like system belong into the special category where not only the entropy but the whole equilibrium probability distribution is constant along the path. Note that in the cycle diagram

(Figures 2 and 3), an adiabatic branch (j) for the hydrogen atom-like system is always a straight line (that can be continued through the origin) with slope $\frac{1}{A^{(j)}}$. Of course, the actual value of the ratio A will be different for each adiabatic leg. For an adiabatic leg (j), it follows that $\kappa^{[j+1]}T^{[j]} = \kappa^{[j]}T^{[j+1]}$. For the combination of iso-κ and adiabatic legs, we have $\kappa^{[1]} = \kappa^{[2]} = \kappa_{in}$ and $\kappa^{[3]} = \kappa^{[4]} = \kappa_f$; therefore, we get

$$\frac{\kappa_{in}}{\kappa_f} = \frac{T^{[1]}}{T^{[4]}} = \frac{T^{[2]}}{T^{[3]}}. \tag{54}$$

Analogously, for the combination of adiabatic and isothermal legs, we have the two adiabatic branches (legs 1 and 3) with $A_{1\to 2} \neq A_{3\to 4}$, for which $\kappa^{[1]}T^{[2]} = \kappa^{[2]}T^{[1]}$ and $\kappa^{[4]}T^{[3]} = \kappa^{[3]}T^{[4]}$, and the isothermal legs yield the conditions $T^{[3]} = T^{[2]}$ and $T^{[1]} = T^{[4]}$. Thus, we have the relations

$$\frac{T^{[1]}}{T^{[2]}} = \frac{\kappa^{[1]}}{\kappa^{[2]}} = \frac{\kappa^{[4]}}{\kappa^{[3]}} = \frac{\kappa_{in}}{\kappa^{[2]}} = \frac{\kappa^{[4]}}{\kappa_f}. \tag{55}$$

Regarding the expressions for the thermodynamic lengths of the various legs in this section, we remark that the main effect of dealing with the hydrogen atom-like system is the special adiabaticity of the isentropic paths, such that the contribution of the adiabatic paths to the excess heat or entropy production can be set equal to zero unless we include the "off-target" contributions discussed in Section 3.4.2. In addition, we can exploit Equation (3) to rewrite the specific heat as

$$C(\kappa,T) = \frac{\vec{\pi}\cdot(\vec{E})^2 - \left(\vec{E}\cdot\vec{\pi}\right)^2}{k_B T^2} = \kappa^2 \frac{\vec{\pi}\cdot(\vec{E(1)})^2 - \left(\vec{E(1)}\cdot\vec{\pi}\right)^2}{k_B T^2} = \kappa^2 C^{\kappa}(\kappa,T) = \frac{\kappa^2}{k_B T^2} Var_{\vec{\pi}}(E(1)) = \frac{A^2}{k_B} Var_{\vec{\pi}}(E(1)), \tag{56}$$

where both the variance $Var_{\vec{\pi}}(E(1)) = \vec{\pi}\cdot(\vec{E(1)})^2 - \left(\vec{E(1)}\cdot\vec{\pi}\right)^2 = \frac{1}{\kappa^2} Var_{\vec{\pi}}(E)$ and the specific heat $C(\kappa,T)$ are functions of $A = \left(\frac{\kappa}{T}\right)$. Furthermore, we can rewrite Equation (35) as

$$\frac{\partial \pi_k}{\partial \kappa} = -\frac{1}{k_B T}\pi_k\left[E_k(1) - \sum\nolimits_j E_j(1)\pi_j\right] = -\frac{1}{k_B T}\pi_k\left[E_k(1) - \vec{E(1)}\cdot\vec{\pi}\right], \tag{57}$$

where π_k is a function of $\left(\frac{\kappa}{T}\right)$, and thus Equation (36) becomes

$$\frac{1}{(k_B T)^2}\left(\vec{\pi}\cdot\vec{E(1)}^2 - \left(\vec{E(1)}\cdot\vec{\pi}\right)^2\right) = \frac{1}{k_B} C^{\kappa}(\kappa,T) = \frac{1}{\kappa^2 k_B} C(\kappa,T) = \frac{Var_{\vec{\pi}}(E(1))}{(k_B T)^2}. \tag{58}$$

Note that the variance of $\frac{\partial E}{\partial \kappa}$ in Equation (36) is now transformed into a variance of the energy $E(1)$ of the unmodified hydrogen atom.

For each cycle discussed below, we first write down a formula for the total work done by the atom and the heat absorbed by the atom in the quasi-static approximation, where $\vec{p}_i = \vec{\pi}_i$ everywhere along the cycle, and subsequently, we provide formulas for the efficiency, and the optimality criterion for the minimal excess heat production.

4.1. Iso-κ-Adiabatic Cycle

In the case of the iso-κ-adiabatic cycle where the legs 2 and 4 are adiabatic and do not contribute to the heat production, we can focus on legs 1 and 3 when computing the heat exchange with the

environment. Using Equations (18) and (19), we obtain therefore for the total heat exchange over the full cycle:

$$\begin{array}{l} Q_{cycle} \;=\; \int_{S^{[1]}}^{S^{[2]}} TdS + \int_{S^{[3]}}^{S^{[4]}} TdS \;=\; \left[T^{[2]}S^{[2]} - T^{[1]}S^{[1]}\right] + k_B \int_{T^{[1]}}^{T^{[2]}} \vec{\pi}(T,\kappa_{in})\cdot ln\Big(\vec{\pi}(T,\kappa_{in})\Big)dT + \\ \left[T^{[4]}S^{[4]} - T^{[3]}S^{[3]}\right] + k_B \int_{T^{[3]}}^{T^{[4]}} \vec{\pi}\Big(T,\kappa_f\Big)\cdot ln\Big(\vec{\pi}\Big(T,\kappa_f\Big)\Big)dT \;=\; \vec{E}(\kappa_{in})\cdot\Big(\vec{\pi}\Big(\kappa_{in}T^{[2]}\Big) - \vec{\pi}\Big(\kappa_{in}T^{[1]}\Big)\Big) \\ +\vec{E}\Big(\kappa_f\Big)\cdot\Big(\vec{\pi}\Big(\kappa_f T^{[4]}\Big) - \vec{\pi}\Big(\kappa_{in}T^{[3]}\Big)\Big) \;=\; W_{cycle}. \end{array} \tag{59}$$

Since $T^{[2]} > T^{[1]}$, $T^{[4]} < T^{[3]}$, and furthermore, the equilibrium entropy at higher temperatures is always larger than the one at lower temperatures, the term belonging to leg 1 transfers heat into the system, while along leg 3, the system gives off heat.

Since the legs 2 and 4 represent adiabatic processes, we have, furthermore, $S^{[2]} = S^{[3]}$ and $S^{[1]} = S^{[4]}$, and also $T^{[3]} = \frac{\kappa_f}{\kappa_{in}}T^{[2]}$ and $T^{[4]} = \frac{\kappa_f}{\kappa_{in}}T^{[1]}$. Using Equation (18) and shifting variables back and forth from T to T/κ_{in} and T/κ_f, this implies that

$$\begin{array}{l} Q_{cycle} \;=\; \int_{S^{[1]},leg1}^{S^{[2]}} TdS + \int_{S^{[3]},leg3}^{S^{[4]}} TdS \;=\; \Big(1 - \frac{\kappa_f}{\kappa_{in}}\Big)\Big[T^{[2]}S^{[2]} - T^{[1]}S^{[1]}\Big] + k_B\kappa_{in}\int_{T^{[1]}/\kappa_{in}}^{T^{[2]}/\kappa_{in}} \vec{\pi}(y)\cdot ln\Big(\vec{\pi}(y)\Big)dy \\ +k_B\kappa_f\int_{T^{[3]}/\kappa_f}^{T^{[4]}/\kappa_f} \vec{\pi}(y)\cdot ln\Big(\vec{\pi}(y)\Big)dy \;=\; \Big(1 - \frac{\kappa_f}{\kappa_{in}}\Big)\Big[T^{[2]}S^{[2]} - T^{[1]}S^{[1]}\Big] - \Big(\kappa_{in} - \kappa_f\Big)\frac{1}{\kappa_{in}}\int_{T^{[1]}}^{T^{[2]}} S(T)dT \;= \\ \Big(1 - \frac{\kappa_f}{\kappa_{in}}\Big)\int_{S^{[1]},leg1}^{S^{[2]}} TdS < 0, \end{array} \tag{60}$$

since $\kappa_f > \kappa_{in}$. This shows that the hydrogen atom-like system gives off heat to the environment, when the cycle is run as described.

Of course, this equals the total work around the cycle, which needs to balance the total heat by energy conservation. If we want to compute the expressions for the work along each of the four legs—e.g., in order to talk about the efficiency of the hydrogen atom-like system as working fluid in an engine, we need to add the contribution for the energy change. We then find: $W_{1\to 2} = W_{3\to 4} = 0, W_{2\to 3} = -\vec{E}\Big(\kappa_f\Big)\cdot\vec{\pi}\Big(\kappa_f, T^{[3]}\Big) + \vec{E}(\kappa_{in})\cdot\vec{\pi}\Big(\kappa_{in}, T^{[2]}\Big) = \Big(\vec{E}(\kappa_{in}) - \vec{E}\Big(\kappa_f\Big)\Big)\cdot\vec{\pi}(A_{2\to 3})$, and $W_{4\to 1} = -\vec{E}(\kappa_{in})\cdot\vec{\pi}\Big(\kappa_{in}, T^{[1]}\Big) + \vec{E}\Big(\kappa_f\Big)\cdot\vec{\pi}\Big(\kappa_f, T^{[4]}\Big) = \Big(\vec{E}\Big(\kappa_f\Big) - \vec{E}(\kappa_{in})\Big)\cdot\vec{\pi}(A_{4\to 1})$. This shows that we reduce the internal energy of the hydrogen atom-like system by a certain amount along leg 2 and raise it along leg 4 but by a much larger amount. Taking the sum, we obtain

$$\begin{array}{c} W_{4\to 1} + W_{2\to 3} \;=\; \Big(\vec{E}\Big(\kappa_f\Big) - \vec{E}(\kappa_{in})\Big)\cdot\vec{\pi}(A_{4\to 1}) + \Big(\vec{E}(\kappa_{in}) - \vec{E}\Big(\kappa_f\Big)\Big)\cdot\vec{\pi}(A_{2\to 3}) \;= \\ \Big(\vec{E}\Big(\kappa_f\Big) - \vec{E}(\kappa_{in})\Big)\cdot\Big(\vec{\pi}(A_{4\to 1}) - \vec{\pi}(A_{2\to 3})\Big) = \\ \Big(\kappa_f - \kappa_{in}\Big)\vec{E}(\kappa \;=\; 1)\cdot\Big(\vec{\pi}(A_{4\to 1}) - \vec{\pi}(A_{2\to 3})\Big) < 0, \end{array} \tag{61}$$

since $\kappa_f > \kappa_{in}$ and $\vec{E}(\kappa \;=\; 1)\cdot\vec{\pi}(A_{4\to 1}) < \vec{E}(\kappa \;=\; 1)\cdot\vec{\pi}(A_{2\to 3}) < 0$ because $A_{4\to 1} = \frac{\kappa_{in}}{T^{[1]}} > A_{2\to 3} = \frac{\kappa_{in}}{T^{[2]}}$. Thus, during this cycle, the apparatus performs net work on the system over the legs 2 and 4.

For the efficiency, a possible definition is to take the ratio between the net work along the legs where κ is varied, and total heat added to/extracted from the system. With this definition, we find

$$\eta_{\{\kappa;S\}} \;=\; \frac{W_{4\to 1} + W_{2\to 3}}{Q_{cycle}} \;=\; \frac{W_{cycle}}{Q_{cycle}} \;=\; 1. \tag{62}$$

Of course, one can define many other efficiencies, depending on the quantities and processes of interest.

Regarding the excess heat, we note that due to Equation (52), the adiabatic legs are special. We do not include the effect of being "off-target" during the adiabatic legs, and thus we only consider the two terms from the iso-κ legs 1 and 3:

$$\begin{aligned} I_{Q;total} &= I_{Q;1\to 2} + I_{Q;3\to 4} = \left\{\sum_{i=1}^{N_T}\left(\vec{\pi}_i - \vec{\pi}_{i-1}\right)\cdot\left\{\frac{k_B T_i}{\overleftrightarrow{\pi_i}}\right\}\left(\vec{\pi}_i - \vec{\pi}_{i-1}\right)\right\}_{leg1} + \\ &\left\{\sum_{i=1}^{N_T}\left(\vec{\pi}_i - \vec{\pi}_{i-1}\right)\cdot\left\{\frac{k_B T_i}{\overleftrightarrow{\pi_i}}\right\}\left(\vec{\pi}_i - \vec{\pi}_{i-1}\right)\right\}_{leg3}. \end{aligned} \tag{63}$$

Using Equations (42) and (56), we get for the whole cycle

$$\begin{aligned} L_{Q;cycle} &= L_Q^{(1)} + L_Q^{(3)} = \left|\kappa_{in}\int_{T^{[1]}}^{T^{[2]}}\sqrt{\frac{C^{\kappa}\left(\frac{\kappa}{T}\right)}{T}}dT\right| + \left|\kappa_f\int_{T^{[3]}}^{T^{[4]}}\sqrt{\frac{C^{\kappa}\left(\frac{\kappa}{T}\right)}{T}}dT\right| \\ &= \left|\kappa_{in}\int_{T^{[1]}}^{T^{[2]}}\sqrt{\frac{Var_{\vec{\pi}}(E(1))}{k_B T^3}}dT\right| + \left|\kappa_f\int_{T^{[3]}}^{T^{[4]}}\sqrt{\frac{Var_{\vec{\pi}}(E(1))}{k_B T^3}}dT\right|. \end{aligned} \tag{64}$$

Switching variables to $A = \frac{\kappa}{T}$ for the integration, keeping in mind that $Var_{\vec{\pi}}(E(1))$ is a function of $A = \frac{\kappa}{T}$, and using $A^{[2]} = A^{[3]}$ and $A^{[4]} = A^{[1]}$ since legs (4) and (2) are adiabatic, we find

$$L_Q^{(1)} = \left|\sqrt{\kappa_{in}}\int_{A^{[1]}}^{A^{[2]}}\sqrt{\frac{Var_{\vec{\pi}}(E(1))}{\sqrt{k_B A}}}dA\right| < L_Q^{(3)} = \left|\sqrt{\kappa_f}\int_{A^{[1]}}^{A^{[2]}}\sqrt{\frac{Var_{\vec{\pi}}(E(1))}{\sqrt{k_B A}}}dA\right|, \tag{65}$$

since $\kappa_f > \kappa_{in}$.

In the case of the adiabatic legs considered here, we do have the problem that, to first order, the thermodynamic length vanishes as long as we are perfectly on target with the thermodynamic controls. Thus, the formula for $\tau^{(j)}$ yields zero time for the adiabatic legs of the path, which essentially means we could jump directly from the end of the first leg (= beginning of the second leg) to the beginning of the third leg (= end of the second leg), and analogously for the fourth branch. In practice, this does not make too much sense, and we would want to employ the off-target formula derived above, even though this requires additional information from experiment, or make assumptions about the location of the virtual intermediary points discussed above. Alternatively, we can make heuristic assumptions about the (hopefully short, i.e., $\tau_a \ll \tau$) minimal time $\tau_a = \tau_Q^{(2)} = \tau_Q^{(4)}$ needed to move along the adiabatic leg without noticeable deviations from the ideal adiabatic curve in (κ, T) space and subtract these times from the total available time τ, $\tau_{iso-\kappa} = \tau - 2\tau_a$, before assigning $\tau_Q^{(1)}$ and $\tau_Q^{(3)}$ according the principle of constant thermodynamic speed.

Since $\frac{L_Q^{(3)}}{L_Q^{(1)}} = \frac{\sqrt{\kappa_f}}{\sqrt{\kappa_{in}}}$, the optimal time allocation for the two legs must be

$$\frac{\tau_Q^{(3)}}{\tau_Q^{(1)}} = \frac{L_Q^{(3)}}{L_Q^{(1)}} = \frac{\sqrt{\kappa_f}}{\sqrt{\kappa_{in}}}, \tag{66}$$

and thus we obtain $\tau_Q^{(1)} = \tau_{iso-\kappa}\frac{\sqrt{\kappa_{in}}}{\sqrt{\kappa_f}+\sqrt{\kappa_{in}}}$ and $\tau_Q^{(3)} = \tau_{iso-\kappa}\frac{\sqrt{\kappa_f}}{\sqrt{\kappa_f}+\sqrt{\kappa_{in}}}$. We remark that when we minimize the entropy production and thus use the metric $\overleftrightarrow{M}_S$, we find $L_S^{(3)} = L_S^{(1)}$ and, after subtracting $\tau_a = \tau_S^{(2)} = \tau_S^{(4)}$ from τ, we obtain $\tau_S^{(1)} = \tau_S^{(3)} = \frac{\tau_{iso-\kappa}}{2}$.

Due to the sum over microstates for the heat capacity with nontrivial energy eigenvalues under the square root and the nontrivial temperature dependence of $\vec{\pi}(T,\kappa)$, no further analytical simplifications appear to be possible. Thus, the allocation along the individual legs is an open question, but should depend on the variance $Var_{\vec{\pi}}(E(1))$ as function of $\left(\frac{\kappa}{T}\right)$.

4.2. Iso-κ-Isothermal Cycle

For the iso-κ-isothermal cycle ($T^{[3]} = T^{[2]}$ and $T^{[4]} = T^{[1]}$), we have a non-vanishing heat term along all legs, where the integrals over temperature along the isothermal branches vanish, of course,

$$k_B \int_{T^{[2]}}^{T^{[3]}} \vec{\pi}(\kappa,T)\cdot ln\Big(\vec{\pi}(\kappa,T)\Big)dT \;=\; k_B \int_{T^{[4]}}^{T^{[1]}} \vec{\pi}(\kappa,T)\cdot ln\Big(\vec{\pi}(\kappa,T)\Big)dT \;=\; 0. \tag{67}$$

Using the fact that along the iso-κ branches $Q^{(j)} = (\Delta E)^{(j)}$, we get for the total heat produced on the cycle,

$$\begin{array}{c} Q_{cycle} \;=\; \vec{E}(\kappa_{in})\cdot\Big[\vec{\pi}\Big(\kappa_{in},T^{[2]}\Big)-\vec{\pi}\Big(\kappa_{in},T^{[1]}\Big)\Big]+\Big[T^{[2]}S^{[3]}\Big(\kappa_f,T^{[2]}\Big)-T^{[2]}S^{[2]}\Big(\kappa_{in},T^{[2]}\Big)\Big]+ \\ \vec{E}\Big(\kappa_f\Big)\cdot\Big[\vec{\pi}\Big(\kappa_f,T^{[1]}\Big)-\vec{\pi}\Big(\kappa_f,T^{[2]}\Big)\Big]+\Big[T^{[1]}S^{[1]}\Big(\kappa_{in},T^{[1]}\Big)-T^{[1]}S^{[4]}\Big(\kappa_f,T^{[1]}\Big)\Big]. \end{array} \tag{68}$$

For the work along the legs, we find $W_{1\to2} = W_{3\to4} = 0$, $W_{2\to3} = \Big[T^{[2]}S^{[3]}\Big(\kappa_f,T^{[2]}\Big)-T^{[2]}S^{[2]}\Big(\kappa_{in},T^{[2]}\Big)\Big] - \vec{E}\Big(\kappa_f\Big)\cdot\vec{\pi}\Big(\kappa_f,T^{[2]}\Big) + \vec{E}(\kappa_{in})\cdot\vec{\pi}\Big(\kappa_{in},T^{[2]}\Big)$ and $W_{4\to1} = \Big[T^{[1]}S^{[1]}\Big(\kappa_{in},T^{[1]}\Big)-T^{[1]}S^{[4]}\Big(\kappa_f,T^{[1]}\Big)\Big] - \vec{E}(\kappa_{in})\cdot\vec{\pi}\Big(\kappa_{in},T^{[1]}\Big) + \vec{E}\Big(\kappa_f\Big)\cdot\vec{\pi}\Big(\kappa_f,T^{[1]}\Big)$. The possible net extracted work from the isothermal legs 2 and 4 is now:

$$\begin{array}{c} W_{4\to1}+W_{2\to3} \;=\; \Big[T^{[2]}S^{[3]}\Big(\kappa_f,T^{[2]}\Big)-T^{[2]}S^{[2]}\Big(\kappa_{in},T^{[2]}\Big)+T^{[1]}S^{[1]}\Big(\kappa_{in},T^{[1]}\Big)-T^{[1]}S^{[4]}\Big(\kappa_f,T^{[1]}\Big)\Big] \\ +\vec{E}(1)\cdot\Big\{\kappa_f\Big[\vec{\pi}\Big(\kappa_f,T^{[1]}\Big)-\vec{\pi}\Big(\kappa_f,T^{[2]}\Big)\Big]-\kappa_{in}\Big[\vec{\pi}\Big(\kappa_{in},T^{[1]}\Big)-\vec{\pi}\Big(\kappa_{in},T^{[2]}\Big)\Big]\Big\}. \end{array} \tag{69}$$

Now, $\frac{\kappa_f}{T^{[2]}} > \frac{\kappa_{in}}{T^{[2]}}$ and similarly $\frac{\kappa_f}{T^{[1]}} > \frac{\kappa_{in}}{T^{[1]}}$, and thus the probability distribution $\vec{\pi}\Big(\kappa_f,T^{[2]}\Big)$ is more concentrated at low energies than $\vec{\pi}\Big(\kappa_{in},T^{[2]}\Big)$, leading to the conclusion that $S\Big(\kappa_f,T^{[2]}\Big) < S\Big(\kappa_{in},T^{[2]}\Big)$, and analogously $S\Big(\kappa_f,T^{[1]}\Big) < S\Big(\kappa_{in},T^{[1]}\Big)$. Similarly, $\vec{E}(1)\cdot\vec{\pi}\Big(\kappa_f,T^{[1]}\Big) < \vec{E}(1)\cdot\vec{\pi}\Big(\kappa_f,T^{[2]}\Big)$ and $\vec{E}(1)\cdot\vec{\pi}\Big(\kappa_{in},T^{[1]}\Big) < \vec{E}(1)\cdot\vec{\pi}\Big(\kappa_{in},T^{[2]}\Big)$. Since $\kappa_f > \kappa_{in}$, the energy contribution to the work along these legs should be negative, resulting in an overall negative work, i.e., the environment performs net work on the hydrogen atom-like system.

Again, we compute the efficiency as

$$\eta_{\{\kappa;T\}} \;=\; \frac{W^{(2)}+W^{(4)}}{Q_{cycle}} \;=\; \frac{W_{cycle}}{Q_{cycle}} \;=\; 1. \tag{70}$$

Regarding the excess heat production, all four legs contribute in this case. Thus, we have

$$\begin{array}{l} I_{Q;total} \;=\; I_{Q;1\to2}+I_{Q;2\to3}+I_{Q;3\to4}+I_{Q;4\to1} \;=\; \Big\{\sum_{i=1}^{N_T}\Big(\vec{\pi}_i-\vec{\pi}_{i-1}\Big)\cdot\Big\{\frac{k_BT_i}{\overleftrightarrow{\pi}_i}\Big\}\Big(\vec{\pi}_i-\vec{\pi}_{i-1}\Big)\Big\}_{leg1}+ \\ k_BT_2\Big\{\sum_{i=1}^{N_\kappa}\Big(\vec{\pi}_i-\vec{\pi}_{i-1}\Big)\cdot\Big\{\frac{1}{\overleftrightarrow{\pi}_i}\Big\}\Big(\vec{\pi}_i-\vec{\pi}_{i-1}\Big)\Big\}_{leg2}+\Big\{\sum_{i=1}^{N_T}\Big(\vec{\pi}_i-\vec{\pi}_{i-1}\Big)\cdot\Big\{\frac{k_BT_i}{\overleftrightarrow{\pi}_i}\Big\}\Big(\vec{\pi}_i-\vec{\pi}_{i-1}\Big)\Big\}_{leg3}+ \\ k_BT_1\Big\{\sum_{i=1}^{N_\kappa}\Big(\vec{\pi}_i-\vec{\pi}_{i-1}\Big)\cdot\Big\{\frac{1}{\overleftrightarrow{\pi}_i}\Big\}\Big(\vec{\pi}_i-\vec{\pi}_{i-1}\Big)\Big\}_{leg4}. \end{array} \tag{71}$$

Note that N_T and N_K of the individual legs will be determined from the ratios $\frac{\tau^{(j)}}{(\Delta t)_{T,\kappa}}$, where we again will assume that the relaxation times are constant. Employing Equations (37), (42) and (56)–(58), the total thermodynamic length of the cycle is then

$$\begin{aligned} L_{Q;cycle} &= L_Q^{(1)} + L_Q^{(2)} + L_Q^{(3)} + L_Q^{(4)} = \left|\kappa_{in}\int_{T^{[1]}}^{T^{[2]}}\sqrt{\frac{C^\kappa\left(\frac{\kappa_{in}}{T}\right)}{T}}dT\right| + \left|\sqrt{T^{[2]}}\int_{\kappa_{in}}^{\kappa_f}\sqrt{C^\kappa\left(\frac{\kappa}{T^{[2]}}\right)}d\kappa\right| + \\ &\left|\kappa_f\int_{T^{[2]}}^{T^{[1]}}\sqrt{\frac{C^\kappa\left(\frac{\kappa_f}{T}\right)}{T}}dT\right| + \left|\sqrt{T^{[1]}}\int_{\kappa_f}^{\kappa_{in}}\sqrt{C^\kappa\left(\frac{\kappa}{T^{[1]}}\right)}d\kappa\right| = \left|\kappa_{in}\int_{T^{[1]}}^{T^{[2]}}\sqrt{\frac{Var_{\overrightarrow{\pi}}(E(1))}{k_BT^3}}dT\right| + \\ &\left|\sqrt{T^{[2]}}\int_{\kappa_{in}}^{\kappa_f}\sqrt{\frac{Var_{\overrightarrow{\pi}}(E(1))}{k_BT^2}}d\kappa\right| + \left|\kappa_f\int_{T^{[1]}}^{T^{[2]}}\sqrt{\frac{Var_{\overrightarrow{\pi}}(E(1))}{k_BT^3}}dT\right| + \left|\sqrt{T^{[1]}}\int_{\kappa_{in}}^{\kappa_f}\sqrt{\frac{Var_{\overrightarrow{\pi}}(E(1))}{k_BT^2}}d\kappa\right|. \end{aligned} \tag{72}$$

Keeping in mind that $Var_{\overrightarrow{\pi}}(E(1))$ depends only on A, we switch variables in all integrals from T and κ to $A = \frac{\kappa}{T}$, to obtain

$$\begin{aligned} L_Q^{(1)} + L_Q^{(2)} + L_Q^{(3)} + L_Q^{(4)} &= \left|\sqrt{\kappa_{in}}\int_{A^{[1]}}^{A^{[2]}}\sqrt{\frac{Var_{\overrightarrow{\pi}}(E(1))}{k_BA}}dA\right| + \left|\sqrt{T^{[2]}}\int_{A^{[2]}}^{A^{[3]}}\sqrt{\frac{Var_{\overrightarrow{\pi}}(E(1))}{k_B}}dA\right| + \\ &\left|\sqrt{\kappa_f}\int_{A^{[3]}}^{A^{[4]}}\sqrt{\frac{Var_{\overrightarrow{\pi}}(E(1))}{k_BA}}dA\right| + \left|\sqrt{T^{[1]}}\int_{A^{[4]}}^{A^{[1]}}\sqrt{\frac{Var_{\overrightarrow{\pi}}(E(1))}{k_B}}dA\right|. \end{aligned} \tag{73}$$

Note that since all legs contribute already to first order to the total thermodynamic length, the times spent in each leg in the optimal case are proportional to the thermodynamic lengths of each leg, $\tau_Q^{(j)} = \frac{L_Q^{(j)}}{L_{cycle}}\tau$. Since the values of A at the corners are all different, no simple general estimate of assigning times to the various legs appears possible. However, for the special case of (approximately) constant variance $Var_{\overrightarrow{\pi}}(E(1))$, we find $L_Q^{(1)} = \kappa_{in}\left(\frac{1}{\sqrt{T_1}} - \frac{1}{\sqrt{T_2}}\right)\sqrt{\frac{Var_{\overrightarrow{\pi}}(E(1))}{k_B}}$, $L_Q^{(2)} = \left(\frac{\kappa_f}{\sqrt{T_2}} - \frac{\kappa_{in}}{\sqrt{T_2}}\right)\sqrt{\frac{Var_{\overrightarrow{\pi}}(E(1))}{k_B}}$, $L^{(3)} = \kappa_f\left(\frac{1}{\sqrt{T_1}} - \frac{1}{\sqrt{T_2}}\right)\sqrt{\frac{Var_{\overrightarrow{\pi}}(E(1))}{k_B}}$ and $L_Q^{(4)} = \left(\frac{\kappa_f}{\sqrt{T_1}} - \frac{\kappa_{in}}{\sqrt{T_1}}\right)\sqrt{\frac{Var_{\overrightarrow{\pi}}(E(1))}{k_B}}$. From this follows

$$L_{Q;cycle} = 2\sqrt{\frac{Var_{\overrightarrow{\pi}}(E(1))}{k_B}}\left(\frac{\kappa_f}{\sqrt{T_1}} - \frac{\kappa_{in}}{\sqrt{T_2}}\right) = 2\sqrt{\frac{Var_{\overrightarrow{\pi}}(E(1))}{k_B}}\frac{\left(\sqrt{T_2}\kappa_f - \sqrt{T_1}\kappa_{in}\right)}{\sqrt{T_1T_2}}, \tag{74}$$

and thus the optimal times for the four legs we obtain $\tau_Q^{(1)} = \frac{\tau}{2}\left[\frac{\sqrt{T_2}\kappa_{in} - \sqrt{T_1}\kappa_{in}}{\sqrt{T_2}\kappa_f - \sqrt{T_1}\kappa_{in}}\right]$, $\tau_Q^{(2)} = \frac{\tau}{2}\left[\frac{\sqrt{T_1}\kappa_f - \sqrt{T_1}\kappa_{in}}{\sqrt{T_2}\kappa_f - \sqrt{T_1}\kappa_{in}}\right]$, $\tau_Q^{(3)} = \frac{\tau}{2}\left[\frac{\sqrt{T_2}\kappa_f - \sqrt{T_1}\kappa_f}{\sqrt{T_2}\kappa_f - \sqrt{T_1}\kappa_{in}}\right]$ and $\tau_Q^{(4)} = \frac{\tau}{2}\left[\frac{\sqrt{T_2}\kappa_f - \sqrt{T_2}\kappa_{in}}{\sqrt{T_2}\kappa_f - \sqrt{T_1}\kappa_{in}}\right]$. Analogous results are obtained using the metric $\overleftrightarrow{M}_S$ for the case of minimum entropy production. In particular, if we again assume an approximately constant variance $Var_{\overrightarrow{\pi}}(E(1))$, we obtain $L_S^{(1)} = \left(\frac{\kappa_{in}}{T_1} - \frac{\kappa_{in}}{T_2}\right)\sqrt{\frac{Var_{\overrightarrow{\pi}}(E(1))}{k_B}}$, $L_Q^{(2)} = \left(\frac{\kappa_f}{T_2} - \frac{\kappa_{in}}{T_2}\right)\sqrt{\frac{Var_{\overrightarrow{\pi}}(E(1))}{k_B}}$, $L^{(3)} = \left(\frac{\kappa_f}{T_1} - \frac{\kappa_f}{T_2}\right)\sqrt{\frac{Var_{\overrightarrow{\pi}}(E(1))}{k_B}}$ and $L_Q^{(4)} = \left(\frac{\kappa_f}{T_1} - \frac{\kappa_{in}}{T_1}\right)\sqrt{\frac{Var_{\overrightarrow{\pi}}(E(1))}{k_B}}$. From this follows for the total thermodynamic length of the path $L_{S;cycle} = 2\sqrt{\frac{Var_{\overrightarrow{\pi}}(E(1))}{k_B}}\frac{\left(T_2\kappa_f - T_1\kappa_{in}\right)}{T_1T_2}$, yielding the optimal time assignments to the legs as $\tau_S^{(1)} = \frac{\tau}{2}\left[\frac{T_2\kappa_{in} - T_1\kappa_{in}}{T_2\kappa_f - T_1\kappa_{in}}\right]$, $\tau_S^{(2)} = \frac{\tau}{2}\left[\frac{T_1\kappa_f - T_1\kappa_{in}}{T_2\kappa_f - T_1\kappa_{in}}\right]$, $\tau_S^{(3)} = \frac{\tau}{2}\left[\frac{T_2\kappa_f - T_1\kappa_f}{T_2\kappa_f - T_1\kappa_{in}}\right]$ and $\tau_S^{(4)} = \frac{\tau}{2}\left[\frac{T_2\kappa_f - T_2\kappa_{in}}{T_2\kappa_f - T_1\kappa_{in}}\right]$.

4.3. Isothermal-Adiabatic Cycle

In the case of the isothermal-adiabatic cycle where the legs 1 and 3 are adiabatic and do not contribute to the heat exchange, we have from legs 2 and 4:

$$\begin{array}{c} Q_{cycle} = \int_{S^{[2]}}^{S^{[3]}} TdS + \int_{S^{[4]}}^{S^{[1]}} TdS = \left[T^{[3]}S^{[3]} - T^{[2]}S^{[2]}\right] + k_B \int_{T^{[2]}}^{T^{[3]}} \vec{\pi}(T,\kappa_{in})\cdot ln\left(\vec{\pi}(T,\kappa_{in})\right)dT + \\ \left[T^{[1]}S^{[1]} - T^{[4]}S^{[4]}\right] + k_B \int_{T^{[4]}}^{T^{[1]}} \vec{\pi}\left(T,\kappa_f\right)\cdot ln\left(\vec{\pi}\left(T,\kappa_f\right)\right)dT = T^{[2]}\left[S^{[3]} - S^{[1]}\right] + T^{[1]}\left[S^{[1]} - S^{[3]}\right] = \\ \left(T^{[2]} - T^{[1]}\right)\left[S^{[3]} - S^{[1]}\right] = W_{cycle}. \end{array} \quad (75)$$

Here, we have used the fact that the temperature does not change along legs 2 and 4, $T^{[2]} = T^{[3]}$ and $T^{[1]} = T^{[4]}$, and that the entropy does not change along the adiabatic legs, i.e., $S^{[1]} = S^{[2]}$ and $S^{[3]} = S^{[4]}$.

Since $T^{[2]} > T^{[1]}$, and furthermore, for equal temperatures, the equilibrium entropy decreases with κ, i.e., $S^{[3]} < S^{[2]} = S^{[1]}$, we have a rejection of heat over the cycle, i.e., the hydrogen atom-like system converts work performed on it into heat transferred to the environment. Furthermore, the term belonging to leg 2 absorbs heat in the system, while along leg 3, we are removing heat from the system.

For the work performed by the system along the four legs, we find $W_{1\to 2} = -\left(\vec{E}(\kappa_2)\cdot\vec{\pi}\left(\kappa_2,T^{[2]}\right) - \vec{E}(\kappa_{in})\vec{\pi}\left(\kappa_{in},T^{[1]}\right)\right)$, $W_{2\to 3} = T^{[2]}\left[S^{[3]}\left(\kappa_f,T^{[2]}\right) - S^{[2]}\left(\kappa_2,T^{[2]}\right)\right] - \left[\vec{E}\left(\kappa_f\right)\cdot\vec{\pi}\left(\kappa_f,T^{[2]}\right) - \vec{E}\left(\kappa_2\right)\cdot\vec{\pi}\left(\kappa_2,T^{[2]}\right)\right]$, $W_{3\to 4} = -\left(\vec{E}(\kappa_4)\cdot\vec{\pi}\left(\kappa_4,T^{[1]}\right) - \vec{E}\left(\kappa_f\right)\vec{\pi}\left(\kappa_f,T^{[2]}\right)\right)$, and $W_{4\to 1} = T^{[1]}\left[S^{[1]}\left(\kappa_{in},T^{[1]}\right) - S^{[4]}\left(\kappa_4,T^{[1]}\right)\right] - \left[\vec{E}(\kappa_{in})\cdot\vec{\pi}\left(\kappa_{in},T^{[1]}\right) - \vec{E}(\kappa_4)\cdot\vec{\pi}\left(\kappa_4,T^{[1]}\right)\right]$. Taking the sum along the two isothermal legs, we obtain

$$\begin{array}{l} W_{4\to 1} + W_{2\to 3} = T^{[1]}\left[S^{[1]}\left(\kappa_{in},T^{[1]}\right) - S^{[4]}\left(\kappa_4,T^{[1]}\right)\right] - \left[\vec{E}(\kappa_{in})\cdot\vec{\pi}\left(\kappa_{in},T^{[1]}\right) - \vec{E}(\kappa_4)\cdot\vec{\pi}\left(\kappa_4,T^{[1]}\right)\right] \\ + T^{[2]}\left[S^{[3]}\left(\kappa_f,T^{[2]}\right) - S^{[2]}\left(\kappa_2,T^{[2]}\right)\right] - \left[\vec{E}\left(\kappa_f\right)\cdot\vec{\pi}\left(\kappa_f,T^{[2]}\right) - \vec{E}\left(\kappa_2\right)\cdot\vec{\pi}\left(\kappa_2,T^{[2]}\right)\right] \\ = \left[T^{[2]} - T^{[1]}\right]\left[S^{[3]} - S^{[1]}\right] - \left(1 - \frac{T_1}{T_2}\right)\kappa_f\vec{E}(\kappa = 1)\cdot\left\{\vec{\pi}(A_{3\to 4}) - \frac{\kappa_{in}}{\kappa_f}\left(\frac{T_2}{T_1}\right)\vec{\pi}(A_{1\to 2})\right\}, \end{array} \quad (76)$$

where we have used $S^{[1]} = S^{[2]}$, $S^{[3]} = S^{[4]}$, $A_{1\to 2} = \frac{\kappa_{in}}{T^{[1]}} = \frac{\kappa_2}{T^{[2]}}$, and $A_{3\to 4} = \frac{\kappa_f}{T^{[2]}} = \frac{\kappa_4}{T^{[1]}}$. We note that $\vec{E}(1)\cdot\vec{\pi}(A_{3\to 4}) < \vec{E}(1)\cdot\vec{\pi}(A_{1\to 2}) < 0$ and thus

$$-\kappa_f\left(1 - \frac{T_1}{T_2}\right)\vec{E}(\kappa = 1)\cdot\left\{\vec{\pi}(A_{3\to 4}) - \frac{\kappa_{in}}{\kappa_f}\left(\frac{T_2}{T_1}\right)\vec{\pi}(A_{1\to 2})\right\} > 0 \quad (77)$$

as long as $\frac{\kappa_{in}}{\kappa_f}\left(\frac{T_2}{T_1}\right) < 1$; note that this is exactly the feasibility condition for the special adiabatic-isothermal cycle, Equation (5). Furthermore, $S^{[3]} < S^{[1]}$ and thus $\left[T^{[2]} - T^{[1]}\right]\left[S^{[3]} - S^{[1]}\right] < 0$, suggesting that the net work for these two legs is likely to be negative, i.e., the apparatus does work on the atom and increases its internal energy in the process.

For the "efficiency", we again compute the ratio between the net work along the isothermal legs and the total heat exchanged

$$\eta_{\{S;T\}}^{isothermal} = \frac{W_{4\to 1} + W_{2\to 3}}{Q_{cycle}} = 1 - \frac{-\kappa_f\left(1 - \frac{T_1}{T_2}\right)\vec{E}(\kappa = 1)\cdot\left\{\vec{\pi}(A_{3\to 4}) - \frac{\kappa_{in}}{\kappa_f}\left(\frac{T_2}{T_1}\right)\vec{\pi}(A_{1\to 2})\right\}}{\left(T^{[2]} - T^{[1]}\right)\left[S^{[1]} - S^{[3]}\right]} < 1. \quad (78)$$

Alternatively, we could use the two adiabatic legs to extract/perform work, i.e.,

$$\begin{array}{rl} W_{1\to 2}+W_{3\to 4} &= -\Big(\vec{E}(\kappa_4)\cdot\vec{\pi}\big(\kappa_4,T^{[1]}\big)-\vec{E}\big(\kappa_f\big)\vec{\pi}\big(\kappa_f,T^{[2]}\big)\Big) \\ & \quad -\Big(\vec{E}(\kappa_2)\cdot\vec{\pi}\big(\kappa_2,T^{[2]}\big)-\vec{E}(\kappa_{in})\vec{\pi}\big(\kappa_{in},T^{[1]}\big)\Big) \\ &= \big(1-\frac{T_1}{T_2}\big)\kappa_f\vec{E}(\kappa\ =\ 1)\cdot\Big\{\vec{\pi}(A_{3\to 4})-\frac{\kappa_{in}}{\kappa_f}\big(\frac{T_2}{T_1}\big)\vec{\pi}(A_{1\to 2})\Big\}; \end{array} \tag{79}$$

in that case, we get for the efficiency

$$\eta^{adiabatic}_{\{S;T\}} \ = \ \frac{W_{1\to 2}+W_{3\to 4}}{Q_{cycle}} \ = \ \frac{\big(1-\frac{T_1}{T_2}\big)\kappa_f\vec{E}(\kappa\ =\ 1)\cdot\Big\{\vec{\pi}(A_{3\to 4})-\frac{\kappa_{in}}{\kappa_f}\big(\frac{T_2}{T_1}\big)\vec{\pi}(A_{1\to 2})\Big\}}{\big(T^{[2]}-T^{[1]}\big)\big[S^{[3]}-S^{[1]}\big]}. \tag{80}$$

Clearly, $\eta^{isothermal}_{\{ad;T\}}+\eta^{adiabatic}_{\{ad;T\}} \ = \ 1$, since $W_{cycle} \ = \ Q_{cycle}$.

Regarding minimizing the excess heat, we do not include the effect of being "off-target" during the adiabatic legs, and thus we only have the two terms from the isothermal legs 2 and 4:

$$\begin{array}{rl} I_{Q;total} &= \ I_{Q;2\to 3}+I_{Q;4\to 1} \ = \ \Big\{\sum_{i\ =\ 1}^{N_T}\big(\vec{\pi}_i-\vec{\pi}_{i-1}\big)\cdot\Big\{\frac{k_BT_i}{\overleftrightarrow{\pi}_i}\Big\}\big(\vec{\pi}_i-\vec{\pi}_{i-1}\big)\Big\}_{leg2}+ \\ & \quad \Big\{\sum_{i\ =\ 1}^{N_T}\big(\vec{\pi}_i-\vec{\pi}_{i-1}\big)\cdot\Big\{\frac{k_BT_i}{\overleftrightarrow{\pi}_i}\Big\}\big(\vec{\pi}_i-\vec{\pi}_{i-1}\big)\Big\}_{leg4}. \end{array} \tag{81}$$

We can use Equations (37) and (58) to write an expression for the thermodynamic length of the cycle:

$$\begin{array}{rl} L_{Q;cycle} &= \ L^{(2)}_Q+L^{(4)}_Q \ = \ \Big|\sqrt{T^{[2]}}\int_{\kappa^{[2]}}^{\kappa_f}\frac{1}{\kappa}\sqrt{C\big(\frac{\kappa}{T^{[2]}}\big)}d\kappa\Big|+\Big|\sqrt{T^{[1]}}\int_{\kappa^{[4]}}^{\kappa_{in}}\frac{1}{\kappa}\sqrt{C\big(\frac{\kappa}{T^{[1]}}\big)}d\kappa\Big| = \\ & \quad \Big|\sqrt{T^{[2]}}\int_{\kappa^{[2]}}^{\kappa_f}\sqrt{\frac{Var_{\vec{\pi}}(E(1))}{k_BT^2}}d\kappa\Big|+\Big|\sqrt{T^{[1]}}\int_{\kappa^{[4]}}^{\kappa_{in}}\sqrt{\frac{Var_{\vec{\pi}}(E(1))}{k_BT^2}}d\kappa\Big|. \end{array} \tag{82}$$

We note that for the hydrogen atom-like system, the integrand in the thermodynamic length integrals of the isothermal legs is the square root of the heat capacity, just as in the case of the iso-κ legs. We again switch to integration over $A \ = \ \frac{\kappa}{T}$, and find for the thermodynamic lengths

$$L^{(2)}_Q \ = \ \Big|\sqrt{T^{[2]}}\int_{A^{[2]}}^{A^{[3]}}\sqrt{\frac{Var_{\vec{\pi}}(E(1))}{k_B}}dA\Big| > L^{(4)}_Q \ = \ \Big|\sqrt{T^{[1]}}\int_{A^{[4]}}^{A^{[1]}}\sqrt{\frac{Var_{\vec{\pi}}(E(1))}{k_B}}dA\Big|, \tag{83}$$

since $\sqrt{T^{[2]}} > \sqrt{T^{[1]}}$, $A^{[2]} \ = \ A^{[1]}$, and $A^{[4]} \ = \ A^{[3]}$ along the special adiabatic legs, and $Var_{\vec{\pi}}(E(1))$ depends only on A.

As far as distributing the available time over the four legs, we again have to face the problem of the adiabatic legs being of zero thermodynamic length as long as we can keep the controls on target along these legs. We assume a short (i.e., $\tau_a \ll \tau$) time $\tau_a \ = \ \tau^{(1)}_Q \ = \ \tau^{(3)}_Q$ needed to move along the adiabatic leg without noticeable deviations from the ideal adiabatic curve in (κ, T) space and subtract these times from the total available time τ, $\tau_{iso-T} \ = \ \tau-2\tau_a$, before assigning $\tau^{(2)}_Q$ and $\tau^{(4)}_Q$ according the principle of constant thermodynamic speed. Assuming constant relaxation times, we determine the optimal times using the ratio of the thermodynamic lengths,

$$\frac{\tau^{(2)}_Q}{\tau^{(4)}_Q} \ = \ \frac{L^{(2)}_Q}{L^{(4)}_Q} \ = \ \frac{\sqrt{T^{[2]}}}{\sqrt{T^{[1]}}}, \tag{84}$$

to be $\tau_Q^{(2)} = \tau_{iso-T}\frac{\sqrt{T^{[2]}}}{\sqrt{T^{[2]}}+\sqrt{T^{[1]}}}$ and $\tau_Q^{(4)} = \tau_{iso-T}\frac{\sqrt{T^{[1]}}}{\sqrt{T^{[2]}}+\sqrt{T^{[1]}}}$. Analogously, when minimizing the entropy production instead of the excess heat, we obtain $L_S^{(2)} = L_S^{(4)}$, and thus with $\tau_a = \tau_S^{(1)} = \tau_S^{(3)}$, the optimal time assignment to the two legs is $\tau_S^{(2)} = \tau_S^{(4)} = \frac{\tau_{iso-T}}{2}$.

Again, due to the sum over microstates with nontrivial energy eigenvalues under the square root, further analytical calculations require additional simplifications; in particular, the optimal placement of the steps along each of the isothermal paths remains open but is expected to vary according to the specific heat.

5. Approximation of the Hydrogen Atom-Like System as a Two-Level System

5.1. Preliminaries

In many cases of statistical mechanical systems, one can find analytical solutions for a problem, if we can restrict ourselves to a two-state model; perhaps the most straightforward example for our purposes is the spin 1/2 system [27,28]. This is also the case here, since we can employ the probability π_1 of one of the two states as the integration variable, $\pi = \pi_1$. Probability conservation then determines the occupation probability of the second state as $\pi_2 = 1-\pi_1 = 1-\pi$, thus eliminating the complicated sum over the microstates. This was demonstrated in [35], where the thermodynamic length was computed for a paramagnet in a magnetic field for an isothermal path along which the energy of the paramagnet was changed by varying the magnetic field in finite time. In this fashion, one could compute the thermodynamic length and subsequently assign the steps by the equal thermodynamic length criterion, thus solving the optimal control problem.

However, the situation is more complex in the case of the cycle of the hydrogen atom-like system, because along the iso-κ legs the temperature varies, adding a nontrivial function $T(\pi)$ to the integrand for the case of minimizing the excess heat. On the other hand, the approximation of any statistical mechanical system by a two-state system actually leads to many generic properties associated with the thermodynamic cycles of the two-state system, i.e., many of the results obtained below do not depend on the specific property in Equation (3), $\widetilde{E}_n(\kappa) = \kappa\widetilde{E}_n(1)$, of the hydrogen atom-like system.

If we take two energy levels, n_1 and n_2 with $n_1 < n_2$ and thus $E_{n_1}(\kappa) = \widetilde{E}_{n_1}(\kappa) = \kappa\widetilde{E}_{n_1}(1) < E_{n_2}(\kappa) = \widetilde{E}_{n_2}(\kappa) = \kappa\widetilde{E}_{n_2}(1)$, with degeneracies $g(n_1) = (n_1)^2$ and $g(n_2) = (n_2)^2$, respectively—recall: we ignore the spin degeneracy of the electron in this study—, then we obtain the following expressions, for given (κ, T): For the probabilities, we have

$$\widetilde{\pi}(n_1) = g(n_1)\rho(n_1) = \pi = \frac{g(n_1)exp\left(\frac{-\widetilde{E}_{n_1}(\kappa)}{k_BT}\right)}{g(n_1)exp\left(\frac{-\widetilde{E}_{n_1}(\kappa)}{k_BT}\right)+g(n_2)exp\left(\frac{-\widetilde{E}_{n_2}(\kappa)}{k_BT}\right)} \tag{85}$$

and

$$\widetilde{\pi}(n_2) = g(n_2)\rho(n_2) = 1-\pi = \frac{g(n_2)exp\left(\frac{-\widetilde{E}_{n_2}(\kappa)}{k_BT}\right)}{g(n_1)exp\left(\frac{-\widetilde{E}_{n_1}(\kappa)}{k_BT}\right)+g(n_2)exp\left(\frac{-\widetilde{E}_{n_2}(\kappa)}{k_BT}\right)}. \tag{86}$$

For the equilibrium entropy, we have the expression

$$\begin{array}{c} S(\pi) = -k_B\left[\pi ln\left(\frac{\pi}{g(n_1)}\right)+(1-\pi)ln\left(\frac{1-\pi}{g(n_2)}\right)\right] = \\ -k_B[\pi(ln(\pi)-ln(g(n_1)))+(1-\pi)(ln(1-\pi)-ln(g(n_2)))] = \\ k_Bln(Z(\kappa,T))-\pi(\kappa,T)\frac{Bk_B}{T}; \end{array} \tag{87}$$

and for the temperature,

$$T(\pi) \;=\; \frac{B}{ln\Big[\Big(\frac{g(n_2)}{g(n_1)}\Big)\Big(\frac{\pi}{1-\pi}\Big)\Big]}. \tag{88}$$

Here, $B \;=\; -\Big(\widetilde{E}_{n_1}(\kappa) - \widetilde{E}_{n_2}(\kappa)\Big)/k_B > 0$, for a generic two-state system; specifically for the hydrogen atom-like system, we have $B \;=\; \kappa B_0/k_B$ with $B_0 \;=\; -\Big(\widetilde{E}_{n_1}(1) - \widetilde{E}_{n_2}(1)\Big) \;=\; \alpha\Big(\frac{1}{(n_1)^2} - \frac{1}{(n_2)^2}\Big) > 0$. Note that $\Big(\frac{g(n_2)}{g(n_1)}\Big)\Big(\frac{\pi}{1-\pi}\Big) \geq 1$, with equality only possible in the infinite temperature limit when $\pi \;=\; \frac{g(n_1)}{g(n_1)+g(n_2)}$.

With this, we get for the expectation value of the energy

$$\langle E\rangle(\kappa, T) \;=\; \widetilde{E}_{n_2}(\kappa) + \pi(\kappa, T)\Big(\widetilde{E}_{n_1}(\kappa) - \widetilde{E}_{n_2}(\kappa)\Big) \;=\; \kappa\Big[\widetilde{E}_{n_2}(1) - \pi\Big(\frac{\kappa}{T}\Big)B_0\Big], \tag{89}$$

where the second equality holds for the hydrogen atom-like system. For the derivative of the entropy with respect to π, we find

$$\tfrac{dS}{d\pi} \;=\; -k_B[ln(\pi) - ln(g(n_1)) - ln(1-\pi) + ln(g(n_2)) + 1 - 1] \;=\; -k_B ln\Big(\Big(\tfrac{g(n_2)}{g(n_1)}\Big)\Big(\tfrac{\pi}{1-\pi}\Big)\Big) \;=\; -k_B\tfrac{B}{T} < 0 \tag{90}$$

for all temperatures. From this follows that for all valid values of π, $\frac{g(n_1)}{g(n_1)+g(n_2)} \leq \pi \leq 1$, we have a one-to-one correspondence between the entropy S and the occupation probability of the low energy state π. As a consequence, every adiabatic path for any two-state system is automatically special adiabatic, because S = constant along the path implies π = constant, too.

5.2. Thermodynamic Cycles

With the formulas derived above, we can compute some of the expressions given in the previous section for the work and heat transfer along the legs of the cycles explicitly, such as, e.g.,

$$Q^{(j)} \;=\; \int_{S^{[j]}}^{S^{[j+1]}} TdS \;=\; \int_{\pi_{in}}^{\pi_f} T(\pi)\frac{dS}{d\pi}d\pi \;=\; \int_{\pi_{in}}^{\pi_f} T(\pi)\Big(-\frac{B(\pi)k_B}{T(\pi)}\Big)d\pi \;=\; -B_0\int_{\pi_{in}}^{\pi_f}\kappa(\pi)d\pi, \tag{91}$$

where the last equality only holds for the hydrogen atom-like system. Here, $\pi_{in} \;=\; \pi^{[j]}$ and $\pi_f \;=\; \pi^{[j+1]}$ are the values of π at the beginning and at the end of the leg (j). If we are considering an iso-κ branch, then we have $\kappa(\pi) \;=\; \kappa^{(j)}$ = constant, and thus $B(\pi) \;=\; B^{(j)}$ = constant, from which follows $Q^{(j)} \;=\; -k_B B^{(j)}\big(\pi_f - \pi_{in}\big)$. Furthermore, if in addition the temperature increases along the leg, then $\pi(T)$ will decrease, $\langle E\rangle\big(\kappa^{(j)}, T\big)$ will increase, and thus $Q^{(j)} > 0$. We note that along such a branch, we also have $(\Delta E)^{(j)} \;=\; \langle E\rangle\big(\kappa^{(j)}, T^{[j+1]}\big) - \langle E\rangle\big(\kappa^{(j)}, T^{[j]}\big) \;=\; -k_B B^{(j)}\big(\pi_f - \pi_{in}\big)$, and thus for any two-state system, we have $Q^{(j)} \;=\; (\Delta E)^{(j)}$ and $W^{(j)} \;=\; 0$ along the iso-κ branches. This is a special case of the earlier general result, Equation (19).

For the adiabatic path (j), we recall that these paths are special for any two-state system, i.e., π = constant, and thus the heat term yields $Q^{(j)} \;=\; -\int_{\pi_{in}}^{\pi_f} k_B B(\pi)d\pi \;=\; 0$ since $\pi_f \;=\; \pi_{in}$. Finally, for an isothermal leg, we have

$$\begin{aligned} Q^{(j)} \;&=\; -k_B T^{(j)}\Big[\Big(\pi_f ln\Big(\tfrac{\pi_f}{g(n_1)}\Big) + \big(1-\pi_f\big)ln\Big(\tfrac{1-\pi_f}{g(n_2)}\Big)\Big) - \Big(\pi_{in} ln\Big(\tfrac{\pi_{in}}{g(n_1)}\Big) + (1-\pi_{in})ln\Big(\tfrac{1-\pi_{in}}{g(n_2)}\Big)\Big)\Big] \\ &= k_B T^{(j)} ln\Big[\tfrac{Z\left(\kappa^{[j+1]}/T^{(j)}\right)}{Z\left(\kappa^{[j]}/T^{(j)}\right)}\Big] + B_0\Big[\pi_{in}\kappa^{[j]} - \pi_f\kappa^{[j+1]}\Big], \end{aligned} \tag{92}$$

where the last equality holds for the hydrogen atom-like system.

In the following, we are not going to re-compute for the two-state hydrogen atom-like system all the general work and heat-related expressions derived in Section 4. We only note that for the cycles with iso-κ legs, we find again that $\eta_{\{\kappa;T\}} \;=\; 1$ and $\eta_{\{\kappa;S\}} \;=\; 1$, which are the same results as

we had obtained for the complete hydrogen atom-like system, Equations (62) and (70). Thus, for the two-state system, the net work performed by the "atom" along the isothermal or adiabatic legs equals the net heat added to the system over the whole cycle because $Q^{(j)} = (\Delta E)^{(j)}$ along the iso-κ legs. Finally, for the adiabatic-isothermal path, we find $\eta^{adiabatic}_{\{S;T\}} = \{1+Y\}^{-1}$ and $\eta^{isothermal}_{\{S;T\}} = \left\{1+\frac{1}{Y}\right\}^{-1}$, where $Y = \frac{k_B(T_1-T_2)ln\left[\frac{Z(\kappa_{in}/T_1)}{Z(\kappa_f/T_2)}\right]}{\kappa_f\left(1-\frac{T_1}{T_2}\right)\left\{\widetilde{E}_{n_2}(1)\left[1-\left(\frac{\kappa_{in}/T_1}{\kappa_f/T_2}\right)\right]-B_0\left[\pi(\kappa_f/T_2)-\left(\frac{\kappa_{in}/T_1}{\kappa_f/T_2}\right)\pi(\kappa_{in}/T_1)\right]\right\}}$.

Instead, we will focus on the optimal control problem of minimizing the excess heat production instead. Applying the general formulas in Equations (23) and (24), we observe that the expression for the square length of an infinitesimal distance in probability space yields in terms of π:

$$\left(dL_Q\right)^2 = k_BT(\pi)\begin{pmatrix} d\pi & -d\pi \end{pmatrix}\begin{Bmatrix} \left(\frac{g(n_1)}{\pi}\right)\frac{g(n_1)}{(g(n_1))^2} & 0 \\ 0 & \left(\frac{g(n_2)}{1-\pi}\right)\frac{g(n_2)}{(g(n_2))^2} \end{Bmatrix}\begin{pmatrix} d\pi \\ -d\pi \end{pmatrix} = k_BT(\pi)\left[(d\pi)^2\right]\left(\tfrac{1}{\pi}+\tfrac{1}{1-\pi}\right). \quad (93)$$

The metric for the energy levels is a compactified (2×2) version of the true $(g(n_1)+g(n_2))\times(g(n_1)+g(n_2))$ microstate metric $\left\{\frac{1}{\pi}\right\}_{kl} = \delta_{kl}\frac{1}{r_1} = \delta_{kl}\frac{g(n_1)}{\pi}$ for $k = 1,\ldots,g(n_1)$ and $\left\{\frac{1}{\pi}\right\}_{kl} = \delta_{kl}\frac{1}{r_2} = \delta_{kl}\frac{g(n_2)}{1-\pi}$ for $k = g(n_1)+1,\ldots,g(n_1)+g(n_2)$. Similarly, $\begin{pmatrix} d\pi \\ -d\pi \end{pmatrix}$ is a compactified version of the $(g(n_1)+g(n_2))$-dimensional microstate probability difference vector $(d\rho_1,\ldots,d\rho_1,-d\rho_2,\ldots,-d\rho_2) = \left(\frac{d\pi}{g(n_1)},\ldots,\frac{d\pi}{g(n_1)},\frac{-d\pi}{g(n_2)},\ldots,\frac{-d\pi}{g(n_2)}\right)$. As mentioned earlier, we assume that the microstates with the same energy exhibit the same occupation probability, and that we do not have "mixing" among the states for the same energy, i.e., all $g(n_1)$ states with energy "gain" the same amount of probability $d\rho_1 = \frac{d\pi}{g(n_1)}$, and similarly, all states with energy "lose" the same amount of probability.

Taking this into account, we find for the infinitesimal element of thermodynamic length:

$$dL_Q = \sqrt{k_BT(\pi)}\sqrt{\frac{1}{\pi}+\frac{1}{1-\pi}}|d\pi| = \pm\sqrt{\frac{k_BT(\pi)}{\pi(1-\pi)}}d\pi, \quad (94)$$

where the $(+)$-sign is employed if π increases along the path ($d\pi > 0$) and the $(-)$-sign is employed if π decreases along the path ($d\pi < 0$). We note that Equations (93) and (94) apply to any two-state system and are not restricted to hydrogen atom-like systems. As mentioned above, the adiabatic pieces of the cycle are special for a two-state system, and thus there is no excess heat production to first order since π is constant along these legs, and thus $|d\pi| = 0$; alternatively, we can note that the initial and final values of π, π_{in}, and π_f, respectively, for an adiabatic path are the same, $\pi_f = \pi_{in}$, and thus $\pm\int_{\pi_{in}}^{\pi_f}\frac{\sqrt{k_BT(\pi)}}{\sqrt{\pi(1-\pi)}}d\pi = \pm\int_{\pi_{in}}^{\pi_{in}}\frac{\sqrt{k_BT(\pi)}}{\sqrt{\pi(1-\pi)}}d\pi = 0$. However, we should introduce a phenomenological time τ_a required for the external controls to follow the ideal path along an adiabatic leg.

For the isothermal pieces of the cycle, we can compute the corresponding thermodynamic lengths L_Q analytically, since

$$\pm\int_{\pi_{in}}^{\pi_f}\frac{d\pi}{\sqrt{\pi(1-\pi)}} = \pm\Big(arcsin(1-2\pi_{in})-arcsin\Big(1-2\pi_f\Big)\Big). \quad (95)$$

Assuming constant relaxation times $(\Delta t)_T$ along the path, the optimal assignment of time follows automatically; along the optimal path with optimal times $\tau^{(2)}$ and $\tau^{(4)}$, and thus $N^{(2)} = \frac{\tau^{(2)}}{(\Delta t)_T}$ and $N^{(4)} = \frac{\tau^{(4)}}{(\Delta t)_T}$ given, we find

$$\pi_i^{(2)} = \frac{1}{2}\Big[1 - sin\Big(arcsin\Big(1-2\pi_{in}^{(2)}\Big) - \Big[arcsin\Big(1-2\pi_{in}^{(2)}\Big) - arcsin\Big(1-2\pi_f^{(2)}\Big)\Big]\frac{i}{N^{(2)}}\Big)\Big] \tag{96}$$

along leg 2, and

$$\begin{aligned}\pi_i^{(4)} &= \tfrac{1}{2}\Big[1 - sin\Big(arcsin\Big(1-2\pi_f^{(4)}\Big) - \Big[arcsin\Big(1-2\pi_f^{(4)}\Big) - arcsin\Big(1-2\pi_{in}^{(4)}\Big)\Big]\tfrac{N^{(4)}-i}{N^{(4)}}\Big)\Big] \\ &= \tfrac{1}{2}\Big[1 - sin\Big(arcsin\Big(1-2\pi_{in}^{(4)}\Big) + \Big[arcsin\Big(1-2\pi_f^{(4)}\Big) - arcsin\Big(1-2\pi_{in}^{(4)}\Big)\Big]\tfrac{i}{N^{(4)}}\Big)\Big]\end{aligned} \tag{97}$$

along leg 4. Note that we have employed the $(+)$-sign in the integral for leg 2 since $\pi_f^{(2)} > \pi_{in}^{(2)}$, and similarly the $(-)$-sign for leg 4 since $\pi_{in}^{(4)} > \pi_f^{(4)}$.

However, for the iso-κ leg, we need to compute the integral

$$(\pm)\int_{\pi_{in}}^{\pi_f} \frac{\sqrt{Bk_B}d\pi}{\sqrt{(\pi(1-\pi))ln\Big[\Big(\frac{g(n_2)}{g(n_1)}\Big)\Big(\frac{\pi}{1-\pi}\Big)\Big]}} = (\pm)\sqrt{\kappa}\int_{\pi_{in}}^{\pi_f} \frac{\sqrt{B_0}d\pi}{\sqrt{(\pi(1-\pi))ln\Big[\Big(\frac{g(n_2)}{g(n_1)}\Big)\Big(\frac{\pi}{1-\pi}\Big)\Big]}}, \tag{98}$$

which is not straightforward even for constant B. Here, the $(+)$-sign refers to legs with increasing π (i.e., leg 3) and the $(-)$-sign to legs with decreasing π (i.e., leg 1), and we have used Equation (88) to replace $T(\pi)$. Thus, any cycle containing an iso-κ leg does not allow us to compute the actual distribution of steps along the leg once the optimal time assignment to the legs has been performed. Note that the $\sqrt{\kappa}$ dependence of the thermodynamic length of an iso-κ branch is specific to the hydrogen atom-like system and is not a property of a general two-state system.

Nevertheless, we note that for an iso-κ-adiabatic cycle, $\pi^{[2]} = \pi^{[3]}$ and $\pi^{[1]} = \pi^{[4]}$ because of the special adiabaticity of legs (2) and (4), where we assume as usual that we need the time τ_a to proceed along an adiabatic leg without generating excess heat such that the available time is $\tau_{iso-\kappa} = \tau - 2\tau_a$. Then we determine the optimal assignment of times as $\tau_Q^{(1)} = \tau_{iso-\kappa}\frac{\sqrt{\kappa_{in}}}{\sqrt{\kappa_{in}}+\sqrt{\kappa_f}}$ and $\tau_Q^{(3)} = \tau_{iso-\kappa}\frac{\sqrt{\kappa_f}}{\sqrt{\kappa_{in}}+\sqrt{\kappa_f}}$, according to the ratio of the optimal times, $\frac{\tau_Q^{(3)}}{\tau_Q^{(1)}} = \frac{L_Q^{(3)}}{L_Q^{(1)}} = \frac{\sqrt{\kappa_f}}{\sqrt{\kappa_{in}}}$; we had found the same result for the general hydrogen atom-like system in Equation (66). In contrast to this result, for the iso-κ-isothermal cycle, the relative sizes of the four legs are unknown, and thus we cannot assign optimal times to the four legs of this cycle, even though we have an analytical expression for the thermodynamic lengths of the two isothermal legs.

Among the three cycles we have considered, only the isothermal-adiabatic one can be completely solved analytically when minimizing excess heat, yielding $L_Q^{(1)} = L_Q^{(3)} = 0$ and

$$L_Q^{(2)} = \sqrt{k_B T^{[2]}}\Big(arcsin\Big(1-2\pi^{[2]}\Big) - arcsin\Big(1-2\pi^{[3]}\Big)\Big) \tag{99}$$

and

$$L_Q^{(4)} = \sqrt{k_B T^{[1]}}\Big(arcsin\Big(1-2\pi^{[1]}\Big) - arcsin\Big(1-2\pi^{[4]}\Big)\Big). \tag{100}$$

Due to the special adiabaticity of legs 1 and 3, we have $\pi^{[1]} = \pi^{[2]}$ and $\pi^{[3]} = \pi^{[4]}$, and thus

$$L_Q^{(4)} = \sqrt{k_B T^{[1]}}\Big(arcsin\Big(1-2\pi^{[2]}\Big) - arcsin\Big(1-2\pi^{[3]}\Big)\Big) = \sqrt{\frac{T^{[1]}}{T^{[2]}}}L_Q^{(2)}. \tag{101}$$

Subtracting the time needed for the adiabatic legs, we can split the remaining time $\tau_{iso-T} = \tau - 2\tau_a$ over the legs 2 and 4, i.e.,

$$\tau_Q^{(2)} = \tau_{iso-T}\frac{L_Q^{(2)}}{L_{cycle}} = \tau_{iso-T}\frac{\sqrt{T^{[2]}}}{\sqrt{T^{[1]}}+\sqrt{T^{[2]}}} \tag{102}$$

and

$$\tau_Q^{(4)} = \tau_{iso-T}\frac{L_Q^{(4)}}{L_{cycle}} = \tau_{iso-T}\frac{\sqrt{T^{[1]}}}{\sqrt{T^{[1]}}+\sqrt{T^{[2]}}}. \tag{103}$$

The ratio of the two assigned times is the same as that which we had found in Equation (84),

$$\frac{\tau_Q^{(2)}}{\tau_Q^{(4)}} = \frac{L_Q^{(2)}}{L_Q^{(4)}} = \sqrt{\frac{T^{[2]}}{T^{[1]}}}, \tag{104}$$

i.e., we need to spend more time in the high-temperature leg than in the low-temperature leg when minimizing the excess heat of the system. The assignment of the step points along each leg now follows directly from Equations (96) and (97).

We note that we did not need to employ the special properties of the hydrogen atom-like system to derive the finite-time thermodynamics results in Equations (95)–(97) and (99)–(104). Thus, the optimal ratio of assigned times $\sqrt{T^{[2]}/T^{[1]}}$ is the optimality criterion for the adiabatic-isothermal cycle of any two-state system. This agrees with the analysis of a spin 1/2 two-state system in finite time where the power along the cycle was maximized [28], and is reminiscent of similar general results obtained in the analysis of Carnot cycles in finite time [10].

The above analysis was performed using the metric $\overleftrightarrow{M}_Q$ in the optimality criterion for minimizing excess heat/work. If we employ the metric $\overleftrightarrow{M}_S$ appropriate for minimizing entropy production, we note that we now have $dL_S = \sqrt{k_B}\sqrt{\frac{1}{\pi}+\frac{1}{1-\pi}}|d\pi| = \pm\sqrt{\frac{k_B}{\pi(1-\pi)}}d\pi$. Thus, for every leg (j), we can use Equation (95) to compute the thermodynamic length $L_S^{(j)}$, regardless of whether we are dealing with an adiabatic, isothermal, or iso-κ leg. As a consequence, all three cycles considered can be solved analytically. For the Carnot-like cycle, we obtain an assignment of equal times to the isothermal legs, $\tau_S^{(2)} = \tau_S^{(4)}$, like we had obtained for the full hydrogen atom; this assignment is again analogous to results obtained for minimal entropy production in the spin 1/2 two-state model [28], as one would have expected from the universal aspects of two-level systems. For the Otto-like cycle, we also find equal time assignments for the iso-κ legs, $\tau_S^{(1)} = \tau_S^{(3)}$, as we did already for the full hydrogen atom. Finally, for the Stirling-like cycle, the total thermodynamic length is $L_{S;cycle} = 2\Big[arcsin\Big(1-2\pi^{[2]}\Big) - arcsin\Big(1-2\pi^{[4]}\Big)\Big]$, and thus the optimal time assignment to the four legs is $\tau_S^{(1)} = \frac{\tau}{2}\frac{\left[arcsin\left(1-2\pi^{[2]}\right)-arcsin\left(1-2\pi^{[1]}\right)\right]}{\left[arcsin\left(1-2\pi^{[2]}\right)-arcsin\left(1-2\pi^{[4]}\right)\right]}$, $\tau_S^{(2)} = \frac{\tau}{2}\frac{\left[arcsin\left(1-2\pi^{[2]}\right)-arcsin\left(1-2\pi^{[3]}\right)\right]}{\left[arcsin\left(1-2\pi^{[2]}\right)-arcsin\left(1-2\pi^{[4]}\right)\right]}$, $\tau_S^{(3)} = \frac{\tau}{2}\frac{\left[arcsin\left(1-2\pi^{[3]}\right)-arcsin\left(1-2\pi^{[4]}\right)\right]}{\left[arcsin\left(1-2\pi^{[2]}\right)-arcsin\left(1-2\pi^{[4]}\right)\right]}$ and $\tau_S^{(4)} = \frac{\tau}{2}\frac{\left[arcsin\left(1-2\pi^{[1]}\right)-arcsin\left(1-2\pi^{[4]}\right)\right]}{\left[arcsin\left(1-2\pi^{[2]}\right)-arcsin\left(1-2\pi^{[4]}\right)\right]}$. Since we have analytical expressions for the thermodynamic length for every leg, it is straightforward to also assign the times along the legs for all three cycles, analogous to Equations (96) and (97).

6. Summary and Discussion

In the previous sections, we have presented three thermodynamic cycles for a hydrogen atom-like system in (κ, T) space, where κ allows us to control the electronic energy levels of the system: iso-κ-isothermal, iso-κ-adiabatic, and adiabatic-isothermal. We have written down expressions for heat and work along the legs of these cycles and derived conditions that yield optimal ways to run through the cycles in finite time such that the entropy production or the excess heat production is minimal.

In particular, we found that the optimal allocation of time—in units of relaxation-to-equilibrium times—including the allocation of discrete steps along the cycle, should take place in such a way that a) the path in (κ, T) space, for given corners ([1], [2], [3], [4]) and prescribed types of branches, should be chosen such that the total thermodynamic length of the cycle is a minimum, b) the time allocated to each leg of the cycle should be proportional to the thermodynamic length of each leg separately, and c) the discrete steps along each leg should be spaced in such a way that the thermodynamic lengths between all pairs of consecutive points along the branch are identical. We showed that the thermodynamic length could be evaluated using an appropriate metric, $\overleftrightarrow{M}_Q = \left\{\frac{k_B T_i}{\overleftrightarrow{\pi}_i}\right\}$ or $\overleftrightarrow{M}_S = \left\{\frac{k_B}{\overleftrightarrow{\pi}_i}\right\}$, in probability distribution space, which was obtained as part of the optimal control analysis.

We note that condition a) is trivial for the cycles chosen in the present study, since each leg is completely determined by the assignment of its end points and the type of path, i.e., whether it is iso-κ, isothermal, or adiabatic. If there were several control parameters $\kappa_{a,b,\ldots}$ that influence the change in the energy levels of the system, then step a) would be a major part of the optimal control problem of minimizing entropy or excess heat production, of course.

Furthermore, we discussed the minimization of excess heat along special adiabatic branches, which by construction equals zero due to the condition that the equilibrium probability distribution is constant along such a special adiabatic path, and thus never an imbalance between actual and equilibrium distribution can build up; for example, by construction, all two-state statistical mechanical systems constitute examples where adiabatic paths are special. Thus, only our inability in practice to keep the control parameters on-target while moving along a special adiabatic path generates deviations from the equilibrium occupation of the microstates of the system, which are the main source of excess heat or entropy production. We derived approximate expressions for the thermodynamic length of generic off-target paths that still remain close to the ideal adiabatic path.

We note that the issue of on-target path control arises for every leg of any cycle, but that one usually ignores these contributions to the entropy or excess heat production. The reason for discounting them is twofold; for one, they tend to be overwhelmed by the effects of having only finite time available to run through the legs of the cycle. Perhaps more important is the fact that an analysis would require information about the apparatus employed to move the system in the (κ, T) space, which is specific to each experiment, and thus usually not within the purview of the theoretical study.

Related finite-time analyses have been performed for thermodynamic engines in the past by assuming, e.g., a generic heat leakage or (inefficient) heat conduction during the processes of the cycle, which are described by phenomenological laws [43–45]. However, this leakage was not connected to the issue of being "on-target" vs. "off-target"; instead, the thermodynamic controls were assumed to be perfect, and the inefficiencies associated with, e.g., friction or heat conduction were considered part of the working of the engine.

These optimality criteria and the associated thermodynamic metrics are very general and apply to essentially all statistical mechanical systems, as long as the energy levels can be controlled by a generic parameter κ or set of parameters $\vec{\kappa} = (\kappa_a, \kappa_b, \ldots)$. Thus, there are connections to other general results [35,46–50]. For example, the excess heat we consider corresponds to the excess work investigated by Sivak and Crooks [47], and thus Equations (28) and (29) for the thermodynamic lengths $L_{Q/S}$ correspond to the generalized thermodynamic length they define via the time-integrated force covariance matrix [47]. Furthermore, the relationship $\overleftrightarrow{M}_Q = T\overleftrightarrow{M}_S$ for statistical mechanical systems observed in this study corresponds to the conformal equivalence of the energy and entropy metric demonstrated by Salamon and co-workers for thermodynamic equilibrium systems [50]. This also shows that the excess heat metric $\overleftrightarrow{M}_Q$ measures the dissipation or loss of availability when proceeding along the path in finite time, as had been shown earlier in the context of optimally measuring free energy differences in statistical mechanical systems [35] and computing thermodynamic lengths within computer simulations [46].

Specific to the hydrogen atom-like system is the observation that $E_n(\kappa) = \kappa E_n(\kappa = 1)$ for all energy levels n. From this follow certain simplifications, such as the fact that κ and T appear only in the combination $A = \frac{\kappa}{T}$ in the equilibrium probability distribution $\vec{\pi}$, and therefore all adiabatic paths in (κ, T) space are special and lie on straight lines that contain the origin $(\kappa = 0, T = 0)$. In particular, we observed that for the isothermal-adiabatic cycle the time allocation to the two isothermal branches should be proportional to the square roots of the temperatures associated with these branches when minimizing the excess heat production. Similarly, for the iso-κ-adiabatic cycle, the time allocation for the two iso-κ branches should be proportional to the square roots of the κ values associated with these branches. In contrast, when minimizing the entropy production of the cycles that contain two adiabatic branches, the optimal times assigned to the two isothermal or iso-κ-legs should be equal. Here, we note that the results obtained in Section 4 would be applicable to any system whose energy spectrum scales with the control parameter κ according to Equation (3), such as, e.g., a quantum harmonic oscillator if one modifies only the basic frequency, $\omega_0 \to \kappa\omega_0$, or a spin system with N_L energy levels in a magnetic field as long as we only change the strength of the applied magnetic field, $B_0 \to \kappa B_0$. For an analysis of the influence of the eigenvalue spectrum of a system on the finite-time performance, we refer to [51].

For the case of the hydrogen atom-like system, we have also considered a two-state approximation, which allows us to perform further analytical evaluations of the optimal control conditions. When minimizing excess heat, we can analytically solve the isothermal-adiabatic cycle, while for minimal entropy production, all three cycles can now be solved analytically. These results are quite general and hold for any two-state system, as can be seen from the agreement with results obtained from, e.g., a spin-1/2 system [28]. Furthermore, the result for the Carnot cycle is reminiscent to the outcome of some finite time optimal control calculations for heat engines, working between two reservoirs [10], and agrees with corresponding results for the spin 1/2 system [28].

However, thermal interactions with the environment affect all energy levels, making the two-state approximation of the hydrogen atom somewhat artificial. On the other hand, enforcing transitions via narrow band radiation allows us to focus on single pairs of energy levels, thus providing a more realistic example of a two-state system at the price of dealing with an a-thermal cycle.

A possible four-leg cycle for the two-state version of a single hydrogen atom-like system (i.e., only two of the electronic energy levels n_1 and $n_2 > n_1$ participate in the process) without contact to a heat bath is shown in Figure 5 for the case $n_1 = 1$ and $n_2 = 2$. No temperature is involved, and the cycle runs as follows, where we take as starting point the atom in the state n_1 with energy $E^{[1]} = E_{n_1}(\kappa_{in})$ for $\kappa^{[1]} = \kappa_{in}$. In leg 1, we excite the atom from $n = n_1$ to $n = n_2$ via irradiation at frequency ν_{in} ($h\nu_{in} = E^{[2]} - E^{[1]} = E_{n_2}(\kappa_{in}) - E_{n_1}(\kappa_{in})$), while we keep κ at the value κ_{in}, $\kappa^{[2]} = \kappa_{in}$. Next, we increase κ to $\kappa^{[3]} = \kappa_f$, while keeping the atom in the excited state $n = n_2$, i.e., $E^{[3]} = E_{n_2}\left(\kappa_f\right)$. This is followed by the reverse operations, i.e., we de-excite the atom back to $n = n_1$ via irradiation at frequency ν_f ($h\nu_f = E^{[3]} - E^{[4]} = E_{n_2}\left(\kappa_f\right) - E_{n_1}\left(\kappa_f\right)$), while keeping κ at the value κ_f, $\kappa^{[4]} = \kappa_f$, followed by the decrease of κ to $\kappa = \kappa_{in}$, while keeping the atom in the state $n = n_1$, thus closing the cycle.

Note that legs 2 and 4 would be the analogues to adiabatic branches in the thermal cycle. There, we perform or extract work on the system by changing the energy content of the hydrogen atom-like system from $E_{n_2}(\kappa_{in})$ to $E_{n_2}\left(\kappa_f\right)$ and from $E_{n_1}\left(\kappa_f\right)$ to $E_{n_1}(\kappa_{in})$, respectively. The total amount of work (done by the atom) associated with these two legs would be

$$\begin{aligned} W = -\Delta E = -\left[E_{n_2}\left(\kappa_f\right) - E_{n_2}(\kappa_{in})\right] - \left[E_{n_1}(\kappa_{in}) - E_{n_1}\left(\kappa_f\right)\right] = \\ \left(\kappa_{in} - \kappa_f\right)\left[E_{n_2}(\kappa = 1) - E_{n_1}(\kappa = 1)\right] = \alpha\left(\frac{1}{(n_1)^2} - \frac{1}{(n_2)^2}\right)\left(\kappa_{in} - \kappa_f\right) < 0, \end{aligned} \tag{105}$$

since $\kappa_f > \kappa_{in}$ and $n_2 > n_1$. Thus, our external apparatus, which changes κ, performs a net amount of work on the atom along these two legs.

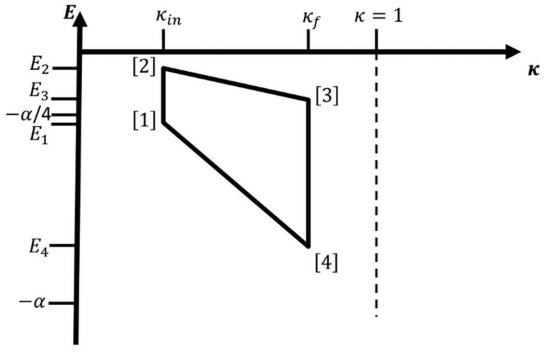

Figure 5. Sketch of an a-thermal iso-κ-"adiabatic" cycle for a two-state system comprising the ground state and the first excited state of the hydrogen-like atom. Branches [1] $\rightarrow$ [2] and [3] $\rightarrow$ [4] are iso-κ-legs and branches [2] $\rightarrow$ [3] and [4] $\rightarrow$ [1] are "adiabatic" legs, respectively. Note that the adiabatic legs run along straight lines that pass through the origin and through the point $(\kappa, E) = (1, -\alpha)$ for the adiabatic leg in the ground state, and through the origin and through the point $(\kappa, E) = (1, -\alpha/4)$ for the adiabatic leg in the first excited state, respectively. The four corners of the cycle are the points $[1] = \left(\kappa^{[1]}, E^{[1]}\right) = (\kappa_{in}, E_1)$, $[2] = \left(\kappa^{[2]}, E^{[2]}\right) = (\kappa_{in}, E_2)$, $[3] = \left(\kappa^{[3]}, E^{[3]}\right) = \left(\kappa_f, E_3\right)$, and $[4] = \left(\kappa^{[4]}, E^{[4]}\right) = \left(\kappa_f, E_4\right)$ in the (κ, E) plane. Note that $E^{[1]} = \kappa_{in} E_1(\kappa = 1)$, $E^{[2]} = \kappa_{in} E_2(\kappa = 1)$, $E^{[3]} = \kappa_f E_2(\kappa = 1)$, and $E^{[4]} = \kappa_f E_1(\kappa = 1)$.

Concerning legs 1 and 3, which would be the analogues to the heating and cooling branches of a typical thermodynamic cycle, it is not obvious how to account for the equivalent of heat transferred from and to the heat reservoir at different temperatures, and thus make a connection to thermodynamic cycles. If the radiation fields had a black-body frequency distribution, the formulas of radiation thermodynamics would apply [52–54], but this would weaken the desired approximation of the system through only two energy levels. What we can consider is a "reservoir" of photons with frequencies ν_{in} and ν_f, which the hydrogen atom-like system is in contact with during the excitation and de-excitation processes in legs 1 and 3, respectively. However, such a radiation field that consists of narrow frequency bands does not act as a standard thermal heat source as far as the hydrogen atom-like system is concerned. Instead, we treat the radiation field as part of the external apparatus for the purpose of this discussion, analogous to the pressure we might apply to the material to change the properties of the excitons representing the hydrogen atom-like system. As a consequence, the net work done by the radiation field on the atom equals

$$h\nu_{in} - h\nu_f = [E_{n_2}(\kappa_{in}) - E_{n_1}(\kappa_{in})] - \left[E_{n_2}\left(\kappa_f\right) - E_{n_1}\left(\kappa_f\right)\right] = \left(\kappa_{in} - \kappa_f\right)[E_{n_2}(1) - E_{n_1}(1)] < 0, \quad (106)$$

i.e., the energy of the radiation field shows a net increase along legs 1 and 3 by the same amount as the atom gained in energy when we applied work along legs 2 and 4.

We can thus visualize the two-state approximation of our hydrogen atom-like system as an "engine" that acts as a "frequency conversion pump" while keeping the number of photons conserved. A possible co-efficient of performance would be

$$\eta^{conv} = \frac{W^{(1)} + W^{(3)}}{W^{(2)} + W^{(4)}} = 1, \quad (107)$$

i.e., the a-thermal cycle of the single controllable hydrogen atom-like system represents a perfect energy conversion apparatus from photons with one frequency to photons with another frequency. We note that this perfect restriction of the hydrogen atom-like system to a two-state system would also work if

the modification of the Hamiltonian breaks the symmetry of the Coulomb field, as might be the case by exposing the hydrogen atom to an anisotropic external electric field inside a cavity.

Of course, in practice, this a-thermal cycle will encounter finite-time losses, too. The sources of possible finite-time losses have to be identified in an analysis of the quantum processes involved when changing the Hamiltonian and exciting/de-exciting the electrons between the two levels, including the degree of coherence maintained in the system along each leg. An analysis of these issues would go beyond the purview of this study, however. Possible approaches on how to analyze these issues can be found in some of the cited references dealing explicitly with the quantum aspects of heat engines [18–29,48,49,51].

A final question is whether there are experimental systems where the thermodynamic or a-thermal cycles discussed in this study might be realized. The most straightforward suggestion would be to take an individual hydrogen atom inside a cavity whose shape can be changed, such that the energy levels can be modified in some way [31]. This system should allow an a-thermal cycle, but the momentum transfer during absorption would start injecting kinetic energy, which would re-appear as a source of heat to the system. In the case of a thermodynamic cycle, where we were to expose the atom to a heat reservoir over a sufficiently large temperature range for exciting the hydrogen atom(s) to a noticeable degree, the system's translational degrees of freedom would quickly establish thermal movement with all that implies, possibly overwhelming the thermodynamic quantities of interest in the electronic two-state system. However, since the experimental control of the hydrogen atom as a thermal engine based on the translational degrees of freedom has been quite successful already [13], a quasi-a-thermal or a thermodynamic engine based on the occupation of the electronic states and on the modification of their energy levels should be feasible.

An alternative would be an excitonic defect in a solid, since this is usually more localized (but still mobile, in principle) and thus probably less susceptible to the kinetic thermal contributions. Furthermore, the reference value of κ, κ_{in}, should be rather small, and thus small changes in temperature would already lead to noticeable changes in the occupation probabilities of the excitonic states. On the other hand, as mentioned earlier, varying κ in a solid can be nontrivial, since the quantities entering κ will depend on both pressure—which would be a suitable control variable—and temperature. As a consequence, in a (p, T) space representation, the iso-κ branches would involve closely coordinated changes both in pressure and temperature. Additionally, an a-thermal cycle might be difficult to achieve, due to the strong thermal coupling of the exciton to the rest of the solid. Nevertheless, it appears that a variety of systems exist which might serve as substrates for the realization of an electronic states-based engine with a single hydrogen atom-like system as the working fluid.

Funding: This research received no external funding.

Acknowledgments: I would like to thank the participants of the 2017 workshop on "Optimizing Thermodynamics" at the Telluride Science Research Center in Telluride, CO, USA, for valuable discussions, and Karl Heinz Hoffmann for a careful reading of the manuscript.

Conflicts of Interest: The author declares no conflict of interest.

References

1. Fernandez-Cara, E.; Zuazua, E. Control Theory: History, Mathematical Achievements and Perspectives. *Bol. Soc. Esp. Mat. Apl.* **2003**, *26*, 79–140.
2. Sussmann, H.J.; Willems, J.C. 300 years of Optimal Control: From the Brachystorochrone to the Maximum Principle. In Proceedings of the History Session, 35th Conference on Decision and Control, Kobe, Japan, 11–12 December 1996.
3. Von den Hoff, P.; Thallmair, S.; Kowalewski, M.; Siemering, R.; de Vivie-Riedle, R. Optimal control theory—Closing the gap between theory and experiment. *Phys. Chem. Chem. Phys.* **2012**, *14*, 14460–14485. [CrossRef] [PubMed]
4. Werschnik, J.; Gross, E.K.U. Quantum optimal control theory. *J. Phys. B* **2007**, *40*, R175–R211. [CrossRef]
5. Landau, L.D.; Lifshitz, E.M. *Statistical Physics*, 3rd ed.; Pergamon Press: Oxford, UK, 1980; Part 1.

6. Gobrecht, H. *Bergmann-Schaefer: Lehrbuch der Experimentalphysik: Mechanik, Akustik, Wärme*; De Gruyter: Berlin, Germany, 1975.
7. Giedt, W. *Thermophysics*; Van Nostrand Reinhold Company: New York, NY, USA, 1971.
8. Andresen, B.; Berry, R.S.; Nitzan, A.; Salamon, P. Thermodynamics in finite time. I. The step Carnot cycle. *Phys. Rev. A* **1977**, *15*, 2086–2093. [CrossRef]
9. Salamon, P.; Nitzan, A.; Andresen, B.; Berry, R.S. Minimum entropy production and the optimization of heat engines. *Phys. Rev. A* **1980**, *21*, 2115–2129. [CrossRef]
10. Salamon, P.; Nitzan, A. Finite time optimizations of a Newton's law Carnot cycle. *J. Chem. Phys.* **1981**, *74*, 3546–3560. [CrossRef]
11. Andresen, B. Current Trends in Finite-Time Thermodynamics. *Angew. Chem. Int. Ed.* **2011**, *50*, 2690–2704. [CrossRef]
12. Seifert, U. Stochastic thermodynamics, fluctuation theorems and molecular machines. *Rep. Prog. Phys.* **2012**, *75*, 126001. [CrossRef]
13. Roßnagel, J.; Dawkins, S.T.; Tolazzi, R.N.; Abah, O.; Lutz, E.; Schmidt-Kaler, F.; Singer, K. A single-atom heat engine. *Science* **2016**, *352*, 325–329. [CrossRef]
14. Leibfried, D.; Blatt, R.; Monroe, C.; Wineland, D. Quantum dynamics of single trapped ions. *Rev. Mod. Phys.* **2003**, *75*, 281–324. [CrossRef]
15. Scully, M.O.; Zubairy, M.S.; Agarwal, G.S.; Walther, H. Extracting Work from a Single Heat Bath via Vanishing Quantum Coherence. *Science* **2003**, *299*, 862–864. [CrossRef]
16. Zhao, N.; Honert, J.; Schmid, B.; Klas, M.; Isoya, J.; Markham, M.; Twithen, D.; Jelezko, F.; Liu, R.-B.; Fedder, H.; et al. Sensing single remote nuclear spins. *Nat. Nanotechnol.* **2012**, *7*, 657–662. [CrossRef] [PubMed]
17. Vicarelli, L.; Heerema, S.J.; Dekker, C.; Zandbergen, H.W. Controlling Defects in Graphene for Optimizing the Electrical Properties of Graphene Nanodevices. *ACS Nano* **2015**, *9*, 3428–3435. [CrossRef]
18. Salamon, P.; Hoffmann, K.H.; Rezek, Y.; Kosloff, R. Maximum work in minimum time from a conservative quantum system. *Phys. Chem. Chem. Phys.* **2009**, *11*, 1027–1032. [CrossRef] [PubMed]
19. Hoffmann, K.H.; Andresen, B.; Salamon, P. Optimal control of a collection of parametric oscillators. *Phys. Rev. E* **2013**, *87*, 062106. [CrossRef]
20. Insinga, A.; Andresen, B.; Salamon, P. Thermodynamic analysis of a quantum heat engine based on harmonic oscillators. *Phys. Rev. E* **2018**, *94*, 12119. [CrossRef] [PubMed]
21. Rezek, Y.; Kosloff, R. Irreversible performance of a quantum harmonic heat engine. *New J. Phys.* **2006**, *8*, 83. [CrossRef]
22. Chen, L.; Liu, X.; Ge, Y.; Wu, F.; Feng, H.; Xia, S. Power and efficiency optimization of an irreversible quantum Carnot heat engine working with harmonic oscillators. *Phys. A* **2020**, *550*, 124140. [CrossRef]
23. Kosloff, R.; Rezek, Y. The Quantum Harmonic Otto cycle. *Entropy* **2017**, *19*, 136. [CrossRef]
24. Lee, S.; Ha, M.; Park, J.-M.; Jeong, H. Finite-time quantum Otto engine: Surpassing the quasistatic efficiency due to friction. *Phys. Rev. E* **2020**, *101*, 022127. [CrossRef] [PubMed]
25. Deffner, S.; Lutz, E. Thermodynamic length for far-from-equilibrium quantum systems. *Phys. Rev. E* **2013**, *87*, 022143. [CrossRef] [PubMed]
26. Quan, H.T.; Liu, Y.-X.; Sun, C.P.; Nori, F. Quantum thermodynamic cycles and quantum heat engines. *Phys. Rev. E* **2007**, *76*, 031105. [CrossRef] [PubMed]
27. Geva, E.; Kosloff, R. A quantum-mechanical heat engine operating in finite time. A model consisting of spin-1/2 systems as the working fluid. *J. Chem. Phys.* **1992**, *96*, 3054–3067. [CrossRef]
28. Geva, E.; Kosloff, R. On the classical limit of quantum thermodynamics in finite time. *J. Chem. Phys.* **1992**, *97*, 4398–4412. [CrossRef]
29. Xu, H.; Yung, M.-H. Unruh quantum Otto heat engine with level degeneracy. *Phys. Lett. B* **2020**, *801*, 135201. [CrossRef]
30. Ashcroft, N.W.; Mermin, N.D. *Solid State Physics*; Saunders College Publishing: Orlando, FL, USA, 1976.
31. Sen, K.D. (Ed.) *Electronic Structure of Quantum Confined Atoms and Molecules*; Springer: Heidelberg, Germany, 2014.
32. Young, K.F.; Frederikse, H.P.R. Temperature and Pressure Dependence of Dielectric Constant of Cadmium Fluoride. *J. Appl. Phys.* **1969**, *40*, 3115–3118. [CrossRef]

33. Sasabe, H.; Saito, S. Effects of Temperature and Pressure on the Dielectric Constant in Non-Polar Polymers. *Polym. J.* **1972**, *3*, 749–755. [CrossRef]
34. Dubbers, D.; Stöckmann, H.-J. *Quantum Physics: The Bottom-Up Approach: From the Simple Two-Level System to Irreducible Representations*; Springer: Heidelberg, Germany, 2013.
35. Schön, J.C. A thermodynamic distance criterion of optimality for the calculation of free energy changes from computer simulations. *J. Chem. Phys.* **1996**, *105*, 10072–10083. [CrossRef]
36. Nulton, J.; Salamon, P.; Andresen, B.; Anmin, Q. Quasistatic processes as step equilibrations. *J. Chem. Phys.* **1985**, *83*, 334–338. [CrossRef]
37. Salamon, P.; Berry, R.S. Thermodynamic Length and Dissipated Availability. *Phys. Rev. Lett.* **1983**, *51*, 1127–1130. [CrossRef]
38. Salamon, P.; Nulton, J.D.; Harland, J.R.; Pedersen, J.; Ruppeiner, G.; Liao, L. Simulated annealing with constant thermodynamic speed. *Comp. Phys. Commun.* **1988**, *49*, 423–428. [CrossRef]
39. Kirkwood, J.G. Statistical Mechanics of Fluid Mixtures. *J. Chem. Phys.* **1935**, *3*, 300–313. [CrossRef]
40. Zwanzig, R. High-Temperature Equation of State by a Perturbation Method. I. Nonpolar Gases. *J. Chem. Phys.* **1954**, *22*, 1420–1426. [CrossRef]
41. Watanabe, M.; Reinhardt, W.P. Direct dynamical calculation of entropy and free energy by adiabatic switching. *Phys. Rev. Lett.* **1990**, *65*, 3301–3304. [CrossRef] [PubMed]
42. Diosi, L.; Kulacsy, K.; Lukacs, B.; Racz, A. Thermodynamic length, time, speed, and optimum path to minimize entropy production. *J. Chem. Phys.* **1996**, *105*, 11220–11225. [CrossRef]
43. Curzon, F.L.; Ahlborn, B. Efficiency of a Carnot engine at maximum power output. *Am. J. Phys.* **1975**, *43*, 22–24. [CrossRef]
44. Hoffmann, K.H. Recent Developments in Finite Time Thermodynamics. *Techn. Mech.* **2002**, *22*, 14–25.
45. Sienutycz, S.; Salamon, P. (Eds.) *Finite-Time Thermodynamics and Thermoeconomics*; Taylor&Francis: New York, NY, USA, 1990.
46. Crooks, G.E. Measuring Thermodynamic Length. *Phys. Rev. Lett.* **2007**, *99*, 100602. [CrossRef]
47. Sivak, D.A.; Crooks, G.E. Thermodynamic Metrics and Optimal Paths. *Phys. Rev. Lett.* **2012**, *108*, 190602. [CrossRef]
48. Brandner, K.; Saito, K. Thermodynamic Geometry of Microscopic Heat Engines. *Phys. Rev. Lett.* **2020**, *124*, 040602. [CrossRef]
49. Abiuso, P.; Miller, H.J.D.; Perarnau-Llobet, M.; Scandi, M. Geometric optimisation of quantum thermodynamic processes. *arXiv* **2020**, arXiv:2008.13593v1.
50. Salamon, P.; Nulton, J.D.; Ihrig, E. On the relation between entropy and energy versions of thermodynamic length. *J. Chem. Phys.* **1984**, *80*, 436. [CrossRef]
51. Allahverdyan, A.E.; Johal, R.S.; Mahler, G. Work extremum principle: Structure and function of quantum heat engines. *Phys. Rev. E* **2008**, *77*, 041118. [CrossRef] [PubMed]
52. Tervo, E.; Bagherisereshki, E.; Zhang, Z. Near-field radiative thermoelectric energy converters: A review. *Front. Energy* **2018**, *12*, 5–21. [CrossRef]
53. Mungan, C.E. Radiation thermodynamics with applications to lasing and fluorescent cooling. *Am. J. Phys.* **2005**, *73*, 315–322. [CrossRef]
54. Essex, C.; Kennedy, D.C.; Berry, R.S. How hot is radiation? *Am. J. Phys.* **2003**, *71*, 969–978. [CrossRef]

entropy

MDPI

Article

Optimization, Stability, and Entropy in Endoreversible Heat Engines

Julian Gonzalez-Ayala [1,2,*], José Miguel Mateos Roco [1,2], Alejandro Medina [1,2] and Antonio Calvo Hernández [1,2]

[1] Instituto de Física Fundamental y Matemáticas, Universidad de Salamanca, 37008 Salamanca, Spain; roco@usal.es (J.M.M.R.); amd385@usal.es (A.M.); anca@usal.es (A.C.H.)

[2] Departamento de Física Aplicada, Universidad de Salamanca, 37008 Salamanca, Spain

* Correspondence: jgonzalezayala@usal.es

Received: 28 September 2020; Accepted: 18 November 2020; Published: 20 November 2020

Abstract: The stability of endoreversible heat engines has been extensively studied in the literature. In this paper, an alternative dynamic equations system was obtained by using restitution forces that bring the system back to the stationary state. The departing point is the assumption that the system has a stationary fixed point, along with a Taylor expansion in the first order of the input/output heat fluxes, without further specifications regarding the properties of the working fluid or the heat device specifications. Specific cases of the Newton and the phenomenological heat transfer laws in a Carnot-like heat engine model were analyzed. It was shown that the evolution of the trajectories toward the stationary state have relevant consequences on the performance of the system. A major role was played by the symmetries/asymmetries of the conductance ratio σ_{hc} of the heat transfer law associated with the input/output heat exchanges. Accordingly, three main behaviors were observed: (1) For small σ_{hc} values, the thermodynamic trajectories evolved near the endoreversible limit, improving the efficiency and power output values with a decrease in entropy generation; (2) for large σ_{hc} values, the thermodynamic trajectories evolved either near the Pareto front or near the endoreversible limit, and in both cases, they improved the efficiency and power values with a decrease in entropy generation; (3) for the symmetric case ($\sigma_{hc} = 1$), the trajectories evolved either with increasing entropy generation tending toward the Pareto front or with a decrease in entropy generation tending toward the endoreversible limit. Moreover, it was shown that the total entropy generation can define a time scale for both the operation cycle time and the relaxation characteristic time.

Keywords: multiobjective optimization; Pareto front; stability; maximum power regime; entropy behavior

1. Introduction

The optimization of energy converters has never been as relevant as it is now. Energy production requirements, efficient use of heat sources, and heat waste reduction are continually pushing technological edges. Linked to this degree of specialization are the control and stability of operation regimes yielding a desirable stable production, despite the possible variations of external or internal conditions. In many cases, this requires the fine-tuning of control parameters with intrinsic energetic costs. In this regard, there are some hints as to the possibility of seizing the stability of heat engine operation regimes to enhance their performance by relaxing the control over the operation parameters [1–3]. Studies regarding the weakly dissipative limit [4] thus far have pointed out the special role played by the endoreversible model [5,6]. These studies consider that after the system experiences a perturbation in its operation variables, the trajectories that lead the system back to its steady state tend to evolve toward the endoreversible limit. This limit has been proven to be associated with thermodynamic states, with the best compromise between maximum efficiency, maximum power output, and minimum entropy production as given by the Pareto front of the system. Although the

equivalence of the low dissipation model (based on entropy generation) and the endoreversible model (based on specific heat transfer laws) has been established for several heat transfer laws [7–9], it is not obvious that the endoreversible behavior appears interconnected to the stability of the low dissipation model. A natural concern is to look for this very same behavior in the context of endoreversible heat engines.

On the other side, the stability of heat engines is not a novel topic. Especially in the realm of finite-time thermodynamics, endoreversible and irreversible models have, in their assets, a good number of works in this regard. From the pioneering work of Santillan et al. [10], a number of studies have analyzed the local and global stability of a variety of operation regimes [11–18], including economic factors [19], and have extended the analysis to heat pumps, refrigerators, and generalized heat engines [17,20–27].

The validation and applicability of the endoreversible hypothesis has been widely analyzed and discussed in the specialized literature [28–31], and although it constitutes an idealization of an irreversible device, recent studies on molecular dynamics simulation [32] have validated its predictions for a finite-time Carnot cycle of a weakly interacting gas (considered as a nearly ideal gas) and considering the local equilibrium for a Maxwell–Boltzmann distribution with a spatially uniform temperature and a spatially varying local center-of-mass velocity. In particular, these results also point to the validity of the paradigmatic Curzon–Ahlborn efficiency at maximum power [33,34]. These molecular dynamics simulations of a two-dimensional Carnot engine allowed to investigate not only the optimization of power output, but also some other figures of merit involving entropy production as the ecological figure of merit [32]. This reinforces the validity of the Carnot-like endoreversible model, where the quasistatic conditions linked to endoreversibility rely on the thermalization due to the internal dynamic speed. Lastly, a recent work reported some new conceptual insights (simulation and reconstruction) on the endoreversibility hypothesis [35] by considering that subsystems are out of equilibrium, i.e., including internal irreversibilities: First, by means of the contact temperature of the heat flows and the non-equilibrium molar entropy for material flows. This new feature is beyond the traditional endoreversible thermodynamics, which considers internal subsystems as reversible, i.e., without internal entropy production. Second, the mentioned work [35] goes beyond the use of paradigmatic, simple models and thus sheds light on the modeling characteristics of endoreversible systems in relation to real running heat engines.

Despite the extensive literature, the possibility of inducing optimization from stability in finite-time thermodynamics has not been studied. This is one of the goals of the present paper, which is focused on irreversible Carnot-like heat engine models with linear and inverse heat transfer laws, as two representative examples, assuming that the maximum power state behaves as a steady state. The kind of perturbations assumed in this analysis are from external sources or variations in the external control, such as those stemming from variations in the velocity of a piston. A benefit of this study is that, unlike the low-dissipation scheme, based on entropy production, the finite-time thermodynamics scheme allows a more straightforward analysis of its consequences on the working fluid and design of the heat engine, as it accounts for explicit heat transfer laws.

This paper is structured as follows: In Section 2, an overview of the endoreversible model is presented, along with some results on the maximum power regime for both the Newton and the phenomenological heat transfer laws. In Section 3, a multiobjective optimization is realized and the Pareto front is faced with endoreversible behavior. In Section 4, the stability dynamics are obtained from basic assumptions and the operation and relaxation times are compared in order to achieve a useful stability. In Section 5, the relaxation trajectories are analyzed in the space of the control variables as in the energetic space composed by power output, efficiency, and entropy generation. Finally some concluding remarks are presented.

2. A Quick Look at the Endoreversible Model

The most basic endoreversible model consists on a baseline Carnot cycle whose working fluid operates with effective temperatures T_{hw} and T_{cw} (isotherms of the Carnot cycle), irreversibly connected to two external reservoirs at temperature T_h and T_c ($T_h > T_{hw} > T_{cw} > T_c$), as depicted in Figure 1.

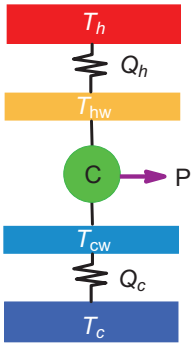

Figure 1. Schematic representation of an endoreversible heat engine. The working fluid realizes a Carnot cycle operating between the isothermal processes at effective temperatures T_{hw} and $T_{cw} < T_{hw}$. The working fluid is irreversibly coupled to external reservoirs at temperatures T_h and $T_c < T_h$.

The endoreversible scheme requires knowledge of the heat transfer laws to model the heat fluxes between the external reservoirs and the working fluid. In a somewhat general case of heat transfer laws, Q_h and Q_c are expressed as:

$$Q_h = \sigma_{hc}\sigma_c \left(T_h^k - T_{hw}^k\right) sgn\,(k)\, t_h > 0, \tag{1}$$

$$Q_c = \sigma_c \left(T_c^k - T_{cw}^k\right) sgn\,(k)\, t_c < 0, \tag{2}$$

where $k \neq 0$ is the exponent of the heat transfer law ($k = 1$ refers to the known Newton law, $k = -1$ is known as the phenomenological law, $k = 4$ is the Stefan–Boltzmann law, and so on); σ_c and σ_h are the thermal conductances with units of J·K^{-k}/s, here considered as constant since only small fluctuations around the operation regime are addressed. The function $sgn\,(k)$ is defined as:

$$sgn\,(k) = \begin{cases} 1 & if \quad k > 0 \\ -1 & if \quad k < 0 \end{cases},$$

which is introduced for consistency with the convention that the heat flux entering the working fluid is positive and that the outgoing heat is negative; t_h and t_c are the times at which the working fluid is in contact with the external heat reservoirs T_h and T_c, respectively. In Equation (1), the $\sigma_{hc} \equiv \sigma_h/\sigma_c$ ratio is introduced, which is an important ingredient to obtain the upper and lower bounds of the efficiency of a given operation regime. The endoreversible hypothesis states that the entropy generation in the inner part of the engine is zero. Mathematically, this means that:

$$\frac{Q_h}{T_{hw}} + \frac{Q_c}{T_{cw}} = 0, \tag{3}$$

and from this constraint, the ratio of the operation time is given as:

$$\frac{t_c}{t_h} = \frac{T_h^k - T_{hw}^k}{T_{cw}^k - \tau^k T_h^k} \frac{T_{cw}}{T_{hw}} \sigma_{hc}, \tag{4}$$

where $\tau \equiv T_c/T_h$. With the endoreversible hypothesis constraining t_c, in Equations (3) and (4), the efficiency η, power output P, and total entropy generation S become functions of $\{T_h, T_c, T_{hw}, T_{cw}, \sigma_{hc}, t_h, \sigma_c\}$. By using Equations (1) and (2), the explicit equations of these key thermodynamic magnitudes are the following:

$$\begin{aligned}
\eta &= 1+\frac{Q_c}{Q_h} = 1-\frac{T_{cw}}{T_{hw}}, \quad k=\{1,-1\} \\
P &= \frac{Q_h+Q_c}{t_c+t_h} = \begin{cases} \frac{\sigma_c\sigma_{hc}(T_{cw}-T_{hw})(T_h-T_{hw})(T_{cw}-\tau T_h)sgn(k)}{T_{cw}T_{hw}(\sigma_{hc}-1)+T_h(\tau T_{hw}-\sigma_{hc}T_{cw})} & k=1 \\ \frac{\sigma_c\sigma_{hc}(T_{cw}-T_{hw})(T_h-T_{hw})(T_{cw}-\tau T_h)sgn(k)}{T_h\left(T_{hw}^2(T_{cw}-\tau T_h)+T_{cw}^2(T_h-T_{hw})\tau\sigma_{hc}\right)} & k=-1 \end{cases}, \\
S &= -\frac{Q_h}{T_h}-\frac{Q_c}{T_c} = \begin{cases} \frac{t_h\sigma_c\sigma_{hc}(T_h-T_{hw})(T_{cw}-\tau T_{hw})sgn(k)}{T_hT_{hw}\tau} & k=1 \\ \frac{t_h\sigma_c\sigma_{hc}(T_h-T_{hw})(\tau T_{hw}-T_{cw})sgn(k)}{T_h^2T_{hw}^2\tau} & k=-1 \end{cases}.
\end{aligned} \tag{5}$$

As can be seen in the definition of the power output, instantaneous adiabatic processes were considered. In order to deal with non-instantaneous adiabatics, a more detailed analysis of the working fluid and the geometry of the device needs to be made (for example, see [36]). In some works, these features have been analyzed by showing their influence in the power output and efficiency, but under certain circumstances, such as the large compression ratios in a piston, these times produce small effects on η and P, remaining compatible with the quasistatic nature of the internal process.

Notice that only S is proportional to t_h. As is shown later in Section 4 (see Equation (15)), the relaxation times are also proportional to this partial time; thus, a relationship between relaxation time and total entropy generation can be found. By fixing the value of S, a time scale for stability can be established. Besides this time scale (establishing the speed of the restitution dynamics), it is possible to analyze the energetic consequences of stability independently of t_h if one works with entropy production per cycle time, defined as $\dot{S} \equiv S/(t_c+t_h) = S/t_h(1+t_c/t_h)$, taking advantage of the constraint on the total operation time through Equation (4).

The maximum power (MP) regime is specified by the temperatures T_{cw}^* resulting from the constraint $\partial P/\partial T_{cw} = 0$ and T_{hw}^* under the condition $\partial P/\partial T_{hw} = 0$. The resulting values are given by:

$$T_{hw}^* = \frac{T_h\left(\sqrt{\tau}+\sqrt{\sigma_{hc}}\right)}{1+\sqrt{\sigma_{hc}}} \quad k=1, \tag{6}$$

$$T_{cw}^* = \frac{T_h\left(\tau+\sqrt{\sigma_{hc}\tau}\right)}{1+\sqrt{\sigma_{hc}}} \quad k=1, \tag{7}$$

$$T_{hw}^* = \frac{2T_h\tau\left(1+\sqrt{\sigma_{hc}}\right)}{1+\tau+2\tau\sqrt{\sigma_{hc}}} \quad k=-1, \tag{8}$$

$$T_{cw}^* = \frac{2T_h\tau\left(1+\sqrt{\sigma_{hc}}\right)}{2+\sqrt{\sigma_{hc}}(1+\tau)} \quad k=-1. \tag{9}$$

From the optimal T_{cw}^* values, parametrization of P, η, and $\dot{S}$ can be made (see dashed curve in Figure 2). The obtained parametric curve exhibits a parabolic-like behavior, where the values of η vary from 0 to $\eta_C \equiv 1-\tau$, the Carnot efficiency (both limits corresponding to a zero power output), and with a single maximum in P. This is what is known in the literature as an endoreversible behavior, a kind of signature of the model. Some relevant features regarding the efficiency at maximum power from these endoreversible models with $k=1$ and $k=-1$ are pointed out:

- The Newton case ($k=1$) gives an efficiency at maximum power, $\eta_{MP} = \eta_{CAN} \equiv 1-\sqrt{\tau}$, the well-known Curzon–Ahlborn–Novikov (CAN) efficiency, which does not depend on the σ_{hc} ratio and appears in a large variety of contexts linked to the maximization of power output, work, and kinetic energy [37].
- The $k=-1$ case, frequently called the phenomenological law, referring to the natural results arising in the linear irreversible thermodynamics framework. It allows to obtain the same limits of

efficiency as in the low-dissipation model, where the self-optimization property has been studied. In this case ($k = -1$), η_{MP} is σ_{hc}-dependent, bounded by $\eta_{MP} \in \left(\frac{\eta_C}{2}, \frac{\eta_C}{2-\eta_C}\right)$, according to whether σ_{hc} varies from 0 to ∞ [7].

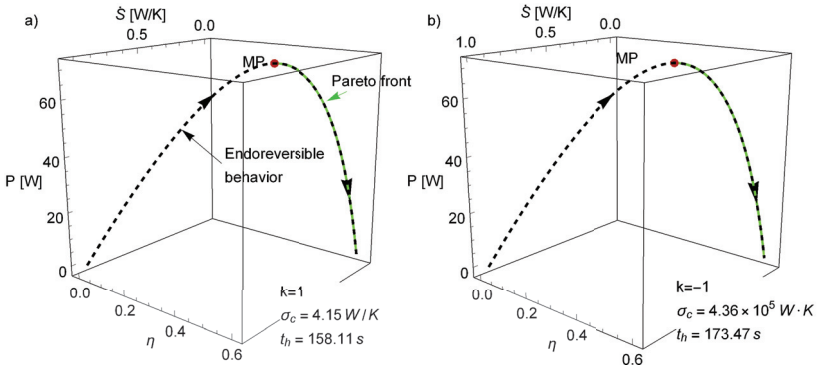

Figure 2. Parabolic behavior of the η, P, and $\dot{S}$ curve typical of the endoreversible model for (**a**) the $k = 1$ case and (**b**) the $k = -1$ case. The values T_h = 500 K, $\sigma_{hc} = 1$, and $\tau = 0.4$ weer fixed. Additionally, σ_c was chosen (for representation/comparison purposes) in such a way that the maximum power (MP) was 70 W in both cases, so that η, P, and $\dot{S}$ ranged in similar intervals.

3. The Relevant Region for Optimization: The Pareto Front

Before exploring stability dynamics, it is convenient to introduce a multiobjective optimization of the model. When looking for the best compromise among a variety of objective functions, the result is the so-called Pareto front (in the space of energetic functions) and the corresponding Pareto optimal set (in the space of operation variables).

To this end, a sorting algorithm is used by applying the concept of dominance [38]: A vector $v = (v_1, \ldots, v_n)$ dominates another one $w = (w_1, \ldots, w_n)$ if, and only if, $v_i \geq w_i \; \forall \, i \in \{1, \ldots, n\}$ (if one is looking for a maximum, $\leq$ for a minimum) and there is at least one j, such that $v_j > w_j$, if one is interested in those vectors that are not dominated by any other. In other words, vectors that have the best value at least in one objective function. In this case, such a vector is formed by η, P, and $\dot{S}$. The algorithm introduced here is a modification of the one introduced in [1–3], as follows:

1. In the phase space (T_{hw}, T_{cw}), the region of physical relevance is defined ($T_h \geq T_{hw} \geq T_{cw} \geq T_c$).
2. A random set of points in the phase space is obtained and the thermodynamic functions are evaluated (energetic space).
3. A set of non-dominated points in the energetic space is obtained, giving a provisional Pareto front.
4. From the corresponding Pareto optimal set (phase space), a convex region is defined and extended in order to cover a larger region for searching new points in the Pareto front. Details on the definition of the extended region are given below.
5. From the new region, a new set of random points is proposed and a new set of non-dominated points in the energetic space is obtained.

In the present analysis, and in order to ensure convergence in the results, Kullback–Leibler (KL) divergence was introduced as a measure of the relative entropy D_{KL} [39]. D_{KL} was calculated between the probability distribution of the efficiencies of the Pareto front in the ith and the $i-1$th iterations. As the probability distribution of η converges to the true Pareto front distribution, the entropy of the distribution converges as well. In such a case, the relative entropy D_{KL} tends toward zero. The radius to extend the search region in the phase space decreases with the D_{KL} value. When this relative entropy

is very small, there is no information gain in iterating more times; then, the search for new points in the Pareto optimal set stops. As mentioned before, D_{KL} provides a measure of statistical convergence by indicating how distant two distributions are. If $D_{KL} = 0$, then the information stemming from both distributions is the same. This is a relevant issue to demonstrate that the obtained trend is not due to the lack of additional iterations.

To obtain D_{KL}, the range of possible values of η, each iteration was divided into $\sqrt{N}$ (rounded to the upper next integer [40], with N being the number of random points added to the search in each iteration) equal intervals (or bins). In this way, the same partition was used to compute the discrete probability distributions, ρ_k (for the k iteration). D_{KL} was calculated by comparing ρ_{k-1} with ρ_k. $D_{KL,k}$ is given by:

$$D_{KL,k}(\rho_{k-1}\|\rho_k) = -\sum_i \rho_{k-1,i}\, log\left(\frac{\rho_{k,i}}{\rho_{k-1,i}}\right), \tag{10}$$

allowing to determine how much information is gained by narrowing the search. In Figure 2, the Pareto front is depicted (green points), along with the endoreversible curve for η, P, and $\dot{S}$ (dashed line), obtained from the parametric elimination of T_{hw} (T_{cw} is constant for the fixed values of the σ_{hc}, σ_c, τ, and T_h parameters; see Equations (7) and (9)). Notice that even when the endoreversible curve depends on a first constraint (T_{cw} satisfies $\partial P/\partial T_{cw} = 0$), the Pareto front has nothing to do with. Nonetheless, the Pareto front lies over the endoreversible curve, covering the regions from maximum power to maximum efficiency and minimum entropy production. This is consistent with the literature, where the mentioned part of the curve has been denoted as the relevant region for optimization. For optimization purposes, additional figures of merit as compromise functions between these three (such as the Ecological function [41] or the Omega function [42]) will not provide further information to the Pareto front. After all of these considerations, analysis of stability dynamics can be made.

4. Stability Dynamics and Relaxation Times

One goal of this analysis was to recover the previous results obtained in the low-dissipation scheme (with no direct connection to working fluid particularities) and to lay the groundwork for a more direct connection with the properties of the working fluid and design parameters. The perturbations we were interested in involved only those of an external nature. The temperature of the external reservoirs remained constant, as well as the conductances of the heat transfer laws (lastly depending on temperature) for only small variations in the operation regime. To illustrate these points, consider a 2-D piston describing a Carnot cycle. The velocity of the piston will determine the effective temperatures of the isotherms of the particles inside the piston (see [32]). The external control (and its energetic cost) needs to remain constant as the velocity of the piston is not accounted for in the thermodynamic description of the gas inside of it. However, fluctuations in this velocity, as well as possible cyclic variability, will lead to variations in the effective temperatures T_{hw} and T_{cw}. Then, a compromise between the energetic cost of the control and the thermodynamic consequences due to stability is of interest.

A simple approach to tackle this problem is the following: Since the operation regime is entirely defined by T_{hw} and T_{cw}, the dynamics involving only these two variables are to be addressed. Fluctuations in these temperatures will affect the heat exchanged between the working fluid and the external reservoirs, Q_h and Q_c. From a Taylor expansion in the first order, Q_h and Q_c near the MP state can be written in matrix form as:

$$\begin{pmatrix} Q_h - Q_h^* \\ Q_c - Q_c^* \end{pmatrix} = \begin{pmatrix} \frac{\partial Q_h}{\partial T_{hw}}\Big|_* & \frac{\partial Q_h}{\partial T_{cw}}\Big|_* \\ \frac{\partial Q_c}{\partial T_{hw}}\Big|_* & \frac{\partial Q_c}{\partial T_{cw}}\Big|_* \end{pmatrix} \cdot \begin{pmatrix} T_{hw} - T_{hw}^* \\ T_{cw} - T_{cw}^* \end{pmatrix} = \begin{pmatrix} \alpha & 0 \\ \beta & \gamma \end{pmatrix} \cdot \begin{pmatrix} T_{hw} - T_{hw}^* \\ T_{cw} - T_{cw}^* \end{pmatrix} \tag{11}$$

$$\Rightarrow \quad \begin{pmatrix} T_{hw} - T_{hw}^* \\ T_{cw} - T_{cw}^* \end{pmatrix} = -\begin{pmatrix} \frac{1}{\alpha} & 0 \\ -\frac{\beta}{\alpha\gamma} & \frac{1}{\gamma} \end{pmatrix} \cdot \begin{pmatrix} Q_h^* - Q_h \\ Q_c^* - Q_c \end{pmatrix}, \tag{12}$$

where α, β, and γ are the elements of the Jacobian matrix evaluated in the MP state (denoted by $*$). It is noted again that this analysis assumes that the MP state is a steady stationary state. Within the first order scheme [43], the simplest relationship for an autonomous system for the two variables T_{hw} and T_{cw} is:

$$\begin{pmatrix} \dot{T}_{hw} \\ \dot{T}_{cw} \end{pmatrix} = -\begin{pmatrix} A & 0 \\ 0 & B \end{pmatrix} \cdot \begin{pmatrix} T_{hw} - T^*_{hw} \\ T_{cw} - T^*_{cw} \end{pmatrix}, \tag{13}$$

which is a good approximation near a stable point. The coefficients A and B determine the restitution strength (with units of s^{-1}). The bigger they are, the faster the system will return to the steady state. By substituting Equation (12) into Equation (13), with the resulting dynamics:

$$\begin{pmatrix} \dot{T}_{hw} \\ \dot{T}_{cw} \end{pmatrix} = \begin{pmatrix} \frac{A}{\alpha} & 0 \\ -\frac{B\beta}{\alpha\gamma} & \frac{B}{\gamma} \end{pmatrix} \cdot \begin{pmatrix} Q^*_h - Q_h \\ Q^*_c - Q_c \end{pmatrix}. \tag{14}$$

The magnitudes of the relaxation times $t_1 = -1/\lambda_1$ and $t_2 = -1/\lambda_2$ are obtained from the eigenvalues, $\lambda_{1,2}$, of the square matrix in the right-hand side of Equation (14). For the cases $k = 1$ and $k = -1$, they are:

$$\begin{aligned} t_1 &= \begin{cases} \frac{t_h \sigma_c \sigma_{hc}}{A} & k = 1 \\ \frac{t_h \sigma_c \sigma_{hc}\left(1+\tau+2\tau\sqrt{\sigma_{hc}}\right)}{4AT_h^2\tau^2\left(1+\sqrt{\sigma_{hc}}\right)^2} & k = -1, \end{cases} \\ t_2 &= \begin{cases} \frac{t_h \sigma_c \sigma_{hc}\left(1-\sqrt{\tau}\right)}{B\left(\sqrt{\sigma_{hc}}+\sqrt{\tau}\right)} & k = 1 \\ \frac{t_h \sigma_c \sigma_{hc}\left(1+\tau+2\tau\sqrt{\sigma_{hc}}\right)(1-\tau)}{4BT_h^2\tau^2\left(1+\sqrt{\sigma_{hc}}\right)^2} & k = -1. \end{cases} \end{aligned} \tag{15}$$

Due to the units of the two matrices, a K/J unit factor should be accounted for in the final expression on the right-hand side of Equations (15), providing the correct units for the relaxation times (in s). As mentioned before, A and B provide the strength of the restitution dynamics, i.e., if they have large values, then the relaxation times are short. Notice that both the relaxation times and the total entropy generation are proportional to the contact time t_h; then, S can be used to define a characteristic time scale for relaxation. Since there are no reasons to provide a preferred relaxation in the heat exchange Q_c or Q_h, it can be assumed that $t_1 = t_2$ (this requirement can be tuned according to the specific conditions of a heat device at hand). Additionally, when looking for stability of a cyclic process, it is desirable that the stability is achieved in times shorter than those of the operation time; that is:

$$t_1 + t_2 = 2t_1 \leq t_h + t_c = t_h\left(1 + \frac{t_c}{t_h}\right). \tag{16}$$

From this constraint and Equation (4), the relaxation times are bounded by:

$$t_1 = t_2 \leq \begin{cases} \frac{t_h}{2}\left(1+\sqrt{\sigma_{hc}}\right) & k = 1 \\ \frac{t_h\left(1+\sqrt{\sigma_{hc}}\right)\left(1+\tau\sqrt{\sigma_{hc}}\right)}{2+\sqrt{\sigma_h \tilde{c}}(1+\tau)} & k = -1, \end{cases} \tag{17}$$

where the equality corresponds to the case where $t_c + t_h = t_1 + t_2$. From now on, equality is assumed. Then, the resulting dynamics (Equation (14)) for $k = 1$ are:

$$\begin{aligned}\dot{T}_{hw} &= -\frac{2\sigma_c\sigma_{hc}\left(T_{hw}\left(1+\sqrt{\sigma_{hc}}\right)-T_h\left(\sqrt{\sigma_{hc}}+\sqrt{\tau}\right)\right)}{\left(1+\sqrt{\sigma_{hc}}\right)^2},\\ \dot{T}_{cw} &= -\frac{2\sigma_c\sigma_{hc}T_h\sqrt{\tau}}{1+\sqrt{\sigma_{hc}}}\left(\frac{T_{hw}\left(1+\sqrt{\sigma_{hc}}\right)}{T_h\left(\sqrt{\sigma_{hc}}+\sqrt{\tau}\right)}+\frac{T_{cw}}{T_h\sqrt{\tau}}\left(\frac{T_h}{T_{hw}}-1\right)-\frac{1-\tau+2\left(\sqrt{\sigma_{hc}}+\sqrt{\tau}\right)}{\left(1+\sqrt{\sigma_{hc}}\right)\left(1+\sqrt{\tau}\right)}\right),\end{aligned} \tag{18}$$

and for $k=-1$,

$$\begin{aligned}\dot{T}_{hw} &= -\frac{4\sigma_c\sigma_{hc}}{T_{hw}}\cdot\frac{\left(\frac{T_{hw}}{T_h}\left(\frac{1+\tau}{2\tau}+\sqrt{\sigma_{hc}}\right)-1-\sqrt{\sigma_{hc}}\right)\left(1+\sqrt{\sigma_{hc}}\left(\frac{1+\tau}{2}\right)\right)}{\left(1+\sqrt{\sigma_{hc}}\right)^2\left(1+\tau\sqrt{\sigma_{hc}}\right)},\\ \dot{T}_{cw} &= -\frac{4\sigma_c\sigma_{hc}}{T_{hw}}\cdot\frac{\frac{\tau T_{hw}}{T_h}\left(\frac{1+\tau}{2\tau}+\sqrt{\sigma_{hc}}\right)^2-\left(1+\sqrt{\sigma_{hc}}\right)\left(1+\tau\sqrt{\sigma_{hc}}+\frac{T_{cw}}{T_h}\left(1+\sqrt{\sigma_{hc}}\left(\frac{1+\tau}{2}\right)\right)\right)+\frac{T_{cw}}{T_{hw}}\left(1+\sqrt{\sigma_{hc}}\right)\left(1+\tau\sqrt{\sigma_{hc}}\right)}{\left(1+\sqrt{\sigma_{hc}}\right)^2\left(1+\tau\sqrt{\sigma_{hc}}\right)}.\end{aligned} \tag{19}$$

From these dynamic equations, it is possible to calculate a relaxation velocity, $v=\sqrt{\dot{T}_{hw}^2+\dot{T}_{cw}^2}$ (in K/s), which indicates how fast the system is evolving toward the steady state. In Figure 3, iso-velocity contours are depicted for the $k=\{1,-1\}$ cases. Two trajectories are represented to provide an idea of how fast the system can return to the MP state. In both cases, the operation time is indicated, along with the time of evolution of each curve. As can be seen, 1 or 2 s are enough to drive the system close to the stationary state; meanwhile, the cycle time is approximately 300 s. Another feature in Figure 3 is that far from the steady state, the system evolves faster. Different marks at equal time intervals are placed over the trajectories, and in every case, the system travels a longer distance in the first interval. In both cases, the T_{cw} direction is slower. It can be confirmed that the depicted trajectories evolve more quickly in the horizontal direction, while the final approach is mostly in the vertical direction. Notice also that the $k=-1$ case has the fastest dynamics.

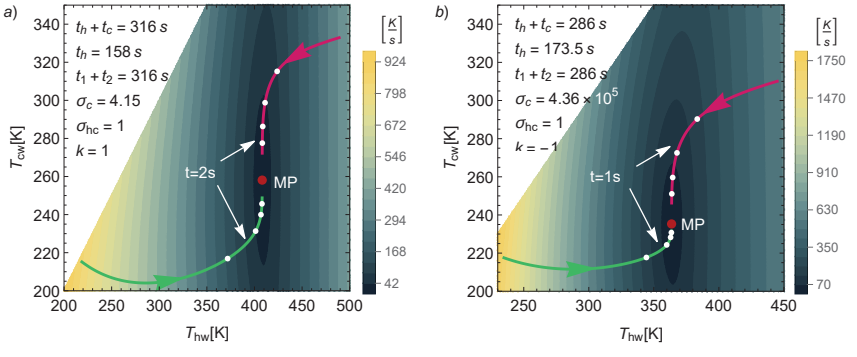

Figure 3. Isocontours of the relaxation velocity for (**a**) the $k=1$ case and (**b**) the $k=-1$ case. The values $T_h=500$ K, $\sigma_{hc}=1$, and $\tau=0.4$ were fixed. As in Figure 2, σ_c and t_h were chosen (for representation/comparison purposes) in such a way that the MP was 70 W and the entropy at MP was 70 J/K in both cases. By fixing S at MP conditions, a time scale for t_h was established, and therefore, a scale for the relaxation time. The qualitative behavior for the other values of S was similar to the one presented here.

5. Thermodynamics of the Relaxation Trajectories

From the analysis of the evolution of trajectories toward the steady state, it is not obvious which energetic implications arise. To address this issue, the dynamic equations were numerically solved. Several trajectories with a starting point within a radius of 30 K (in the T_{hw}–T_{cw} space) from the MP state were analyzed. Then, these trajectories were mapped into the energetic space (η, P, and $\dot{S}$).

As it can be checked in Equations (4), (17) and (18), the conductance ratio σ_{hc} plays a key role both in the dynamic equations and in the energetic properties of the system. In this regard, it is noted that the limits $\sigma_{hc} \to \{0, \infty\}$ are not physical from a dynamic point of view. For both the $k = \{-1, 1\}$ cases, the limit $\sigma_{hc} \to 0$ leads to null power output P, entropy S (Equation (5)), and also null restitution strengths (see Equation (18)), i.e., $\{P, S, A, B\} \to 0$; thus, there is no power output and there are no restitution forces. In comparison, the limit $\sigma_{hc} \to \infty$ leads to $\{S, A, B\} \to \infty$; thus, there is an infinite entropy generation and infinite restitution forces. For this reason, in the present analysis, the more realistic cases $\sigma_{hc} = \{10^{-6}, 1, 10^{6}\}$ were considered.

In Figure 4, the four rows display the trajectories obtained from numerically solving the dynamics in Equation (18) for the $k = 1$ case. The first row displays the trajectories in the T_{hw} and T_{cw} space, while the next rows show, respectively, the mapping of the same trajectories over the η–P, $\dot{S}$–P, and $\dot{S}$–η spaces. The three columns are for the abovementioned representative conductance values: (a) $\sigma_{hc} = 10^{-6}$, (b) $\sigma_{hc} = 1$, and (c) $\sigma_{hc} = 10^{6}$. In the first row, according to the initial state in each trajectory, a clock hour analogy was used; in this way, the purple line corresponds to 12 o'clock and red line to 3 o'clock. The Pareto optimal set is displayed (green points), together with some iso-velocity contours. The white curve indicates the position of the MP state as σ_{hc} varies from 0 to ∞. All of these points produce the same efficiency at MP given by $\eta^* = \eta_{CAN}$. For the rest of the rows, the Pareto front and the endoreversible curve are presented as well. Note also that in the three configurations (columns), the total operation time is the same, but the t_c/t_h (and σ_c) ratio varies, as can be seen in the legend in each case. This figure reveals several key features:

(a) For a small σ_{hc} (left column), only trajectories between 9 and 3 o'clock are present in the T_{hc}–T_{cw} space (denoted in colors ranging from red to blue). Most of the observed trajectories (especially those with darker colors) evolve to the stable state near the endoreversible curve in such a way that the power and efficiency progressively increase their values, while entropy production decreases (see rows 2–4 in the first column). In other words, the relaxation process mainly drives the system toward a thermodynamic steady state, thereby enhancing the thermodynamic performance of the engine (η and P increase and $\dot{S}$ decreases).

(b) For $\sigma_{hc} = 1$ (second column), the trajectories arriving at the stable point from all directions are clearly observed. Those in darker colors (from 9 to 3 o'clock) evolve, as in the above case, but closer to the endoreversible curve, showing an increase in power and efficiency and a decrease in entropy generation. In contrast, the trajectories denoted in colors ranging from orange to green (between 3 and 7 o'clock) evolve to the steady state near the Pareto front, with an increase in power output but a decrease in efficiency and higher entropy production. Note also in this configuration how the relaxation is well balanced between the trajectories approaching the endoreversible limit on the Pareto front side and to the other side. However, the curves near the Pareto front are longer, meaning that random perturbations tend to favor a locus directed toward the Pareto front.

(c) For a large σ_{hc} (last column), the trajectories evolve directly toward the endoreversible curve first. In this part of the trajectory, η, P, and $\dot{S}$ are enhanced simultaneously. Later on, the system evolves to the steady state, either through the endoreversible limit or the Pareto front.

(d) Although the sizes of the perturbations in the T_{hw}–T_{cw} space are the same, the case with the small σ_{hc} allows larger variations of power output, while the case where $\sigma_{hc} = 1$ exhibits the smallest fluctuations in the η–$\dot{S}$ plane.

(e) The relaxation times (Equation (17)) are directly proportional to t_h, and from the expressions of P, η, and S (see Equation (5)), only entropy generation depends on t_h. Thus, the characteristic time scale of the relaxation is linked to the entropy scale of the system, a feature that connects the stability with the thermodynamics of the system. In this entropy–control point of view, the dynamics for the small values of σ_{hc} in the left column apply to greater t_h values and, as a consequence, when the contact time of the heat engine with the cold reservoir is small. On the contrary, the dynamics for the large values of σ_{hc} in the right column apply to smaller t_h values, i.e., when the contact time of the heat engine with the cold reservoir is large.

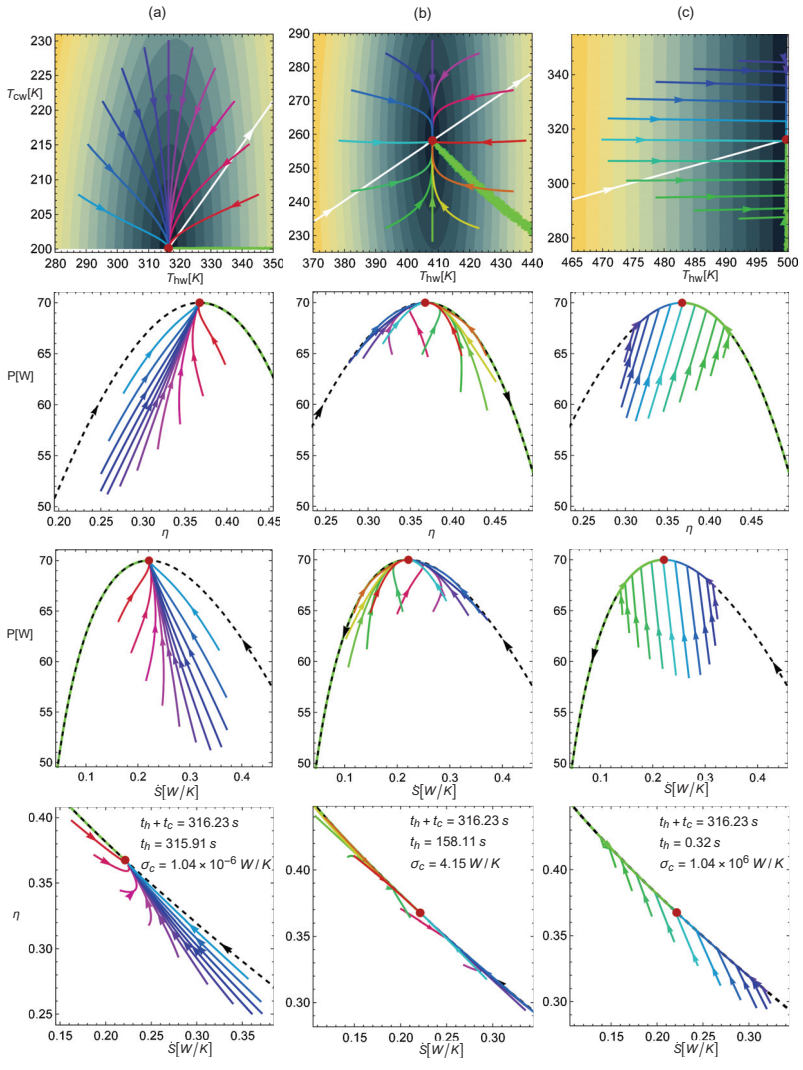

Figure 4. Trajectories in the T_{hw}–T_{cw} space and the mapping over the η–P, $\dot{S}$–P, and $\dot{S}$–η spaces for $k = 1$. (**a**) the $\sigma_{hc} = 10^{-6}$ case; (**b**) the $\sigma_{hc} = 1$ case; (**c**) the $\sigma_{hc} = 10^{6}$ case. The values $T_h = 500$ K and $\tau = 0.4$ were fixed. As in Figure 2, σ_c and t_h were chosen (for representation/comparison purposes) in such a way that the MP was 70 W and the entropy at MP was 70 J/K in both cases.

In Figure 5, the corresponding configurations for $k = -1$ are depicted. Notice that the behavior of the trajectories is almost the same as that in the $k = 1$ case, but here, the maximum power stationary state is linked to different efficiencies as σ_{hc} increases from 0 to ∞. In particular, when $\sigma_{hc} \to 0$, the efficiency at maximum power is $\eta^* = \frac{1-\tau}{2} = \frac{\eta_c}{2}$; when $\sigma_{hc} \to 1$, $\eta^* = \frac{2(1-\tau)}{3+\tau} = \frac{2\eta_C}{4-\eta_C}$; when $\sigma_{hc} \to \infty$, $\eta^* = \frac{1-\tau}{1+\tau} = \frac{\eta_C}{2-\eta_C}$. The dynamics for different σ_{hc} are no longer linked to equal operation times $t_c + t_h$. Another difference is that the relaxation times are noticeably smaller and, therefore, the restitution forces are stronger. Additionally, as σ_{hc} decreases (η^* also decreases), the same temperature perturbations lead to the farthest starting points in the energetic planes. In this way, the case of tlarge σ_{hc} (with a high efficiency) is the one with the smallest

drops in η, P, and $\dot{S}$ (with shorter trajectories). This suggests that the system becomes more stable as the efficiency in the steady state increases.

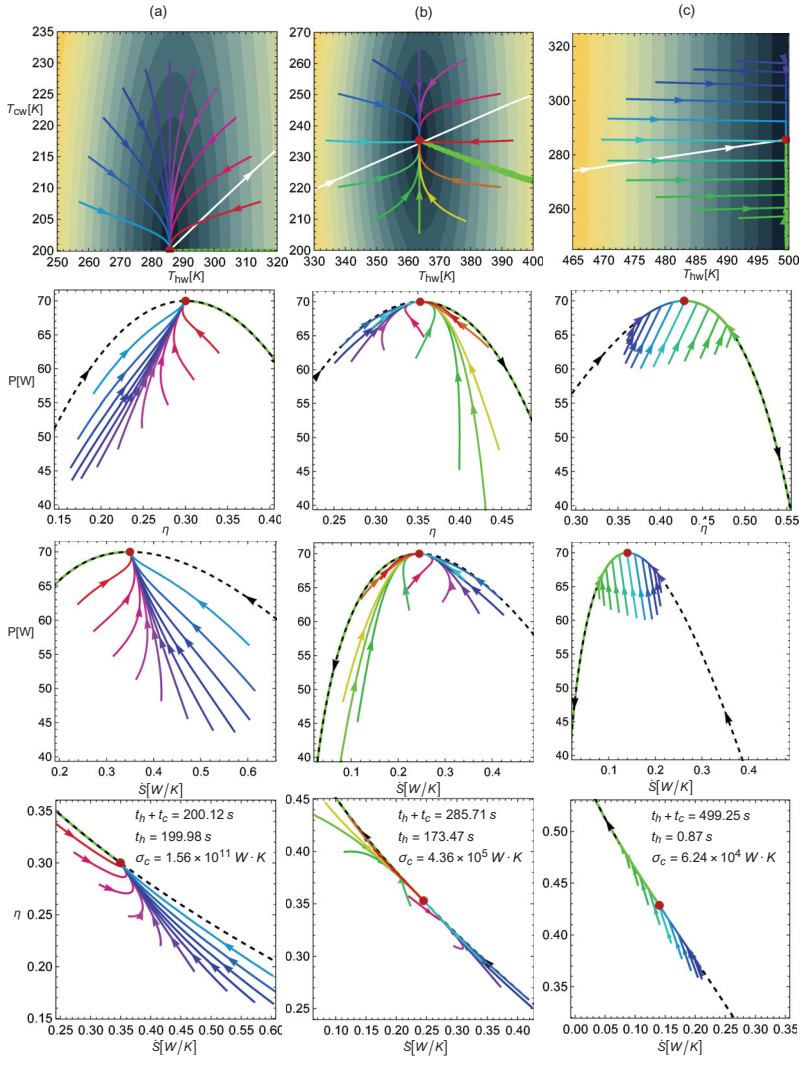

Figure 5. Trajectories in the T_{hw}–T_{cw} space and mapping over the η–P, $\dot{S}$–P, and $\dot{S}$–η spaces for $k = -1$. In column (**a**) the $\sigma_{hc} = 10^{-6}$ case; (**b**) the $\sigma_{hc} = 1$ case; (**c**) the $\sigma_{hc} = 10^{6}$ case. The values $T_h = 500$ K and $\tau = 0.4$ were fixed. As in Figure 2, σ_c and t_h were chosen (for representation/comparison purposes) in such a way that the MP was 70 W and the entropy at MP was 70 J/K in both cases.

6. Concluding Remarks

It was shown that the Pareto front, which represents the best compromise among power output, efficiency, and entropy generation is related to endoreversible behavior, obtained herein by analyzing the Newton and phenomenological heat transfer laws in the context of Carnot-like models. These findings corroborate those obtained in the low-dissipation scheme.

A set of dynamic equations were found based only on the assumption that the endoreversible heat engine has a stationary state and from a Taylor expansion of the input/output heat fluxes in the first order. A relationship between relaxation times and total operation time was obtained. It was shown that the trajectories that lead the system back to the stationary state require much shorter times than the cycle time, allowing the system to work under continuous cyclic operation.

Mapping of the relaxation trajectories into the energetic space allowed for an analysis of the performance consequences of stability. The degree of symmetry of the conductance ratio in the input/output heat exchange is the main valuable factor for stability dynamics. For small σ_{hc} values, the thermodynamic trajectories improve the efficiency and power values with a decrease in entropy generation, evolving near the endoreversible behavior. For larger σ_{hc} values, the first part of the thermodynamic trajectories improve the efficiency and power values with a decrease in entropy generation, evolving toward the endoreversible behavior and the Pareto front. In between these two situations, i.e., for equal conductance values, ($\sigma_{hc} = 1$) trajectories with decreasing efficiencies and increasing entropy generation can be found, with a preference for evolving near the Pareto front.

In summation, the stability of the irreversible Carnot-like heat engine exhibits two interesting behaviors in which the fluctuations around the stationary state (due to external perturbations) would likely maintain the system in an optimum state, or produce self-optimization induced by the stability. A biased control of the operation parameters could result in an economic saving, as energy is needed for the fine-tuning of parameter control. Finally, in this work the thermodynamic functions that were selected as the most relevant for this heat engine model were η, P, and $\dot{S}$. It is very likely that by analyzing different stationary states, such as those predicted by the compromise Ecological [41] or Omega [42] operation performances, the role of the Pareto front would be more evident, as occurred in the case of the low-dissipation heat engine and refrigerator [1,2].

Another valuable remark is that the total entropy generation defines a time scale for both the operation and relaxation times. Finally, this analysis laid down the grounds to analyze heat devices dependent on working fluid properties, where the endoreversible hypothesis plays a relevant role. Especially when the thermalization mechanisms are fast enough compared to the cycle time in agreement with local equilibrium. This allows to incorporate, in a straightforward way, stochastic-type perturbations into the analysis through additive noise in Equation (14).

Author Contributions: The authors contributed equally to the paper. All authors have read and agreed to the published version of the manuscript.

Funding: Junta de Castilla y León, Project No. SA017P17; J.G.A. acknowledges partial financial support from Instituto Universitario de Física Fundamental y Matemáticas (IUFFyM) at Universidad de Salamanca.

Conflicts of Interest: The authors declare no conflict of interest.

References

1. Gonzalez-Ayala, J.; Guo, J.; Medina, A.; Roco, J.M.M.; Hernández, A.C. Energetic Self-Optimization Induced by Stability in Low-Dissipation Heat Engines. *Phys. Rev. Lett.* **2020**, *124*, 050603. [CrossRef]
2. Gonzalez-Ayala, J.; Medina, A.; Roco, J.M.M.; Hernández, A.C. Thermodynamic optimization subsumed in stability phenomena. *Sci. Rep.* **2020**, *10*, 14305. [CrossRef]
3. Gonzalez-Ayala, J.; Guo, J.; Medina, A.; Roco, J.M.M.; Hernández, A.C. Optimization induced by stability and the role of limited control near a steady state. *Phys. Rev. E* **2019**, *100*, 062128. [CrossRef]
4. Esposito, M.; Kawai, R.; Lindenberg, K.; van den Broeck, C. Efficiency at maximum power of low-dissipation Carnot engines. *Phys. Rev. Lett.* **2010**, *105*, 150603. [CrossRef] [PubMed]
5. Curzon, F.; Ahlborn, B. Efficiency of a Carnot engine at maximum power output. *Am. J. Phys.* **1975**, *43*, 22. [CrossRef]
6. Berry, R.S.; Salamon, P.; Andresen, B. How It All Began. *Entropy* **2020**, *22*, 908. [CrossRef]
7. Gonzalez-Ayala, J.; Roco, J.M.M.; Medina, A.; Hernández, A.C. Carnot-like heat engines versus low-dissipation models. *Entropy* **2017**, *19*, 182. [CrossRef]

8. Johal, R.S. Heat engines at optimal power: Low-dissipation versus endoreversible model. *Phys. Rev. E* **2017**, *96*, 012151. [CrossRef]
9. Gonzalez-Ayala, J.; Medina, A.; Roco, J.M.M.; Hernández, A.C. Entropy generation and unified optimization of Carnot-like and low-dissipation refrigerators. *Phys. Rev. E* **2018**, *97*, 022139. [CrossRef]
10. Santillán, M.; Maya, G.; Angulo-Brown, F. Local stability analysis of an endoreversible Curzon-Ahborn-Novikov engine working in a maximum-power-like regime. *J. Phys. D* **2001**, *34*, 2068. [CrossRef]
11. Guzmán-Vargas, L.; Reyes-Ramírez, I.; Sánchez, N. The effect of heat transfer laws and thermal conductances on the local stability of an endoreversible heat engine. *J. Phys. D* **2005**, *38*, 1282. [CrossRef]
12. Chimal-Eguia, J.; Guzmán-Vargas, L.; Reyes-Ramírez, I. Local Stability of an Endoreversible Heat Engine Working in an Ecological Regime. *Open Syst. Inf. Dyn.* **2007**, *14*, 411. [CrossRef]
13. Huang, Y.; Sun, D.; Kang, Y. Local stability characteristics of a non-endoreversible heat engine working in the optimum region. *Appl. Therm. Eng.* **2009**, *29*, 358. [CrossRef]
14. Ladino-Luna, D.; Portillo-Díaz, P.; Páez-Hernández, R.T. Local Stability of Curzon-Ahlborn Cycle with Non-Linear Heat Transfer for Maximum Power Output Regime. *J. Mod. Phys.* **2013**, *4*, 22. [CrossRef]
15. Reyes-Ramírez, I.; Barranco-Jiménez, M.; Rojas-Pacheco, A.; Guzmán-Vargas, L. Global Stability Analysis of a Curzon–Ahlborn Heat Engine under Different Regimes of Performance. *Entropy* **2014**, *16*, 5796. [CrossRef]
16. Reyes-Ramírez, I.; Barranco-Jiménez, M.; Rojas-Pacheco, A.; Guzmán-Vargas, L. Global stability analysis of a Curzon–Ahlborn heat engine using the Lyapunov method. *Physica A* **2014**, *399*, 98. [CrossRef]
17. Chen, L.; Wu, X.; Xiao, Q.; Ge, Y.; Sun, F. Local stability of a generalized irreversible heat engine with linear phenomenological heat transfer law working in an ecological regime. *Ther. Sci. Eng. Prog.* **2018**, *8*, 537–541. [CrossRef]
18. Valencia-Ortega, G.; Levario-Medina, S.; Barranco-Jiménez, M.A. Local and global stability analysis of a Curzon-Ahlborn model applied to power plants working at maximum κ-efficient power. *arXiv* **2020**, arXiv:2005.10397.
19. Barranco-Jiménez, M.; Sánchez-Salas, N.; Reyes-Ramírez, I. Local Stability Analysis for a Thermo-Economic Irreversible Heat Engine Model under Different Performance Regimes. *Entropy* **2015**, *17*, 8019. [CrossRef]
20. Huang, Y.; Sun, D.; Kang, Y. Local stability analysis of a class of endoreversible heat pumps. *J. Appl. Phys.* **2007**, *102*, 034905. [CrossRef]
21. Huang, Y.; Sun, D. The effect of cooling load and thermal conductance on the local stability of an endoreversible refrigeratorImpact de la charge thermique et de la conductivité thermique sur la stabilité locale d'un réfrigérateur endoréversible. *Int. J. Refrig.* **2008**, *31*, 483. [CrossRef]
22. Nie, W.; He, J.; Yang, B.; Qian, X. Local stability analysis of an irreversible heat engine working in the maximum power output and the maximum efficiency. *Appl. Therm. Eng.* **2008**, *28*, 699. [CrossRef]
23. Nie, W.; He, J.; Deng, X. Local stability analysis of an irreversible Carnot heat engine. *Int. J. Therm. Sci.* **2008**, *47*, 633. [CrossRef]
24. Huang, Y. Local asymptotic stability of an irreversible heat pump subject to total thermal conductance constraint. *Energy Convers. Manag.* **2009**, *50*, 1444. [CrossRef]
25. He, J.; Miao, G.; Nie, W. Local stability analysis of an endoreversible Carnot refrigerator. *Phys. Scr.* **2010**, *82*, 025002. [CrossRef]
26. Wouagfack, P.A.N.; Keune, G.F.; Tchinda, R. Local stability analysis of an irreversible refrigerator working at the maximum thermo-ecological functions: A comparison. Analyse de la stabilité locale d'un réfrigérateur irréversible fonctionnant au maximum de ses fonctions thermo-écologiques: Une comparaison. *Int. J. Refrig.* **2017**, *75*, 38. [CrossRef]
27. Lü, K.; Nie, W.; He, J. Dynamic robustness of endoreversible Carnot refrigerator working in the maximum performance per cycle time. *Sci. Rep.* **2018**, *8*, 12638. [CrossRef]
28. Sekulic, D.P. A fallacious argument in the finite time thermodynamics concept of endoreversibility. *J. Appl. Phys.* **1998**, *83*, 4561. [CrossRef]
29. Andresen, B. Comment on "A fallacious argument in the finite time thermodynamic concept of endoreversibility" [J. Appl. Phys. 83, 4561 (1998)]. *J. Appl. Phys.* **2001**, *90*, 6557. [CrossRef]
30. Chen, J.; Yan, Z.; Lin, G.; Andresen, B. On the Curzon–Ahlborn efficiency and its connection with the efficiencies of real heat engines. *Energy Convers. Manag.* **2001**, *42*, 173. [CrossRef]
31. Gyftopoulos, E.P. On the Curzon–Ahlborn efficiency and its lack of connection to power producing processes. *Energy Convers. Manag.* **2002**, *43*, 609–615. [CrossRef]

32. Rojas-Gamboa, D.A.; Rodríguez, J.I.; Gonzalez-Ayala, J.; Angulo-Brown, F. Ecological efficiency of finite-time thermodynamics: A molecular dynamics study. *Phys. Rev. E* **2018**, *98*, 022130. [CrossRef] [PubMed]
33. Izumida, Y.; Okuda, K. Molecular kinetic analysis of a finite-time Carnot cycle. *EPL* **2008**, *83*, 60003. [CrossRef]
34. Izumida, Y.; Okuda, K. Molecular kinetic analysis of a local equilibrium Carnot cycle. *Phys. Rev. E* **2017**, *96*, 012123. [CrossRef] [PubMed]
35. Muschik, W.; Hoffmann, K.H. Modeling, Simulation, and Reconstruction of 2-Reservoir Heat-to-Power Processes in Finite-Time Thermodynamics. *Entropy* **2020**, *22*, 997. [CrossRef]
36. Agrawal, D.C.; Gordon, J.M.; Huleihil, M. Endoreversible engines with finite-time adiabats. *Indian J. Eng. Mater. Sci.* **1994**, *1*, 195–198.
37. Hernandez, A.C.; Roco, J.M.M.; Medina, A.; Velasco, S.; Guzmán-Vargas, L. The maximum power effciency $1-\sqrt{\tau}$: Research, education, and bibliometric relevance. *Eur. Phys. J. Spec. Top.* **2015**, *224*, 809–823. [CrossRef]
38. Deb, K. *Multi-Objective Optimization Using Evolutionary Algorithms*; John Wiley & Sons, Inc.: New York, NY, USA, 2001; ISBN 978-0-471-87339-6.
39. Kullback, S.; Leibler, R.A. On information and sufficiency. *Ann. Math. Stat.* **1951**, *22*, 79–86. [CrossRef]
40. Venables, W.N.; Ripley, B.D. *Modern Applied Statistics with S*; Springer: New York, NY, USA, 2002.
41. Angulo-Brown, F. An ecological optimization criterion for finite-time heat engines. *J. Appl. Phys.* **1991**, *69*, 7465. [CrossRef]
42. Hernández, A.C.; Medina, A.; Roco, J.M.M.; White, J.A.; Velasco, S. Unified optimization criterion for energy converters. *Phys. Rev. E* **2001**, *63*, 037102. [CrossRef]
43. Strogatz, S.H. *Nonlinear Dynamics and Chaos: With Applications to Physics, Biology, Chemistry, and Engineering*; Westview Press: Boulder, CO, USA, 2014.

entropy

MDPI

Article

Endoreversible Models for the Thermodynamics of Computing

Alexis De Vos

Vakgroep elektronika en informatiesystemen, Universiteit Gent, Technologiepark 126, B-9052 Gent, Belgium; alexis.devos@ugent.be

Received: 20 May 2020; Accepted: 10 June 2020; Published: 15 June 2020

Abstract: Landauer's principle says that, in principle, a computation can be performed without consumption of work, provided no information is erased during the computational process. This principle can be introduced into endoreversible models of thermodynamics.

Keywords: macroentropy; microentropy; endoreversible engine; reversible computing; Landauer's principle

1. Introduction

Thermodynamics of computing has a peculiar history. Many years, scientists have searched for the minimum energy needed to perform an elementary computing step. It was Landauer [1–4] who demonstrated in the period 1960–1990 that, in principle, computing can be performed without energy consumption, provided the computing process applies exclusively logically reversible computing steps. As long as information is not destroyed and computing is performed infinitely slowly, no work has to be supplied to the computer. Only erasure of information requires energy input. It is remarkable that we had to wait until the period 2012–2018 to have experimental confirmation [5–8] of Landauer's principle.

Basic thermodynamics, i.e., the Carnot theory, describes thermal engines acting infinitely slowly. In 1975, Curzon and Ahlborn [9] presented a thermodynamical model for an engine working at non-zero speed: the endoreversible engine. It consists of a reversible core, performing the actual conversion (of heat into work) and two irreversible channels for the heat transport. The approach turned out to be very fruitful: not only processes in engineering, but also in physics, chemistry, economics, etc. can successfully profit from endoreversible modelling, especially when processes happen at non-zero speed and thus tasks are performed in a finite time [10,11].

The present paper is an attempt to apply the endoreversible scheme to the Landauer principle, thus to thermodynamically describe computing at a non-zero speed.

2. Logic Gates

Any computer is built from basic building blocks, called gates. In a conventional electronic computer, such building block is e.g., a `not` gate, an `or` gate, a `nor` gate, an `and` gate, a `nand` gate, etc. Such gate has both a short input (denoted with subscript 1) and a short output (denoted with subscript 2). As an example, Table 1a defines the `and` gate, by means of its truth table. We see an input word A_1B_1 and the corresponding output word A_2. If the input word is given, the table suffices to read what the output 'will be'. If, however, the value of the output word is given, this information is not sufficient to recover what the input word 'has been'. Indeed, output $A_2 = 0$ can equally well be the result of either $A_1B_1 = 00$ or $A_1B_1 = 01$, or $A_1B_1 = 10$. For this reason, we say that the gate is logically irreversible. In contrast, the `not` gate is logically reversible, as can be verified from its truth table in Table 1b. Indeed, knowledge of A_1 suffices to know A_2, but also: knowledge of A_2 suffices to know A_1.

Table 1. Truth tables of two conventional logic gates: (**a**) the `and` gate and (**b**) the `not` gate.

(**a**)		
$\mathbf{A}_1$	$\mathbf{B}_1$	$\mathbf{A}_2$
0	0	0
0	1	0
1	0	0
1	1	1
(**b**)		
	$\mathbf{A}_1$	$\mathbf{A}_2$
	0	1
	1	0

We not only can distinguish logically irreversible gates from logically reversible gates. We also can quantify how strongly a gate is irreversible. For this purpose, we apply Shannon's entropy:

$$S = -k \sum q_i \log(q_i) \,,$$

where k is Boltzmann's constant and q_i is the probability that a word $ABC...$ (either an input word $A_1B_1C_1...$ or an output word $A_2B_2C_2...$) has a particular value. As an example, we examine Table 1a in detail. Let $(q_{00})_1$ be the probability that input word A_1B_1 equals 00, let $(q_{01})_1$ be the probability that A_1B_1 equals 01, let $(q_{10})_1$ be the probability that it equals 10, and let $(q_{11})_1$ be the probability that it equals 11. We, of course, assume $0 \leq (q_i)_1 \leq 1$ for all i, as well as $\sum(q_i)_1 = 1$. Let $(q_0)_2$ be the probability that output word A_2 equals 0 and let $(q_1)_2$ be the probability that A_2 equals 1. Inspection of Table 1a reveals that

$$\begin{aligned} (q_0)_2 &= (q_{00})_1 + (q_{01})_1 + (q_{10})_1 \\ (q_1)_2 &= (q_{11})_1 \,. \end{aligned}$$

Automatically, we have $0 \leq (q_i)_2 \leq 1$ for both i, as well as $\sum(q_i)_2 = 1$. We now compare the entropies of input and output:

$$\begin{aligned} S_1 &= -k \sum (q_i)_1 \, \log\left((q_i)_1\right) \\ S_2 &= -k \sum (q_i)_2 \, \log\left((q_i)_2\right) \,. \end{aligned}$$

We find that these two quantities are not necessarily equal. For example, if the inputs 00, 01, 10, and 11 are equally probable, i.e., if

$$(q_{00})_1 = (q_{01})_1 = (q_{10})_1 = (q_{11})_1 = 1/4 \,,$$

then we have

$$(q_0)_2 = 3/4 \;\text{ and }\; (q_1)_2 = 1/4 \,,$$

such that

$$\begin{aligned} S_1 &= 2\,k \log(2) = 2\,b \\ S_2 &= \left[2 - \frac{3\log(3)}{4\log(2)}\right] k \log(2) \approx 0.811\,b \,, \end{aligned}$$

where $b = k\log(2)$ is called 'one bit of information'. Thus, evolving from input to output is accompanied by a loss of entropy $S_1 - S_2$ of about 1.189 bits. A similar examination of Table 1b leads to $S_1 = S_2 = 1\,b$. Thus, both input and output contain one bit of information. There is no change in entropy: $S_1 - S_2 = 0$.

A reversible computer is a computer exclusively built from reversible logic gates [12,13]. As among the conventional logic gates, only the `not` gate is logically reversible, we need to introduce unconventional reversible gates, in order to be able to build a general-purpose reversible computer. Table 2 shows two examples: the `controlled not` gate (a.k.a. the `Feynman` gate) and the `controlled controlled not` gate (a.k.a. the `Toffoli` gate). The truth table of the `controlled not` gate has the following properties:

$$\begin{aligned} (q_{00})_2 &= (q_{00})_1 \\ (q_{01})_2 &= (q_{01})_1 \\ (q_{10})_2 &= (q_{11})_1 \\ (q_{11})_2 &= (q_{10})_1 \,, \end{aligned}$$

such that $\sum (q_i)_2 \log((q_i)_2) = \sum (q_i)_1 \log((q_i)_1)$ and thus $S_2 = S_1$. This result is true whatever the values of the input probabilities $(q_{00})_1$, $(q_{01})_1$, $(q_{10})_1$, and $(q_{11})_1$, thus not only if these four numbers all are equal to $1/4$. The reason of this property is clear: the output words A_2B_2 of Table 2a are merely a permutation of the input words A_1B_1. Analogously, in Table 2b, the output words $A_2B_2C_2$ form a permutation of the input words $A_1B_1C_1$. Therefore, the `controlled controlled not` gate also satisfies $S_2 = S_1$ and hence is logically reversible.

Table 2. Truth tables of two reversible logic gates: (**a**) the `controlled not` gate and (**b**) the `controlled controlled not` gate.

(**a**)			
$\mathbf{A_1}$	$\mathbf{B_1}$	$\mathbf{A_2}$	$\mathbf{B_2}$
0	0	0	0
0	1	0	1
1	0	1	1
1	1	1	0

(**b**)					
$\mathbf{A_1}$	$\mathbf{B_1}$	$\mathbf{C_1}$	$\mathbf{A_2}$	$\mathbf{B_2}$	$\mathbf{C_2}$
0	0	0	0	0	0
0	0	1	0	0	1
0	1	0	0	1	0
0	1	1	0	1	1
1	0	0	1	0	0
1	0	1	1	0	1
1	1	0	1	1	1
1	1	1	1	1	0

Figure 1 shows a c-MOS (i.e., complementary metal–oxide–semiconductor) implementation of these two reversible gates in a silicon chip.

The reader may easily verify that, in general, we are allowed to summarize as follows:

- if the logic gate is logically reversible, then entropy is neither increased nor decreased;
- if the logic gate is logically irreversible, then entropy is decreased.

Of course, in the framework of the second law, any entropy decrease sounds highly suspicious. The next section will demonstrate that fortunately there is no need to worry.

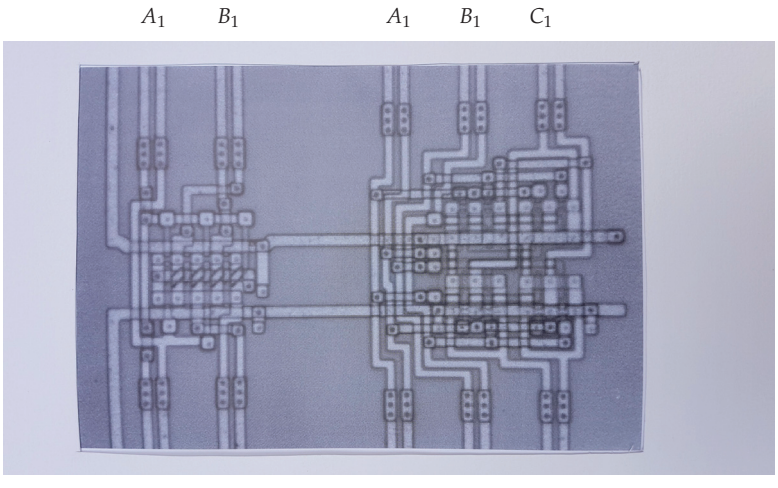

Figure 1. Silicon c-MOS inplementation of two reversible logic gates: (**a**) the `controlled not` gate and (**b**) the `controlled controlled not` gate.

3. Macroentropy and Microentropy

Let the phase space of a system be divided into N parts. Let p_m be the probability that the system finds itself in part # m of the phase space. Then, the entropy of the system is

$$\sigma = -k \sum_{m=1}^{N} p_m \log(p_m) \, . \tag{1}$$

Figure 2a shows an example with $N = 15$.

We now assume that the division of phase space happens in two steps. First, we divide it into M large parts (with $M \ll N$), called macroparts. Then, we divide each macropart into microparts: macropart # 1 into n_1 microparts, macropart # 2 into n_2 microparts, ..., and macropart # M into n_M microparts:

$$n_1 + n_2 + ... + n_M = N \, .$$

We denote by $p_{i,j}$ the probability that the system is in microcell # j of macrocell # i. Let q_i be the probability that the system finds itself in macropart # i:

$$q_i = \sum_{j=1}^{n_i} p_{i,j} \, .$$

Figure 2b shows an example with $N = 15$ and $M = 4$ ($n_1 = 4$, $n_2 = 5$, $n_3 = 3$, and $n_4 = 3$); Figure 2c shows an example with $N = 15$ and $M = 2$ ($n_1 = 12$ and $n_2 = 3$).

Let σ be the entropy of the system consisting of the M macrocells. We have

$$\sigma = -k \sum_{i=1}^{M} \sum_{j=1}^{n_i} p_{i,j} \log(p_{i,j}) \, . \tag{2}$$

One can easily check that this expression can be written as

$$\sigma = -k\sum_{i=1}^{M} q_i \log(q_i) - k\sum_{i=1}^{M} q_i \sum_{j=1}^{n_i} \frac{p_{i,j}}{q_i} \log\left(\frac{p_{i,j}}{q_i}\right) . \tag{3}$$

The former contribution to the rhs of Equation (3) is called the macroentropy S, whereas the latter contribution is called the microentropy s. We identify the macroentropy with the information entropy of Section 2. We associate the microentropy with the heat Q, i.e., with the energy exchange which would occur, if the microentropy enters or leaves the system at temperature T, according to the Gibbs formula

$$s = \frac{Q}{T} .$$

Hence:

$$\sigma = S + \frac{Q}{T} .$$

This decomposition can be expressed in several ways:

$$\begin{aligned} \text{total entropy} &= \text{macroentropy} + \text{microentropy} \\ &= \text{Shannon entropy} + \text{Gibbs entropy} \\ &= \text{information entropy} + \text{heat entropy} . \end{aligned}$$

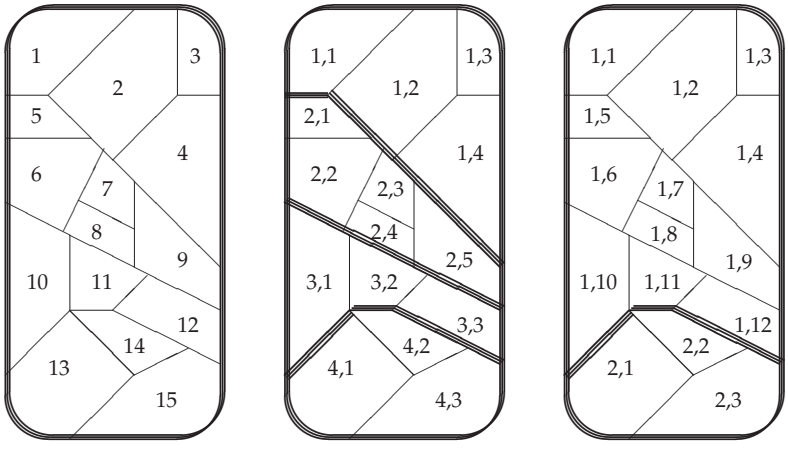

(**a**) (**b**) (**c**)

Figure 2. A same phase space divided into three different numbers M of macrocells: (**a**) $M = 1$; (**b**) $M = 4$; and (**c**) $M = 2$.

We now assume that the probabilities of being in a particular microcell is the same in the three cases of Figure 2. For example, p_6 of Figure 2a equals both $p_{2,2}$ of Figure 2b and $p_{1,6}$ of Figure 2c. Then, Equations (1) and (2) tell us that the entropy σ is the same in the three cases:

$$\sigma_a = \sigma_b = \sigma_c .$$

Assuming all probabilities $p_{i,j}$ are non-zero, it is clear that the macroentropies satisfy

$$0 = S_a < S_c < S_b .$$

Therefore, the microentropies satisfy

$$\sigma = s_a > s_c > s_b \,.$$

In particular, the inequality $S_c < S_b$ corresponds with the inequality $S_2 < S_1$ in Section 2 for the and gate in Table 1a. Indeed: Figure 2b corresponds with the left part of the truth table, whereas Figure 2c corresponds with the right part of the table. The decrease of macroentropy ($S_2 < S_1$) thus is compensated by the increase of microentropy ($s_2 > s_1$), leading to $\sigma_2 = \sigma_1$, thus saving the second law: $\sigma_2 \geq \sigma_1$.

4. Reversible Engine

Figure 3a is the classical model of the Carnot engine, consisting of

- a heat reservoir at temperature T_1, providing a heat Q_1,
- a heat reservoir at temperature T_2, absorbing a heat Q_2, and
- a reversible convertor, generating the work E.

For our purpose, we provide each reservoir with a second parameter, i.e., the macroentropy S. See Figure 3b.

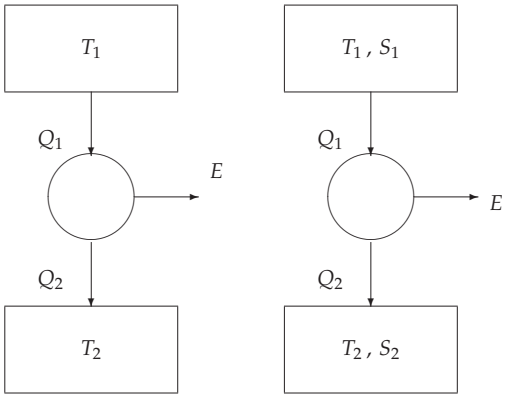

Figure 3. Core engines: (**a**) basic model and (**b**) extended model.

We write the two fundamental theorems of reversible thermodynamics:

- conservation of energy: the total energy leaving the convertor is zero:

$$-Q_1 + E + Q_2 = 0 \,;$$

- conservation of entropy: the total entropy leaving the convertor is zero:

$$-\left(\frac{Q_1}{T_1} + S_1\right) + 0 + \left(\frac{Q_2}{T_2} + S_2\right) = 0 \,.$$

Eliminating the variable Q_2 from the above two equations yields

$$E = \left(1 - \frac{T_2}{T_1}\right) Q_1 + (S_2 - S_1)\, T_2 \,. \tag{4}$$

We can distinguish two special cases (Figure 4):

- If $S_2 = S_1$, then we obtain from Equation (4) that

$$E = \left(1 - \frac{T_2}{T_1}\right) Q_1 \,,$$

known as Carnot's law.
- If $T_2 = T_1$ (say T), then we obtain from (4) that

$$E = (S_2 - S_1)\, T \,,$$

known as Landauer's law.

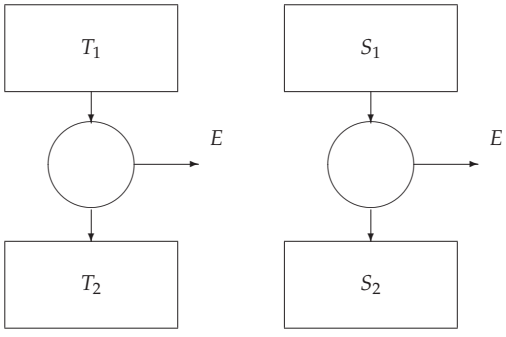

Figure 4. Core engines: (**a**) the Carnot engine and (**b**) the Landauer engine.

We thus retrieve, besides Carnot's formula, the priciple of Landauer: if no information is erased ($S_2 = S_1$), then no work E is involved; if information is erased ($S_2 < S_1$), then a negative work E is produced, meaning that we have to supply a positive work $-E$.

We note that, in Figure 4a, the arrows indicate the sence of positive Q_1 (heat leaving the upper heat reservoir) and positive Q_2 (heat entering the lower heat reservoir). Analogously, in Figure 4b, the arrows indicate the sence of positive S_1 (macroentropy leaving the upper memory register) and S_2 (macroentropy entering the lower memory register). In order to actually perform the computation in the positive direction, an external driving force is necessary. The next section introduces this 'arrow of computation'.

5. Reversible Engine Revisited

Information is carried by particles. Therefore, we have to complement the reservoirs of Figure 3b with a third parameter, i.e., the chemical potential μ of the particles. See Figure 5. Besides a heat flow Q, a reservoir also provides (or absorbs) a matter flow N.

In conventional electronic computers, the particles are electrons and holes within silicon and copper. There, the particle flow N is (up to a constant) equal to the electric current I:

$$N = I/q \,,$$

where q is the elementary charge. The chemical potential μ is (up to a constant) equal to the voltage V:

$$\mu = qV \,.$$

In the present model, we maintain the quantities N and μ, in order not to exclude unconventional computing, e.g., computation by means of ions, photons, Majorana fermions, ... or even good old abacus beads.

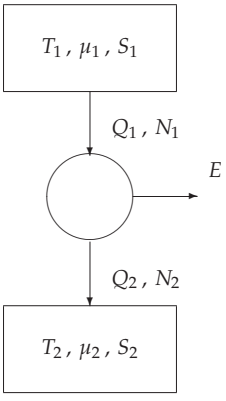

Figure 5. Core engine.

We write the three fundamental theorems of reversible thermodynamics:

- conservation of matter: the total amount of matter leaving the convertor is zero:

$$-N_1 + 0 + N_2 = 0\,;$$

- conservation of energy: the total energy leaving the convertor is zero:

$$-(Q_1 + \mu_1 N_1) + E + (Q_2 + \mu_2 N_2) = 0\,;$$

- conservation of entropy: the total entropy leaving the convertor is zero:

$$-\left(\frac{Q_1}{T_1} + S_1\right) + 0 + \left(\frac{Q_2}{T_2} + S_2\right) = 0\,.$$

The first equation leads to $N_2 = N_1$, which we simply denote by N. Eliminating the variable Q_2 from the remaining two equations yields the output work:

$$E = \left(1 - \frac{T_2}{T_1}\right) Q_1 + (\mu_1 - \mu_2)\, N + (S_2 - S_1)\, T_2\,.$$

We can distinguish three special cases (Figure 6):

- If $\mu_2 = \mu_1$ and $S_2 = S_1$, then we obtain

$$E = \left(1 - \frac{T_2}{T_1}\right) Q_1\,,$$

  i.e., Carnot's law.
- If $T_2 = T_1$ and $S_2 = S_1$, then we obtain

$$E = (\mu_1 - \mu_2)\, N\,,$$

  known as Gibb's law.
- If $T_2 = T_1$ (say T) and $\mu_2 = \mu_1$, then we obtain

$$E = (S_2 - S_1)\, T\,,$$

  i.e., Landauer's principle.

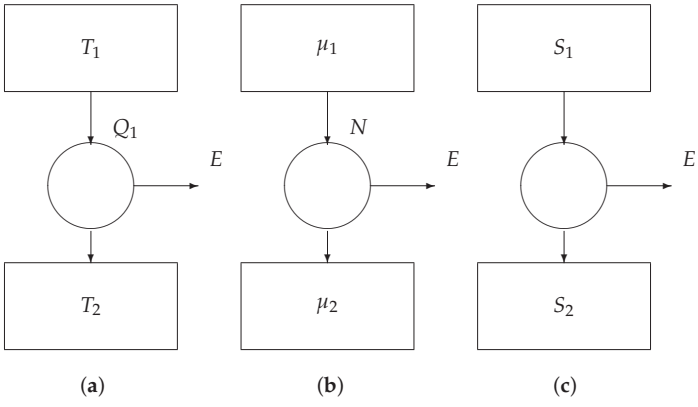

Figure 6. Core engines: (**a**) the Carnot engine, (**b**) the Gibbs engine, and (**c**) the Landauer engine.

6. Irreversible Transport

Figure 7a represents a transport channel between two reservoirs. The upper reservoir has parameter values T', μ', and S'; the lower reservoir has parameter values T'', μ'', and S''. We assume that the computer hardware is at a uniform temperature. Hence, $T'' = T'$ (say T). Furthermore, we assume that $S'' = S'$ (say S). This means, e.g., that noise does not cause random bit errors during the transport of the information. Thus, reservoirs only differ by μ' and μ''. See Figure 7b.

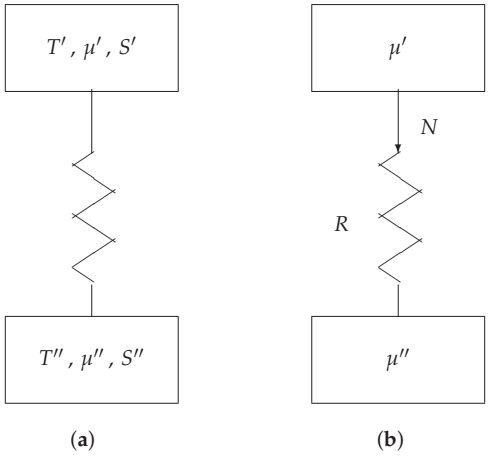

Figure 7. Irreversible transport: (**a**) general model and (**b**) simplified model.

The particle drift N is caused by the difference of the two potentials μ' and μ''. The law governing the current is not necessarily linear. Hence, we have

$$N = \frac{1}{R}\,[\,f(\mu') - f(\mu'')\,]\,,$$

where $f(\mu)$ is an appropriate (monotonically increasing) function of μ and R (called resistance) is a constant depending primarily on the material properties and geometry of the particle channel. Many different functions f are applicable in different circumstances. For example, in classical c-MOS

technology, an electron or hole diffusion process in silicon [14,15] can successfully be modeled by the function

$$f(\mu) = \exp\left(\frac{\mu}{kT}\right) ,$$

such that

$$N = \frac{1}{R}\left[\exp\left(\frac{\mu'}{kT}\right) - \exp\left(\frac{\mu''}{kT}\right)\right] .$$

Below, however, for sake of mathematical transparency, we will apply

$$f(\mu) = \mu ,$$

such that we have a linear transport equation, i.e., Ohm's law:

$$N = \frac{1}{R}\left(\mu' - \mu''\right) .$$

7. Endoreversible Engine

Figure 8 shows an endoreversible computer gate. It consists of

- a core part with reversible gate and
- two transport channels: one for providing the input information and one for draining the output information.

The core is modeled according to Section 5; the two transport channels are modeled according to Section 6. In Figure 8a, the two outermost reservoirs (i.e., the input and output data registers) have fixed boundary conditions: T_1, μ_1, S_1 and T_2, μ_2, S_2, respectively. The inner parameters T_3, μ_3, S_3, T_4, μ_4, and S_4 are variables. In accordance with Section 6, we choose T_3 and S_3 equal to T_1 and S_1, respectively, as well as T_4 and S_4 equal to T_2 and S_2, respectively. Finally, we assume the whole engine is isothermal, such that $T_2 = T_1$. This results in Figure 8b. We thus only hold back as variable parameters the chemical potentials μ_3 and μ_4.

According to Section 5, we have, for the core of the endoreversible engine:

$$E = (\mu_3 - \mu_4)N + (S_2 - S_1)T . \tag{5}$$

According to Section 6, the two transport laws are

$$N = \frac{1}{R_1}(\mu_1 - \mu_3) \tag{6}$$

$$N = \frac{1}{R_2}(\mu_4 - \mu_2) . \tag{7}$$

We remind that, in the present model, the intensive quantities T, μ_1, S_1, μ_2, and S_2 have given values, whereas the quantities μ_3 and μ_4 have variable values. We eliminate the two parameters μ_3 and μ_4 from the three Equations (5)–(7). We thus obtain

$$E(N) = (\mu - RN)\,N + T(S_2 - S_1) ,$$

where $\mu = \mu_1 - \mu_2$ and $R = R_1 + R_2$. The total energy dissipated in the endoreversible engine is

$$F = N\mu_1 - E - N\mu_2 .$$

We thus find

$$F(N) = RN^2 + T(S_1 - S_2) . \tag{8}$$

The former term on the rhs of Equation (8) consists of the energy R_1N^2 dissipated in resistor R_1 and the energy R_2N^2 dissipated in resistor R_2; the latter term is the energy dissipated in the information loss in the core of the engine.

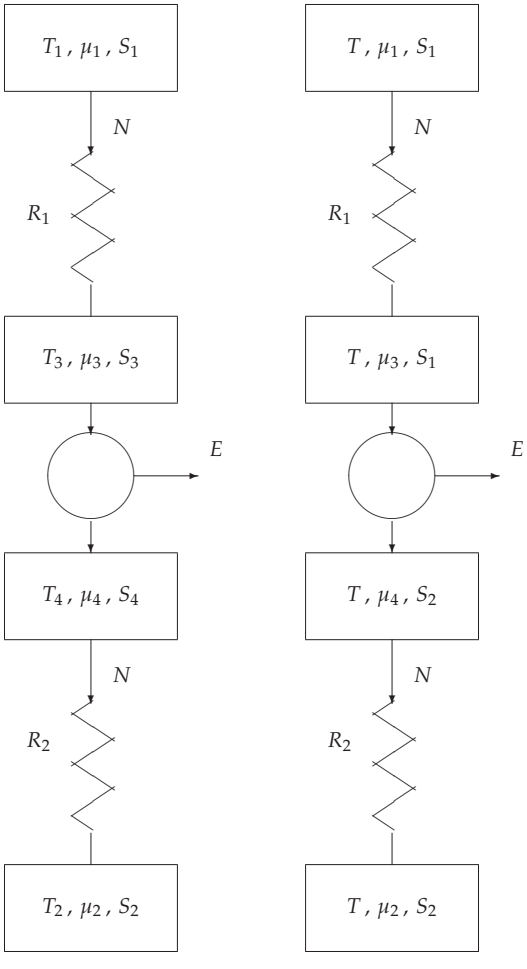

Figure 8. Endoreversible engine: (**a**) general model and (**b**) simplified model.

If $N = 0$, then we dissipate a minimum of energy $F_{min} = F(0) = T(S_1 - S_2)$. Unfortunately, $N = 0$ corresponds with an engine computing infinitely slowly (just like a heat engine produces power with a maximum, i.e., Carnot, efficiency when driven infinitely slowly). For reasons of speed, a computer is usually operated in so-called short-circuit mode: $N = N_{sc} = \mu/R$. This operation

corresponds with a short circuit between the two inner reservoirs of Figure 8: $\mu_3 = \mu_4$. Under such condition, we have

$$\begin{aligned} F = F_{sc} = F(N_{sc}) = F\left(\frac{\mu}{R}\right) &= \frac{1}{R}\,\mu^2 + T(S_1 - S_2) \\ &= RN_{sc}^2 + T(S_1 - S_2) \\ &= \mu N_{sc} + T(S_1 - S_2)\,. \end{aligned} \tag{9}$$

For the sake of energy savings, we aim at low F_{sc}. As N_{sc} is large for sake of speed, we thus need both small R and small μ.

8. Discussion

Figure 8b acts as our thermodynamical model of classical (i.e., non-quantum) computing. It is equally applicable to a single elementary logic gate as it is to a complete supercomputer. In the use of the model, we distinguish two cases: logically irreversible computation and logically reversible computation:

8.1. Conventional Computing

In conventional computers, information is erased during the computational process: $S_1 - S_2 > 0$. The computation happens in one direction: from reservoir # 1 to reservoir # 2. In other words: $N > 0$ and thus $\mu_1 > \mu_2$.

During several decades, classical MOS technology succeeded in minimizing both parameters R and μ. Indeed, according to Moore's law, we have known a continuous (exponential) shrinking of computer components. As a consequence, energy consumption per computational step diminished accordingly. In spite of this, the former term in (9) is still several orders of magnitude larger than the latter contribution. For a single computational step with e.g., a `nand` gate, in a 10 nanometer c-MOS technology, run with a power-supply voltage of 0.6 volt and operating at room temperature (i.e., at about 300 K), the dissipation in the resistor R is of the order of one attojoule (i.e., 10^{-18} J), whereas the dissipation $T(S_1 - S_2)$ is of order one zeptojoule (i.e., 10^{-21} J) only (corresponding with an entropy production of 3 zJ/K and 0.003 zJ/K, respectively). An attojoule may sound as an irrelevant miniscule amount of energy. However, because of present-day computer speeds (i.e., clock rates of about 3 GHz) and computation parallelism, it is responsible for the approximately 50 W dissipation in a single silicon chip (CPU or central processing unit) and hence for the megawatt power consumption in today's data centres. Further improvement of technology could lead to less energy dissipation. However, breaking the Landauer barrier will be impossible without radically changing computation architecture, i.e., without switching from logically irreversible computing to reversible computing.

8.2. Reversible Computing

In reversible computers, no information is erased: $S_1 - S_2 = 0$. The computation can happen in either direction: either from reservoir # 1 to reservoir # 2 or from reservoir # 2 to reservoir # 1. The former operation is activated by choosing $\mu_1 > \mu_2$ (and hence $N > 0$); the latter operation is activated by choosing $\mu_2 > \mu_1$ (and hence $N < 0$). For example, the circuits in Figure 1 indeed can be operated from top to bottom as well as from bottom to top, depending on the applied voltages.

Because the contribution $T(S_1 - S_2)$ to the dissipated energy F is absent from (8), we can, in the limit, make F as small as we like, by letting N go to zero, either from the positive side or from the negative side. This reminds us of the fundamental law: things only can happen without dissipation if they happen infinitely slowly.

9. Conclusions

Endoreversible schemes have proven to be very useful in many branches of science: both in thermodynamics and in many disciplines far beyond. In the present paper, we have applied it to informatics and computing. The simple model presented brings together Carnot's law, Landauer's principle, Ohm's law, and even Moore's law.

Funding: This research received no external funding.

Acknowledgments: The author thanks Bjarne Andresen and Robert Glueck, both from Københavns Universitet, at the physics and information department, respectively, for many years of fruitful discussions and collaborations.

Conflicts of Interest: The author declares no conflicts of interest.

References

1. Landauer, R. Irreversibility and heat generation in the computational process. *IBM J. Res. Dev.* **1961**, *5*, 183–191. [CrossRef]
2. Keyes, R.; Landauer, R. Minimal energy dissipation in logic. *IBM J. Res. Dev.* **1970**, *14*, 153–157. [CrossRef]
3. Bennett, C.; Landauer, R. The fundamental physical limits of computation. *Sci. Am.* **1985**, *253*, 38–46. [CrossRef]
4. Landauer, R. Information is physical. *Phys. Today* **1991**, *44*, 23–29. [CrossRef]
5. Bérut, A.; Arakelyan, A.; Petrosyan, A.; Ciliberto, S.; Dillenschneider, R.; Lutz, E. Experimental verification of Landauer's principle linking information and thermodynamics. *Nature* **2012**, *483*, 187–190. [CrossRef] [PubMed]
6. Orlov, A.; Lent, C.; Thorpe, C.; Boechler, G.; Snider, G. Experimental test of Landauer's principle at the sub-k_BT level. *Jpn. J. Appl. Phys.* **2012**, *51*, 06FE10. [CrossRef]
7. Jun, Y.; Gavrilov, M.; Bechhoefer, J. High-precision test of Landauer's principle in a feedback trap. *Phys. Rev. Lett.* **2014**, *113*, 190601. [CrossRef] [PubMed]
8. Yan, L.; Xiong, T.; Rehan, K.; Zhou, F.; Liang, D.; Chen, L.; Zhang, J.; Yang, W.; Ma, Z.; Feng, M. Single-atom demonstration of the quantum Landauer principle. *Phys. Rev. Lett.* **2018**, *120*, 210601. [CrossRef] [PubMed]
9. Curzon, F.; Ahlborn, B. Efficiency of a Carnot engine at maximum power output. *Am. J. Phys.* **1975**, *43*, 22–24. [CrossRef]
10. Andresen, B. *Finite-Time Thermodynamics*; Københavns Universitet: København, Denmark, 1983; ISBN 87-88318-02-8.
11. De Vos, A. *Thermodynamics of Solar Energy Conversion*; Wiley–VCH: Weinheim, Germany, 2008; ISBN 978-3-527-40841-2.
12. Fredkin, E.; Toffoli, T. Conservative logic. *Int. J. Phys.* **1982**, *21*, 219–253. [CrossRef]
13. De Vos, A. *Reversible Computing*; Wiley–VCH: Weinheim, Germany, 2010; ISBN 978-3-527-40992-1.
14. Mead, M. *Analog VLSI and Neural Systems*; Addison–Wesley: Reading, MA, USA, 1989; ISBN 0-201-05992-4.
15. Desoete, B.; De Vos, A. Optimal charging of capacitors. In Proceedings of the 8th International Workshop Patmos, Lyngby, Denmark, 7–9 October 1998; pp. 335–344.

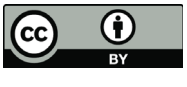

entropy

MDPI

Article

Optimized Piston Motion for an Alpha-Type Stirling Engine

Robin Masser, Abdellah Khodja, Mathias Scheunert, Karsten Schwalbe, Andreas Fischer, Raphael Paul and Karl Heinz Hoffmann *

Institut für Physik, Technische Universität Chemnitz, 09107 Chemnitz, Germany;
robin.masser@physik.tu-chemnitz.de (R.M.); abdellah.khodja@physik.tu-chemnitz.de (A.K.);
mathias.scheunert@mailserver.tu-freiberg.de (M.S.); karsten.schwalbe@physik.tu-chemnitz.de (K.S.);
andreas.fischer@physik.tu-chemnitz.de (A.F.); raphael.paul@physik.tu-chemnitz.de (R.P.)
* Correspondence: hoffmann@physik.tu-chemnitz.de

Received: 26 May 2020; Accepted: 19 June 2020; Published: 23 June 2020

Abstract: The Stirling engine is one of the most promising devices for the recovery of waste heat. Its power output can be optimized by several means, in particular by an optimized piston motion. Here, we investigate its potential performance improvements in the presence of dissipative processes. In order to ensure the possibility of a technical implementation and the simplicity of the optimization, we restrict the possible piston movements to a parametrized class of smooth piston motions. In this theoretical study the engine model is based on endoreversible thermodynamics, which allows us to incorporate non-equilibrium heat and mass transfer as well as the friction of the piston motion. The regenerator of the Stirling engine is modeled as ideal. An investigation of the impact of the individual loss mechanisms on the resulting optimized motion is carried out for a wide range of parameter values. We find that an optimization within our restricted piston motion class leads to a power gain of about 50% on average.

Keywords: piston motion optimization; endoreversible thermodynamics; stirling engine; irreversibility; power; efficiency; optimization

1. Introduction

In the 1970s, finite-time thermodynamics evolved in Steve Berry's group as an extension to traditional thermodynamics [1]. The aim of this extension was to describe dissipative heat engines operating in finite time or with finite rates as opposed to the reversible description. Finite-time thermodynamics focuses on irreversibilities within the system in question and incorporates them into the analysis. The goal was not so much to capture every little bit of dissipation occurring, the goal was to incorporate the most dominant dissipation contributions in order to get performance features—like efficiencies—much closer to the observed ones than the reversible treatment would give. New concepts [2–5] were developed and then applied not only to heat engines, but also to chemical processes [6]. Already this early work emphasized the importance of process optimization [7]. Later the field widened and different aspects of finite-time thermodynamics were studied such as its usage for power or efficiency optimization [8–10], the influence of different descriptions of irreversibilities [11–15] and the analysis of a broad range of thermodynamic systems [16–19]. Of particular interest are efficiency considerations. From the seminal work of Curzon and Ahlborn [20], to recent publications concerning non-linear irreversible systems [21–24], stochastic fluctuations [25–27], thermoelectric generators [28], biological processes [29] or general realizability domains [30] a multitude of investigations were carried out.

One of the central question in finite-time thermodynamics is: how large is the minimum necessary dissipation to perform a certain process in a specific time? This question can be treated by optimizing

that process—often using control theory—with respect to a certain performance goal, for instance maximizing the power output or minimizing the entropy production. In particular for heat engines a power optimization can be performed by improving the piston motion. Such piston trajectories have been studied for engines with Otto [31–33], Diesel [34–37], and Miller cycles [38] as well as the special paths needed for light-driven engines [39–44].

In this work we will use finite-time thermodynamics methods to study the performance features for Stirling engines. Stirling engines are considered to be good candidates for the use of waste heat, which occurs in many technical applications and which is often dumped into the environment without use. In such situations it is not so much the saved fuel—which comes more or less for free—it is the economical choice of an appropriate engine size (and the connected capital costs) which requires knowledge about performance features and in particular of the power output of the engines. Investigations into such performance features for Stirling engines and their optimization have already been conducted, see for instance [45–50], where especially the piston motion has been considered [51–53].

Here, our goal is to analyze in particular the power output of a Stirling engine in alpha configuration, for which the piston motion is characterized by two independently acting pistons. We determine possible performance improvements for ideal regeneration by varying its piston movement. Finding its performance optima by using the classical approach based on control theory would be a formidable task. Here, we take a simpler route, based on a parameter optimization of the piston motion with especially chosen smooth functions from the AS class of functions introduced below. The advantage of our approach is the simplicity of its technical implementation and a much reduced numerical effort. This turned out to be very favorable in treating the wide range of cases needed in the application which started this investigation: the recovery of waste heat from machine tools. We note that our method will provide lower bounds for the gain achievable by a control theory based optimization. Our investigation will be based on an endoreversible model incorporating the essential losses due to friction of the moving pistons and the resistances in the heat transport in and out of the engine, as well as the impact of the non-vanishing flow resistance in moving the working fluid through the regenerator.

2. Piston Motion Optimization

The standard harmonic piston motion used in Stirling engine modeling is given by

$$V(t) = V_{\mathrm{dead}} + \Delta V(1 + \sin(2\pi t/t_0))/2, \tag{1}$$

where V_{dead} and ΔV are the dead volume and the displacement, respectively, and where t_0 is the period of the motion, which is here chosen to be $t_0 = 1\,\mathrm{s}$. In our analysis we want to capture the effects of two important variations of this standard piston motion. One is a variation in the piston speed as it travels from its minimum displacement to its maximum displacement and back. The other is a variation of the time a working volume is above its average value $V_{\mathrm{dead}} + \Delta V/2$ compared to the time it spends at volumes below its average value. Both variations influence the different loss mechanisms in subtle ways, where the influence of the piston speed on the piston velocity dependent friction loss is most obvious.

Of course the class of piston motions we consider must be periodic, moreover we will consider only motions for which all time derivatives of the piston position exist and are continuous. Making use of the fact that the cross sectional area of the cylinder is constant we directly specify the cylinder volume rather than the piston position. As a result of these considerations we will use the following newly developed piston motion:

$$V(t) = V_{\mathrm{dead}} + \Delta V f(t/t_0; \sigma, \delta), \tag{2}$$

where the function $f(x;\sigma,\delta)$ and the dimensionless parameters σ and δ are explained in more detail below. The function $f(x;\sigma,\delta)$ is a composition of two functions f_1 and f_2

$$f(x;\sigma,\delta) = f_1(f_2(x;\delta);\sigma), \tag{3}$$

where f_1 and f_2 are given by

$$f_1(y;\sigma) = (\sin(2\pi y + \sigma\sin(4\pi y)) + 1)\,/2 \tag{4}$$

and

$$f_2(x;\delta) = x + \delta(1 - \cos(2\pi x)), \tag{5}$$

respectively.

Below we will refer to this class of piston motions as "adjustable sinusoidal" and will label the corresponding items by "AS". Once the piston motion has been optimized by an appropriate choice of parameters we will call it "optimized sinusoidal" and will label the corresponding items "OS". Note that the standard harmonic motion belongs to the class of adjustable sinusoidal motions and can be regained by the choice $\sigma = \delta = 0$. We will label items corresponding to this motion "STD". The advantageous feature that the STD case belongs to the AS class of motions allows for an easy comparison and a continuous transition from the STD case to the OS case.

The influence of the parameters σ and δ on the piston motion is demonstrated in the following figures. Figure 1 shows the changes induced by a variation of σ.

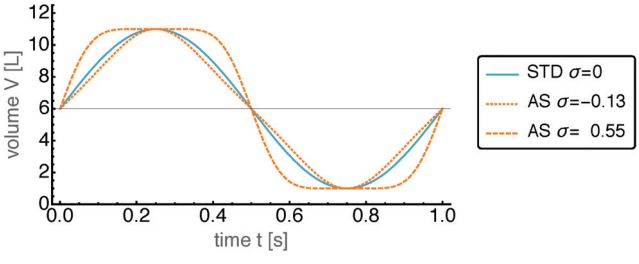

Figure 1. Piston volume V over time t for the standard harmonic motion (STD), and the "adjustable sinusoidal" motion (AS) with $\delta = 0$ and different values for σ. Negative values for σ decrease the maximum piston velocity resulting in shorter times spent at the extreme values of the volume, while positive values for σ lead to the opposite effect.

As can be seen, an increasing σ leads to a faster piston speed (corresponding to steeper slopes of $V(t)$) during the compression and expansion phases, while the speed close to the minimum and maximum position is considerably reduced such that the volume stays close to its extreme values for an extended fraction of the overall time period. The figure also shows the effects of negative σ. Here, the rest times of the piston at its extreme positions are reduced compared to the standard harmonic motion. This property of the AS motion class is important as it is well known from earlier work on power optimization by motion control [34] that sometimes it is beneficial to let the piston rest for a while at a extreme position.

The effects caused by variations of the parameter δ are shown in Figure 2, where the AS motion is displayed for $\delta = -0.05$ and $\delta = 0.05$. It is apparent that the fraction of time spend above the mean displacement can be extended considerably by setting δ to negative values, and can be shortened by setting δ to positive values.

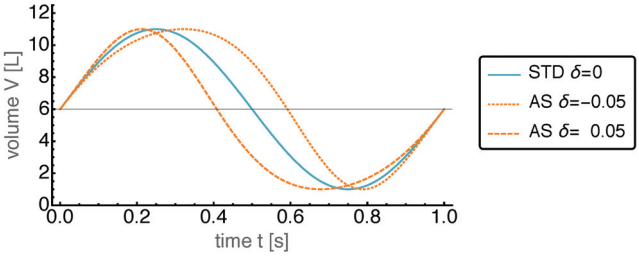

Figure 2. Piston volume V over time t for the standard harmonic motion (STD), and the "adjustable sinusoidal" motion (AS) with $\sigma = 0$ and different values for δ. Negative values for δ extend the fraction of time with a volume larger than the mean volume. Positive values lead to the opposite effect.

The above discussed features of the AS motion can be observed within certain limits of the parameters σ and δ, which have been determined by a systematic search of the parameter space. Hence, we will use the following restrictions on these parameters: $-0.13 < \sigma < 0.6$ and $-0.08 < \delta < 0.08$. Beyond these limits the desirable features decline.

While the above discussion described the dynamics of one of the two pistons of the considered Stirling engine, we will now turn to the overall combined dynamics of both pistons. In the subsequent analysis of the potential power improvements through optimized piston dynamics we will use

$$V_1(t) = V_{\text{dead}} + \Delta V f(t/t_0; \sigma_1, \delta_1), \tag{6}$$

$$V_2(t) = V_{\text{dead}} + \Delta V f(t/t_0 + \Delta t/t_0; \sigma_2, \delta_2), \tag{7}$$

where we have introduced the additional parameter Δt. This parameter induces a time shift between the two piston motions. In the standard case of harmonic dynamics this parameter is set by the usual phase shift of $-\pi/2$ which translates into a $\Delta t = -0.25\, t_0$. In summary, we will use the five dimensionless parameters σ_1, δ_1, σ_2, δ_2, and $\Delta t/t_0$ in our optimization.

3. Endoreversible Stirling Engine

The Stirling engine model used here is based on endoreversible thermodynamics. While a brief description of its concepts is given below, a more extensive description can be found in these two reviews [54,55]. After early work [56–58] the approach became more formalized and is now used in a variety of applications as for instance dealing with chemical reactions [59–63], engines of different kinds [64–67] and in particular with efficiencies of energy transformation devices [68–73].

In the subsequent subsections the endoreversible modeling of the alpha Stirling engine is shown.

3.1. Endoreversible Modeling

The main aspect of endoreversible modeling is the description of a system as well as the processes occurring in it by specifying its subsystems and the reversible or irreversible interactions between those. The subsystems are divided into (in)finite reservoirs with state variables, and engines, which serve for energy conversion. Finite reservoirs are typically described by their energy E_i as a function of its extensities, where i denotes the i-th subsystem. For each extensity X_i^α a corresponding intensity Y_i^α can be calculated by

$$Y_i^\alpha = \frac{\partial E_i(X_i^\alpha)}{\partial X_i^\alpha}. \tag{8}$$

Here, the superscript α specifies the corresponding extensity, e. g. the intensity Y^S is the temperature T, which is the corresponding intensity to the extensity entropy S. The change in energy

of the subsystem can thus be expressed as the sum of changes in extensities times the corresponding intensities of the subsystem:

$$\mathrm{d}E_i = \sum_\alpha Y_i^\alpha \, \mathrm{d}X_i^\alpha. \tag{9}$$

According to this relation, each flux of extensity J_i^α carries an accompanying flux of energy

$$I_i^\alpha = Y_i^\alpha J_i^\alpha. \tag{10}$$

Infinite reservoirs, on the other hand, are only described by their intensities, which stay constant and do not change when extensity or energy is transferred to or from them.

The second type of endoreversible subsystems are engines, which transfer energy from one carrying extensity to another. Unlike reservoirs, they are not intended to store extensities. Hence, extensities and energy are balanced over all incoming and outgoing fluxes:

$$0 = \sum_k J_{i,k}^\alpha \text{ for all } \alpha \text{ and} \tag{11}$$

$$0 = \sum_{k,\alpha} I_{i,k}^\alpha, \tag{12}$$

where k serves to differentiate the contact points of subsystem i, at which the $I_{i,k}^\alpha$ and $J_{i,k}^\alpha$ of the various interactions enter the subsystem. Typically, k consecutively numbers the contact points of a subsystem, or denotes the linked subsystem. The latter might be favorable when there are only interactions connecting no more than two subsystems—as it is the case in this paper.

The fluxes themselves are defined by either the requirement of equal intensities of two subsystems $Y_i^\alpha = Y_j^\alpha$ or by transport laws for the transferred extensity or energy. While in the first case the fluxes can technically become infinite in order to instantaneously equalize the intensities, in the latter case often phenomenological relationships are used resulting in finite rates. Of course, energy conservation applies to all interactions. In addition, the other extensities must be balanced, with the exception of entropy, since interactions can be irreversible and therefore generate entropy.

Often it is not necessary to describe the energy carrying extensity of an interaction. Instead a power flux is used describing only the rate of transferred energy or work.

3.2. Stirling Engine

Using the described aspects of endoreversible modeling, we build the Stirling engine model as shown in Figure 3. The subsystems shown as circles are engines representing the regenerator R and the transmission units T1 and T2. The latter are converting the volume work flux of the stroke into some form of power we do not need to specify here. The regenerator is connected to an entropy reservoir SR and a work reservoir WR. It is also connected to the reservoirs representing the gas in the hot cylinder 1 and the cold cylinder 2 of the Stirling engine, respectively. Those in turn are thermally coupled to a hot heat bath H and a cold heat bath C. The remaining reservoirs are work reservoirs collecting the net power WT from the volumetric processes and the frictional power loss WF of the transmission units, as well as volume reservoirs representing the environment E. All reservoirs and interactions are explained in more detail below.

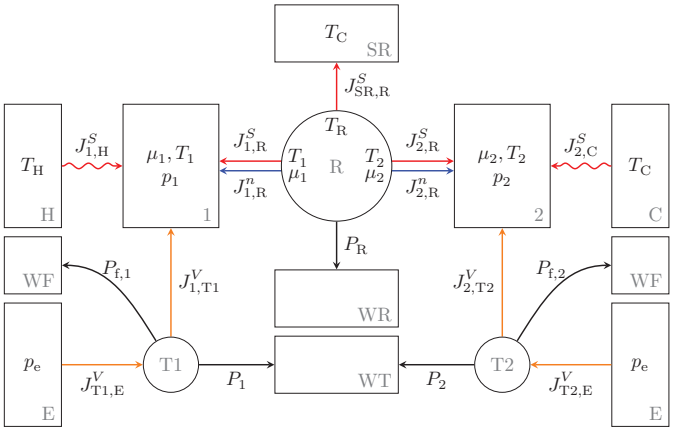

Figure 3. Endoreversible model of the Stirling engine with reservoirs (rectangles), endoreversible engines (circles) and reversible (straight lines) and irreversible (wavy lines) interactions. On the left side the hot cylinder 1 is located with its interactions to the hot heat bath H and a transmission unit T1 while on the right side the cold cylinder 2 is displayed with corresponding interactions and the cold heat bath C. Both are connected by the regenerator R in the middle which interacts with an entropy and work reservoir, SR and WR, respectively. Further reservoirs are work reservoirs WT and WF collecting the net power and friction losses, respectively, from the energy converting engines T1 and T2 as well as volume reservoirs E representing the environment.

3.3. The Working Fluid

The working fluid in cylinder 1 and 2 is described by the equation of state for an ideal gas:

$$pV = nRT, \tag{13}$$

where p, V, n and T are the pressure, volume, mole number and temperature, respectively, and R is the gas constant. The caloric equation of state is given by

$$U = \hat{c}_V nRT, \tag{14}$$

where U is the internal energy and $\hat{c}_V$ is the dimensionless specific heat capacity at constant volume. Here, this is chosen to be $\hat{c}_V = 5/2$ as usual for di-atomic gases.

Endoreversible modelling of reservoirs gets particularly simple, if one uses the extensities to describe its state, which in our case are the entropy S, the volume V and the mole number n of the fluid. We start from the fluid's entropy

$$S = nR\left(\hat{c}_V \ln\frac{T}{T_0} + \ln\frac{V}{V_0} - \ln\frac{n}{n_0}\right) + n\frac{S_0}{n_0}, \tag{15}$$

with T_0, V_0 and n_0 being the reference temperature, volume and mole number, respectively, for the reference entropy $S_0(T_0, V_0, n_0)$. By solving Equation (15) for the temperature T we obtain

$$T(S, V, n) = \left(\frac{V_0 T_0^{\hat{c}_V}}{n_0}\frac{n}{V}\exp\left(\frac{S}{nR} - \frac{S_0}{n_0 R}\right)\right)^{\frac{1}{\hat{c}_V}}. \tag{16}$$

Now, the internal energy U can be expressed in terms of the extensities S, V and n:

$$U = \hat{c}_V nRT(S,V,n) = \hat{c}_V nR \left(\frac{V_0 T_0^{\hat{c}_V}}{n_0} \frac{n}{V} \exp\left(\frac{S}{nR} - \frac{S_0}{n_0 R} \right) \right)^{\frac{1}{\hat{c}_V}}. \tag{17}$$

This equation is also called the principle equation of state [74]. According to Equation (8) the pressure p and the chemical potential μ of the fluid can then be derived from the principle equation of state:

$$p(S,V,n) = -\left(\frac{\partial U}{\partial V} \right)_{S,n} = \frac{nR}{V} T(S,V,n), \tag{18}$$

$$\mu(S,V,n) = \left(\frac{\partial U}{\partial n} \right)_{S,V} = \left(\hat{c}_V R + R - \frac{S}{n} \right) T(S,V,n). \tag{19}$$

For a given working fluid databases typically provide the standard molar entropy $S_{m,0}(p_0, T_0)$ at reference pressure and reference temperature. In this case, using Equation (13) and $S_{m,0} = S_0/n_0$ the temperature can also be expressed as

$$T(S,V,n) = \left(\frac{R T_0^{1+\hat{c}_V}}{p_0} \frac{n}{V} \exp\left(\frac{S}{nR} - \frac{S_{m,0}}{R} \right) \right)^{\frac{1}{\hat{c}_V}}. \tag{20}$$

3.4. Heat Transfer and Power Losses

The heat transfer between the hot heat bath H and the gas reservoir 1 as well as between the gas reservoir 2 and the cold heat bath C is assumed to be Newtonian. Thus, the heat flows $I^S_{1,\mathrm{H}}$ and $I^S_{2,\mathrm{C}}$ from the hot and cold heat baths are proportional to the temperature differences between the gas reservoirs and the hot and cold heat baths with temperature T_H and T_C, respectively:

$$I^S_{1,\mathrm{H}} = \kappa(T_\mathrm{H} - T_1), \tag{21}$$

$$I^S_{2,\mathrm{C}} = \kappa(T_\mathrm{C} - T_2), \tag{22}$$

where κ is the heat transfer coefficient, which for simplicity is here chosen to be equal for the hot and cold side. The resulting entropy fluxes into or out of the reservoirs are

$$J^S_{1,\mathrm{H}} = I^S_{1,\mathrm{H}}/T_1, \tag{23}$$

$$J^S_{2,\mathrm{C}} = I^S_{2,\mathrm{C}}/T_2. \tag{24}$$

The hot and cold heat baths are modeled as infinite reservoirs so that their temperature remains constant at T_H and T_C, respectively, regardless of the incoming entropy flux.

In order to capture the mechanical friction due to the piston motion, we make the often used assumption of a power loss P_f proportional to the piston velocity squared. Again, since the cross sectional area of the cylinder is constant, this loss can be expressed using the volume change of reservoir $i = 1, 2$:

$$P_{\mathrm{f,i}} = \beta \dot{V}_i^2, \tag{25}$$

where β is the mechanical friction coefficient [32]. This power loss is transferred to the work reservoir WF for bookkeeping purposes, from which it is then dissipated to heat and dumped into the environment. The resulting power connected to changes of the volume of reservoir i is then given by

$$P_i = p_i \dot{V}_i - P_{\mathrm{f},i} \tag{26}$$

according to the energy balance equations of the transmission units and is flowing to or from the work reservoir WT.

3.5. Ideal Regenerator and Mass Transfer

The regenerator of the Stirling engine is designed to cool and heat the gas flowing back and forth between the cylinders. A real regenerator acts like a short-term heat storage, which during one cycle alternately absorbs energy and then releases it again. Here, we consider an ideal regenerator. We define it in a way such that no irreversibilities occur in the process of regeneration by requiring that the flowing gas leaves or enters the regenerator with the temperature and pressure of the cylinder it flows to or comes from. In addition, the ideal regenerator does not contain any gas itself.

Such an ideal regenerator can be modeled as an engine. The incoming particle flux is passed on directly to the other gas reservoir. The chemical potential and temperature of the incoming and outgoing particle fluxes as well as the associated entropy fluxes are equal to those of the adjacent reservoirs. Hence, these interactions are reversible. We assume a mass transport that is proportional to the difference of the pressures within the two cylinders. Hence, using a mass transfer coefficient α the particle flux through the regenerator is given as

$$J^n_{1,\mathrm{R}} = \alpha(p_2 - p_1) = -J^n_{2,\mathrm{R}}. \tag{27}$$

The corresponding entropy fluxes entering or leaving the reservoirs 1 and 2 are then given by

$$J^S_{1,\mathrm{R}} = S_{m,1} J^n_{1,\mathrm{R}}, \tag{28}$$

$$J^S_{2,\mathrm{R}} = S_{m,2} J^n_{2,\mathrm{R}}, \tag{29}$$

respectively, where $S_{m,i} = S_i/n_i$ is the molar entropy of the subsystem i. We point out that such coupled fluxes can be combined to a multi-extensity flux [75].

Since these two entropy fluxes generally are not equal, a third entropy flux is needed to maintain entropy balance within the ideal regenerator. This third entropy flux $J^S_{\mathrm{SR,R}}$ reversibly flows into the entropy reservoir SR

$$J^S_{\mathrm{SR,R}} = -J^S_{1,\mathrm{R}} - J^S_{2,\mathrm{R}}. \tag{30}$$

We set the temperature $T_\mathrm{R} = T_\mathrm{C}$, as the cold heat bath is considered to be the environment from which entropy or energy can be taken or dumped into at no cost. Likewise, to fulfill energy conservation within the regenerator, an additional energy flux is needed:

$$P_\mathrm{R} = T_1 J^S_{1,\mathrm{R}} + \mu_1 J^n_{1,\mathrm{R}} + T_2 J^S_{2,\mathrm{R}} + \mu_2 J^n_{2,\mathrm{R}} + T_\mathrm{C} J^S_{\mathrm{SR,R}}. \tag{31}$$

This necessary or excess energy for the ideal regeneration process is accounted for in the work reservoir WR and will enter the overall power output. Finally we note, that kinetic energy and mechanical inertia of the gas and mass leakages have been neglected.

3.6. The Dynamics

From the balance equations for the extensities derived above and the transport laws we obtain a coupled system of differential equations to be integrated

$$\dot{n}_1 = \alpha(p_2 - p_1), \qquad \dot{n}_2 = \alpha(p_1 - p_2), \tag{32}$$

$$\dot{S}_1 = \kappa(T_\mathrm{H} - T_1)/T_1 + S_{m,1}\dot{n}_1, \qquad \dot{S}_2 = \kappa(T_\mathrm{C} - T_2)/T_2 + S_{m,2}\dot{n}_2, \tag{33}$$

$$V_1 = V_1(t; \sigma_1, \delta_1), \qquad V_2 = V_2(t + \Delta t; \sigma_2, \delta_2), \tag{34}$$

where all the intensities can be expressed in terms of the extensities. For given parameters $\sigma_1, \delta_1, \sigma_2, \delta_2$ and Δt, the above equations are integrated until the system has reached a steady cyclic operation. Resetting the time we obtain the resulting useful work output per cycle

$$W_{\text{out}} = \int_0^{t_0} P_{\text{R}} + P_1 + P_2 \, \mathrm{d}t. \tag{35}$$

The overall friction losses can be calculated by

$$P_{\text{f}} = P_{\text{f},1} + P_{\text{f},2}. \tag{36}$$

If W_{out} is positive, the Stirling engine provides an average power output

$$P = W_{\text{out}}/t_0. \tag{37}$$

Otherwise, energy must be supplied to the engine to maintain its operation.

Finally we define the efficiency of the Stirling engine as ratio of the total work output over the integrated heat flux from the hot reservoir for one cycle

$$\eta = \frac{W_{\text{out}}}{Q_{\text{in}}} = \frac{W_{\text{out}}}{\int_0^{t_0} I^{\text{S}}_{1,\text{H}} \, \mathrm{d}t} = \frac{W_{\text{out}}}{\int_0^{t_0} \kappa (T_{\text{H}} - T_1) \, \mathrm{d}t}. \tag{38}$$

Based on these quantities we now turn to the optimized operation of the Stirling engine.

4. Results

Our aim was to determine the potential gains in the average power output which could be achieved by an optimized piston motion as compared to the standard motion. To achieve that aim we optimized the parameters $\sigma_1, \delta_1, \sigma_2, \delta_2$ and Δt of the AS motion numerically based on a Nelder–Mead approach [76]. In general we found that the power output was not very sensitive with respect to the motion control parameters in the sense that one got large power variations for small parameter changes.

We presented the results for the piston motion optimized with regard to the average power output (OS) and compared them to those of the standard harmonic piston motion (STD). The results were obtained for model parameters representing a somewhat typical Stirling engine in the few kW range. The temperatures $T_{\text{H}} = 400\,\text{K}$ and $T_{\text{C}} = 300\,\text{K}$ reflected the application area of waste heat usage, while the dead volume $V_{\text{dead}} = 1\,\text{L}$ and the displacement $\Delta V = 10\,\text{L}$, leading to a typical value of 0.1 for their ratio. The amount of working fluid was $n = 1\,\text{mol}$, which with the volumes chosen led to a moderate pressure engine. The above engine parameters were kept fixed at their values in the entire results section.

There are three further parameters, for which we investigated their influence on the engine performance in more detail. These were the friction coefficient β determining losses due to mechanical friction, the heat transfer coefficient κ determining losses due to finite heat conduction, and the mass transfer coefficient α which determines the mass flow rate through the regenerator.

We started our analysis by investigating a case in which the power limiting impacts of these three parameters are negligible. In particular the minimum value for the friction coefficient was set to zero, and the values for κ and α were chosen such that their further increase would no longer lead to a sizable power increase: $\beta_0 = 0\,\text{Js/m}^6$, $\alpha_0 = 100\,\text{mol}/(\text{s bar})$, $\kappa_0 = 10^5\,\text{W/K}$. With these choices the temperature of the working fluid was always very close to the temperature of the connected heat bath and the pressures in the two cylinders were nearly equal. This minimum value for the friction coefficient and the maximum values for κ and α are referred to as "base values", and the results obtained for these values are referred to as the "base case".

4.1. Optimized Piston Motion: The Base Case

First, we present the results for the base case. The power output for the OS motion is 962 W and for the STD motion 608 W. Thus, the power output for the OS motion turned out to be about 50 % larger than that for the STD motion. The corresponding dynamics of the state variables are shown in Figures 4–8.

In Figure 4 the volumes of the two cylinders are shown as a function of time.

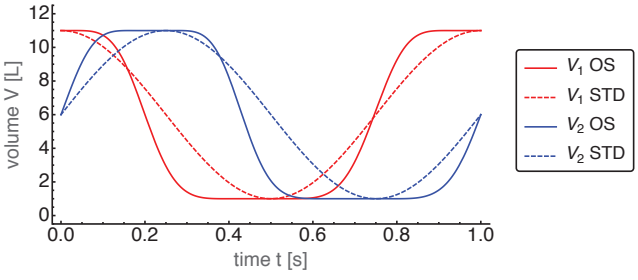

Figure 4. Resulting cylinder volumes V_1 and V_2 over time t for the optimized sinusoidal (OS) motion with base case parameters. For comparison the STD motion is plotted with dashed lines.

The optimal volume dynamics showed a number of interesting and surprising features. It is apparent that both volumes varied more like a trapezoid wave than a harmonic wave, leading to a faster transition between the minimal and maximum volumes. Moreover, the extrema were slightly shifted with respect to those of the STD motion. It turned out that the time shift $\Delta t_{\mathrm{OS}} = -0.255 t_0$ differed only little from its STD value $\Delta t_{\mathrm{STD}} = -0.25 t_0$. The values of $\delta_{1,\mathrm{OS}} = 0.0217$ and $\delta_{2,\mathrm{OS}} = 0.036$ were positive indicating a preference for smaller volumes for both cylinders, while the relatively large positive values $\sigma_{1,\mathrm{OS}} = 0.573$ and $\sigma_{2,\mathrm{OS}} = 0.565$ reflected the tendency to the square wave behavior. All four parameters differed considerably from the STD case.

The optimized piston motion led to the entropy and mole number dynamics as shown in Figures 5 and 6, respectively. Both figures showed a high degree of similarity, which in part is due to the entropy being roughly proportional to the mole number. Small differences between them were visible around $t = 0.6$ s which indicates that the specific entropy changed there.

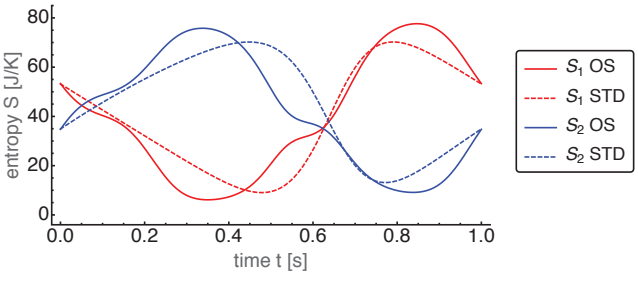

Figure 5. Entropies S_1 and S_2 of the hot and cold cylinder, respectively, over time t for the OS motion with base case parameters. For comparison those for the STD motion are plotted with dashed lines.

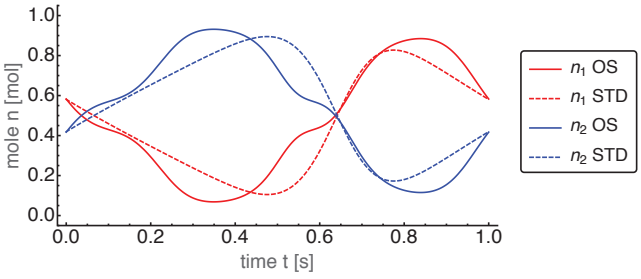

Figure 6. Mole numbers n_1 and n_2 of the hot and cold cylinder, respectively, over time t for the OS motion with base case parameters. For comparison those for the STD motion are plotted with dashed lines.

For the further discussion it is helpful to consider the dynamics of the intensities temperature and pressure in the two cylinders. The temperatures of the working fluid in both cylinders were very close to the bath temperatures due to our choice of the base value for the heat conduction. In Figure 7 we show the difference between the cylinder temperature and the corresponding heat bath temperature for both cylinders. One sees that T_1 and T_2 showed rich dynamics as a consequence of the heat exchange, the volume changes, and the mass transfer through the regenerator. One interesting feature is that during one cycle the cylinder temperature was sometimes largerand sometimes smaller than the corresponding bath temperature. Thus heat entered and returns from each cylinder in relation to its bath. Another feature was the larger variations of the OS temperatures compared to the STD case. The strongly increased power output compared to the STD case required a larger heat supply from the hot bath (and implicitly a larger heat delivery to the cold bath) and therefore larger temperature differences.

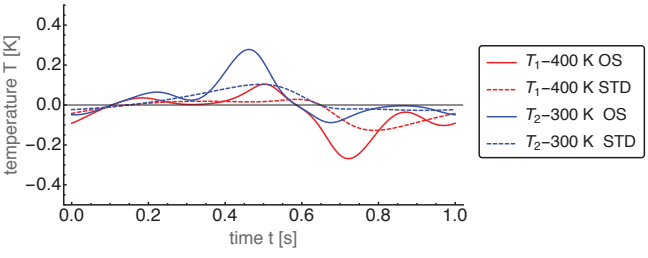

Figure 7. Temperatures T_1 and T_2 of the hot and cold cylinder, respectively, over time t for the OS and STD motions with base case parameters. Note that the difference to the corresponding heat bath temperature is shown. The temperatures for the OS motion feature a much stronger variation than for the STD case. The rich dynamical structure is due to the interaction of the volume changes in both cylinders.

The pressure dynamics is displayed in Figure 8. Here, the dominating feature was the absence of any noticeable pressure difference between the cylinders during the whole cycle. Again, this feature was caused by our choice of the mass transport coefficient α, allowing a sufficiently large mass flow through the regenerator to almost instantaneously equilibrate the pressures of both sides. This common pressure, which was now a global pressure in the whole Stirling engine, showed a much higher peak for the OS motion than for the STD motion. This peak occurred around $t = 0.6\,\mathrm{s}$, where both volumes reach their minimal values (see Figure 4).

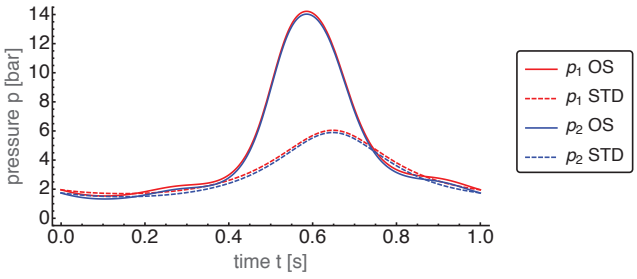

Figure 8. Pressures p_1 and p_2 of the hot and cold cylinder, respectively, over time t for the OS motion with base case parameters. For comparison those for the STD motion are plotted with dashed lines. The curves for p_1 and p_2 lie on top of each other, for better visibility the p_1 curves have been moved up by 0.2 bar.

Based on the common pressure $p = p_1 \approx p_2$ the infinitesimal total volume work done by both pistons can be expressed as $\mathrm{d}W = p\,\mathrm{d}V_{\mathrm{tot}}$ with the total volume $V_{\mathrm{tot}} = V_1 + V_2$. Then the gain in power output can easily be understood by looking at the p-V_{tot}-plot, which is displayed in Figure 9.

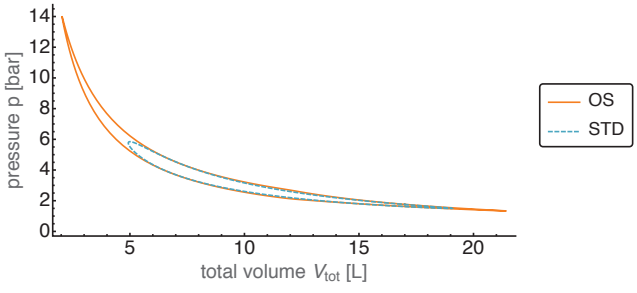

Figure 9. Pressure $p = p_1 \approx p_2$ over total volume $V_{\mathrm{tot}} = V_1 + V_2$ for both the OS and STD motion in base case. The OS motion leads to lower volumes and higher pressures resulting in a higher usable work output.

We first noticed that the total volume traversed a larger range for the OS motion than for the STD motion. Especially for small V_{tot} this automatically led to much higher pressure values for the given heat bath temperatures. This opened the route to exhaust the work potentially gainable from the considered cycle by reaching into the "corners" of the ideal Stirling cycle with its constant volume branches.

After establishing the base case we then turned to the investigation of the possible power gains by an optimized piston motion in dependence of the loss terms present. We varied the three coefficients one by one to capture the regions of interest for the power output: The minimum value of β and the maximum values of κ and α were chosen to be the base values and the maximum value of β and the minimum values of κ and α were set by a vanishing power output. When varying one of the parameters, the base values were used for the other parameters.

4.2. Optimized Piston Motion: Friction

First, we looked at achievable power gains for different friction losses. To that end we varied the friction coefficient β between zero and about $7 \times 10^5\,\mathrm{Js/m^6}$, for which all the power produced was dissipated by the friction losses.

Indeed the optimized piston motion led to an increase in the average power output compared to the standard motion, as shown in Figure 10. On average the gain in power output was about 50 %, even

though the piston motion was only optimized within the AS class considered. While for small friction the power gain was maximal it declined towards larger values of the friction coefficient. Astonishingly it kept a constant power gain from about $\beta = 4 \times 10^5\,\mathrm{Js/m^6}$ down to vanishing power, which means that there was strong increase in relative performance.

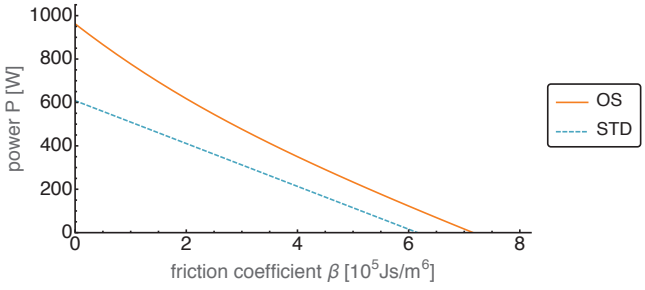

Figure 10. Average power output P over varied friction coefficient β for both OS and STD motion. The friction coefficient has been increased from zero until no positive average power output was reached.

In Figure 11 we show the efficiencies corresponding to the power optimized motion and the standard motion.

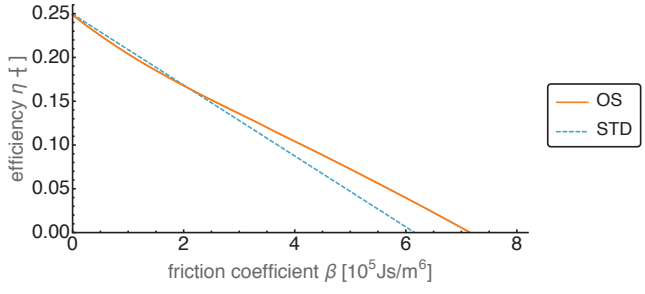

Figure 11. Efficiency η over varied friction coefficient β for both OS and STD motion.

It is interesting to note that for vanishing friction losses the efficiencies both started at about 0.25 which corresponded to the Carnot efficiency for the given heat bath temperatures. Moreover the OS efficiency was initially lower than the STD efficiency while the power output was higher by more than 50 %. This means that the large increase in power needed disproportionately more heat input than the STD case, which for a waste heat application was not so crucial.

4.3. Optimized Piston Motion: Heat Conduction

The second dissipative process present in the Stirling engine is the finite heat conduction. While for high heat conduction the temperatures in the working volumes were close to the temperatures of the associated heat baths, this was different for a low heat conduction. The heat transfer coefficient κ was varied between its base value and nearly zero.

As can be seen in Figure 12, the average power output at high heat conduction for the OS motion reached values of about 150 % of that of the STD motion. With κ getting smaller the OS power output decreased faster than the STD power output. When κ reached values about 4 kW/K the decay in OS power became stronger, but it stayed always above the STD one. For even smaller heat transfer coefficients the power output decreased towards zero. A similar behavior can be observed for the standard motion, however with a considerably smaller power output. While for the OS motion the

average power output became negative for κ close to zero, this happened for the standard motion already at κ values around 200 W/K.

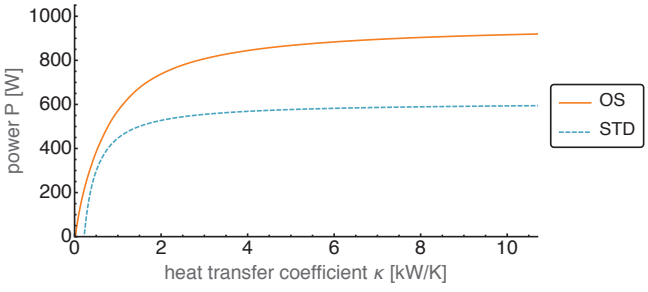

Figure 12. Average power output P over varied heat transfer coefficient κ for both OS and STD motion. The OS motion reaches average power output values of around 150 % compared to the STD motion as well as positive values of P with κ close to zero.

The efficiency is shown in Figure 13 as a function of the heat transfer coefficient. It is apparent that the efficiency was mostly higher for the standard motion than for the OS motion. However at smaller values of κ it dropped below that for the OS motion. It stayed close to the Carnot value 0.25 over most of the considered κ range and dropped off around the values where the power output also decreased. This led to a crossing point of the STD and OS graphs in Figure 13 which was not present in Figure 12. There the STD graph was always below the OS graph and thus the decline of the power output for the STD case to zero at larger values of κ did not necessitate such a crossing.

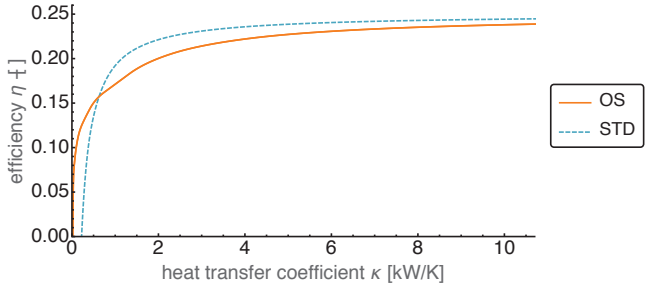

Figure 13. Efficiency η over varied heat transfer coefficient κ for both OS and STD motion. For higher values of κ the efficiency of the OS motion is slightly lower than that of the STD motion. For lower κ the OS motion leads to better efficiency values.

4.4. Optimized Piston Motion: Mass Transport

The third non-equilibrium process in our model is the mass transport between working volumes 1 and 2. This transport was assumed to be proportional to the pressure difference, with the proportionality constant being the mass transport coefficient α. However, even though it was a non-equilibrium transport, it described a reversible exchange of working fluid between the working volumes 1 and 2 through the regenerator. This is due to the regenerator being modeled as ideal which corresponded to a fully reversible operation.

In Figure 14 the average power output is shown as a function of the mass transport coefficient α for the range between zero and 10 mol/(s bar). For large values the power output saturated, while for smaller values the power output slowly decreased. Around 1.5 mol/(s bar) it started to fall off towards zero. Initially for large enough values of α the gain in the power output of the OS motion

compared to that of the standard motion was more than 50 %. The gain increased towards smaller α and became infinite in the range where the OS power output was positive while the STD power output was negative.

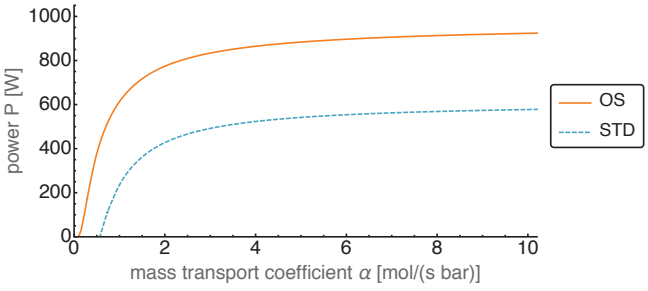

Figure 14. Average power output P over varied mass transfer coefficient α for both OS and STD motion. The OS motion leads to an increase in P of more than 50 % and to lower feasible values of α compared to the STD motion.

In Figure 15 the efficiency is shown as a function of the mass transport coefficient α. This figure shows efficiencies very close to the Carnot efficiency $\eta_C = 0.25$, which is due to the reversible modeling of the regenerator. For very small α the finite—but large—heat transfer coefficient κ led to negative power output, for which we set the efficiency to zero. The surprising feature here was the steep decline of efficiency once it left the Carnot value level.

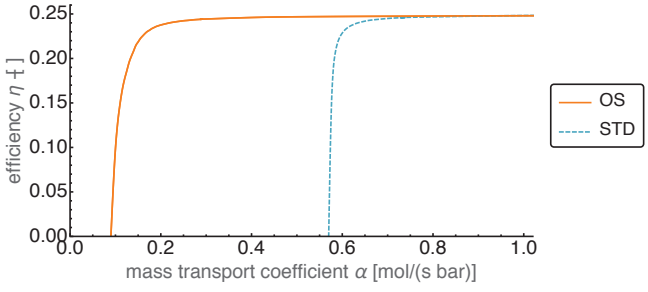

Figure 15. Efficiency η over varied mass transfer coefficient α for both OS and STD motion. Despite the equally high efficiency values above $\alpha > 0.8\,\mathrm{mol/(s\,bar)}$, the OS motion maintains such high values for much lower mass transfer coefficients than the STD motion.

5. Conclusions

In this paper we investigated possible performance improvements for an endoreversible Stirling engine through an optimized piston motion. The motion of the two pistons of the Stirling engine was limited to the smooth adjustable sinusoidal (AS) motion which is controlled by five parameters. The underlying endoreversible model that was build for the Stirling engine takes into account friction losses, irreversible heat transfers as well as the impact of a finite gas flow through the regenerator. The regenerator itself was assumed to be ideal.

For comparison a "base case" was defined without friction losses and where heat and mass transfer coefficients have been chosen such that their further increase would no longer lead to a sizable increase in power output. Already in this case, the piston motion optimization shows that the average power output can be increased by about 50 %. These surprising gains could be achieved by the fact that the optimized piston motion resulted in higher temporal pressure variations within

the system. This brought the process closer to the ideal Stirling cycle as is well illustrated in the pressure-volume diagram.

In all cases considered, there was an astonishing gain in average power output. This effect is especially pronounced in cases with "unfavorable" coefficients, that means high friction or low heat and mass transfer coefficients. This extends to conditions, where the Stirling engine with standard piston motion can no longer be profitably operated, but where it can still be operated with good performance using an optimized sinusoidal (OS) piston motion.

The efficiency of the Stirling engine with optimized piston motion was larger or smaller, depending on each case, compared to the standard motion. This is a consequence of the optimization being done with the objective to maximize the average power rather than the efficiency.

The fact that we have used an ideal regenerator has a large impact on the system behavior as well as the optimization of the piston motion. This work was carried out to show the potential gains in power output that can be achieved by optimizing the piston motion. While the results indicate a considerable performance increase for the investigated model with an ideal regenerator, real engines will have non-ideal regeneration. Our future work will therefore focus on a modified endoreversible Stirling engine with a non-ideal regenerator.

Author Contributions: All authors contributed equally to this article. All authors have read and agreed to the published version of the manuscript.

Funding: This research has been funded by the German Federal Ministry of Education and Research under support code 01LY1218C. The publication of this article was funded by Chemnitz University of Technology.

Conflicts of Interest: The authors declare no conflict of interest.

References

1. Andresen, B.; Salamon, P.; Berry, R.S. Thermodynamics in Finite Time. *Phys. Today* **1984**, *37*, 62–70. [CrossRef]
2. Andresen, B.; Berry, R.S.; Nitzan, A.; Salamon, P. Thermodynamics in Finite Time. I. The Step-Carnot Cycle. *Phys. Rev. A* **1977**, *15*, 2086–2093. [CrossRef]
3. Salamon, P.; Andresen, B.; Berry, R.S. Thermodynamics in Finite Time. II. Potentials for Finite-Time Processes. *Phys. Rev. A* **1977**, *15*, 2094–2102. [CrossRef]
4. Andresen, B.; Salamon, P.; Berry, R.S. Thermodynamics in finite time: Extremals for imperfect heat engines. *J. Chem. Phys.* **1977**, *66*, 1571–1577. [CrossRef]
5. Salamon, P.; Nitzan, A.; Andresen, B.; Berry, R.S. Minimum Entropy Production and the Optimization of Heat Engines. *Phys. Rev. A* **1980**, *21*, 2115–2129. [CrossRef]
6. Ondrechen, M.J.; Andresen, B.; Berry, R.S. Thermodynamics in Finite Time: Processes with Temperature-Dependent Chemical Reactions. *J. Chem. Phys.* **1980**, *73*, 5838–5843. [CrossRef]
7. Salamon, P.; Nitzan, A. Finite Time Optimizations of a Newton's Law Carnot Cycle. *J. Chem. Phys.* **1981**, *74*, 3546–3560. [CrossRef]
8. Gordon, J.M. Observations on Efficiency of Heat Engines Operating at Maximum Power. *Am. J. Phys.* **1990**, *58*, 370–375. [CrossRef]
9. Esposito, M.; Kawai, R.; Lindenberg, K.; Van den Broeck, C. Efficiency at Maximum Power of Low-Dissipation Carnot Engines. *Phys. Rev. Lett.* **2010**, *105*, 150603. [CrossRef]
10. Blaudeck, P.; Hoffmann, K.H. Optimization of the Power Output for the Compression and Power Stroke of the Diesel Engine. In *Efficiency, Costs, Optimization and Environmental Impact of Energy Systems*; Gögüş, Y.A., Öztürk, A., Tsatsaronis, G., Eds.; International Centre for Applied Thermodynamics (ICAT): Istanbul, Turkey, 1995; Volume 2, p. 754.
11. Chen, L.; Sun, F.; Wu, C. Optimal configuration of a two-heat-reservoir heat-engine with heat-leak and finite thermal-capacity. *Appl. Energy* **2006**, *83*, 71–81. [CrossRef]
12. Song, H.; Chen, L.; Sun, F. Endoreversible heat-engines for maximum power-output with fixed duration and radiative heat-transfer law. *Appl. Energy* **2007**, *84*, 374–388. [CrossRef]
13. Hoffmann, K.H. An introduction to endoreversible thermodynamics. *AAPP Phys. Math. Nat. Sci.* **2008**, *86*, 1–19. [CrossRef]

14. Lu, C.; Bai, L. Nonlinear Dissipation Heat Devices in Finite-Time Thermodynamics: An Analysis of the Trade-Off Optimization. *J. Non-Equilib. Thermodyn.* **2017**, *42*, 277–286. [CrossRef]
15. Feidt, M.; Costea, M. From Finite Time to Finite Physical Dimensions Thermodynamics: The Carnot Engine and Onsager's Relations Revisited. *J. Non-Equilib. Thermodyn.* **2018**, *43*, 151–161. [CrossRef]
16. Ge, Y.; Chen, L.; Sun, F. Finite-time thermodynamic modeling and analysis for an irreversible Dual cycle. *Math. Comput. Model.* **2009**, *50*, 101–108. [CrossRef]
17. Michaelidies, E.E. Entropy production and optimization of geothermal power plants. *J. Non-Equilib. Thermodyn.* **2012**, *37*, 233–246. [CrossRef]
18. Andresen, B. Current Trends in Finite-Time Thermodynamics. *Angew. Chem.* **2011**, *50*, 2690–2705. [CrossRef]
19. Badescu, V. Upper Bounds for the Conversion Efficiency of Diluted Blackbody Radiation Energy into Work. *J. Non-Equilib. Thermodyn.* **2018**, *43*, 273–287. [CrossRef]
20. Curzon, F.L.; Ahlborn, B. Efficiency of a Carnot Engine at Maximum Power Output. *Am. J. Phys.* **1975**, *43*, 22–24. [CrossRef]
21. Páez-Hernández, R.T.; Portillo-Díaz, P.; Ladino-Luna, D.; Ramírez-Rojas, A.; Pacheco-Paez, J.C. An analytical study of the endoreversible Curzon-Ahlborn cycle for a non-linear heat transfer law. *J. Non-Equilib. Thermodyn.* **2016**, *41*, 19–27. [CrossRef]
22. Xia, S.; Chen, L.; Sun, F. Maximum cycle work output optimization for generalized radiative law Otto cycle engines. *Eur. Phys. J. Plus* **2016**, *131*, 394. [CrossRef]
23. Ponmurugan, M. Attainability of Maximum Work and the Reversible Efficiency of Minimally Nonlinear Irreversible Heat Engines. *J. Non-Equilib. Thermodyn.* **2019**, *44*, 143–153. [CrossRef]
24. Zhang, Y.; Guo, J.; Lin, G.; Chen, J. Universal Optimization Efficiency for Nonlinear Irreversible Heat Engines. *J. Non-Equilib. Thermodyn.* **2017**, *42*, 253–263. [CrossRef]
25. Schwalbe, K.; Hoffmann, K.H. Stochastic Novikov engine with time dependent temperature fluctuations. *Appl. Therm. Eng.* **2018**, *142*, 483–488. [CrossRef]
26. Schwalbe, K.; Hoffmann, K.H. Performance Features of a Stationary Stochastic Novikov Engine. *Entropy* **2018**, *20*, 52 . [CrossRef]
27. Schwalbe, K.; Hoffmann, K.H. Stochastic Novikov Engine with Fourier Heat Transport. *J. Non-Equilib. Thermodyn.* **2019**, *44*, 417–424. [CrossRef]
28. Narducci, D. Efficiency at Maximum Power of Dissipative Thermoelectric Generators: A Finite-time Thermodynamic Analysis. *J. Mat. Eng. Perform.* **2018**, *27*, 6274–6278. [CrossRef]
29. Roach, T.N.; Salamon, P.; Nulton, J.; Andresen, B.; Felts, B.; Haas, A.; Calhoun, S.; Robinett, N.; Rohwer, F. Application of finite-time and control thermodynamics to biological processes at multiple scales. *J. Non-Equilib. Thermodyn.* **2018**, *43*, 193–210. [CrossRef]
30. Zaeva, M.A.; Tsirlin, A.M.; Didina, O.V. Finite Time Thermodynamics: Realizability Domain of Heat to Work Converters. *J. Non-Equilib. Thermodyn.* **2019**, *44*, 181–191. [CrossRef]
31. Mozurkewich, M.; Berry, R.S. Optimal Paths for Thermodynamic Systems: The ideal Otto Cycle. *J. Appl. Phys.* **1982**, *53*, 34–42. [CrossRef]
32. Fischer, A.; Hoffmann, K.H. Can a quantitative simulation of an Otto engine be accurately rendered by a simple Novikov model with heat leak? *J. Non-Equilib. Thermodyn.* **2004**, *29*, 9–28. [CrossRef]
33. Ge, Y.; Chen, L.; Sun, F. Optimal path of piston motion of irreversible Otto cycle for minimum entropy generation with radiative heat transfer law. *J. Energy Inst.* **2012**, *85*, 140–149. [CrossRef]
34. Hoffmann, K.H.; Watowich, S.J.; Berry, R.S. Optimal Paths for Thermodynamic Systems: The Ideal Diesel Cycle. *J. Appl. Phys.* **1985**, *58*, 2125–2134. [CrossRef]
35. Burzler, J.M.; Blaudeck, P.; Hoffmann, K.H. Optimal Piston Paths for Diesel Engines. In *Thermodynamics of Energy Conversion and Transport*; Stanislaw Sieniutycz, S.; de Vos, A., Eds.; Springer: Berlin, Germany, 2000; pp. 173–198. [CrossRef]
36. Chen, L.; Xia, S.; Sun, F. Optimizing piston velocity profile for maximum work output from a generalized radiative law Diesel engine. *Math. Comput. Model.* **2011**, *54*, 2051–2063. [CrossRef]
37. Xia, S.; Chen, L.; Sun, F. Engine performance improved by controlling piston motion: Linear phenomenological law system Diesel cycle. *Int. J. Therm. Sci.* **2012**, *51*, 163–174. [CrossRef]
38. Lin, J.; Chang, S.; Xu, Z. Optimal motion trajectory for the four-stroke free-piston engine with irreversible Miller cycle via a Gauss pseudospectral method. *J. Non-Equilib. Thermodyn.* **2014**, *39*, 159–172. [CrossRef]

39. Watowich, S.J.; Hoffmann, K.H.; Berry, R.S. Intrinsically Irreversible Light-Driven Engine. *J. Appl. Phys.* **1985**, *58*, 2893–2901. [CrossRef]
40. Watowich, S.J.; Hoffmann, K.H.; Berry, R.S. Optimal Paths for a Bimolecular, Light-Driven Engine. *Il Nuovo Cim. B* **1989**, *104*, 131–147. [CrossRef]
41. Ma, K.; Chen, L.; Sun, F. Optimal paths for a light-driven engine with a linear phenomenological heat transfer law. *Sci. China. Chem.* **2010**, *53*, 917–926. [CrossRef]
42. Chen, L.; Ma, K.; Ge, Y.; Sun, F. Minimum entropy generation path for light-driven engine with [a]-[b] system and heat transfer law. *Environ. Eng. Manag. J.* **2017**, *16*, 2035–2043. [CrossRef]
43. Chen, L.; Ma, K.; Ge, Y. Optimal Configuration of a Bimolecular, Light-Driven Engine for Maximum Ecological Performance. *Arab J. Sci. Eng.* **2017**, *38*, 341–350. [CrossRef]
44. Ma, K.; Chen, L.; Sun, F. Ecological performance improved by controlling piston motion: Linear phenomenological system bimolecular, light driven engine. *J. Energy Inst.* **2013**, *86*, 210–219. [CrossRef]
45. Ladas, G.H.; Ibrahim, O.M. Finite-Time View of the Stirling Engine. *Energy* **1994**, *19*, 837–843. [CrossRef]
46. Wu, F.; Chen, L.; Wu, C.; Sun, F. Optimum performance of irreversible stirling engine with imperfect regeneration. *Energy Convers. Manag.* **1998**, *39*, 727–732. [CrossRef]
47. Timoumi, Y.; Tlili, I.; Nasrallah, S.B. Performance optimization of Stirling engines. *Renew. Energy* **2008**, *33*, 2134–2144. [CrossRef]
48. Chen, C.H.; Yu, Y.J. Combining dynamic and thermodynamic models for dynamic simulation of a beta-type Stirling engine with rhombic-drive mechanism. *Renew. Energy* **2012**, *37*, 161–173. [CrossRef]
49. Ahmadi, M.H.; Ahmadi, M.A.; Bayat, R.; Ashouri, M.; Feidt, M. Thermo-economic optimization of Stirling heat pump by using non-dominated sorting genetic algorithm. *Energy Convers. Manag.* **2015**, *91*, 315–322. [CrossRef]
50. Ahmadi, M.H.; Ahmadi, M.A.; Pourfayaz, F.; Bidi, M.; Hosseinzade, H.; Feidt, M. Optimization of powered Stirling heat engine with finite speed thermodynamics. *Energy Convers. Manag.* **2016**, *108*, 96–105. [CrossRef]
51. Kojima, S. Maximum Work of Free-Piston Stirling Engine Generators. *J. Non-Equilib. Thermodyn.* **2017**, *42*, 169–186. [CrossRef]
52. Craun, M.; Bamieh, B. Optimal Periodic Control of an Ideal Stirling Engine Model. *J. Dyn. Syst. Meas. Control* **2015**, *137*, 071002. [CrossRef]
53. Craun, M.; Bamieh, B. Control-Oriented Modeling of the Dynamics of Stirling Engine Regenerators. *J. Dyn. Syst. Meas. Control* **2018**, *140*, 041001. [CrossRef]
54. Hoffmann, K.H.; Burzler, J.M.; Schubert, S. Endoreversible Thermodynamics. *J. Non-Equilib. Thermodyn.* **1997**, *22*, 311–355.
55. Hoffmann, K.H.; Burzler, J.M.; Fischer, A.; Schaller, M.; Schubert, S. Optimal Process Paths for Endoreversible Systems. *J. Non-Equilib. Thermodyn.* **2003**, *28*, 233–268. [CrossRef]
56. De Vos, A. Reflections on the power delivered by endoreversible engines. *J. Phys. D Appl. Phys.* **1987**, *20*, 232–236. [CrossRef]
57. Chen, J.; Yan, Z. Optimal Performance of an Endoreversible-Combined Refrigeration Cycle. *J. Appl. Phys.* **1988**, *63*, 4795–4798. [CrossRef]
58. De Vos, A. Is a solar cell an edoreversible engine? *Sol. Cells* **1991**, *31*, 181–196. [CrossRef]
59. Andresen, B.; Salamon, P. Distillation by Thermodynamic Geometry. In *Thermodynamics of Energy Conversion an Transport*; Sieniutycz, S., De Vos, A., Eds.; Springer: New York, NY, USA, 2000; Chapter 12, pp. 319–331.
60. Wagner, K.; Hoffmann, K.H. Endoreversible modeling of a PEM fuel cell. *J. Non-Equilib. Thermodyn.* **2015**, *40*, 283–294. [CrossRef]
61. Tsirlin, A.; Sukin, I.A.; Balunov, A.; Schwalbe, K. The Rule of Temperature Coefficients for Selection of Optimal Separation Sequence for Multicomponent Mixtures in Thermal Systems. *J. Non-Equilib. Thermodyn.* **2017**, *42*, 359–369. [CrossRef]
62. Xia, S.; Chen, L.; Sun, F. Maximum power configuration for multireservoir chemical engines. *J. Appl. Phys.* **2009**, *105*, 1–6. [CrossRef]
63. Marsik, F.; Weigand, B.; Thomas, M.; Tucek, O.; Novotny, P. On the Efficiency of Electrochemical Devices from the Perspective of Endoreversible Thermodynamics. *J. Non-Equilib. Thermodyn.* **2019**, *44*, 425–437. [CrossRef]
64. Huleihil, M.; Andresen, B. Optimal piston trajectories for adiabatic processes in the presence of friction. *J. Appl. Phys.* **2006**, *100*, 114914 . [CrossRef]

65. Aragón-González, G.; Canales-Palma, A.; León-Galicia, A.; Morales-Gómez, J.R. Maximum Power, Ecological Function and Efficiency of an Irreversible Carnot Cycle. A Cost and Effectiveness Optimization. *Braz. J. Phys.* **2008**, *38*, 1–8. [CrossRef]
66. Paéz-Hernández, R.T.; Chimal-Eguía, J.C.; Sánchez-Salas, N.; Ladino-Luna, D. General Properties for an Agrowal Thermal Engine. *J. Non-Equilib. Thermodyn.* **2018**, *43*, 131–139. [CrossRef]
67. Masser, R.; Hoffmann, K.H. Dissipative Endoreversible Engine with Given Efficiency. *Entropy* **2019**, *21*, 1117. [CrossRef]
68. Ding, Z.; Chen, L.; Sun, F. Finite time exergoeconomic performance for six endoreversible heat engine cycles: Unified description. *Appl. Math. Mod.* **2011**, *35*, 728–736. [CrossRef]
69. Rogolino, P.; Sellitto, A.; Cimmelli, V.A. Minimal entropy production and efficiency of energy conversion in nonlinear thermoelectric systems with two temperatures. *J. Non-Equilib. Thermodyn.* **2017**, *42*, 287–303. [CrossRef]
70. Schwalbe, K.; Hoffmann, K.H. Optimal Control of an Endoreversible Solar Power Plant. *J. Non-Equilib. Thermodyn.* **2018**, *43*, 255–271. [CrossRef]
71. Schwalbe, K.; Hoffmann, K.H. Novikov engine with fluctuating heat bath temperature. *J. Non-Equilib. Thermodyn.* **2018**, *43*, 141–150. [CrossRef]
72. Açıkkalp, E.; Yamık, H. Modeling and optimization of maximum available work for irreversible gas power cycles with temperature dependent specific heat. *J. Non-Equilib. Thermodyn.* **2015**, *40*, 25–39. [CrossRef]
73. Masser, R.; Hoffmann, K.H. Endoreversible Modeling of a Hydraulic Recuperation System. *Entropy* **2020**, *22*, 383. [CrossRef]
74. Essex, C.; Andresen, B. The principal equation of state for classical particles, photons, and neutrinos. *J. Non-Equilib. Thermodyn.* **2013**, *38*, 293–312. [CrossRef]
75. Wagner, K.; Hoffmann, K.H. Chemical reactions in endoreversible thermodynamics. *Eur. J. Phys.* **2016**, *37*, 015101. [CrossRef]
76. Nelder, J.A.; Mead, R. A Simplex Method for Function Minimization. *Comput. J.* **1965**, *7*, 308–313. [CrossRef]

entropy

MDPI

Article

Re-Optimization of Expansion Work of a Heated Working Fluid with Generalized Radiative Heat Transfer Law

Lingen Chen [1,2,*], Kang Ma [3], Yanlin Ge [1,2] and Huijun Feng [1,2]

[1] Institute of Thermal Science and Power Engineering, Wuhan Institute of Technology, Wuhan 430205, China; geyali9@hotmail.com (Y.G.); huijunfeng@139.com (H.F.)
[2] School of Mechanical & Electrical Engineering, Wuhan Institute of Technology, Wuhan 430205, China
[3] Unit 92941 of PLA, Huludao 125001, China; delmarco1981@sina.com
* Correspondence: lingenchen@hotmail.com; Tel.: +86-27-8361-5046; Fax: +86-27-83638709

Received: 8 June 2020; Accepted: 27 June 2020; Published: 29 June 2020

Abstract: Based on the theoretical model of a heated ideal working fluid in the cylinder, the optimal motion path of the piston in this system, for the maximum work output, is re-studied by establishing the changed Lagrangian function and applying the elimination method when the initial internal energy, initial volume, finial volume and the process time are given and generalized radiative heat transfer law between the working fluid and heat bath is considered. The analytical solutions of the intermediate Euler-Lagrange arc with square, cubic and radiative heat transfer laws are taken as examples and obtained. The optimal motion path of the piston with cubic heat transfer law, which is obtained by applying the elimination method, is compared with that obtained by applying the Taylor formula expansion method through numerical example. The comparing result shows that the accuracy of the result which is obtained by applying the elimination method is not affected by the length of time of the expansion process of the working fluid, so this result is more universal.

Keywords: generalized radiative heat transfer law; optimal motion path; maximum work output; elimination method; finite time thermodynamics

1. Introduction

Finding the optimal configurations of thermodynamic processes and systems under different given optimal objectives is one of the most active research directions of the finite time thermodynamics (FTT) theory [1–10]. For the system of a heated ideal working fluid (WF) in the cylinder, Refs. [11,12] studied the optimal motion path (MP) of the piston under the maximum work output. In this system, the WF was assumed to be ideal gas and the heat transfer law (HTL) between the WF and heat bath was Newton's HTL. Refs. [13–16] used the optimization results obtained in Refs. [11,12] to study the optimal MPs of the piston under the maximum power output [13] and the maximum work output [14] when the power input was given, as well as the optimal operation processes of internal [15] and external [16] combustion engines. In practical process, HTL is not always Newton's HTL and also obeys other laws, and HTLs will affect the optimal configurations of thermodynamic processes and systems. Ref. [17] studied the optimal MP of the piston of a heated ideal WF in the cylinder with linear phenomenological HTL and obtained the analytical solution. Refs. [18,19] used the optimization results obtained in Ref. [17] to optimize the operation processes of internal [18] and external [19] combustion engines with linear phenomenological HTL. Refs. [20–22] studied the optimal MPs of the piston of a heated ideal WF in the cylinder under generalized radiative [20], Dulong–Petit [21] and convective-radiative [22] HTLs, respectively, and obtained the first-order approximate analytical solutions by using the Taylor formula expansion method. Refs. [20–22] applied the Taylor formula expansion method to simplify a

complex differential equation to a linear equation, obtained the equation set of the system, and solved the problem that the analytical solution could not be obtained for the too complex differential equation. The results obtained in Refs. [20–22] have certain theoretical guiding significance. However, the Taylor formula expansion method has its own limitation, and the approximate analytical solution obtained by using the first order Taylor formula expansion method also has limitation. The Taylor formula expansion method is only suitable for the expansion process in which the total process time is very short (for example, the expansion time in Refs. [20–22]). Considering time-dependent heat conductance, Chen et al. [23,24] also studied the optimal MPs of the piston of a heated ideal WF in the cylinder under Newton's [23] and generalized radiative [24] HTLs, respectively. Chen et al. [25] studied the optimal MPs of the piston of a heated ideal WF in the cylinder under generalized convective HTL.

In this paper, on the basis of Refs. [11,12,17,20–22], using the elimination method to eliminate the variable $V(t)$ by applying optimal control theory (OCT), the optimal MP of the piston of a heated ideal WF in the cylinder is studied by using the single variable $E(t)$ when the HTL between the WF and heat bath is generalized radiative HTL. The analytical solutions of intermediate arc, with square, cubic and radiative HTLs, will be taken as examples in this paper. Numerical examples of the optimal MP of the piston for cases of cubic HTL, which is obtained by using the elimination method, will be provided in this paper, and will be compared with those obtained by using the Taylor formula expansion method. The research on the effect of HTL on the optimal MP of a heated ideal WF in the cylinder can enrich FTT.

2. Modeling

Figure 1 shows the model diagram of a cylinder with a moveable piston. In this system, assuming there is 1 mol ideal WF contained in the cylinder, the rate of heat flow $f(t)$ pumped into the cylinder is given, and the HTL between the WF and heat bath is generalized radiative HTL. $q \propto \Delta(T^n)$ is the heat flow rate through the cylinder wall. K is the heat conductance, T_{ex} and T are the temperatures of the heat bath and WF, respectively, n is the power exponent and $Sign(n)$ is a symbolic function: if $n > 0$, then $Sign(n) = 1$, and if $n < 0$, then $Sign(n) = -1$. Furthermore, both the inertia impacts of the WF and the piston, and the friction loss of the piston are all ignored.

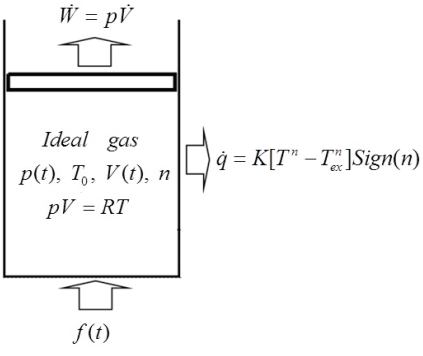

Figure 1. Model diagram of the cylinder with a moveable piston.

In this system, the first law of thermodynamics can be written as

$$f(t) - \dot{E}(t) - \dot{W}(t) - Sign(n)[T^n(t) - {T_{ex}}^n]K = 0 \tag{1}$$

where $W(t)$ is the work, E is the internal energy, the dot above the variable represents the rate of change of this variable with time.

When the WF in the cylinder is heated, the WF will expand, and the work W produced during this process in the time interval $(0, t_m)$ is

$$W = \int_0^{t_m} p(t)\dot{V}(t)dt \tag{2}$$

where V and p are the volume and pressure of the WF, respectively. As demonstrated by Ref. [12], the irreversible efficiency η of the process can be written as

$$\eta = W/\left\{RT_{ex}\ln[V_m/V(0)] + E_p\right\} \tag{3}$$

where $RT_{ex}\ln[V_m/V(0)]$ is the maximum work produced by the WF expanding from $V(0)$ to V_m under constant temperature T_{ex}, and $E_p = \int_0^{t_m} f(t)dt$ is the total energy added to the WF.

3. Optimal Solutions

The general solution is provided first, and three special cases are then provided.

3.1. General Solution

As the WF is an ideal gas, the equations $E = C_V T$ and $pV = RT$ can also be used, where R is the gas constant, and C_V is molar specific heat at constant volume. One can have $p = ER/VC_V$ by combining the above two equations. Substituting it into Equation (2) yields

$$W = \int_0^{t_m} \frac{ER}{C_V}\frac{\dot{V}(t)}{V(t)}dt \tag{4}$$

Combining Equations (1) and (4) yields

$$W = \int_0^{t_m} F(t)dt - \int_0^{t_m}\left[\dot{E}(t) + \frac{Sign(n)K}{{C_V}^n}E^n(t)\right]dt \tag{5}$$

where $F(t) = f(t) + Sign(n)K{T_{ex}}^n$.

As demonstrated by Ref. [20], the optimization problem is

$$\text{maximize } W = \int_0^{t_m} \frac{\dot{V}(t)E(t)R}{V(t)C_V}dt \tag{6}$$

The constraint condition is Equation (1).

For the above problem, the changed Lagrangian function is established [20]

$$L = \frac{\dot{V}(t)E(t)R}{V(t)C_V} + \lambda(t)\left\{\dot{E}(t) - F(t) + \frac{\dot{V}(t)E(t)R}{V(t)C_V} + Sign(n)\left[\frac{E(t)}{C_V}\right]^n K\right\} \tag{7}$$

The Lagrange multiplier $\lambda(t)$ in Equation (7) is a function of time.

Solving the Euler-Lagrange ($E - L$) equation for the problem of Equation (7) gives [20]

$$\dot{E} = \frac{E\dot{F}(t)}{(n-1)K(\frac{E}{C_V})^n Sign(n) + F(t)(n+1)} \tag{8}$$

When $n = 2$, 3 and 4, if the expansion process time is short (for example $t_m = 0.05$ s), the first-order approximate analytical solution for Equation (8) can be obtained by applying Taylor formula expansion method [20], and the first-order approximate analytical solution is

$$\begin{aligned} E(t) &= E'(0) + \dot{E}'(0)t + O(t) \\ &\approx E'(0) + \frac{E\dot{F}(t)}{(n+1)F(t)+Sign(n)(n-1)(\frac{E}{C_V})^n K}t \end{aligned} \tag{9}$$

In this paper, the elimination method introduced in Appendix B of Ref. [12] is adopted to obtain an analytical solution about the $E-L$ arc. Using the OCT to eliminate the variable $V(t)$, the above optimization problem becomes a one-variable problem, and the optimal MP of the piston can be obtained by the single variable $E(t)$.

Since the MP only depends on the term $\int_0^{t_m}\left[\dot{E}(t) + \frac{Sign(n)K}{{C_V}^n}E^n(t)\right]dt$ of Equation (5), the optimization problem can be changed to the problem

$$\text{minimize} \int_0^{t_m}\left[E(t) + \frac{Sign(n)K}{{C_V}^n}E^n(t)\right]dt \tag{10}$$

When Equation (1) is divided by $E(t)$, one can have

$$\frac{F(t) - K[E(t)/C_V]^n Sign(n) - \dot{E}(t)}{E(t)} = \frac{\dot{V}(t)R}{V(t)C_V} \tag{11}$$

Since the values of $V(0)$ and V_m are assumed to be given, the constraint of the equivalent optimization problem can be obtained by integrating Equation (11) over time

$$\begin{aligned} &\int_0^{t_m}\frac{F(t)-K[E(t)/C_V]^n Sign(n)-\dot{E}(t)}{E(t)}dt \\ &= (R/C_V)\ln[V_m/V(0)] = \text{constant} \end{aligned} \tag{12}$$

To minimize Equation (10) under the constraint of Equation (12), the modified Lagrangian function is formed as:

$$L = \dot{E}(t) + \frac{Sign(n)K}{{C_V}^n}E^n(t) + \frac{\lambda}{E}\left\{F(t) - K[E(t)/C_V]^n Sign(n) - \dot{E}(t)\right\} \tag{13}$$

where λ is the constant Lagrange multiplier. The problem has become the one-variable optimization problem.

The $E-L$ equation for Equation (13) is

$$0 = C_V^n E^2\left(\frac{\partial L}{\partial E} - \frac{d}{dt}\frac{\partial L}{\partial \dot{E}}\right) = nKE^{n+1} - Sign(n)(n-1)\lambda KE^n - \lambda C_V^n F \tag{14}$$

Since Lagrange multiplier λ is a constant, it can be obtained by substituting initial values of $E(0)$ and $F(0)$ into Equation (14)

$$\lambda = \frac{nKE^{n+1}(0)}{Sign(n)(n-1)KE^n(0) + {C_V}^n F(0)} \tag{15}$$

Substituting λ from Equation (15) into Equation (14) yields

$$\begin{aligned} &E^{n+1}(t) - E^n(t)\frac{KE^{n+1}(0)(n-1)Sign(n)}{KE^n(0)(n-1)Sign(n)+F(0){C_V}^n} \\ &-F(t)\frac{E^{n+1}(0){C_V}^n}{KE^n(0)(n-1)Sign(n)+F(0){C_V}^n} = 0 \end{aligned} \tag{16}$$

Solving Equation (16), the analytical solution of $E(t)$ can be obtained. Substituting the analytical solution of $E(t)$ into Equation (1) and integrating, the analytical solution of $V(t)$ can be written as

$$V(t) = \left[\frac{E}{E(0)}\right]^{\frac{C_V}{R}} \exp\left[\frac{C_V}{R}\int_0^t \frac{F - Sign(n)K(\frac{E}{C_V})^n}{E}dt\right]V(0) \tag{17}$$

The optimal process that is determined by Equations (16) and (17) is named $E-L$ arc.

As the same with the results obtained in Ref. [12], one can also conclude that the optimal MP of the piston when the work output is the maximum consists of three segments; this problem is called the linkage problem of OCT. The solution for this problem consists of following three segments: an initial adiabatic process, a middle $E-L$ arc, and a final adiabatic process.

Two items of $f(t)$ and $K[T^n(t) - T_{ex}^n]$ are all equal to zero in the adiabatic process; integrating Equation (1), one can obtain

$$E(V) = (V/V_i)^{-R/C_V}E(V_i) \tag{18}$$

For the initial adiabatic process, assuming the initial values of $E(0)$ and $V(0)$ are given, $E'(0)$ and $V'(0)$ are the final values of internal energy and volume, respectively. The motion equations of the three segments are as follows.

Segment (1) is the adiabatic process of the WF expanding form $V(0)$ to $V'(0)$ at $t = 0$. For this process, one has

$$E'(0) = E(0)[V(0)/V'(0)]^{R/C_V} \tag{19}$$

Segment (2) is the $E-L$ arc between $t = 0$ and $t = t_m$. In this segment, the WF expands from the initial state [$V'(0)$ and $E'(0)$] at $t = 0$ to $t = t_m$. For different HTLs, i.e., n equals to different values, the shapes of $E-L$ arc and the corresponding solution methods are all different. When $n = -1, 1, 2$ and 3, solving Equation (16), the analytical solutions of $E(t)$ can be obtained, and corresponding $E-L$ arcs can also be obtained. When n equals to other values, the analytical solutions cannot be obtained by Equation (16), and numerical algorithm must be used to obtain the numerical solutions.

Segment (3) is the adiabatic process of WF expanding to final volume V_m at t_m. For this process, one can use

$$E_m = [V(t_m)/V_m]^{R/C_V}E(t_m) \tag{20}$$

where $E(t_m)$ and $V(t_m)$ can be solved by Equations (16) and (17) at time t_m.

When $E(0)$, $V(0)$ and V_m are given, the above linkage problem becomes the one-dimensional optimization problem of expansion work W and $E'(0)$, i.e., solving the optimal final state [$E'(0)$, $V'(0)$] of initial adiabatic expansion to obtain the maximum expansion work W.

Combining Equations (1) and (4), one can obtain

$$W = \int_0^{t_m} F(t)dt + E'(0) - E_m - \frac{Sign(n)K}{{C_V}^n}\int_0^{t_m} E^n(t)dt \tag{21}$$

The maximum expansion work W is a function of the variable $E'(0)$, and solving the equation $dW/dE'(0) = 0$, the optimal value of $E'(0)$ can be obtained. Substituting W from Equation (21) into the differential equation $dW/dE'(0) = 0$ yields

$$\frac{dE_m}{dE'(0)} + \frac{d\left[Sign(n)K\int_0^{t_m}(E/C_V)^n dt\right]}{dE'(0)} = 0 \tag{22}$$

The analytical solutions of the $E-L$ arc obtained in this paper for $n = 1$ and $n = -1$ are the same as those of obtained in Refs. [12,17], and the corresponding numerical examples have been also given in Ref. [20]. Herein, other three cases are provided.

3.2. Case of $n = 2$

Substituting $n = 2$ into Equation (16) yields

$$E^3(t) - \frac{KE'^3(0)}{KE'^2(0) + {C_V}^2F(0)}E^2(t) - \frac{{C_V}^2E'^3(0)}{KE'^2(0) + {C_V}^2F(0)}F(t) = 0 \tag{23}$$

There are three roots of Equation (23), and the acceptable one is as following

$$E(t) = \frac{2A_1K + 2\sqrt[3]{2}{A_1}^2K^2/B_1 + \sqrt[3]{4}B_1}{6} \tag{24}$$

where

$$A_1 = \frac{E'^3(0)}{KE'^2(0) + {C_V}^2F(0)} \tag{25}$$

$$B_1 = \left[27A_1{C_V}^2F(t) + 2{A_1}^3K^3 + 3\sqrt{3}\sqrt{27{A_1}^2C_V^4F^2(t) + 4{A_1}^4{C_V}^2K^3F(t)}\right]^{1/3} \tag{26}$$

Substituting Equation (24) into Equation (17) yields

$$V(t) = V'(0)\left[\frac{E}{E'(0)}\right]^{-C_v/R}\exp\left\{\frac{1}{C_VR}\int_0^t\frac{C_V^2F - KE^2}{E}dt\right\} \tag{27}$$

The $E - L$ arc in stage (2) is determined by Equations (24)–(27).

Substituting $n = 2$ into Equation (5) yields

$$W = \int_0^{t_m}F(t)dt + E(0) - E_m - \frac{K}{{C_V}^2}\int_0^{t_m}E^2(t)dt \tag{28}$$

Substituting $t = t_m$ into Equations (24) and (27) yields

$$E(t_m) = \frac{2A_1K + 2\sqrt[3]{2}{A_1}^2K^2/B'_1 + \sqrt[3]{4}B'_1}{6} \tag{29}$$

$$V(t_m) = V'(0)\left[\frac{E(t_m)}{E'(0)}\right]^{-C_v/R}\exp\left\{\frac{1}{C_VR}\int_0^{t_m}\frac{C_V^2F - KE^2}{E}dt\right\} \tag{30}$$

where

$$B'_1 = \left[27A_1{C_V}^2F(t_m) + 2{A_1}^3K^3 + 3\sqrt{3}\sqrt{27{A_1}^2C_V^4F^2(t_m) + 4{A_1}^4{C_V}^2K^3F(t_m)}\right]^{1/3} \tag{31}$$

Combining Equations (19), (20), (29) and (30) yields

$$E_m = E(0)\left(\frac{V_m}{V(0)}\right)^{-R/C_v}\left\{\exp\left[\frac{1}{C_VR}\int_0^{t_m}\frac{C_V^2F - KE^2}{E}dt\right]\right\}^{R/C_V} \tag{32}$$

Taking the derivation of Equation (28) with respect to $E'(0)$ and setting it equal to zero, the optimal value of $E'(0)$ should satisfy the following equation

$$\frac{dE_m}{dE'(0)} + \frac{K}{{C_V}^2}\frac{d\int_0^{t_m}E^2(t)dt}{dE'(0)} = 0 \tag{33}$$

3.3. Case of $n = 3$

Substituting $n = 3$ into Equation (16) yields

$$E^4(t) - \frac{2KE'^4(0)}{2KE'^3(0) + {C_V}^3F(0)}E^3(t) - \frac{{C_V}^3E'^4(0)}{2KE'^3(0) + {C_V}^3F(0)}F(t) = 0 \tag{34}$$

There are four roots of Equation (34), and the acceptable one is as following

$$\begin{aligned} E(t) = \tfrac{1}{2}\Bigg[A_2^2K^2 - \tfrac{2A_2C_V^3F(t)}{(3B_2/4)^{1/3}} + \left(\tfrac{2B_2}{9}\right)^{1/3}\Bigg]^{1/2} + \tfrac{A_2K}{2} + \tfrac{1}{2}\Bigg[2A_2^2K^2 + \tfrac{2A_2C_V^3F(t)}{(3B_2/4)^{1/3}} - \left(\tfrac{2B_2}{9}\right)^{1/3} \\ + \tfrac{2A_2^3K^3}{\left[A_2^2K^2 - 2A_2C_V^3F(t)/(3B_2/4)^{1/3} + (2B_2/9)^{1/3}\right]^{1/2}}\Bigg]^{1/2} \end{aligned} \tag{35}$$

where

$$A_2 = \frac{E'^4(0)}{2KE'^3(0) + {C_V}^3F(0)} \tag{36}$$

$$B_2 = -9A_2^3C_V^3K^2F(t) + \sqrt{3}\sqrt{16A_2^3C_V^9F^3(t) + 27A_2^6C_V^6K^4F^2(t)} \tag{37}$$

Substituting Equation (35) into Equation (17) yields

$$V(t) = \left[\frac{E'(0)}{E}\right]^{C_V/R}\exp\left\{\frac{1}{C_V^2R}\int_0^t \frac{FC_V^3 - E^3K}{E}dt\right\}V'(0) \tag{38}$$

The $E - L$ arc in stage (2) is determined by Equations (35)–(38).

Substituting $n = 3$ into Equation (5) yields

$$W = \int_0^{t_m} F(t)dt + E(0) - E_m - (K/{C_V}^3)\int_0^{t_m} E^3(t)dt \tag{39}$$

Substituting $t = t_m$ into Equations (35) and (38) yields

$$\begin{aligned} E(t_m) = \tfrac{1}{2}\Bigg[A_2^2K^2 - \tfrac{2A_2C_V^3F(t)}{\left(3B_2'/4\right)^{1/3}} + \left(\tfrac{2B_2'}{9}\right)^{1/3}\Bigg]^{1/2} + \tfrac{A_2K}{2} + \\ \tfrac{1}{2}\Bigg[\begin{array}{c} 2A_2^2K^2 + \tfrac{2A_2C_V^3F(t)}{\left(3B_2'/4\right)^{1/3}} - \left(\tfrac{2B_2'}{9}\right)^{1/3} + \\ \tfrac{2A_2^3K^3}{\left[A_2^2K^2 - 2A_2C_V^3F(t)/\left(3B_2'/4\right)^{1/3} + \left(2B_2'/9\right)^{1/3}\right]^{1/2}} \end{array}\Bigg]^{1/2} \end{aligned} \tag{40}$$

$$V(t_m) = V'(0)\left[\frac{E(t_m)}{E'(0)}\right]^{\frac{C_V}{R}}\exp\left\{\frac{1}{C_V^2R}\int_0^{t_m}\frac{C_V^3F - KE^3}{E}dt\right\} \tag{41}$$

where

$$B_2' = -9A_2^3C_V^3K^2F(t_m) + \sqrt{3}\sqrt{16A_2^3C_V^9F^3(t_m) + 27A_2^6C_V^6K^4F^2(t_m)} \tag{42}$$

Combining Equations (19), (20), (40) and (41) yields

$$E_m = E(0)\left(\frac{V_m}{V(0)}\right)^{-R/C_v}\left\{\exp\left[\frac{1}{C_V^2R}\int_0^{t_m}\frac{C_V^3F - KE^3}{E}dt\right]\right\}^{R/C_V} \tag{43}$$

Taking the derivation of Equation (39) with respect to $E'(0)$, and setting it equal to zero, the optimal value of $E'(0)$, should satisfy the following equation

$$\frac{dE_m}{dE'(0)} + \frac{K}{{C_V}^3}\frac{d\int_0^{t_m} E^3(t)dt}{dE'(0)} = 0 \tag{44}$$

3.4. Case of $n = 4$

Substituting $n = 4$ into Equation (16) yields

$$E^5(t) - \frac{3K{E'}^5(0)}{3K{E'}^4(0) + {C_V}^4F(0)}E^4(t) - \frac{{C_V}^4{E'}^5(0)}{3K{E'}^4(0) + {C_V}^4F(0)}F(t) = 0 \tag{45}$$

The analytical solution of $E(t)$, with respect to $F(t)$ and $E'(0)$, cannot be obtained because Equation (45) cannot be solved directly. As a result, the method used for cases of $n = 1$, $n = -1$, $n = 2$ and $n = 3$ cannot be adopted for case of $n = 4$. Such an optimization problem can only be solved numerically.

Substituting $n = 4$ into Equation (5) yields

$$W = \int_0^{t_m} F(t)dt + E(0) - E_m - \frac{K}{{C_V}^4}\int_0^{t_m} E^4(t)dt \tag{46}$$

4. Numerical Example

In this section, only the numerical examples when $n = 3$ are taken as examples and provided.

In this case, $V(0) = 1 \times 10^{-3}\,\mathrm{m}^3$, $C_V = 1.5R$, $E(0) = 3780\,\mathrm{J}$, $T_{ex} = 300\,\mathrm{K}$, $V_m = 8 \times 10^{-3}\,\mathrm{m}^3$ and $f(t) = 4200te^{-t}\,\mathrm{W}$ are selected. Tables 1 and 2 list the values of the state variables obtained by using the elimination method with variable K for cases of $t_m = 2$ s and $t_m = 0.05$ s. Table 3 lists the values of the state variables obtained by using the Taylor formula expansion method with variable K for case of $t_m = 0.05$ s. Figures 2 and 3 show the optimal E and V versus t in the $E - L$ arc obtained by using the elimination method for the case of $t_m = 2$ s. Figure 4 shows the optimal E versus t in the $E - L$ arc obtained, respectively, by using the elimination and Taylor formula expansion methods for the case of $t_m = 0.05$ s. Figure 5 shows the optimal V versus t in the $E - L$ arc obtained, respectively, by using the elimination and Taylor formula expansion methods for case of $t_m = 0.05$ s.

The error percentage of internal energy between results obtained by using the elimination method and those obtained by using the Taylor formula expansion method for case of $n = 3$ is approximately 1.92%, and that of volume is approximately 2.54%.

Table 1. Parameters versus K obtained by using the elimination method for case of $n = 3$ when $t_m = 2$ s.

$K\,(\mathrm{W/K}^3)$	7×10^{-5}	8×10^{-5}	9×10^{-5}
$V'(0)\left(10^{-3}\mathrm{m}^3\right)$	1.341	1.316	1.295
$E'(0)\,(\mathrm{J})$	3108.480	3147.350	3181.910
$V(t_m)\left(10^{-3}\mathrm{m}^3\right)$	4.9940	5.205	5.388
$E(t_m)\,(\mathrm{J})$	3412.680	3419.810	3428.710
$E_m\,(\mathrm{J})$	2492.780	2567.670	2634.600
$W\,(\mathrm{J})$	4630.820	4661.790	4690.000
η	0.603	0.607	0.611

Table 2. Parameters versus K obtained by using the elimination method for case of $n = 3$ when $t_m = 0.05$ s.

K (W/K^3)	7×10^{-5}	8×10^{-5}	9×10^{-5}
$V'(0)\left(10^{-3}\mathrm{m}^3\right)$	2.226	2.221	2.216
$E'(0)$(J)	2217.500	2220.850	2224.2000
$V(t_m)\left(10^{-3}\mathrm{m}^3\right)$	2.2677	2.288	2.306
$E(t_m)$(J)	2268.590	2265.820	2264.350
E_m(J)	978.929	983.553	988.173
W(J)	2880.230	2886.190	2892.120
η	0.555	0.556	0.557

Table 3. Parameters versus K obtained by using the method of Taylor series expansion for case of $n = 3$ when $t_m = 0.05$ s.

K (W/K^3)	7×10^{-5}	8×10^{-5}	9×10^{-5}
$V'(0)\left(10^{-3}\mathrm{m}^3\right)$	2.280	2.282	2.284
$E'(0)$(J)	2181.93	2181.100	2179.820
$V(t_m)\left(10^{-3}\mathrm{m}^3\right)$	2.326	2.355	2.382
$E(t_m)$(J)	2237.070	2229.330	2222.680
E_m(J)	981.919	986.471	991.195
W(J)	2896.100	2904.8000	2913.4000
η	0.558	0.560	0.561

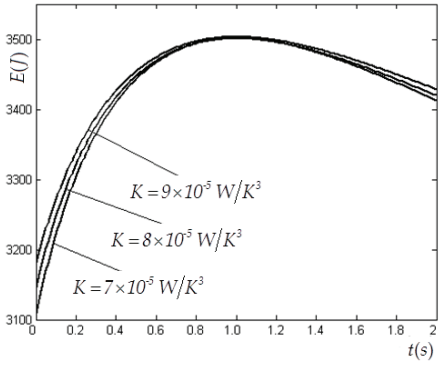

Figure 2. Optimal E versus t obtained by using the elimination method for case of $n = 3$ when $t_m = 2$ s.

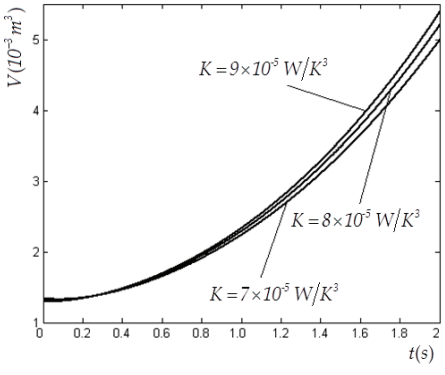

Figure 3. Optimal V versus t obtained by using the elimination method for case of $n = 3$ when $t_m = 2$ s.

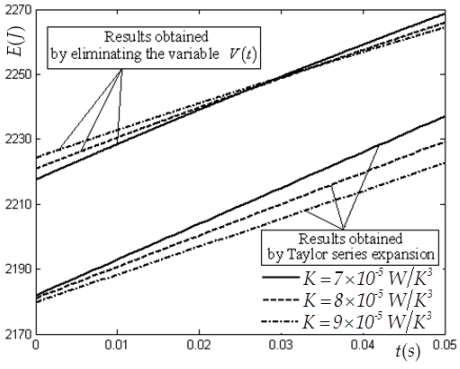

Figure 4. Optimal E versus t obtained by using the elimination and Taylor series expansion methods for case of $n = 3$ when $t_m = 0.05$ s.

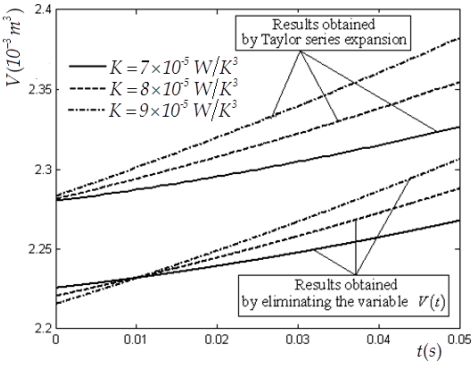

Figure 5. Optimal V versus t obtained by using the elimination and Taylor series expansion methods for case of $n = 3$ when $t_m = 0.05$.

5. Conclusions

Based on the Refs. [11,12,17,20–22], using the elimination method to eliminate the variable $V(t)$ by applying OCT, the optimal MP of the piston of a heated ideal WF in the cylinder is studied by the single variable $E(t)$ when the HTL between the WF and heat bath is generalized radiative HTL. The general solution and those for three special cases of $n = 2$, $n = 3$ and $n = 4$ are provided.

Numerical examples obtained by using the elimination method for the optimal MP when $n = 3$ are provided in this paper, and compared with those obtained by using the Taylor formula expansion method. The expansion process time t_m has great influences not only on the values of initial $E'(0)$ and $V'(0)$, but also on the optimal MP of the piston. Finally, it can be found that the optimal MPs obtained by using the elimination method are similar to those obtained by using the Taylor formula expansion method when the expansion process time is very short.

The model utilized herein includes only heat transfer loss, without considering friction and the inertia of the piston. Therefore, it is an endoreversible model as those discussed in Refs. [26–37]. It can be extended by adding some other dissipations, such as those discussed by Mozurkewich and Berry [38,39] and Hoffmann et al. [40]. Using the elimination method, a more accurate semi-analytical solution is obtained for the optimal MP of the piston in general. The work in this paper can enrich FTT theory.

Author Contributions: Conceptualization, L.C.; funding acquisition, L.C.; methodology, K.M.; software, K.M.; supervision, L.C.; validation, H.F. and Y.G.; writing—original draft, K.M.; writing—review & editing, L.C. All authors have read and agreed to the published version of the manuscript.

Funding: This research was funded the National Natural Science Foundation of China (project number 51779262).

Acknowledgments: The authors wish to thank the academic editor and the reviewers for their careful, unbiased and constructive suggestions, which led to this revised manuscript.

Conflicts of Interest: The authors declare no conflict of interest.

Nomenclature

C_v	Molar heat capacity, J/(mol·K)
E	Internal energy, J
f	Rate of heated, W
K	Heat conductance, W/K^n
L	Modified Lagrangian, W
n	Heat transfer power exponent
p	Pressure, Pa
q	Heat flow rate through the cylinder wall, W
R	Gas constant, J/(mol·K)
$Sign(n)$	Sign function
T	Temperature, K
t	Time, s
V	Volume, m^3
W	Work output, J
Greek symbols	
η	Efficiency
λ	Lagrange multiplier
Subscripts	
ex	External heat bath
m	Final state of expansion process
0	Ambient or reference

References

1. Andresen, B.; Salamon, P.; Berry, R.S. Thermodynamics in finite time. *Phys. Today* **1984**, *37*, 62–70. [CrossRef]
2. Bejan, A. Entropy generation minimization: The new thermodynamics of finite-size devices and finite-time processes. *J. Appl. Phys.* **1996**, *79*, 1191–1218. [CrossRef]
3. Chen, L.G.; Wu, C.; Sun, F.R. Finite time thermodynamic optimization or entropy generation minimization of energy systems. *J. Non-Equilib. Thermodyn.* **1999**, *24*, 327–359. [CrossRef]
4. Andresen, B. Current trends in finite-time thermodynamics. *Angew. Chem. Int. Ed.* **2011**, *50*, 2690–2704. [CrossRef]
5. Chen, L.G.; Meng, F.K.; Sun, F.R. Thermodynamic analyses and optimizations for thermoelectric devices: The state of the arts. *Sci. China Technol. Sci.* **2016**, *59*, 442–455. [CrossRef]
6. Ge, Y.L.; Chen, L.G.; Sun, F.R. Progress in finite time thermodynamic studies for internal combustion engine cycles. *Entropy* **2016**, *18*, 139. [CrossRef]
7. Feidt, M. The history and perspectives of efficiency at maximum power of the Carnot engine. *Entropy* **2017**, *19*, 369. [CrossRef]
8. Chen, L.G.; Xia, S.J. Progresses in generalized thermodynamic dynamic-optimization of irreversible processes. *Sci. Sin. Technol.* **2019**, *49*, 981–1022. [CrossRef]
9. Chen, L.G.; Xia, S.J.; Feng, H.J. Progress in generalized thermodynamic dynamic-optimization of irreversible cycles. *Sci. Sin. Technol.* **2019**, *49*, 1223–1267. [CrossRef]
10. Badescu, V. *Optimal Control in Thermal Engineering*; Springer: New York, NY, USA, 2017.
11. Band, Y.B.; Kafri, O.; Salamon, P. Maximum work production from a heated gas in a cylinder with piston. *Chem. Phys. Lett.* **1980**, *72*, 127–130. [CrossRef]
12. Band, Y.B.; Kafri, O.; Salamon, P. Finite time thermodynamics: Optimal expansion of a heated working fluid. *J. Appl. Phys.* **1982**, *53*, 8–28. [CrossRef]

13. Salamon, P.; Band, Y.B.; Kafri, O. Maximum power from a cycling working fluid. *J. Appl. Phys.* **1982**, *53*, 197–202. [CrossRef]
14. Aizenbud, B.M.; Band, Y.B. Power considerations in the operation of a piston fitted inside a cylinder containing a dynamically heated working fluid. *J. Appl. Phys.* **1981**, *52*, 3742–3744. [CrossRef]
15. Aizenbud, B.M.; Band, Y.B.; Kafri, O. Optimization of a model internal combustion engine. *J. Appl. Phys.* **1982**, *53*, 1277–1282. [CrossRef]
16. Band, Y.B.; Kafri, O.; Salamon, P. Optimization of a model external combustion engine. *J. Appl. Phys.* **1982**, *53*, 29–33. [CrossRef]
17. Chen, L.G.; Sun, F.R.; Wu, C. Optimal expansion of a heated working fluid with phenomenological heat transfer. *Energy Convers. Manag.* **1998**, *39*, 149–156. [CrossRef]
18. Song, H.J.; Chen, L.G.; Sun, F.R. Optimization of a model external combustion engine with linear phenomenological heat transfer law. *J. Energy Inst.* **2009**, *82*, 180–183. [CrossRef]
19. Chen, L.G.; Song, H.J.; Sun, F.R. Optimization of a model internal combustion engine with linear phenomenological heat transfer law. *Int. J. Ambient Energy* **2010**, *31*, 13–22. [CrossRef]
20. Song, H.J.; Chen, L.G.; Sun, F.R. Optimal expansion of a heated working fluid for maximum work output with generalized radiative heat transfer law. *J. Appl. Phys.* **2007**, *102*, 094901. [CrossRef]
21. Ma, K.; Chen, L.G.; Sun, F.R. Optimum expansion of a heated under Dulong-Petit heat transfer law. *J. Eng. Therm. Energy Power* **2009**, *24*, 447–451. (in Chinese)
22. Chen, L.G.; Song, H.J.; Sun, F.R. Optimal expansion of a heated working fluid with convective-radiative heat transfer law. *Int. J. Ambient Energy* **2010**, *31*, 81–90. [CrossRef]
23. Chen, L.G.; Ma, K.; Sun, F.R. Optimal expansion of a heated ideal gas with time-dependent heat conductance. *Int. J. Low-Carbon Technol.* **2013**, *8*, 230–237. [CrossRef]
24. Chen, L.G.; Ma, K.; Sun, F.R. Optimal expansion of a heated working fluid for maximum work output with time-dependent heat conductance and generalized radiative heat transfer law. *J. Non-Equilib. Thermodyn.* **2011**, *36*, 99–122. [CrossRef]
25. Chen, L.G.; Ma, K.; Feng, H.J.; Ge, Y.L. Optimal configuration of a gas expansion process in a piston-type cylinder with generalized convective heat transfer law. *Energies* **2020**, *13*, 3229. [CrossRef]
26. Hoffmann, K.H.; Burzler, J.; Fischer, A.; Schaller, M.; Schubert, S. Optimal process paths for endoreversible systems. *J. Non-Equilib. Thermodyn.* **2003**, *28*, 233–268. [CrossRef]
27. Schwalbe, K.; Hoffmann, K.H. Novikov engine with fluctuating heat bath temperature. *J. Non-Equilib. Thermodyn.* **2018**, *43*, 141–150. [CrossRef]
28. Schwalbe, K.; Hoffmann, K.H. Stochastic Novikov engine with Fourier heat transport. *J. Non-Equilib. Thermodyn.* **2019**, *44*, 417–424. [CrossRef]
29. Paéz-Hernández, R.T.; Chimal-Eguía, J.C.; Sánchez-Salas, N.; Ladino-Luna, D. General properties for an Agrawal thermal engine. *J. Non-Equilib. Thermodyn.* **2018**, *43*, 131–140. [CrossRef]
30. Feidt, M.; Costea, M. From finite time to finite physical dimensions thermodynamics: The Carnot engine and Onsager's relations revisited. *J. Non-Equilib. Thermodyn.* **2018**, *43*, 151–162. [CrossRef]
31. Zaeva, M.A.; Tsirlin, A.M.; Didina, O.V. Finite time thermodynamics: Realizability domain of heat to work converters. *J. Non-Equilib. Thermodyn.* **2019**, *44*, 181–191. [CrossRef]
32. Schwalbe, K.; Hoffmann, K.H. Optimal control of an endoreversible solar power plant. *J. Non-Equilib. Thermodyn.* **2018**, *43*, 255–272. [CrossRef]
33. Wu, Z.X.; Chen, L.G.; Feng, H.J. Thermodynamic optimization for an endoreversible Dual-Miller cycle (DMC) with finite speed of piston. *Entropy* **2018**, *20*, 165. [CrossRef]
34. Dumitrascu, G.; Feidt, M.; Popescu, A.; Grigorean, S. Endoreversible trigeneration cycle design based on finite physical dimensions thermodynamics. *Energies* **2019**, *12*, 3165.
35. Meng, Z.W.; Chen, L.G.; Wu, F. Optimal power and efficiency of multi-stage endoreversible quantum Carnot heat engine with harmonic oscillators at the classical limit. *Entropy* **2020**, *22*, 457. [CrossRef]
36. de Vos, A. Endoreversible models for the thermodynamics of computing. *Entropy* **2020**, *22*, 660. [CrossRef]
37. Masser, R.; Khodja, A.; Scheunert, M.; Schwalbe, K.; Fischer, A.; Paul, R.; Hoffmann, K.H. Optimized piston motion for an alpha-type Stirling engine. *Entropy* **2020**, *22*, 700. [CrossRef]
38. Mozurkewich, M.; Berry, R.S. Finite-time thermodynamics: Engine performance improved by optimized piston motion. *Proc. Natl. Acad. Sci. USA* **1981**, *78*, 1986–1988. [CrossRef]

39. Mozurkewich, M.; Berry, R.S. Optimal paths for thermodynamic systems. The ideal Otto cycle. *J. Appl. Phys.* **1982**, *53*, 34–42. [CrossRef]
40. Hoffmann, K.H.; Watowich, S.J.; Berry, R.S. Optimal paths for thermodynamic systems. The ideal Diesel cycle. *J. Appl. Phys.* **1985**, *58*, 2125–2134. [CrossRef]

entropy

MDPI

Article

Radiative Transfer and Generalized Wind

Christopher Essex * and Indrani Das

Department of Applied Mathematics, the University of Western Ontario, London, ON N6A 5B7, Canada; idas2@uwo.ca

* Correspondence: essex@uwo.ca

Received: 12 August 2020; Accepted: 9 October 2020; Published: 14 October 2020

Abstract: Dissimilar flows can be compared by exploiting the fact that all flux densities divided by their conjugate volume densities form velocity fields, which have been described as generalized winds. These winds are an extension of the classical notion of wind in fluids which puts these distinct processes on a common footing, leading to thermodynamical implications. This paper extends this notion from fluids to radiative transfer in the context of a classical two-stream atmosphere, leading to such velocities for radiative energy and entropy. These are shown in this paper to exhibit properties for radiation previously only thought of in terms of fluids, such as the matching of velocity fields where entropy production stops.

Keywords: entropy production; radiative energy transfer; radiative entropy transfer; two-stream grey atmosphere; energy flux density; entropy flux density; generalized winds

1. Introduction

We understand wind as a phenomenon in a gas or plasma where an impulsive load is delivered by the anisotropic distribution of individual particle velocities realized in the form of a vector field stemming from the collective behaviour of gas particles. Currents in liquids might also be termed "winds" in a general sense. The mechanical wind velocity field can similarly be thought of as the mass flux, $\rho\mathbf{v}$, divided by the volume density of mass ρ. A mechanical wind vector field is the central product of fluid mechanics, typically extracted via the Navier–Stokes equations. Its solutions form a vector field of velocities with a classical rest frame.

The wind velocity can also be seen as implying a rest frame without wind. In that rest frame, the fluid is at rest and local thermodynamic conditions can then be considered. However, out of full thermodynamic equilibrium, that frame does not truly represent a state of rest. There are still currents of other thermodynamical and dynamical physical properties passing though that frame, like energy and momentum to mention a few. These velocity fields also represent frames. An observer riding with the classical wind is not at rest in these other frames.

These fluxes each have different units and as such are difficult to compare, unless one observes that each flux density, $\mathbf{G}$, and its associated volume density, ϕ, induces a velocity vector field of its own, $\mathbf{v}_\phi = \mathbf{G}/\phi$. S. Sieniutycz [1,2] observed that all such vector fields must become identical in thermodynamic equilibrium. He used this insight to explore covariant fluid dynamics and thermodynamics. Each of these fluxes inducing its own vector field, implies a distinct rest frame. When all of these vector fields are the same, there is one reference an observer could ride in where all currents stop. The term "generalized wind" was later coined to describe these vector fields [3]. When a single "generalized wind" velocity exists for all currents there exists a frame where no process occurs. The one-frame condition for all winds becomes a necessary condition for thermodynamic equilibrium. This implies that the entropy production rate must vanish when all generalized wind frames agree.

Fluid dynamics are normally considered distinct from radiative transfer. However, they both can be traced to a common structure in momentum space, wherein the total time derivative of the

mean occupation number $n(\mathbf{r}(t), \mathbf{p}(t), t)$ leads to the primary transport equations for both fluids and radiative transfer. The outcomes through their respective moment equations are very different however. The classical Navier–Stokes equations can be seen as providing rest frames, while radiative transfer concerns photons with no rest frame. Generalized winds must exist for photons too in radiative transfer. There is an energy velocity, $\mathbf{v_e} = \mathbf{F}/u$ stemming from the energy flux density, $\mathbf{F}$, and the volume radiation energy density, u. There is also an entropy velocity, $\mathbf{v_s} = \mathbf{H}/s_r$, arising from the entropy flux density, $\mathbf{H}$, and the entropy volume density, s_r. This paper addresses whether these generalized winds for radiation follow the prescription that velocity fields must agree when entropy production is zero and not elsewhere.

The static plane parallel grey atmosphere was instrumental in the development of the theory of integral equations in the first half of the twentieth century by Hopf, Milne, Schwarzschild and others and of course essential to astrophysics. In this regard, this is a classical subject, but the notion of generalized winds has not been considered. This paper explores the extent to which $\mathbf{v_e}$ and $\mathbf{v_s}$ follow the necessary conditions on the entropy production rate in a classical plane parallel, two-stream atmosphere, while considering the notion of rest frames for generalized winds. This paper shows that the thermodynamical expectations for radiation generalized winds hold within the limitations of the simplified classical radiative transfer problem.

2. Preliminaries

This section has two goals. It lays down the radiative transfer framework for those unfamiliar with the subject, and it introduces radiative entropy transfer for those already familiar with radiative transfer of energy. We proceed in a parallel manner between energy and entropy in order to highlight the close parallels intuitively. This representation is used where possible throughout our paper.

2.1. Energy and Entropy Radiation: The Specific Intensities, Fluxes and Volume Densities

We proceed from the mean occupation number, but expressed in terms of a time-varying number flux density per unit volume and unit solid angle defined in terms of position, frequency and direction: $n(\mathbf{r}(t), \nu, \hat{\mathbf{m}}, t)$ [4]. It is straightforward to connect this primary statistical mechanical object to the specific intensity (also called radiance) which is energy flux density per unit solid angle and frequency, and similarly for entropy. Thus, the frequency dependent specific intensity for photon energy, I_ν, and the same for entropy, J_ν, are,

$$I_\nu = \frac{2h\nu^3}{c^2} n \quad ; \quad J_\nu \equiv \frac{2k_B\nu^2}{c^2}[(1+n)\ln(1+n) - n\ln n]. \tag{1}$$

The factor of 2 in each indicates unpolarised radiation. The entropy expression comes directly from counting Bosons [4].

Moment integrals, in $\hat{\mathbf{m}}$, over all solid angles and frequencies provide well-known integrals for volume densities and flux densities for both energy and entropy, respectively,

$$u = \frac{1}{c}\int I_\nu \, d\Omega d\nu \quad ; \quad s_r = \frac{1}{c}\int J_\nu \, d\Omega d\nu \tag{2}$$

where c is the speed of light.

Accordingly, vector energy flux density ($\mathbf{F}$) and entropy flux density ($\mathbf{H}$) represent first moments,

$$\mathbf{F} = \int I_\nu \hat{\mathbf{m}} \, d\Omega d\nu \quad ; \quad \mathbf{H} = \int J_\nu \hat{\mathbf{m}} \, d\Omega d\nu \tag{3}$$

where $\mathbf{F}$ and $\mathbf{H}$ are presented as the first order moment of the corresponding energy and entropy density function. Note that (2) represents the zeroth order moment of their respective density function.

2.2. Radiative Energy and Entropy Transfer Equations

The equation of radiative energy and entropy transfer can simply be written in the following differential form:

$$\frac{1}{c}\frac{\partial I_\nu}{\partial t} + \hat{\mathbf{m}} \cdot \nabla I_\nu = -\kappa_\nu I_\nu + j_\nu \quad ; \quad \frac{1}{c}\frac{\partial J_\nu}{\partial t} + \hat{\mathbf{m}} \cdot \nabla J_\nu = -\kappa_\nu J_\nu + i_\nu \tag{4}$$

These are easily deduced by differentiating the mean occupation number in time and then applying (1). The right sides are general if j_ν and i_ν are left unspecified. Kirchhoff's law is easily generalized to include entropy too by considering entropy transfer in (4) and considering the equilibrium case when derivatives vanish leaving,

$$j_\nu = \kappa_\nu B_\nu \quad ; \quad i_\nu = \kappa_\nu L_\nu \tag{5}$$

where in thermodynamic equilibrium, $I_\nu = B_\nu$, the Planck function intensity, and $J_\nu = L_\nu$, the intensity of the equilibrium entropy distribution corresponding to the Planck function. That latter can be easily determined through (1).

Classical radiative transfer due to Kirchhoff [5] holds that the equilibrium value for i_ν holds out of equilibrium too. One may make a similar claim for entropy, j_ν. Both assumptions fail in the small ν limit on account of stimulated emission, but hold very well generally simultaneously [6].

Now, integrating (4) over the entire range of frequencies and solid angles and using (2) and (3), one obtains

$$\frac{\partial u}{\partial t} + \nabla \cdot \mathbf{F} = \epsilon \quad ; \quad \frac{\partial s_r}{\partial t} + \nabla \cdot \mathbf{H} = \xi \tag{6}$$

where ϵ and ξ present the source strengths for energy and entropy radiation, respectively.

In the latter case, if radiative absorption and emission are the only irreversible processes, as it is in classical radiative transfer, then ξ is the entropy production rate and $\xi > 0$ according to the second law of thermodynamics. Energy radiation under similar conditions is in radiative equilibrium, i.e., $\epsilon = 0$ or $\nabla \cdot \mathbf{F} = 0$ under steady conditions.

2.3. Classical Grey RT in Plane Parallel Geometry under Steady State Conditions

For simplicity, we proceed with a classical steady state grey atmosphere [5,7]. In keeping with the classical picture, we employ a plane parallel geometry. Then, (4) and (5) are reduced to the following form,

$$\mu\frac{dI_\nu}{dz} = -\kappa_\nu I_\nu + \kappa_\nu B_\nu \quad ; \quad \mu\frac{dJ_\nu}{dz} = -\kappa_\nu J_\nu + \kappa_\nu L_\nu \tag{7}$$

where μ is the direction cosine from the spherical geometry of the moment integrals, arising from $\hat{\mathbf{m}} \cdot \hat{\mathbf{k}}$, where $\hat{\mathbf{k}}$ is the upward direction vector in the atmosphere. Recall that the plane parallel geometry has only one meaningful dimension. On symmetry grounds we find that $\mathbf{F} = F\,\hat{\mathbf{k}}$, and $\mathbf{H} = H\,\hat{\mathbf{k}}$. Thus,

$$F = \int I_\nu\, \mu\, d\Omega\, d\nu \quad ; \quad H = \int J_\nu\, \mu\, d\Omega\, d\nu \tag{8}$$

The grey approximation means that the volume absorption coefficient, κ_ν, has no dependence on frequency ν. Thus, $\kappa_\nu \Rightarrow \kappa$. We introduce the optical depth in the classical way to employ a coordinate

system natural to the physical process in radiative transfer. $\tau = 0$ is the top of the atmosphere and it increases with decreasing altitude, z.

$$d\tau = -\kappa dz \tag{9}$$

Returning to (7), with these conditions and definitions, we find the classical result for energy and a close analogue for entropy,

$$\mu \frac{dI}{d\tau} = I - B \quad ; \quad \mu \frac{dJ}{d\tau} = J - L. \tag{10}$$

Here, I and J are the frequency integrated specific intensity for energy and entropy, respectively. B and L can be found by integrating B_ν and L_ν over all frequencies. These too are well known [4],

$$B = \int_0^\infty B_\nu d\nu = \frac{\sigma}{\pi} T^4 \quad ; \quad L = \int_0^\infty L_\nu d\nu = \frac{4}{3}\frac{\sigma}{\pi} T^3 \tag{11}$$

where σ is the Stefan–Boltzmann constant. One can relate B and L in the following way,

$$\frac{4}{3}\left(\frac{\sigma}{\pi}\right)^{\frac{1}{4}} B^{\frac{3}{4}} = L \tag{12}$$

2.4. Moment Equations and Radiative Equilibrium

Integrating (10) over all solid angles, one obtains

$$\frac{dF}{d\tau} = cu - 4\pi B \quad ; \quad \frac{dH}{d\tau} = cs_r - 4\pi L \tag{13}$$

We write the radiation energy pressure per volume, P, and entropy pressure analogue, R, in as the second moment of respective intensities,

$$P = \frac{1}{c}\int I\mu^2 d\Omega \quad ; \quad R = \frac{1}{c}\int J\mu^2 d\Omega \tag{14}$$

Multiplying (10) by μ, integrating over solid angle, then using the definitions (14) yields,

$$\frac{dP}{d\tau} = \frac{1}{c}F \quad ; \quad \frac{dR}{d\tau} = \frac{1}{c}H \tag{15}$$

Radiative equilibrium requires, $\epsilon = 0 \;\Rightarrow\; \frac{dF}{d\tau} = 0$. It breaks the parallelism between energy and entropy radiation as $\frac{dH}{d\tau} = \xi > 0$ by the second law of thermodynamics. The energy equations significantly simplify in radiative equilibrium. That is exemplified by (13), which becomes

$$u = \frac{4\pi B}{c} \tag{16}$$

2.5. Classical Two Stream Atmosphere with Entropy Radiation

Further progress is made with the classical two-stream assumptions. When moments are taken, instead of assuming that the intensities vary with μ we assume that they are independent of μ, except that intensities only differ between the upper and lower hemispheres (e.g., [7]). The problem becomes a complex computational problem without this assumption, which will be explored in future work. We may use this approximation here to eliminate P and R from (15). First we find

$$u = \frac{2\pi}{c}(I^+ + I^-) \quad ; \quad s_r = \frac{2\pi}{c}(J^+ + J^-) \tag{17}$$

$$F = \pi(I^+ - I^-) \quad ; \quad H = \pi(J^+ - J^-) \tag{18}$$

$$P = \frac{2\pi}{3c}(I^+ + I^-) \quad ; \quad R = \frac{2\pi}{3c}(J^+ + J^-) \tag{19}$$

where the upward intensities of I and J are denoted by I^+ and J^+, respectively, while the downward ones are denoted by I^- and J^-, respectively.

An interesting outcome emerges in passing, as we know radiation pressure volume density is one-third of energy volume density in thermodynamic equilibrium. This emerges for our two-stream atmosphere too, as well as, intriguingly, for entropy,

$$P = \frac{u}{3} \quad ; \quad R = \frac{s_r}{3}. \tag{20}$$

Differentiating (20) with respect to τ then using (15) yields

$$\frac{du}{d\tau} = \frac{3}{c}F \quad ; \quad \frac{ds_r}{d\tau} = \frac{3}{c}H \tag{21}$$

Differentiating (13) w.r.t. τ and using (21) gives,

$$\frac{d^2F}{d\tau^2} - 3F = -4\pi\frac{dB}{d\tau} \quad ; \quad \frac{d^2H}{d\tau^2} - 3H = -4\pi\frac{dL}{d\tau} \tag{22}$$

Differentiating the latter part of (21) w.r.t. τ, and substituting the corresponding part from (13) yields,

$$\frac{d^2s_r}{d\tau^2} - 3s_r = -\frac{12\pi}{c}L \tag{23}$$

In radiative equilibrium (22) yields,

$$\frac{dB}{d\tau} = \frac{3}{4\pi}F \Rightarrow B = \frac{3}{4\pi}F\tau + B(0) \tag{24}$$

At $\tau = 0$, $I^- = 0$; thus, (16) through (18) require $\frac{F}{2\pi} = B(0)$ or

$$B = \frac{F}{2\pi}\left(\frac{3}{2}\tau + 1\right) \tag{25}$$

and substituting into (12) gives,

$$L = \frac{4}{3}\left(\frac{\sigma}{\pi}\right)^{1/4}\left(\frac{F}{2\pi}\right)^{3/4}\left[\frac{3}{2}\tau + 1\right]^{3/4} \tag{26}$$

As τ increases, the radiation state approaches thermodynamic equilibrium. The field approaches isotropy and the energy intensity approaches the ambient black body function, B. We see this by using (25) and by breaking up (16) through (18) to find I^+ and I^- as following

$$I^+ = B\left(\frac{\frac{3}{2}\tau + 2}{\frac{3}{2}\tau + 1}\right) \quad ; \quad I^- = B\left(\frac{\frac{3}{2}\tau}{\frac{3}{2}\tau + 1}\right) \tag{27}$$

As τ increases both intensities become the same and approach the integrated Planck function.

This is a key observation because it implies that we must require that $J^+ \to J^- \to L$ in the large τ limit. Similarly $H \to 0$ and $cs_r \to 4\pi L$ and their derivatives above (see (13) and (21)) vanish in that limit.

3. Generalized Winds

A vector velocity field is associated with a vector flux density and a scalar volume density. This vector field is defined as a generalized wind, which is simply the ratio of a flux density with its corresponding volume density. Thus, radiative energy velocity ($\mathbf{v}_e$) and entropy velocity ($\mathbf{v}_s$) are given by,

$$\mathbf{v}_e = \frac{\mathbf{F}}{u} \quad ; \quad \mathbf{v}_s = \frac{\mathbf{H}}{s_r} \tag{28}$$

Simplifying using (27), we find

$$v_e = \frac{F}{u} = \frac{c}{3\tau + 2} \tag{29}$$

Solving for v_s is more complicated. From above (see the latter part of (13) and (21) each) we have the coupled system as follows,

$$\begin{pmatrix} H' \\ cs_r' \end{pmatrix} = \begin{pmatrix} 0 & 1 \\ 3 & 0 \end{pmatrix} \begin{pmatrix} H \\ cs_r \end{pmatrix} - 4\pi L \begin{pmatrix} 1 \\ 0 \end{pmatrix} \tag{30}$$

where H' and s_r' denote derivatives of H and s_r w.r.t. τ, respectively.

After diagonalization of the above, (30) gives

$$\begin{pmatrix} z_1' \\ z_2' \end{pmatrix} = \begin{pmatrix} \sqrt{3} & 0 \\ 0 & -\sqrt{3} \end{pmatrix} \begin{pmatrix} z_1 \\ z_2 \end{pmatrix} - 4\pi L \begin{pmatrix} 1 \\ 1 \end{pmatrix} \tag{31}$$

where $z_1 = (H + \frac{cs_r}{\sqrt{3}})$ and $z_2 = (H - \frac{cs_r}{\sqrt{3}})$. z_1' and z_2' denote derivatives of z_1 and z_2 w.r.t. τ, respectively.

Now, solving (31) for z_1 and z_2 yields,

$$\begin{pmatrix} z_1 \\ z_2 \end{pmatrix} = \begin{pmatrix} -4\pi \int_0^\tau L e^{-\sqrt{3}(t-\tau)} dt + z_1(0) e^{\sqrt{3}\tau} \\ -4\pi \int_0^\tau L e^{\sqrt{3}(t-\tau)} dt + z_2(0) e^{-\sqrt{3}\tau} \end{pmatrix} \tag{32}$$

In the above equation, there are two conditions that define $z_1(0)$ and $z_2(0)$. The first condition is that at the top of the atmosphere $J^- = 0$. Using the two stream definitions above (see Section 2.5) this implies that $H(0) = cs_r(0)/2$. Thus, it follows

$$\begin{pmatrix} z_1 \\ z_2 \end{pmatrix} = \begin{pmatrix} -4\pi \int_0^\tau L e^{-\sqrt{3}(t-\tau)} dt + H(0)(1 + \frac{2}{\sqrt{3}}) e^{\sqrt{3}\tau} \\ -4\pi \int_0^\tau L e^{\sqrt{3}(t-\tau)} dt + H(0)(1 - \frac{2}{\sqrt{3}}) e^{-\sqrt{3}\tau} \end{pmatrix} \tag{33}$$

The other physical condition on the atmosphere is that thermodynamic equilibrium must be approached asymptotically with optical depth. This is realized by an asymptotic approach to zero of $\frac{dH}{d\tau}$ and $\frac{ds_r}{d\tau}$ with increasing τ. That implies, using z_1, that $z_1' \to 0$, as τ grows. Thus,

$$H(0) \sim \frac{4\pi}{1+\frac{2}{\sqrt{3}}}\int_0^{\tau} Le^{-\sqrt{3}t}dt \Rightarrow H(0) = \frac{4\pi}{1+\frac{2}{\sqrt{3}}}\int_0^{\infty} Le^{-\sqrt{3}t}dt \tag{34}$$

This means that the entropy flux at the top of the atmosphere is the sum of the entropy emissions from the whole atmosphere.

Finally, we obtain

$$v_s = \frac{c}{\sqrt{3}}\frac{z_1+z_2}{z_1-z_2} = \frac{c}{\sqrt{3}}\frac{\{-\chi(\tau)+\chi(\infty)\}e^{\sqrt{3}\tau}+\{-\psi(\tau)+\chi(\infty)\frac{\sqrt{3}-2}{\sqrt{3}+2}\}e^{-\sqrt{3}\tau}}{\{-\chi(\tau)+\chi(\infty)\}e^{\sqrt{3}\tau}-\{-\psi(\tau)+\chi(\infty)\frac{\sqrt{3}-2}{\sqrt{3}+2}\}e^{-\sqrt{3}\tau}} \tag{35}$$

where $\chi(\tau) = \int_0^{\tau}\left[\frac{3}{2}t+1\right]^{3/4}e^{-\sqrt{3}t}dt$ and $\psi(\tau) = \int_0^{\tau}\left[\frac{3}{2}t+1\right]^{3/4}e^{\sqrt{3}t}dt$ arriving at the curious fact that both v_s and v_e are functions of τ only. Thus, Figure 1 is unchanged no matter what atmosphere it represents: planetary atmosphere or star!

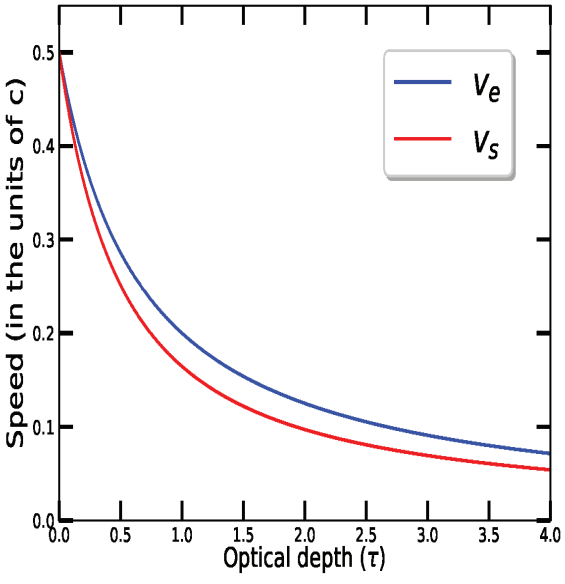

Figure 1. Energy speed (v_e) and entropy speed (v_s) as a function of optical depth (τ). Both of these are evaluated in the units of speed of light (c).

The speeds of the generalized winds are plotted in Figure 1 using (29) and (35). The top of the atmosphere (i.e., up) is at the left ($\tau = 0$) and the atmosphere's interior (i.e., down) is off to the right—truncated at $\tau = 4$ in Figure 1 for convenience. This configuration of coordinates is the standard in radiative transfer.

In Figure 1 we see that both v_e and v_s increase with altitude. This might be interpreted as the result of a net force if we were considering bodies with mass. No such mechanical thinking is appropriate here. The very general picture of equilibrium presented in the introduction does not require such mechanics to be in play.

Off of the right side of the figure, the velocities are both asymptotically approaching zero as densities increase while F is a constant and H is decreasing to zero. Thermodynamic conditions

approach equilibrium in that limit too, agreeing with expectations that $v_e \to v_s$ in that limit. Thus, we expect that the blue and red curves will grow apart with decreasing optical depth. This will continue until the influences of the top of the atmosphere are encountered. Classically this is expected to occur at optical depth 1 or so. Indeed, this appears to be so in Figure 1 where $v_e - v_s$ begins to decrease with decreasing optical depth near $\tau = 1$. The top of the atmosphere $\tau = 0$ is where irreversible absorption and re-emission stops in the absence of any absorbing material, and so we expect that $v_e = v_s$.

It is remarkable that this result is independent of the particulars of any atmosphere. That is, these functions hold for a two-stream approximation for any star or planet. The special case of a finite optical depth only requires an energy and entropy flux to be supplied at the largest τ.

4. Conclusions

This paper provided a quick introduction to classical radiative transfer while appending a new parallel development for radiative entropy transfer. This allowed us to address the classical plane parallel, two-stream, grey atmosphere in a new way. That geometry is applicable to both stellar and planetary atmospheres. With this foundation we were able to turn to the thermodynamics question; in particular, the proposition that all generalized wind vector fields must become identical in thermodynamic equilibrium, or at least in the absence of irreversible processes.

The results within the two-stream assumption strongly suggest that this concept holds for radiation too, extending it beyond its origins in fluid mechanics. The entropy production in this paper does indeed stop at the top of the atmosphere where its generalized winds become the same. Similarly, in the infinite optical depth limit, where equilibrium is approached, the velocities become the same too.

There are however a number of questions. Some need to be addressed in a full, non-two-stream treatment. Some are simpler than others. One of these is the significance of the speed $c/2$ at the top of the atmosphere. Is this top speed the same value in the full non-two-stream treatment? Another question concerns where the largest separation in the functions v_s and v_e occurs at $\tau \approx 1$. Is there a maximum in the entropy production rate there? The functions v_s and v_e are invariant across stellar and planetary atmospheres. Is this true for a full non-two-stream treatment too?

A convenience in thinking about congruent vector fields is the existence of a rest frame that one can imagine travelling with the flow on. While this is easily imagined with vector fields of nearly zero magnitude in the deep interior of the atmosphere, there clearly is a problem at the top of the atmosphere. There is no rest frame there, because there is no radiation coming down to be blue shifted there and the rest of the radiation is red shifted, even that coming from the sides because of time dilation. Photons have no rest frame, but radiation flows can have one. Is there a transition between a rest-frame flow and a more streaming-like flow without one? At what τ would the transition occur? Is it connected with optical depth 1? Is the existence of a rest frame necessary to the concept?

Additionally, we have not even considered the role of scattering which has rich complications as well. These are all interesting questions that our forthcoming work will address.

Author Contributions: The contributions of authors are not denumerable. All authors have read and agreed to the published version of the manuscript.

Acknowledgments: Special thanks goes to Shantanu Basu for helpful discussions and support.

Conflicts of Interest: The authors declare no conflict of interest.

References

1. Sieniutycz, S. Thermal Momentum, heat inertia and a macroscopic extension of de Broglie thermodynamics I. *Adv. Thermodyn.* **1990**, *3*, 328–368.
2. Sieniutycz, S. Thermal Momentum, heat inertia and a macroscopic extension of de Broglie thermodynamics II. *Adv. Thermodyn.* **1992**, *7*, 408–447.

3. Essex, C. Does laboratory-scale physics obstruct the development of a theory for climate? *J. Geophys. Res. Atmos.* **2013**, *118*, 1218–1225. [CrossRef]
4. Essex, C.; Kennedy, D.C. Minimum Entropy Production of Neutrino Radiation in the Steady State. *J. Stat. Phys.* **1999**, *94*, 253–267. [CrossRef]
5. Chandrasekhar, S. *An Introduction to Stellar Structure*; University of Chicago Press: Chicago, IL, USA, 1939.
6. Essex, C. Minimum entropy production in the steady state and radiative transfer. *Astrophys. J.* **1984**, *285*, 279–293. [CrossRef]
7. Chamberlain, J. *Theory of Planetary Atmospheres*; International Geophysics Series, Academic Press: New York, NY, USA, 1978.

entropy

MDPI

Article

Thermodynamics at Very Long Time and Space Scales

Bjarne Andresen [1,†,*] and Christopher Essex [2,†]

[1] Niels Bohr Institute, University of Copenhagen, Blegdamsvej 17, DK-2100 Copenhagen Ø, Denmark
[2] Department of Applied Mathematics, The University of Western Ontario, London, ON N6A 5B7, Canada; essex@uwo.ca
* Correspondence: andresen@nbi.ku.dk
† These authors contributed equally to this work.

Received: 20 July 2020; Accepted: 26 September 2020; Published: 28 September 2020

Abstract: Any observation, and hence concept, is limited by the time and length scale of the observer and his instruments. Originally, we lived on a timescale of minutes and a length scale of meters, give or take an order of magnitude or two. Therefore, we devloped laboratory sized concepts, like volume, pressure, and temperature of continuous media. The past 150 years we managed to observe on the molecular scale and similarly nanoseconds timescale, leading to atomic physics that requires new concepts. In this paper, we are moving in the opposite direction, to extremely large time and length scales. We call this regime "slow time". Here, we explore which laboratory concepts still apply in slow time and which new ones may emerge. E.g., we find that temperature no longer exists and that a new component of entropy emerges from long time averaging of other quantities. Just as finite-time thermodynamics developed from the small additional constraint of a finite process duration, here we add a small new condition, the very long timescale that results in a loss of temporal resolution, and again look for new structure.

Keywords: very long timescales; slow time; ideal gas law; new and modified variables

1. Introduction

Any observer perceives effects and structure only within a limited time window within which it is able to achieve time resolution and thus establishing 'before and after' and causality. At shorter times, we cannot resolve that, at longer times we do not observe any change. We have always experienced laboratory/human scales directly. In more recent times, through inference and some observations, we have extended our time window to shorter timescales, to molecular behavior. This means moving downward by a factor of about 12 or more orders of magnitude. In the slow-time project, we are trying to look the other way, to very long timescales by similarly roughly 12 or more orders of magnitude, in order to search for structures that are invisible on the timescales we experience routinely.

Statistical mechanical modelling of e.g., spin glasses has taken a first step in that direction and found new phenomena, called glassy dynamics, e.g., polynomial time evolution, memory, and recurrence, but still within the laboratory scale universe of variables. An excellent review may be found in [1] and references therein. These phenomena often extend over several decades of time and they involve logarithmic laws, but eventually the usual exponential decay toward equilibrium sets in. These behaviors all involve metastability, i.e., they appear stable for long periods of time. They are also found outside thermodynamics, e.g., describing the decline in extinction rates and scale invariance in the fossil record and the magnetic creep-rate of type-II superconductors [2,3]. In the present study, we go many orders of magnitude beyond those studies and seek possibly new concepts and variables. Does thermodynamics as we know it exist at those time and corresponding length scales?

Our approach is an extension of standard thermodynamics into a new realm very much like finite-time thermodynamics (FTT) was at its conception. FTT added one small condition, a limit on the duration of the process considered. Similarly, slow-time thermodynamics adds the extrapolation to very long times where laboratory dynamics disappears into fluctuations—not the usual equilibrium limit.

The traditional thermodynamic limit in which the system is assumed in equilibrium at uniform intensive parameters (e.g., temperature) throughout no longer exists. The laboratory variables fluctuate faster than what is observable in slow time, and position has similarly been coarsegrained. The system never reaches even quasi-equilibrium in our usual variables. However, perhaps some other variables do?

The aim is to treat directly the effects of long timescales on physics or chemistry as time resolution is lost. The distinct regimes of physics, such as the atomic and laboratory regimes, are familiar. There is a clear hierarchy which has the distinctive property that each regime can "ignore" underlying ones, even though they must be in fundamental agreement. That property is known as closure [4], following the terminology arising from the historical problem of turbulence. Closure emerges through a process that induces new relationships between existing or modified quantities in some limit, yielding a system of equations that can be solved without reference to the underlying regime.

The central question the slow-time approach asks is whether a new regime or new regimes emerge on long timescales and since equilibration expands at a certain rate, correspondingly coarsened space scales. Loosely speaking that question puts an observer in a situation not unlike trying to view the laboratory regime from atomic or kinetic scales. From the standpoint of such scales, the laboratory regime induces new physical variables such as temperature, while burying specific dynamical variables in the loss of resolution whereby entropy emerges.

Our first experiments consisted of flowing water, in this case the Niagara River just below the falls. The left picture of Figure 1 has a 1/2 s exposure. The right picture is exactly the same but with a strong filter allowing a 50 s exposure. The unsteady flow disappears in favor of smooth streamlines turning to the right and vivid standing and bow waves previously invisible in the "noise" of local fluctuations. We see similar "tranquil" situations in slow-time pictures of trees in the wind and of busy traffic in Figure 2. These pictures illustrate the presence of structure appropriate to different timescales.

Figure 1. Two images of the same Niagara Falls downstream flow. The left image is an exposure of 1/2 sec, while the right hand image is exposed for 50 sec. Note the flow features visible in the right hand image (stream lines, bow waves, standing waves, vortices, etc.) that are not clearly visible or simply invisible in the left image due to the "noise" of local fluctuations.

Figure 2. A busy intersection with lots of students, cars, trucks, and busses moving about. The left frame is a normal picture taken at 1/100 sec, the right frame is exposed for 10 min. No moving objects are seen anymore, except for a few very faint shadows. The multiple cars in the left turning lane sit waiting for green, leading to multiple images of running lights in that position. The red-yellow-green traffic lights are all lit at the same time, on average.

2. The Slow-Time Probability Density Function

In our first exploration of a fluctuating system at long times [5], we let temperature and flow velocity fluctuate in a simple homogenous system to produce probability density functions (PDF's) appropriate for long timescales. It identified key features of PDF's that must arise without consideration of the small-scale local equilibrium systems per se.

The standard thermal Gaussian molecular velocity distribution that is centered around u is

$$p_u(v) = \left(\frac{m}{2kT}\right)^{1/2} \frac{1}{\sqrt{\pi}}\, e^{-\frac{m}{2kT}(v-u)^2}, \tag{1}$$

where m is the particle mass, k the Boltzmann constant, and T the standard temperature. Fluctuating the rest velocity u (wind) about zero with a given variance σ_u results in a new Gaussian distribution [5],

$$p_\theta(v) = \left(\frac{m}{2k\theta}\right)^{1/2} \frac{1}{\sqrt{\pi}}\, e^{-\frac{m}{2k\theta}v^2} \tag{2}$$

but with a modified temperature θ,

$$\theta = T + \frac{\sigma_u^2 m}{k} \tag{3}$$

that embeds the fluctuations of the wind velocity u in the form of its variance. In other words, the wind has been thermalized. However the particle velocity v has not been. v persists as a valid quantity on long timescales. Similar quantities that carry over to slow time are particle number, energy, and under certain conditions volume. The fluctuations in wind velocity have become thermalized just like the molecular velocities are on the laboratory timescale, a sort of mega Brownian motion. Because the expression (2) is still a standard thermal Gaussian distribution, just with a new temperature variable in the exponent, θ is indeed a real temperature for its regime, not some sort of "noise temperature". The wind has simply been thermalized. Fluctuating wind on the laboratory scale is no different from fluctuating molecular velocities on the atomic scale. We could, of course, equally well have fluctuated the reference velocity u around a

non-zero value; that would not have changed the conclusions above. A realistic wind fluctuation in our daily weather is $\sigma_u \sim 5$ m/s, which makes the correction term $\sigma_u^2 m/k \sim 0.1$ K, a change that is negligible under normal conditions. θ is not a generalization of temperature, it is an emerging feature of long-time fluctuations of wind and will, therefore, in all places replace the laboratory scale temperature T.

Fluctuating temperature, on the other hand, is more delicate, because it does not only appear in the exponent of the molecular velocity distribution (1), but also in the prefactor. That leads to the very interesting normalized functional form [5]

$$p_{uT}(v) = \int_{-\infty}^{\infty} p_u p_\xi d\xi = \frac{w^3 \psi_0}{\sqrt{\pi}(v^2+w^2)^{3/2}} \, e^{-\frac{w^2\psi_0^2 v^2}{v^2+w^2}}, \tag{4}$$

valid for $w\psi_0 \gtrsim 2$. In this equation, v is the particle velocity and $\psi(\theta)$ is the precision of the Gaussian velocity distribution (1), which is itself fluctuating around the central value

$$\psi_0 \equiv \psi(\theta)\Big|_{\theta=\theta_0} = \sqrt{m/2k\theta_0} \tag{5}$$

according to the Gaussian distribution

$$p_\xi = \frac{w}{\sqrt{\pi}} \, e^{-w^2\xi^2} \tag{6}$$

where ξ is the fluctuating part of ψ, $\psi = \psi_0 + \xi$ and with θ defined in (3). Thus, w is the Gaussian precision of the fluctuations in ψ with units of velocity. For mathematical convenience, we work with the Gaussian precision instead of the standard deviation. For standard deviation σ the precision $\psi = 1/\sigma$. Thus a larger precision means a tighter distribution. We could, of course, have chosen another type of fluctuation for ψ than the Gaussian (6) as long as it approaches zero at large argument values sufficiently rapidly to be normalizable. The results would have been qualitatively the same, the mathematics just more complicated.

$p_{uT}(v)$, Equation (4), is a very interesting function in that it is a conventional Gaussian for large w (i.e., very narrow fluctuation of ψ), but becomes a power function for small w. That means that (4) is not a proper thermal distribution, in other words, the concept of temperature does not extend to long timescales where also the precision of the velocity distribution fluctuates. Besides formally being the precision of the precision of the v fluctuations, w is the transition velocity above which the effects of temperature fluctuations become unthermalizable due to the heavy tails. Figure 3 showing the function $\Phi = p_{uT}/p_u$, i.e., the PDF for fluctuating temperature (4) as compared to the Gaussian PDF for fluctuating wind (1), illustrates this. As long as $v \ll w$, the value is 1, but, outside that range, considerable deviations appear.

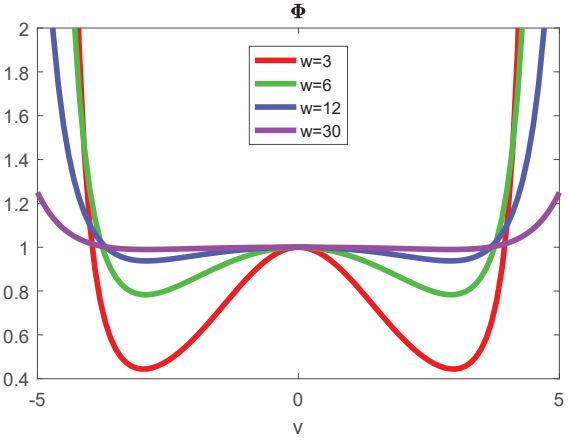

Figure 3. The function $\Phi = p_{uT}/p_u$ relating the PDF for fluctuating velocity as well as temperature for four different precisions of precisions w to the PDF with an exact precision of temperature. The two distributions are identical, i.e., $\Phi = 1$, for $v \ll w$.

So far, we have been considering a one-dimensional system which fluctuated as a whole. Especially for very long time and spatial scales we need to be more realistic and allow for local fluctuations around local equilibria. Such local equilibria are widespread in physics from the smallest to the largest scales. Those systems do not even need to be in steady state. We define this situation as *fluctuating local equilibrium* (FLE). It implies the existence of fluctuating scalar and vector fields throughout the system, each local pocket will fluctuate by itself. We use these properties to determine a slow-time relationship between moments in an FLE system that does not employ usual variables in the laboratory regime valid for finite w in order to arrive at a long timescale equation for an ideal gas in an FLE system. In addition, we assume spatial isotropy for mathematical convenience.

3. The Slow Time Ideal Gas Law

Because the physical world is not continuous to the extreme but eventually discrete, all moments of $p_{uT}(v)$ (4) are convergent for sufficiently large w. Let $\mathcal{M}_n\{g(v)\} \equiv \int_D v^n g(v)\, dv$ be the n^{th} moment of $g(v)$. Subsequently, $\mathcal{M}_0\{p_{uT}(v)\} = 1$, and $\mathcal{M}_1\{p_{uT}(v)\} = 0$ while the second moments add up to the energy E involving all components of $\mathbf{v}$,

$$E = \frac{mN}{2}\sum_i \mathcal{M}_2\{p_{uT}(v_i)\} = \frac{mN}{2}\sum_i \mathcal{M}_2\{p_u(v_i)\} + \frac{mN}{2}\sum_i \mathcal{M}_2\{p_{uT}(v_i) - p_u(v_i)\}, \tag{7}$$

where N is the number of particles in the entire FLE system and the summations over i are the three dimensions of physical space, x, y, z. For some suitable function $f(w, v_*)$, this may be written as

$$E = \frac{3}{2}Nk\theta + Nf(w, v_*). \tag{8}$$

The first term is the standard energy expression for the thermal distribution (1), i.e., the first term on the right hand side of (7), while $f(w, v_*)$ represents the second right hand term. Those are the effects due to the

thermal fluctuations that depend on their precision of precision w and a parameter v_* indicating the largest velocity for which a continuous PDF is physically meaningful. I.e., realistically, no particle in the system has a velocity $v > v_*$ even though the continuous PDF does have a tiny but non-vanishing value all the way to infinity. This observation of discreteness in Nature allows us to truncate the normalization v integral of $p_{uT}(v)$ from ∞ to v_* and thus ensure normalization of the PDF (4) in all situations. The properties of $f(w, v_*)$ require w and v_* to be fully determined in terms of the specific structures in play.

The correspondence principle for the FLE systems requires that the energy equation reduces to the classical equation $E = \frac{3}{2}NkT$ in the absence of fluctuations. Clearly, $\theta \to T$ in that case, but we must also have $\lim_{w\to\infty} f(w, v_*) = 0$. This follows if $\lim_{w\to\infty} p_{uT}(v) = p_u$. To ensure these results, we must either ignore v_* or require $w \ll v_*$. This allows for us to introduce an expansion at infinity of the form $f(w, v_*) = w^{-2}h + O(w^{-4})$, or

$$E = \frac{3}{2}Nk\theta + Nw^{-2}h + O(w^{-4}), \tag{9}$$

where h is a constant to be determined. We do not at present know this slow-time behavior and, thus, must expect $h \neq 0$. Its value will depend on specifics unavailable to us a priori with our laboratory scale knowledge, but it is, in principle, something measurable with appropriate instruments from the [deleted the extra 'the'] slow-time regime.

Discarding higher order terms in (9),

$$E = \frac{3}{2}Nk\theta + Nw^{-2}h \tag{10}$$

becomes the slow-time version of the *ideal gas law*, where θ, w, and h are the natural slow-time regime variables.

4. Discussion and Conclusions

To summarize, the slow-time temperature θ reduces to T in the no fluctuation limit, but the classical temperature T itself no longer exists. The transition velocity, w, the statistical precision of fluctuations in the temperature variable, ψ, (5), represents the transition from Gaussian to heavy tail (polynomial) behavior. h is the residual at infinity of the correction term in the slow-time ideal gas law (10).

Hoping to define an appropriate slow-time temperature, distinct from θ, analogously to the laboratory regime requires that we have a definite entropy of the FLE in order to be able to calculate a derivative that is analogous to $\partial E/\partial S$. However, there is no fundamental reason to carry over the notion of intensities that are generated from partial derivatives of a function of extensities. Like classical temperature, this analogy may prove to be unsuitable for the slow time regime.

Entropy does not exist at the atomic scale, since all motion in principle can be monitored and, thus, is represented as kinetic energy. On the laboratory scale that small random motion is coarse grained away (blurred), but its average effect remains in the form of entropy. In slow time, an analogous effect turns randomly variable winds into a temperature contribution to the new thermalized wind temperature θ.

However, h (9) is different, because it describes the large-scale behavior of the system. The integral h should have a measurable value, but that value is not knowable from classical theoretical principles on the laboratory scale. We still lack an expression that is analogous to $S = -k\sum_i p_i \ln p_i$. The Maxwellian has unsuitable tail behavior to address this matter. The new term in the slow-time ideal gas law (10), h, captures features that are invisible on shorter timescales, e.g., the laboratory scale. In principle, h is a new observable of the slow-time regime. We call it *epitropy*.

Similar slow-time behavior, not seen on shorter timescales, may be found in simple numerical simulations. Consider the Rösler equations,

$$\dot{x} = -y - z \tag{11}$$

$$\dot{y} = x + Ay \tag{12}$$

$$\dot{z} = xz - Cz + B. \tag{13}$$

They describe a chaotic three-dimensional system, where the long-time behavior cannot be observed through a short calculation. Figure 4 shows the XY projection of a long-time calculation (10^7 steps) with the parameters $A = B = 0.2$ and $C = 5.981$ (left) and $C = 5.982$ (right). We can make two observations from these pictures: (i) the many trajectories have a clear large-scale structure with bands of dense population (yellow) and bands of minimal population (brown) very clearly separated although adjacent. Neither the equations nor a few individual trajectories indicate such a behavior. (ii) The tiny difference in the C parameter, from 5.981 to 5.982, dramatically changes the picture. This is slow-time behavior, not seen on cursory plots.

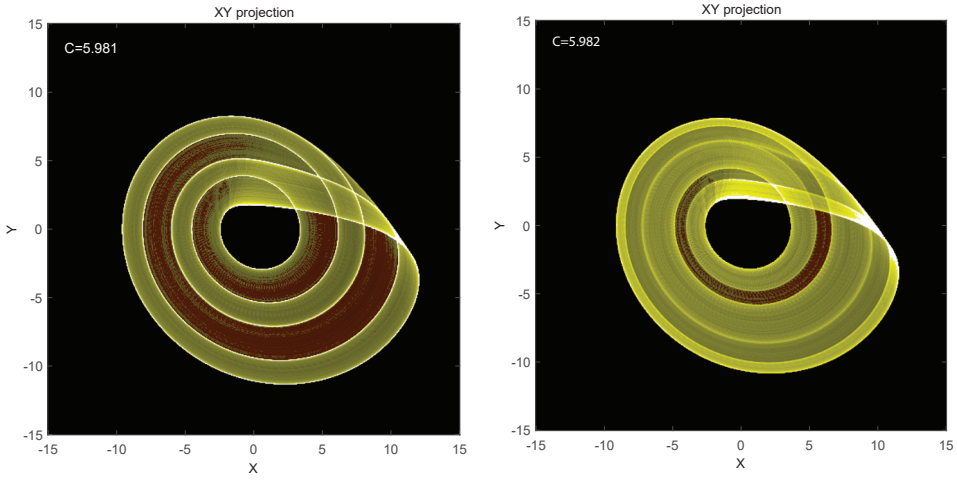

Figure 4. XY-projections of a 10^7 step iteration of the Rösler equations with the parameters $A = B = 0.2$ and $C = 5.981$ (left) and $C = 5.982$ (right). We see that: (i) the many trajectories have a clear large-scale structure with bands of dense population (yellow) and bands of minimal population (brown) very clearly separated although adjacent. (ii) The tiny difference in the C parameter, from 5.981 to 5.982, dramatically changes the picture.

A strange attractor gives some insight into the slow-time picture. Figure 4 shows two instances of the attractor with slightly different parameter settings. Someone computing the trajectory over short time sees trajectories and not densities. Outside of a bifurcation point, they will not detect any qualitative differences in the attractor in the two cases, but, after long time integrations, one notices shifts in the densities of trajectories that only become visible and understandable in the coarsegraining that is implied by densities. One might connect density distributions in space with the system parameters to gain

a qualitative understanding of long-time behaviors without revealing any obvious differences to the short-time trajectories. The long-time behaviors are invisible on the short timescales.

Finite-time thermodynamics added the seemingly small additional constraint that the process in question proceed during a finite time. However, it had a profound effect and led to concepts, like maximum power, minimum entropy production, time dependent potentials, optimal paths, and a lot more and spread to a much wider range of applications than usually called thermodynamic. In this paper, we use the same approach by adding a small new condition, a very long timescale, and again look for new structure. We do not claim to have built a full new theory of slow time, only defined some new concepts, and found surprising observations for particular functional dependencies, like the Gaussian fluctuations laws (6). Other explicit PDF's would have resulted in somewhat different behavior, but the new effects, like a modified temperature (3), a non-Gaussian long-time behavior (4), and the appearance of epitropy (9) would not have been affected. So far, we have only scratched the surface, there is much more to come. The derivation of an "ideal gas law" and a new contribution (epitropy) to the entropy in slow-time are encouraging.

Author Contributions: These authors contributed equally to this work—Conceptualization, B.A. and C.E.; Writing–original draft, B.A. and C.E. All authors have read and agreed to the published version of the manuscript.

Funding: This research received no external funding.

Conflicts of Interest: The authors declare no conflict of interest.

References

1. Sibani, P.; Boettcher, S.; Jensen, H.J. Record dynamics of evolving metastable systems: Theory and applications. *arXiv* **2020**, arxiv:2008.12684.
2. Newman, M.E.J.; Eble, G.J. Decline in extinction rates and scale invariance in the fossil record. *Paleobiology* **1999**, *25*, 434–439. [CrossRef]
3. Oliveira, L.P.; Jensen, H.J.; Nicodemi, M.; Sibani, P. Record dynamics and the observed temperature plateau in the magnetic creep-rate of type-II superconductors. *Phys. Rev. B* **2005**, *71*, 104526. [CrossRef]
4. Essex, C. Climate theory versus a theory for climate. *Int. J. Bifurcation Chaos* **2011**, *21*, 3477–3487. [CrossRef]
5. Essex, C.; Andresen, B. Maxwellian velocity distributions in slow time. *J. Non-Equil. Thermod.* **2015**, *40*, 139–151. [CrossRef]

entropy

MDPI

Article

Modeling, Simulation, and Reconstruction of 2-Reservoir Heat-to-Power Processes in Finite-Time Thermodynamics †

Wolfgang Muschik [1,*] and Karl Heinz Hoffmann [2]

[1] Institut für Theoretische Physik, Technische Universität Berlin, Hardenbergstr. 36, 10623 Berlin, Germany
[2] Institut für Physik, Technische Universität Chemnitz, 09107 Chemnitz, Germany; hoffmann@physik.tu-chemnitz.de
* Correspondence: muschik@physik.tu-berlin.de
† In memory of József Verhás.

Received: 30 July 2020; Accepted: 2 September 2020 ; Published: 7 September 2020

Abstract: The connection between endoreversible models of Finite-Time Thermodynamics and the corresponding real running irreversible processes is investigated by introducing two concepts which complement each other: *Simulation* and *Reconstruction*. In that context, the importance of particular machine diagrams for *Simulation* and (reconstruction) parameter diagrams for *Reconstruction* is emphasized. Additionally, the treatment of internal irreversibilities through the use of contact quantities like the contact temperature is introduced into the Finite-Time Thermodynamics description of thermal processes.

Keywords: simulation; modeling; reconstruction; finite time thermodynamics; endoreversible thermodynamics; nonequilibrium thermodynamics; entropy production; contact temperature

1. Introduction

"Finite-Time Thermodynamics" (FTT) is a field in nonequilibrium thermodynamics that evolved over the past 45 years and that has, and still does, attract a lot of interest. Its central theme is that finishing a thermodynamic task in a finite amount of time is different from doing it with an infinite time horizon. If only limited time is available for a cyclic process to convert heat into work with a macroscopic heat engine, then one usually has to pay a "price" in form of a reduced efficiency. Finite-Time Thermodynamics set out to quantify that price.

This theme has been investigated in a vast variety of paradigmatic examples. If one wants to stress the fact that nonequilibrium processes will have performance features different from an equilibrium description, then one has to make that point for the present with the help of simple examples and not with the complexity of a real running heat engine like, for instance, a jet turbine. Such a simple paradigmatic example is the Curzon–Ahlborn efficiency [1] for a maximum power heat-to-work conversion:

$$\eta_{\mathrm{CA}} = 1 - \sqrt{\frac{T_L}{T_H}}, \tag{1}$$

where T_L and T_H are, respectively, the temperatures of the low- and high-temperature heat baths a Carnot engine is operating between under the restriction that the heat flows to and from the engine are limited by a finite heat conduction. The idea in that example is not to predict the efficiencies of real

running power stations for a quantitative analysis, but to show that the Curzon–Ahlborn efficiency is a much better predictor for observed efficiencies than the Carnot efficiency,

$$\eta_{\text{Carnot}} = 1 - \frac{T_L}{T_H}. \tag{2}$$

Later, it became clear that already earlier Novikov [2] and others [3] had used an even simpler model by considering only one heat flow to be restricted by a limited heat conductance, while the the other flow is reversible. Nonetheless, the Curzon–Ahlborn efficiency also applies to these models.

Finite-Time Thermodynamics evolved over the years and different aspects of nonequilibrium processes were analyzed. Early work started in Steve Berry's group [4–7], and later the field evolved into different directions, for a review see in [8]. While originally the focus was on macroscopic heat engines and their optimization [9–12], lately also quantum engines have attracted interest [13–15]. Again, the goal is to find performance extrema of heat to power conversion [16,17], but also generalizations of the classical availability concept to the quantum level have been considered [18,19].

Finite-Time Thermodynamics as a field is open for different methods, but always with goal to capture the impact of "haste" in performing a thermodynamic process. This is for instance apparent in the work on finite-time potentials [5] or, more recently, on the implementation of finite-time concepts in the realm of biological processes [20]. When it comes to quantifying the necessary irreversibility with its performance losses due to "haste", Endoreversible Thermodynamics [21–27] has shown its great potential as a modeling tool. Its basic concept is to describe a system undergoing nonequilibrium processes as consisting of reservoirs, engines, and reactors, which are modeled as reversible systems, such that the usual thermodynamic equilibrium relations apply. All dissipation is confined to the interactions between those systems, which capture the nonequilibrium transport of energy and other thermodynamic extensities. Usually these are characterized by transport equations for the irreversible processes, which contain characteristic and often fixed parameters like a heat conduction or a flow viscosity. Endoreversible Thermodynamics has been used, for instance, in the treatment of heat-to-power conversion [28–33], in the context of chemical processes [34,35], in thermo-economic applications, [36,37] and in the thermodynamics of computing [38].

In this paper two advancements beyond FTT are presented: The first one goes beyond the limitations of Endoreversible Thermodynamics, following from the assumption of endoreversibility for the subsystems in question. While Endoreversible Thermodynamics uses the fact that it treats subsystems as reversible without internal entropy production, here it is demonstrated that the use of nonequilibrium quantities like contact temperature for heat flows or nonequilibrium molar entropies for material flows allows to include internal irreversibilities for describing nonequilibrium states appropriately. The second advancement is to go beyond the use of paradigmatic but simple models. It thus sheds light on the modeling character of endoreversible systems in relation to real running heat engines. To elucidate the different perspectives taken—on the one hand, starting from a model and, on the other hand, starting from the performance of *real running* heat engine—the concepts of *simulation* and *reconstruction* are introduced. For the presentation of both advancements, two simple and well-known cyclic 2-reservoir heat-to-power model processes are chosen.

The paper is organized as follows. After this introduction, the nonequilibrium time rate of discrete (Schottky) systems is repeated for elucidation of the sequel and for defining a nonequilibrium temperature—the contact temperature—in the third section. The contact temperature is essential for describing real running (irreversible) cyclic 2-reservoir heat-to-power processes in the fourth section. Because contact and reservoir temperatures are used side by side, two different entropy productions appear which are connected by a function of the net heat flows and the contact and reservoir (baths) temperatures—the *non-reversibility.* In the fifth section, a process class is introduced by which the tools of simulation and modeling are defined. These are then applied to two historical basic endoreversible models of FTT: the reversible Carnot process with heat leak and the Curzon–Ahlborn

model, both subjected to a simulation of a real running process and conversely subjected to a reconstruction of a model of an engine.

2. Entropy Time Rate of Discrete Systems

2.1. Equilibrium

A discrete system (also named Schottky system [39]) $\mathcal{G}^*$ in equilibrium is considered which is presupposed to be a reservoir. This implies that the relaxation times of the system are arbitrarily high and that $\mathcal{G}^*$ can be described as being always in equilibrium. Consequently, $\mathcal{G}^*$ is subjected to thermostatics whose validity is presupposed. The *"time rate" of entropy* of the reservoir is

$$\dot{S}^* = \frac{1}{T^*}\,\dot{Q}^* + \boldsymbol{s}^*\cdot\dot{\boldsymbol{n}}^{*e}, \tag{3}$$

and the differentials of thermostatics are written as derivatives

$$d\oplus \equiv \dot{\oplus} \tag{4}$$

because of adapting the formalism to nonequilibrium in the sequel (more details in [40]). The entropy flux in (3) is a factorized decomposition into the reciprocal thermostatic temperature T^* of $\mathcal{G}^*$ and the heat exchange through its surface $\partial\mathcal{G}^*$. Moreover, the components of the external material exchange $\dot{\boldsymbol{n}}^{*e}$ are in reference to $\mathcal{G}^*$. The molar entropies of the components in $\mathcal{G}^*$ are $\boldsymbol{s}^*$. An entropy production does not appear in (3), because $\mathcal{G}^*$ is an equilibrium system and consequently described by thermostatics.

2.2. Non-Equilibrium, 2nd Law and Compound Systems

The *time rate of entropy* of a system $\mathcal{G}$ in nonequilibrium has the form (more details in [40])

$$\dot{S} = \frac{1}{\Theta}\,\dot{Q} + \boldsymbol{s}\cdot\dot{\boldsymbol{n}}^{e} + \Sigma. \tag{5}$$

Here, $\dot{Q}$ and $\dot{\boldsymbol{n}}^{e}$ are the heat exchange and the external material exchange through the surface $\partial\mathcal{G}$ of $\mathcal{G}$. The thermostatic temperature T^* in (3) as well as the equilibrium molar entropies $\boldsymbol{s}^*$ have to be replaced by nonequilibrium quantities, contact temperature, Θ and nonequilibrium molar entropies $\boldsymbol{s}$, which are defined in the sequel. The entropy production Σ is independent of the exchange quantities $\dot{Q}$ and $\dot{\boldsymbol{n}}^{e}$, and consequently, Σ is the time rate of entropy in isolated systems ($\dot{Q}\equiv 0$ and $\dot{\boldsymbol{n}}^{e} \equiv \boldsymbol{0}$).

According to the *Second Law*, the entropy production is not negative [41–43] (a statement which is in such a way not valid in Stochastic Thermodynamics [44]),

$$\Sigma \geq 0. \tag{6}$$

A comparison of (5) with (3) shows that the entropy production $\Sigma^* \equiv 0$ vanishes identically in equilibrium systems.

Now, a nonequilibrium system $\mathcal{G}$ is considered which is embedded into an equilibrium reservoir $\mathcal{G}^*$ having a joint surface $\partial\mathcal{G} \equiv \partial\mathcal{G}^*$, which means a compound system $\mathcal{G}\cup\mathcal{G}^*$ is considered whose sub-systems have mutual exchanges of heat and material. Usually, $\mathcal{G}^*$ is denoted as the system's controlling environment. The joint surface represents the partition between the two subsystems. Especially, inert partitions are considered which are defined as follows. An inert partition does not absorb or emit heat, power, and material [45], as described by the following equations [46,47],

$$\dot{Q} = -\dot{Q}^*, \qquad W = \mathbf{A}\cdot\dot{\boldsymbol{a}} = \mathbf{A}^*\cdot\dot{\boldsymbol{a}} = -W^*, \qquad \dot{\boldsymbol{n}}^{e} = -\dot{\boldsymbol{n}}^{*e}. \tag{7}$$

Here, the *-quantities belong to the system's controlling environment $\mathcal{G}^*$. The work done on the system is performed by the environment using its generalized forces $\mathbf{A}^*$ and orientated at the work variables of the system (which do not appear according to (3) and (4)). The permeability of $\partial\mathcal{G}$ to heat, power, and material is described by (7). The time rate of entropy of the compound system is set by an

Axiom: The partial entropies of sub-systems are additive.

The entropy of the isolated total system $\mathcal{G}^* \cup \mathcal{G}$ is according to this axiom and $(7)_{1,3}$ (a subscript i of an equation reference refers to the ith (in)equalitiy or ith element in the referenced equation; here, $(7)_{1,3}$ refers to the first and last equation in (7))

$$\begin{aligned} \dot{S}^{tot} := \dot{S} + \dot{S}^* &= \frac{1}{\Theta}\,\dot{Q} + \boldsymbol{s}\cdot\dot{\boldsymbol{n}}^e + \frac{1}{T^*}\,\dot{Q}^* + \boldsymbol{s}^*\cdot\dot{\boldsymbol{n}}^{*e} + \Sigma = \\ &= \left(\frac{1}{\Theta} - \frac{1}{T^*}\right)\dot{Q} + (\boldsymbol{s} - \boldsymbol{s}^*)\cdot\dot{\boldsymbol{n}}^e + \Sigma \geq 0. \end{aligned} \tag{8}$$

The inequality sign is due to the isolation of the compound system and the definition of entropy production. The inequality $(8)_3$ allows to define the contact temperature Θ and the nonequilibrium molar entropies $\boldsymbol{s}$ in Section 3. Now, another property of the time rate of nonequilibrium entropy (5) is considered.

2.3. Non-Equilibrium Entropy as a State Function

For defining the time rate of nonequilibrium entropy, a *state space* $\mathcal{Z}$ for $\mathcal{G}$ is needed,

$$\dot{S}\,(\boldsymbol{Z}(t)) = \frac{\partial S}{\partial \boldsymbol{Z}}\cdot\dot{\boldsymbol{Z}}\,(t), \qquad \boldsymbol{Z} \in \mathcal{Z}. \tag{9}$$

Such a nonequilibrium state space is spanned by the equilibrium variables internal energy U, the work variables $\boldsymbol{a}$ and the mol numbers $\boldsymbol{n}$ of the system, supplemented by the nonequilibrium variables contact temperature Θ and the internal variables $\boldsymbol{\xi}$ [48,49]

$$\boldsymbol{Z} = (\boldsymbol{a}, \boldsymbol{n}, U, \Theta, \boldsymbol{\xi}) \in \mathcal{Z}. \tag{10}$$

The choice of such a state space is possible, because in nonequilibrium U and Θ are independent variables, and the entropy production depends on the time rates of the nonequilibrium variables $\Sigma(\dot{\Theta}, \dot{\boldsymbol{\xi}})$ [50].

The time rate of the nonequilibrium entropy has to be in accordance with the equilibrium entropy. This fact is enforced by the embedding theorem: the nonequilibrium entropy rate integrated along an irreversible process $\mathcal{T}$ starting and ending in equilibrium states—A_{eq} and B_{eq}—has the same value as the difference of the equilibrium entropies between the initial and final states of $\mathcal{T}$,

$$\mathcal{T}\int_{A_{eq}}^{B_{eq}} \dot{S}\,(\boldsymbol{Z}(t))dt = S(B_{eq}) - S(A_{eq}). \tag{11}$$

Beyond the embedding theorem, an other property is necessary for establishing a nonequilibrium entropy to be a state function on $\mathcal{Z}$: adiabatical uniqueness defined as follows [45].

Definition 1. *A Schottky system is called* adiabatically unique, *if, for each arbitrary but fixed nonequilibrium state B, after isolation of the system the relaxation process ends always in the same final equilibrium state, independently of how the process into B was performed.*

Considering a cyclic process in $\mathcal{Z}$, taking into account (6) and that $S(\boldsymbol{Z})$ is a state function on $\mathcal{Z}$, (5) results in

$$\oint \dot{S}\, dt \;=\; 0 \;=\; \oint \Big(\frac{1}{\Theta}\,\dot{Q} + \boldsymbol{s}\cdot\dot{\boldsymbol{n}}^{e}\Big)dt + \oint \Sigma dt \;\geq\; \oint \Big(\frac{1}{\Theta}\,\dot{Q} + \boldsymbol{s}\cdot\dot{\boldsymbol{n}}^{e}\Big)dt. \tag{12}$$

Consequently, the entropy production of a cyclic process becomes according to $(12)_2$ and (6)

$$\oint \Sigma dt \;=\; -\oint \Big(\frac{1}{\Theta}\,\dot{Q} + \boldsymbol{s}\cdot\dot{\boldsymbol{n}}^{e}\Big)dt \;\geq\; 0. \tag{13}$$

The definitions of the contact temperature Θ and the nonequilibrium molar entropy $\boldsymbol{s}$ which appear in $(8)_2$ and in the Clausius-like inequality (13) are given in the next section.

3. Contact Temperature and Neq-Molar Entropy

Up to now, Θ and $\boldsymbol{s}$ are placeholders in the dissipation inequality $(8)_2$ for the unknown contact quantities, whereas Σ, the internal entropy production of the system according to (5), is represented by $(1/\Theta - 1/T^{*})\,\dot{Q}$ and $(\boldsymbol{s}-\boldsymbol{s}^{*})\cdot\dot{\boldsymbol{n}}^{e}$ is the entropy production of the heat and material exchanges between the subsystems of the compound system. If the system is a reversible one ($\Sigma = 0$), these exchanges have to be compatible with the dissipation inequality $(8)_2$. Because heat and material exchanges are independent of each other, the following inequalities

$$\Big(\frac{1}{\Theta} - \frac{1}{T^{*}}\Big)\,\dot{Q} \geq 0 \qquad (\boldsymbol{s}-\boldsymbol{s}^{*})\cdot\dot{\boldsymbol{n}}^{e} \;\geq\; \boldsymbol{0} \tag{14}$$

are demanded for defining the placeholders Θ and $\boldsymbol{s}$ which are ascribed to the subsystem $\mathcal{G}$ (the system) of the compound system $\mathcal{G}^{*}\cup\mathcal{G}$.

For defining these place holders, the following proposition [51] for a vector quantity is used:

$$\boldsymbol{X}\cdot f(\boldsymbol{X}) \;\geq\; 0 \,(\text{for all } \boldsymbol{X} \wedge f \text{ continuous at } \boldsymbol{X}=\boldsymbol{0}) \;\Longrightarrow\; f(\boldsymbol{0}) = \boldsymbol{0}. \tag{15}$$

Without any restriction of generality, the left hand brackets in (14) can be presupposed as being continuous, if the right hand factors vanish. These factors vanish, if suitable equilibrium environments $\mathcal{G}^{*}$ are chosen for contacting

$$\mathcal{G}^{*}_{\odot} \;\longrightarrow \dot{Q}_{\odot} = 0, \qquad \mathcal{G}^{*}_{j0} \;\longrightarrow \dot{n}^{e}_{j0} = 0, \quad j = 1,2,...,N \text{ components.} \tag{16}$$

$\mathcal{G}^{*}_{\odot}$ and $\mathcal{G}^{*}_{j0}$ are equipped with equal temperatures $T^{*}_{\odot}$ and T^{*}_{0} which is the same for all $\mathcal{G}^{*}_{j0}$. Consequently, according to the proposition (15) contact quantities can be defined, a temperature Θ and N molar entropies $\boldsymbol{s}$, which belong to the special chosen environments $\mathcal{G}^{*}_{\odot}$ and $\mathcal{G}^{*}_{j0}$:

$$\dot{Q}_{\odot} = 0 \;\Longleftrightarrow\; \Theta = T^{*}_{\odot}, \qquad \dot{\boldsymbol{n}}^{e}_{0} = \boldsymbol{0} \;\Longleftrightarrow\; \boldsymbol{s} = \boldsymbol{s}^{*}_{0}. \tag{17}$$

Here, $(17)_2$ holds true for each chemical component. The $T^{*}_{\odot}$ and $\boldsymbol{s}^{*}_{0}$ are known and belong to the special equilibrium environments (16) which generate the vanishing RHS factors of (14). According to $(17)_1$, the following definition is made [52–54]

Definition 2. *The system's* contact temperature Θ *is that thermostatic temperature $T^{*}_{\odot}$ of the system's equilibrium environment for which the net heat exchange $\dot{Q}_{\odot}$ between the system and this environment through an inert partition vanishes by change of sign.*

Inserting the defining inequalities (14) into the expression $(12)_3$ for cyclic processes results in

$$0 \geq \oint \Big(\frac{1}{\Theta} \dot{Q} + \boldsymbol{s} \cdot \dot{\boldsymbol{n}}^e \Big) dt \geq \oint \Big(\frac{1}{T^*} \dot{Q} + \boldsymbol{s}^* \cdot \dot{\boldsymbol{n}}^e \Big) dt, \tag{18}$$

representing a proof and an extension of Clausius inequality: the thermostatic temperature T^* and the molar entropies $\boldsymbol{s}^*$ of the controlling equilibrium reservoirs which enforce the cyclic process are replaced by nonequilibrium quantities of the system, the contact temperature Θ, and the nonequilibrium molar entropies $\boldsymbol{s}$. Because the inequalities (6) and (14) change into equalities in equilibrium, the entropy rate in equilibrium is (3)

$$\dot{S}^{\,eq} = \frac{1}{T^*} \dot{Q} + \boldsymbol{s}^* \cdot \dot{\boldsymbol{n}}^e, \tag{19}$$

which is a state function (or a total differential) on the equilibrium sub-space [55]

$$\boldsymbol{Z}^{eq} = (\boldsymbol{a}, \boldsymbol{n}, U, \Theta(\boldsymbol{a}, \boldsymbol{n}, U), \boldsymbol{\xi}(\boldsymbol{a}, \boldsymbol{n}, U)) \in \mathcal{Z}^{eq} \subset \mathcal{Z}. \tag{20}$$

Even if the entropy production is added to the equilibrium entropy rate

$$\dot{S}^{\,eq} + \Sigma = \frac{1}{T^*} \dot{Q} + \boldsymbol{s}^* \cdot \dot{\boldsymbol{n}}^e + \Sigma \neq \dot{S}, \tag{21}$$

a comparison with (5) demonstrates that this expression is different from the nonequilibrium entropy rate. Consequently, it is not a state function because of the reservoir quantities T^* and $\boldsymbol{s}^*$ which do not belong to the system.

The utility of the contact quantities from a conceptual point of view is obvious. Their usage acknowledges the fact that real systems exchanging heat and work are not in equilibrium, and thus the assumption of endoreversibility is thus certainly not correct in the strict sense. From a practical point of view, the difference between a nonequilibrium contact temperature and an equilibrium temperature as a proxy in an overall description of thermodynamic systems depends very much on the "nonequilibrium" nature of the situation in question: In some cases the usage of an equilibrium proxy might be possible without much loss of accuracy, in other cases, for instance, when the local temperature field at the inert partition is highly nonuniform or if the assumption of local equilibrium no longer applies, the errors might be considerable. If in particular cases the contact temperature can be obtained in terms of the variables of a nonequilibrium state space, then also from a practical point of view their utility is even larger.

The short sketch of nonequilibrium thermodynamics given here uses explicitly the time and therefore includes Finite-Time Thermodynamics, which deals with irreversible cyclic processes in Schottky systems which are considered in the next sections.

4. Cyclic 2-Reservoir Processes

4.1. First Law

We consider two heat reservoirs (H and L) of different thermostatic (equilibrium) temperatures $T_H > T_L$. A real, cyclic, irreversible 2-reservoir process of a Schottky system is running between these two reservoirs exchanging the heat flows $\dot{Q}_H(t) > 0$ and $\dot{Q}_L(t) < 0$ with H and L, respectively. No mass and no work exchange appear between the reservoirs and the system undergoing the cyclic process. The heat flows depend on the contact temperature and of that of the reservoir

$$\dot{Q}_H(t) = \mathcal{U}_H(\Theta_H, T_H), \qquad \dot{Q}_L(t) = \mathcal{U}_L(\Theta_L, T_L), \tag{22}$$

representing constitutive heat conduction properties which are not specialized here, because constitutive properties are out of scope in this section. Consequently, also the material which performs the considered cyclic process is not specified: the theoretical concept of cyclic 2-reservoir processes, developed here, includes arbitrary cyclic processes of arbitrary materials. Because the non-negative definiteness of the entropy production is presupposed in the sequel, items concerning Stochastic Thermodynamics are out of scope.

The *net heat exchanges per cycle* of the cycle time $\tau > 0$ are ($[Q_H]$=Nm/cycle, $[\tau]$=s/cycle)

$$Q_H := \int_0^\tau \dot{Q}_H(t)dt = \oint \dot{Q}_H\, dt, \qquad Q_L := \int_0^\tau \dot{Q}_L(t)dt = \oint \dot{Q}_L\, dt. \tag{23}$$

Throughout the paper we will consider *heat-to-work conversion processes*, which are characterized by a non-positive work $W \leq 0$, i.e., the system delivers work per cycle to the environment. Therefore, the *First Law* for heat-to-power processes writes

$$Q_H + Q_L + W = 0, \quad W \leq 0, \quad \Longrightarrow \quad Q_H \geq -Q_L > 0. \tag{24}$$

The well-known thermodynamic diagram of a 2-reservoir cyclic heat-to-power process is shown in Figure 1.

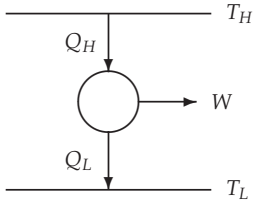

Figure 1. Schematic sketch of a 2-reservoir cyclic heat-to-power process. The arrows indicate the flow direction of energy (heat or work) in this particular heat-to-power process. Using the standard physics convention of heat and work entering a system being positive, one has $Q_H > 0$, $Q_L < 0$, and $W < 0$.

4.2. Contact and Reservoir Temperatures

In order to establish a relation between the contact temperature and the reservoir temperatures below, we introduce the cycle mean values of these contact temperatures, which are defined by

$$\frac{1}{\Theta^+} := \frac{1}{Q_H}\oint \frac{\dot{Q}_H}{\Theta_H}dt > 0, \qquad \frac{1}{\Theta^-} := \frac{1}{Q_L}\oint \frac{\dot{Q}_L}{\Theta_L}dt > 0. \tag{25}$$

The Θ^+ and Θ^- are the mean values of the contact temperatures of the system generated by the cyclic process which is controlled by the constant reservoir temperatures T_H and T_L. Starting with $(14)_1$, we obtain two inequalities valid for the reservoirs H and L

$$\oint \frac{\dot{Q}_H}{\Theta_H}dt \geq \oint \frac{\dot{Q}_H}{T_H}dt \quad \longrightarrow \quad \frac{1}{\Theta^+}Q_H \geq \frac{1}{T_H}Q_H \longrightarrow \Theta^+ \leq T_H, \tag{26}$$

$$\oint \frac{\dot{Q}_L}{\Theta_L}dt \geq \oint \frac{\dot{Q}_L}{T_L}dt \quad \longrightarrow \quad \frac{1}{\Theta^-}Q_L \geq \frac{1}{T_L}Q_L \longrightarrow \Theta^- \geq T_L. \tag{27}$$

The contact temperatures Θ^+ and Θ^- belong in contrast to the reservoir temperatures T_H and T_L to the irreversibly running system. Because Θ^+ and Θ^- are "closer to the system" than T_H and T_L, results are expected which are more realistic than those obtained by using the reservoir temperatures.

4.3. Entropy Production and Efficiency

According to (13), the *entropy production per cycle* Ω appearing in a closed ($\dot{\boldsymbol{n}}^e \equiv \mathbf{0}$) 2-reservoir system of controlling reservoirs H and L of constant thermostatic temperatures is by use of $(13)_1$ and $(14)_1$ ([Ω]=Nm/(K cycle))

$$0 \leq \Omega := \oint \Sigma dt = -\oint \frac{1}{\Theta} \dot{Q}\, dt \leq -\oint \frac{1}{T^*} \dot{Q}\, dt = -\frac{Q_H}{T_H} - \frac{Q_L}{T_L}. \tag{28}$$

This inequality represents the special form of *Clausius' inequality* for 2-reservoir systems [56]. Using $(28)_3$, the entropy production per cycle becomes by use of (25)

$$0 \leq \Omega = -\oint \frac{1}{\Theta} \dot{Q}\, dt = -\frac{1}{\Theta^+} \oint \dot{Q}_H\, dt - \frac{1}{\Theta^-} \oint \dot{Q}_L\, dt = -\frac{Q_H}{\Theta^+} - \frac{Q_L}{\Theta^-}. \tag{29}$$

The second equality is due to the mean value theorem establishing the mean values of the system's contact temperatures averaged over the cyclic process as already done in (26) and (27). In contrast to Clausius' inequality (28) which represents an estimation of the entropy production, (29) is an equation for it.

From $(29)_4$ it follows by taking (24) into account that

$$-\frac{Q_L}{\Theta^-} \geq \frac{Q_H}{\Theta^+} \longrightarrow \frac{Q_H + W}{\Theta^-} \geq \frac{Q_H}{\Theta^+} \longrightarrow Q_H\Big(\frac{1}{\Theta^-} - \frac{1}{\Theta^+}\Big) \geq \frac{-W}{\Theta^-} \geq 0, \tag{30}$$

that together with (26) and (27) results in

$$T_L \leq \Theta^- \leq \Theta^+ \leq T_H. \tag{31}$$

The *efficiency* of the 2-reservoir process is defined by the *work per cycle* and the heat input [57]

$$0 \leq \eta := \frac{-W}{Q_H} = \frac{Q_H + Q_L}{Q_H} = 1 + \frac{Q_L}{Q_H} \leq 1 - \frac{\Theta^-}{\Theta^+} \leq 1 - \frac{T_L}{T_H} \tag{32}$$

and is transformed by taking $(24)_1$, $(30)_1$ and (31) into account. Consequently, two upper limits of the efficiency are obtained, one formulated with the contact temperatures, the other one with the reservoir temperatures.

4.4. Heat Exchange Coefficient, Non-Reversibility, and Power

From $(32)_{5,6}$ follows the *heat exchange coefficient* α

$$1 \leq \alpha := -\frac{Q_H}{Q_L} \leq \frac{\Theta^+}{\Theta^-} \leq \frac{T_H}{T_L} \longrightarrow Q_H = -\alpha Q_L. \tag{33}$$

These inequalities demonstrate that each work producing thermodynamic cyclic process belongs to a heat exchanging coefficient which is located in the angle between $\alpha = 1$ and $\alpha = \alpha_{max}$ in Figure 2.

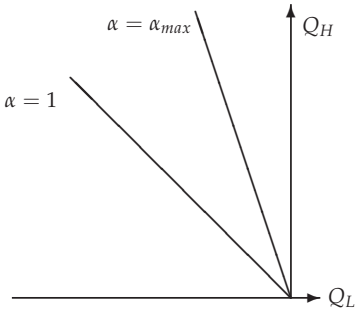

Figure 2. Different values of the heat exchanging coefficient α characterizing different work producing thermodynamic cyclic processes which all are located between $\alpha = 1$ and $\alpha = \alpha_{max} > 1$.

By taking $(33)_2$ into account, the efficiency $(32)_4$ results in

$$0 \le \eta(\alpha) = 1 - \frac{1}{\alpha} \le 1 - \frac{1}{\alpha_{max}} =: \eta_{max}. \tag{34}$$

The entropy production per cycle $(29)_4$ becomes by taking $(28)_4$ and $(33)_2$ into account

$$0 \le \Omega = -\frac{Q_H}{\Theta^+} - \frac{Q_L}{\Theta^-} =: -\Lambda\Big(\frac{Q_H}{T_H} + \frac{Q_L}{T_L}\Big) = -\Lambda\frac{Q_H}{T_L}\Big(\frac{T_L}{T_H} - \frac{1}{\alpha}\Big), \quad 0 < \Lambda \le 1. \tag{35}$$

The parameter Λ is called the *non-reversibility*. Its range is generated by the inequality $(28)_4$. It is defined by $(35)_3$ and makes possible to replace the mean process values of the contact temperature, Θ^+ and Θ^-, (quantities which are difficult to determine experimentally) by one parameter $\Lambda(\alpha, \Theta^+, \Theta^-, T_H, T_L)$ according to (35) which is limited by $(35)_5$ and which describes the correction, if the contact temperatures are replaced by the reservoir temperatures. As shown Appendix A.1, the non-reversibility is

$$\Lambda(\alpha, \Theta^+, \Theta^-, T_H, T_L) = \frac{(\alpha\Theta^- - \Theta^+)T_H T_L}{(\alpha T_L - T_H)\Theta^+\Theta^-}. \tag{36}$$

From (35) follows by use of $(34)_2$ and $(32)_2$

$$T_L\frac{\Omega}{\Lambda} = -Q_H\Big(\frac{T_L}{T_H} - 1 + 1 - \frac{1}{\alpha}\Big) = Q_H\Big(1 - \frac{T_L}{T_H}\Big) - Q_H\eta = Q_H\Big(1 - \frac{T_L}{T_H}\Big) + W. \tag{37}$$

Here, $\Omega/\Lambda \ge \Omega$ is the *reservoir-related entropy production* $(28)_5$, which exceeds the regular entropy production $(29)_4$. Consequently, the work per cycle which is done on the system's environment is according to (37),

$$0 \le -W = Q_H\Big(1 - \frac{T_L}{T_H}\Big) - T_L\frac{\Omega}{\Lambda} \le Q_H\Big(1 - \frac{T_L}{T_H}\Big) - T_L\Omega. \tag{38}$$

The somewhat strange fact that two different entropy productions occur (namely, Ω and Ω/Λ) is due to the side by side use of contact and reservoir temperatures, whereas the entropy production is based on the time rate of entropy necessarily formulated with the contact temperature, the work belongs to the greater reservoir-related entropy production according to (38). Another shape of $(35)_{3,2}$ or $(38)_1$ is

$$\frac{Q_H}{T_H} + \frac{Q_L}{T_L} = -\frac{\Omega}{\Lambda} \le 0, \qquad \frac{Q_H}{\Theta^+} + \frac{Q_L}{\Theta^-} = -\Omega \le 0. \tag{39}$$

The *power per cycle* becomes by use of the cycle time τ and of $(32)_1$

$$P := \frac{-W}{\tau} = Q_H\frac{\eta}{\tau} \ge 0. \tag{40}$$

Inserting $(34)_2$ and $(33)_6$, the power per cycle results according to $(34)_2$ in

$$P = \frac{Q_H}{\tau}\left(1-\frac{1}{\alpha}\right) = \frac{Q_L}{\tau}(1-\alpha) = \frac{Q_L}{\tau}\frac{\eta}{\eta-1}. \tag{41}$$

From $(38)_2$ and $(40)_2$ follows

$$P = \frac{P}{\eta}\Big(1-\frac{T_L}{T_H}\Big) - \frac{T_L}{\tau}\frac{\Omega}{\Lambda} \implies \Big(\frac{1}{\eta}(1-\frac{T_L}{T_H})-1\Big)P = \frac{T_L}{\tau}\frac{\Omega}{\Lambda}, \tag{42}$$

resulting in

$$\Big(1-\frac{T_L}{T_H}-\eta\Big)P = \frac{T_L}{\tau}\frac{\Omega}{\Lambda}\eta \quad \implies \quad \eta \le 1-\frac{T_L}{T_H}, \tag{43}$$

a relation which come again into consideration, if reversible processes are taken into account (53).

4.5. Reversible "Processes"

Because endoreversible models are considered in the sequel, reversible processes have to be defined, and the thermodynamic relations of Sectons 4.1–4.4 are translated for reversible processes. These "processes" are defined by vanishing entropy production

$$\Omega_{rev} \equiv 0. \tag{44}$$

From (39) and $(44)_1$ follows *Clausius' equality*

$$\frac{Q_H^{rev}}{T_H} + \frac{Q_L^{rev}}{T_L} = 0 = \frac{Q_H^{rev}}{\Theta_{rev}^+} + \frac{Q_L^{rev}}{\Theta_{rev}^-}, \tag{45}$$

by use of (31) and $(24)_4$ resulting in

$$0 \ge Q_H^{rev}\Big(\frac{1}{T_H}-\frac{1}{\Theta_{rev}^+}\Big) = Q_L^{rev}\Big(\frac{1}{\Theta_{rev}^-}-\frac{1}{T_L}\Big) \ge 0. \tag{46}$$

Consequently,

$$\Theta_{rev}^+ = T_H, \qquad \Theta_{rev}^- = T_L \tag{47}$$

follows, that means, the difference between contact and reservoir temperatures vanishes for reversible processes, and from (36) and (47) follows for the non-reversibility

$$\Lambda_{rev} = 1. \tag{48}$$

Starting with $(32)_2$ written down for reversible processes, $(38)_2$ results by use of $(34)_2$ in

$$Q_H^{rev}\eta_{rev} = -W^{rev} = Q_H^{rev}\Big(1-\frac{T_L}{T_H}\Big) \quad \implies \quad \eta_{rev} = 1-\frac{T_L}{T_H} \implies \alpha_{rev} = \frac{T_H}{T_L}. \tag{49}$$

Taking $(49)_3$ into account, (38) becomes

$$0 \le -W = Q_H\eta_{rev} - T_L\frac{\Omega}{\Lambda} \le Q_H\eta_{rev} - T_L\Omega, \tag{50}$$

that results in two statetments: (i) the reversible work is maximal

$$\Omega \doteq 0 \implies -W_{max} = Q_H\Big(1-\frac{T_L}{T_H}\Big) = -W^{rev} \tag{51}$$

and (ii) the reservoir-related entropy production is maximal, if the work vanishes

$$W \doteq 0 \implies \Big(\frac{\Omega}{\Lambda}\Big)_{max} = Q_H\Big(\frac{1}{T_L} - \frac{1}{T_H}\Big). \tag{52}$$

and finally, the power (43) becomes

$$(\eta_{rev} - \eta)P = \frac{T_L}{\tau}\frac{\Omega}{\Lambda}\eta \geq 0 \quad \implies \quad \eta \leq \eta_{max} = \eta_{rev}. \tag{53}$$

The expressions for the entropy production, power and efficiency, which are derived here, will be needed in the next sections for simulating real cyclic 2-reservoir processes by endoreversible models.

4.6. Maximal Power and Cycle Time: The Machine Diagrams

Considering a special engine, its "fuel consumption" Q_H and its "heat loss" Q_L depend on the cycle time [58]

$$Q_H = \Psi(\zeta), \quad Q_L = \Xi(\zeta), \qquad \zeta \equiv (T_H, T_L, \tau) \tag{54}$$

relations which are called *machine diagrams* and which characterize the considered engine. Consequently, the machine diagrams tranfer the cycle time to the thermodynamic quantities which are discussed in Section 4

$$\alpha(\zeta) = -\frac{\Psi(\zeta)}{\Xi(\zeta)}, \quad \eta(\zeta) = 1 + \frac{\Xi(\zeta)}{\Psi(\zeta)}, \quad P(\zeta) = \frac{1}{\tau}\Big(\Psi(\zeta) + \Xi(\zeta)\Big), \tag{55}$$

$$\Omega(\zeta) = -\Lambda(\vartheta)\Big(\frac{\Psi(\zeta)}{T_H} + \frac{\Xi(\zeta)}{T_L}\Big), \quad \Lambda(\vartheta) = \chi(\zeta, \Theta^+, \Theta^-). \tag{56}$$

Taking a reversible process into account, (54) becomes

$$Q_H^{rev} = \Psi(\zeta_{rev}), \quad Q_L^{rev} = \Xi(\zeta_{rev}), \qquad \zeta_{rev} \equiv (T_H, T_L, \infty) \tag{57}$$

Taking the machine diagrams (54) into consideration, the relation $(55)_2$ of the efficiency depends on the cycle time. If the solubility of $(55)_2$ for the cycle time is presupposed,

$$\tau = \Pi(T_H, T_L, \eta), \tag{58}$$

the power $(40)_2$ results in

$$0 \leq \frac{P}{Q_H} = \frac{\eta}{\tau(\eta)}, \quad \implies \quad \Big(\frac{P}{Q_H}\Big)\Big|_{\eta=0} = 0, \quad \Big(\frac{P}{Q_H}\Big)\Big|_{\eta=\eta_{rev}} = 0 \tag{59}$$

Now the question arises: Is there any efficiency η^* for which the power per fuel consumption is maximal? According to (59), the answer depends on the cycle time $\tau(\eta)$:

$$\frac{d}{d\eta}\Big(\frac{P}{Q_H}\Big) = \frac{\tau(\eta) - \eta(d\tau/d\eta)}{\tau^2(\eta)} \doteq 0. \tag{60}$$

There is a local maximum of P/Q_H with respect to the efficiency, because the equation

$$\eta^*\Big(\frac{d\tau}{d\eta}\Big)\Big|_{\eta^*} = \tau(\eta^*), \quad \implies \quad \Big(\frac{d\ln\tau}{d\eta}\Big)\Big|_{\eta^*} = \frac{1}{\eta^*} \tag{61}$$

has a solution η^* due to $P/Q_H \not\equiv 0$ and $(59)_{3,4}$.

The local maximum of another quantity, $P/(\Omega/\Lambda)$, with respect to the efficiency is found out in the Appendix A.2. These two examples demonstrate that the machine diagrams determine for what efficiency the power is maximal. According to the machine diagrams (54), the power $(55)_3$

depends on the cycle time. That is the reason why the machine diagrams have to be taken into account. If other quotients like P/Q_H, P/Q_L, or $P/(\Omega/\Lambda)$, in which the power is measured relative to Q_H, etc., are optimized, then the maxima of these quotients belong to different efficiencies.

4.7. Universality

The cyclic 2-reservoir heat-to-power processes considered in the above section are universal in the following sense.

- The cyclic process between the two heat reservoirs is arbitrary: it may be a Carnot, Otto, Diesel, Brayton, or another cyclic reversible or irreversible process.
- The working material which perform this cyclic process under control of the two heat reservoirs is arbitrary: it may be a perfect or real gas, a fluid, a liquid crystal, or radiation in classical or quantumtheoretical description, the only restriction is that the chosen substance allows such a cyclic 2-reservoir process.

Consequently, the general concepts developed above in Section 4 can be applied to the items considered below. The simulation of an irreversible cyclic 2-reservoir heat-to-power process by different endoreversible models which do not represent real processes because of their reversible parts. To explain what simulation means, two well-known examples are again considered for remembrance [58]: the reversible Carnot process with heat leak in Section 6.1 and the Curzon–Ahlborn model in Section 6.2.

5. Simulation and Modeling

5.1. Process Class

All real cyclic 2-reservoir processes can be described by the reservoir temperatures, by the cycle mean values of the contact temperatures (25), by the heat exchanges (23), and by the cycle time. Instead of the contact temperatures, one can use for our purpose the non-reversibility Λ. Consequently, a 6-dimensional manifold, the *process class* is introduced:

$$z \;:=\; (T_H, T_L, \Lambda, Q_H, Q_L, \tau) \;\in\; \mathcal{M}^6. \tag{62}$$

The physical meaning of the parameters spanning this manifold induces some restrictions: $T_H > T_L > 0$, $\tau > 0$, $Q_H \geq -Q_L > 0$ satisfying $(33)_2$, $0 < \Lambda \leq 1$, according to $(35)_5$, depending on the reservoir and contact temperatures and on the heat exchanges according to (36).

For arbitrary, but fixed allowed values of the quantities $(T_H, T_L, \Lambda, Q_H, Q_L, \tau)$, we call z a *process class* and $\mathcal{M}^6$ the *set of all process classes*. According to its definition, the process class contains all processes having the same values for z, not implying that the process mean values of the contact temperatures are equal: Consider two processes, I and II, of the same process class

$$\Lambda_I \;=\; \frac{(\alpha\Theta_I^- - \Theta_I^+)T_H T_L}{(\alpha T_L - T_H)\Theta_I^+\Theta_I^-} \;=\; \Lambda_{II} \;=\; \frac{(\alpha\Theta_{II}^- - \Theta_{II}^+)T_H T_L}{(\alpha T_L - T_H)\Theta_{II}^+\Theta_{II}^-}, \tag{63}$$

resulting in

$$\frac{\alpha\Theta_I^- - \Theta_I^+}{\Theta_I^+\Theta_I^-} \;=\; \frac{\alpha\Theta_{II}^- - \Theta_{II}^+}{\Theta_{II}^+\Theta_{II}^-} \;\longrightarrow\; \Theta_I^\pm \text{ may be different from } \Theta_{II}^\pm. \tag{64}$$

Introducing the process class, we concern ourselves no longer with the particular time dependence of the heat flows during the cyclic process, but we group together all processes having the same values of z forming the process class. All processes of a process class are equivalent to each other.

5.2. Simulating Processes

Now, we want to simulate a real irreversible cyclic 2-reservoir heat-to-power process which is contained in the process class (62). That means, we have to replace the original irreversible cyclic process by a special other one. Of course this replacement is not unique: there are many other processes simulating the original one. "Simulating" means that the process replacing the original one has the same $\boldsymbol{z}$ as the original process: Simulating processes $_{SP}$ and original process $_{OP}$ belong to the same process class $\boldsymbol{z}$ [58]

$$\boldsymbol{z}_{OP} \;=\; \boldsymbol{z}^{I}_{SP} \;=\; \boldsymbol{z}^{II}_{SP} \;=\; \boldsymbol{z}^{III}_{SP} \;=\; ..... \tag{65}$$

Whereas the original process is a real running one, a simulating process may also be a real running one, but also reversible "processes" (not real running) are allowed. Because the simulating process is in the same process class (62) as the original one, it cannot be distinguished from the original process by elements of $\boldsymbol{z}$. These simulating processes can be modeled differently. Here, we are using endoreversible models, but other modeling for generating simulating processes is possible.

5.3. Process Family and Machine Diagrams

The heat exchanges Q_H and Q_L of a real running cyclic engine between the fixed controlling heat reservoirs of the temperatures T_H and T_L depend on the cycle time τ. Consequently, the *process family* of such an engine is described by a family of subsets of the process class

$$\boldsymbol{Z}(\tau) \;:=\; \Big(T_H, T_L, \Lambda(\tau), Q_H(\tau), Q_L(\tau), \tau\Big) \tag{66}$$

with the cycle time as a family parameter. The $\boldsymbol{Z}(\tau)$ which characterize the engine are denoted as *machine diagrams*. These machine diagrams group together process classes by making its variables dependent of each other. The process class depicts the variables of a 2-reservoir system, whereas the process family describes the constitutive properties of the considered engine.

5.4. Endoreversible Models

For simulating processes of an engine, endoreversible models are here used because they can be of nearly arbitrary complexity [25,26]. In this paper, a reversible Carnot "process" combined with an irreversible transport process like the Fourier or the Newton heat conduction, which simulate the entropy production of the original process, is chosen as an endoreversible model. Consequently, two steps appear in the simulation procedure: the reversibility condition related to the Carnot process and irreversibility conditions related to the entropy production. These two steps will be reflected in two corresponding types of *simulation parameters:* The first and second simulation parameters.

In the next section, we will consider endoreversible systems, and we will show how to construct special simulation parameters which determine the simulating process.

6. Simulation by Special Endoreversible Models

Explaining the concept of simulation [58] in more detail, two well-known endoreversible models are chosen: the reversible Carnot process with a Fourier heat leak and the Curzon–Ahlborn model with Newton heat conduction. We make this choice because these two models have accompanied the historical development of Finite-Time Thermodynamics (FTT): they are chosen because everyone is familiar with them, helping to understand what simulation means.

6.1. Reversible Carnot "Process" with Fourier Heat Leak

The model structure of the reversible Carnot process with heat leak [59] is shown in Figure 3. The reservoir-related entropy production per cycle $(28)_5$ of the original process can be identically transformed into

$$\frac{\Omega}{\Lambda} = -\frac{Q_H - \Delta Q}{T_H} - \frac{Q_L + \Delta Q}{T_L} + \Delta Q \left(\frac{1}{T_L} - \frac{1}{T_H} \right). \tag{67}$$

Because the heat leak can only be described by taking place between the heat reservoirs, the expression $(35)_3$ which contains the reservoir temperatures and the non-reversibility is chosen instead of $(35)_2$ which is defined by using the mean values of the contact temperatures. The introduced *heat leak per cycle* ΔQ is according to (67) arbitrary without influencing the process class z (62).

For constructing a particular endoreversible model, we choose ΔQ in such a way, that the sum of the first two terms on the right-hand side of (67) become zero, thus representing a Clausius' equality describing a reversible process

$$-\frac{Q_H - \Delta Q}{T_H} - \frac{Q_L + \Delta Q}{T_L} \doteq 0. \tag{68}$$

This *reversibility condition* represents a reversible process having the heat exchanges $Q_H - \Delta Q$ and $Q_L + \Delta Q$ between the system and the two controlling reservoirs of the temperatures T_H and T_L, respectively (see Figure 3). The reversible work

$$-W^{rev} = (Q_H - \Delta Q) + (Q_L + \Delta Q) = -W \tag{69}$$

is equal to that of the original process. According to (68), the reservoir-related entropy production per cycle (67) of the original process results in

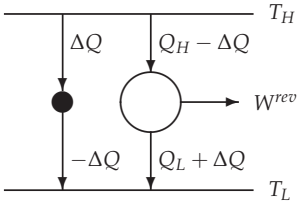

Figure 3. Model structure of the reversible Carnot engine with heat leak ΔQ. The black dot symbolizes that part of the endoreversible model through which the heat leak flows. From the perspective of the endoreversible model (black dot + white circle), the same total heat exchanges ($\Delta Q + Q_H - \Delta Q$ and $-\Delta Q + Q_L + \Delta Q$) as in the simulated process class occur: Q_H and Q_L.

$$\frac{\Omega}{\Lambda} = \Delta Q \left(\frac{1}{T_L} - \frac{1}{T_H} \right) \geq 0 \Longrightarrow \Delta Q \geq 0. \tag{70}$$

The reversibility condition (68) determines the heat leak ΔQ which is connected to the entropy production. From (70) follows with $(49)_3$

$$\frac{\Omega}{\Lambda} \frac{T_H T_L}{T_H(1 - T_L/T_H)} = \Delta Q = \frac{\Omega T_L}{\Lambda \eta_{rev}}. \tag{71}$$

The heat leak ΔQ is called a *first simulation parameter*. The endoreversible model of a real 2-reservoir process class is determined by specializing this first simulation parameter which is given by the reversibility condition (68) resulting in (71).

Now a *second simulation parameter* λ^{hl} is introduced by a "constitutive equation" for the heat leak per cycle

$$\Delta Q =: \lambda^{hl}\tau\left(\frac{1}{T_L}-\frac{1}{T_H}\right) = \lambda^{hl}\tau\frac{\eta_{rev}}{T_L} \implies \lambda^{hl} \geq 0. \tag{72}$$

This equation looks like a Fourier heat conduction ansatz, but it is not, because (72) determines the "heat conductivity" λ^{hl} which of course is in general not a constant, but a function of Q_L, α, and τ according to (72), (71) and $(56)_1$. From (72) follows with (71)

$$\lambda^{hl}(\boldsymbol{\zeta}) = \frac{1}{\tau}\frac{\Omega(\boldsymbol{\zeta})}{\Lambda}\Big(\frac{T_L}{\eta_{rev}}\Big)^2, \tag{73}$$

and $(72)_1$ inserted into (70) results in

$$\frac{\Omega(\boldsymbol{\zeta})}{\Lambda} = \lambda^{hl}(\boldsymbol{\zeta})\tau\left(\frac{1}{T_L}-\frac{1}{T_H}\right)^2 \geq 0, \qquad \boldsymbol{\zeta} = (T_H, T_L, \tau) \tag{74}$$

according to (54). The equations (73) and (74) demonstrate that the cycle time dependence of the "heat conductivity" induced by the machine diagrams has to be taken into account.

For given temperatures of the heat reservoirs, the simulation parameter λ^{hl} depends via the reservoir-related entropy production per cycle on the cycle time. If λ^{hl} would be set constant,

$$\frac{\Omega}{\tau\Lambda} \doteq const. \implies -\frac{1}{\tau}\Big(\frac{\Psi(\boldsymbol{\zeta})}{T_H}+\frac{\Xi(\boldsymbol{\zeta})}{T_L}\Big) = const. \tag{75}$$

follows according to (73) and (56). However, then for arbitrary machine diagrams, $(75)_2$ is in general not satisfied because its LHS depends on the cycle time. Only very special machine diagrams would make the LHS constant. Consequently, the reversible Carnot process with Fourier heat leak and an as CONSTANT chosen "heat conduction coefficient" λ^{hl} does not represent a simulation of a general real running irreversible engine and is thus not suited for a general simulation task.

In the reversible case we obtain according to $(44)_1$ from (71), that there is no heat leak

$$\Delta Q_{rev} = 0. \tag{76}$$

From (73) it follows that

$$\lambda^{hl}\tau\left(\frac{\eta_{rev}}{T_L}\right)^2 = \frac{\Omega}{\Lambda} = -\frac{Q_H}{T_H}-\frac{Q_L}{T_L}. \tag{77}$$

As shown in the Appendix A.3, we obtain from (77) the power

$$P = \lambda^{hl}\frac{1}{T_H}\frac{(\alpha_{rev}-1)^2}{\alpha_{rev}-\alpha}(\alpha-1). \tag{78}$$

In summary, the original 2-reservoir process is simulated by an endoreversible model consisting of the reversible part described by (68) (the right-hand part in Figure 3), and of an irreversible heat conducting part, the heat leak (the left-hand part in Figure 3), described by $(71)_2$. The endoreversible model undergoes the same "process" as the original one: the original process is simulated by an endoreversible model.

Another example of endoreversible modeling is considered in the next section.

6.2. Curzon–Ahlborn Model

Now the original 2-reservoir process class (62), shown in Figure 1, is simulated by using another endoreversible model, the Curzon–Ahlborn model [1] with two internal temperatures T_{iH} and T_{iL}, $T_H > T_{iH} > T_{iL} > T_L$ (see Figure 4). Because the situation is as in Figure 1 represented, we can use the results of Section 4.

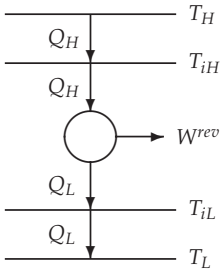

Figure 4. Model structure of the Curzon–Ahlborn model.

The entropy production $(35)_3$ is now identically transformed into

$$\Omega \;=\; \Lambda\Big(-\frac{Q_H}{T_H}-\frac{Q_L}{T_L}\Big) = -\Lambda\Big(\frac{Q_H}{T_{iH}}+\frac{Q_L}{T_{iL}}\Big)+\Lambda Q_H\left(\frac{1}{T_{iH}}-\frac{1}{T_H}\right)+\Lambda Q_L\left(\frac{1}{T_{iL}}-\frac{1}{T_L}\right), \tag{79}$$

by introducing T_{iH} and T_{iL} as two *first simulation parameters*. The reversibility condition of the reversible part of the endoreversible Novikov process is chosen as

$$\frac{Q_H}{T_{iH}}+\frac{Q_L}{T_{iL}} \doteq 0 \quad\Longrightarrow\quad \alpha \;=\; \frac{T_{iH}}{T_{iL}}, \quad \eta \;=\; 1-\frac{T_{iL}}{T_{iH}}, \tag{80}$$

that means, one of the first simulation parameters can be freely chosen. From (79) it follows that by use of $(41)_2$, the reservoir-related entropy production is

$$\frac{\Omega}{\Lambda} \;=\; Q_H\left(\frac{1}{T_{iH}}-\frac{1}{T_H}\right)+Q_L\left(\frac{1}{T_{iL}}-\frac{1}{T_L}\right) \;=\; \frac{Q_L}{T_H}(\alpha-\alpha_{rev}) \;=\; \frac{-W}{T_H}\frac{(\alpha-\alpha_{rev})}{1-\alpha}. \tag{81}$$

It is evident that the reservoir-related entropy production does not depend on the two first simulation parameters because α and W are determined by the original process according to $(33)_2$ and $(24)_1$.

Two *second simulation parameters* λ_H and λ_L are introduced generating "constitutive equations" in the same fashion as in (72) which represent definitions of λ_H and λ_L

$$Q_H \;=:\; \lambda_H\tau(T_H-T_{iH}), \quad Q_L \;=:\; \lambda_L\tau(T_L-T_{iL}), \quad \lambda_H,\lambda_L>0, \tag{82}$$

and the reservoir-related entropy production $(81)_2$ results in

$$\frac{\Omega}{\Lambda} \;=\; \frac{\lambda_L}{T_H}\tau(T_L-T_{iL})(\alpha-\alpha_{rev}). \tag{83}$$

Because the LHS of (83) is independent of T_{iL} according to $(81)_3$, λ_L depends on T_{iL}. A simple (and boring) calculation in the Appendix A.4 (A17) results in

$$\frac{\Omega}{\Lambda} \;=\; \tau\frac{\lambda_L\lambda_H}{\lambda_L+\lambda_H}\Big(\frac{\alpha_{rev}}{\alpha}-1\Big)\Big(1-\frac{\alpha}{\alpha_{rev}}\Big). \tag{84}$$

Starting with $(32)_2$ and $(82)_1$, a simple, but well known [58] (also boring) calculation presented in Appendix A.5 (A21) results in

$$P \;=\; \lambda_H(T_H-T_{iH})\eta \;=\; \frac{\lambda_L\lambda_H}{\lambda_L+\lambda_H}T_H\frac{\eta_{rev}-\eta}{1-\eta}\eta. \tag{85}$$

This expression is of course different from (78) due to the different models for the original process, although the values of the power in (78) and (85) are equal to that of the original process of the engine in $(40)_2$.

From (82) it follows that

$$\lambda_H \tau \;=\; \frac{Q_H}{T_H - T_{iH}}, \qquad \lambda_L \tau \;=\; \frac{Q_L}{T_L - T_{iL}}, \tag{86}$$

A short calculation results in

$$\begin{aligned} \frac{\lambda_L \lambda_H}{\lambda_L + \lambda_H} \;&=\; \tau^{-1} \frac{Q_H Q_L}{Q_L(T_H - T_{iH}) + Q_H(T_L - T_{iL})} \;=\; \tau^{-1} \frac{Q_H}{T_H - T_{iH} - \alpha(T_L - T_{iL})} \;= \\ &=\; \tau^{-1} \frac{Q_H}{T_H - \alpha T_L} \end{aligned} \tag{87}$$

demonstrating that in general

$$\frac{\lambda_L \lambda_H}{\lambda_L + \lambda_H} \;=\; \mathcal{F}(Q_H, \alpha, T_H, T_L, \tau) \;\neq\; const. \tag{88}$$

The heat exchange coefficient $(33)_2$ becomes with (82) and $(80)_2$

$$-\frac{Q_H}{Q_L} \;=\; \alpha \;=\; -\frac{\lambda_H}{\lambda_L} \frac{(T_H - T_{iH})}{(T_L - T_{iL})} \;=\; \frac{T_{iH}}{T_{iL}}, \tag{89}$$

resulting in

$$\lambda_L \;=\; \frac{T_{iL}(T_H - T_{iH})}{T_{iH}(T_{iL} - T_L)} \lambda_H \;=\; \frac{T_H - \alpha T_{iL}}{\alpha(T_{iL} - T_L)} \lambda_H. \tag{90}$$

According to (80), one of the first simulation parameters can be chosen freely. With respect to the machine diagrams (54) and $(55)_1$, T_{iL} is not determined by the original process

$$T_{iH}(\zeta) \;=\; \alpha(\zeta) T_{iL}, \quad \zeta \;\equiv\; (T_H, T_L, \tau), \tag{91}$$

and (86) results in

$$\lambda_H(\zeta; T_{iL}) \;=\; \frac{1}{\tau} \frac{\Psi(\zeta)}{T_H - \alpha(\zeta) T_{iL}}, \qquad \lambda_L(\zeta; T_{iL}) \;=\; \frac{1}{\tau} \frac{\Xi(\zeta)}{T_L - T_{iL}}. \tag{92}$$

Consequently, λ_H and λ_L are as T_{iL} not determined by the original process of the engine. However, because $\mathcal{F}$ in (88) does not depend on T_{iL}, the reservoir-related entropy production (84) and the power (85) are determined by the original process.

Up to here, the problem was as follows. How can the original process described in Section 4 be simulated by use of an endoreversible model? In the next section, the question is inverted: Given an endoreversible model, what real running process can belong to it?

7. Reconstruction, Parameter and Model Diagrams

During the 45 years since the Curzon–Ahlborn paper [2], a huge number of endoreversible models have been considered. Many of these models were simple ones considering continuously running or cyclic processes and analyzed basic features like power production or efficiencies of heat-to-power conversions. Most of those can be considered as paradigmatic examples not directly connected to any real existing heat-to-power engine. Nonetheless, the question arises, whether there exists a connection between these numerous not running endoreversible models and real running processes. More precisely, is it possible to generate an endoreversible model such that it can approximate a real

running engine? This question is now shortly discussed for the example of the Curzon–Ahlborn model (CAM) described in Section 6.2.

For distinguishing all quantities X of the endoreversible model (CAM) from those of a real running engine, they are denoted by X^+. The reconstruction procedure starts always with the choice of the endoreversible model; here, the CAM and its thermodynamic relations which are described in Section 6.2. The simulation parameters which are determined by simulation can now be chosen freely and are denoted as *reconstruction parameters* for characterizing their free choice in contrast to the simulation parameters.

In the endoreversible CAM we have two first *reconstruction parameters*, T_{iH}^+ and T_{iL}^+, and two second *reconstruction parameters*, λ_H^+ and λ_L^+. These are not independent of each other, because of the reversibility condition $(80)_1$

$$\frac{Q_H^+}{T_{iH}^+} + \frac{Q_L^+}{T_{iL}^+} = 0 \tag{93}$$

where, according to (82), the heat exchanges Q_H^+ and Q_L^+ depend on the second *reconstruction parameters* λ_H^+ and λ_L^+ as well as on the first *reconstruction parameters* T_{iH}^+ and T_{iL}^+.

$$Q_H^+ = \lambda_H^+ \tau^+ (T_H - T_{iH}), \quad Q_L^+ = \lambda_L^+ \tau^+ (T_L - T_{iL}), \quad \lambda_H^+, \lambda_L^+ > 0. \tag{94}$$

The first and second *reconstruction parameters* are fixed as functions of the cycle time τ^+ through the choice of their *parameter diagrams*

$$T_{iH} = T_{iH}(\tau^+), \qquad T_{iL} = T_{iL}(\tau^+), \tag{95}$$

$$\lambda_H^+ = \lambda_H^+(\tau^+), \qquad \lambda_L^+ = \lambda_L^+(\tau^+), \tag{96}$$

which have to respect the usual positivity requirements for temperatures and heat conductances as well as the reversibility condition (80). With that choice also the heat exchange coefficient and internal efficiency can be determined

$$\alpha^+ = \frac{T_{iH}^+}{T_{iL}^+} = -\frac{Q_H^+}{Q_L^+}, \quad \eta^+ = 1 - \frac{T_{iL}^+}{T_{iH}^+}. \tag{97}$$

as well as the power and the reservoir-related entropy production

$$P^+ = \lambda_H^+ (T_H - T_{iH}) \eta^+ = \frac{\lambda_L^+ \lambda_H^+}{\lambda_L^+ + \lambda_H^+} T_H \frac{\eta_{rev} - \eta^+}{1 - \eta^+} \eta^+, \tag{98}$$

$$\left(\frac{\Omega}{\Lambda}\right)^+ = \tau^+ \frac{\lambda_L^+ \lambda_H^+}{\lambda_L^+ + \lambda_H^+} \left(\frac{\alpha_{rev}^+}{\alpha^+} - 1\right)\left(1 - \frac{\alpha^+}{\alpha_{rev}}\right). \tag{99}$$

From here the endoreversible analog to the machine diagrams, the *model diagrams*, are generated

$$Q_H^+(\tau^+) = \lambda_H^+(\tau^+) \tau^+ (T_H - \alpha^+ T_{iL}^+(\tau^+)), \qquad Q_L^+(\tau^+) = \lambda_L^+(\tau^+) \tau^+ (T_L - T_{iL}^+(\tau^+)), \tag{100}$$

which can be compared with the machine diagrams of an engine.

Consequently, the quality of an endoreversible model for describing an engine can be tested by a comparison of the model diagrams with the corresponding machine diagrams. With the choice of simple parameter diagrams—like constant heat conductances—it is apparent, that the model diagrams will not model given machine diagrams exactly, but they may serve as a more or less good approximation. Then, an approximation procedure can be established: changing the reconstruction parameters and the parameter diagrams of the endoreversible model in such a way that the resulting model diagrams are approaching the given machine diagrams of the engine. If the parameter diagrams

are chosen in such a way that model diagrams and machine diagrams are identical, the reconstruction annuls the simulation.

– –

Simulation:
engine + machine diagrams $\longrightarrow$
$\longrightarrow$ endoreversible model + simulation parameter diagrams

– –

Reconstruction:
endoreversible model + reconstruction parameter diagrams $\longrightarrow$
$\longrightarrow$ model diagrams + model of engine

– –

Simulation and reconstruction have different starting points. For simulation, the process family of an engine with its machine diagrams is given, whereas for reconstruction, the reconstruction parameter diagrams together with the structure of the considered endoreversible model are at the beginning.

Diagrams which introduce the cycle time to the thermodynamic quantities are necessary in both cases: in simulation these are the machine diagrams, whereas in reconstruction a cycle time is introduced by the parameter diagrams. It are the parameter and the resulting model diagrams which generate the utility of endoreversible models by reconstructing them to models of an engine.

8. Simulation, Modeling, Reconstruction, and FTT

As already pointed out in the introduction, the original goal of Finite-Time Thermodynamics was to capture the influence of “haste” on the performance of thermodynamic processes and in particular on heat-to-power conversion. The observed efficiencies differ widely from the well-known Carnot efficiency, and thus better estimates were desired. Moreover, the knowledge on realistic performance measures allows to ask whether existing processes can be optimized by minimizing the dissipation necessary to reach a target output.

If a particular heat engine performing a cyclic 2-reservoir process is considered, then by the choice of an operating point the process class (62) is fixed. To find out whether that is a good or bad operating point one needs other processes [58] with which a comparison with the original process can be performed. Such processes can be taken either from the machine diagrams of a real engine, or from the model diagrams induced by reconstruction parameter diagrams of an (endoreversible) model. While the first point of view puts its focus on the *simulation* of the process and can thus be used to optimize the particular heat engine under consideration, the second view puts its focus on the *modeling* of the process and its *reconstruction*, thus allowing for simple calculations and for insight into (more) realistic efficiencies for instance at maximum power.

The first point of view—simulating the processes of real engines by an endoreversible model—becomes particularly important, when such a model becomes part of a larger endoreversible description. Using *simulations* enlarges the tool box of Endoreversible Thermodynamics and allows to include irreversible engines with given machine diagrams into the description [60]. Using the appropriate complexity, the interesting entropy production sources can be *quantitatively* mapped into the description. Based on the resulting features, the design and optimization of the entire system can then be performed. Such building blocks have for instance been used to model a full hydraulic recuperation system for trucks [61]. In that sense Endoreversible Thermodynamics has left the level treating only simple but paradigmatic cases; it can now also be used as an engineering design tool.

The second point of view is particularly useful if one searches for paradigmatic models with which important insights can be gained. It turned out that the efficiencies calculated at maximum power for the Curzon–Ahlborn model are independent of the values of the used heat conductances. The differences between the efficiencies obtained for different types of heat conduction (Newton, Fourier etc.) immediately show that the results depend very much on the chosen model.

Recently the search for such paradigmatic models have led to the study of Novikov models with fluctuating heat bath. The results again are paradigmatic in sense of a certain universality with respect to stochastic features of the fluctuations [62–64].

Endoreversible Thermodynamics has also shown its usefullness in describing systems in a relatively coarse fashion to analyze for instance the optimization potential for a given real process. As an example we mention the optimization of the piston motion in cyclic heat engines, which has been investigated for engines with Otto [65–67], Diesel [68–71], and Miller cycles [72], as well as the special paths needed for light-driven engines [73–78]. For instance, in [32] this approach has been used to get a good guess of the potential power output gains for an alpha-type Stirling engine by using an optimized control of the piston motion. Based on a special class of piston motions, the power-optimized motion showed a power output gain of about 50% and more over a large parameter range. As long as the goal is to establish whether gains of 10% as in the Diesel case [68] or 50% as in this case are possible, the simple model with fixed transport coefficients, which can be varied during the analysis, suffices thus providing a fast and effective solution approach.

Finally, if the performance of a real heat-to-power thermodynamic device should be analyzed, simple endoreversible heat engine models with one or two fixed model parameters will not capture the important features due to their oversimplified structure. In order to reach the level of an engineering description, the complexity of the *model structure* can be increased. It is one of the great advantages of endoreversible modeling, that it allows to adjust the level of complexity to the desired level of accuracy by providing more reconstruction parameters. After having introduced the endoreversibility condition, and following the philosophy of FFT, the most important dissipative loss terms of the engine are modeled and then supplemented by model elements for further dissipative loss terms of less and less importance until the appropriate modeling level is reached. Together with its reconstruction parameter diagrams, the endoreversible model can then be checked against experimental data.

9. Test

engine means always a real running engine with its → machine diagrams.

process without addendum means a real running irreversible process. The other "processes" need an addendum: → reversible or → endoreversible.

reversible means vanishing → entropy production.

endoreversible model is a system of → reversible parts which interact irreversibly with each other, thus generating → entropy production. → "Processes" in such a system are called endoreversible. It is characzerized by a chosen structure and parameters (→ simulation parameters or → reconstruction parameters).

set of process classes is the manifold $\mathcal{M}^6$ spanned by the independent data of all cyclic 2-reservoir processes $(T_H, T_L, \Lambda, Q_H, Q_L, \tau)$.

process class $\boldsymbol{z} = (T_H, T_L, \Lambda, Q_H, Q_L, \tau)$ is a member of the → set of all process classes $\mathcal{M}^6$. It includes all → processes (reversible or irreversible, real running or endoreversible) with the same $\boldsymbol{z}$.

non-reversibility Λ, $0 < \Lambda \leq 1$, is a function of $(T_H, T_L, Q_H, Q_L, \tau)$ and of the cycle mean values of the contact temperature (Θ^+, Θ^-). The non-reversibility distinguishes between different → entropy productions

process family is given by → machine diagrams or by → model diagrams. It includes all → process classes belonging to the same → engine or → endoreversible model.

machine diagrams determine $\Lambda(\tau)$, $Q_H(\tau)$, and $Q_L(\tau)$ as functions of the cycle time τ. The sub-set $(T_H, T_L, \Lambda(\tau), Q_H(\tau), Q_L(\tau), \tau)$ of the → set of all process classes represents a → process family with

the cycle time τ as a family parameter.

entropy production appears twofold: entropy production with respect to the cycle mean values of the contact temperature of the considered system, and entropy production with respect to the reservoir temperatures of the controlling heat bathes. These two kinds of entropy production are connected by the → non-reversibility.

simulation parameters characterize an → endoreversible model and performing a → simulation, their functional dependence on τ, → the simulation parameter diagram, is determined by the → machine diagram

simulation is the procedure of generating an → endoreversible model including the choice of appropriate → simulation parameter diagrams (for the → simulation parameters), such that the resulting model diagram belongs to the same → process family as a *given* → engine.

simulation parameter diagrams determine the τ-dependence of the → simulation parameters.

reconstruction is the procedure of starting with an → endoreversible model including *chosen* → reconstruction parameter diagrams (for the → reconstruction parameters) and then generating a → model diagram. Consequently, reconstruction is the reciprocal procedure to simulation.

reconstruction parameters correspond to the → simulation parameters by change of name. The difference between them: The values of the → simulation parameters are determined by the → simulation parameter diagrams, which in turn are determined by the → machine diagrams of the → engine, whereas the values of the reconstruction parameters can be chosen.

model parameters are → simulation or → reconstruction parameters.

reconstruction parameter diagrams determine the τ-dependence of the → reconstruction parameters. The reconstruction parameter diagrams can be chosen freely. Inserted into the thermodynamic relations of the chosen → endoreversible model, they generate the → model diagrams.

model diagrams are generated for a given → endoreversible model from its *chosen* → parameter diagrams. The model diagrams include the same variables as the → machine diagrams, but they differ from each other: → machine diagrams belong to an → engine, whereas parameter diagrams generated by → reconstruction belong to an → endoreversible model. Because model diagrams and → machine diagrams have the same range, they can be compared, that means, the quality of an → endoreversible model for describing an → engine can be tested by a comparison of the model diagrams with the corresponding → machine diagrams.

10. Summary

The paper starts with the basic facts of nonequilibrium thermodynamics of discrete systems: time rate of entropy of compound systems and cyclic processes are considered and the contact temperature is introduced enforcing the nonequilibrium entropy to be a state function and generating a Clausius-like inequality describing the 2nd law. Using these items, irreversible and reversible cyclic 2-heat-reservoir heat-to-power processes are discussed elucidating the difference beween contact and reservoir temperatures. This difference generates two different entropy productions, a contact temperature orientated and a reservoir-related one. This difference is described by a contact and reservoir temperature dependent function, called non-reversibility. The definitions of efficiency and heat exchange coefficient are not affected by the difference beween contact and reservoir temperatures, but their values differ because of different heat exchanges due to different contact and reservoir temperatures. To bring the cycle time to the thermodynamical quantities, machine diagrams have

to be introduced. At the end of this section, the universality of the considered cyclic 2-reservoir heat-to-power processes is emphasized.

Then the concepts of endoreversible modeling, simulation and reconstruction are introduced:

- Endoreversible modeling means: Creating a model structure of reversible systems which interact by irreversible exchange processes supplemented with model parameters.
- Simulation means: Generating an endoreversible model in such a way, that the external exchanges are identical with those of an irreversible real running process.
- Reconstruction means: Generating model diagams from a given endoreversible model structure and chosen (cycle time dependent) reconstruction parameter diagrams (e.g., for testing the chosen endoreversible model by comparison with machine diagrams).

For elucidation, two very well-known endoreversible models are examplarily considered: the reversible Carnot process with Fourier heat leak as a first model parameter and a corresponding heat conductance as a second model parameter, and the Curzon–Ahlborn model, i.e., a reversible Carnot process with Newton heat conduction containing two internal temperatures as first model parameters and two heat conductances as second model parameters.

In the case of simulation, the model parameters—now called simulation parameters—depend on the machine diagrams of the real running engine which is simulated: for instance, for the first model the heat leak and the corresponding heat conductance are proportional to the reservoir-related entropy production, which follows from the machine diagrams.

In the case of reconstruction, the model parameters—now called reconstruction parameters—are *chosen* as functions of the cycle time by specifying the reconstruction parameter diagrams. These in connection with the endoreversible model structure provide the external heat exchanges in the form of the model diagrams. For instance, for the Curzon–Ahlborn model, the heat conductances are set constant and the intermediate temperatures are optimized for power output.

From a historical point of view, in the literature usually the reconstruction route has been taken, so that the connection between chosen endoreversible models and corresponding real running processes needs more elucidation which is the aim of this paper.

Author Contributions: This research was developed following the work in [58]. Basics of non-equilibrium thermodynamics, contact quantities, reconstruction, and appendices, mainly W.M.; Endoreversible models, parameter, and model diagrams, finite-time thermodynamics, and references, mainly K.H.H.; For most of the topics the authors contributed equally. All authors have read and agreed to the published version of the manuscript.

Funding: This research received no external funding.

Conflicts of Interest: The authors declare no conflicts of interest.

Appendix A

Appendix A.1. Non-Reversibility

From $(35)_3$ follows

$$Q_H\Big(\frac{\Lambda}{T_H}-\frac{1}{\Theta^+}\Big) = Q_L\Big(\frac{1}{\Theta^-}-\frac{\Lambda}{T_L}\Big) \longrightarrow \alpha\Big(\frac{1}{\Theta^+}-\frac{\Lambda}{T_H}\Big) = \frac{1}{\Theta^-}-\frac{\Lambda}{T_L} \tag{A1}$$

by use of $(33)_2$. This results in

$$\Lambda\Big(\frac{1}{T_L}-\frac{\alpha}{T_H}\Big) = \frac{1}{\Theta^-}-\frac{\alpha}{\Theta^+} \longrightarrow \Lambda = \frac{(\alpha\Theta^- - \Theta^+)T_HT_L}{(\alpha T_L - T_H)\Theta^+\Theta^-}. \tag{A2}$$

Appendix A.2. Maximal Power (General)

From (53) follows

$$0 \leq \frac{P}{\Omega/\Lambda} = \frac{T_L}{\tau(\eta)}\frac{\eta}{(\eta_{rev}-\eta)}, \quad \Longrightarrow \quad \left(\frac{P}{\Omega/\Lambda}\right)\Big|_{\eta=0} = 0, \quad \left(\frac{P}{\Omega/\Lambda}\right)\Big|_{\eta=\eta_{rev}} = 0, \tag{A3}$$

if

$$\lim_{\eta\to\eta_{rev}} [\tau(\eta)(\eta_{rev}-\eta)] \to \infty \tag{A4}$$

is presupposed. From $(A3)_2$ follows

$$\frac{d}{d\eta}\left(\frac{P}{\Omega/\Lambda}\right) = T_L\frac{\tau(\eta_{rev}-\eta)-\eta[(d\tau/d\eta)(\eta_{rev}-\eta)-\tau]}{[\tau(\eta_{rev}-\eta)]^2} \doteq 0, \tag{A5}$$

resulting in

$$\tau\eta_{rev} = \frac{d\tau}{d\eta}\eta(\eta_{rev}-\eta) \quad \Longrightarrow \quad \frac{d\ln\tau}{d\eta} = \frac{\eta_{rev}}{\eta(\eta_{rev}-\eta)}. \tag{A6}$$

An η^* is sought for satisfying $(A6)_2$

$$\frac{d}{d\eta}\ln\tau(\eta)\Big|_{\eta^*} = \frac{\eta_{rev}}{\eta^*(\eta_{rev}-\eta^*)} \neq \frac{1}{\eta^*}, \tag{A7}$$

determining the cycle time $\tau(\eta^*)$ and the efficiency η^* for which $P/(\Omega/\Lambda)$ is maximal. A comparison with $(61)_2$ demonstrates that $P/(Q_H)$ and $P/(\Omega/\Lambda)$ are maximal for different efficiencies.

Appendix A.3. Power (Carnot Process with Fourier Heat Leak)

Starting with (77)

$$\lambda^{hl}\tau\left(\frac{\eta_{rev}}{T_L}\right)^2 = -\frac{Q_H}{T_H}-\frac{Q_L}{T_L}, \tag{A8}$$

resulting by use of $(49)_3$ in

$$\lambda^{hl}\tau\frac{T_H}{Q_L}\left(\frac{\eta_{rev}}{T_L}\right)^2 = -\frac{Q_H}{Q_L}-\frac{T_H}{T_L} = \alpha-\alpha_{rev} = \lambda^{hl}\tau\frac{T_H}{Q_L}\frac{1}{T_H^2}\left(\frac{T_H}{T_L}-1\right)^2. \tag{A9}$$

Using $(41)_2$, this results in

$$\frac{Q_L}{\tau} = \frac{P}{1-\alpha} = \lambda^{hl}\frac{1}{T_H}\frac{(\alpha_{rev}-1)^2}{\alpha-\alpha_{rev}} \tag{A10}$$

which is identical with (78).

Appendix A.4. Reservoir-Related Entropy Production

Starting with $(33)_2$ and (82),

$$\alpha = -\frac{Q_H}{Q_L} = \frac{\lambda_H(T_H-T_{iH})}{\lambda_L(T_{iL}-T_L)} = \frac{\lambda_H(T_H-\alpha T_{iL})}{\lambda_L(T_{iL}-T_L)}, \tag{A11}$$

$$\lambda_L(T_{iL}-T_L) = \lambda_H(T_H/\alpha-T_{iL}), \tag{A12}$$

$$T_{iL}(\lambda_L+\lambda_H) = \lambda_H T_H/\alpha+\lambda_L T_L, \tag{A13}$$

$$T_{iL} = \frac{\lambda_H T_H/\alpha+\lambda_L T_L}{\lambda_L+\lambda_H}. \tag{A14}$$

Consequently, the reservoir-related entropy production (83) becomes

$$\frac{\Omega}{\Lambda} = \frac{\lambda_L}{T_H}\tau(T_L - T_{iL})(\alpha - \alpha_{rev}) = \frac{\lambda_L}{T_H}\tau\Big(T_L - \frac{\lambda_H T_H/\alpha + \lambda_L T_L}{\lambda_L + \lambda_H}\Big)(\alpha - \alpha_{rev}). \tag{A15}$$

Inserting $(49)_4$, this results in

$$\frac{\Omega}{\Lambda} = \frac{\lambda_L}{\alpha_{rev}}\tau\Big(1 - \frac{\lambda_H \alpha_{rev}/\alpha + \lambda_L}{\lambda_L + \lambda_H}\Big)(\alpha - \alpha_{rev}) = \frac{\lambda_L}{\alpha_{rev}}\tau\Big(\frac{\lambda_H(1 - \alpha_{rev}/\alpha)}{\lambda_L + \lambda_H}\Big)(\alpha - \alpha_{rev}) = \tag{A16}$$

$$= \tau\frac{\lambda_L\lambda_H}{\lambda_L + \lambda_H}\Big(1 - \frac{\alpha_{rev}}{\alpha}\Big)\Big(\frac{\alpha}{\alpha_{rev}} - 1\Big). \tag{A17}$$

Appendix A.5. Work (Curzon–Ahlborn Model, Newton Heat Conduction)

Starting with (85), the work becomes, by the use of (A14), $(80)_2$, and $(49)_4$,

$$-W = \lambda_H\tau(T_H - T_{iH})\eta = \lambda_H\tau\Big(T_H - \frac{\lambda_H T_H + \alpha\lambda_L T_L}{\lambda_L + \lambda_H}\Big)\eta = \tag{A18}$$

$$= \lambda_H\tau T_H\Big(1 - \frac{\lambda_H + \alpha\lambda_L/\alpha_{rev}}{\lambda_L + \lambda_H}\Big)\eta. \tag{A19}$$

Taking $(34)_2$ into account, the work becomes

$$-W = \lambda_H\tau T_H\Big(\frac{\lambda_L - \alpha\lambda_L(1 - \eta_{rev})}{\lambda_L + \lambda_H}\Big)\eta = \lambda_L\lambda_H\tau T_H\Big(\frac{1 - (1 - \eta_{rev})/(1 - \eta)}{\lambda_L + \lambda_H}\Big)\eta = \tag{A20}$$

$$= \tau\frac{\lambda_L\lambda_H}{\lambda_L + \lambda_H}T_H\Big(1 - \frac{1 - \eta_{rev}}{1 - \eta}\Big)\eta = \tau\frac{\lambda_L\lambda_H}{\lambda_L + \lambda_H}T_H\frac{\eta_{rev} - \eta}{1 - \eta}\eta, \tag{A21}$$

resulting in (85).

References

1. Curzon, F.L.; Ahlborn, B. Efficiency of a Carnot Engine at Maximum Power Output. *Am. J. Phys.* **1975**, *43*, 22–24. [CrossRef]
2. Novikov, I.I. The Efficiency of Atomic Power Stations. *J. Nucl. Energy* **1958**, *7*, 125–128. Translated from *Atomnaya Energiya* **1957**, *3*, 409. [CrossRef]
3. Vaudrey, A.; Lanzetta, F.; Feidt, M. HB Reitlinger and the origins of the efficiency at maximum power formula for heat engines. *J. Non-Equilib. Thermodyn.* **2014**, *39*, 199–203. [CrossRef]
4. Andresen, B.; Berry, R.S.; Nitzan, A.; Salamon, P. Thermodynamics in Finite Time. I. The Step-Carnot Cycle. *Phys. Rev. A* **1977**, *15*, 2086–2093. [CrossRef]
5. Salamon, P.; Andresen, B.; Berry, R.S. Thermodynamics in Finite Time. II. Potentials for Finite-Time Processes. *Phys. Rev. A* **1977**, *15*, 2094–2102. [CrossRef]
6. Andresen, B.; Salamon, P.; Berry, R.S. Thermodynamics in finite time: extremals for imperfect heat engines. *J. Chem. Phys.* **1977**, *66*, 1571–1577. [CrossRef]
7. Andresen, B.; Salamon, P.; Berry, R.S. Thermodynamics in Finite Time. *Phys. Today* **1984**, *37*, 62–70. [CrossRef]
8. Andresen, B. Current Trends in Finite-Time Thermodynamics. *Angew. Chem.* **2011**, *50*, 2690–2705. [CrossRef]
9. Angulo-Brown, F. An Ecological Optimization Criterion for Finite-Time Heat Engines. *J. Appl. Phys.* **1991**, *69*, 7465–7469. [CrossRef]
10. Barranco-Jiménez, M.A.; Páez-Hernández, R.T.; Reyes-Ramírez, I.; Guzmán-Vargas, L. Local Stability Analysis of a Thermo-Economic Model of a Chambadal-Novikov-Curzon–Ahlborn Heat Engine. *Entropy* **2011**, *13*, 1584–1594. [CrossRef]
11. Açıkkalp, E.; Yamık, H. Modeling and optimization of maximum available work for irreversible gas power cycles with temperature dependent specific heat. *J. Non-Equilib. Thermodyn.* **2015**, *40*, 25–39. [CrossRef]
12. Lu, C.; Bai, L. Nonlinear Dissipation Heat Devices in Finite-Time Thermodynamics: An Analysis of the Trade-Off Optimization. *J. Non-Equilib. Thermodyn.* **2017**, *42*, 277–286. [CrossRef]

13. Wu, F.; Chen, L.; Sun, F.; Wu, C.; Hua, P. Optimum performance parameters for a quantum Carnot heat pump with spin-1/2. *Energy Convers. Manag.* **1998**, *39*, 1161–1167. [CrossRef]
14. Rezek, Y.; Kosloff, R. Irreversible performance of a quantum harmonic heat engine. *New J. Phys.* **2006**, *8*, 1–27. [CrossRef]
15. Deffner, S. Efficiency of Harmonic Quantum Otto Engines at Maximal Power. *Entropy* **2018**, *20*, 875. [CrossRef]
16. Wu, F.; Chen, L.; Sun, F.; Wu, C. Finite-time exergoeconomic performance bound for a quantum Stirling engine. *Int. J. Eng. Sci.* **2000**, *38*, 239–247. [CrossRef]
17. Smith, Z.; Pal, P.S.; Deffner, S. Endoreversible Otto Engines at Maximal Power. *JNET* **2020**, *45*, 305–310. [CrossRef]
18. Hoffmann, K.H.; Salamon, P. Finite-time availability in a quantum system. *EPL* **2015**, *109*, 40004-p1–40004-p6. [CrossRef]
19. Hoffmann, K.H.; Schmidt, K.; Salamon, P. Quantum finite time availability for parametric oscillators. *J. Non-Equilib. Thermodyn.* **2015**, *40*, 121–129. [CrossRef]
20. Roach, T.N.F.; Salamon, P.; Nulton, J.; Andresen, B.; Felts, B.; Haas, A.; Calhoun, S.; Robinett, N.; Rohwer, F. Application of finite-time and control thermodynamics to biological processes at multiple scales. *J. Non-Equilib. Thermodyn.* **2018**, *43*, 193–210. [CrossRef]
21. Rubin, M.H. Optimal Configuration of a Class of Irreversible Heat Engines. I. *Phys. Rev. A* **1979**, *19*, 1272–1276. [CrossRef]
22. De Vos, A. Reflections on the power delivered by endoreversible engines. *J. Phys. D Appl. Phys.* **1987**, *20*, 232–236. [CrossRef]
23. Chen, J.; Yan, Z. Optimal Performance of an Endoreversible-Combined Refrigeration Cycle. *J. Appl. Phys.* **1988**, *63*, 4795–4798. [CrossRef]
24. De Vos, A. Is a solar cell an edoreversible engine? *Sol. Cells* **1991**, *31*, 181–196. [CrossRef]
25. Hoffmann, K.H.; Burzler, J.M.; Schubert, S. Endoreversible Thermodynamics. *J. Non-Equilib. Thermodyn.* **1997**, *22*, 311–355.
26. Hoffmann, K.H.; Burzler, J.M.; Fischer, A.; Schaller, M.; Schubert, S. Optimal Process Paths for Endoreversible Systems. *J. Non-Equilib. Thermodyn.* **2003**, *28*, 233–268. [CrossRef]
27. Hoffmann, K.H. An introduction to endoreversible thermodynamics. *AAPP Phys. Math. Nat. Sci.* **2008**, *86*, 1–19. [CrossRef]
28. Arias-Hernández, L.A.; Angulo-Brown, F. Thermodynamic optimization of endoreversible engines. *Rev. Mex. Fís.* **1994**, *40*, 866–877.
29. Huleihil, M.; Andresen, B. Optimal piston trajectories for adiabatic processes in the presence of friction. *J. Appl. Phys.* **2006**, *100*, 114914-1–114914-6. [CrossRef]
30. Aragón-González, G.; Canales-Palma, A.; León-Galicia, A.; Morales-Gómez, J.R. Maximum Power, Ecological Function and Efficiency of an Irreversible Carnot Cycle. A Cost and Effectiveness Optimization. *Braz. J. Phys.* **2008**, *38*, 543–550. [CrossRef]
31. Paéz-Hernández, R.T.; Chimal-Eguía, J.C.; Sánchez-Salas, N.; Ladino-Luna, D. General Properties for an Agrawal Thermal Engine. *J. Non-Equilib. Thermodyn.* **2018**, *43*, 131–139. [CrossRef]
32. Masser, R.; Khodja, A.; Scheunert, M.; Schwalbe, K.; Fischer, A.; Paul, R.; Hoffmann, K.H. Optimized Piston Motion for an Alpha-Type Stirling Engine. *Entropy* **2020**, *22*, 700. [CrossRef]
33. Chen, L.; Ma, K.; Ge, Y.; Feng, H. Re-Optimization of Expansion Work of a Heated Working Fluid with Generalized Radiative Heat Transfer Law. *Entropy* **2020**, *22*, 720. [CrossRef]
34. Marsik, F.; Weigand, B.; Thomas, M.; Tucek, O.; Novotny, P. On the Efficiency of Electrochemical Devices from the Perspective of Endoreversible Thermodynamics. *J. Non-Equilib. Thermodyn.* **2019**, *44*, 425–437. [CrossRef]
35. Wagner, K.; Hoffmann, K.H. Chemical reactions in endoreversible thermodynamics. *Eur. J. Phys.* **2016**, *37*, 015101. [CrossRef]
36. Ding, Z.; Chen, L.; Sun, F. Finite time exergoeconomic performance for six endoreversible heat engine cycles: Unified description. *Appl. Math. Mod.* **2011**, *35*, 728–736. [CrossRef]
37. Ahmadi, M.H.; Ahmadi, M.A.; Bayat, R.; Ashouri, M.; Feidt, M. Thermo-economic optimization of Stirling heat pump by using non-dominated sorting genetic algorithm. *Energ. Convers. Manag.* **2015**, *91*, 315–322. [CrossRef]

38. De Vos, A. Endoreversible Models for the Thermodynamics of Computing. *Entropy* **2020**, *22*, 660. [CrossRef]
39. Schottky, W. *Thermodynamik, Erster Teil*, 2nd ed.; Springer: Berlin, Germany, 1929.
40. Muschik, W. Second Law and Non-Equilibrium Entropy of Schottky Systems—Doubts and Verification. *Entropy* **2018**, *20*, 740. [CrossRef]
41. Kestin, J. (Ed.) *The Second Law of Thermodynamics*; Hutchinson and Ross: Stroudsburg, PA, USA, 1976.
42. Muschik, W. Formulations of the Second Law - Recent Developments. *J. Phys. Chem. Solids* **1988**, *49*, 709–720. [CrossRef]
43. Muschik, W. Different Formulations of the Second Law. In Proceedings of the International Symposium on Trends in Continuum Physics (Trecop '04), Poznan, Poland, 17–19 November 2004; pp. 1–12.
44. Muschik, W. Non-equilibrium thermodynamics and stochasticity: A phenomenological look on Jarzynski's equality. *Contin. Mech. Thermodyn.* **2016**, *28*, 1887–1903. [CrossRef]
45. Muschik, W. Contact quantities and non-equilibriun entropy of discrete systems. *JNET* **2009**, *34*, 75–92. [CrossRef]
46. Muschik, W. Thermodynamic interaction between two discrete systems in nonequilibrium. *JNET* **2004**, *29*, 237–255. [CrossRef]
47. Muschik, W.; Berezovski, A. Non-equilibrium contact quantities and compound deficiency at interfaces between discrete systems. *Proc. Est. Acad. Sci. Phys. Math.* **2007**, *56*, 133–145.
48. Muschik, W. Internal variables in nonequilibrium thermodynamics. *JNET* **1990**, *15*, 127–137. [CrossRef]
49. Maugin, G.; Muschik, W. Thermodynamics with internal variables. *JNET* **1994**, *19*, 217–289.
50. Muschik, W. Contact Temperature as an Internal Variable of Discrete Systems in Non-Equilibrium. In *Generalized Models and Non-Classical Approaches in Complex Materials 1*; Altenbach, H., Pouget, J., Rousseau, M., Collet, B., Michelitsch, T., Eds.; Springer: London, UK, 2018; pp. 605–618.
51. Muschik, W. Recent developments in nonequilibrium thermodynamics. *Lect. Notes Phys.* **1984**, *199*, 387.
52. Muschik, W. Temperatur und Irreversibilität in der Rationalen Mechanik. *ZAMM* **1975**, *55*, T102–T105.
53. Muschik, W. Empirical foundation and axiomatic treatment of nonequilibrium temperature. *Arch. Ration. Mech. Anal.* **1977**, *66*, 379–401. [CrossRef]
54. Muschik, W.; Brunk, G. A concept of non-equilibrum temperature. *Int. J. Eng. Sci.* **1977**, *15*, 377–389. [CrossRef]
55. Muschik, W. Contact temperature and internal variables: A glance back, 20 years later. *JNET* **2014**, *39*, 113–121. [CrossRef]
56. Muschik, W. *Aspects of Non-Equilibrium Thermodynamics*; World Scientific: Singapore, 1990.
57. Kestin, J. *A Course in Thermodynamics*, 1st ed.; Hemisphere Pub. Corp.: Washington, DC, USA; London, UK, 1979.
58. Muschik, W.; Hoffmann, K.H. Endoreversible Thermodynamics: A Tool for Simulating and Comparing Processes of Discrete Systems. *JNET* **2006**, *31*, 293–317.
59. Gordon, J.M.; Huleihil, M. General performance characteristics of real heat engines. *J. Appl. Phys.* **1992**, *72*, 829–837. [CrossRef]
60. Masser, R.; Hoffmann, K.H. Dissipative Endoreversible Engine with Given Efficiency. *Entropy* **2019**, *21*, 1117. [CrossRef]
61. Masser, R.; Hoffmann, K.H. Endoreversible Modeling of a Hydraulic Recuperation System. *Entropy* **2020**, *22*, 383. [CrossRef]
62. Schwalbe, K.; Hoffmann, K.H. Performance Features of a Stationary Stochastic Novikov Engine. *Entropy* **2018**, *20*, 52. [CrossRef]
63. Schwalbe, K.; Hoffmann, K.H. Novikov engine with fluctuating heat bath temperature. *J. Non-Equilib. Thermodyn.* **2018**, *43*, 141–150. [CrossRef]
64. Schwalbe, K.; Hoffmann, K.H. Stochastic Novikov Engine with Fourier Heat Transport. *J. Non-Equilib. Thermodyn.* **2019**, *44*, 417–424. [CrossRef]
65. Mozurkewich, M.; Berry, R.S. Optimal Paths for Thermodynamic Systems: The ideal Otto Cycle. *J. Appl. Phys.* **1982**, *53*, 34–42. [CrossRef]
66. Fischer, A.; Hoffmann, K.H. Can a quantitative simulation of an Otto engine be accurately rendered by a simple Novikov model with heat leak? *J. Non-Equilib. Thermodyn.* **2004**, *29*, 9–28. [CrossRef]
67. Ge, Y.; Chen, L.; Sun, F. Optimal path of piston motion of irreversible Otto cycle for minimum entropy generation with radiative heat transfer law. *J. Energ Inst.* **2012**, *85*, 140–149. [CrossRef]

68. Hoffmann, K.H.; Watowich, S.J.; Berry, R.S. Optimal Paths for Thermodynamic Systems: The Ideal Diesel Cycle. *J. Appl. Phys.* **1985**, *58*, 2125–2134. [CrossRef]
69. Burzler, J.M.; Blaudeck, P.; Hoffmann, K.H. Optimal Piston Paths for Diesel Engines. In *Thermodynamics of Energy Conversion and Transport*; Stanislaw Sieniutycz, S., de Vos, A., Eds.; Springer: Berlin, Germany, 2000; pp. 173–198. [CrossRef]
70. Chen, L.; Xia, S.; Sun, F. Optimizing piston velocity profile for maximum work output from a generalized radiative law Diesel engine. *Math. Comput. Model.* **2011**, *54*, 2051–2063. [CrossRef]
71. Xia, S.; Chen, L.; Sun, F. Engine performance improved by controlling piston motion: Linear phenomenological law system Diesel cycle. *Int. J. Therm. Sci.* **2012**, *51*, 163–174. [CrossRef]
72. Lin, J.; Chang, S.; Xu, Z. Optimal motion trajectory for the four-stroke free-piston engine with irreversible Miller cycle via a Gauss pseudospectral method. *J. Non-Equilib. Thermodyn.* **2014**, *39*, 159–172. [CrossRef]
73. Watowich, S.J.; Hoffmann, K.H.; Berry, R.S. Intrinsically Irreversible Light-Driven Engine. *J. Appl. Phys.* **1985**, *58*, 2893–2901. [CrossRef]
74. Watowich, S.J.; Hoffmann, K.H.; Berry, R.S. Optimal Paths for a Bimolecular, Light-Driven Engine. *Il Nuovo Cim. B* **1989**, *104*, 131–147. [CrossRef]
75. Ma, K.; Chen, L.; Sun, F. Optimal paths for a light-driven engine with a linear phenomenological heat transfer law. *Sci. China Chem.* **2010**, *53*, 917–926.
76. Chen, L.; Ma, K.; Ge, Y.; Sun, F. Minimum entropy generation path for light-driven engine with [a]-[b] system and heat transfer law. *Environ. Eng. Manag. J.* **2017**, *16*, 2035–2043. [CrossRef]
77. Chen, L.; Ma, K.; Ge, Y. Optimal Configuration of a Bimolecular, Light-Driven Engine for Maximum Ecological Performance. *Arab. J. Sci. Eng.* **2017**, *38*, 341–350. [CrossRef]
78. Ma, K.; Chen, L.; Sun, F. Ecological performance improved by controlling piston motion: Linear phenomenological system bimolecular, light driven engine. *J. Energy Inst.* **2013**, *86*, 210–219. [CrossRef]

entropy

MDPI

Article

Averaged Optimization and Finite-Time Thermodynamics

Anatoly Tsirlin [1,*] and Ivan Sukin [2,*]

Ailamazyan Program Systems Institute of Russian Academy of Sciences, Petra Pervogo st., 4a, Veskovo, Yaroslavl oblast 152021, Russia

* Correspondence: tsirlin@sarc.botik.ru (A.T.); ivsukin@gmail.com (I.S.); Tel.: +7-915-973-44-42 (I.S.)

Received: 1 July 2020; Accepted: 18 August 2020; Published: 20 August 2020

Abstract: The paper considers typical extremum problems that contain mean values of control variables or some functions of these variables. Relationships between such problems and cyclic modes of dynamical systems are explained and optimality conditions for these modes are found. The paper shows how these problems are linked to the field of finite-time thermodynamics.

Keywords: averaged; optimization; thermodynamics; heat transfer; cyclic mode

1. Introduction

Averaging plays a very important role in optimization problems applied to engineering. Here are a few examples:

1. Assume that there is a bound on the source flow g_s and this constraint lowers the possible optimal value of the production. If we introduce some buffer (container) in such a way that the source flow is its feed, we can raise the possible value of the feed flow to the actual process without violating this constraint. Actual values of the feed flow will oscillate between values that are greater than and less than g_s. Only the mean value of the feed flow will be bounded in this case. Using this approach we can replace the strict constraint on g_s by the averaged one. If we use such a buffer to store the product flow, we can maximize not this flow itself, but its mean value (Figure 1).

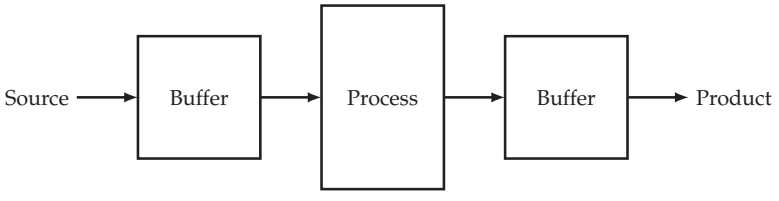

Figure 1. Flowsheet of a simple process with averaging of both source and product flows.

Let us assume that the relationship between production rate g and consumption q has the form presented at Figure 2.

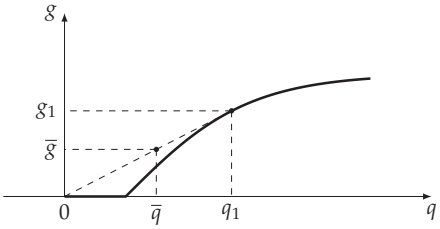

Figure 2. Relationship between production and consumption. Effect of averaging.

With the help of buffers this relationship could be improved on interval from 0 to q_1. The process must operate with consumption q_1 during some fraction of time and with zero consumption during the remaining time. Relationship between average production and average consumption is represented by dashed slope line at Figure 2. This is the way pumps of water towers operate.

2. Controls often can have only discrete values. For example, the light switch can be either on or off. None of these discrete values satisfy the constraints of the original problem. If there are devices that smooth out any oscillations of control variables, the optimal mode can correspond to the switching strategy that maintains given average values of flows. This kind of switching is the basis of electronic light dampers.
3. In a heat engine the working fluid periodically makes contacts with the hot and cold sources, and the properties of these contacts must be chosen such that the average properties of the working fluid satisfy the constraints of the optimum cycle problem.

Averaged problems arise in finite-time thermodynamics for two main reasons:

1. Many processes are periodic and their constraints must be satisfied on average per cycle.
2. Interactions of thermodynamic systems are characterized by values of extensive variables X (volume, amount of substance, internal energy, entropy), and flows of mass and energy emerging in these interactions depend on intensive variables y (temperature, pressure, molar fraction). The rate of change of extensive variables depend on a flow, and of course on y. This means that the governing equations for thermodynamic interactions have the form:

$$\frac{dX}{dt} = F(y) \tag{1}$$

The right hand side of (1) does not contain X and this means that the increase in extensive variables during some given amount of time depends only on the mean value of F. It does not depend on the order in which intensive variables have different values, if the mean value of F remains constant. Equations such as (1) are called Lyapunov-type. They allow us to formulate the problem of optimal control for thermodynamic systems in averaged form.

Below we will consider some of these problems. The last section contains applications of methods developed in the paper to finite-time thermodynamics.

We consider dynamical systems characterized by a finite number of variables.

By a *steady-state mode* of a system we mean a mode such that, for every variable $y_\nu(t)$ characterizing the system, there exists a period T_ν such that the average value of $y_\nu(t)$ over this period is constant in time. Formally, this can be written as [1]

$$\frac{1}{T_\nu} \int_{t-T_\nu}^{t} y_\nu(\tau) d\tau = \overline{y}_\nu. \tag{2}$$

Clearly, static modes, under which $y_\nu(t)$ are constant for all ν, satisfy this definition.

Another, more general, subclass of steady-state modes is formed by modes for which there exists a period T that is a multiple of all periods T_ν. Such modes are called *cyclic* ones.

There are also steady modes for which there does not exist a common period T for all variables $y_\nu(t)$. This corresponds to the case where the ratio of at least two periods T_ν and T_μ is irrational. Such modes are called *quasi-cyclic* steady-state modes.

If the system is affected by external factors represented by stationary random processes and the mean values of the variables characterizing the system tend to some limits as the period T of averaging increases, then the steady mode is said to be *stochastic*.

A switch to a non-static steady-state mode may be caused either by the absence of a static mode admitted by the operating conditions of the system or by the fact that the efficiency of the system in a static mode is lower than in other modes.

Consider some examples.

1. The human organism in a steady mode in the absence of external perturbations is characterized by a constant temperature, a constant composition of arterial blood, etc. However, some factors such as the blood pressure and the lung volume periodically change. This is related to the "structure" of the respiration and circulation organs.
2. A system consisting of a pump connected with a tank (e.g., a water tower) and consumers operates so that, even if the liquid consumption $\overline{G}$ is constant, the pump is sometimes completely switched off (and the liquid does not flow into the tank) and is sometimes switched on and operates with delivery higher than $\overline{G}$, with the average delivery being $\overline{G}$. If the dependence of the pump delivery g on the power expenditure S is described by a strictly convex function, then the average pump delivery is higher than that in the static mode at the same average power expenditure.

   In the rest of the paper, we mainly consider cyclic steady-state modes, among which two limit classes are distinguished. The first class includes modes in which each of the periods T_ν significantly exceeds the time of relaxation processes in the system. Moreover, each of the static steady states is assumed to be stable. In this case, we can neglect the dynamics of the system and assume that under variation of the mode variables, the state variables change in accordance with the static characteristics. Such modes are said to be *quasi-static*.

   The second class is formed by *sliding* steady-state modes, in which all or some of the control variables vary with frequency so high that, due to the inertia of the object, the state variables remain virtually constant, and their values depend only on the averaged influence of the control variables.

   Although static modes are a special case of cyclic modes, below by cyclic modes we mean modes under which at least one variable of the process changes periodically in time. A cyclic mode is said to be efficient if the passage to this mode improves the efficiency of the process in comparison with the static mode.
3. Cyclic modes are typical of systems with no admissible static modes. Often a system has no static modes if the set V of admissible values of variables is non-convex; e.g., this set may include only discrete values. This is so, for example, in a heat engine in which a working fluid contacts a heat source whose temperature can take only two values, T_+ (a hot source) and T_- (a cold source), and the average power over a cycle is required to be maximal under certain constraints.

Cyclic processes may be organized not only in time; variables may also depend on a spatial coordinate. In this case, the parameters of the system are constant in each section of the apparatus and vary periodically from section to section.

When passing from a static mode to a cyclic mode, one needs to replace the objective function by its mean value over the cycle and to replace all or some constraints imposed at each moment of time by averaged constraints. Thus, this passage involves an operation of averaging. Before passing to a cyclic mode, one must answer the following questions:

1. Does there exist a cyclic mode satisfying the constraints of the problem?
2. Is the transition from the optimal static mode to the cyclic mode efficient?
3. What is the gain in the optimality criterion from this passage?
4. What are the optimal forms of variation of the control and state variables, optimality conditions, computational algorithms?

It is desirable to answer questions 1—3 without solving problem 4, which is rather difficult in most cases.

Usually the problem of choosing an optimal static mode of an apparatus reduces to the problem of finding the extremal value of the objective function under certain equality and inequality constraints on the variables, i.e., to a non-linear programming problem. The transition to cyclic modes extends the set of possible solutions and, depending on a particular setting, leads either to an averaged non-linear programming problem or to a variational control problem. If the problem has an optimal static mode, then we refer to this problem as the initial problem.

In the rest of the paper we consider various methods for constructing problems with larger sets of admissible solutions as compared with the initial problem; we show that there are relationships between such extended problems, which allows one to estimate solutions and values of some of them by solving others.

2. Averaged Optimization Problems and Their Optimality Conditions

In this section, we consider various methods for introducing averaging into a non-linear programming (NLP) problem and obtain optimality conditions for averaged problems. To obtain these conditions, we use a trick based on reducing any averaged problem to a canonical form and deriving necessary optimality conditions for a particular problem from those for a general problem.

2.1. Averaging of Functions Included in the Formulation of an Optimization Problem

Consider an initial NLP problem [2] in the form

$$f_0(x) \to \max \Big/ f_i(x) = 0, \quad i = \overline{1,m}, \quad x \in V_x. \tag{3}$$

On the set V_x , we define a probability measure $p(x)$ such that

$$\int\limits_{V_x} p(x)dx = 1, \quad p(x) \geq 0. \tag{4}$$

The average value of the function $f(x)$ on the interval $[0, \tau]$ can be calculated as follows:

$$\overline{f(x)} = \frac{1}{\tau} \int\limits_0^\tau f(x(t))dt = \int\limits_{V_x} f(x)p(x)dx. \tag{5}$$

Let us assume that x varies with time or one solves the problem (3) and maximizes the mean value of f_0, but not the value of this function itself. If functions f_i vanish on average, then we will arrive at a problem of the form

$$\overline{f_0(x)} \to \max \Big/ \overline{f_i(x)} = 0, \quad i = \overline{1,m}. \tag{6}$$

A sought solution of problem (6) is a measure $p(x)$ on V_x rather than a vector x. The variable x is called a *randomized* one, and $p(x)$ is called a *generalized* solution. Following A.D. Ioffe and V.M. Tikhomirov [3], we call the value of the objective functional at the optimal solution as *the value of a problem*.

2.2. Convex Hulls—Carathéodory's Theorem

The notion of *convexity* is very important for optimization problems.

1. The convex hull of a set V is the minimum convex set CoV such that $V \subset CoV$.
2. The set of points lying on or below the graph of a function is called its *hypograph*. The convex hull Cof of a function f is the upper boundary of the convex hull of its hypograph.
3. Alternatively, the convex hull of a function f is the minimum convex function defined on the convex hull of the domain of f. For every $\tilde{x}$ from the domain of f the following holds: $Cof(\tilde{x}) \geq f(\tilde{x})$.

Carathéodory's theorem is the most important theorem of convex analysis and geometry. It states that coordinates of every point of the convex hull of the set $V \subset \mathbb{R}^n$ could be calculated as the weighted arithmetic mean of some points of V and the maximum necessary number of these points is no more than $n+1$. The beautiful exposition of this theorem is given in [4].

2.3. Optimal Distribution in An Averaged NLP Problem

Let us take some $x_0 \in V_x$. If $p(x) = \delta(x - x_0)$, then problem (6) coincides with the initial problem. If the set of admissible solutions of a problem includes the set of admissible solution of the initial NLP problem and the optimality criteria in both problems coincide on the set of admissible solutions of the NLP problem, then the former problem is called an extension of the NLP problem.

First, consider the special form of problem (6) with $f_i(x) = x_i$:

$$\overline{f_0(x)} \to \max \Big/ \overline{x}_i = 0, \quad i = \overline{1,n}. \tag{7}$$

The value of the problem (7) is equal to the ordinate of the convex hull of the function $f_0(x)$ on the set V_x at the point $x = 0$. According to Carathéodory's theorem, constructing any ordinate of the convex hull of a function of n variables requires averaging at most $n+1$ ordinates of the function $f_0(x)$; therefore, we can rewrite problem (7) in the form

$$\sum_{\nu=0}^{n} \gamma_\nu f_0(x^\nu) \to \max \Big/ \sum_{\nu=0} \gamma_\nu x_i^\nu = 0, \quad i = \overline{1,n}, \quad \gamma_\nu \geq 0, \quad \sum_{\nu=0}^{n} \gamma_\nu = 1. \tag{8}$$

Let us return to problem (6) and try to reduce it to simple calculation. We need to calculate the ordinate of a convex hull of the given function. Please note that problem (6) can be solved in two stages. At the first stage, we find the maximum of the function $f_0(x)$ subject to the constraint $f(x) = C$, where C takes all values for which the level surface $f(x) = C$ intersects V_x. The problem

$$f_0(x) \to \max / f_i(x) = C, \quad i = \overline{1,m}, \quad x \in V_x \tag{9}$$

is a non-linear programming problem. Solving (9), we obtain a set of conditionally optimal solutions $x^*(C)$ and the corresponding values of the *reachability function* $f_0^*(C) = f_0(x^*(C))$ of the non-linear programming problem.

The following assertion holds: *The optimal distribution $p^*(x)$ in problem (6) is concentrated at the points $x^*(C)$*. In other words, *one needs to average only over conditionally optimal values of f_0*.

2.4. Necessary Conditions of Optimality—Kuhn-Tucker Theorem

The Kuhn-Tucker theorem generalizes Lagrange multipliers method to problems with inequality constraints:

$$f_0(x) \to \max_x \Big/ f_i(x) = 0, \quad \varphi_j(x) \geq 0, \quad i = \overline{1,k}, \quad j = \overline{k+1,m}, \tag{10}$$

where all functions are smooth.

The theorem states that *there is nonzero vector of Lagrange multipliers with components* λ_i, $\mu_j \leq 0$ *such that Lagrange function*

$$L = \lambda_0 f_0(x) + \sum_i \lambda_i f_i(x) + \sum_j \mu_j \varphi_j(x) = R(\lambda, x) + \sum_j \mu_j \varphi_j(x) \tag{11}$$

is stationary on the optimal solution of the problem (10). The multiplier λ_0 *could equal to zero or one. In the former case the solution is called degenerate.*

It follows from this theorem that when $\varphi_j(x) = x_j$ we have inequality $\frac{\partial R}{\partial x_j} \leq 0$ for the optimal solution. More detailed explanation could be found in [5].

2.5. Reduction to an Ordinary NLP Problem

The above considerations allow us to formulate the second stage in solving problem (6). This stage is the maximization of the average value of the function $f_0^*(C)$ with the constraint that the vector C has zero mean, i.e.,

$$\overline{f_0^*(C)} \to \max \Big/ \overline{C}_i = 0, \quad i = \overline{1,m}, \quad C_i \in V_C. \tag{12}$$

This problem is similar to the problem (7). Its value, and hence the value of problem (6), is equal to the ordinate of the convex hull of the reachability function $f_0^*(C)$ at $C = 0$:

$$\sup_{x \in D} \overline{f_0(x)} = \sup \overline{f_0^*(C)} \Big/ \overline{C} = 0, \quad C \in V_C. \tag{13}$$

Since the vector C is m-dimensional, the number of base points C^ν in problem (9) is at most $m + 1$. Thus, the distribution $p(C)$ in problem (9) can be sought in the form

$$p(C) = \sum_{\nu=0}^{m} \gamma_\nu \delta(C - C^{nu}). \tag{14}$$

Since each of the base values C^ν corresponds to a conditionally optimal solution $x^*(C^\nu)$, the optimal distribution $p(x)$ is also concentrated at no more than $m + 1$ points:

$$p(x) = \sum_{\nu=0}^{m} \gamma_\nu \delta(x - x^\nu). \tag{15}$$

Substituting the distribution (15) into the expressions for $\overline{f_0(x)}$ and $\overline{f_i(x)}$, we reduce problem (6) to the form

$$\begin{aligned} &I = \sum_{\nu=0}^{m} \gamma_\nu f_0(x^\nu) \to \max \Big/ \sum_{\nu=0}^{m} \gamma_\nu f_i(x^\nu) = 0, \\ &i = \overline{1,m}, \quad x^\nu \in V_x, \quad \gamma_\nu \geq 0, \quad \sum_{\nu=0}^{m} \gamma_{nu} = 1. \end{aligned} \tag{16}$$

Thus, we have reduced the problem to an ordinary NLP problem whose variables are the base values x^ν of the vector x and the weight factors γ_ν.

2.6. Relationship between Averaged NLP Problem and the Lagrangian Function of the NLP Problem without Averaging

The Lagrangian function

$$\begin{aligned} &\overline{R} = \sum_{\nu=0}^{m} \gamma_\nu f_0(x^\nu) + \sum_{i=1}^{m} \lambda_i \sum_{\nu=0}^{m} \gamma_\nu f_i(x^\nu) + \Lambda \left(1 - \sum_{\nu=0}^{m} \gamma_\nu\right) = \\ &= \sum_{\nu=0}^{m} \gamma_\nu \left[f_0(x^\nu) + \sum_{i=1}^{m} \lambda_i f_i(x^\nu) - \Lambda\right] + \Lambda \end{aligned} \tag{17}$$

of problem (16) is related to the Lagrangian function

$$R = f_0(x) + \sum_{i=1}^{m} \lambda_i f_i(x) \tag{18}$$

of the initial NLP problem by

$$\overline{R} = \sum_{\nu=0}^{m} \gamma_\nu (R(x^\nu, \lambda) - \Lambda) + \Lambda. \tag{19}$$

Since $\sum\limits_{\nu} \gamma_\nu = 1$, the Lagrangian function of the averaged problem equals the average value of the Lagrangian function of the initial problem over all base values x^ν. Some of the weight factors γ_ν may vanish; then the number of base points is less than $m + 1$.

Let us find conditions that must hold for those x^ν that have non-zero weights in (19). For this purpose, we apply the Kuhn–Tucker theorem and write the optimality conditions for problem (16) with respect to the variables γ_ν:

$$\frac{\partial \overline{R}}{\partial \gamma_\nu} \delta\gamma_\nu \le 0. \tag{20}$$

Since γ_ν are bounded only from below ($\gamma_\nu \ge 0$), it follows that $\delta\gamma_\nu \ge 0$; therefore,

$$\frac{\partial \overline{R}}{\partial \gamma_\nu} = R(x^\nu) - \Lambda \le 0, \tag{21}$$

or $R(x^\nu) \ge \Lambda$. If $\gamma_\nu^* > 0$, then $\delta\gamma_\nu$ may be of any sign, and so inequality (21) transforms into the equality

$$R(x^\nu) = \Lambda. \tag{22}$$

Thus, *for all x^ν involved in the averaged problem with non-zero weights, the Lagrangian function R of the initial non-linear programming problem attains an absolute maximum*. Of course, this maximum is the same for all x^ν.

The requirements that the function R must take the same value at all points $x^{\nu *}$ and that this value must be maximum give equations for the variables to be found. Thus, applying Kuhn–Tucker theorem the problem (6), we obtain the vector of Lagrange multipliers λ for which the function $\overline{R}$ attains an absolute maximum with respect to the variables $x^\nu \in V_x$ and $\gamma_\nu \in V_\gamma$ at an element of the set D of admissible solutions to problem (6), and these multipliers λ satisfy the condition

$$\overline{R}(\lambda^*, \gamma_\nu^*, x^{\nu *}) = \inf_{\lambda \in V_\lambda} \sup_{\gamma_\nu, x^\nu} \overline{R}(\lambda, \gamma_\nu, x^\nu) = \inf_{\lambda \in V_\lambda} \sup_{x \in V_x} R(\lambda, x). \tag{23}$$

Thus, when the attainability function $f_0^*(C)$ coincides with its convex hull at $C = 0$, the transition to the averaged problem is not efficient (the values of the NLP problem and problem (6) coincide). By virtue of (23), we can look for the value of the averaged problem in the form $\inf\limits_{\lambda \in V_\lambda} \sup\limits_{x \in V_x} R(\lambda, x)$. If the extended problem is inefficient, then we say that it is equivalent to the initial problem.

In the general case, the dimension of the vector of unknown variables and the computational complexity of problem (6) are much greater than those for the NLP problem. However, in many cases, we are interested not in the solution but in the value of the averaged problem, which shows the gain obtained by transition to the averaged setting. Some methods for estimating the value of problem (6) from above and below were proposed in [6].

2.7. Other Forms of Averaged Extensions of the NLP Problem

Problem (6) is not the only possible extension of the NLP problem by averaging. The optimality criteria, relations, and constraints in real-life problems often include the mean values of variables x rather than the variables themselves. For example, the performance of a distillation column

is characterized by the mean not current composition of output flows, because these flows are accumulated in some containers or apparatuses at the exit of the column (or attached to the column). Below, we describe several possible modifications of the averaged extension [7].

1. *Problem of maximizing a function of the mean value of the argument.* When D is the set of admissible solutions of the initial NLP problem, i.e., D is defined by the condition $f(x) = 0$, and $\overline{x}$ is the mean value of the vector x on the set D, we have:

$$f_0(\overline{x}) \to \sup \,/\, p(x) = 0 \quad \forall x \notin D. \tag{24}$$

Since the set of values $\overline{x}$ satisfying this condition is the convex hull of D, problem (24) is equivalent to the NLP problem on the convex hull of D:

$$f_0(x) \to \sup \,/\, x \in \operatorname{Co} D. \tag{25}$$

2. *Problem of maximizing the mean value of a function under constraints imposed on the mean value of the argument:*

$$\overline{f_0(x)} \to \sup \Big/ f_i(\overline{x}) = 0, \quad i = \overline{1,m} \tag{26}$$

or, in more detail,

$$\int\limits_{V_x} f_0(x)p(x)dx \to \sup_{p(x)} \Big/ f_i\left(\int\limits_{V_x} x \cdot p(x)dx\right) = 0, \quad i = \overline{1,m}. \tag{27}$$

3. *Problem of maximizing a function of the mean value of x under averaged constraints:*

$$f_0(\overline{x}) \to \sup \,/\, \overline{f_i(x)} = 0, \quad i = \overline{1,m}. \tag{28}$$

Each of the above problems is an extension of the non-linear programming problem, and the solutions of these problems are distributions $p(x)$.

Averaged problems with two types of variables. An NLP problem can be extended only with respect to some components of the solution rather than with respect to the whole solution. In practice, this situation occurs when the problem is solved repeatedly and some components (we denote them by x) can vary from one solution to another, while the remaining components must be chosen only once and then fixed. We denote the latter group of variables by y. For example, x may be the operating conditions of the process (such as flow, pressure, temperature, etc.) and y may be the design parameters of an apparatus.

If we denote

$$\overline{f(y,x)}^{x} = \int\limits_{C_x} f(y,x)p(x)dx, \tag{29}$$

a problem in which averaging is performed over only part of variables has the form

$$\overline{f_0(y,x)}^{x} \to \sup \Big/ \overline{f_i(y,x)}^{x} = 0, \quad i = \overline{1,m}. \tag{30}$$

One need to find the vector y and distribution $p(x)$ in (30).

For each fixed y, this problem coincides with the usual setting of problem (6). If we separate the randomized variables $x \in E^r$ and the deterministic variables $y \in E^s$ in the Lagrangian function R of the initial NLP problem, then we can write optimality conditions with respect to x by analogy with problem (6) in the form (see (23))

$$R(\lambda, \gamma_\nu^*, y, x^{\nu *}) = \sup_{x \in V_x} R(\lambda, y, x), \quad \nu = \overline{0,m}. \tag{31}$$

In this case, if we denote the admissible set of (30) as $\overline{D_x(y)}^x$, for each $y \in V_y$, there exist $\lambda(y)$ such that

$$\inf_{\lambda} \sup_{x \in V_x} R(\lambda, y, x) = \sup_{x \in \overline{D_x(y)}^x} \overline{f_0(y, x)}. \tag{32}$$

The Lagrangian function attains an absolute maximum at the base values of x.

At the same time, for a fixed function $p(x)$, problem (30) becomes a usual non-linear programming problem with respect to the variables y. The Kuhn–Tucker conditions hold for this problem, which include in this case the complementary slackness conditions as well as the requirement that the function $R(\lambda, \gamma_\nu, y, x^\nu)$ be stationary with respect to y, which in turn, leads to the equations

$$\frac{\partial}{\partial y_j} \left[\sum_{\nu=0}^{m} \gamma_\nu R(\lambda, y, x^\nu) \right] = 0, \quad j = \overline{1, s}. \tag{33}$$

where R is the Lagrangian function for the NP problem.

Averaged problems with two types of variables are in a sense close to optimal control problems, and optimality conditions for such problems are close to the Pontryagin maximum principle.

2.8. The Algorithm for Obtaining Optimality Conditions in Averaged Problems

By *an averaged problem of static optimization* we mean any NLP problem in which either functions or variables are averaged with respect to all or part of the variables.

As shown above, the settings of averaged problems are very diverse. The reason for this is that a problem may contain both the mean values of functions and functions of the mean values of variables. Moreover, averaging may involve only part of the variables. Under these conditions, it is inexpedient to study each possible setting of an averaged problem. It is significantly more convenient to obtain optimality conditions for some canonical form of an averaged problem and apply them to each particular problem after having reduced the latter to this canonical form [8].

Before obtaining optimality conditions, we must answer the following two questions:

1. Is the optimal distribution, which is one of the components of the solution of an averaged problem, always concentrated at finitely many base points?
2. If the answer to the previous question is "yes," then what is the limit number of these points?

The necessary optimality conditions given below yield an affirmative answer to the first question and allow one to determine the limit number of base points.

Let y denote the vector of deterministic variables, and let x be the vector of randomized variables. For the former, we must find an optimal value, and for the latter, an optimal measure. The canonical form of the averaged problem is

$$F_0(\overline{f(x, y)}, y, x) \to \max \tag{34}$$

under the constraints

$$\begin{aligned} &F_\nu(\overline{f(x, y)}, \varphi(x, y), \overline{x}) = 0, \quad \nu = \overline{1, r}, \\ &F_\nu(\overline{f(x, y)}, \varphi(x, y), \overline{x}) \geq 0, \quad \nu = \overline{r+1, m}. \end{aligned} \tag{35}$$

Here the bar over the symbol of a function denotes averaging over the set V_x of randomized variables x, which is assumed to be compact.

Suppose that the vector x has dimension k and the vector function f has dimension n. The function F is assumed to be continuously differentiable with respect to all its variables, and f and φ are continuous in x and continuously differentiable in y.

In [8], one of the authors (*A.T.*) proved that *the optimal measure $p^*(x)$ on the set of randomized variables is concentrated at no more than $L + 1$ base points, where $L = n + k$.* Thus,

$$p^*(x) = \sum_{l=0}^{L} \gamma_l \delta(x - x^l), \quad \gamma_l \geq 0, \quad \sum_{l=0}^{L} \gamma_l = 1. \tag{36}$$

Therefore, for the optimal solution, we have

$$\overline{f^*(x,y)} = \sum_{l=0}^{L} \gamma_l f(x^l, y), \quad \overline{x} = \sum_{l=0}^{L} \gamma_l x^l, \tag{37}$$

and constraints (35) take the form

$$\begin{array}{l} F_\nu(\overline{f}, \varphi(x^l, y), \overline{x}) = 0, \quad \nu = \overline{1, r}, \\ F_\nu(\overline{f}, \varphi(x^l, y), \overline{x}) \geq 0, \quad \nu = \overline{r+1, m}. \end{array} \tag{38}$$

for all values of x^l.

These expressions turn problem (34), (35) into an ordinary NLP problem with respect to γ_l, y and x^l. The Kuhn–Tucker conditions reduce to the following: the Lagrangian function

$$R = F_0(\overline{f}, y, \overline{x}) + \sum_{\nu=1}^{m} \lambda_\nu F_\nu(\overline{f}, \varphi(x^l, y), \overline{x}) \tag{39}$$

of this problem is stationary with respect to x^l and y and is unimprovable with respect to γ_l (we assume the solution is non-degenerate, so $\lambda_0 = 1$). To write down the optimality conditions, we introduce the notation

$$a_j = \frac{\partial R}{\partial \overline{f}_j}, \quad \beta_i = \frac{\partial R}{\partial x_i}, \quad r_{\mu l} = \frac{\partial R}{\partial \varphi_\mu}(x^l, y). \tag{40}$$

Using this notation, we can write the condition that R is unimprovable with respect to γ_l as follows: the expression

$$C(x) = \sum_j a_j f_j(x, y^*) + \sum_i \beta_i x_i \tag{41}$$

attains its maximum with respect to $x \in V_x$ at the points x^l, so that

$$x^{l*} = \arg\max_x C(x), \quad l = \overline{1, L}; \tag{42}$$

the condition that R is stationary with respect to y has the form

$$\nabla_y \left[\sum_j a_j \overline{f_j(x,y)} + F_0(\overline{f}, x, y) + \sum_{\mu,l} r_{\mu l} \varphi_\mu(x^l, y) \right] = 0. \tag{43}$$

The maximality of $C(x)$, together with equations (42), constraints (35), and the complementary slackness conditions

$$\sum_{\nu=r+1}^{m} \lambda_\nu F_\nu(\overline{f}^*, \varphi^*, x^*) = 0, \quad \lambda_\nu \geq 0, \quad \nu = \overline{r+1, m} \tag{44}$$

allows one to find a solution γ_l^*, y^*, x^l.

When formulating a specific averaged problem, one

1. writes the conditions of the problem in the canonical form (34), (35);
2. separates the randomized and deterministic variables;
3. calculates the total number L of averagings, which is equal to the sum of the dimensions of the vector of randomized variables and of the vector of functions to be averaged;
4. constructs the functions R and C and substitutes them into expressions (42)–(44).

For example, in problem (26), we have

$$F_0 = \overline{f_0(x)}, \quad F_\nu = f_\nu(\overline{x}), \quad \nu = \overline{1, m}. \tag{45}$$

The number L equals k, and

$$R = \lambda_0 \overline{f_0(x)} + \sum_{\nu=1}^{m} \lambda_\nu f_\nu(\overline{x}). \tag{46}$$

In (42), we have $a_0 = \lambda_0 = 1$, $a_\nu = 0$ for $\nu > 0$ and

$$\beta_i = \sum_{\nu=1}^{m} \lambda_\nu \left(\frac{\partial f(\overline{x})}{\partial \overline{x}_i} \right)_{\overline{x}}, \quad i = \overline{1,k}. \tag{47}$$

At the base points x^l, the number of which does not exceed $k+1$, the expression

$$C(x) = f_0(x) + \sum_{i=1}^{k} x_i \sum_{\nu=1}^{m} \lambda_\nu \left(\frac{\partial f(\overline{x})}{\partial \overline{x}_i} \right)_{x^*} \tag{48}$$

attains its maximum, and conditions (35) hold, which have the form

$$f_\nu \left(\sum_{l=0}^{k} \gamma_l x^l \right) = 0, \quad \nu = \overline{1,m}. \tag{49}$$

3. Non-Stationary Problems of Averaged Optimization

Consider an extremal problem of the form

$$\overline{f}_0 = \frac{1}{\tau} \int_0^\tau f_0(J(t), u(t))dt \to \max_u \tag{50}$$

subject to the constraints

$$\overline{f}_\nu = \frac{1}{\tau} \int_0^\tau f_\nu(J(t), u(t))dt = 0, \quad \nu = \overline{1,n}, \tag{51}$$

where the functions $f_\nu : \mathbb{R}^{k_1} \times \mathbb{R}^{k_2} \to \mathbb{R}$, $\nu = \overline{0,n}$, are continuous in J and u, $u \in V_u \subset \mathbb{R}^{k_1}$ is a measurable function, the set V_u is compact, and $J(t) \in V_J \subset \mathcal{R}^{k_2}$ is a given measurable function of time. With $J(t)$ we can associate a probability measure (distribution) $p(J)$. If $J(t)$ takes a value J^k on a part of the interval $(0,\tau)$ of relative length α_k, then $p(J)$ contains a term of the form $\alpha_k \delta(J - J^k)$. The length of the interval $(0,\tau)$ may tend to infinity, and $J(t)$ may be a stationary random process with distribution $p(J)$.

The distribution $p(J)$ can be written in the form

$$p(J) = \overline{p}(J) + \sum_k \alpha_k \delta(J - J^k). \tag{52}$$

For problem (50), (51), let $\alpha\tau$ be the length of the part of $(0,\tau)$ on which $J(t)$ takes one of the constant values J^k; we have $\alpha = \sum\limits_k \alpha_k$. We refer to $\alpha\tau$ as the total constancy interval of $J(t)$. The remaining part $(1-\alpha)\tau$ is called the interval of variation of the parameter J.

Theorem 1. *Let $u^*(t)$ be an optimal solution; then there exists a non-zero vector $\lambda = \{\lambda_0, \ldots, \lambda_n\}$ with $\lambda_0 \in \{0,1\}$ such that*

- *on the interval of variation of the parameter $J(t)$*

$$u^*(J,\lambda) = \arg\max_{u \in V_u} \sum_{\nu=0}^{n} \lambda_\nu f_\nu(J,u); \tag{53}$$

- *on the total constancy interval of $J(t)$, the optimal solution switches between at most $n+1$ base values u^j, and each of these values satisfies the condition*

$$u^j = \arg\max_{u \in V_u} \sum_k \alpha_k \sum_{\nu=0}^{n} \lambda_\nu f_\nu(J^k, u), \quad j = \overline{0,n}; \tag{54}$$

- *the portions γ_j of the constancy interval $\alpha\tau$ on which $u^*(t)$ takes the respective values u^j satisfy the conditions*

$$\begin{gathered} \int_{V_J} \overline{p}(J) f_\nu(J, u^*(J)) dJ + \sum_{j=0}^{n} \gamma_j \sum_k \alpha_k f_\nu(J^k, u^j) = 0, \quad \nu = \overline{1,n}, \\ \sum_{j=0}^{n} \gamma_j = 1, \quad \gamma_j \geq 0; \end{gathered} \tag{55}$$

- *the vector of multipliers λ_ν, $\nu = \overline{1,n}$, is determined by the conditions*

$$\lambda^* = \arg\min_{\lambda} \left[\int_{V_J} \overline{p}(J) \sum_{\nu=0}^{n} \lambda_\nu f_\nu(J, u^*(J,\lambda)) dJ + \sum_{j=0}^{n} \gamma_j \sum_{\nu=0}^{n} \lambda_\nu \sum_k \alpha_k f_\nu(J^k, u^j(\lambda)) \right]. \tag{56}$$

Thus, on the constancy intervals, the optimal solution of a problem with non-stationary parameters coincides with the solution of an averaged mathematical programming problem, and on the interval of variation of the parameter, it varies as the solution of a problem with integral constraints. This theorem was proved in [9].

Example 1. *Consider the problem of maximizing the average power $\overline{p}$ of a heat engine in which the working fluid contacts a source of variable temperature $T_0(t)$. This problem has the form*

$$\overline{p} = \frac{1}{\tau} \int_0^\tau q(T_0(t), T(t)) dt \to \max_T \tag{57}$$

subject to the constraint

$$\overline{\sigma} = \frac{1}{\tau} \int_0^\tau \frac{q(T_0(t), T(t))}{T(t)} dt = 0. \tag{58}$$

Here $T(t)$ is the temperature of the working substance, q is the heat flux from the source to the working fluid, and $\overline{\sigma}$ is the mean rate of variation of the entropy of the working substance. A substantiation of the setting (56), (57) can be found in [10–12]. The optimality conditions (53) imply the following relation for the interval of variation of $T_0(t)$:

$$\frac{1}{T^2} \frac{q(T_0, T)}{\partial q(T_0, T)/\partial T} - \frac{1}{T} = \text{const}. \tag{59}$$

In particular, for the Newtonian law $q(T_0, T) = \beta(T_0 - T)$ of heating, (59) implies

$$T^*(T_0) = m\sqrt{T_0}, \tag{60}$$

where m is the constant equal to the mean value of the square root of the source temperature.

For example, suppose that $T_0(t)$ has a uniform distribution (for a regular function $T_0(t)$, this means that the source temperature depends linearly on time) and T_{02} and T_{01} are the maximal and minimal source temperatures, respectively. Then

$$T^*(T_0) = \frac{2(T_{02}^{3/2} - T_{01}^{3/2})}{3(T_{02} - T_{01})} \sqrt{T_0}. \tag{61}$$

The maximum power is given by

$$\overline{p}_{max} = \beta \left[\frac{T_{02} + T_{01}}{2} - \frac{4}{9} \frac{(T_{02}^{3/2} - T_{01}^{3/2})}{T_{02} - T_{01}} \right]. \tag{62}$$

Thus, a heat engine with one source may have non-zero power if the variance of the source temperature is positive.

For some laws $q(T_0, T)$, the optimal temperature $T^*(t)$ may switch between two base values on intervals of constancy of the parameter T_0.

4. Estimation of the Performance of Cyclic Modes

Suppose that the dynamics of a system is characterized by the differential equations

$$\dot{x}_\nu = f_\nu(x, u, a), \quad \nu = \overline{1, m}, \tag{63}$$

whose right-hand sides do not explicitly depend on t. Here, as in the preceding sections, x denotes the state variables, u are the control ones, and a denotes parameters to be optimized. As a rule, boundary conditions are not fixed for equations (63), but the state variables are required to vary periodically:

$$x_\nu(\tau) = x_\nu(0) \Rightarrow \int_0^\tau f_\nu(x, u, a)dt = 0, \quad \nu = \overline{1, m}. \tag{64}$$

The performance averaged over the cycle plays the role of the optimality criterion for such a cyclic process and can be written in the form

$$I = \frac{1}{\tau} \int_0^\tau f_0(x, u, a)dt \to \max. \tag{65}$$

The duration τ of each cycle is one of the components of the vector a; in the general case, it is not fixed. The parameters and controls are subject to constraints $a \in V_a$ and $u \in V_u$; in addition to the integral constraints (64), which follow from the periodicity of the process, the problem usually contains integral constraints determined by given mean rates of consumption of some resources (resource constraints):

$$J_j = \int_0^\tau \varphi_j(x, u, a)dt = 0, \quad j \in \overline{1, r}. \tag{66}$$

It is assumed that each of the functions determining the problem is continuous in all its variables and is continuously differentiable with respect to x and a.

Optimality conditions. Optimality conditions for problem (63)–(66) can be obtained by using the maximum principle [6]. Namely, if an optimal solution x^*, a^*, u^* exists and is non-degenerate, then there exist a non-zero vector λ and a differentiable vector function $\psi(t)$ such that the function

$$R = \frac{1}{\tau} f_0 + \sum_\nu [\dot{\psi}_\nu x_\nu + (\psi_\nu + \lambda_\nu) f_\nu] + \sum_j \lambda_j \varphi_j. \tag{67}$$

is stationary with respect to x and attains a maximum with respect to u, and the integral S of this function is locally unimprovable with respect to a. Thus,

$$\frac{\partial R}{\partial x_i} = 0 \quad \Rightarrow \quad \dot{\psi}_i = -\frac{\partial}{\partial x_i} \left\{ \frac{1}{\tau} f_0 + \sum_\nu (\psi_\nu + \lambda_\nu) f_\nu + \sum_j \lambda_j \varphi_j \right\}. \tag{68}$$

Since the values $x_\nu(\tau)$ and $x_\nu(0)$ are not fixed, it follows that $\psi_\nu(\tau)$ and $\psi_\nu(0)$ vanish. Introducing the notation $\tilde{\psi}_\nu = \psi_\nu + \lambda_\nu$ and taking into account the equality $\dot{\tilde{\psi}}_\nu = \dot{\psi}_\nu$, we can rewrite condition (68) in the form

$$\dot{\tilde{\psi}}_i = -\frac{\partial}{\partial x_i}\left\{\frac{1}{\tau}f_0 + \sum_\nu \psi_\nu f_\nu + \sum_j \lambda_j \varphi_j\right\} = -\frac{\partial}{\partial x_i}H. \tag{69}$$

For these equations, since $\psi(0)$ and $\psi(\tau)$ vanish, the costate variables satisfy the periodicity conditions

$$\widetilde{\psi}_\nu(0) = \widetilde{\psi}_\nu(\tau) \quad \Rightarrow \quad \int_0^\tau \frac{\partial H}{\partial x_\nu}dt = 0, \quad \nu = \overline{1,m}. \tag{70}$$

The conditions of maximality of R with respect to u have the form

$$u^*(t) = \arg\max_{u \in V_u}\left\{\frac{f_0}{\tau} + \sum_\nu \tilde{\psi}_\nu f_\nu + \sum_j \lambda_j \varphi_j\right\}. \tag{71}$$

Finally, the optimality conditions with respect to each component a_k of the vector a, including the duration τ of the cycle, yield the inequalities

$$\frac{\partial S}{\partial a_k}\delta a_k \le 0, \quad k = 1, 2, \ldots \tag{72}$$

Here δa is the cone of variations of the vector a that are admissible with respect to the inclusion $a \in V_a$.

Please note that the phase trajectory corresponding to an optimal cyclic process has no self-intersections [13].

5. Estimation of the Efficiency of Transition to a Cyclic Process

5.1. Conditions of Equivalence and Efficiency of a Cyclic Extension

The optimal cyclic mode problem (63)–(66) (we refer to it as Problem C) is an extension of a non-linear programming problem. Indeed, imposing the additional constraints $x = \text{const}$ and $u = \text{const}$ on the solution of this problem, we obtain the following optimal static mode problem (Problem S):

$$I_S = f_0(x,u,a) \to \max \Big/ \begin{array}{l} f_\nu(x,u,a) = 0, \quad \varphi_j(x,u,a) = 0 \\ u \in V_u, \quad a \in V_a, \quad \nu = \overline{1,m}, \quad j = 1,2. \end{array} \tag{73}$$

Since the set of admissible solutions of problem (63)–(66) is larger than that of Problem S, it follows that

$$I_S^* \le I_C^*. \tag{74}$$

where I_C^* denotes the value of the optimal cyclic mode problem.

One of the problems in designing cyclic processes consists of distinguishing a class of problems for which inequality (74) turns into an equality, i.e., the cyclic extension is equivalent to the static problem. An important role in solving this problem is played by the Lagrangian function of Problem S,

$$R_S = f_0(x,u,a) + \sum_\nu \lambda_\nu f_\nu(x,u,a) + \sum_j \xi_j \varphi_j(x,u,a) \tag{75}$$

To determine whether a cyclic process is equivalent to a static one or efficient without solving problem (63)–(66), we form averaged problems, which are in turn extensions for Problem S or C or for both. Comparing the values of these problems with I_C^*, we find conditions for the equivalence of a cyclic extension.

1. *An upper bound for I^*_{C} and sufficient conditions for the equivalence of a cyclic extension*. Let us enlarge the set of admissible solutions of Problem C by removing the differential equations (63). We obtain Problem $\overline{S}$, which we call an *estimating* problem:

$$I_{\bar{S}} = \overline{f_0(x,u,a)}^{x,u} \to \max \Big/ \begin{array}{l} \overline{f_\nu(x,u,a)}^{x,u} = 0, \quad \overline{\varphi_j(x,u,a)}^{x,u} = 0 \\ \nu = \overline{1,m}, \quad u \in V_u, \quad a \in V_a, \quad j = \overline{1,r}. \end{array} \tag{76}$$

Clearly,

$$I^*_{\bar{S}} \geq I^*_{\mathrm{C}}, \tag{77}$$

and Problem $\overline{S}$ is an averaged extension of Problem S with the variables x and u and the parameters a. The roles of the variables x and u in the conditions of Problem $\overline{S}$ are similar, and we unite these variables and denote them by $y = (x,u)$. In shorthand notation, this problem has the form

$$I_{\bar{S}} = \overline{f_0(y,a)}^{y} \to \max / \overline{f_\nu(y,a)}^{y} = 0, \quad \overline{\varphi_j(y,a)}^{y} = 0, \quad \nu = \overline{1,m}, \quad j = \overline{1,r}. \tag{78}$$

The value of problem (78) as an extension of the optimal static mode problem can be expressed in terms of the function R_S as

$$I^*_{\bar{S}} = \inf_{\lambda,\xi} \sup_{y} R_{\mathrm{S}}(y, a^*, \lambda, \xi). \tag{79}$$

For determining the vector of parameters, we have the condition

$$\left[\frac{\partial}{\partial a}\overline{R_{\mathrm{S}}(y,a,\lambda,\xi)}^{y}\right]_{a=a^*} = 0. \tag{80}$$

If a^* lies inside V_a, then condition (80) reduces to the condition of stationarity of R_S with respect to a.

If the value I^*_5 given by (79) equals I^*_{S} (i.e., Problem $\overline{\mathrm{S}}$ has a unique base solution), then inequalities (74) and (77) imply $I^*_{\mathrm{C}} = I^*_{\mathrm{S}}$; i.e., the static mode cannot be improved by passing to a cyclic mode. If $I^*_{\bar{S}} > I^*_{\mathrm{S}}$, then the difference $\Delta_{\overline{\mathrm{S}}}$ between these values gives an upper bound for the possible gain from the passage to a cyclic mode.

2. *A lower bound for I^*_{C}. Quasi-static and sliding modes*. Consider the case when $x(t)$ and $u(t)$ vary so that the time derivatives of $x(t)$ can be neglected. Then the relations between x and u are given, as in the static case, by $f(x(t),u(t),a) = 0$ for all t. The corresponding modes are said to be quasi-static. The problem of an optimal choice of $x(t)$ and $u(t)$ under the quasi-static conditions (Problem QS) has the form

$$I_{\mathrm{QS}} = \frac{1}{\tau}\int_0^\tau f_0(x,u,a)dt \to \max / f(x,u,a) = 0, \quad \int_0^\tau \varphi(x,u,a)dt = 0, \quad u \in V_u, \quad a \in V_a.$$

or, in shorthand notation,

$$I_{\mathrm{QS}} = \overline{f_0(y,a)}^{y} \to \max / \overline{\varphi(y,a)}^{y} = 0, \quad y \in V_y, \quad a \in V_a. \tag{81}$$

Here $y = (x,u)$, and the set V_y is determined by the conditions $u \in V_u, a \in V_a$, and $f(x,u,a) = 0$. Since any solution of Problem QS is admissible for Problem C, it follows that

$$I^*_{\mathrm{QS}} \leq I^*_{\mathrm{C}}. \tag{82}$$

At the same time, the value I^*_{QS} of Problem QS, being the value of an averaged problem, is given by the expression

$$I^*_{\mathrm{QS}} = \inf_{\xi} \left\{ \sup_{y} \left[f_0(y, a^*) + \xi \varphi(y, a^*) \right] \Big/ f(y, a^*) = 0, u \in V_u \right\}. \tag{83}$$

Here a^* is the optimal value of a subject to the constraint

$$\frac{\partial}{\partial a} \left[\overline{f_0(y,a)}^y + \left(\xi, \overline{\varphi(y,a)}^y \right) + \sum_{i=0}^{r} \lambda^i f\left(y^i, a\right) \right]_{a^*} \delta a \le 0. \tag{84}$$

in which δa is the set of variations allowed by the inclusion $a \in V_a$.

We choose the Lagrange multipliers λ^i in (84) so that $f(y^i, a) = 0$ for any base value y^i of the vector y. The number of base values of y is determined by the dimension r of the vector function φ; thus, the problem takes the form

$$\bar{f}_0 = \sum_{i=0}^{r} \gamma_i f_0\left(y^i, a\right), \quad \bar{\varphi} = \sum_{i=0}^{r} \gamma_i \varphi\left(y^i, a\right), \quad \sum_{i=0}^{r} \gamma_i = 1, \quad \gamma_i \ge 0. \tag{85}$$

Consider the case when the control vector in the steady state of the system changes with a frequency so high that the state vector x remains virtually constant. Such a mode is called a *sliding* steady mode. The optimization problem for such a mode is formulated as

$$I_{\mathrm{SL}} = \overline{f_0(b,u)}^u \to \sup / \overline{f(b,u)}^u = 0, \quad u \in V_u, \quad \overline{\varphi(b,u)}^u = 0, \quad b \in V_b. \tag{86}$$

This problem is known as Problem SL. In (86), b denotes the vector formed by x and a. This mode is the limit case of the cyclic mode, so we have

$$I^*_{\mathrm{SL}} \le I^*_{\mathrm{C}}.$$

Problem (86) is an averaged extension of Problem S with two types of variables; its value is given by

$$I^*_{\mathrm{SL}} = \min_{\lambda,\xi} \max_{u} R(u, b^*, \lambda, \xi) = \min_{\lambda,\xi} \max_{u \in V_u} \left[f_0(u, b^*) + \lambda f(u, b^*) + \xi \varphi(u, b^*) \right], \tag{87}$$

where b^* satisfies the condition

$$\frac{\partial}{\partial b} \overline{R(u, b^*, \lambda, \xi)}^u \delta b \le 0. \tag{88}$$

The number of base values of the vector function u in Problem SL is at most $m + r + 1$.

A necessary condition for the efficiency of the transition to a cyclic mode can be stated in terms of I^*_{QS} and I^*_{SL}. Consider the quantity

$$I_{\mathrm{K}} = \max \left[I^*_{\mathrm{QS}}, I^*_{\mathrm{SL}} \right].$$

If I_{K} is greater than I^*_{S}, then the passage to a cyclic mode is efficient, and the difference

$$\Delta_K = I_K - I^*_S$$

provides a lower bound for the efficiency.

5.2. The Frequency Criterion for the Efficiency of the Passage to a Cyclic Mode

Suppose that an optimal static mode x^0, u^0 in Problem S is known. As above, it is required to determine whether the cyclic extension of Problem S is efficient. In [14], a frequency criterion for the efficiency of a cyclic mode was proposed. This criterion is based on the analysis of the increment in the optimality criterion I as compared to its maximal static value I^0 for small harmonic oscillations of the control about u^0.

Let λ^0 and μ^0 be the values of Lagrange multipliers λ and μ corresponding to the optimal static mode in the Lagrangian function

$$R = f_0(x,u) + \sum_i \lambda_i f_i(x,u) + \sum_j \mu_j \varphi_j(x,u)$$

for Problem S.

In a neighborhood of the optimal static mode and the corresponding Lagrange multipliers, we calculate the first and second derivatives of the functions that determine the problem with respect to x and u (if x and u are vectors, then these derivatives are matrices):

$$A = \frac{\partial f}{\partial x}, \quad B = \frac{\partial f}{\partial u}, \quad P = \frac{\partial^2 R}{\partial x^2}, \quad Q = \frac{\partial^2 R}{\partial x \partial u}, \quad H = \frac{\partial^2 R}{\partial u^2}, \quad K = \frac{\partial \varphi}{\partial x}, \quad M = \frac{\partial \varphi}{\partial u}.$$

In a neighbourhood of the optimal static mode, the increment of the functional I under small variations $\delta x(t)$ and $\delta u(t)$ is given by

$$\Delta I = \frac{1}{2T} \int_0^T \left(\delta x' P \delta x + \delta x' Q \delta u + \delta u' Q' \delta x + \delta u' H \delta u \right) dt.$$

The transition to a cyclic mode is efficient if there is a variation δu such that the quantity ΔI is positive under the linearized constraints (63), i.e.,

$$\delta \dot{x} = A \delta x + B \delta u, \quad \delta x(T) = \delta x(0). \tag{89}$$

To get rid of these constraints, we consider only harmonic variations, i.e., those of the form

$$\delta u(t) = \sum_{\nu=-\infty}^{\infty} u_\nu e^{i\nu \frac{2\pi}{T} t}.$$

Applying the Fourier transform to the linear differential constraints (89), we obtain

$$\delta x(i\omega) = \delta u(i\omega) \frac{B}{i\omega E - A} = \delta u(i\omega) W(i\omega).$$

Here E is the identity matrix ($E = 1$ for scalar x). It is assumed that the matrix A has no eigenvalues with zero real part; otherwise, small deviations $\delta u(t)$ may correspond to large deviations $\delta x(t)$, and the linearization may be incorrect.

Let us express the quantity ΔI by Parseval's identity in the frequency domain, replacing $\delta x(i\omega)$ by its expression in terms of δu. The increment in the criterion under harmonic oscillations of the control with frequencies that are multiples of $2\pi/T$ takes the form

$$\Delta I = \frac{1}{2} \int_{-\infty}^{\infty} \delta u'(-i\omega) A(\omega) \delta u(i\omega) d\omega.$$

Here $A(\omega)$ is defined by the matrices P, Q, and H and the relation between δu and δx; it is easy to show that

$$A(\omega) = W'(-i\omega) P W(i\omega) + Q' W(i\omega) + W'(-i\omega) Q + H,$$

where the prime denotes transposition.

For the scalar problem, we have

$$A(\omega) = P|W(i\omega)|^2 + 2Q\,\mathrm{Re}\,W(i\omega) + H$$

If the matrix $A(\omega)$ for some ω is such that the integrand in the expression for ΔI is positive for at least one vector δu, then the static mode can be improved and the passage to a cyclic mode is efficient.

For the scalar problem, we have

$$\Delta I = \frac{1}{2}\int_{-\infty}^{\infty} |\delta u(i\omega)|^2 A(\omega) d\omega,$$

and the static mode improves if $A(\omega)$ is positive for some ω.

5.3. Lyapunov Problems

For an important class of problems, the inequality (77) turns into an equality. In these problems, the functions f_0, f, and φ in relations (63)–(66) depend only on u and a, so that

$$\dot{x} = f(u, a) \tag{90}$$

Such equations are called *Lyapunov-type equations*, and the corresponding problems are known as Lyapunov problems. If we discard equations (63), which have the form (90), in Problem C, thereby transitioning to Problem S, then we can find its solution $u^*(t)$, a^*. Substituting this solution into equation (90), we determine an optimal trajectory. Clearly, in this problem, $I_S^* = I_C^*$, $u^*(t)$ takes at most $m + r + 1$ base values, and the function $x^*(t)$ is a polygonal line with at most $m + r$ (internal) vertices.

Problems that include, in addition to Lyapunov-type equations, equations of the form

$$\dot{x}_\nu = f_\nu(u, a) F_\nu\,(x_\nu)$$

can also be reduced to Lyapunov problems. Indeed, such equations can be reduced to the form (90) by the change

$$y_\nu\,(x_\nu) = \int \frac{dx_\nu}{F_\nu\,(x_\nu)}, \tag{91}$$

so that $\dot{y}_\nu = f_\nu(u, a)$. The optimal solution $y_\nu(t)$ is piecewise linear, and $x_\nu(t)$ can be found from (91) by solving the equation

$$\frac{dx_\nu}{F_\nu\,(x_\nu)} = y_\nu(t) dt.$$

6. Average Optimization in Finite-Time Thermodynamics

The field of finite-time thermodynamics is one of the most important examples of application of averaged optimization techniques. The reasons for this are the following:

1. Problems of optimal thermodynamic cycles.

   There are a very important kind of thermodynamic systems — intermediary ones. These systems contact different subsystems (reservoirs) alternately while producing power and thus lowering the irreversibility arising from a continuous contact of the above-mentioned subsystems. The main example here is the heat engine, where the working fluid contacts two sources of different temperature.

   One of the most essential problems in finite-time thermodynamics is the problem of maximum average power of heat engines, when the average rate of the heat flow from the hot source is given.

Similar problems arise also in absorption-desorption systems, where the working fluid contacts with the multi-component mixture and picks one component out from one source, releasing it at another one.

In reverse cycles, the working fluid obtains the energy from the exterior system. Upon contact with the source that loses energy or matter in the regular cycle, the working fluid enriches it with the corresponding resource.

In all of these problems, the working fluid restores its state at the beginning of every cycle. One needs to average all of the variables determining the process.

2. Relations between intensive and extensive variables are Lyapunov-type equations. Thermodynamic variables are divided into two classes: intensive (temperature, pressure, chemical potential, ...) and extensive (volume, internal energy, entropy, amount of substance, ...) ones. Flow rates of transport processes between subsystems depend only on intensive variables. This value determines in turn the rate of change of extensive variables. This means that equations determining the change of state of the thermodynamic system have the form [10–12]:

$$\frac{dZ_j}{dt} = F_j(u_i, u_j). \tag{92}$$

Here i and j are indices of the contacting subsystems, u is the vector of intensive variables, Z is the vector of extensive variables. Equations of this type are called Lyapunov-type equations earlier in this paper. The right hand side of these equations does not depend on Z, and the increase of Z is determined by the average value of the function F. As we have shown above, one can obtain the limiting capabilities of systems characterized by Lyapunov-type equations using techniques of the averaged optimization.

7. Example: Averaged Optimization of a Heat Engine

7.1. Maximum Average Power Output

We will assume that there is a heat engine with constant temperature of sources T_+ and T_- [15]. If we denote the temperature of the source contacting with the working fluid at the moment as T_n and the temperature of the working fluid itself as T, we will obtain that the average output per cycle is

$$\overline{p} = \overline{q(T_n, T)}. \tag{93}$$

Now we can formulate the averaged optimization problem, given that the average entropy generation within the working fluid per cycle is zero:

$$\overline{q(T_n, T)} \to \max_T, \Big/ \begin{array}{l} \overline{\left(\frac{q(T_n,T)}{T}\right)} = 0, \\ T_n = (T_+; T_-), \quad T > 0. \end{array} \tag{94}$$

This is the problem in the form (6). Using the algorithm described earlier (see (42)–(44)) we find the number of base points is two. This means that the Lagrange function

$$R = q(T_n, T) + \lambda \frac{q(T_n, T)}{T} = q(T_n, T)\left(1 + \frac{\lambda}{T}\right) \tag{95}$$

has two maxima, so

$$\begin{aligned} T_1 &= \arg\max_T q(T_+, T)\left(1 + \tfrac{\lambda}{T}\right), \\ T_2 &= \arg\max_T q(T_-, T)\left(1 + \tfrac{\lambda}{T}\right). \end{aligned} \tag{96}$$

Both maxima are global and therefore they must be equal [16]. It means that the Lagrange multiplier is the solution of

$$q(T_+, T_1)\left(1+\frac{\lambda}{T_1}\right) = q(T_+, T_2)\left(1+\frac{\lambda}{T_2}\right). \tag{97}$$

When the heat transfer law is linear

$$q(T_+, T) = \alpha_+(T_+ - T), \quad q(T_-, T) = \alpha_-(T_- - T), \tag{98}$$

solution of equations (94)–(96) with notation $\alpha = \frac{\alpha_+\alpha_-}{\left(\sqrt{\alpha_+}+\sqrt{\alpha_-}\right)^2}$ leads to

$$p_{max} = \alpha\left(\sqrt{T_+} - \sqrt{T_-}\right)^2. \tag{99}$$

The relationship between entropy generation and heat flows is shown at Figure 3. It is clear from this picture that the point of maximum power output lies on the convex hull of original output curves, so it is attainable only when averaged control is used.

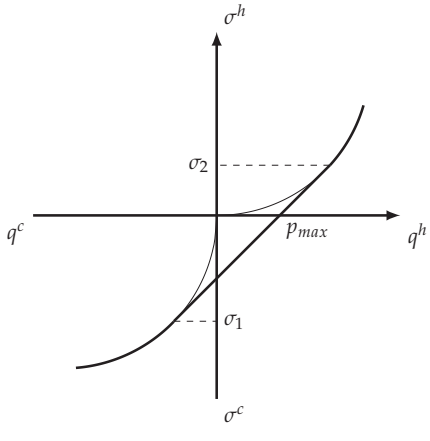

Figure 3. Relationship between entropy generation and heat flows and its convex hull. Here q^h and q^c are heat exchange rates upon contact with the hot and cold reservoirs, respectively, and σ^h, σ^c are the corresponding entropy generation rates. The optimal solution is attained when $\sigma^c = \sigma_1$, $\sigma^h = \sigma_2$, $q^1 = q^c(\sigma_1)$, $q^2 = q^h(\sigma^2)$ and $p_{max} = q^1 + q^2$.

7.2. Maximum Efficiency

When the power output p_0 is given, the problem of maximum efficiency is equivalent to the problem of minimum entropy generation within the system. Using again that the average entropy generation within the working fluid is zero for a cyclic process, we obtain the problem:

$$-\sigma = \overline{\left(\frac{q(T_n, T)}{T_n}\right)} \to \max_T \Big/ \begin{array}{l} \overline{q(T_n, T)} = p_0, \\ \overline{\left(\frac{q(T_n,T)}{T}\right)} = 0, \\ T_n = (T_+; T_-), \quad T > 0. \end{array} \tag{100}$$

One may notice that this problem allows three base points in general, because there are three averaging operations in (100). This is the case when the entropy generation as a function of $q(T_+, T)$ is not convex. We will not consider this case here, because this function is convex for most of heat transfer laws.

Another possibility corresponds to two base points. In this case, we have the following equations for T_1 and T_2:

$$\begin{aligned} T_1 &= \arg\max_T \left[q(T_+, T) \left(\tfrac{1}{T_+} + \lambda + \tfrac{\mu}{T} \right) - \lambda p_0 \right], \\ T_2 &= \arg\max_T \left[q(T_-, T) \left(\tfrac{1}{T_-} + \lambda + \tfrac{\mu}{T} \right) - \lambda p_0 \right]. \end{aligned} \tag{101}$$

These maxima must be equal, which leads to:

$$q(T_+, T) \left(\frac{1}{T_+} + \lambda + \frac{\mu}{T} \right) = q(T_-, T) \left(\frac{1}{T_-} + \lambda + \frac{\mu}{T} \right). \tag{102}$$

The averaged constraints must also be satisfied:

$$\begin{aligned} &\gamma q(T_+, T_1) + (1-\gamma) q(T_-, T_2) = p_0, \\ &\gamma \tfrac{q(T_+, T_1)}{T_1} + (1-\gamma) \tfrac{q(T_-, T_2)}{T_2} = 0. \end{aligned} \tag{103}$$

Equations (101)–(103) allow one to find values of T_1, T_2, λ, μ and γ.

For the linear heat transfer law we have the following value of maximum efficiency:

$$\eta_{max}(p) = \frac{1}{2} \left(\frac{p}{\alpha T_+} + \eta_c \right) \pm \sqrt{\frac{1}{4} \left(\frac{p}{\alpha T_+} + \eta_c \right)^2 - \frac{p}{\alpha T_+}}. \tag{104}$$

When $p \to 0$, the value of (104) approaches η_c (Carnot efficiency) and when $p = p_{max}$ (99), we have

$$\eta_{max}(p_{max}) = 1 - \sqrt{\frac{T_-}{T_+}} = 1 - \sqrt{1 - \eta_c}, \tag{105}$$

which is the well-known result of Novikov [17], Chambadal [18], Curzon and Ahlborn [19]. Important results for other types of heat transfer laws and different processes are presented in [20–22].

8. Results

We obtained the general necessary conditions of optimality for averaged optimization problems. These conditions can be written down using the algorithmic procedure given in the paper, which allows one to use them for problems of any structure. We showed how these techniques can be applied to the problems of finite-time thermodynamics leading to new results in the field.

Author Contributions: Conceptualization, A.T. and I.S.; methodology, A.T.; validation, I.S.; writing–original draft preparation, A.T.; writing–review and editing, I.S.; supervision, A.T. All authors have read and agreed to the published version of the manuscript.

Funding: This research received no external funding.

Conflicts of Interest: The authors declare no conflict of interest.

References

1. Tsirlin, A.M. Problems and methods of averaged optimization. *Proc. Steklov Inst. Math.* **2008**, *261*, 270–286. [CrossRef]
2. Kaplinski, A.M.; Propoi, A.I. Stochastic Approach to Nonlinear Programming Problems. *Automat. Remote Control* **1970**, *31*, 448–459.
3. Ioffe, A.; Tikhomirov, V. *Theory of Extremal Problems*; Elsevier North-Holland: New York, NY, USA, 1979; p. 459.
4. Rockafellar, R.T. *Convex Analysis*; Princeton University Press: Princeton, NJ, USA, 1996; p. 472.
5. Boltyanski, V.G; Martini, H.; Soltan, V. *Geometric Methods and Optimization Problems*; Springer: New York, NY, USA, 1999; p. 432.

6. Tsirlin, A. *Averaged Optimization Methods and Their Applications (Metody usrednjonnoj optimizatsii i ikh prilozhenija)*; Fizmatlit: Moscow, Russia, 1997. (In Russian)
7. Tsirlin A. *Optimal Cycles and Cyclic Modes (Optimal'nye tsikly i tsiklicheskie rezhimy)*; Energoatomizdat: Moscow, Russia, 1985. (In Russian)
8. Tsirlin, A.M. Conditions for Optimality of Solutions to Average Problems in Mathematical Programming. *Sov. Phys. Dokl.* **1992**, *37*, 117–119.
9. Tsirlin, A.M. The Optimal Conditions for Averaged Problems with Time-Dependent Parameters. *Dokl. Math.* **2000**, *62*, 297–299.
10. Rozonoer, L.I.; Tsirlin, A.M. Optimal Control of Thermodynamic Processes. I. *Automat. Remote Control* **1983**, *44*, 55–62.
11. Rozonoer, L.I.; Tsirlin, A.M. Optimal Control of Thermodynamic Processes. II. *Automat. Remote Control* **1983**, *44*, 209–220.
12. Rozonoer, L.I.; Tsirlin, A.M. Optimal Control of Thermodynamic Processes. III. *Automat. Remote Control* **1983**, *44*, 314–326.
13. Zevin, A.A. Optimal Control of Periodic Processes. *Automat. Remote Control* **1980**, *41*, 304–308.
14. Guardabassi, G.; Locatelli, A.; Rinaldi, S. Periodic Optimization of Continuous Systems. In Proceedings of the International Conference on Cybernetics and Society, Washington, DC, USA, 9–12 October 1972; pp. 261–263.
15. Tsirlin, A. *Minimum Dissipation Processes in Irreversible Thermodynamics (Protsessy minimalnoj dissipatsii v neobratimoj termodinamike)*; Lan: Saint-Petersburg, Russia, 2020; p. 400. (In Russian)
16. Tsirlin, A. *Optimization Methods in Irreversible Thermodynamics and Microeconomics (Metody optimizatsii v neobratimoj termodinamike i mikroekonomike)*; Fizmatlit: Moscow, Russia, 2003. (In Russian)
17. Novikov, I.I. The efficiency of atomic power stations (a review). *J. Nucl. Energy* **1958**, *7*, 125–128. [CrossRef]
18. Chambadal, P. *Atomic Power Stations (Les centrales nucleaires)*; Colin: Paris, France, 1957; p. 188. (In French)
19. Curzon, F.L.; Ahlborn, B. Efficiency of a Carnot engine at maximum power output. *Am. J. Phys.* **1975**, *43*, 22–24. [CrossRef]
20. Berry, R.; Kazakov, V.; Sieniutycz, S.; Szwast, Z.; Tsirlin, A. *Thermodynamic Optimization of Finite-Time Processes*; Wiley: Chichester, UK, 1999.
21. Boehme, B.; Sofieva, Y.N.; Tsirlin, A.M. On the characteristic of steady state for some types of dynamic plants. *Automat. Remote Control* **1979**, *40*, 5–11.
22. Kuznetsov, A.G.; Rudenko, A.V.; Tsirlin, A.M. Optimal control in thermodynamic systems with sources of finite capacity. *Automat. Remote Control* **1985**, *46*, 20–32.

entropy

MDPI

Article

Thermodynamic Curvature of the Binary van der Waals Fluid

George Ruppeiner [1,*] and Alex Seftas [2]

[1] Division of Natural Sciences, New College of Florida, 5800 Bay Shore Road, Sarasota, FL 34243, USA
[2] Department of Physics, Applied Physics, and Astronomy, Rensselaer Polytechnic Institute, 110 Eighth Street, Troy, NY 12180-3590, USA; seftaa@rpi.edu
* Correspondence: ruppeiner@ncf.edu

Received: 28 September 2020; Accepted: 22 October 2020; Published: 26 October 2020

Abstract: The thermodynamic Ricci curvature scalar R has been applied in a number of contexts, mostly for systems characterized by 2D thermodynamic geometries. Calculations of R in thermodynamic geometries of dimension three or greater have been very few, especially in the fluid regime. In this paper, we calculate R for two examples involving binary fluid mixtures: a binary mixture of a van der Waals (vdW) fluid with only repulsive interactions, and a binary vdW mixture with attractive interactions added. In both of these examples, we evaluate R for full 3D thermodynamic geometries. Our finding is that basic physical patterns found for R in the pure fluid are reproduced to a large extent for the binary fluid.

Keywords: information geometry of thermodynamics; thermodynamic curvature; critical phenomena; binary fluids; van der Waals equation

1. Introduction

The thermodynamic Ricci curvature scalar R has yielded a number of interesting results in the study of fluids [1]. However, to this point, the great majority of the calculations of R have been made for pure fluids. Much less examined has been R for binary fluids. Pure fluids offer many research topics in a relatively simple thermodynamic geometric scenario. One element of this simplicity is that pure fluids may be represented by a two-dimensional (2D) thermodynamic Riemannian geometry, where just the scalar R gives the full curvature picture.

The dimension of the thermodynamic phase space grows by one for each added fluid component, and, as the dimension grows, the curvature rapidly becomes more complicated. For example, the binary fluid corresponds to a three-dimensional (3D) phase space, where there are six independent components of the full Riemannian curvature tensor [2]. Which of these components do we focus on for physical interpretation? In this paper, our results suggest that the curvature scalar R remains the fundamental physical quantity. (We offer no rigorous proof, but we do note that classical general relativity, based on four-dimensional Riemannian geometry, may be expressed as a variational principle based on the Hilbert action, with R as the Lagrangian [2]. This variational principle is certainly not in play in this paper, but we do hope that this significance for R translates to the thermodynamic scenario as well).

We calculate R for two thermodynamic examples represented by a 3D thermodynamic geometry: (1) a binary van der Waals (vdW) fluid with just repulsive interactions, and (2) a binary vdW fluid with attractive interactions added. To add conceptual structure to our presentation, we discuss to what extent the 3D results for R follow the same physical principles as the 2D ones. As we show, there is a great deal of correspondence. (Scenarios with a thermodynamic geometric dimension greater than two have also been considered for black hole thermodynamics; see Sahay for a brief review [3]. This theme is beyond the scope of this paper.)

A few cases have been worked out for R for the full 3D thermodynamic geometry. Ruppeiner and Davis [4] worked out R for the multicomponent ideal gas, with an arbitrary number of components. Kaviani and Dalafi-Rezaie [5] worked out R for the paramagnetic ideal gas, where, in addition to the temperature and the density, there is an external organizing magnetic field. Erdem [6] worked out R for the antiferromagnetic Ising model with a temperature and two ordering fields, with special attention to the critical phenomena near the Neel point.

One may also approach 3D thermodynamic geometries by working out R over 2D slices of the full 3D thermodynamic geometry. This has physical relevance if, for example, one of the independent variables is irrelevant to a phase transition. Ginoza [7] considered the binary fluid mixture in generality, and calculated R 2D along surfaces of constant T. Jaramillo-Gutiérrez et al. [8] calculated a constrained R 2D by fixing the sum of the mole numbers. These authors made several comments about how their constrained R relates to that of the pure fluid. Generally, the calculation is simplified in 2D, but, in an age of powerful mathematics software, considerations of simplicity should maybe no longer be so much of a driving force.

2. Expectations for 3D Outcomes for R

For guidance as to what 3D thermodynamic geometry might tell us, let us pose some questions motivated by findings in the pure fluid [9–12]: (a) In the ideal gas limit, is $|R|$ either zero or small? "Small" means $|R|\rho < 1$, with ρ the number density. In this event, the volume measured by $|R|$ is less than the average volume occupied by a single particle, and we are under the low $|R|$ limit [10,11]. Thermodynamics is challenged at such a size scale, and a precise physical interpretation for R is harder to come by (though researchers do try if the opportunity arises). (b) As a critical point is approached, does $|R|$ diverge in proportion to the correlation volume ξ^3? (c) Near a critical point, is the sign of R negative? A negative sign is consistent with effectively attractive interactions. (d) Are the values of R in two coexisting phases equal to each other near a critical point? (e) Are there interesting regimes of positive R? A positive sign is consistent with effectively repulsive interactions. (f) Does the binary repulsive fluid have instances of anomalous negative R, such as is present for the hard-sphere pure fluid [13]?

We find considerable physical correspondence between R for the pure fluid and for the binary fluid.

3. Thermodynamic Geometry of a Binary Fluid

For a binary fluid, the Helmholtz free energy per volume may be written in terms of its appropriate coordinates [4,14],

$$f = f(T, \rho_1, \rho_2), \tag{1}$$

where T is the temperature, and $\rho_1 = n_1/V$ and $\rho_2 = n_2/V$ are the molar densities of the two components 1 and 2. Here, n_1 and n_2 are the mole numbers of the components, and V is the volume.

The thermodynamic entropy metric originates from the thermodynamic fluctuation theory [1,15]. Consider a finite open subsystem $\mathcal{A}_V$, with fixed volume V, of an infinite closed thermodynamic fluid system $\mathcal{A}$; see Figure 1. The thermodynamic state (T, ρ_1, ρ_2) of $\mathcal{A}_V$, fluctuates in time about the state of $\mathcal{A}$. The Gaussian fluctuation probability density is proportional to

$$\exp\left[-\frac{V}{2}(\Delta\ell)^2\right], \tag{2}$$

where the entropy metric is [1]

$$(\Delta\ell)^2 = \frac{1}{k_B T}\left(\frac{\partial s}{\partial T}\right)(\Delta T)^2 + \frac{1}{k_B T}\sum_{i,j=1}^{2}\left(\frac{\partial \mu_i}{\partial \rho_j}\right)\Delta\rho_i \Delta\rho_j. \tag{3}$$

Here, the entropy per volume of $\mathcal{A}_V$ is

$$s = -\frac{\partial f}{\partial T}, \tag{4}$$

and the chemical potentials of the two fluid components are

$$\mu_i = \frac{\partial f}{\partial \rho_i}. \tag{5}$$

ΔT, $\Delta\rho_1$, and $\Delta\rho_2$ are the differences in the temperature and density coordinates of $\mathcal{A}_V$ and $\mathcal{A}$. In addition, k_B is Boltzmann's constant. The thermodynamic metric is employed here in fluctuation theory. It has also been used in finite time thermodynamics [16] as a measure of dissipation.

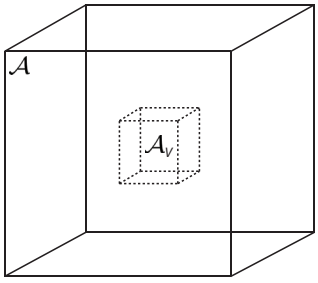

Figure 1. A standard structure in thermodynamic fluctuation theory, a single open subsystem $\mathcal{A}_V$, with fixed volume V, of an infinite closed environment $\mathcal{A}$.

Let us emphasize a point not always appreciated in the metric geometry of thermodynamic fluctuations. A major project in this geometry is to calculate the thermodynamic curvature R. We want R to tell us something about the intrinsic properties of the material comprising the system $\mathcal{A}$. This goal naturally requires the use of an open subsystem $\mathcal{A}_V$, so as to leave particles free to move in or out of $\mathcal{A}_V$, unimpeded by any surrounding artificial wall or membrane. Such a physical constraint would change the value of R in a way involving more than just the properties of the particles; this should be avoided. As emphasized by Callen [14], fluid thermodynamics requires us to set one of the thermodynamic variables aside as the fixed subsystem scale. For an open system, this scale is the volume V. We recommend that authors always work with open subsystems for calculating R.

In the coordinates (T, ρ_1, ρ_2), the metric tensor $\mathbf{g}$ is composed of five nonzero elements, which can be read off from Equation (3):

$$\mathbf{g} = \frac{1}{k_B T} \begin{pmatrix} -\frac{\partial^2 f}{\partial T^2} & 0 & 0 \\ 0 & \frac{\partial^2 f}{\partial \rho_1^2} & \frac{\partial^2 f}{\partial \rho_1 \partial \rho_2} \\ 0 & \frac{\partial^2 f}{\partial \rho_2 \partial \rho_1} & \frac{\partial^2 f}{\partial \rho_2^2} \end{pmatrix}. \tag{6}$$

The fourth-rank curvature tensor has elements [2]

$$R^{\alpha}_{\beta\gamma\delta} = \Gamma^{\alpha}_{\beta\gamma,\delta} - \Gamma^{\alpha}_{\beta\delta,\gamma} + \Gamma^{\mu}_{\beta\gamma}\Gamma^{\alpha}_{\delta\mu} - \Gamma^{\mu}_{\beta\delta}\Gamma^{\alpha}_{\gamma\mu}, \tag{7}$$

where the Greek indices range from $1, 2, 3$, and denote the coordinates (T, ρ_1, ρ_2), respectively. The Christoffel symbols are defined as

$$\Gamma^{\alpha}_{\beta\gamma} = \frac{1}{2} g^{\alpha\mu}(g_{\mu\gamma,\beta} + g_{\mu\beta,\gamma} - g_{\beta\gamma,\mu}), \tag{8}$$

where $g^{\alpha\beta}$ denotes the elements of the inverse of the metric $\mathbf{g}$ with elements $g_{\alpha\beta}$. We use the comma notation (e.g., $,\beta$) to denote the partial derivative with respect to some specific coordinate. Repeated indices are summed over. The second-rank Ricci tensor is given by

$$R_{\alpha\beta} = R^{\mu}_{\alpha\mu\beta}, \tag{9}$$

and the Ricci curvature scalar is

$$R = g^{\mu\nu} R_{\mu\nu}. \tag{10}$$

It is straightforward to show that R has units of volume per particle for the binary fluid, the same units as for the pure fluid. These units alone label R as a measure of some sort of size scale within the system. The definition of the Riemannian curvature tensor is ambiguous with respect to a sign, and we use the sign convention of Weinberg [17], where the two spheres have negative R.

4. Thermodynamic Stability

Fluctuations must satisfy thermodynamic stability, requiring maximum entropy of $\mathcal{A}$ in equilibrium. This is obtained if the line element in Equation (3) is positive definite for all fluctuations. A necessary and sufficient condition for thermodynamic stability is that the metric coefficients in Equation (6) satisfy the three following conditions [1,18]:

$$g_{11} > 0, \tag{11}$$

$$\begin{vmatrix} g_{11} & g_{12} \\ g_{21} & g_{22} \end{vmatrix} > 0, \tag{12}$$

and

$$\begin{vmatrix} g_{11} & g_{12} & g_{13} \\ g_{21} & g_{22} & g_{23} \\ g_{31} & g_{32} & g_{33} \end{vmatrix} > 0. \tag{13}$$

We tested frequently for stability.

5. Helmholtz Free Energy for Binary van der Waals

We take the Helmholtz free energy per mole for binary vdW from Konynenburg and Scott [19]:

$$\begin{aligned} A_m = e(T) - \mathcal{R}\,T \log\left(\frac{V_m - b}{V_{m0}}\right) \\ + \mathcal{R}\,T\,[(1-x)\log(1-x) + x\log(x)] - \frac{a}{V_m}, \end{aligned} \tag{14}$$

where

$$e(T) = -\frac{3}{2}\,\mathcal{R}\,T \ln\left(\frac{T}{T_0}\right) + \epsilon \tag{15}$$

is the purely thermal part of the ideal gas contribution, $\mathcal{R}$ is the universal gas constant, $V_m = V/(n_1 + n_2)$ is the molar volume, V_{m0}, T_0, and ϵ are constants that do not appear in R, and x is the concentration

$$x = \frac{n_2}{n_1 + n_2}. \tag{16}$$

The quantities a and b are functions of x reflecting the purely attractive and repulsive parts of the interparticle interactions, respectively:

$$a(x) = (1-x)^2 a_{11} + 2x(1-x)\,a_{12} + x^2 a_{22}, \tag{17}$$

and

$$b(x) = (1-x)\, b_{11} + x\, b_{22}, \tag{18}$$

with a_{11}, a_{12}, a_{22}, b_{11}, and b_{22} as the five independent vdW coefficients.

The full (extensive) Helmholtz free energy is

$$A(T, n_1, n_2, V) = (n_1 + n_2) A_m, \tag{19}$$

and the Helmholtz free energy per volume is

$$f(T, \rho_1, \rho_2) = \frac{A(T, n_1, n_2, V)}{V}. \tag{20}$$

For the pure fluid, vdW simplifies by using scaled units [15]. For binary vdW, scaling cannot be done in a natural way. One possibility is to scale in terms of the van der Waals coefficients of one of the fluid components [19], but this seems somewhat artificial. In this paper, we avoid scaled units, and simply adopt real units when needed.

6. Repulsive Binary van der Waals

First consider the case with only repulsive interactions, with zero a coefficients, $b_{11} = b_1$, and $b_{22} = b_2$. By Equation (20), we have

$$\begin{aligned} f(T, \rho_1, \rho_2) = &-k_B T(\rho_1 + \rho_2) \log\left[\frac{1 - b_1\rho_1 - b_2\rho_2}{V_{m0}}\right] + k_B T \rho_1 \log(\rho_1) \\ &+ k_B T \rho_2 \log(\rho_2) - \frac{3}{2} k_B T(\rho_1 + \rho_2) \log\left(\frac{T}{T_0}\right) + \epsilon(\rho_1 + \rho_2), \end{aligned} \tag{21}$$

where we send $\mathcal{R} \to k_B$ to convert ρ_1 and ρ_2 to units of particles per volume.

By using Equation (21), and the process described in Section 3, we find:

$$\begin{aligned} R = \frac{1}{2(\rho_1 + \rho_2)} \Big[&1 - 2b_2\rho_1 - 2b_1\rho_2 - 4b_1\rho_1 - 4b_2\rho_2 + 5b_1^2\rho_1\rho_2 \\ &+ 5b_2^2\rho_1\rho_2 + 5b_1^2\rho_1^2 + 5b_2^2\rho_2^2 \Big]. \end{aligned} \tag{22}$$

Note, R for repulsive vdW has no dependence on T, nor does it depend on the constants in Equation (21), other than the b's.

Since R has units of volume per particle, $R \times (\rho_1 + \rho_2)$ is dimensionless. Setting $b_1 = b_2 = b$ yields

$$R \times (\rho_1 + \rho_2) = \frac{1}{2} [1 - b(\rho_1 + \rho_2)] [1 - 5b(\rho_1 + \rho_2)]. \tag{23}$$

If $b \to 0$, this expression agrees with Ruppeiner and Davis [4] for the binary ideal gas with the thermal contribution in Equation (15). $R \times (\rho_1 + \rho_2)$ is shown as a contour graph in Figure 2.

With only the b coefficients nonzero, we would naively expect $R > 0$, consistent with repulsive interactions. Cases with $R < 0$ clearly occur, mirroring the situation in the pure fluid where, for example, the gas of hard-spheres has negative R [13]. Such anomalous results might be dismissed as aberrations since we are below the low $|R|$ limit. However, it is interesting that the negative sign persists from the pure fluid into the binary fluid. This consistency contributes to the need for a more nuanced interpretation for the sign of R.

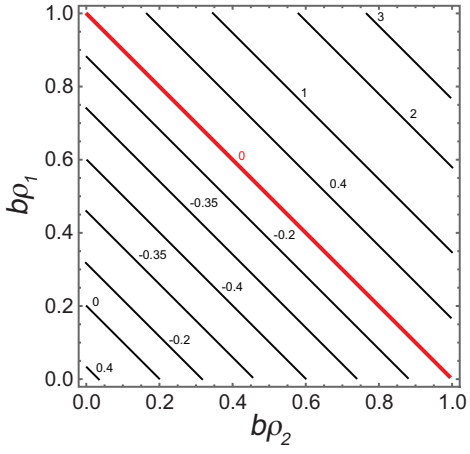

Figure 2. The contour graph of $R \times (\rho_1 + \rho_2)$. On approaching the bold red line from below, the pressure $P \to +\infty$. Above the line P is negative. The physical regime is below the line, where R has both positive and negative values, with a minimum of $R \times (\rho_1 + \rho_2) = -0.4$. In the physical regime, values of $R \times (\rho_1 + \rho_2)$ are all less than the low $|R|$ limit. The value at the origin is $1/2$.

7. Attractive Binary van der Waals

Now turn on the attractive interactions in binary vdW. In this scenario, Konynenburg and Scott [19] classified nine distinct possibilities, depending on the values of the vdW a and b coefficients. We consider here only an instance of their Type I possibility, with a single curve of critical points continuously connecting the critical points of the pure fluid components $x = 0$ and $x = 1$. Our example has vdW coefficients $a_{11} = 0.002$, $a_{22} = 0.005$, $a_{12} = 0.004$, and $b_{11} = b_{22} = 0.00002$. (In MKS units, the units of the a's are Joules meters^3/mole^2, and the units of the b's are meters^3/mole. These vdW coefficients produce critical points very roughly in the zone of normal fluid Helium.)

To structure the discussion, note that if T is high, the attraction between the particles has little effect, and we expect no phase transitions. Now consider lowering T slowly, with the particle numbers and the volume held fixed. We might move along such an isochore in a laboratory PVT experiment; see Figure 3. As T decreases, attractive interatomic interactions become more effective, and the binary fluid could eventually break into two phases.

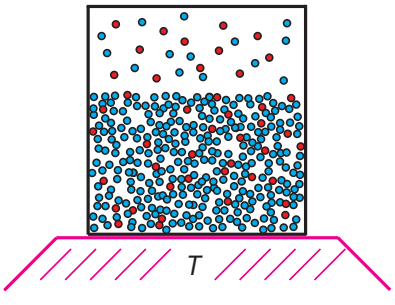

Figure 3. The binary fluid inside a closed container fixing the number of particles and the volume. As the temperature is lowered, the kinetic energy decreases, and the fluid generally breaks into two phases at some temperature. The phases have different x's.

These phase transitions have associated second-order curves of critical points [19]. For Type 1, every x has a single critical point with critical coordinates $T = T_c$, $P = P_c$, and $V_m = V_{mc}$. In their

Appendix A, Konynenburg and Scott [19] describe an explicit procedure $x \rightarrow (T_c, P_c, V_{mc})$ for locating these critical points.

The critical curve is shown in Figure 4. The $\det(\mathbf{g})$ switches signs upon crossing this critical curve, with the thermodynamics stable above the curve and unstable below it, according to Equations (11)–(13). R diverges to negative infinity on the critical curve.

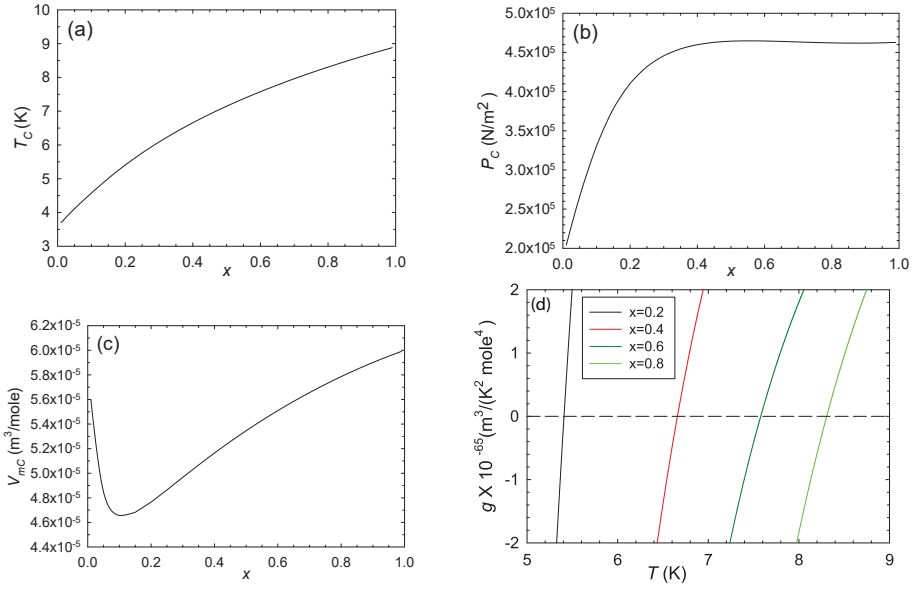

Figure 4. The critical parameters (T_c, P_c, V_{mc}) as functions of x (**a**–**c**). On crossing the critical curve, $\det(\mathbf{g})$ switches sign, as shown in (d), with $g = \det(\mathbf{g})$ calculated along critical isochores (x, T, V_{mc}). The thermodynamics is thus stable above the critical curve and unstable below it. R diverges to negative infinity on the critical curve.

The theoretical expectations on approaching the critical curve are well-known. A general physical argument was given by Widom [20] in the context of the hyperscaling critical exponent relation

$$d\,\nu = 2 - \alpha, \tag{24}$$

where d is the spatial dimension ($d = 3$ here), α is the heat capacity critical exponent ($\alpha = 0$ here), and ν is the correlation length critical exponent. On approaching the critical curve from above along a critical isochore with fixed x, fixed $V_m = V_{mc}$, and decreasing T, the correlation length is expected to diverge according to:

$$\xi^d \propto \left(\frac{T - T_c}{T_c}\right)^{\alpha - 2}. \tag{25}$$

A key finding in previous research is that $|R| \propto \xi^d$ near a critical point [1,21–23], (The constant of proportionality between R and ξ^3 calculated for both fluid and magnetic systems in distinct spatial dimensions appears to be $-1/2$: $-\frac{1}{2}R = \xi^d$; see [23] for a brief review.) and so we expect

$$|R| \propto \left(\frac{T - T_c}{T_c}\right)^{-2} \tag{26}$$

along a critical isochore.

An interesting contrast to binary vdW is offered by pure fluid vdW, where R is computed with 2D thermodynamic geometry. It was shown [1] that the asymptotic divergence of R for the pure vdW fluid, with the thermal ideal gas contribution as in Equation (15), along the critical isochore is

$$R = -b\left(\frac{T - T_c}{T_c}\right)^{-2}, \tag{27}$$

independent of the vdW constant a. Here, $b = b_{11}$ if $x = 0$ and $b = b_{22}$ if $x = 1$.

Physically, ξ^3 should be the same for a binary fluid in the limits $x \to 0$ or $x \to 1$ as for the corresponding pure fluids. Since R in the critical region is a measure of ξ^3, we might then physically expect the limiting R 3D's to be at least approximately equal to the corresponding R 2D's. Remarkably, this limiting correspondence holds very well, even though the 2D and 3D formulas for R are quite different.

We computed R along four critical isochores in 3D thermodynamic geometry, $x = 0.2, 0.4, 0.6$, and 0.8. Results near the critical point are shown in Figure 5. The four curves clearly overlap each other very closely, and show very little dependence on x. The asymptotic R is always negative, in accordance with expectations for effectively attractive interactions. The critical curves have asymptotic power law divergences, in accordance with Equation (26). The critical exponents of the four curves are all within better than 0.3% of the expected value 2, with the power law fits done over the full range of the data shown in Figure 5. Erdem [6] got similar 3D power law behavior in the Ising antiferromagnet. Note as well that the smallest values of $|R|$ in Figure 5 are about 4 nm^3/atom, so values near the particle level are on the asymptotic power law line. Such a large span of the critical regime was seen also in magnetic systems [23].

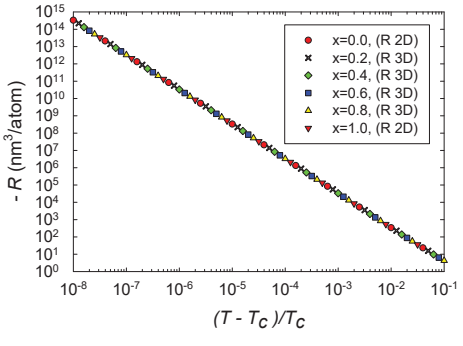

Figure 5. $-R$ computed with the R 3D formula versus the reduced temperature for four critical isochores in the critical region. Points all fall nearly on the same straight line with slope -2. The values of R are all negative. Additionally shown is $-R$ computed with the R 2D formula for the two pure fluids $x = 0$ and 1 along the critical isochores. Somewhat remarkably, these points also fall on the common line.

Additionally shown in Figure 5 is $-R$ for the pure fluids $x = 0$ and 1 calculated with the 2D thermodynamic geometry. Asymptotically, we expect these curves to obey Equation (27), and we found that they do. The R 2D curves are in excellent agreement with the corresponding R 3D curves.

Next, we consider letting the binary fluid expand into the binary ideal gas state, which has the dimensionless quantity [4]

$$R \times (\rho_1 + \rho_2) = \frac{1}{2}. \tag{28}$$

We approached the binary ideal gas limit for four fixed values of x by starting at (T_c, V_{mc}) for each x, and increasing V_m at constant $T = T_c$. Results of this expansion are shown in Figure 6. Clearly, for each x, $R \times (\rho_1 + \rho_2) \to 1/2$, in accord with Equation (28).

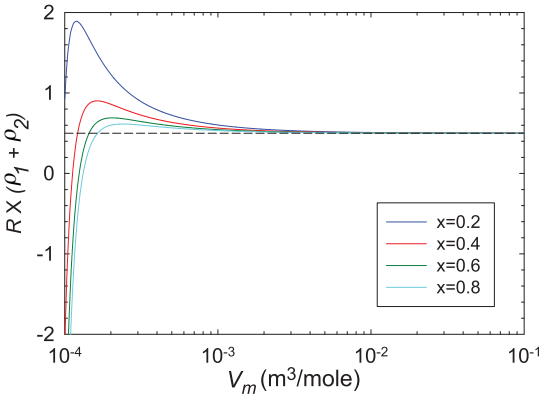

Figure 6. The approach to the ideal gas limit. For each fixed x, we proceed at constant $T = T_c$ by increasing V_m, starting from V_{mc}. This leads to the ideal gas where we expect $R \times (\rho_1 + \rho_2) = 1/2$.

8. Conclusions

We have made a start in calculating the full three-dimensional thermodynamic Ricci curvature scalar R in an interacting binary fluid system. Our main finding is that the physical interpretation of R for the pure fluid extends very naturally to the binary fluid. The emerging physical picture for the thermodynamic R is thus quite robust. We calculated R for two scenarios involving the van der Waals model for the binary fluid. The first had exclusively repulsive interactions, and the second added attractive interactions, and critical phenomena.

Let us place our results in the context of the expectations in Section 2. (a) In the binary ideal gas limit, we expect $R \times (\rho_1 + \rho_2) = 1/2$ from an earlier exact calculation. Figure 6 clearly shows this known limit. This limit is also shown at the origin of Figure 2. Both these figures (in the ideal gas limit) have $|R|$ smaller than the low $|R|$ limit, and so the results here are not as strong as those in the critical regime, where $|R|$ is much larger. (b) Near critical points, $|R|$ was found to diverge with the expected critical exponent of 2, as shown in Figure 5. In the limits as the binary fluid goes to the pure fluid, we found excellent concordance with the pure fluid results calculated with the 2D thermodynamic geometry. These critical point results are the strongest that we present in this paper. (c) Near critical points, R was found to be negative, as shown in Figure 5. This negative sign is expected when interactions are effectively attractive. (d) Evaluating R along coexistence curves was beyond the scope of our paper. (e) Our regimes of positive R were all more or less expected, with values all under the low $|R|$ limit. A more systematic search of the thermodynamic phase space for more interesting cases (above the low $|R|$ limit) was beyond the scope of our paper. (f) We found that the repulsive vdW was negative at large densities, in accord with the anomaly found by Brańka et al., for the hard sphere [13]; see Figure 2. That this anomaly translates from the 2D to the 3D thermodynamic geometry is interesting.

Author Contributions: Formal analysis, G.R. and A.S.; Project administration, G.R.; Writing—original draft, G.R. and A.S.; Writing—review & editing, G.R. and A.S. All authors have read and agreed to the published version of the manuscript.

Funding: This research received no external funding.

Conflicts of Interest: The authors declare no conflict of interest.

References

1. Ruppeiner, G. Riemannian geometry in thermodynamic fluctuation theory. *Rev. Mod. Phys.* **1995**, *67*, 605; Erratum in **1996**, *68*, 313. [CrossRef]
2. Carroll, S.M. *Spacetime and Geometry*; Addison Wesley: San Franciso, CA, USA, 2004.
3. Sahay, A. Restricted thermodynamic fluctuations and the Ruppeiner geometry of black holes. *Phys. Rev. D* **2017**, *95*, 064002. [CrossRef]
4. Ruppeiner, G.; Davis, C. Thermodynamic curvature of the multicomponent ideal gas. *Phys. Rev. A* **1990**, *41*, 2200. [CrossRef] [PubMed]
5. Kaviani, K.; Dalafi-Rezaie, A. Pauli paramagnetic gas in the framework of Riemannian geometry. *Phys. Rev. E* **1999**, *60*, 3520. [CrossRef] [PubMed]
6. Erdem, R. Antiferromagnetic Ising model in the framework of Riemannian geometry. *Acta Phys. Pol. B* **2018**, *49*, 1823. [CrossRef]
7. Ginoza, M. Riemannian geometry of equilibrium thermodynamics in a liquid mixture. *Rep. Math. Phys.* **1993**, *32*, 167. [CrossRef]
8. Jaramillo-Gutiérrez, J.; López-Picón, J.L.; Torres-Arenas, J. Thermodynamic geometry for binary mixtures: A constrained approach. *J. Mol. Liq.* **2020**, *319*, 114213. [CrossRef]
9. Ruppeiner, G. Thermodynamic curvature measures interactions. *Am. J. Phys.* **2010**, *78*, 1170. [CrossRef]
10. Ruppeiner, G.; Sahay, A.; Sarkar, T.; Sengupta, G. Thermodynamic geometry, phase transitions, and the Widom line. *Phys. Rev. E* **2012**, *86*, 052103. [CrossRef]
11. Ruppeiner, G. Thermodynamic curvature from the critical point to the triple point. *Phys. Rev. E* **2012**, *86*, 021130. [CrossRef] [PubMed]
12. May, H.-O.; Mausbach, P.; Ruppeiner, G. Thermodynamic curvature for attractive and repulsive intermolecular forces. *Phys. Rev. E* **2013**, *88*, 032123. [CrossRef] [PubMed]
13. Brańka, A.C.; Pieprzyk, S.; Heyes, D.M. Thermodynamic curvature of soft-sphere fluids and solids. *Phys. Rev. E* **2018**, *97*, 022119. [CrossRef] [PubMed]
14. Callen, H.B. *Thermodynamics and an Introduction to Thermostatistics*; John Wiley & Sons: New York, NY, USA, 1985.
15. Landau, L.D.; Lifshitz, E.M. *Statistical Physics*; Elsevier: New York, NY, USA, 1980.
16. Andresen, B.; Salamon, P.; Berry, R.S. Thermodynamics in finite time. *Phys. Today* **1984**, *37*, 62. [CrossRef]
17. Weinberg, S. *Gravitation and Cosmology*; Wiley: New York, NY, USA, 1972.
18. Eves, H. *Elementary Matrix Theory*; Dover: New York, NY, USA, 1966.
19. van Konynenburg, P.; Scott, R. Critical lines and phase equilibria in binary van der Waals mixtures. *Philos. Trans. Math. Phys. Sci.* **1980**, *298*, 495.
20. Widom, B. The critical point and scaling theory. *Physica* **1974**, *73*, 107. [CrossRef]
21. Ruppeiner, G. Thermodynamics: A Riemannian geometric model. *Phys. Rev. A* **1979**, *20*, 1608. [CrossRef]
22. Johnston, D.A.; Janke, W.; Kenna, R. Information geometry, one, two, three (and four). *Acta Phys. Pol. B* **2003**, *34*, 4923.
23. Ruppeiner, G.; Bellucci, S. Thermodynamic curvature for a two-parameter spin model with frustration. *Phys. Rev. E* **2015**, *91*, 012116. [CrossRef] [PubMed]

entropy

MDPI

Article

Thermoelectric Efficiency of Silicon–Germanium Alloys in Finite-Time Thermodynamics

Patrizia Rogolino [1] and Vito Antonio Cimmelli [2,*]

[1] Department of Mathematical and Computer Sciences, Physical Sciences and Earth Sciences, University of Messina, Viale F. Stagno d'Alcontres, 31, 98166 Messina, Italy; progolino@unime.it
[2] Department of Mathematics, Computer Science and Economics, University of Basilicata, Viale dell'Ateneo Lucano, 10, 85100 Potenza, Italy
* Correspondence: vito.cimmelli@unibas.it; Tel.: +39-0971205885

Received: 30 July 2020; Accepted: 29 September 2020; Published: 2 October 2020

Abstract: We analyze the efficiency in terms of a thermoelectric system of a one-dimensional Silicon–Germanium alloy. The dependency of thermal conductivity on the stoichiometry is pointed out, and the best fit of the experimental data is determined by a nonlinear regression method (NLRM). The thermoelectric efficiency of that system as function of the composition and of the effective temperature gradient is calculated as well. For three different temperatures ($T = 300$ K, $T = 400$ K, $T = 500$ K), we determine the values of composition and thermal conductivity corresponding to the optimal thermoelectric energy conversion. The relationship of our approach with Finite-Time Thermodynamics is pointed out.

Keywords: finite-time thermodynamics; Silicon–Germanium alloys; minimum of thermal conductivity; efficiency of thermoelectric systems; minimal energy dissipation

1. Introduction

In recent years, Silicon–Germanium $(SiGe)$ alloys have become very important in technology, since some of their properties such as, for example, their efficiency in energy conversion, may be improved by adjusting their stoichiometry. Indeed, alloys of the type Si_cGe_{1-c}, where $c \in [0,1]$ is a stoichiometric parameter which varies along a direction z in the system, are widely used in energy production and management [1–6]. The thermoelectric efficiency is defined as $\eta_{el} = \frac{P_{\rm el}}{\dot{Q}_{\rm tot}}$, with $P_{\rm el}$ the obtained electric power and $\dot{Q}_{\rm tot}$ the heat per unitary time entering the system, [7–9]. It can be proven that η_{el} is an increasing function of the material function ZT, where T is the absolute temperature while the figure-of-merit Z is given by $Z = \frac{\epsilon^2 \sigma_e}{\lambda}$, where ϵ is the Seebeck coefficient, σ_e the electrical conductivity, and λ is the thermal conductivity of the material [9]. Then in the literature one can find several methods to enhance Z [10–12]. One of the most successful strategies is the use of nonlinear nanomaterials [13–15], namely nanomaterials in which some nonlinear transport equations hold. Indeed, for those materials an external control of the flux of heat carriers is possible, leading to a reduction of the thermal conductivity, and hence to an increment of Z [16–19]. The efficiency of a homogeneous thermoelectric system has been calculated in [20,21], wherein some strategies to enhance its performance have been pointed out. The thermoelectric efficiency of a nanosystem of variable composition has been studied in several papers by the present authors [22–24]. In particular, in [23], we have obtained the analytical representation of the thermal conductivity of a nanowire as function of its composition c, as the sum of two exponentials, each depending on 3 parameters, whose value was determined by the experimental data through NLRM.

On the other hand, in several cases the constituents of thermoelectric energy generators can have macroscopic dimension, so that the thermoelectric efficiency of graded systems at macroscale needs to

be investigated as well. In such a framework, the possibility of application of the nonlinear model used in [22–24] needs to be tested, since at macroscopic scale nonlinear effects are less evident. Thus, in this paper we explore the possible extension of the model at macroscopic scale, by considering a $SiGe$ graded wire, of length $L = 3$ mm. We investigate the dependence of its performance as thermoelectric energy generator as function of the composition and of the effective temperature gradient applied to its boundaries, and determine the conditions under which such an efficiency is maximum. Our conclusion will be that the model still leads to previsions which are physically sound and acceptable for the system at hand, although they differ from those obtained in [23].

Moreover, as additional result of the present research, going a step further with respect to [23], we also improve the constitutive equation of the thermal conductivity, which now depends by only 4 parameters instead of the 6 parameters used in [23]. Such an improvement is not easy, as it could appear at a first look, because a reduction of the number of free parameters in general increases the numerical error which affects the fit, and the new fit can be used in the applications only if the error on it is kept at an acceptable level. In Section 2 we discuss this problem and show that our fit reproduces accurately the experimental data.

Then, we calculate the heat conductivity at $T = 300$ K, $T = 400$ K, and $T = 500$ K, corresponding to the experimental data at our disposal, and prove that for each temperature there is only one value of c in the interval $[0, 1]$ which minimizes the local rate of entropy production, i.e., which corresponds to the optimal efficiency of the thermoelectric energy production.

The article has the following structure.

In Section 2, we apply a NLRM to obtain the best fit of the curve which represents the thermal conductivity of a wire of length $L = 3$ mm as function of its composition c.

In Section 3, we first give a sketch of the nonlinear model we are facing with, and calculate the form of the local rate of entropy produced along the thermoelectric process. Then, under the assumption that the optimal efficiency is achieved in correspondence of a minimum of the local rate of entropy produced, we determine the theoretical expressions of c which minimize such a rate.

In Section 4, we calculate the effective values of c given by the theoretical expressions found in Section 3 and discuss this result taking into account the characteristic properties of nanosystems.

Finally, in Section 5, we interpret the present approach within the frame of Finite-Time Thermodynamics [25–27]. In particular, we show that our assumption of minimum entropy production can be considered a consequence of a global variational principle which is suitable for application in Finite-Time Thermodynamics.

2. Constitutive Equation of Thermal Conductivity

In this section, by using MATHLAB (http://www.mathlab.mtu.edu/mediawiki/index.php/Main_Page), we apply a NLRM [28,29] to determine the best fit of the experimental data for the heat conductivity of a Si_cGe_{1-c} wire of length $L = 3$ mm as function of its composition parameter $c \in [0, 1]$.

In Ref. [23], starting from the experimental data in [30–32], such a procedure led us to the following constitutive equation

$$\lambda(c) = A' e^{B'c^2 + D'c} + E' e^{F'c^2 + G'c} \tag{1}$$

with A', B', D', E', F' and G' as material parameters, determined by a NLRM. The constitutive Equation (1) led us to a very good accordance with the experimental data [23].

In the present paper, we go a step further, starting from the observation that since we have pure Ge for $c = 0$, and pure Si for $c = 1$, for Equation (1) the following constraints on A', B', D', E', F' and G' must be satisfied for any value of the temperature T

$$\lambda(0) = A' + E' = \lambda_{Ge} \quad \lambda(1) = A' e^{B' + D'} + E' e^{F' + G'} = \lambda_{Si} \tag{2}$$

where λ_{Ge} and λ_{Si} are the thermal conductivity of pure Ge and pure Si, respectively. As a consequence, only 4 independent parameters are necessary, once the experimental values of λ_{Ge} and λ_{Si} at a fixed temperature are known. To obtain a manageable 4-parameters representation is not an easy task, because, in general, the smaller the number of free parameters in the fitting function, the higher the numerical error affecting the fit. In the present paper, we determine a new fit, with 4 independent parameters only, which is reliable and introduces a small error. For the new 4-parameters representation, the analysis of the data in [30–32] suggests us to look for a best-fit curve of the form

$$\lambda(c) = f(A, B, D, E)e^{Ac^2+Bc} + g(A, B, D, E)e^{Dc^2+Ec} \tag{3}$$

where A, B, D, E, are the unknown parameters to be determined by NLRM and $f(A, B, D, E)$ and $g(A, B, D, E)$ are suitable parameters-dependent coefficients. Finally, the conditions $\lambda(0) = \lambda_{Ge}$ and $\lambda(1) = \lambda_{Si}$ give the following expressions of the functions $f(A, B, D, E)$ and $g(A, B, D, E)$

$$f(A, B, D, E) = \frac{\lambda_{Si} - \lambda_{Ge}\, e^{D+E}}{e^{A+B} - e^{D+E}}, \qquad g(A, B, D, E) = \frac{-\lambda_{Si} + \lambda_{Ge}\, e^{D+E}}{e^{A+B} - e^{D+E}}$$

Thus, our fitting curve can be obtained once the parameters A, B, D, and E are determined. In order to calculate them, first we estimate some initial values for parameter entering Equation (3). Then, in the set of the possible couples $(c, \lambda(c))$, i.e., in the strip $\{[0, 1] \times [0, \infty]\} \subset R^2$, we generate the curve determined by the estimated values of the parameters, and adapt them in such a way that the Euclidean distance in R^2 between the fitting curve and the experimental points is as small as possible. Let's notice that the total error affecting the fit, i.e., the sum of the squared distances between the experimental points and the fitting curve, is of the same order of magnitude for all the temperatures considered here.

The values of A, B, D, E at $T = 300$ K, $T = 400$ K and $T = 500$ K are shown in Table 1 for $L = 3$ mm. The values of the heat-conduction parameter for bulk systems of pure Si and pure Ge at $T = 300$ K, $T = 400$ K and $T = 500$ K, are shown in Table 2. The plots in Figures 1–3 show the measured and theoretical values of $\lambda(c)$ expressed by Equation (3), at $T = 300$ K, $T = 400$ K and $T = 500$ K, for $L = 3$ mm. By comparing the pink and black curves in Figures 1–3 we argue that fitting curve reproduces accurately the experimental data. It is evident from the figure the presence of two narrow zones, close to the extremes of the interval $[0, 1]$, in which λ varies steeply, while it remains almost constant in the other points of the interval. The variation of λ with c is more evident in the subintervals $[0, 0.1]$ and $[0.9, 1]$ because a small quantity of impurities is capable of enhancing the phonon scattering, and, as a consequence, to reduce very much heat conductivity with respect to the one of the pure system.

Table 1. Values of A, B, D, E in Equation (3) for a Si_cGe_{1-c} wire of length $L = 3$ mm.

Temperature	A	B	D	E
$T = 300$ K	4.8706	−3.76	109.452	−108.953
$T = 400$ K	91.804	−91.351	4.416	−3.3127
$T = 500$ K	4.0667	−2.9717	80.4998	−80.0781

Table 2. Thermal conductivity in (W m^{-1} K^{-1}) corresponding to the mentioned compositions at $T = 300$ K, $T = 400$ K and $T = 500$ K, for a Si_cGe_{1-c} wire of length $L = 3$ mm.

Temperature	λ_{Si}	λ_{Ge}
$T = 300$ K	149.95	77.95
$T = 400$ K	113.54	59.42
$T = 500$ K	92.01	48.08

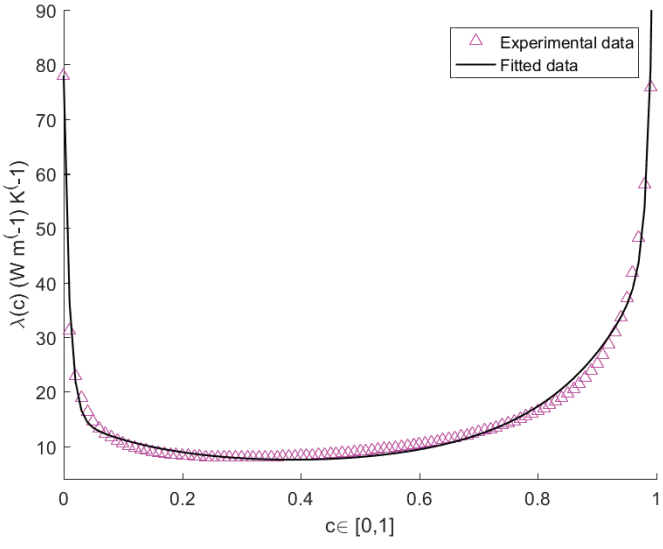

Figure 1. Plots of the calculated vs. measured values of thermal conductivity of a Si_cGe_{1-c} wire of length $L = 3$ mm as function of c, at temperature $T = 300$ K.

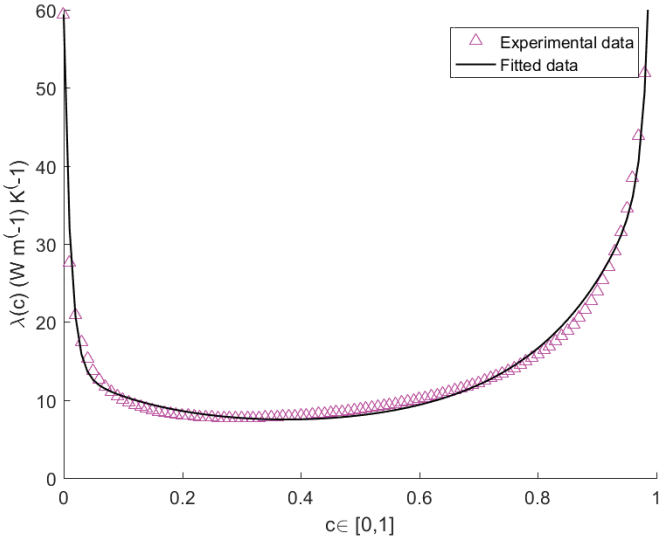

Figure 2. Plots of the calculated vs. measured values of thermal conductivity of a Si_cGe_{1-c} wire of length $L = 3$ mm as function of c, at temperature $T = 400$ K.

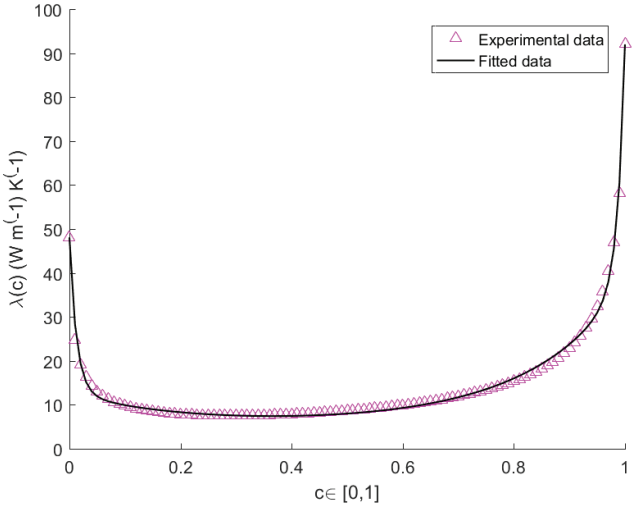

Figure 3. Plots of the calculated vs. measured values of thermal conductivity of a Si_cGe_{1-c} wire of length $L = 3$ mm as function of c, at temperature $T = 500$ K.

3. Best Efficiency in Thermoelectric Energy Conversion

The system analyzed here is a graded Si_cGe_{1-c} wire of length L crossed by an electric current $\mathbf{i}$, on which acts an electric field $\mathbf{E}$. The right-hand side $(z = L)$, is kept at the hot temperature T_h, while the left-hand side, $(z = 0)$, is kept at the cold temperature T_c. Since the material composition changes with position, at right-hand side $(z = L)$ we have only Silicon while at left-hand side, $(z = 0)$ we have only Germanium. Then, the system is similar to a junction of different materials at the ends of which is applied a difference of temperature $T_h - T_c$. As is well known, such a type of junction is capable of generating a difference of electric potential at its ends, and this phenomenon is the classical thermoelectric effect [16,17]. As a consequence of the generation of this difference of potential, there are an electric current $\mathbf{i}$ flowing uniformly inside the system from left to right, and an electric field $\mathbf{E}$ acting on the system. The difference of temperature at the ends of the wire is generated by given amount of heat per unit time $\dot{Q}_{\text{tot}}$ which enters uniformly into the hot side of the element.

The model is represented by:

- The local energy balance [21]

$$\rho \frac{du}{dt} + \nabla \cdot \mathbf{q} = \mathbf{E} \cdot \mathbf{i} \tag{4}$$

  where ρ is the mass density, u the specific internal energy and $\mathbf{q}$ the heat flux;
- the constitutive equation for the heat flux

$$\mathbf{q} = -\nabla \mathbf{q} \cdot \mathbf{l} - \lambda \left(1 - b\right) \nabla T + \Pi \mathbf{i} \tag{5}$$

  where $\mathbf{l}$ denotes a characteristic-length vector, proportional to the heat flux $\mathbf{q}$, b is a dimensionless quantity smaller than 1 and depending on q^2, and Π is the Peltier coefficient [9,17];
- the constitutive equation for the electric current

$$\mathbf{i} = -\sigma_e \epsilon \nabla T + \sigma_e \mathbf{E} \tag{6}$$

Here the Peltier and Seebeck coefficients Π and ϵ, as well as the electric conductivity σ_e, are supposed to be constant. It is worth noticing that for the nonlinear heat conductor presented here the classical second Kelvin relationship $\Pi = \epsilon T$, which holds in Linear Irreversible Thermodynamics [9,17], in general, is no longer true (see [21] for a detailed discussion of this point). In our analysis we assume also that the thermal conductivity $\lambda(c, T)$ can be approximated with its expression at the hottest side, namely $\lambda(c, T_h)$.

From the physical point of view, the previous hypotheses mean that we restrict our investigation to rigid conductors whose thermal and electric functions have small variations with respect to temperature, and the variation of λ with the composition is preeminent in influencing the thermoelectric behavior. Of course, this is not the most general case, and the present investigation must be considered only as a first step toward a complete analysis of the thermoelectric behavior of composition graded materials.

From the mathematical point of view, as it will be shown below, the previous hypotheses lead to a problem of determination of the points of minimum of a function of two independent variables. In such a case, some conditions ensuring that such minima always exist can be determined. On the other hand, if the material functions would depend on the temperature too, the same problem should be considered for a function of three independent variables, as in Ref. [24]. In such a case, it is much more difficult to determine the conditions which ensure the existence of minima. Moreover, more data on the dependence of the material functions on temperature are necessary. Indeed, currently we are considering such a problem, and the results will be included in a forthcoming article.

Under the conditions discussed above, if we further assume that both $\mathbf{q}$ and $\mathbf{E}$ depend only on the position on the longitudinal axis z, and that $\mathbf{q}$ and $\mathbf{i}$ are parallel, by some lengthy calculations we obtain that the local rate of energy dissipated along a thermoelectric process is [23]

$$\mathscr{E} = \frac{i^2}{\sigma_e} + i[\epsilon\, T_h - (\Pi - \overline{E}\ \overline{l})]\nabla T + \lambda(1-b)(\nabla T)^2 \tag{7}$$

where $\overline{E}$, and $\overline{l}$ denote the mean values of $|\mathbf{E}|$, and $|\mathbf{l}|$ on the interval $[0, L]$, respectively. In what follows we restrict ourselves to steady-state situations, which are usual for thermoelectric converters, and exploit Equation (7) in order to determine the situation in which the efficiency as thermoelectric energy converter of the system under consideration is maximum. Indeed, our main assumption is that the optimal efficiency is achieved in correspondence of a minimum of the rate of energy dissipated. Such a hypothesis lies on the observation that the efficiency is reduced by dissipative effects induced by the heat and electric transport. In Section 4 we will discuss it within the framework of Finite-Time Thermodynamics [25–27].

Equation (7) provides an expression of the local rate of energy dissipated, depending on the temperature gradient and on T_h and c through the thermal conductivity $\lambda(T_h, c)$. Thus, if T_h is fixed at one of the constant values $T = 300$ K, $T = 400$ K and $T = 500$ K, function $\mathscr{E}$ depends only on the gradient of temperature, and on the composition c. Furthermore, the hypothesis that the temperature gradient is parallel to z allows the further approximation $\nabla T = \dfrac{dT}{dz} \simeq \dfrac{T_h - T_c}{L}$. Then, Equation (7) rewrites as follows

$$\mathscr{E}\,(c, x) = \frac{i^2}{\sigma_e} + i[\epsilon\, T_h - (\Pi - \overline{E}\ \overline{l})]x^2 + \lambda(c)(1-b)x^4 \tag{8}$$

where

$$x \equiv \sqrt{\frac{T_h - T_c}{L}} \tag{9}$$

In the following we look for the possible minima of function $\mathscr{E}\,(c, x)$. It is easily proved that those points, which will be denoted by (c_s, x_s), are the stationary points c_s of $\lambda(c)$, and the values

$$x_s = \sqrt{\frac{-i\,[\epsilon\, T_h - (\Pi - \overline{E}\ \overline{l})]}{4\,\lambda_s(1-b)}} \tag{10}$$

with $\lambda_s \equiv \lambda(c_s)$. They exist if the inequality

$$i\,[\epsilon\, T_h - (\Pi - \overline{E}\,\overline{l})] < 0 \tag{11}$$

holds. The relationship (11) can be considered as a unilateral constraint on the physical parameters which characterize the model.

By the analysis of the Hessian matrix of the function $\mathscr{E}\,(c, x)$, it follows that the condition that must be fulfilled for the existence of a minimum for it is that the thermal conductivity has a minimum in c_s, and that the further constraint

$$2i[\epsilon\, T_h - (\Pi - \overline{E}\,\overline{l})] + 12\lambda_s x_s^2(1-b) > 0 \tag{12}$$

is satisfied. Although the first addendum in the left-hand side of Equation(12) is negative because of the constraint (11), the second one is positive, and hence the inequalities (11) and (12) can be satisfied contemporarily. Thus, the points of minimum for $\mathscr{E}\,(c, x)$ exist. From now on we denote by (c_{opt}, x_{opt}) such points.

4. Results

In this section, we discuss the properties of the minima (c_{opt}, x_{opt}) of $\mathscr{E}\,(c, x)$, calculated by using MATHEMATICA (https://www.wolfram.com/mathematica/).

At $T = 300$ K, $\mathscr{E}\,(c, x)$ attains a minimum at $c = 0.385989$. In this point λ=7.51235 $\mathrm{Wm^{-1}K^{-1}}$.
At $T = 400$ K, $\mathscr{E}\,(c, x)$ attains a minimum at $c = 0.375079$. In this point λ = 7.48291 $\mathrm{Wm^{-1}K^{-1}}$.
At $T = 500$ K, $\mathscr{E}\,(c, x)$ attains a minimum at $c = 0.36537$. In this point λ = 7.42273 $\mathrm{Wm^{-1}K^{-1}}$.
The previous results are summarized in Table 3, wherein $\lambda_{opt} \equiv \lambda(c_{opt})$.

Table 3. Values of λ_{opt} (in W $\mathrm{m^{-1}\ K^{-1}}$) for the compositions c_{opt} at $T = 300$ K, $T = 400$ K and $T = 500$ K, for $L = 3$ mm.

Temperature (K)	c_{opt}	λ_{opt} (in W $\mathrm{m^{-1}\ K^{-1}}$)
$T = 300$	0.385989	7.51235
$T = 400$	0.375079	7.48291
$T = 500$	0.36537	7.42273

Let us now compare the present results with those obtained in [23]. In both cases, there are no local minima of λ in the zones where λ is more steep, namely the optimal efficiency takes place in the zone where λ is almost constant. The values of c_{opt} are a little bit smaller (from 0.36 to 0.38) with respect to the values found in [23] (from 0.44 to 0.41). However, in both cases we got three points of minimum very close each other, which correspond to small differences in λ. Meantime, the values of λ_{opt} obtained here for a wire of length $L = 3$ mm are almost an order of magnitude higher with respect to those obtained in [23] for $L = 100$ nm, and comparable with (but smaller than) those obtained for $L = 30$ nm. It is worth noting that in [23] we obtained a marked difference between the values of λ_{opt} for $L = 30$ nm and those for $L = 100$ nm. It can be considered a size effect, i.e., a strong dependency of the material properties on the dimension of the system. This is just what we observed in [23], since for $L = 30$ nm we obtained λ_{opt} of the order of magnitude of 30 W $\mathrm{m^{-1}\ K^{-1}}$, while for $L = 100$ nm we obtained λ_{opt} of the order of magnitude of 0.4 W $\mathrm{m^{-1}\ K^{-1}}$. Size effects are very frequent in heat conduction in nanosystems, and manifest themselves when the physical dimension of the heat conductor becomes comparable with, or smaller than, the mean free path of the heat carriers [16,17]. These effects disappear at macroscopic length-scale. To verify such a property in our case, the dependency of λ_{opt} on the size of the system at macroscopic scale deserves further investigation. For such a study we need new experimental data, for length smaller and higher than 3 mm. Currently we are not aware of such data, but we are looking for them in the literature.

5. Relation with Finite-Time Thermodynamics

The early studies on the efficiency of thermodynamic engines were based on the concept of Carnot cycle, which means a quasi-static, i.e., reversible, thermodynamic cycle constituted by two isothermal and two adiabatic arcs in the state space, in which a thermodynamic system adsorbs, at constant temperature, a quantity of heat Q_H by a hottest source at temperature T_H and gives, at constant temperature, a quantity of heat Q_C to a cold reservoir at temperature T_C. Along the cycle, the system produces a net amount of work $W = Q_H - Q_C$. The efficiency of this cycle is $\eta \equiv W/Q_H = (Q_H - Q_C)/Q_H = 1 - Q_C/Q_H$. Carnot was the first to prove that such efficiency takes the form $\eta_C = 1 - T_C/T_H$. Since a quasi-static transformation requires an infinite time, the Carnot efficiency η_C is not suitable to describe the efficiency of real processes, which take over in a finite time. For those processes it is more useful to calculate the efficiency as the ratio $\eta = P_{\text{ex}}/\dot{Q}_{\text{tot}}$, where P_{ex} is the extracted work per unitary time and $\dot{Q}_{\text{tot}}$ is the heat supplied to the system per unitary time. A simple model of system operating in finite time is provided by the Curzon-Ahlborn endoreversible engine [33]. For that system the efficiency at maximum power, i.e., when the system extracts the maximum power, can be proved to be $\eta_{CA} = 1 - \sqrt{T_C/T_H}$, so that $\eta_{CA} < \eta_C$. Thus, for real processes, the central question is to investigate how much the efficiency deteriorates when the cycle is operated in a finite time. This is the task of Finite-Time Thermodynamics, a modern nonequilibrium theory, which has been developed in the last four decades by Andresen, Salamon, Stephen Berry et al. [25–27,34].

Classical thermoelectricity can be considered to lay within the frame of Finite-Time Thermodynamics for the following reasons:

- The definition of the thermoelectric efficiency as $\eta_{el} = P_{\text{el}}/\dot{Q}_{\text{tot}}$ (see Section 1) does not require quasi-static transformations along an infinite time. Indeed, if one remains in the frame of linear thermodynamics, i.e., with linear constitutive equations for heat flux and electrical current, it can be proved that the maximum efficiency is [9]

$$\eta_{max} = \eta_C \frac{1 - 1/\xi}{1 + 1/\xi} \tag{13}$$

  wherein $\xi \equiv \sqrt{ZT + 1}$. Hence, $\eta_{max} < \eta_C$, in accordance with the tenets of Finite-Time Thermodynamics.
- In the situation considered in the present investigation, two time scales appear: the scale of the electric effects, and that of the thermal ones. Indeed, according to the general tenets of Extended Irreversible Thermodynamics, the constitutive Equations (5) and (6) can be obtained by the following balance laws for the heat flux and for the electric-charge flux, namely the electric current **i** [16,17]:

$$\tau_q \dot{\mathbf{q}} + \mathbf{q} = -\nabla \mathbf{q} \cdot \mathbf{l} - \lambda (1 - b) \nabla T + \Pi \mathbf{i} \tag{14}$$

$$\tau_i \dot{\mathbf{i}} + \mathbf{i} = -\sigma_e \epsilon \nabla T + \sigma_e \mathbf{E} \tag{15}$$

  where τ_q is the relaxation time of the heat flux and τ_i the relaxation time of the electric current. On the other hand, at the macroscopic length-scale electric phenomena are faster of the thermal ones, so that the electric relaxation time is much shorter that the thermal one. Thus, the condition $\tau_i << \tau_q$ allows the regarding of the thermal evolution as a finite-time process with respect to the electric one.

Equation (13) implies that the higher ξ, the higher η_{max}, so that several researches in recent decades focused on the methods to enhance ξ, i.e., to enhance ZT. However, this is not an easy task. For instance, still remaining in a linear theory, it can be easily proved that for the wire considered here, $\dot{Q}_{\text{tot}} = \lambda(T_h - T_c)/L + \Pi i$ [21], so that for fixed $T_h - T_c$ and i, a reduction of $\dot{Q}_{\text{tot}}$ can be realized, from the technical point of view, only by a reduction of λ, i.e., by an increment of $Z = \epsilon^2 \sigma_e/\lambda$, producing so an enhancement of the efficiency. However, a reduction of λ is connected with an increment of the phonon scattering inside the thermoelectric solid [16,17], and this produces dissipation

which, in turn, reduces P_{el}. Thus, numerator and denominator cannot be controlled independently in the expression of η_{el}. On the other hand, to optimize only one of them is not sufficient to obtain the best efficiency, as argued by Hoffmann in [34], where it is shown by a meaningful example that the maximum power does not correspond to the minimum dissipation, and hence to the best efficiency.

In the present investigation we propose a new procedure in the realm of Irreversible Thermodynamics (Classical and Extended) which is capable of overcoming the difficulties mentioned above, since it does not focus on the power output but on the energy dissipated along the thermoelectric process. We proceed as follows. We disregard all the losses related to the production of $\dot{Q}_{\mathrm{tot}}$ and to the management of the generated difference of electrical potential, and we focus only on the thermodynamic process inside the thermoelectric wire. As illustrated in Section 3, it consists of the generation of an electric potential after that an amount of heat per unit time $\dot{Q}_{\mathrm{tot}}$ entered uniformly inside the system. Such a heat flow produces dissipation by Joule effect, which, in any point z of the system and at any time t, is given by the rate of energy dissipated $\mathscr{E}(c(z),\, x(z,t))$ calculated in Equation (8). Please note that since we suppose the absence of any mechanical friction, the sole dissipation of energy is due to the Joule effect. Then, we argue that the smaller the energy dissipated by Joule effect, the higher the efficiency in the process of thermoelectric energy conversion. It is worth remarking that $\mathscr{E}(c(z),\, x(z,t))$ is a local quantity, so that our hypothesis of minimum energy dissipated is local.

At this point one may wonder if our point of view can follow by a global variational principle which holds for a wider class of thermoelectric systems. To investigate such a possibility, let's consider a thermoelectric system, and let Σ its state space, spanned by a set of n thermodynamic variables $X_1, \ldots, X_n$. Moreover, let $A \equiv (X_{1A}, \ldots, X_{nA})$ and $B \equiv (X_{1B}, \ldots, X_{nB})$ denote two generic points of Σ. The following statement can be expected to hold.

Principle of Minimum Energy Dissipated

Let $\mathscr{S}$ a thermoelectric system undergoing a thermodynamic process of conversion of a given amount of heat per unit time into an electric-power output, and let such a process represented by a regular curve between two fixed thermodynamic states A and B of the system. Then, among all the possible processes represented by a curve of extremes A and B in Σ, the most efficient one is the process in which the total energy dissipated by Joule effect achieves a minimum.

If a thermoelectric process is represented by a regular curve γ in the state space, the total energy dissipated is given by

$$E_{tot} = \int_{\gamma} \mathscr{E}(c,\, x) dl \tag{16}$$

where dl denotes the infinitesimal arc-length of γ.

The Principle of minimum energy dissipated states that the most efficient thermoelectric process is the one in which E_{tot} is minimum.

For the one-dimensional system considered here, the previous principle implies that the best efficiency is obtained when the local energy dissipated per unit time (i.e., the local power dissipated) $\mathscr{E}(c,\, x)$ is minimum. To prove that, we first observe that at the constant temperature T_h, the constitutive Equations (5) and (6) depend only on the composition c and on the temperature gradient ∇T, which we have approximated by the effective gradient x. Thus, the sole thermodynamic variables are the couple $(c,\, x)$. Moreover, we are considering the steady-state situation, in which a process of thermoelectric energy conversion takes place with the system in a constant state. In such a case the different curves reduce to different points of Σ, and among them, we are looking for the state for which the energy dissipated is minimum. In such a situation the total energy dissipated in any point is given by

$$E_{tot} = \int_0^L \int_0^\tau \bar{\mathscr{E}}(z,\, t)) dz dt \tag{17}$$

where τ is the duration of the thermodynamic process, and the superposed bar means that $\mathscr{E}(c(z),\, x(z,t))$ was explicated as function of z and t.

On the other hand, being $\bar{\mathscr{E}}(z,\, t))$ a positive quantity, the right-hand side of Equation (17) is minimum if, and only if, the integrand function is minimum in any point of the domain of integration, or, equivalently, if, and only if, $\mathscr{E}(c,\, x)$ is evaluated in the state (c_{opt}, x_{opt}) found in Sections 3 and 4.

In the technical applications the previous result allows the determination a priori of the part of the conductor where the energy conversion is optimal by modulating the dependence of c on z.

This proves that for the system considered in the present investigation, the global and local forms of the principle are equivalent. Of course, this is a very particular case, and it is important to underline that the previous conclusions are no longer true for different systems and in non-stationary situations. In future research, we plan to extend such investigation to more general systems, for instance, to deformable graded continua, in order to verify the possible extensions of the Principle of minimum energy dissipated.

It is important to note the different physical dimensions of $\mathscr{E}$ and E_{tot}: the first one is a power density, measured in $Jm^{-1}s^{-1}$, the second one is the total energy dissipated along the process, which is measured in J. We observe that the local form of our principle requires that the power density $\mathscr{E}(c,\, x)$ takes a minimum, the global form, instead, requires that the total energy E_{tot} takes a minimum.

Remark 1. *The results above are in accordance with Gyarmati approach to Irreversible Thermodynamics. According to this approach, the fundamental laws of the thermodynamics of dissipative processes can be resumed into a very general variational principle, formulated by Gyarmati both in local and global forms [35]. Such a principle allows several particular formulations, and it is very useful in optimization problems, as those which are typical of Finite-Time Thermodynamics. For a general analysis of the principle we refer the reader to the paper [36]. The investigation of a possible formulation of the general tenets of Finite-Time Thermodynamics in view of the Gyarmati variational principle for dissipative processes constitutes a very interesting field of investigation, which, however, is beyond the scope of the present article.*

It is worth noticing that the Principle of minimum energy dissipated is only one of the possible criteria for the optimization of the performance of finite-time heat engines. For instance, some authors proposed the maximization of the power output, some others the maximization of the ratio between the power output and the heat adsorbed, i.e., the quantity $\eta = \dfrac{P_{\text{out}}}{\dot{Q}_{\text{tot}}}$, and others the minimization of the entropy production (see [25] for a discussion of this topic). Each of those approaches presents vantages and disadvantages. For instance, the power maximization aims at designing highly performant heat engines, the maximization of the η aims at obtaining good performance with acceptable costs in energy, the minimization of entropy production, or, equivalently, of energy dissipated, aims at preserving the natural resources. Regarding this aspect, in the literature one can also find an ecological criterion which requires maximization of the difference between the power output and the energy dissipated [37]. Such a criterion seems to be a good compromise between power enhancement and acceptable entropy production.

The analysis of the efficiency of thermoelectric graded systems in view of the different criteria illustrated above offers interesting perspectives for future research.

At the very end, we underline again that the previous analysis regards only the process of thermoelectric energy conversion inside the wire, while the dissipation inside the surrounding is neglected. Of course, this working hypothesis is only an approximation since, in general, is not easy to separate the entropy production of the surrounding from that of the heat conductor. Hence, a complete analysis of thermoelectric energy conversion should take into account the dissipation due to the production of $\dot{Q}_{\text{tot}}$ and that due to the transport and management of the obtained difference of electric potential. However, such a study is outside the scopes of the present research, and is more pertinent to the field of Engineering. The previous considerations serve only to explain why the problem

investigated here, especially the procedure carried out in Sections 2 and 3, can be considered to be typical of Finite-Time Thermodynamics.

Author Contributions: In this article, both P.R. and V.A.C. were fully involved in: substantial conception and design of the paper; analysis and development of the calculations; drafting of the article and critical revision of it; final approval of the version to be submitted. Both authors have read and agreed to the published version of the manuscript.

Funding: P.R. and V.A.C.: Financial support of the National Group of Mathematical Physics (GNFM-INdAM). P.R.: University of Messina, grant FFABR 2019. V.A.C.: University of Basilicata, grants RIL 2013 and RIL 2015.

Acknowledgments: The authors gratefully thank the Guest Editors, B. Andresen (University of Copenhagen), R. Stephen Berry (University of Chicago), and P. Salamon (San Diego State University), for the kind invitation to contribute to this special issue of Entropy devoted to Finite-Time Thermodynamics.

Conflicts of Interest: The authors declare no conflict of interest. The funders had no role in the design of the study; in the collection, analyses, or interpretation of data; in the writing of the manuscript, or in the decision to publish the results.

References

1. Gelbstein, Y.; Dashevsky, Z.; Dariel, M. High performance n-type PbTe-based materials for thermoelectric applications. *Phys. B* **2005**, *363*, 196–205. [CrossRef]
2. Olatunji-Ojo, A.O.; Boetcherb, S.K.S.; Cundaria, T.R. Thermal conduction analysis of layered functionally graded materials. *Comput. Mater. Sci.* **2012**, *54*, 329–335. [CrossRef]
3. Lebon, G. Heat conduction at micro and nanoscales: A review through the prism of Extended Irreversible Thermodynamics. *J. Non-Equilib. Thermodyn.* **2014**, *39*, 35–59. [CrossRef]
4. Cimmelli, V.A. Different thermodynamic theories and different heat conduction laws. *J. Non-Equilib. Thermodyn.* **2009**, *34*, 299–333. [CrossRef]
5. Yang, N.; Zhang, G.; Li, B. Carbon nanocone: A promising thermal rectifier. *Appl. Phys. Lett.* **2008**, *93*, 243111. [CrossRef]
6. Gonzalez-Noya, E.; Srivastava, D.; Menon, M. Heat-pulse rectification in carbon nanotube Y junctions. *Phys. Rev. B* **2009**, *79*, 115432. [CrossRef]
7. Mingo, N. Thermoelectric figure of merit and maximum power factor in III–V semiconductor nanowires. *Appl. Phys. Lett.* **2004**, *84*, 2652. [CrossRef]
8. Nolas, G.S.; Sharp, J.; Goldsmid, H.J. *Thermoelectrics: Basic Principles and New Materials Developments*; Springer: New York, NY, USA, 2001.
9. Lebon, G.; Jou, D.; Casas-Vázquez, J. *Understanding Nonequilibrium Thermodynamics*; Springer: Berlin, Germany, 2008.
10. Balandin, A.; Wang, K.L. Effect of phonon confinement on the thermoelectric figure of merit of quantum wells. *J. Appl. Phys.* **1998**, *84*, 6149. [CrossRef]
11. Kuznetsov, V.L. Functionally graded materials for termoelectric applications. In *Thermoelectrics Handbook: Macro to Nano—Sec. 38*; Rowe, D.M., Ed.; CRC Press: Boca Raton, FL, USA, 2005.
12. Li, D.; Wu, Y.; Kim, P.; Shi, L.; Yang, P.; Majumdar, A. Thermal conductivity of individual silicon nanowires. *Appl. Phys. Lett.* **2003**, *83*, 2934–2936. [CrossRef]
13. Ferry, D.K.; Goodnick, S.M. *Transport in Nanostructures*, 2nd ed.; Cambridge University Press: Cambridge, UK, 2009.
14. Goodson, K.E.; Flik, M.I. Electron and Phonon Thermal Conduction in Epitaxial High-T_c Superconducting Films. *J. Heat Transfer.* **1993**, *115*, 17–25. [CrossRef]
15. Joshi, G.; Lee, H.; Lan, Y.; Wang, X.; Zhu, G.; Wang, D.; Gould, R.W.; Cuff, D.C.; Tang, M.Y.; Dresselhaus, M.S.; et al. Enhanced Thermoelectric Figure-of-Merit in Nanostructured p-type Silicon Germanium Bulk Alloys. *Nano Lett.* **2008**, *8*, 4670–4674. [CrossRef] [PubMed]
16. Jou, D.; Casas-Vázquez, J.; Lebon, G. *Extended Irreversible Thermodynamics*, 4th ed.; Springer: Berlin, Germany, 2010.
17. Sellitto, A.; Cimmelli, V.A.; Jou, D. *Mesoscopic Theories of Heat Transport in Nanosystems*; Springer: Berlin, Germany, 2016.

18. Cimmelli, V.A.; Sellitto, A.; Jou, D. Nonlocal effects and second sound in a nonequilibrium steady state. *Phys. Rev. B* **2009**, *79*, 014303. [CrossRef]
19. Cimmelli, V.A.; Sellitto, A.; Jou, D. Nonequilibrium temperatures, heat waves, and nonlinear heat transport equations. *Phys. Rev. B* **2010**, *81*, 054301. [CrossRef]
20. Rogolino, P.; Sellitto, A.; Cimmelli, V.A. Influence of the electron and phonon temperature and of the electric-charge density on the optimal efficiency of thermoelectric nanowires. *Mech. Res. Commun.* **2015**, *68*, 77–82. [CrossRef]
21. Rogolino, P.; Sellitto, A.; Cimmelli, V.A. Influence of nonlinear effects on the efficiency of a thermoelectric generator. *Zeitschrift fur Angewandte Mathematik und Physik* **2015**, *66*, 2829–2842. [CrossRef]
22. Rogolino, P.; Cimmelli, V.A. Thermoelectric efficiency of graded $S_c\,Ge_{1-c}$ alloys. *J. Appl. Phys.* **2018**, *124*, 094301. [CrossRef]
23. Rogolino, P.; Cimmelli, V.A. Fitting thermal conductivity and optimizing thermoelectric efficiency of functionally graded $Si_c\,Ge_{1-c}$ nanowires. *Math. Comput. Simul.* **2020**, *176*, 279–291. [CrossRef]
24. Rogolino, P.; Cimmelli, V.A. Thermal conductivity and enhanced thermoelectric efficiency of composition graded $Si_c\,Ge_{1-c}$ alloys. *Zeitschrift fur Angewandte Mathematik und Physik* **2020**, *71*, 92. [CrossRef]
25. Andresen, B.; Berry, R.S.; Nitzan, A.; Salomon, P. Thermodynamics in finite time. I. The step-Carnot cicle. *Phys. Rev. A* **1977**, *15*, 2086–2093. [CrossRef]
26. Andresen, B.; Berry, R.S.; Ondrechen, M.J.; Salomon, P. Thermodynamics for Processes in Finite Time. *Acc. Chem. Res.* **1984**, *17*, 266–271. [CrossRef]
27. Andresen, B.; Salomon, P.; Berry, R.S. Thermodynamics in finite time. *Phys. Today* **1984**, *37*, 62–70. [CrossRef]
28. Caim, J.W. Mathematics of Fitting Sicientific Data. In *Molecular Life Sciences*; Bell, E., Ed.; Springer: New York, NY, USA, 2014.
29. Motulsky, J.H.; Ransnas, A.L. Fitting Curves to Data Using Nonlinear Regression: A Practical and Nonmathematical Review. *FASEB J.* **1987**, *1*, 365–374. [CrossRef] [PubMed]
30. Glassbrenner, C.; Slack, G. Thermal conductivity of silicon and germanium from 3° K to the melting point. *Phys. Rev.* **1964**, *134*, 1058–1069. [CrossRef]
31. Steele, M.; Rosi, F. Thermal conductivity and thermoelectric power of germanium-silicon alloys. *J. Appl. Phys.* **1958**, *29*, 1517–1520. [CrossRef]
32. Abeles, B.; Beers, D.; Cody, G.; Dismukes, J. Thermal conductivity of Ge-Si alloys at high temperatures. *Phys. Rev.* **1962**, *125*, 44–46. [CrossRef]
33. Curzon, F.L.; Ahlborn, B. Efficiency of a Carnot engine at maximum power output. *Am. J. Phys.* **1975**, *43*, 22–24. [CrossRef]
34. Hoffmann, K.H. Recent Developments in Finite Time Thermodynamics. *Tech. Mech.* **2002**, *22*, 14–25.
35. Gyarmati, I. On the Governing Principle of Dissipative Processes and its Extension to Non-Linear Problems. *Annalen der Physik* **1969**, *23*, 353–378. [CrossRef]
36. Verhás, J. Gyarmati's Variational Principle of Dissipative Processes. *Entropy* **2014**, *16*, 2362–2383. [CrossRef]
37. Angulo-Brown, F. An ecological optimization criterion for finite-time heat engines. *J. Appl. Phys.* **1991**, *69*, 7465. [CrossRef]

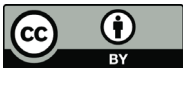

entropy

MDPI

Article

Minimum Entropy Generation Rate and Maximum Yield Optimization of Sulfuric Acid Decomposition Process Using NSGA-II

Ming Sun [1], Shaojun Xia [1], Lingen Chen [2,3,*], Chao Wang [1] and Chenqi Tang [1]

[1] College of Power Engineering, Naval University of Engineering, Wuhan 430033, China; 17862989281@163.com (M.S.); 15994280441@139.com (S.X.); victoria329@163.com (C.W.); tangchenqi7@163.com (C.T.)
[2] Institute of Thermal Science and Power Engineering, Wuhan Institute of Technology, Wuhan 430205, China
[3] School of Mechanical & Electrical Engineering, Wuhan Institute of Technology, Wuhan 430205, China
* Correspondence: lgchenna@yahoo.com or lingenchen@hotmail.com

Received: 24 July 2020; Accepted: 19 September 2020; Published: 23 September 2020

Abstract: Based on the theory of finite-time thermodynamics (FTT), the effects of three design parameters, that is, inlet temperature, inlet pressure, and inlet total mole flow rate, of a tubular plug-flow sulfuric acid decomposition reactor on the total entropy generation rate (EGR) and SO_2 yield are analyzed firstly. One can find that when the three design parameters are taken as optimization variables, the minimum total EGR and the maximum SO_2 yield of the reference reactor restrict each other, i.e., the two different performance objectives cannot achieve the corresponding extremum values at the same time. Then, the second-generation non-dominated solution sequencing genetic algorithm (NSGA-II) is further used to pursue the minimum total EGR and the maximum SO_2 yield of the reference reactor by taking the three parameters as optimization design variables. After the multi-objective optimization, the reference reactor can be Pareto improved, and the total EGR can be reduced by 9% and the SO_2 yield can be increased by 14% compared to those of the reference reactor. The obtained results could provide certain theoretical guidance for the optimal design of actual sulfuric acid decomposition reactors.

Keywords: finite-time thermodynamics; sulfuric acid decomposition; tubular plug-flow reactor; entropy generation rate; SO_2 yield; multi-objective optimization

1. Introduction

At present, the Hybrid-Sulphur (H-S) thermochemical cycle and the Sulphur-Iodine (S-I) thermochemical cycle are considered to be the two most promising recycling methods in the preparation of hydrogen from water by thermochemical cycles [1], and the schematic diagram of S-I thermochemical cycle is shown in Figure 1. Both the H-S and the S-I cycles contain the sulfuric acid decomposition process. Therefore, it is important and necessary to improve the performance of the sulfuric acid decomposition process.

The S-I thermochemical cycle consists of three main chemical reactions: (1) the endothermic decomposition of hydrogen iodide in gas phase; (2) the spontaneous absorption of sulfur dioxide in liquid phase; (3) the sulfuric acid decomposition reaction. The corresponding reaction equations are given as follows:

$$H_2SO_4 \overset{800K}{\rightarrow} SO_3 + H_2O \quad \text{(I)}$$

$$SO_3 \overset{1100K}{\rightarrow} SO_2 + \frac{1}{2}O_2 \quad \text{(II)}$$

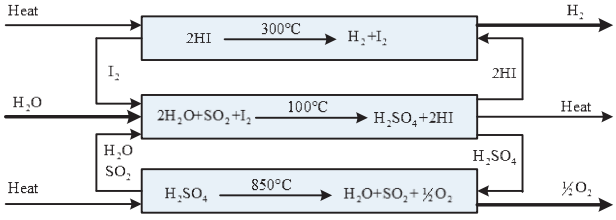

Figure 1. The schematic diagram of S-I thermochemical cycle.

Reaction type (I) is the spontaneous decomposition of H_2SO_4 into SO_3 and H_2O at 400–500 °C. Reaction type (II) is the reaction of SO_3 over 750 °C to produce SO_2 and O2 under the action of a catalyst. In this process, a great deal of heat is consumed, which is also the main energy consumption process in the S-I and H-S thermochemical cycles.

In the aspect of thermodynamic analysis and optimization of sulfuric acid decomposition, Van der ham et al. [1] assumed that the reaction mixture satisfies the ideal gas equation of state, established the physical model of sulfuric acid decomposition reaction, and analyzed the minimization of entropy generation rate (EGR) of a sulfuric acid decomposition reactor by using the optimal control theory. Kuchi et al. [2] carried out a numerical simulation of a high-temperature shell and tube heat exchanger and decomposer, investigated the fluid flow, heat transfer, and chemical reaction processes in the decomposer by using the porous media method, and established a two-dimensional axisymmetric tubular plug-flow reactor model. Ponyavin et al. [3] studied the sulfuric acid decomposer process in a high-temperature ceramic heat exchanger and established a three-dimensional calculation model of the reactor. Van der ham et al. [4] further compared two methods to improve the efficiency of sulfuric acid decomposition reactor and proposed two design schemes to improve the efficiency of the reactor. On the basis of Ref. [1], Wang et al. [5,6] optimized the decomposition of sulfuric acid in the tubular plug-flow reactor with the goal of maximum yield [5], further analyzed the influences of the design parameters of the reactor on the SO_2 yield and specific EGRs [6], and obtained the optimal parameters corresponding to the minimum specific EGRs.

Many scholars have optimized other types of thermochemical reaction processes by using the theory and method of finite-time thermodynamics (FTT) [7–22]. For example, Wang et al. [23] investigated the isotherm chemical reaction $A \Leftrightarrow B \Leftrightarrow C$ and obtained the best concentration configuration of the reaction. Johannessen and Kjelstrup [24] studied the EGR minimization of sulfur dioxide oxidation process. The second-generation non-dominated solution sequencing genetic algorithm (NSGA-II) has been widely used in multi-objective optimization of various engineering problems [25–30].

On the basis of Refs. [1,5,6], this paper will further analyze the effects of reactant inlet temperature, pressure, and total molar flow rate on total EGR and SO_2 yield, and perform the multi-objective optimization of the process by using the NSGA-II algorithm by applying FTT.

2. Modeling of the Sulfuric Acid Decomposition Process

A reference reactor used in the performance analysis and optimization as well as the kinetics and thermodynamics models will be introduced in this section.

2.1. Reference Reactor

The model of a tubular plug-flow reactor for sulfuric acid decomposition is shown in Figure 2. It is assumed that the temperature (T_w) of the outer wall of tubular plug-flow reactor does not change with time and its distribution is linear along the axial direction of the reactor. The distribution follows $T_w = 975 + 148z/L$ (K). The reaction mixture in the reactor is regarded as an ideal gas and only flows along the axial direction of the reactor. The radial concentration gradient and temperature gradient of

the reaction mixture in the reactor are ignored without both radial diffusion and back-mixing. The total molar flow rate and velocity of the reaction mixture at the cross-section of the reactor are as follows:

$$F_{tot} = \sum_i F_i \tag{1}$$

$$\mathrm{v} = \frac{F_{tot}}{A_c} \frac{R\,T}{P \times 10^5} \tag{2}$$

where F_i is the molar flow rate of reaction component i, i.e., H_2SO_4, SO_3, H_2O, SO_2 and O_2; A_c is the radial cross section area of the reactor, and R is the universal gas constant.

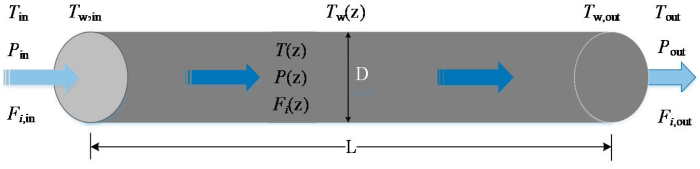

Figure 2. Schematic of tubular plug-flow reactor.

The data of catalyst selection, reactor structure, and thermodynamic parameters of the reaction mixture are determined according to Ref. [1], as listed in Table 1.

Table 1. Parameters of the reference reactor.

Parameter	Symbol	Value
Overall heat transfer coefficient/J/$\left(\mathrm{K{\cdot}m^2{\cdot}s}\right)$	U	170
Dynamic viscosity/kg/(m·s)	η	4×10^{-5}
Catalyst bed porosity	ε	0.45
Catalyst pellet density/kg/m^3	ρ_p	4200
Catalyst pellet diameter/m	D_p	0.003
Inner diameter of reactor/m	D	0.030
Length of reactor/m	L	3.090
Inlet temperature/K	T_in	800
Inlet pressure/bar	P_in	7.1
Inlet total molar flow rate	$F_\mathrm{tot,in}$	0.034
Molar fraction of inlet H_2SO_4	$F_{H_2SO_4,in}$	0.094
Molar fraction of inlet SO_3	$F_{SO_3,in}$	0.425
Molar fraction of inlet H_2O	$F_{H_2O,in}$	0.481
Molar fraction of inlet SO_2	$F_{SO_2,in}$	0.000
Molar fraction of inlet O_2	$F_{O_2,in}$	0.000

2.2. Models of Kinetics and Thermodynamics

The fluid flow, heat transfer, and chemical reaction of the reaction mixture in a tubular plug-flow reactor follow momentum, energy, and mass conservation equations, respectively, which are given by:

$$\frac{\mathrm{d}P}{\mathrm{d}z} = -\left[\frac{150\eta}{D_\mathrm{p}^2}\frac{(1-\varepsilon)^2}{\varepsilon^3} + \frac{1.75\rho_\mathrm{in}\mathrm{v}_\mathrm{in}}{D_\mathrm{p}}\frac{1-\varepsilon}{\varepsilon^3}\right]\mathrm{v} \tag{3}$$

$$\frac{dT}{dz} = \frac{\pi D J_q + A_c \rho_p \sum_j \left[r_{m,j} (-\Delta_r H_j) \right]}{\sum_i (F_i C_{p,i})} \tag{4}$$

$$\frac{dF_{H_2SO_4}}{dz} = -A_c \rho_p r_{m,1} \tag{5}$$

$$\frac{dF_{H_2O}}{dz} = A_c \rho_p r_{m,1} \tag{6}$$

$$\frac{dF_{SO_3}}{dz} = A_c \rho_p (r_{m,1} - r_{m,2}) \tag{7}$$

$$\frac{dF_{SO_2}}{dz} = A_c \rho_p r_{m,2} \tag{8}$$

$$\frac{dF_{O_2}}{dz} = \frac{1}{2} A_c \rho_p r_{m,2} \tag{9}$$

where ρ_{in} and v_{in} are the density and flow velocity of the reaction mixture on the entrance section, respectively; subscript $j = 1, 2$ represents the reaction types (I) and (II); $r_{m,j}$ is the reaction rate of mass per unit catalyst, and they are $r_{m,1} = r_1/\rho_p$ and $r_{m,2} = r_2$; $C_{p,i}$ and $\Delta_r H_j$ are the component molar constant-pressure heat capacity and the reaction enthalpy of the reaction type j, and their expressions are given in the Appendix A.

The heat transfer from the heat source outside the tube to the reaction mixture inside the tube follows Newtonian heat transfer law:

$$J_q = U(T_w - T) \tag{10}$$

For different reaction conditions and mechanisms, the driving force in the kinetic equation could be written as different mathematical forms, and the corresponding coefficients in the kinetic equation should be determined by experiments and also be different for different choices of the driving force. According to Ref. [1], the condition that the chemical reaction occurred at the vicinity of the equilibrium is assumed to be satisfied, and all components are assumed to have stoichiometric reaction order, so the chemical reaction rates of reaction types (I) and (II) are as follows:

$$r_1 = k_1 \left(P_{H_2SO_4} - \frac{P_{H_2O} P_{SO_3}}{K_1} \right) \tag{11}$$

$$r_2 = k_2 \left(P_{SO_3} - \frac{P_{SO_2} \sqrt{P_{O_2}}}{K_2} \right) \tag{12}$$

where k_1 and k_2 are the reaction rate constants of reaction types (I) and (II), according to Ref. [1], $k_1 = 10^{-3} \mathrm{mol}(SO_3)/(\mathrm{Pa \cdot m^3 \cdot s})$, $k_2 = 4.7 \times 10^{-3} \exp^{\left(\frac{-99 \cdot 10^3}{RT}\right)} \mathrm{mol}(SO_3)/(\mathrm{Pa \cdot kg \cdot s})$; P represents the partial pressure of the corresponding component; $K_j = \exp\left(\frac{\Delta_r G^{\circ}_{T,j}}{-RT} \right)$ is the equilibrium constant of the chemical reaction type j; $\Delta_r G^{\circ}_{T,j}$ is the standard Gibbs free enthalpy of the reaction type j, and the expression is given in the Appendix A. The driving force in the kinetic Equation (12) is written as $r_2 = k_2 \left(P_{SO_3} - P_{SO_2} \sqrt{P_{O_2}} / K_2 \right)$, and effects of the different forms of the driving force on the optimization results will be considered in another paper in the future.

The SO_2 yield of the tubular plug-flow reactor is as follows:

$$\Delta F_{SO_2} = F_{SO_2,out} - F_{SO_2,in} \tag{13}$$

The local EGR of the tubular plug-flow reactor is as follows:

$$\begin{aligned}\sigma_{\mathrm{tot}} &= \sigma_{\mathrm{ht}} + \sigma_{\mathrm{f}} + \sigma_{\mathrm{cr}} \\ &= \pi D J_{\mathrm{q}}\left(\tfrac{1}{T} - \tfrac{1}{T_{\mathrm{w}}}\right) + A_{\mathrm{c}} \mathrm{v}\left[-\tfrac{1}{T}\left(\tfrac{\mathrm{d}P}{\mathrm{d}z}\right)\right] + A_{\mathrm{c}}\rho_{\mathrm{b}} \sum_j r_{m,j}\left(-\tfrac{\Delta_r G_j}{T}\right)\end{aligned} \tag{14}$$

where subscripts ht, f, and cr represent the local EGRs of heat transfer, fluid flow, and chemical reaction, respectively.

The total EGR is obtained by integrating the local EGR, i.e.,

$$\Sigma_{tot} = \int_0^L \sigma_{tot} dz \tag{15}$$

3. Parameter Analyses of Sulfuric Acid Decomposition Reactor

By changing the inlet parameters of the reference reactor, including the inlet temperature T_{in}, pressure P_{in} and the total molar flow rate $F_{\mathrm{tot,in}}$, the total EGR and the SO_2 yield of the reference reactor are analyzed, and the influences of the initial inlet conditions on the two performance objectives can be obtained. The variation ranges of the initial inlet parameters are: 750 K $\leq T_{\mathrm{in}} \leq$ 900 K, 4 MPa $\leq P_{\mathrm{in}} \leq$ 9.5 MPa, and 0.0027 mol/s $\leq F_{\mathrm{tot,in}} \leq$ 0.1 mol/s.

Figure 3 shows the effects of the temperature T_{in} of the reaction mixture on the total EGR and the SO_2 yield. It can be seen that the total EGR decreases nonlinearly with the increase of the temperature T_{in}, and the decreasing trend is fast firstly and then slow; when the temperature T_{in} increases from 750 °C to 900 °C, the total EGR decreases from 0.331 W/K to 0.189 W/K, i.e., decreases by 43%. The main reason is that with the temperature T_{in} of the reaction mixture increases, the heat transfer temperature difference between the reaction mixture and the external heat source decreases, which reduces the local EGR of heat transfer and the total EGR. The SO_2 yield increases very slowly with the increase of the temperature T_{in}, and when the temperature T_{in} increases from 750 °C to 900 °C, the SO_2 yield increases by only 0.4%. It can be seen that the total EGR can be reduced by increasing the temperature T_{in} of the reaction mixture, i.e., the irreversibility of the sulfuric acid decomposition process could be reduced by increasing the T_{in} of the reaction mixture. However, it is not significant to increase the SO_2 yield by increasing the temperature T_{in} of the reaction mixture.

Figure 4 shows the effects of the pressure P_{in} of the reaction mixture on the total EGR and the SO_2 yield. It can be seen that the curve of the total EGR is concave and parabolic-like with the increase of the pressure P_{in}, and the minimum value is 0.224 W/K when the pressure P_{in} is about 0.85 MPa. The SO_2 yield decreases linearly with the increase of the pressure P_{in}. When the pressure P_{in} increases from 0.4 MPa to 1 MPa, the SO_2 yield decreases from 0.0118 mol/s to 0.0105 mol/s, i.e., decreases by 11.02%.

Figure 5 shows the effects of the molar flow rate $F_{\mathrm{tot,in}}$ of the reaction mixture on the total EGR and the SO_2 yield. It can be seen that the total EGR and the SO_2 yield increase with the increase of the molar flow rate $F_{\mathrm{tot,in}}$, and the minimum total EGR and the maximum SO_2 yield are mutually restricted. When the molar flow rate $F_{\mathrm{tot,in}}$ increases from 0.027 mol/s to 0.10 mol/s, the total EGR and the SO_2 yield increases by 4.8 times and 1.8 times, respectively.

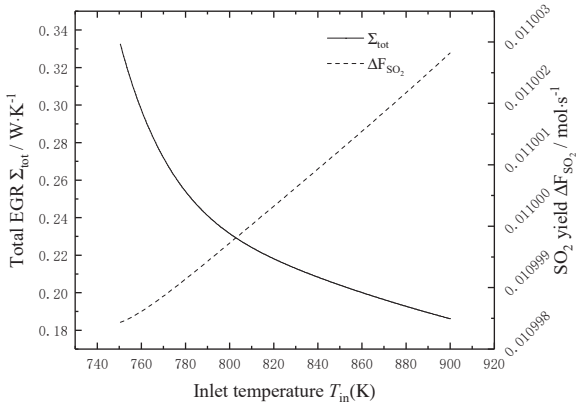

Figure 3. The effects of T_{in} on the total EGR and the SO_2 yield.

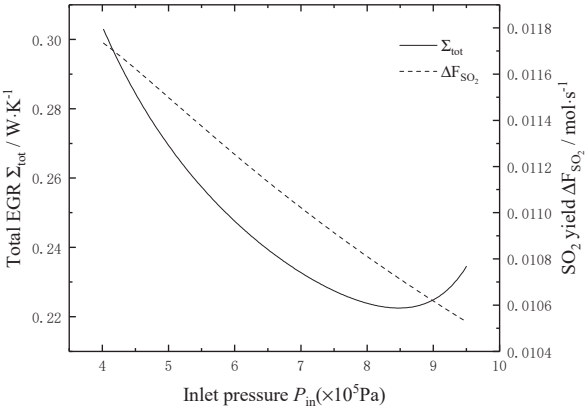

Figure 4. Effects of P_{in} on the total EGR and the SO_2 yield.

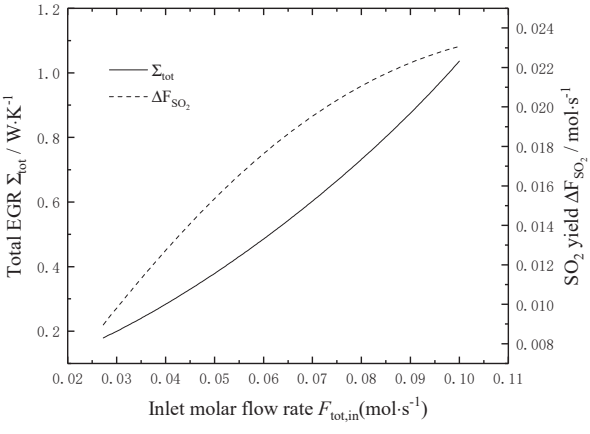

Figure 5. Effects of $F_{tot,in}$ on the total EGR and the SO_2 yield.

4. Multi-Objective Optimization and Result Analyses

From the analyses in Section 3, when the three inlet parameters are chosen as optimization variables, and the minimum total EGR and the maximum SO_2 yield are taken as optimization objectives, respectively, there is no optimal solution to achieve the extremum values of the total EGR and SO_2 yield at the same time. Therefore, how to select the appropriate initial inlet conditions to achieve the relative optimal total EGR and SO_2 yield is very important. The NSGA-II algorithm is one of the excellent algorithms to solve multi-objective optimization problems, and can give a series of non-inferior solutions (solutions that cannot be optimized for arbitrary objectives without making other objectives worse) of multi-objective problems. The corresponding improvement process is called Pareto improvement, the corresponding set of non-inferior solutions is called the Pareto-optimal solution set, and the corresponding objective function solution is called the Pareto-optimal front.

Figure 6 shows the flow chart of the NSGA-II algorithm. In this section, all of the T_{in}, P_{in} and $F_{tot,in}$ are taken as the optimization variables to minimize the total EGR and maximize the SO_2 yield. The optimization intervals of the variables are consistent with the previous single-variable analysis.

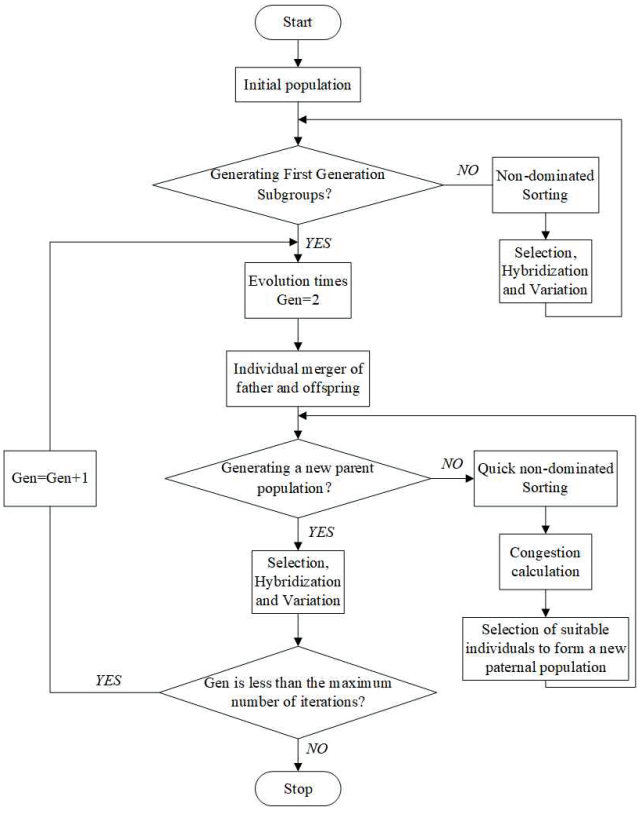

Figure 6. Basic flow chart of NSGA-II algorithm.

Figure 7 is Pareto optimal frontier of a reference reactor based on the objective of minimizing total EGR and maximizing SO_2 yield, where points A and B represent the solution of the maximum SO2 yield and the minimum total EGR, respectively. At point A, the weighting coefficient of SO_2 yield in multi-objective optimization is 1, and the weighting coefficient of total EGR is 0, it is also the solution of maximizing the SO_2 yield. Similarly, point B is the solution of minimizing the total

EGR. From Figure 7, it can be seen that the minimum total EGR and the maximum SO_2 yield are mutually constrained, and they cannot achieve the extremum values at the same time. Only the relative optimal solutions of the two objectives under different weighting coefficients can be found, that is, the non-inferior solution. One can select the appropriate optimal solution from the Pareto-optimal solution set according to different needs to meet the different demands of decision-making purposes. Commonly used multi-objective decision-making methods are Shannon, LINMAP, and TOPSIS, but in the actual decision-making process, decision-making is usually based on actual engineering experience and personal preferences of decision-makers, there is no universal way to make decisions.

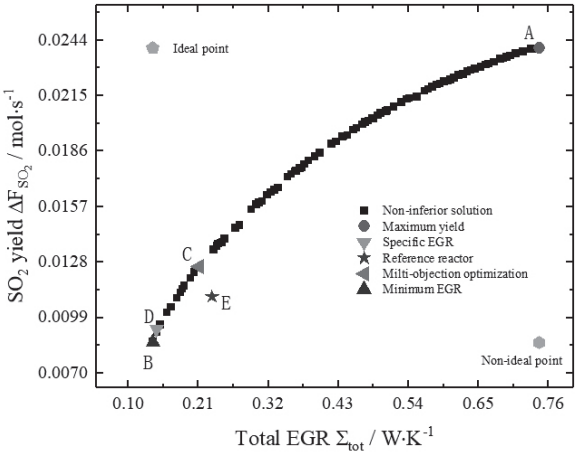

Figure 7. Pareto optimal frontiers of reference reactor.

In this paper, in order to facilitate the comparison with the reference reactor, a suitable multi-objective decision point (point C) is selected for comparison. Because the solution of the minimum specific EGRs is the solution of the total EGR and the yield under a certain ratio, the decision point of the minimum specific EGR must be on the Pareto-optimal front, which can be used as an important basis to verify the accuracy of the NSGA-II algorithm results.

Figure 8 is the bar chart of the target value of the reference reactor under optimization and non-optimization. Table 2 lists the results of each optimization target condition. It can be seen that compared with the reference reactor, the SO_2 yield of the reactor with the maximum yield increases by 118%, but the total EGR increases by 222%; the total EGR of the minimum EGR reactor decreases by 40%, and the corresponding SO_2 yield also decreased by 22%; the total EGR and the SO_2 yield of the reactor with the minimum specific EGR decrease by 38% and 16%, respectively. From Figure 7, it can be easily concluded that the reference reactor is not located at the Pareto optimal frontier, so the reference reactor can be optimized by Pareto improvement. A non-inferior solution (point C) is obtained by the multi-objective optimization method, in which the total EGR of the reactor decreases by 9% and the SO_2 yield of the reactor increases by 14% compared to the reference reactor. Also, from Figure 7, it can be seen that a series of non-inferior solutions located at the upper left of the decision point (point E) of the reactor have good properties of reducing the total EGR and increasing the SO_2 yield.

Figures 9–11 show the distribution of the T_{in}, P_{in} and $F_{tot,in}$ in Pareto-optimal fronts, and the black and white dots in the figures represent the total EGR and the SO_2 yield, respectively, which exist in pairs. As seen from Figures 9 and 10, the T_{in} and P_{in} of the reaction mixture in Pareto-optimal fronts are mainly distributed in high-temperature (892–896 K) and high-pressure (9.0–9.2 bar) area, so increasing the T_{in} and P_{in} of the reaction mixture is an important means for Pareto improvement. Figure 11 shows that the $F_{tot,in}$ of the reaction mixture in Pareto-optimal fronts distributes uniformly in

its optimal range, which indicates that adjusting the $F_{tot,in}$ of the reaction mixture in Pareto-optimal fronts is an important means to reconcile the contradiction between the minimum total EGR and the maximum SO_2 yield.

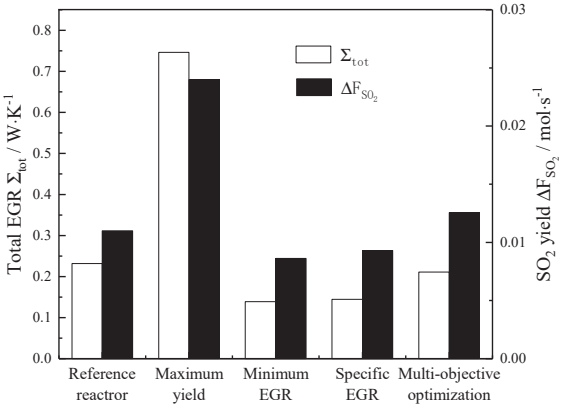

Figure 8. Comparison of total EGR and the yield of optimized objectives.

Table 2. Calculation results of each target.

	Reactor Inlet Parameters			EGR		SO_2 Yield	
	Temperature T_{in}(K)	Pressure P_{in}(1×10^5Pa)	Molar Rate $F_{tot,in}$(mol·s^{-1})	Σ_{tot}/W·K^{-1}		ΔF_{SO_2}/mol·s^{-1}	
Reference reactor	800	7.10	0.034	0.2316	——	0.01100	——
Maximum yield	896	8.97	0.010	0.7450	↑ 222%	0.02395	↑ 118%
Minimum EGR	893	8.69	0.027	0.1388	↓ 40%	0.00862	↓ 22%
Specific EGR	900	8.62	0.030	0.1446	↓ 38%	0.00930	↓ 16%
Multi-objective optimization	894	9.18	0.041	0.2111	↓ 9%	0.01256	↑ 14%

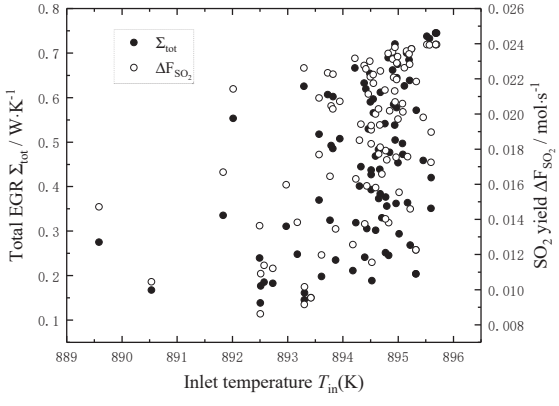

Figure 9. Distribution of inlet temperature in Pareto-optimal fronts.

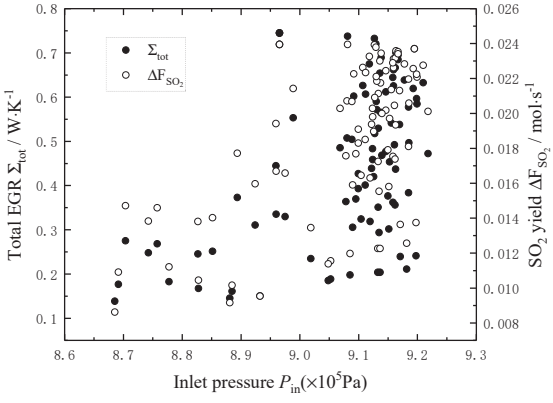

Figure 10. Distribution of inlet pressure in Pareto-optimal fronts.

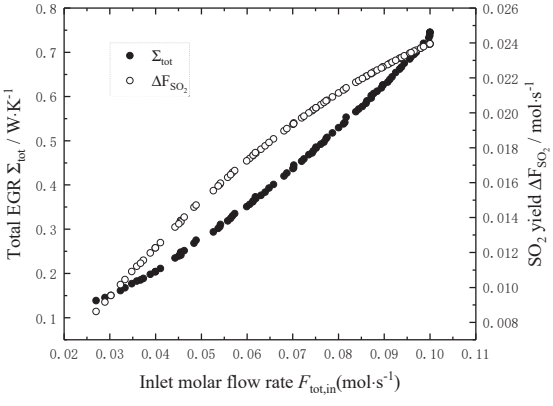

Figure 11. Distribution of total inlet molar flow rate in Pareto-optimal fronts.

5. Conclusions

In this paper, the effects of reaction mixture inlet parameters on the total EGR and SO_2 yield of the tubular plug-flow sulfuric acid decomposition reactor are analyzed, and the multi-objective optimization for the two performance objectives are carried out by using FTT. The results show that:

(1) When the T_{in} increases from 750 °C to 900 °C, the total EGR decreases by 43% and the SO_2 yield increases by 0.4%. When the P_{in} increases from 0.4 MPa to 1 MPa, the curve of the total EGR versus the P_{in} is a concave parabolic-like, the minimum value of the total EGR is 0.224 W/K when the P_{in} equals to 0.85 MPa, and the corresponding SO_2 yield decreases by 11%. When the $F_{tot,in}$ increases from 0.027mol/s to 0.10mol/s, the total EGR and the SO_2 yield increase by 4.8 times and 1.8 times, respectively.

(2) The reference reactor can be Pareto improvement, one of the non-inferior solutions can reduce the total EGR by 9% and increase the SO_2 yield by 14% compared to those of the reference reactor.

(3) FTT is a powerful theoretical tool for the performance analysis and optimization of tubular plug-flow sulfuric acid decomposition reactor. The NSGA-II algorithm is an effective mathematical tool for the multi-objective optimization of tubular plug-flow sulfuric acid decomposition reactor. The Pareto-optimal fronts obtained in this paper has a certain theoretical guiding significance for the optimal designs of the actual sulfuric acid decomposition reactors.

Author Contributions: Conceptualization, M.S., S.X. and L.C.; Funding acquisition, S.X.; Methodology, M.S., S.X. and L.C.; Software, M.S., C.W. and C.T.; Supervision, L.C.; Validation, M.S. and C.T.; Writing—original draft, M.S. and S.X.; Writing—review & editing, L.C. All authors have read and agreed to the published version of the manuscript.

Funding: This research was funded by National Natural Science Foundation of China (Grant Nos. 51976235) and 51606218) and the Hubei Province Natural Science Foundation of China (Grant No, 2018CFB708).

Acknowledgments: The authors wish to thank the Academic Editor and reviewers for their careful, unbiased and constructive suggestions, which led to this revised manuscript.

Conflicts of Interest: The authors declare no conflict of interest.

Nomenclature

A	area m^2
C_P	molar constant-pressure heat capacity, KJ/(mol·K)
D_p	catalyst pellet diameter, m
F	molar flow rate, mol/s
J_q	heat flux density, W/m^2
K	equilibrium constant
L	length, m
P	pressure, bar
R	universal gas constant, J/(mol·K)
r	reaction rate, mol/(kg·s)
T	temperature, K
v	flow velocity, m/s
z	length, m
Greek letters	
ε	catalyst bed porosity
η	dynamic viscosity, kg/(m·s)
κ	rate constant of chemical reaction
ν_i	the stoichiometric number of reaction component i
ρ	density, $kg{\cdot}m^{-3}$
σ	local EGR, J/K
Σ	total
$\Delta_r G$	Gibbs free energy change of chemical reaction, J
$\Delta_r H$	enthalpy change of chemical reaction, J
Subscripts	
c	cross section of tubular plug-flow reactor
cr	chemical reaction
f	fluid flow
ht	heat transfer
i	component
in	inlet
j	reaction types (I) and (II)
out	outlet
p	catalyst pellet
q	quantity of heat
r	reaction
tot	total
w	wall of tubular plug-flow reactor
Abbreviations	
EGR	entropy generation rate
FTT	finite-time thermodynamics
H-S	hybrid-Sulphur thermochemical cycle
NSGA-II	second generation non-dominated solution sequencing genetic algorithm
S-I	sulphur-Iodine thermochemical cycle

Appendix A

According to the Refs. [31], the component molar constant-pressure heat capacity, molar enthalpy and molar Gibbs energy can be calculated by the following formula:

$$C^{\circ}_{p,i} = A_i + B_i\frac{T}{1000} + C_i\left(\frac{T}{1000}\right)^2 + D_i\left(\frac{T}{1000}\right)^3 + E_i\left(\frac{1000}{T}\right)^2 \tag{A1}$$

$$H^{\circ}_{T,i} = A_i\frac{T}{1000} + \frac{B_i}{2}\left(\frac{T}{1000}\right)^2 + \frac{C_i}{3}\left(\frac{T}{1000}\right)^3 + \frac{D_i}{4}\left(\frac{T}{1000}\right)^4 - E_i\left(\frac{1000}{T}\right) + F_i \tag{A2}$$

$$S^{\circ}_{T,i} = A_i In\left(\frac{T}{1000}\right) + B_i\frac{T}{1000} + \frac{C_i}{2}\left(\frac{T}{1000}\right)^2 + \frac{D_i}{3}\left(\frac{T}{1000}\right)^3 - \frac{E_i}{2}\left(\frac{1000}{T}\right)^2 + G_i \tag{A3}$$

$$\Delta_r H^{\circ}_T = \sum_i v_i H^{\circ}_{T,i} \tag{A4}$$

$$\Delta_r S^{\circ}_T = \sum_i v_i S^{\circ}_{T,i} \tag{A5}$$

$$\Delta_r G^{\circ}_T = \Delta_r H^{\circ}_T - T\Delta_r S^{\circ}_T \tag{A6}$$

where A_i~G_i are the thermodynamic coefficients of the formula, which are listed in Table A1; v_i is the stoichiometric number of reaction component i.

Table A1. Thermodynamic coefficients.

Gas	$M_{W,i}$/kg·mol^{-1}	A_i	B_i	C_i	D_i	E_i	F_i	G_i	T_{min}/K	T_{max}/K
SO_2	6.40×10^{-2}	21.430	74.351	−57.752	16.355	0.087	−305.769	254.887	298	1200
O_2	3.20×10^{-2}	29.659	6.137	−1.187	0.096	−0.220	−9.861	237.948	298	6000
SO_3	8.01×10^{-2}	24.025	119.461	−94.387	26.926	−0.118	−407.853	253.51	298	1200
H_2O	1.80×10^{-2}	30.092	6.833	6.793	−2.534	0.082	−250.881	223.397	500	1700
H_2SO_4	9.81×10^{-2}	47.289	190.331	−148.123	43.868	−0.740	−758.953	301.296	298	1200

References

1. Van der Ham, L.V. Minimising Entropy Production in a H_2SO_4 Decomposer for the Thermochemical Production of H_2 from H_2O. Master's Thesis, Delft University of Technology, Delft, Norway, 2008.
2. Kuchi, G.; Ponyavin, V.; Chen, Y. Numerical modeling of high-temperature shell-and-tube heat exchanger and chemical decomposer for hydrogen production. *Int. J. Hydrog. Energy* **2008**, *33*, 5460–5468. [CrossRef]
3. Ponyavin, V.; Chen, Y.; Mohamed, T. Parametric study of sulfuric acid decomposer for hydrogen production. *Prog. Nucl. Energy* **2008**, *50*, 427–433. [CrossRef]
4. Van der Ham, L.V.; Gross, J.; Verkooijen, A. Efficient conversion of thermal energy into hydrogen: Comparing two methods to reduce exergy losses in a sulfuric acid decomposition reactor. *Ind. Eng. Chem. Res.* **2009**, *48*, 8500–8507. [CrossRef]
5. Wang, C.; Chen, L.G.; Xia, S.J.; Sun, F.R. Maximum production rate optimization for sulphuric acid decomposition process in tubular plug-flow reactor. *Energy* **2016**, *99*, 152–158. [CrossRef]
6. Wang, C.; Xia, S.J.; Chen, L.G.; Ge, Y.L.; Zhang, L.; Feng, H.R. Effects of design parameters on entropy generation rate of sulphuric acid decomposition process. *Int. J. Ambient Energy* **2020**, *41*. [CrossRef]
7. Andresen, B.; Berry, R.S.; Ondrechen, M.J.; Salamon, P. Thermodynamics for processes in finite time. *Acc. Chem. Res.* **1984**, *17*, 266–271. [CrossRef]
8. Bejan, A. Entropy generation minimization: The new thermodynamics of finite-size devices and finite-time processes. *J. Appl. Phys.* **1996**, *79*, 1191–1218. [CrossRef]
9. Chen, L.G.; Wu, C.; Sun, F.R. Finite time thermodynamic optimization or entropy generation minimization of energy systems. *J. Non-Equilib. Thermodyn.* **1999**, *24*, 327–359. [CrossRef]
10. Berry, R.S.; Kazakov, V.A.; Sieniutycz, S.; Szwast, Z.; Tsirlin, A.M. *Thermodynamic Optimization of Finite Time Processes*; Wiley: Chichester, UK, 1999.
11. Chen, L.G. *Finite-Time Thermodynamic Analysis of Irreversible Processes and Cycles*; Higher Education Press: Beijing, China, 2005.

12. Andresen, B. Current trends in finite-time thermodynamics. *Angew. Chem. Int. Edition.* **2011**, *50*, 2690–2704. [CrossRef]
13. Roach, T.N.F.; Salamon, P.; Nulton, J.; Andresen, B.; Felts, B.; Haas, A.; Calhoun, S.; Robinett, N.; Rohwer, F. Application of finite-time and control thermodynamics to biological processes at multiple scales. *J. Non-Equilibr. Thermodyn.* **2018**, *43*, 193–210. [CrossRef]
14. Gonzalez-Ayala, J.; Santillán, M.; Santos, M.J.; Calvo-Hernández, A.; Roco, J.M.M. Optimization and stability of heat engines: The role of entropy evolution. *Entropy* **2018**, *20*, 865. [CrossRef]
15. Fontaine, K.; Yasunaga, T.; Ikegami, Y. OTEC maximum net power output using Carnot cycle and application to simplify heat exchanger selection. *Entropy* **2019**, *21*, 1143. [CrossRef]
16. Feidt, M.; Costea, M. Progress in Carnot and Chambadal modeling of thermomechnical engine by considering entropy and heat transfer entropy. *Entropy* **2019**, *21*, 1232. [CrossRef]
17. Masser, R.; Hoffmann, K.H. Dissipative endoreversible engine with given efficiency. *Entropy* **2019**, *21*, 1117. [CrossRef]
18. Dumitrascu, G.; Feidt, M.; Popescu, A.; Grigorean, S. Endoreversible trigeneration cycle design based on finite physical dimensions thermodynamics. *Energies* **2019**, *12*, 3165.
19. Yasunaga, T.; Ikegami, Y. Finite-time thermodynamic model for evaluating heat engines in ocean thermal energy conversion. *Entropy* **2020**, *22*, 211. [CrossRef]
20. Masser, R.; Hoffmann, K.H. Endoreversible modeling of a hydraulic recuperation system. *Entropy* **2020**, *22*, 383. [CrossRef]
21. De Vos, A. Endoreversible models for the thermodynamics of computing. *Entropy* **2020**, *22*, 660. [CrossRef]
22. Masser, R.; Khodja, A.; Scheunert, M.; Schwalbe, K.; Fischer, A.; Paul, R.; Hoffmann, K.H. Optimized piston motion for an alpha-type Stirling engine. *Entropy* **2020**, *22*, 700. [CrossRef]
23. Wang, C.; Chen, L.G.; Xia, S.J.; Sun, F.R. Optimal concentration configuration of consecutive chemical reaction $A \Leftrightarrow B \Leftrightarrow C$ for minimum entropy generation. *J. Non-Equili. Thermodyn.* **2016**, *41*, 313–326. [CrossRef]
24. Johannessen, E.; Kjelstrup, S. Minimum entropy production rate in plug flow reactors: An optimal control problem solved for SO_2 oxidation. *Energy* **2004**, *29*, 2403–2423. [CrossRef]
25. Yang, H.Z.; Wen, J.; Wang, S.M.; Li, Y.Z. Thermal design and optimization of plate-fin heat exchangers based global sensitivity analysis and NSGA-II algorithm. *Appl. Thermal Eng.* **2018**, *136*, 444–453. [CrossRef]
26. Mann, G.W.; Eckels, S. Multi-objective heat transfer optimization of 2D helical micro-fins using NSGA-II algorithm. *Int. J. Heat Mass Transf.* **2019**, *132*, 1250–1261. [CrossRef]
27. Valencia, G.; Núñez, J.; Duarte, J. Multi-objective optimization of a plate heat exchanger in a waste heat recovery organic Rankine cycle system for natural gas engines. *Entropy* **2019**, *21*, 655. [CrossRef]
28. Zhang, L.; Chen, L.G.; Xia, S.K.; Ge, Y.L.; Wang, C.; Feng, H.J. Multi-objective optimization for helium-heated reverse water gas shift reactor by using NSGA-II. *Int. J. Heat Mass Transf.* **2020**, *148*, 119025. [CrossRef]
29. Tang, C.Q.; Feng, H.J.; Chen, L.G.; Wang, W.H. Power density analysis and multi- objective optimization for a modified endoreversible simple closed Brayton cycle with one isothermal heat process. *Energy Rep.* **2020**, *6*, 1648–1657. [CrossRef]
30. Wu, Z.X.; Feng, H.J.; Chen, L.G.; Ge, Y.L. Performance optimization of a condenser in ocean thermal energy conversion (OTEC) system based on constructal theory and multi-objective genetic algorithm. *Entropy* **2020**, *22*, 641. [CrossRef]
31. NIST Chemistry WebBook, NIST Standard Reference Database Number 69. June 2005. Available online: http://webbook.nist.gov/chemistry/ (accessed on 4 April 2020).

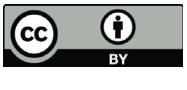

entropy

MDPI

Perspective

Use and Abuse of Entropy in Biology: A Case for Caliber

Ty N. F. Roach

Hawai'i Institute of Marine Biology, University of Hawai'i at Mānoa, Kāne'ohe, HI 96744, USA; smokinroachjr@gmail.com

Received: 7 October 2020; Accepted: 19 November 2020; Published: 25 November 2020

Abstract: Here, I discuss entropy and its use as a tool in fields of biology such as bioenergetics, ecology, and evolutionary biology. Statistical entropy concepts including Shannon's diversity, configurational entropy, and informational entropy are discussed in connection to their use in describing the diversity, heterogeneity, and spatial patterning of biological systems. The use of entropy as a measure of biological complexity is also discussed, and I explore the extension of thermodynamic entropy principles to open, nonequilibrium systems operating in finite time. I conclude with suggestions for use of caliber, a metric similar to entropy but for time-dependent trajectories rather than static distributions, and propose the complementary notion of path information.

Keywords: biophysics; biochemistry; dynamical systems; diversity; complexity; path information

1. Introduction

Entropy principles have been used to describe biological patterns and processes at a range of scales [1]. Perhaps the most well-known use of entropy in biology stems from the use of Shannon's entropy (H) [2] to describe the diversity of an ecological community. Entropy has also been used in ecology to describe spatial patterning [3] and interconnectedness of organisms in systems [4]. In evolutionary biology, entropy principles have been used to describe the irreversible change of systems through time [5] and to quantify the organization and complexity of populations and communities [6,7]. Other uses include quantifying the thermal efficiency of organismal metabolism [8,9] and creating orientors for in silico models [10,11]. Herein, I review the general uses and misuses of entropy methods in biology and discuss other, more process-focused methods such as caliber and path information.

2. Uses of Entropy in Biology

In classical thermodynamics, entropy (S) is an extensive state variable (i.e., a state variable that changes proportionally as the size of the system changes, and is thus additive for subsystems,) which describes the relationship between the heat flow (δQ) and the temperature (T) of a system. Mathematically denoted, the relationship is $dS = \delta Q/T$. This formalism of entropy and Clausius's statement of the second law of thermodynamics led to the interpretation of entropy as a measure of unavailability (i.e., entropy as a measure of the energy dispersed as heat, which cannot perform work at a given temperature). It is also this formalism which has allowed for entropy production as a measure of spontaneity, unidirectionality, and dissipation. This formalism has proven particularly useful in biology for measuring the energy dissipation and thermodynamic efficiency in biological systems including cells, organisms, and ecosystems [8,9,12,13].

The direct relationship of entropy to temperature and heat allows for the precise calculations of entropy production in systems via calorimetry and spectroscopy. These methods have proven quite valuable as a means to collect data on energetics and entropy production in biological

systems, and improvements in resolution and accuracy in both technologies continue to advance bioenergetics research.

2.1. Statistical Entropy

The thermodynamic entropy function proposed by Clausius was extended to the field of statistical mechanics by Boltzmann with the introduction of statistical entropy [14]. In Boltzmann's formalism, entropy is a measure of the number of possible microscopic states (or microstates) of a system in thermodynamic equilibrium, consistent with its macroscopic thermodynamic properties (or macrostate). Thus, the popular expression of entropy as $S = k_B ln\Omega$, where Ω is the number of microstates consistent with the equilibrium macrostate and k_B is a constant, which serves to keep entropy in the units of heat capacity (i.e., Joules·Kelvin^{-1}). Gibbs extended Boltzmann's analysis of a single multiparticle system to the analysis of an ensemble of infinitely many copies of the same system, demonstrating that the entropy of a system is related to the probability of being in a given microstate during the system's fluctuations (p_i), and resulting in the well-known Gibbs entropy equation:

$$S = -k_B \sum_i p_i \ln p_i \tag{1}$$

It is notable that the Gibbs entropy less the Boltzmann constant is identical to the Shannon entropy (H) where

$$H = -\sum_{i=1}^{n} p_i \log p_i \tag{2}$$

As the Gibbs entropy approaches the Clausius entropy in the thermodynamic limit, this interesting link between Shannon's entropy and thermodynamic entropy has often led to misinterpretations of the second law of thermodynamics in biological systems (e.g., the postulation of macroscopic second laws acting at the scale of organisms and ecosystems). However, it is this same link that has made possible the idea of information engines (e.g., [15,16]) and has allowed for use of entropy concepts in many systems far removed from the heat engine (e.g., chemical systems, electrical systems, biological systems).

In biology, perhaps the most well-known application of entropy is the use of Shannon's entropy as a measure of diversity [17,18]. More precisely, the Shannon entropy of a biological community describes the distribution of individuals (these could be individual biomolecules, genes, cells, organism, or populations) into distinct states (these states could be different types of molecules, types of cells, species of organism, etc.). The Shannon entropy normalized by the richness (i.e., the number of states) yields another diversity metric known as evenness [19–21], which is typically interpreted as a measure of how similar the abundances of different states are.

Beyond allowing for the calculation of diversity, entropy concepts have also been quite useful as a metric to quantify the organization, complexity, and order of biological systems. Often, this is accomplished by comparing the entropy of the system to the system's maximum entropy (i.e., the entropy of the system without the informational constraints of history) to estimate its departure from maximum homogeneity and randomness [7]. By extending entropy-based biodiversity and complexity measures into spatially explicit landscapes, the field of landscape ecology has made particular use of entropy methods to describe spatial and topological patterning at different scales. Recent advances in the field have made use of more generalized statistical entropy formulations such as Renyi's entropy [22] and generalized Boltzmann entropy for landscape mosaics and landscape gradients [23,24]. See *Entropy* Special Issue: *Entropy in Landscape Ecology* for other uses of entropy in this field [25].

2.2. Information

In the post-Shannon age, information (I) has been conceptualized as a form of negative entropy—that is to say that entropy is the information missing about a system, which would allow that same system to do work at a given temperature. To state it more explicitly, $I = -S$.

This relationship has allowed for many interesting applications of entropy methods to the informational content of biological systems (e.g., informational content in a single biomolecule, a genome, a metagenome). Several biologists have applied these information theoretic approaches to model ecological and evolutionary systems. Of particular note are the infodynamic formalisms proposed by Jeff Wicken [26–28], Stanley Salthe [29–31], and Robert Ulanowicz's concept of *ascendency* for the development and succession of ecological systems [32].

3. Abuse of Entropy in Biology

3.1. Entropy and Order

Despite the numerous uses of entropy concepts in biology, there has also been some confusion concerning entropy and its applications in the life sciences. One such issue is the interpretation of entropy as the disorder of a system. While entropy has often been taught in college chemistry and physics classes as synonymous with disorder, this is not actually the case. In fact, in many systems, order increases as a direct result of increasing entropy (e.g., [7]). This is because both order and disorder are functions of entropy [33]. The mathematical relationship between entropy (S) and disorder (D) is $D = S/S_{max}$. This leads to the complementary notion of order (O), where $O = 1 - S/S_{max}$, where S_{max} is the maximum entropy (i.e., the entropy the system would have if it were free of informational constraints). The misinterpretation of entropy as disorder has led some authors to assert that the increase in biological order observed through time in many systems is a violation of the second law of thermodynamics, which is simply wrong. This relationship between entropy and maximum entropy has been useful in the areas of complexity science and autopoiesis (the study of systems capable of maintaining and reproducing themselves) [34,35]. It should be noted that the relationship of entropy to notions of order, organization, and complexity all transform the extensivity of entropy into an intensive quantity by normalizing to some other variable. This emphasizes that these metrics, although derived from entropy, are not synonymous with entropy itself.

3.2. Entropy-Driven Systems

Another abuse of entropy in biology is the claim that biological systems are driven by entropy (or entropy production). This notion may have begun with Schrödinger's statement that life feeds off negative entropy [36]. However, just because entropy increases in spontaneous processes does not mean that entropy (or its production) is the ultimate thermodynamic driving force. In fact, only in the case of isolated systems does entropy alone determine the direction of thermodynamic equilibrium. For non-isolated systems such as biological systems, where there are flows of matter, energy, and entropy into and out of the systems, the movement of the system toward equilibrium is determined by both the maximization of entropy and the minimization of free energy. Only in isolated systems where internal energy (U) is held constant will entropy reach its maximum [37]. In the thermodynamic limit where systems undergo isentropic change (i.e., they change without production of entropy), equilibrium is only determined by the minimization of free energy. Thus, it is seen that non-isolated systems are driven by free energy flux or, more precisely, exergy flux. (Note: For those not familiar with exergy, it is the work that could be extracted in a process that reversibly brings a system to equilibrium with the environment. At constant environmental temperature and pressure, exergy change is equal to the change in free energy.) It is noted that biological systems increase the global entropy and dissipation by using free energy to create local entropy minima (i.e., building up local information and order). However, this increase in universal entropy (ΔS^U) is not the driving force in biological processes but is merely a requisite of the system operating in finite time. Thus, for biological systems, just as for heat engines, the entropy production is simply a byproduct due to dissipative processes such as friction and turbulence, which should be minimized insofar as the constraints of finite time and resources allow. Consequently, it is seen that biological systems are not selected to maximize dissipation and entropy

production, as is often claimed (e.g., [38]), but rather to minimize these quantities to perform work to ultimately survive and reproduce.

3.3. Mischaracterization of Biological Systems

Much of the confusion concerning the entropy-driven nature of biological systems stems from the mischaracterization of biological systems as isolated or closed systems (i.e., a system with no exchange of matter and/or energy). However, biological systems are not closed systems; rather, they are open to the exchange of both matter and energy. This means that they can create and maintain localized decreases in entropy by using exogenous sources of free energy and matter. It is by maintaining their localized entropy at lower levels than the surrounding environment that biological systems are able to build up information and order. This highlights the fact that biological systems must dissipate entropy into the surrounding environment to build up local order. Incorporating the role of the environment into thermodynamic studies emphasizes the ecological nature (i.e., the interconnectedness of multiple systems and subsystems to each other and to their physical surroundings) of biological systems and allows for a more complete systems view of biology.

Similar to the mischaracterization of biological systems as closed systems is the mischaracterization of biological systems as being at equilibrium. Almost by definition, living systems are not at equilibrium. Of course, some degrees of freedom may be at or near equilibrium; however, many degrees of freedom are actually quite far from thermodynamic equilibrium. The formalization of nonequilibrium approaches to open thermodynamic systems has allowed for better use of entropy principles in biology [39–42]. However, thermodynamic entropy (e.g., Clausius, Gibbs, and Boltzmann) is undefined in nonequilibrium states, as there is no well-defined temperature. This can be overcome with the use of von Neumann entropy, an extension of classical entropy to quantum mechanics. The von Neumann entropy can be calculated for any quantum state, equilibrium or otherwise, as $S = -tr(\rho\, ln\rho)$, where ρ is the density matrix describing the quantum state and tr is the trace of this matrix. Although von Neumann's formulation allows for the calculation of nonequilibrium entropy, it is still a state function. Thus, one can only infer the change in entropy in a system by comparing the difference in entropy between states. This serves to highlight that thermodynamics is not really dynamics at all; rather, it is a form of comparative statics (i.e., comparing the difference between states). However, many biologists are not interested in merely comparing states, but instead aim to understand the underlying dynamics of biological processes.

4. Caliber

To begin to shift biological thermodynamics from a state-focused form of comparative statics to process-focused dynamics, I propose the use of caliber concepts and methodologies. *Caliber* (*C*), also known as path entropy (a notion similar to Feynman's path integral formulation [43]), is a thermodynamic quantity that defines the distribution of flows over pathways in dynamical processes. Mathematically, this amounts to an entropy-like equation: $C = -\sum_i p_i ln p_i$, where the p_is here are the relative populations of flow paths [44]. This is contrary to the formulation of entropy where the p_is are relative populations of states, whereas for caliber the probabilities represent the distributions of dynamical trajectories between states. Thus, caliber is to dynamics as entropy is to comparative statics. Another way to say this is that while entropy provides a state-focused, equilibrium approach to problems, caliber provides a process-focused, nonequilibrium approach. As biological systems are inherently nonequilibrium dynamical systems, caliber provides a function, which may be better suited to accurately describe the processes occurring in cells, organisms, populations and ecosystems.

Maximum caliber approaches have been used to accurately predict dynamical distribution functions that characterize the relative probabilities of different microtrajectories, including so-called "bad actors" that contribute net motion in the direction opposite to the macroflux predicted by the second law of thermodynamics [45]. Furthermore, caliber approaches have been shown to be particularly useful in systems with a small number of individuals, where maximum caliber methods have been

used to successfully model autoactivation in single-gene circuits [46]. Caliber approaches have also been shown to work well in systems involving feedback mechanisms, such as the feedback produced by the changing fitness landscape topologies arising from ecological interactions in evolutionary systems [47]. In addition to being a more informative and accurate method for predicting trajectories in changing biological systems, maximum caliber methodologies are also more parsimonious than other methods involving master equations and mass action laws, as maximum caliber requires fewer model assumptions and parameters. Thus, generalizable stochastic models utilizing caliber may be the best approach to model biological processes, such as evolution and succession, based on thermodynamic principles. For more on caliber methods and their use in biology, see the review by Ghosh et al. [48]

5. Discussion

5.1. Connecting Caliber to Other Thermodynamic Quantities

Despite the seeming advantages of caliber approaches over entropy to describe nonequilibrium dynamical systems, there are still some advantages of using entropy for certain problems. One of the major advantages to entropy methods is the strong fundamental connection between entropy and other thermodynamic metrics such as heat, free energy, work, and efficiency. The relationship between these metrics and caliber is less well-defined in the existing literature and offers an area rich for further research.

5.2. Informed Pathways

The link between information and entropy demonstrates that local decreases in entropy essentially amount to local increases in information. These local accumulations of information represent constraints on specific degrees of freedom which allow for control of a system as it relaxes toward equilibrium. As the approach to equilibrium is inherently a dynamical process, I propose a complementary notion to caliber which I call *path information*. Path information serves to quantify the informational constraints, which limit the possible flow paths, and ultimately allow a system to extract work from flows of free energy through these informed pathways.

This is precisely how many biological systems function: they use free energy to locally decrease entropy (i.e., create informational constraints on the flow of free energy through the system) in order to perform work. In the case of organisms, these informational constraints include the information encoded in DNA sequences and complex biochemical modifications (e.g., methylation, ubiquitination, phosphorylation). At the biochemical level, these informed pathways can be seen in the form of enzymes and molecular motors which carefully control biochemical processes. It should be noted here that the flow of free energy through informed pathways to do work does not necessarily lead to entropy production; instead, it is the thermalization of free energy which causes entropy production. This highlights a major difference between the biological mechanism of energy use and many other technologies, such as the heat engine. Rather than converting chemical energy—"food"—to heat and then using that heat to do work as it flows to a cooler subsystem, biological pathways extract work in a nonthermal manner by carefully choregraphing molecular motions to better maximize their efficiency. The buildup of path information is what allows biology to extract work from flows of free energy in this manner and ultimately what determines the thermodynamic efficiency of biological processes. This emphasizes the fact that the efficiency of living systems—that is, the degree to which they can approach the thermodynamic limits—is a matter of engineering-informed energy flux pathways, not a matter of the available free energy quantity or quality.

The formulation of path information, much like entropy and caliber, has the potential to be used in both a physical, thermodynamic sense and in a macroscopic, descriptive manner. For example, path information can be used to define the relative flows of molecules through specific biochemical pathways and quantify how this relates to metabolic efficiency. At the macroscopic scale, path information could be useful to describe dynamical processes such as organismal migration,

epidemiological spread of pathogens, evolutionary gene flow, and trophic cascades. Other areas where path information formulations may prove particularly useful include hydrology, hydrodynamics, aerodynamics, and economics.

5.3. Ergodicity

Many authors have asserted that biological systems are ergodic (e.g., [49–51]). A system is ergodic if its dynamics sample phase space such that, in the long run, time averages over a single trajectory and ensemble averages over many independent trajectories yield the same result. Thus, it follows that in ergodic systems all accessible microstates are equiprobable over a long period of time and that long-term behaviors are essentially independent of initial conditions. However, this is most certainly not a characteristic of biological systems, which typically have strong signatures of history and initial conditions [52]. Furthermore, one cannot exchange space and time averages in biological systems. For one illustrative example at the microscopic scale, consider a circular, unidirectional process such as A→B→C→A in steady state. Many biochemical processes are exactly of this circular type—e.g., the buildup and breakdown of glycogen. Since this cycling of glycogen costs ATP for every cycle, there is no energetic equiprobability among the states, even though their numbers (concentrations) may remain constant. Thus, these systems are not an equilibrium ensemble and are not ergodic. This becomes even more blatantly obvious at the macroscale where ecological and evolutionary systems typically evolve to different forms over long time periods. Take, for example, the death of an organism. Once the organism has died, there is no chance of it spontaneously returning to the previous state of being alive. It should be noted here that, despite the claim of some authors, death is not synonymous with reaching equilibrium; although the organism's metabolism has stopped, the macromolecules contained in the biomass still have a relatively high energetic potential and will continue to be oxidized to lower and lower energetic states before being recycled and assimilated into new forms. Throughout all the stages of life, death, and decomposition, there is extraordinarily little chance of spontaneously returning to the previous phase space. The non-ergodicity of biological systems is even more conspicuous in the process of mass death, or extinction, in which whole groups of organisms are lost, and although similar organisms may eventually evolve, the return to the previous biological phase space is nearly infinitesimal (especially without energetic inputs). Therefore, it is noted that biological systems are strongly constrained by history and the arrow of time, which by definition makes them non-ergodic.

Some subset of ecological and evolutionary systems may explore only a small portion of their phase space over relatively short timescales, and in this sense may have local ergodic periods characterized by macroscopic stationary states. However, over long timescales, these systems typically evolve to search a new, small area of phase space. Thus, it is seen that biological systems at all scales are largely non-ergodic.

6. Conclusions

The applications of thermodynamics to biological systems have been largely focused on state functions (e.g., entropy). However, this approach does not allow for the observation of process dynamics that occur in biological systems. Thus, the dynamics are only inferred from comparative statics. To move forward, the field needs to shift from a state-based science to a process-based discipline. This will necessitate the explicit incorporation of time and rate dependency, which will require the integration of other branches of physics such as statistical mechanics and kinetics. Furthermore, the type of biological data collected will need to explicitly include time as a variable. Although some authors approach biological systems as ergodic [49–51], allowing for the exchange of space averages for time averages or vice versa, living systems are not actually ergodic. This means that temporally resolved data is needed to address path dependency and process functions. Utilizing nonequilibrium, process-focused metrics such as caliber and path information will allow better modeling of biological

processes and will give biologists a more complete and realistic understanding of the dynamics of living systems.

Funding: This research received no external funding.

Acknowledgments: Thanks to Mark Kozak and the Telluride Science Research Center for providing a venue for discussing new ideas concerning physics in biology. Thanks to Gintare Bielkinaite, Joel Huckeba, Forest Rohwer, and Carlo Caruso for reading of the manuscript and thoughtful discussion during the writing process. Lastly, but most certainly not least, thanks to the late R. Stephen Barry for providing the foundations of finite time thermodynamics, without which this and so many other valuable works would not have been possible.

Conflicts of Interest: The author declares no conflict of interest.

References

1. Roach, T.N.F.; Salamon, P.; Nulton, J.; Andresen, B.; Felts, B.; Haas, A.; Calhoun, S.; Robinett, N.; Rohwer, F. Application of Finite-Time and Control Thermodynamics to Biological Processes at Multiple Scales. *J. Non-Equilib. Thermodyn.* **2018**, *43*, 193–210. [CrossRef]
2. Shannon, C.E. A mathematical theory of communication. *Bell Syst. Tech. J.* **1948**, *27*, 379–423. [CrossRef]
3. Cushman, S. Calculation of Configurational Entropy in Complex Landscapes. *Entropy* **2018**, *20*, 298. [CrossRef]
4. Ulanowicz, R.E. *Growth and Development: Ecosystems Phenomenology*; Springer: Berlin, Germany, 2012.
5. Brooks, D.; Wiley, E. Evolution as an entropic phenomenon. In *Evolutionary Theory: Paths into the Future*; Wiley: Hoboken, NJ, USA, 1984.
6. Roach, T.N.F.; Nulton, J.; Sibani, P.; Rohwer, F.; Salamon, P. Entropy in the Tangled Nature Model of evolution. *Entropy* **2017**, *19*, 192. [CrossRef]
7. Roach, T.N.F.; Nulton, J.; Sibani, P.; Rohwer, F.; Salamon, P. Emergent structure in a stochastic model of ecological evolution. *Ecol. Model.* **2019**, *401*, 129–133. [CrossRef]
8. Roach, T.N.F.; Abieri, M.L.; George, E.E.; Knowles, B.; Naliboff, D.S.; Smurthwaite, C.A.; Kelly, L.W.; Haas, A.F.; Rohwer, F.L. Microbial bioenergetics of coral-algal interactions. *PeerJ* **2017**, *5*, e3423. [CrossRef]
9. Gnaiger, E. Physiological calorimetry: Heat flux, metabolic flux, entropy and power. *Thermochim. Acta* **1989**, *151*, 23–34. [CrossRef]
10. Ludovisi, A. Effectiveness of entropy-based functions in the analysis of ecosystem state and development. *Ecol. Indic.* **2014**, *36*, 617–623. [CrossRef]
11. Müller, F.; Leupelt, M. *Eco Targets, Goal Functions, and Orientors*; Springer: Berlin/Heidelberg, Germany, 1998.
12. Walsberg, G.; Hoffman, T. Direct calorimetry reveals large errors in respirometric estimates of energy expenditure. *J. Exp. Biol.* **2005**, *208*, 1035–1043. [CrossRef]
13. McLean, J.A.; Tobin, G. *Animal and Human Calorimetry*; Cambridge University Press: Cambridge, UK, 2007.
14. Boltzmann, L. *Vorlesungen über Gastheorie—I. Theil: Theorie des Gase mit Einatomigen Molekülen, deren Dimensionen Gegen die Mittlere Weglänge Verschwinden*; J.A. Barth: Leipzig, Germany, 1896; Volume 1.
15. Paneru, G.; Lee, D.Y.; Tlusty, T.; Pak, H.K. Lossless Brownian Information Engine. *Phys. Rev. Lett.* **2018**, *120*, 020601. [CrossRef]
16. Rana, S.; Jayannavar, A.M. A multipurpose information engine that can go beyond the Carnot limit. *J. Stat. Mech. Theory Exp.* **2016**, *2016*, 103207. [CrossRef]
17. Jost, L. Entropy and diversity. *Oikos* **2006**, *113*, 363–375. [CrossRef]
18. Simpson, E. Measurement of diversity. *Nature* **1949**, *163*, 688. [CrossRef]
19. Jost, L. The Relation between Evenness and Diversity. *Diversity* **2010**, *2*, 207–232. [CrossRef]
20. Mason, N.W.H.; Mouillot, D.; Lee, W.G.; Wilson, J.B. Functional richness, functional evenness and functional divergence: The primary components of functional diversity. *Oikos* **2005**, *111*, 112–118. [CrossRef]
21. Hill, M.O. Diversity and Evenness: A Unifying Notation and Its Consequences. *Ecology* **1973**, *54*, 427–432. [CrossRef]
22. Carranza, M.L.; Acosta, A.; Ricotta, C. Analyzing landscape diversity in time: The use of Rènyi's generalized entropy function. *Ecol. Indic.* **2007**, *7*, 505–510. [CrossRef]
23. Zhang, H.; Wu, Z.; Lan, T.; Chen, Y.; Gao, P. Calculating the Wasserstein Metric-Based Boltzmann Entropy of a Landscape Mosaic. *Entropy* **2020**, *22*, 381. [CrossRef]
24. Gao, P.; Li, Z. Computation of the Boltzmann entropy of a landscape: A review and a generalization. *Landsc. Ecol.* **2019**, *34*, 2183–2196. [CrossRef]

25. Cushman, S. Entropy in landscape ecology. *Entropy* **2018**, *20*, 314. [CrossRef]
26. Wicken, J.S. Information transformations in molecular evolution. *J. Theor. Biol.* **1978**, *72*, 191–204. [CrossRef]
27. Wicken, J. Entropy, information, and nonequilibrium evolution. *Syst. Zool.* **1983**, *32*, 438–443. [CrossRef]
28. Wicken, J. *Evolution, Information and Thermodynamics: Extending the Darwinian Program*; Oxford University Press: Oxford, UK, 1987.
29. Salthe, S.N. Ecology and infodynamics. *J. Soc. Evol. Syst.* **1998**, *21*, 223–231. [CrossRef]
30. Salthe, S.N. Infodynamics, a Developmental Framework for Ecology/Economics. *Conserv. Ecol.* **2003**, *7*, 3. [CrossRef]
31. Salthe, S.N. What is Infodynamics? In *Understanding Complexity*; Springer: Boston, MA, USA, 2001; pp. 31–38.
32. Ulanowicz, R.E. *Ecology, the Ascendent Perspective*; Columbia University Press: New York, NY, USA, 1997.
33. Landsberg, P.T. Can entropy and "order" increase together? *Phys. Lett. A* **1984**, *102*, 171–173. [CrossRef]
34. Varela, F.G.; Maturana, H.R.; Uribe, R. Autopoiesis: The Organization of Living Systems, lts Characterization and a Model. In *Facets of Systems Science*; International Federation for Systems Research International Series on Systems Science and Engineering; Springer: Boston, MA, USA, 1991; Volume 7, pp. 559–569.
35. Luisi, P.L. Autopoiesis: A review and a reappraisal. *Naturwissenschaften* **2003**, *90*, 49–59. [CrossRef]
36. Schrodinger, E. What Is Life? Cambridge University Press: Cambridge, UK, 1944.
37. Moore, W. *Basic Physical Chemistry*; Prentice Hall: Englewood Cliffs, NJ, USA, 1983.
38. Annila, A.; Salthe, S. Physical foundations of evolutionary theory. *J. Non-Equilib. Thermodyn.* **2010**, *35*, 301–321. [CrossRef]
39. Nicolis, G.; Prigogine, I. Fluctuations in Nonequilibrium Systems. *Proc. Natl. Acad. Sci. USA* **1971**, *68*, 2102–2107. [CrossRef]
40. Prigogine, I.; Nicolis, G. Biological order, structure and instabilities. *Q. Rev. Biophys.* **1971**, *4*, 107–148. [CrossRef]
41. Prigogine, I. *Introduction to Thermodynamics of Irreversible Processes*, 1st ed.; Charles C Thomas Publisher: Springfield, IL, USA, 1955.
42. Prigogine, I.; Nicolis, G.; Babloyantz, A. Thermodynamics of evolution. *Phys. Today* **1972**, *25*, 23–28. [CrossRef]
43. Feynman, R.P. Space-time approach to non-relativistic quantum mechanics. *Rev. Mod. Phys.* **1948**, *20*, 367–387. [CrossRef]
44. Jaynes, E.T. The Minimum Entropy Production Principle. *Annu. Rev. Phys. Chem.* **1980**, *31*, 579–601. [CrossRef]
45. Wu, D.; Ghosh, K.; Inamdar, M.; Lee, H.J.; Fraser, S.; Dill, K.; Phillips, R. Trajectory approach to two-state kinetics of single particles on sculpted energy landscapes. *Phys. Rev. Lett.* **2009**, *103*, 050603. [CrossRef]
46. Firman, T.; Balázsi, G.; Ghosh, K. Building predictive models of genetic circuits using the principle of maximum caliber. *Biophys. J.* **2017**, *113*, 2121–2130. [CrossRef] [PubMed]
47. Nevozhay, D.; Adams, R.M.; van Itallie, E.; Bennett, M.R.; Balázsi, G. Mapping the environmental fitness landscape of a synthetic gene circuit. *PLoS Comput. Biol.* **2012**, *8*, e1002480. [CrossRef] [PubMed]
48. Ghosh, K.; Dixit, P.D.; Agozzino, L.; Dill, K.A. The maximum caliber variational principle for nonequilibria. *Annu. Rev. Phys. Chem.* **2020**, *71*, 213–238. [CrossRef] [PubMed]
49. Rodríguez, R.A.; Delgado, J.D.; Herrera, A.M.; Riera, R.; Navarro, R.M.; Melián, C.; Dieguez, L.; Quirós, Á. Effects of two traits of the ecological state equation on our understanding of species coexistence and ecosystem services. *Ecol. Model.* **2013**, *265*, 1–13. [CrossRef]
50. Herrera, A.M.; Riera, R.; Rodríguez, R.A.; Santander, J.; Miranda, J.V.; Perdomo, M.E.; Quirós, Á.; Fath, B.D. From a stationary to a non-stationary ecological state equation: Adding a tool for ecological monitoring. *Ecol. Model.* **2016**, *320*, 44–51. [CrossRef]
51. Rodríguez, R.A.; Herrera, A.M.; Otto, R.; Delgado, J.D.; Fernández-Palacios, J.M.; Arévalo, J.R. Ecological state equation. *Ecol. Model.* **2012**, *224*, 18–24. [CrossRef]
52. Wiley, E.; Brooks, D. Victims of history—a nonequilibrium approach to evolution. *Syst. Biol.* **1982**, *31*, 1–24. [CrossRef]

entropy

MDPI

Article

Calorimetric Measurements of Biological Interactions and Their Relationships to Finite Time Thermodynamics Parameters

Yuwei Zhang and Gregory J. Kowalski *

Department of Mechanical and Industrial Engineering, Northeastern University, Boston, MA 02115, USA; zhang.yuwei@northeastern.edu

* Correspondence: gkowal@coe.neu.edu; Tel.: +1-508-423-4117

Abstract: A description and examination of the potential for calorimetry for use in exploring the entropy flows in biological and or reacting systems is presented. A calorimeter operation background is provided, and two case studies are investigated using a transient numerical simulation. The first case describes a single cell calorimeter containing a single phase material excited by heat generation source function such as joule heating. The second case is a reacting system. The basic observation parameter, the temperature, cannot be used to separate the entropy property changes and the rate of entropy production in the second case. The calculated transient response can be further analyzed to determine the equilibrium constant once the reaction equation and stoichiometric constants are specified which allows entropy property changes and the rate of entropy production to be determined. In a biological community, the equivalent of the reaction equation and a definition of an equilibrium constant are not available for all systems. The results for the two cases illustrate that using calorimetry measurements to identify the entropy flows in biological community activities requires further work to establish a framework similar to that chemical reacting systems that are based on an equilibrium type parameter.

Keywords: calorimetry; entropy flow; entropy production; biological communities; reacting systems

Citation: Zhang, Y.; Kowalski, G.J. Calorimetric Measurements of Biological Interactions and Their Relationships to Finite Time Thermodynamics Parameters. *Entropy* **2022**, *24*, 561. https://doi.org/10.3390/e24040561

Academic Editors: Bjarne Andresen, R. Stephen Berry and Peter Salamon

Received: 21 January 2022
Accepted: 11 April 2022
Published: 16 April 2022

Publisher's Note: MDPI stays neutral with regard to jurisdictional claims in published maps and institutional affiliations.

1. Introduction

Calorimetry is utilized to measure the thermodynamic properties such as enthalpy, entropy, and Gibbs free energy in biological and chemical reacting systems. While the energy/heat released during these processes is important, the entropic changes which reflect the irreversibility and efficiencies are equally important in the understanding of them. Calculating the heat released from one single microbe has confused biologists for centuries. Most marine microbe studies measure the heat dissipation on a community level since the isolation of individual types of microorganisms is not required. In a drop (one millimeter) of seawater, there are approximately 0.5 million microbes and 10 million viruses. To describe the distribution of individual bacteria is time-consuming and biased in their culture practice. Djamali et al. [1] estimated that the heat release per marine bacteria is 50 nJ after concentrating the population by filtration and backwashing. Roach et al. [2] collected the rate of heat-released data by a TAM III calorimetry from various microbe groups and found it to be approximately 25 J/s per gram of seawater from an aquarium system. Precise thermodynamic data is demanded since the measurement of microbe activities is on a nanotechnology scale, much smaller than observed in pharmaceutical reactions [3,4]. The output from the commercial calorimeters is usually reported as power, μW, or often using units of $\mu cal \cdot s^{-1}$ or $\mu J \cdot s^{-1}$ as a function of time [3] and converting to energy units, J. The observed output is the change in the power used to control the sample and reference cell maintaining the same temperature. Maintaining two cells in a calorimeter at the same temperature is intended to have the same heat exchange rate between them and the surrounding bath in order to observe energy released by the biological process. The issue

is how to determine the entropy changes in biological processes and the entropy flows that occur in these devices.

The Gibbs free energy is considered an important parameter to understanding the thermodynamic information on living organisms and the driving force for chemical processes of metabolism activities. The change in Gibbs free energy can be estimated for known entropy of the biomass or with Roel's correlation [5]. However, current calorimetric studies have not developed a way to directly measure the Gibbs free energy from microbial experiments, nor to measure the entropy change in the reactions occurring in the community [5–7]. The Gibbs energy dissipation is related to entropy production exporting from the cell into the environment. The change in entropy includes entropy flow, which is caused by the exchange of entropy in the system with its surroundings; an entropy property change, the entropy exchange between different states of the system and is related to the mass, heat specific, temperature, and pressure. The entropy production is related to the irreversibility of the process [8]. Having an understanding of the entropy flows and the Gibbs free energy change as a biological community interacts with its surroundings provides a more in-depth knowledge of the efficiency of these systems and the tradeoff between switching to maximum power (energy rate) modes vs. energy efficiency modes.

The actual spontaneous processes in biological systems are irreversible and will have an entropy production that adds to the observed heat dissipation in calorimetric measurements. There is a tradeoff between the efficiency of biological processes and the processes rate, with the maximum rate of operation accompanying a 50% loss of the yield [9]. The biological processes are driven by the flow of exergy through the informed pathways rather than the production of entropy. The concept of dissipative biological structure describes these living systems from microorganisms to ecosystems by the dynamics of a far-from-equilibrium system [9]. In contrast, the calorimeter measurements are closed systems after introducing nutrients or competing phages or viruses to the sample. In both cases, it is desired to have measurements that would lead to identifying the entropy property changes and entropy production parameters.

This paper aims to examine what the calorimetric measurements provide and to introduce potential novel methods that determine the equilibrium constant from calorimetry measurement and use it with the second law of thermodynamics to relate it to the Gibbs free energy change. We demonstrate that calorimetric experiments by themselves do not provide the information to isolate the entropy production term, the irreversibility, in the observed reaction. In the case of the pharmaceutical industry, calorimetry plays an important role but the additional analysis which includes an assumption of the reaction type is required to obtain the necessary entropy information. While this step is part of the commercial calorimetry package, its use toward identifying the irreversibility and potential of a drug–protein interaction is clearly understood in this process. In terms of biological processes, the role of calorimetry is increasing. as is the thermodynamic and entropic interpretation of these processes. The manuscript identifies the missing steps in linking calorimetry and other known means related to growth rate formulations, degree of reduction or reactions that would allow this experiment tool to provide entropic information.The paper focuses on describing the thermodynamic and heat transfer physics in the calorimeter device and their relationship with observed energy transfer and entropy flows. These relationships are fundamental and apply to the different time scales seen in drug discovery processes and biological systems. The method of thermodynamic properties measured from the isothermal titration calorimeter will be discussed and extended to a single injection type of experiment, which is related to that biological sample. In the following section, the calorimeter background with two cases will be provided to illustrate how entropy production and entropy properties become convoluted during the measurements.

2. Calorimetry

2.1. Background

Two different configurations of a calorimeter that could be used to measure the energy released by microbes, phages, and virus, their interactions, or drug-related chemical reactions are shown in Figure 1.

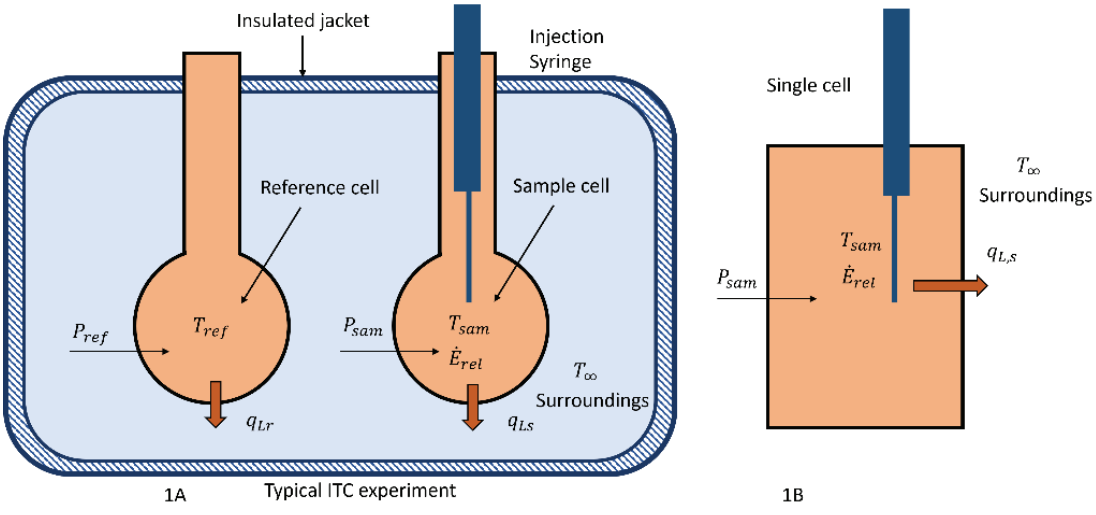

Figure 1. Schematic sketches of two calorimeter configurations used in determining the energy released from biological/reacting systems. (**A**) is a two-cell configuration where both cells are usually maintained at a uniform temperature and the difference between the power of the reference and sample cell is recorded. (**B**) is a single cell configuration where the temperature is monitored during the biological reaction as a function of time.

In Figure 1A, a typical isothermal titration calorimeter (ITC) or two cell configuration that has been involved in the previously cited papers [3] is illustrated. This configuration is usually operated at a constant temperature and in biological situations is not operated in a titration mode [2,10], but the operating principle is similar to that described below. In this device the two cells, reference and sample cells, are similarly constructed so that the heat transfer between them and the surroundings can be considered to be the same if they are maintained at the same temperature using electric heaters. The heaters are controlled by varying the power to them to maintain the same temperature in each cell where the respective cell temperatures are measured by either thermopiles or other accurate devices.

The rate of energy released by the observed reaction in the sample cell; for example, a microbe community with a food source, will cause the temperature of the sample cell to change unless the power to it is adjusted to maintain a constant temperature. The observed variable in these measurements is the difference between the reference and sample power, ΔP, which is stated to be equal to the rate of energy released during this process. The rate of energy released ultimately is transferred as heat to the surrounding large thermal reservoir. The energy released associated with the process under the assumption of constant temperature in each cell and that the cells are similarly constructed lead to a simple relationship, Equation (1).

$$\Delta P = Observed\ Change\ In\ Power = P_{REF} - P_{SAM} = \dot{E}_{REL} \quad (1)$$

where P_{REF} and P_{SAM} are the power to the reference and sample cell, respectively. $\dot{E}_{REL}$ equals the rate of energy released by the reactions occurring in the sample cell. The energy

balance on the sample cell provides additional insights into these assumptions and the mechanisms that occur during the reaction, Equation (2).

$$P_{SAM} + \dot{E}_{REL} = \frac{dU_{SAM}}{dt} + q_{L,s} \tag{2}$$

In Equation (2) U_{SAM} is the internal energy change in the materials in the sample cell, t is time and $q_{L,s}$ is the rate of heat transfer between the sample cell and the surrounding bath. While in most of these devices, there is an injection to the test sample to add food or duplicate injections requiring a transient form of the energy balance to simulate the process. It should be noted that the rate of change of the internal energy depends on the temperature change in the sample, as well as the changes in its mass. In these calorimeters the temperatures of the reference and sample cells are controlled to be equal and set to a constant value. For these conditions, the derivative of the internal energy term will be zero; if the mass of the sample cell remains constant during the measurement, at steady state conditions, or when a balance of the interacting group of various species is reached, the transient term on the RHS of Equation (2) will approach zero. Assuming that the working fluid in the device is an incompressible material yields Equation (5). The time dependence of the mass in the sample cell is related to the mass flow rate of the injection, Equation (3) and the expanded form of the internal energy, Equation (4) is included in the transient energy balance, Equation (5), to emphasize the above assumptions.

$$m_{sam} = \dot{m}_{inj} t \tag{3}$$

$$U_{SAM} = m_{sam} c_s (T_S - T_R) \tag{4}$$

$$P_{SAM} + \dot{E}_{REL} = \frac{d(m_{sam} c_s (T_S - T_R))}{dt} + q_{L,s} \tag{5}$$

In Equation (4), m_{SAM} and c_s equal the mass of material and the specific heat of the material in the sample cell, T_s is the temperature of the sample cell at any time and T_R is the reference temperature for the internal energy. The mass of material, m_{sam}, in a typical titration experiment is related to the injection rate, concentration, and injecting time. $\dot{m_{inj}}$ is the injection of the syringe in Equation (4). A similar energy balance can be written for the reference cell where there is no rate of energy released term. Since the temperature of both cells is controlled to be equal in the theory of two-cells ITC and they are geometrically similar, the heat loss from both cells will be the same at any time. The internal energy balance in the reference cell is constant as its mass does not vary with time. Since the temperature of each cell is controlled to a constant value, the temperature time derivatives are also zero. The implications of these assumptions will be discussed later. Combining these energy balances of sample and reference cell under these conditions yields the following relationship:

$$\dot{E}_{REL} = c_s (T_S - T_R) \frac{d(m_{sam})}{dt} + (P_{REF} - P_{SAM}) \tag{6}$$

The derivative term in Equation (6) was left to illustrate that even if the temperatures are controlled to be equal and constant, a part of the internal energy change will remain if the mass changes. Equation (2) assumes that the preceding condition is satisfied. If it is not, then the result summarized in Equation (2) is not valid.

Commercial ITC/sample and reference cell calorimeters are designed and manufactured to satisfy these conditions for chemical reaction processes. When these calorimeters are used to measure the rate of energy release from the microbe community, as in [1,2,10], the effects of injecting fluids at a different temperature need to be taken into account. As that of the cells, the effects include the changes in mass from gas exchange with the surroundings, separating the growth of the microbes, significant changes in the metabolic rate based on the community dynamics and potential interactions between the microbes

and phages or viruses. If sufficient time is taken one can reach a near steady state condition, which avoids the initial injection region and the growth of the community phases. In standard ITC practice, the power difference which equals the energy release is integrated over the time of reaction to obtain the thermodynamic property of the enthalpy of reaction, ΔH, and is usually expressed per number of microbes or mole of injectant. In the case of the microbial community, this change in power is related to energy released by the microbes and has also been reported [1,2,10]. The heat transfer rate from each cell in these types of measurements is not usually reported, although the difference in the power between the reference and sample as a function of time is as reported in [2].

To understand what is measured by the change in power, the single-cell calorimeter as shown in Figure 1B is analyzed and it is essentially one of the cells from the ITC/ sample and reference cell device. In this case, the energy released, $\dot{E}_{REL}$, is determined from the observed temperature response, the heat input, P_{sam}, if any, and the heat transfer characteristics of the cell, $q_{L,s}$. A calibration relation is required to determine these heat transfer characteristics. The energy balance on this device is similar to that of Equation (2) and can be solved for energy released, $\dot{E}_{REL}$. The integration of the energy release term over the time of the process can be used to determine the enthalpy of reaction as stated above.

$$\dot{E}_{REL} = \frac{dU}{dt} + q_{L,s} - P_{sam} \tag{7}$$

If the energy released by the community or the enthalpy of reaction was the only variable of interest and not the entropy flows in the system, the above experimental protocols would be sufficient [1,2]. In this case, the internal energy of the community is assumed to be a function of the temperature and mass of the fluid containing the microbes and other biological materials. Additional experiments to determine these parameters can be easily designed. The heat transfer from the cell is described in Equation (8) by the temperature difference between it and the surroundings and the overall heat transfer coefficient, ($u_{HT}A$).

$$q_{L,s} = (u_{HT}A)(T - T_{\infty}) \tag{8}$$

What is not obvious in both Equations (2) and (7) is that the heat transfer from the cell also would transport any irreversibility associated with the processes being observed which are convoluted with the heat flowrate from the sample cell. The details of this process are discussed in Section 2.1. The steady-state results stated in Equation (1) do not provide information on the irreversibility directly when a reaction is occurring and only the energy leaving the sample cell can be used to determine the rate of entropy flow from the sample cell. Other means are needed to provide information on the irreversibility or process efficiencies. For example, in (ITC) experiments, one performs the experiments sequentially to observe the reaction as the concentrations change in a prescribed manner in order to develop a relationship between the extents of the reaction and to determine the reaction's equilibrium constant, k_D. The equilibrium constant allows the introduction of second law parameters such as the Gibbs free energy change of the reaction, which then allows the entropy of the system during the reaction to be determined. A second law analysis of the calorimeter is then used to calculate the entropy production rate, which is related to the irreversibility of the reaction (Section 2.3). Procedures and hypotheses concerning the relationships for energy stored in growth, growth rate, and generation times would need to be applied to possibly formulate entropy statements for these processes, similar to that carried out in the ITC analysis [10].

2.2. Case 1: Spatially Uniform System Heating without Reaction

Consider a simple system such as the single-cell, Figure 1B, that corresponds to an incompressible material, water, that is excited using microwave heating. This problem, while simple, provides the base solution to illustrate the determination of the rate of energy released, entropy flow, entropy property changes and the rate of entropy production

from a calorimeter device. Assume that the single cell is a closed system, there is no expansion work nor mass exchange with the surroundings. A steady-state heat source, q_g that represents the microwave or Joule heating per volume is active in the closed system, q_g, and there is heat exchange, $q_{L,s}$ with the surroundings through convection (Equation (9)). The internal energy, u, is determined from the equation of state for the material in the cell. A is the surface area for heat transfer of the closed system of the test cell and the temperature of the surroundings is T_∞. The energy balance is developed as in Equation (5).

$$P_{SAM} + q_g\, V = \frac{d(m_{sam} c_s T)}{dt} + q_{L,s} \tag{9}$$

The initial conditions for this problem are:

$$Time = t = 0\ T(0) = T_\infty \tag{10}$$

$$\text{For } t \geqq 0,\ \dot{q_g} = \text{constant} = 10^6\ \text{W/m}^3 \tag{11}$$

The material in the single-cell system is water with constant properties of specific heat, c_S = 4180 kJ/(kg K), thermal conductivity = 0.6 W/(m K), and density of 997 kg/m^3. P_{SAM} is set to zero in this simulation. The volume of the liquid is fixed at 80 µL and the ($u_{HT}A$) product is 0.0356 W/K. The value of the power into the cell is zero in this experiment. Equation (9) was solved numerically using the code developed by Modaresifar and Kowalski [11] for reactingmixtures in microchambers, which simulates an injection experiment and analyzes its thermal process in a microscale calorimeter. This is a straightforward problem that is easily solved. This code was found to spatially converge to an accurate solution with three nodes for this small volume and uniform heat generation rate. It predicts the temperature time response, as shown in Figure 2, until the steady state is reached, approximately t_f = 130 s. In Figure 2 the temperatures of the three spatial nodes are shown. They are not distinguishable from one another, which confirms that the numerical simulation satisfies the uniformly spatial assumption. Tests at a higher number of nodes, providing more precise resolution in the simulation, confirm that the solution has converged.

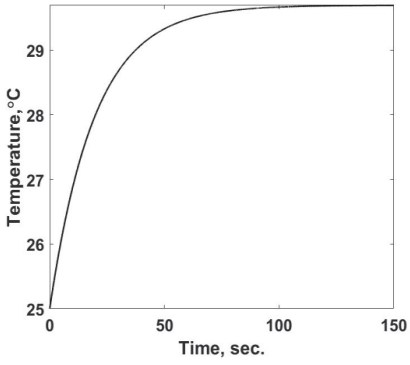

Figure 2. The temperature response of the single sample cell as a function of time for a pure material, water, exposed to a uniform heat generation rate.

This case provides a baseline solution of what is measured in a calorimetric type of device and allows one to investigate the entropy flow from the sample cell, the rate of change of the entropy property of the material within it, and the rate of entropy production for this process involving a single material phase with known properties. To illustrate the above statement, one must view Figure 2 not as an end result of a simulation, but as the observed variable in the calorimetric device. As described in the background section, what one observes in the calorimeter is either the temperature response or the result of a small

change in temperature that alters the power into the cell. For this discussion, Figure 2 is not the outcome, but the starting point to determine the heat generation term, q_g, in Equation (9). This calculation is accomplished by integrating Equation (9) with respect to time under the assumption that q_g is constant. In this step, note that one is specifying the function form of the internal heat generation, a constant, that is occurring in the sample, i.e., a mechanism. The integrated form of Equation (9) is:

$$\int_0^{t_f} q_g(V)dt = q_g\left(Vt_f\right) = (m_{sam}c_s)\left[T\left(t_f\right) - T(0)\right] + \int_0^{t_f} q_{L,S}dt \tag{12}$$

The heat generation term, the LHS of Equation (12), is usually the primary measurement sought, since it can be related to the energy released by the microbe community or a chemical reaction. Further analysis is performed to determine the irreversibility associated with this heating process, using relationships with the entropy flow.

The heat loss, $q_{L,s}$, in Equation (12) is the heat transfer rate and is summarized in Figure 3 as a function of time using Equation (10). As expected, the heat transfer rate starts at zero and increases to its steady value. The difference between the heat transfer rate and the rate of energy released from the heat generation term is the internal energy storage rate, the first term on the RHS of Equation (12).

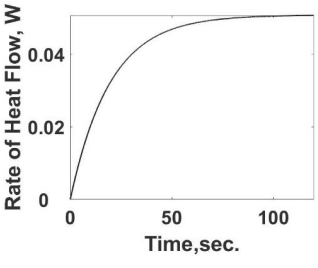

Figure 3. Instantaneous heat transfer rate as a function of time for the sample cell. The results shown are based on the known value of the heat transfer coefficient, ($u_{HT}A$) product, and the observed temperature from Figure 2 as if it were a calorimeter experiment.

The flow of entropy from the sample cell is determined from the calculated heat flow and the temperature of the sample cell. This relationship is summarized in Figure 4. The rate of entropy flow out of the sample cell can be determined from the calorimetric measurements of the temperature and heat transfer information, as demonstrated below. The entropy flow out follows the behavior of the heat transfer rate as expected.

$$S_{out} = rate\ of\ entropy\ flow\ out = \frac{q_{L,s}}{T} \tag{13}$$

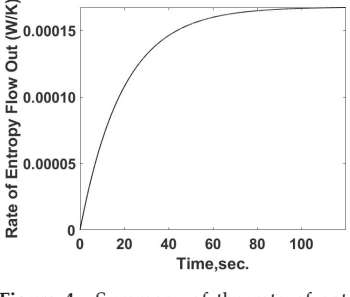

Figure 4. Summary of the rate of entropy flow out of the sample cell as a function of time. The calculations are based on temperatures and heat losses which would be determined from calorimetric measurements.

The entropy property change is determined by the temperature, as observed in Figure 2, and the Gibbs equation. Water at moderate temperatures and pressures is used in this simulation and is treated as an incompressible material

$$\frac{dS_{prop}}{dt} = m_{sam}c_s\frac{dT}{T} + \frac{P}{T}dv = m_{sam}c_s\frac{dT}{T} \tag{14}$$

The rate of entropy property changes at each observed time, Figure 5. This simulation case can be determined because one is using a pure material with a known equation of state. The temperature terms can be calculated for this case from the calorimetric observations. One feature of Figure 5 is the rapid increase in the rate of entropy property changes at the start of the process and then a steady decline until it reaches zero. During this response, the rate of entropy flow from the sample cell is increasing to its steady-state value, Figure 4.

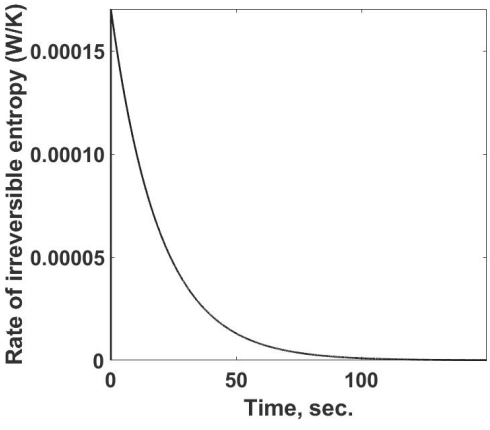

Figure 5. Summary of the rate of entropy property changes within the sample cell as a function of time. The calculations are based on temperatures and heat losses which would be determined from calorimetric measurements.

The preceding calculations and graphs illustrate the different entropy components that are obtained from calorimetric measurements. The entropy balance is used to determine the rate of entropy production, which is related to the irreversibility observed for the constant heating process in this case.

$$\dot{\sigma} = \frac{dS_{prop}}{dt} + \frac{d}{dt}\dot{S}_{out} \tag{15}$$

The rate of entropy production as a function of time is determined from the previously calculated values using Equation (15) and is summarized in Figure 6. One interesting feature is that the rate of entropy production increases rapidly and then slightly decreases, reaching a near-constant value, similar to that of the entropy flow out of the system.

For the heat generation process in this case, the rate of entropy production has a direct link to the irreversibility of this process. If this were a microbe community with a constant energy release rate, the results in Figure 6 would be a measure of the irreversibility and possibly would be related to the efficiency with which the community is using its resources. Such a case of near-constant energy release rates has been reported for *E. coli* during the stationary phase [10].

The above case is simplistic and a direct application of thermodynamics to a calorimetric type device. The results are expected and are presented here to establish; 1. what information could be obtained from a calorimetric type device and, 2. an approach to provide a baseline measure of the irreversibility. It neglects the complications of inter species competition for food sources, different phases such as exponential growth or declining, as

well as changes in the immediate surroundings that one species may cause. These complications go directly to the assumption that the property relationships for calculating the entropy property solely on the observed temperature in an active community are possible. Without these key relationships, other means are needed to describe the interactions. Some of these complications are introduced in the second case, that of a sample cell containing a reacting mixture or interacting group of various species.

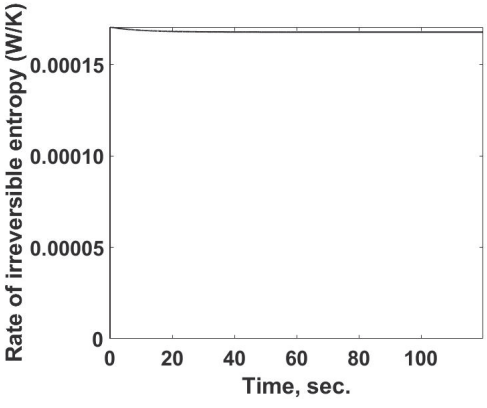

Figure 6. The rate of entropy production within the sample cell as a function of time. The calculations are based on temperatures and heat losses which would be determined from calorimetric measurements.

2.3. Case 2: Spatially Uniform System with Reaction Limited by an Equilibrium Constant

Case 2 considers the same sample cell as shown in Figure 1B and that was discussed in detail for case 1 for the constant heat generation case. In case 2, the sample cell is initially filled with two reacting solutions, where these solutions could reflect chemical reactions or two interacting species; for example, *E. coli* and phages or ligands. From an experimental viewpoint, the same observed property, the temperature, is measured. The reacting solutions will normally be low concentrations of the reacting species in a buffer or low concentrations of microbes in water that contains a food source. From a calorimetric viewpoint, the key rates of energy exchanges are the rate of change in internal energy of the buffer/water and the rate of heat transfer from the sample cell. The driving thermodynamic potential is the reaction that will be characterized in terms of reaction equation, equilibrium constant, growth rate constant, degree of reduction, or equivalent, and the rate of reaction. The reacting compound case will be used as a starting point to illustrate these relationships and what information we can obtain from a calorimeter experiment. The role of the equilibrium constant on the resulting energy release rate is similar to the biological interaction restrictions that determine how fast and to what extent two biological species react with one another. This reaction constraint has direct implications on the flow of entropy and entropy production in these systems. Consider a concentration of compound $[X]$, which reacts with a concentration of $[Y]$, where both are in the same buffer of $[B]$ and produce a concentration $[XY]$, the product. A similar development can be found in [3]

$$[X] + [Y] + [B] \overset{yields}{\rightarrow} [XY] + [B] + [X_F] + [Y_F] \tag{16}$$

The reaction summarized in Equation (16) is constrained by the equilibrium constant, k_B and the products are as shown in Equation (17), which assumes a complete reaction.

$$k_B = \frac{[XY]}{[X][Y]} \tag{17}$$

The correct form of Equation (16) that includes the equilibrium composition of the products is:

$$[X]_1 + [Y]_1 + [B] \overset{yields}{\rightarrow} [XY]_2 + [X]_2 + [Y]_2 + [B] \tag{18}$$

The energy and entropy balances for the described reaction can be written using absolute thermodynamic properties and are simar to that of Equations (8), (9) and (13). The transient energy balance, Equation (8), with $P_{SAM} = 0$ is:

$$q_{g2} = \frac{d(m_{sam} c_s(T))}{dt} + q_{L2} \tag{19}$$

where

$$q_{L2} = (u_{HT} A)(T - T_\infty) \tag{20}$$

In this experiment, the compound $[X]$ is injected into the sample cell that contains a fixed amount of $[Y] = [Y_{TOT}]$. During this injection, the rate of reaction is considered to be very fast and the rate of energy released per volume, q_{g2}, is not a constant and is determined from the equilibrium constant k_B and the enthalpy of reaction per mol of the injected compound, ΔH. The rate of energy release between two specified times is:

$$Q_{g2} = \textit{Energy released per volume between } t_{i+1} \textit{ and } t_i = ([XY]_{i+1} - [XY]_i)\Delta H \tag{21}$$

Differentiating Equation (21) with respect to time determines the rate of energy released per volume:

$$q_{g2} = \frac{d[XY]}{dt}\Delta H \tag{22}$$

To determine the derivative in Equation (22), the equilibrium constant, Equation (17), is used to obtain a quadratic expression for the product $[XY]$ by combining it with the species/mass balance of the species:

$$[X]_i = [X]_{TOT} - [XY]_i \tag{23}$$

$$[Y]_i = [Y]_{TOT} - [XY]_i \tag{24}$$

$$[X]_{TOT} = [X]_{i-1} + \dot{X}_{inj} t \tag{25}$$

where the molar rate of injection is $\dot{X}_{inj}$ and t is the time from the start of the injection. The resulting relationship is

$$\frac{d[XY]}{dt} = \frac{1}{2}\left\{1 - \frac{\left[\left(Y_{TOT} + \dot{X}_{inj} t + \frac{1}{k_B}\right) - 2Y_{TOT}\right]}{\left[\left(Y_{TOT} + \dot{X}_{inj} t + \frac{1}{k_B}\right) - 4Y_{TOT}\dot{X}_{inj} t\right]}\right\} \tag{26}$$

It is observed from Equation (26) that the energy release rate for the reacting compound example is time dependent, unlike that in case 1. Equations (26) and (22) are used to determine the rate of energy release during the injection of compound $[X]$ into the chamber filled with compound $[Y]$. The initial concentration of compound $[Y]$, Y_{TOT}, is known at the start and the injection rate of compound $[X]$ is held constant. Unlike case 1, the rate of energy added to the chamber is not constant but is a function of time that starts at a maximum value and then decreases to zero, or a constant value as the number of reaction sites or available food goes towards zero, Figure 7.

The shape of this curve reflects the trends discussed in [3], which is shown inverted since it is measuring the change in power in the two-cell calorimeter. Numerically solving Equation (19) using the energy release rate given by Equation (22) predicts the temperature response shown in Figure 8. The temperature response corresponds to the observed property in the single-cell calorimeter.

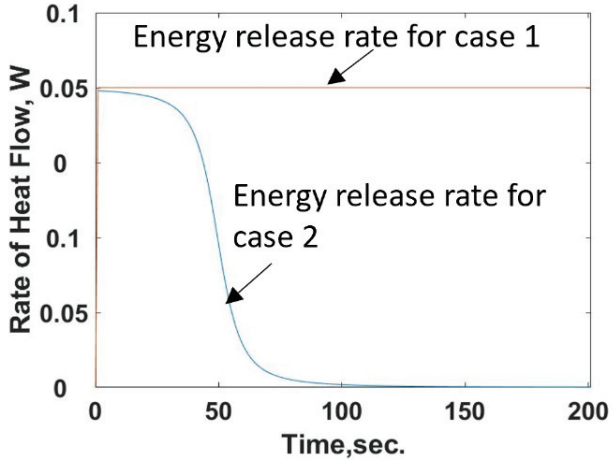

Figure 7. Comparison of the constant energy release rate of case 1 to the time dependent energy release rate of case 2, the reacting compound example. The orange line is the constant energy release of case 1. The blue monotonically decreasing line is for case 2.

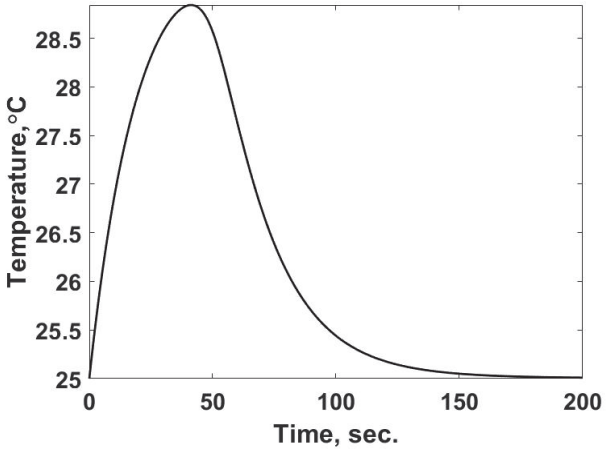

Figure 8. Predicted temperature vs. time response for the reacting calorimeter cell. This response corresponds to the observed parameter of the calorimeter experiment.

The results in Figure 8 are expected: a rise in temperature to the maximum value due to the thermal capacitance of the system, while the rate of energy release is greater than the heat transfer rate. Once the heat transfer rate overcomes the rate of energy, the temperature decreases in the system. The system returns to the temperature of the surroundings at the end of the process as expected. In terms of determining the entropy flows in this case, the observed temperature is shown in Figure 8: the heat transfer characteristics of the cell, and the thermodynamic properties of the buffer and each reactant are needed. Due to the reaction between the reactants, the absolute entropy for the products is unknown for a test case and, unlike case 1, the case of a single, non-reacting material, there are no equations of state to determine the entropy property change from the calorimeter experiment. What can be determined is the entropy flow from the chamber, since the rate of heat flow is determined in the simulation, Equation (21) (Figure 9).

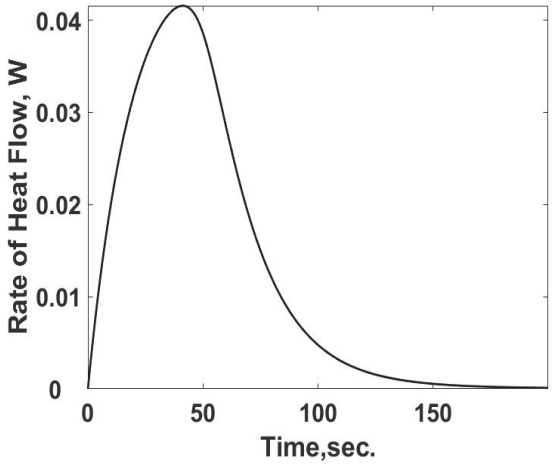

Figure 9. Predicted heat flow rate vs. time response for the reacting calorimeter cell. This parameter is calculated using the predicted temperature response and the heat transfer characteristics of the test cell as determined from a calibration test.

Since the temperature at the system boundary is known as a function of time the rate of entropy flow from the cell can be calculated by Equation (27) and is summarized in Figure 10.

$$\dot{S}_{out} = rate\ of\ entropy\ flow\ out = \frac{q_{g2}}{T} \tag{27}$$

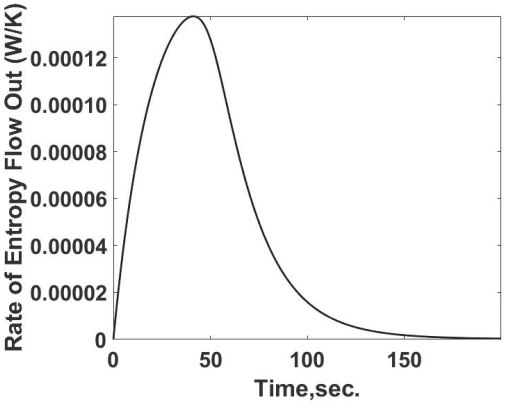

Figure 10. Predicted entropy flow rate out vs. time response for the reacting calorimeter cell. This parameter is calculated using the predicted temperature response and heat transfer rate.

From the entropy balance on the test cell:

$$\dot{\sigma} = \frac{dS_{prop}}{dt} + \dot{S}_{out} \tag{28}$$

where

$$\frac{dS_{prop}}{dt} = \Delta S^{\circ}_{form} + \Delta S_{prop} + \Delta S_{reactants} \tag{29}$$

The rate of entropy flow out of the system can be determined from the observed experimental parameters. In this case, the rate of change in the entropy property cannot

be determined, unless this is a known reaction and the absolute entropy values of the reactants and products are known, Equations (28) and (29). This is not usually the case when testing reacting compounds in a calorimeter because that is the purpose of the experiments. As a result, the only statement that can be made is the calculated value of the confusing parameters of the rate of entropy property change and the entropy production rate. This calculation does not allow the irreversibility of the reaction or interactions, $\dot{\sigma}$, in the biological communities to be determined for possible use in better understanding the dynamics of the community, the efficient use of food sources or evolutionary trends.

In 1999, Battley [12] developed an empirical statistic model to calculate the standard molar entropy ΔS°_{form} with accuracy at 2%. However, the method to calculate the information of ΔS°_{form} from the experiment is still limited. The Gibbs free energy is defined as the maximum amount of non-expansion work in a thermodynamic system and is related to enthalpy, temperature, and entropy. The definition equation can be written as Equation (29) at thermodynamic standard states for the absolute entropy property changes [8].

In the case of drug and protein reactions, there is an additional procedural step that can be used to determine the equilibrium constant, which can then be related to the change in the Gibbs energy from which the rate of entropy property change can be calculated. This step is best illustrated from the ITC version of the calorimeter, in which a series of titrations are performed and the energy released at each step is determined as a function of the mole fraction of the product [3]. This leads to a graph that is similar to that of Figure 8 for the reacting case and the slope of the curve equals the equilibrium constant, k_B. The thermodynamics of the equilibrium composition K_B is related to the change in the Gibbs energy.

$$\Delta G = -RTln\left[\frac{1}{k_B}\right] = \Delta G^{\circ} = \Delta H^{\circ}_{f} - T\Delta S^{\circ} \tag{30}$$

For the case of the single injection experiment described in this section, a similar curve as that developed in the ITC experiment can be determined by calculating the energy release rate within a finite time interval from the observed temperature–time response and the energy balance. The determined value of k_B would then be used in Equation (30) to determine the change in the Gibbs Energy and the change in the absolute entropy property change. These results, together with Equation (26), would allow one to isolate the rate of entropy productions and measure the irreversibility of the reaction.

While the above procedure applies to a reacting system, it does not directly relate to the activities of biological microorganisms due to the lack of a clear definition of what would be the corresponding equilibrium constant. A similar parameter to the equilibrium constant for monotypic microorganisms interacting with their surroundings using a calorimeter-based measurement needs to be defined in order to separate the entropy property changes from the entropy production changes. Using probabilistic methods as described by [7] to identify a constant that characterizes the energy releasing interactions is one approach and is beyond the scope of this paper. From the comparison of case 1 and 2, it is demonstrated that the calorimeter measurement can identify the combined values of the entropy property changes and entropy production, but without further analysis or observed information, it cannot separate these parameters.

3. Discussion: What Is Measured

The two case examples and the calorimetry background provided illustrate that the parameter measured in these experiments is the heat flow from the test cell and it is related to the energy released by the reaction, the biological community activities, or the heat generation source. The energy flow from the cell can be further divided into the amount due to the irreversibility in the system, i.e., the entropy production term, and the amount due to the reaction. Procedures as described for the ITC type measurement that allow a parameter such as the equilibrium constant to be determined and then related to the entropy property change exist in the drug discovery or chemical reaction fields. As shown in case 2,

the dynamics of the reaction in biological fields need to be developed for calorimetry to be used to isolate the entropy flows in the community.

From the perspective of biochemistry, analysis of biomass-based on the empirical formula of various microorganisms is instructive to understand the microbe's thermodynamic properties [12–15]. A method of the degree of reduction from elemental analysis using electron concepts estimitates the enthalpy of combustion of the biomass [14] and biosynthetic efficiency [15]. Through the oxidation reaction of the dry microorganism biomass equation, the enthalpy of formation can be determined [7]. In a living system, it is impossible to concisely express all the intermediate reactions within a microbe or the community. However, it is practicable to describe the typical microbe growth from an initial substance state to a final state comprised of the microorganism and other products by a growth-process equation [16,17]. When monitoring the heat exchange in a microbe growth experiment by an ITC calorimeter, the thermal power can be written as an exponential equation with the growth rate constant in the log growth phase [10]. Assuming there are only monotypic microbes and glucose injected into the sample cell, the growth-process equation can be written to represent the exponential phase in a traditional growth curve. To calculate the equilibrium constant, the concentration and mass of microorganisms are necessary. Makarieva et al. [18,19] developed a comprehensive database including the endogenous (non-growth) and growth metabolic rate of microorganisms and their corresponding microorganism mass involving 3006 species from all kingdoms. With an acknowledged mass of microorganisms, metabolic rate, enthalpy of biomass formation and the growth-process equation in a closed system, an energy balance can be constructed to estimate the equilibrium constant. Similarly, the equilibrium constant in the stationary phase can be determined by introducing the oxidation reaction of biomass representing the death of microbes. For more complicated cases, for example, the lysogeny by virus infection and symbiosis in biological evolution, statistical models are developed to predict the thermodynamic properties. [20,21]

An interesting observation is presented in a paper by Djamali et al. [1] in their Figures 4, 5 and 7, where the transient response of the observed heat flow from the test cell is plotted as a function of time. The observations in this paper are reported using the long-term, greater than approximately 10 h, which is constant heat flow with respect to time. The analysis approach described in case 2 for the single-cell injection experiment to determine an equilibrium constant-like parameter would fail when using this long-term data because of its uniform heat flow. What would be of more interest to determine the entropy flows from the calorimetry measurements are the early time data, in which the dynamics of the biological community are changing.

4. Conclusions

A background on the operation of calorimeters is provided and two case studies are investigated using a numerical simulation. The first case describes a single cell calorimeter containing a single-phase material excited by heat generation source function such as joule heating. In this case, the equations of state can be used to determine the energy released in the cell, as well as the entropy flows: entropy property changes, entropy flow to the surroundings and the rate of entropy production. In the second case, a reacting system, the numerical simulation of the calorimeter experiment provides the energy released and the entropy flow to the surroundings. The basic observation parameter, the temperature, cannot be used to separate the entropy property changes and the rate of entropy production. In the chemical reacting system, the data can be further analyzed to determine the equilibrium constant once the reaction equation and stoichiometric constants are specified. The equilibrium constant is then used to identify the entropy property changes and the entropy balance is used to determine the rate of entropy production. In biological conditions, the equivalent of the reaction equation and a definition of an equilibrium constant is not available for all systems. While an empirical relationship for the absolute entropy property change has been reported, it is not clear if it would apply to all systems being

investigated. To use calorimetry measurements to identify the entropy flows in biological community activities, further work must be carried out to establish a framework similar to that of chemical reacting systems that are based on an equilibrium type parameter.

Author Contributions: Formal analysis, Y.Z. and G.J.K.; Investigation, Y.Z.; Methodology, Y.Z. and G.J.K.; Software, Y.Z. and G.J.K.; Writing—original draft, Y.Z.; Writing—review & editing, G.J.K. All authors have read and agreed to the published version of the manuscript.

Funding: This research received no external funding.

Data Availability Statement: Not applicable.

Acknowledgments: This research was supported by the Department of Mechanical and Industrial Engineering, Northeastern University.

Conflicts of Interest: The authors declare no conflict of interest.

References

1. Djamali, E.; Nulton, J.D.; Turner, P.J.; Rohwer, F.; Salamon, P. Heat Output by Marine Microbial and Viral Communities. *J. Non-Equilib. Thermodyn.* **2012**, *37*, 291–313. [CrossRef]
2. Roach, T.N.F.; Abieri, M.L.; George, E.E.; Knowles, B.; Naliboff, D.S.; Smurthwaite, C.A.; Kelly, L.W.; Haas, A.F.; Rohwer, F.L. Microbial Bioenergetics of Coral-Algal Interactions. *PeerJ* **2017**, *5*, e3423. [CrossRef] [PubMed]
3. Thomson, J.A.; Ladbury, J.E. Isothermal Titration Calorimetry: A Tutorial. *Biocalorimetry* **2005**, *2*, 35–58.
4. Ladbury, J.E.; Klebe, G.; Freire, E. Adding Calorimetric Data to Decision Making in Lead Discovery: A Hot Tip. *Nat. Rev. Drug Discov.* **2010**, *9*, 23–27. [CrossRef] [PubMed]
5. Von Stockar, U.; Liu, J.-S. Does Microbial Life Always Feed on Negative Entropy? Thermodynamic Analysis of Microbial Growth. *Biochim. Et Biophys. Acta (BBA)-Bioenerg.* **1999**, *1412*, 191–211. [CrossRef]
6. Anthenelli, M.; Jasien, E.; Edwards, R.; Bailey, B.; Felts, B.; Katira, P.; Nulton, J.; Salamon, P.; Rohwer, F.; Silveira, C.B.; et al. Phage and Bacteria Diversification through a Prophage Acquisition Ratchet. *bioRxiv* **2020**. [CrossRef]
7. Popovic, M. Thermodynamic Properties of Microorganisms: Determination and Analysis of Enthalpy, Entropy, and Gibbs Free Energy of Biomass, Cells and Colonies of 32 Microorganism Species. *Heliyon* **2019**, *5*, e01950. [CrossRef] [PubMed]
8. Roach, T.N. Use and Abuse of Entropy in Biology: A Case for Caliber. *Entropy* **2020**, *22*, 1335. [CrossRef]
9. Roach, T.N.F.; Salamon, P.; Nulton, J.; Andresen, B.; Felts, B.; Haas, A.; Calhoun, S.; Robinett, N.; Rohwer, F. Application of Finite-Time and Control Thermodynamics to Biological Processes at Multiple Scales. *J. Non-Equilib. Thermodyn.* **2018**, *43*, 193–210. [CrossRef]
10. Xiao, S.-X.; Li, A.-T.; Li, X.; Li, C.-H.; Xiao, H.-Y.; Huang, S.; Chen, Q.-S.; Ye, L.-J.; Li, Q.-G. The research on formation enthalpy of phenanthroline monohydrate and its influence on the growth metabolism of E. coli by microcalorimetry. *J. Therm. Anal. Calorim.* **2014**, *115*, 2211–2217. [CrossRef]
11. Modaresifar, M.; Kowalski, G.J. Numerical Simulation of an Injection Microscale Calorimeter to Identify Significant Thermal Processes and Verify Data Reduction. In Proceedings of the ASME International Mechanical Engineering Congress and Exposition, Tampa, FL, USA, 3–9 November 2017.
12. Battley, E.H. An Empirical Method for Estimating the Entropy of Formation and the Absolute Entropy of Dried Microbial Biomass for Use in Studies on the Thermodynamics of Microbial Growth. *Thermochim. Acta* **1999**, *326*, 7–15. [CrossRef]
13. Kemp, R.B. *Handbook of Thermal Analysis and Calorimetry*; U.S. Department of Energy Office of Scientific and Technical Information: Oak Ridge, TN, USA, 1999.
14. Patel, S.A.; Erickson, L.E. Estimation of heats of combustion of biomass from elemental analysis using available electron concepts. *Biotechnol. Bioeng.* **1981**, *23*, 2051–2067. [CrossRef]
15. Gary, C.; Frossard, J.S.; Chenevard, D. Heat of combustion, degree of reduction and carbon content: 3 interrelated methods of estimating the construction cost of plant tissues. *Agronomie* **1995**, *15*, 59–69. [CrossRef]
16. Battley, E.H. A short review and an empirical method for estimating the absorbed enthalpy of formation and the absolute enthalpy of dried microbial biomass for use in studies on the thermodynamics of Microbial Growth. *J. Therm. Anal. Calorim.* **2010**, *104*, 13–22. [CrossRef]
17. Battley, E.H. A theoretical study of the thermodynamics of microbial growth using *Saccharomyces cerevisiae* and a different free energy equation. *Q. Rev. Biol.* **2013**, *88*, 69–96. [CrossRef] [PubMed]
18. Makarieva, A.M.; Gorshkov, V.G.; Li, B.-L. Energetics of the smallest: Do bacteria breathe at the same rate as whales? *Proc. R. Soc. B Biol. Sci.* **2005**, *272*, 2219–2224. [CrossRef] [PubMed]
19. Makarieva, A.M.; Gorshkov, V.G.; Li, B.-L.; Chown, S.L.; Reich, P.B.; Gavrilov, V.M. Mean mass-specific metabolic rates are strikingly similar across life's major domains: Evidence for life's Metabolic Optimum. *Proc. Natl. Acad. Sci. USA* **2008**, *105*, 16994–16999. [CrossRef] [PubMed]

20. Roach, T.; Nulton, J.; Sibani, P.; Rohwer, F.; Salamon, P. Entropy in the tangled nature model of evolution. *Entropy* **2017**, *19*, 192. [CrossRef]
21. Luque, A.; Silveira, C.B. Quantification of lysogeny caused by phage coinfections in microbial communities from Biophysical Principles. *mSystems* **2020**, *5*, e00353-20. [CrossRef] [PubMed]

entropy

MDPI

Article

Perturbed and Unperturbed: Analyzing the Conservatively Perturbed Equilibrium (Linear Case)

Yiming Xi [1,*], Xinquan Liu [1], Denis Constales [2] and Gregory S. Yablonsky [1]

[1] McKelvey School of Engineering, Department of Energy, Environmental and Chemical Engineering, Washington University in St Louis, St. Louis, MO 63130, USA; liuxinquan@wustl.edu (X.L.); gy@wustl.edu (G.S.Y.)

[2] Department of Electronics and Information Systems, Ghent University, Building S-8, Krijgslaan 281, B-9000 Ghent, Belgium; Denis.Constales@UGent.be

* Correspondence: yiming.xi@wustl.edu

Received: 30 July 2020; Accepted: 12 October 2020; Published: 15 October 2020

Abstract: The "conservatively perturbed equilibrium" (CPE) technique for a complex chemical system is computationally analyzed in a batch reactor considering different linear mechanisms with three and four species. Contrary to traditional chemical relaxation procedures, in CPE experiments only some initial concentrations are modified; other conditions, including the total amount of chemical elements and temperature are kept unchanged. Generally, for "unperturbed" species with initial concentrations equal to their corresponding equilibrium concentrations, unavoidable extreme values are observed during relaxation to the equilibrium. If the unperturbed species is involved in one step only, this extremum is a momentary equilibrium of the step; if the unperturbed species is involved in more reactions, the extremum is not a momentary equilibrium. The acyclic mechanism with four species may exhibit two extrema and an inflection point, which corresponds to an extremum of the rate of the species change. These facts provide essential information about the detailed mechanism of the complex reaction.

Keywords: conservatively perturbed equilibrium; extreme value; momentary equilibrium

1. Introduction

A new kinetic technique, Conservatively Perturbed Equilibrium (CPE), was analyzed theoretically in previous studies [1,2]. It is formulated within a new paradigm of chemical kinetics, the so-called "Joint Kinetics", which was developed during the last decade (see the papers [3–8] and the most recent review [9]). In a batch reactor, in the CPE experiment, the total amounts of chemical elements and the temperature are maintained constant. Then, the CPE procedure is performed as follows:

1. The equilibrium concentration values of all species are determined.
2. Some of the species, at least two, are chosen to have their concentration perturbed from the equilibrium value.
3. At least one species is not chosen, with its concentration value being kept at the equilibrium value.
4. The perturbations mentioned in point 2 are required to satisfy all conservation laws applicable to the system reactions.
5. The evolutions of all species concentrations are observed as they tend towards equilibrium.

It should be stressed that within the CPE procedure, different from the traditional relaxation method, finite perturbations are used, not the small ones. Additionally, the CPE approach is not limited by the linear cases, only by possibilities to meet the balance requirements.

It was shown [1,2] that in such CPE experiments, the concentration of any unperturbed species first evolves away from its initial value, which equals the equilibrium value, and then back to this

value as time tends to infinity, via an unavoidable first extreme value (maximum or minimum), possibly followed by other extreme values. These extreme concentration values and the times of their occurrences present essential information:

(a) on the detailed mechanism
(b) on the values of the kinetic parameters
(c) on the possibility of new regimes with an improved yield and selectivity.

The physico-chemical foundations of the CPE technique are the uniqueness and stability of the chemical equilibrium composition, which are basic properties of complex reactions occurring in a closed chemical system. These properties were first qualitatively proven by Zeldovich in 1938 [10,11]; from 1960 onwards, many researchers studied these problems and presented rigorous proofs of the uniqueness and stability of the equilibrium composition, such as Shapiro and Shapley [12], Aris [13,14], Horn and Jackson [15], Vol'pert and Khudyaev [16,17], Gorban [18], and Gorban and Yablonsky [19,20]. An essential trait of the equilibrium of reversible complex reactions is that it is actually a detailed equilibrium—i.e., for every step considered separately, the rate of the forward reaction equals the rate of the corresponding reverse reaction. Reviews of these results are available in the books [21,22] and in the paper [23].

The developed CPE approach is not limited to the networks of only unimolecular, linear reactions which are utilized as examples in the present work. In recent experiments (B. Peng [24]), the CPE technique was experimentally verified in a batch reactor for a nonlinear complex esterification reaction:

$$\text{Alcohol} + \text{Acid} \rightleftharpoons \text{Ester} + \text{Ester},$$

in which ethanol and benzyl alcohol react with acetic acid, producing two different esters and water. Three possible CPE cases (acetic acid and water unperturbed; ethanol and ethyl acetate unperturbed; benzyl alcohol and benzyl acetate unperturbed) were systematically investigated. For the unperturbed species, the unavoidable extreme values were experimentally observed during the relaxation towards equilibrium. These extreme values were larger than the equilibrium concentration. Generally, the CPE technique accompanied by unavoidable extrema may lead to processes limited by thermodynamic equilibrium achieving a yield higher than the equilibrium. This is probably highly important for some industrial processes—for example, processes of the pharmaceutical industry.

In the 1950s and 1960s, fundamental progress in the analysis of chemical relaxations was achieved by Manfred Eigen (Nobel Price 1967 [25]). An excellent review of results of chemical relaxation studies of the 1950–1970s is presented in Bernasconi's monograph [26]. Typically, in the transient regimes described by Bernasconi, the "perturbed" system goes to the different final composition—i.e., the perturbations of temperature or pressure change the final chemical state. Contrary to classical chemical relaxation procedures, in our CPE approach only some initial concentrations are modified—the "perturbed" ones. Other characteristics, such as the total amounts of chemical elements and the temperature or any other factors that could interfere with the final composition, are kept unchanged to ensure the system returns to the same equilibrium. In the CPE approach, the transient kinetic dependence of unperturbed substances exhibit unavoidable extremum, which are fingerprints of the CPE technique.

1.1. Previous Study Review

In the paper [1], the CPE phenomenon was studied computationally and analytically using the two-step linear mechanism as an example

$$\mathrm{A} \underset{k_1^-}{\overset{k_1^+}{\rightleftarrows}} \mathrm{B} \underset{k_2^-}{\overset{k_2^+}{\rightleftarrows}} \mathrm{C}$$

It exhibits the following properties:

Unavoidability of the concentration extremum of unperturbed species: this fact is independent on the linearity or nonlinearity of the model studied (see Figure 1).

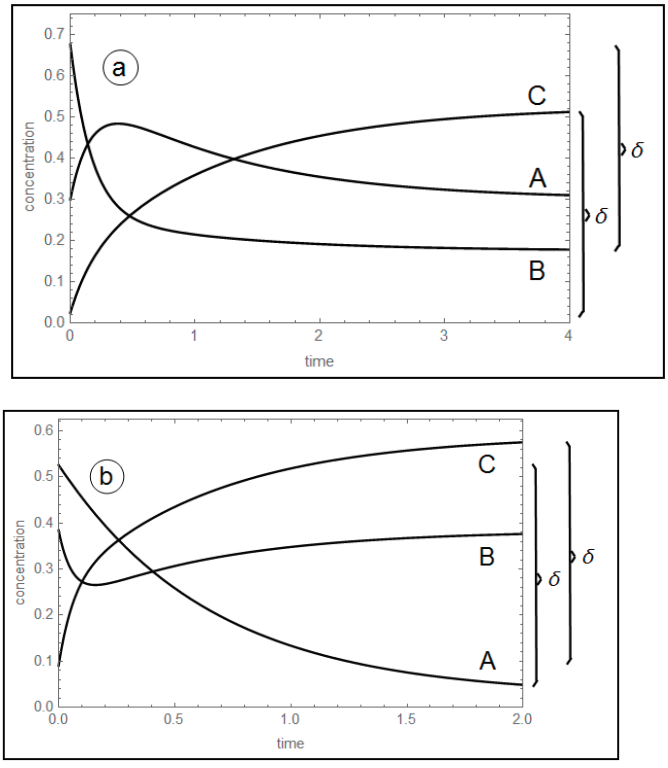

Figure 1. Concentration profiles of A, B and C, for $\delta = 0.5$. (**a**) A maximum of A; $k_1^+ = 1.75$, $k_1^- = 3.00$, $k_2^+ = 1.50$, $k_2^- = 0.50\ s^{-1}$. (**b**) A minimum of B; $k_1^+ = 1.50$, $k_1^- = 0.10$, $k_2^+ = 10.0$, $k_2^- = 6.50\ s^{-1}$.

1.2. Achieving Momentary Equilibrium (ME) at Some Extrema

Preliminarily, the concept of the "equilibrium" must be explained in more detail with some of its modifications. Typically, the equilibrium is understood as the final state of the non-steady-state chemical reaction which occurs in the closed chemical system.

The "equilibrium of the single step" means that the rate of the forward reaction of this step equals the rate of the corresponding reverse reaction. Consequently, the net rate of this step equals zero, and the equilibrium chemical composition is governed by the equilibrium constant. The "detailed equilibrium" means that every chemical step of the complex chemical reaction at the final state is under equilibrium conditions. As the momentary equilibrium of some reaction, we define such temporal behavior when the rate of some step at that moment equals zero.

At the ME point of a linear step, the quotient of the step (i.e., the ratio of the product concentration to reactant concentration) equals the equilibrium constant. However, the absolute values of the concentrations are not equal to the corresponding concentrations at the final detailed equilibrium.

For systems of linear reactions, this holds for so-called end species, which participate only in a single reaction. For example, in the mechanism

$$A \rightleftharpoons B \rightleftharpoons C$$

momentary equilibrium occurs at any extremum of species A and C. In the mechanism

$$\begin{array}{c} A \rightleftharpoons B \rightleftharpoons C \\ \uparrow\downarrow \\ D \end{array}$$

momentary equilibrium holds at any extremum of the species A, C and D. For species that participate in several-step reactions the concentration maximum is not a momentary equilibrium.

The time at which the CPE extremum occurs is independent of the perturbation; in the linear mechanism

$$A \rightleftharpoons B \rightleftharpoons C$$

these extrema occur at a time that is independent of the magnitude of the perturbation.

The goal of this paper is to study further the dynamic properties of CPE experiments, formulating new questions and new problems, in linear models with three and four species, focusing on the following topics:

1. What is the influence of the mechanism structure on the CPE properties?
2. Which differences exist between noncyclic reactions and cyclic ones? Or four cycles with a diagonal step?
3. What is the influence of the strategy of perturbation—i.e., the distribution of perturbed and unperturbed species, their vicinity and interconnectivity within the mechanism?
4. Is it possible to observe more complex dynamic behavior, such as the evolution of events, two extrema, overshooting the equilibrium value, etc.?

2. Materials and Methods

For this study, computational simulations were performed using MATLAB, with ode45 and ode15s as time integration methods for systems of ordinary differential equations that model systems of reactions in batch reactors.

3. Results

As mentioned in the introduction, we distinguish two groups of species, "perturbed" and "un-perturbed". In correspondence with the CPE experiment, the initial concentrations of these species were chosen as equal to the equilibrium concentration ("unperturbed species") or different from the equilibrium ones ("perturbed" species).

Since the perturbation of a single species cannot be conservative (maintaining the same total amount of each element), and at least one species must remain unperturbed, the number of perturbed species allowed in a CPE experiment ranges from 2 to N-1, where N is the total number of species participating in a mechanism. The number of degrees of freedom of the perturbation equals the number of perturbed species minus the number of independent conservation laws—see [1].

For a linear three-species (N = 3) mechanism, the number of perturbed species is 2, of unperturbed is 3−2 = 1, and there are 2−1 = 1 degrees of freedom. For linear four-species (N = 4) mechanisms, the number of perturbed species can be two or three, but in this study, all perturbations will involve only two species, so that there are 4−2 = 2 unperturbed species and still 2−1 = 1 degrees of freedom.

Additionally, for the purpose of future analysis, it is important to distinguish the subset of special unperturbed species that have only unperturbed neighbors, thus being "shielded" from the perturbation. However, among all species, there must be at least one "neighboring pair" of perturbed and unperturbed species; otherwise, the perturbation would have no effect on the unperturbed species.

3.1. Analysis of Perturbed Species in a Three-Species Acyclic Mechanism (Two-Step Mechanism)

$$A \underset{k_1^-}{\overset{k_1^+}{\rightleftarrows}} B \underset{k_2^-}{\overset{k_2^+}{\rightleftarrows}} C$$

The previous work [1] discussed the transient behavior of the unperturbed species only in two-step mechanisms. As a continuation of that analysis, we now consider the perturbed species. A series of simulation experiments with different kinetic constants was performed, from which two experiments were selected as examples—see Table 1.

Table 1. Two-step mechanism, Simulation Experiments 1 and 2.

Experiment Settings	Experiment #1	Experiment #2
Kinetic Parameters (s^{-1}):	$k_1^+ = 5$, $k_1^- = 4$ $k_2^+ = 12$, $k_2^- = 6$	$k_1^+ = 16$, $k_1^- = 4$ $k_2^+ = 12$, $k_2^- = 6$
Perturbed species:	A, B	A, B
Unperturbed species:	C	C

The transient trajectories of the three species in the two experiments are plotted in Figure 2.

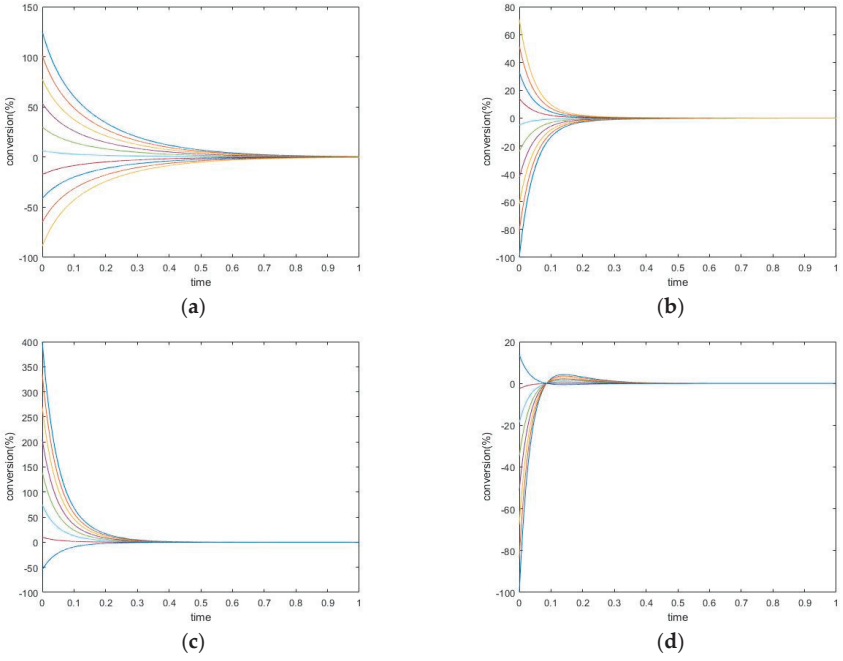

Figure 2. Two-step mechanism, (**a**,**b**) simulation experiment #1, (**c**,**d**) simulation experiment #2. (**a**) Species A Conversion, (**b**) Species B Conversion; (**c**) Species A Conversion; (**d**) Species B Conversion.

New Findings—Perturbed Species May Experience Either Monotone Relaxation or Behavior with one Extremum Peak

Changing the kinetic constants may modify the extremum behavior for the perturbed species. In this case, species A and B both exhibit monotone relaxation when k_1^+ is chosen in a small range. As the forward kinetic constant becomes larger, species B shows transition to more complex behavior. Its

transient regime will come to contain one peak (extremum). Additionally, the concentration of B will overshoot its equilibrium value (in the graphs, this is where conversion = 0).

The concentration extremum indicates the rate of change of the corresponding species when the timepoint is zero. Since this behavior occurs on species B, which is participating in two reactions simultaneously, this extremum is not a momentary equilibrium. It was discovered in a series of computational simulations for this mechanism that when the kinetic constant is above some value, a concentration extremum for species B will become available.

3.2. Three-Species Cyclic Mechanism

The three-species cyclic mechanism (see Figure 3 and Table 2) presents an additional connectivity from species A to species C. The kinetic constants must satisfy the following Onsager condition: the ratio of the third pair of kinetic constants, $\frac{k_3^+}{k_3^-}$, which is also the thermodynamic equilibrium constant of the third reaction K_3, must satisfy the condition $\frac{k_1^+}{k_1^-} \cdot \frac{k_2^+}{k_2^-} = \frac{k_3^+}{k_3^-}$.

Mechanism:

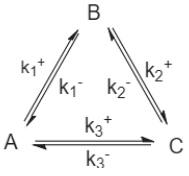

Figure 3. Triangular (three-species cyclic) mechanism.

Table 2. Three-species cyclic conservatively perturbed equilibrium (CPE) example.

Experiment Settings	Value	
Kinetic Parameters (s^{-1}):	$k_1^+ = 16$	$k_1^- = 4$
	$k_2^+ = 12$	$k_2^- = 6$
	$k_3^+ = 8$	$k_3^- = 1$
Perturbed species:	A, B	
Unperturbed species:	C	

Experiments were performed as described in Table 2 and plotted in Figure 4, setting the same first two pairs of reaction parameters as in Experiment 2 above, and in adding the third reaction with kinetic constants satisfying the Onsager condition.

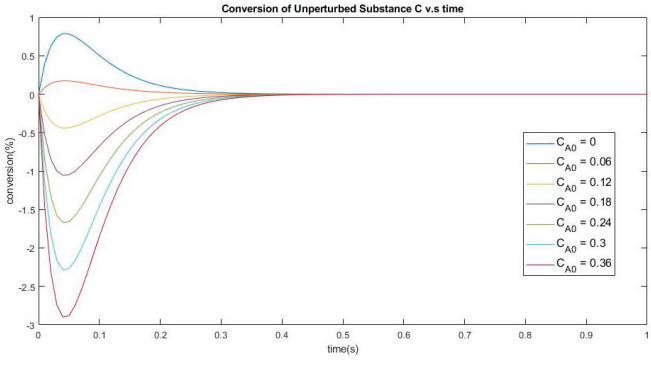

Figure 4. Conversion of the unperturbed species C vs. time. The perturbation consists in changing species (A) from 0 to 0.36 and species (B) from 0.92 down to 0.56.

3.2.1. *New Findings on the Three-Species Cyclic Mechanism*—The Extremum Time for the Cyclic Mechanism Has the Same Analytical Expression as for the Acyclic

Since a three-species mechanism has three eigenvalues, one of which is 0, and the discrepancy from equilibrium of an unperturbed substance is zero both at times zero and infinity, it must be proportional to the difference $e^{\lambda_p t} - e^{\lambda_m t}$. Therefore, the extremum time, when its derivative with respect to time vanishes, is given by

$$t_{exe} = \frac{log\left(\lambda_p / \lambda_m\right)}{\lambda_m - \lambda_p},$$

which is the same as those in the acyclic mechanism case. This is because there are only two nonzero eigenvalues in any linear three-species system, and since there are two boundary conditions at $t = 0$ and as t approaches infinity, the linear combinations of exponentials are fixed up to a factor for the unperturbed species.

3.2.2. The Cyclic Mechanism's Extremum Time is Shorter than that of the Acyclic Mechanism

The cyclic and acyclic exhibit similar properties, however, the major difference between them is the extremum time caused by the reaction between A and C. As mentioned before, the cycle must satisfy the Onsager relation $\frac{k_1^+}{k_1^-} \cdot \frac{k_2^+}{k_2^-} = \frac{k_3^+}{k_3^-}$, otherwise, there are possibilities of complex eigenvalues. To compare the cyclic and the acyclic mechanisms, a simulation is performed fixing $k_1{}^+ = 0.16\ s^{-1}$, $k_1{}^- = 0.04\ s^{-1}$, $k_2{}^+ = 0.12\ s^{-1}$, $k_2{}^- = 0.06\ s^{-1}$, and selecting the value of $k_3{}^+$, which in turn determines the value of $k_3{}^-$ from the thermodynamic condition. The comparison results are illustrated in Figure 5.

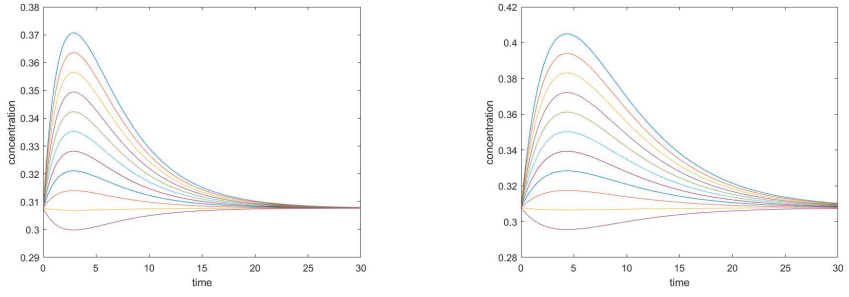

(**a**) (**b**)

Figure 5. (**a**) Conversion of unperturbed species with large $k_3{}^+$. (**b**) Conversion of unperturbed species with small $k_3{}^+$.

The plot on the left is when we have a large $k_3{}^+$ and the plot on the right is when have a small $k_3{}^+$. We observe that with a larger $k_3{}^+$, the extremum time becomes smaller and the extremum concentration gets closer to the equilibrium concentration. With a smaller $k_3{}^+$, the trajectories of a cyclic mechanism become closer to that of an acyclic mechanism with the same $k_1{}^+$, $k_1{}^-$, $k_2{}^+$, and $k_2{}^-$ values. Intuitively, we can consider the reaction between species A and species C as a shortcut, so that a small $k_3{}^+$ will keep the reaction going similar to an acyclic, but a large $k_3{}^+$ will allow the reaction to reach equilibrium faster through this shortcut. Mathematically, the reaction between species A and species C changes the zero entries on the upper right and lower left corner of the kinetic matrix to $k_3{}^+$ and $k_3{}^-$, as can be seen from the matrix form of the kinetic model:

$$\frac{d}{dt}\begin{pmatrix}[A]\\[B]\\[C]\end{pmatrix} = \begin{pmatrix} -k_1^+ - k_3^- & k_1^- & k_3^+ \\ k_1^+ & -k_1^- - k_2^+ & k_2^- \\ k_3^- & k_2^+ & -k_3^+ - k_2^- \end{pmatrix}\begin{pmatrix}[A]\\[B]\\[C]\end{pmatrix}$$

A detailed proof of the faster evolution in a three-species cyclic mechanism is given in Appendix A.

There is No momentary equilibrium due to no single-step species.

All three species are involved in two steps, which means that they cannot exhibit a momentary equilibrium in any of the steps. Nevertheless, for this three-species cyclic mechanism the concentration extremum will occur for unperturbed species during the transient regimes, and some special cases such as unitary kinetic parameters would generate special results. This feature will be explored in a future paper with focus on CPE for reaction systems with special parameters.

3.3. Four-Species Acyclic Mechanism

The results of this case are summarized in Figures 6 and 7 and Table 3.

Mechanism:

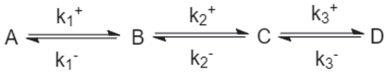

Figure 6. Four-species acyclic mechanism.

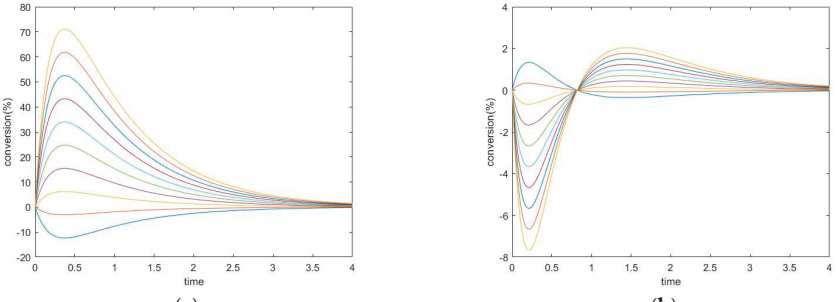

(**a**) (**b**)

Figure 7. Four-species acyclic mechanism, species B and C unperturbed, (**a**) conversion of unperturbed species B, (**b**) conversion of unperturbed species C.

Table 3. A four-species acyclic example.

Experimental Settings	Value	
Kinetic parameters (s^{-1}):	$k_1^+ = 2$	$k_1^- = 1$
	$k_2^+ = 3$	$k_2^- = 1$
	$k_3^+ = 1$	$k_3^- = 1$
Perturbed species:	A, D	
Unperturbed species:	B, C	

3.3.1. *New Findings*—Possibility of Two Extrema and an Inflection Point

Unperturbed species can exhibit two concentration extrema during CPE, a maximum and a minimum, located before and after the point of crossing the equilibrium value in the transient regime. Which extremum occurs first depends on the sign of the perturbations. The times at which the extrema are reached are not dependent upon initial conditions. An inflection point occurs between them, where the second derivative becomes zero for the unperturbed species concentration; the physical meaning is a maximum or minimum of the rate of the substance.

This mechanism leads to six different cases of perturbation when choosing two unperturbed species among four. The simulation settings for all the six combinations are listed in Tables 4 and 5, and two representative cases are plotted in Figure 8. In these experiments, all simulations are performed under the same parameters; only the choice of perturbed species varies.

Table 4. Experiment settings of CPE for a four-species acyclic mechanism.

Experimental Settings	Values	
Kinetic parameters (s^{-1}):	$k_1^+ = 2$	$k_1^- = 1$
	$k_2^+ = 3$	$k_2^- = 1$
	$k_3^+ = 1$	$k_3^- = 1$

Table 5. Cases and results of CPE for a four-species acyclic mechanism.

Experiment	Perturbed Species	Unperturbed Species	Behavior
1	A, B	C, D	2 extrema of [C], 1 of [D]
2	A, C	B, D	1 extremum of [B], 1 of [D]
3	A, D	B, C	2 extrema of [C], 1 of [B]
4	B, C	A, D	1 extremum of [A], 1 of [D]
5	B, D	A, C	1 extremum of [A], 1 of [C]
6	C, D	A, B	1 extremum of [A], 1 of [B]

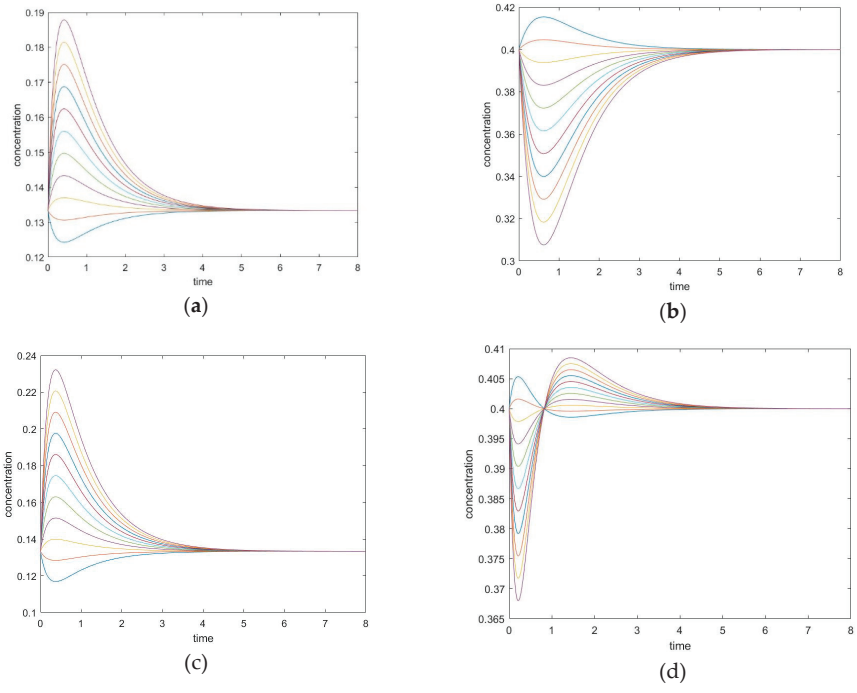

Figure 8. (**a**,**b**) Experiment 2, (**a**) Concentration of the unperturbed species B, and (**b**) concentration of the unperturbed species D. (**c**,**d**) Experiment 3, (**c**) Concentration of the unperturbed species B, (**d**) concentration of the unperturbed species C.

3.3.2. The Initial Rate is Zero for Unperturbed Species that are Connected only with Other Unperturbed Species

In the cases where species A and B are perturbed (i.e., C, D unperturbed), the initial slope of the trajectory of species D is 0 (rate of reaction is 0). The same phenomenon is also observed in species A when C and D are perturbed (A and B unperturbed). See Figure 9.

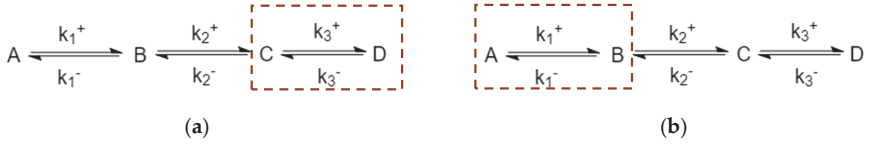

Figure 9. (**a**) Species C and D are unperturbed in experiment #1. (**b**) Species A and B are unperturbed in experiment #6.

In these cases, when the unperturbed species is not connected directly with perturbed species, the initial momentary equilibrium established between the unperturbed species produces a zero initial rate for the species, making the species appear "shielded" by the other species. Nevertheless, this momentary equilibrium will immediately be broken as the other species participate in reactions with perturbed species. The first derivatives of concentrations (i.e., reaction rates) in experiment #1 are plotted in Figure 10. When an initial rate is zero, the extremum rate is unavoidable since the final rate is zero as well. Consequently, an inflexion point of transient concentration is unavoidable.

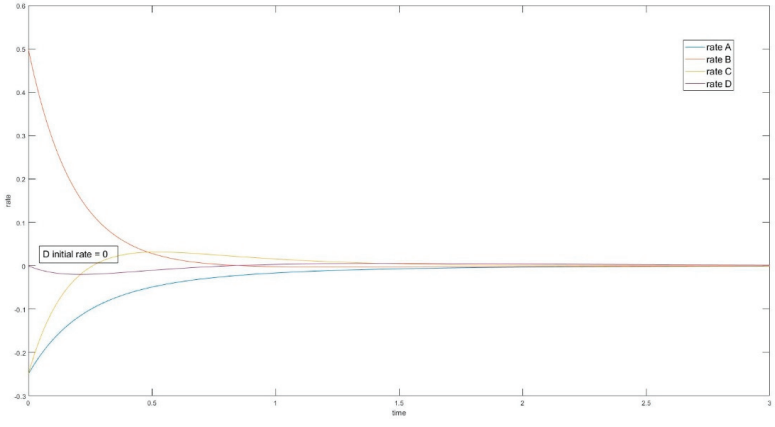

Figure 10. Four-species acyclic reaction, species C and D unperturbed, first derivative. Species D has initial rate equal to 0.

3.3.3. Evolution of Events: Change of the Number of Extrema due to Change in Kinetic Parameter Values

In Experiment #3, species C has two extrema and one inflection point under the given kinetic parameter set. Varying a kinetic parameter such as k_1^+ will lead to a change in the number of extrema, as is plotted in Figure 11.

This shows that a threshold located between $k_1^+ = 1.5$ and $k_1^+ = 1.6$ acts as bifurcation point where switching from the one-extremum to the two-extrema case. This passage from one case to the other may be helpful to identify the source of complexity in this linear dynamic system. Similar bifurcations are discovered for parameters k_1^-, k_2^+ and k_3^-. These questions will motivate future studies of the evolution of events in CPE experiments.

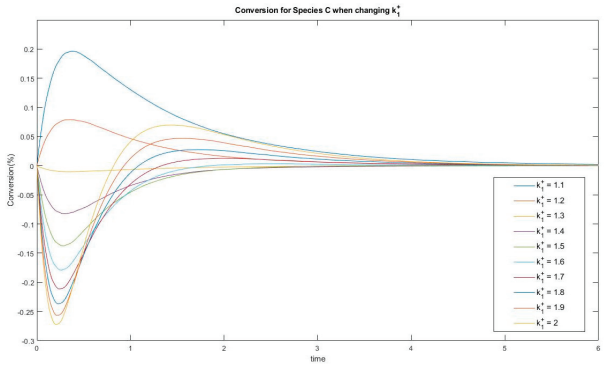

Figure 11. Conversion of species C when changing k_1^+. A passage from one extremum to two extrema behavior is observed.

3.4. Four-Species Cyclic Mechanism

The mechanism is shown in Figure 12. The parameter values used for the simulations are listed in Table 6, along with the choices of perturbed species. Example time evolutions are plotted in Figure 13.

Mechanism:

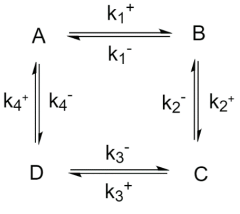

Figure 12. Four-Species Cyclic Mechanism.

Table 6. Kinetic specs of four-species cyclic mechanism.

Experiment Settings	Value	
Kinetic parameters (s^{-1}):	$k_1^+ = 2$	$k_1^- = 1$
	$k_2^+ = 3$	$k_2^- = 1$
	$k_3^+ = 1$	$k_3^- = 1$
	$k_4^+ = 1$	$k_4^- = 6$
Perturbed species:	A, D	
Unperturbed species:	B, C	

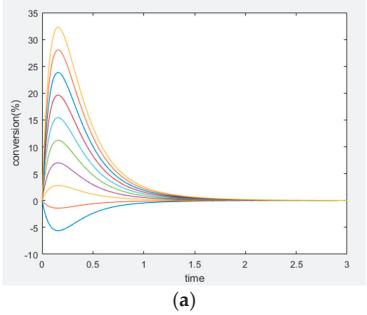

(**a**)

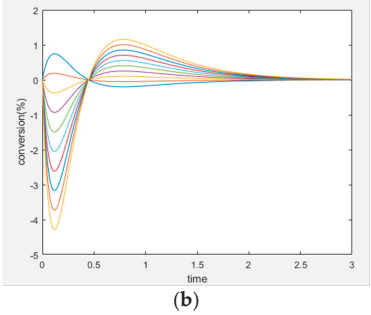

(**b**)

Figure 13. Four-species cyclic mechanism, BC unperturbed, (**a**) conversion of unperturbed species B, (**b**) conversion of unperturbed species C.

3.4.1. *New Findings*—Similarity with Four-Species Acyclic Mechanism: Occurrence of Two Extrema and an Inflection Point

Since the four-species acyclic mechanism is a limit of four-species cyclic mechanisms, it is not surprising to find that the four-species cyclic CPE shares similarity in transient behavior for unperturbed species. Unperturbed species can also exhibit two extrema and one inflection point, as well as crossing their equilibrium concentration during the transient regime. The additional connectivity did not overly modify the complexity of the system behavior.

3.4.2. Zero Initial Rate Behavior for Unperturbed Species Does not Occur

The four-species cyclic mechanism no longer has "end" species participating in only one step; the example plots of rates in Figure 14 illustrates a case where species C and D are unperturbed.

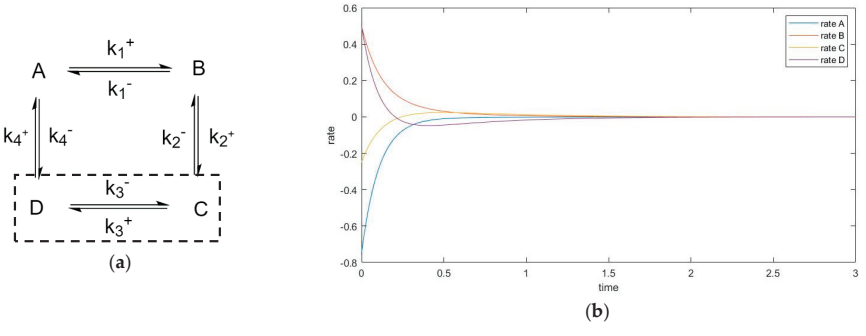

Figure 14. (**a**) Species C and D are unperturbed in the four-species cyclic mechanism experiment. (**b**) plot of first derivatives (rates). Zero initial rate does not occur.

3.5. Four-Species Cyclic Mechanism with Additional Diagonal Connectivity

To investigate further the effect of the mechanism on the behavior of CPE trajectories, we consider systems that are square but connected diagonally, such as the mechanism shown in Figure 15. It is made of two triangles joined into a square, which means that it must satisfy three Onsager relationships: $\frac{k_1^+}{k_1^-}\cdot\frac{k_2^+}{k_2^-}\cdot\frac{k_3^+}{k_3^-}=\frac{k_4^+}{k_4^-}$, $\frac{k_1^+}{k_1^-}\cdot\frac{k_2^+}{k_2^-}=\frac{k_5^+}{k_5^-}$, and $\frac{k_5^+}{k_5^-}\cdot\frac{k_3^+}{k_3^-}=\frac{k_4^+}{k_4^-}$, of which only two are independent.

Mechanism:

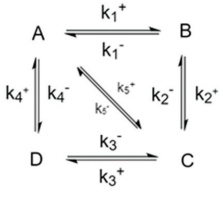

Figure 15. Four-species cyclic mechanism with diagonal connectivity.

An interesting question could be asked regarding the effect of k_5^+ (and k_5^-) on the trajectories. In Figure 16, we see that a system with a larger k_5^+ will behave more akin to a triangular mechanism (or two triangular mechanisms) while a system with a smaller k_5^+ will behave more akin to a square. In particular, when k_5^+ is large, the two extrema become only one.

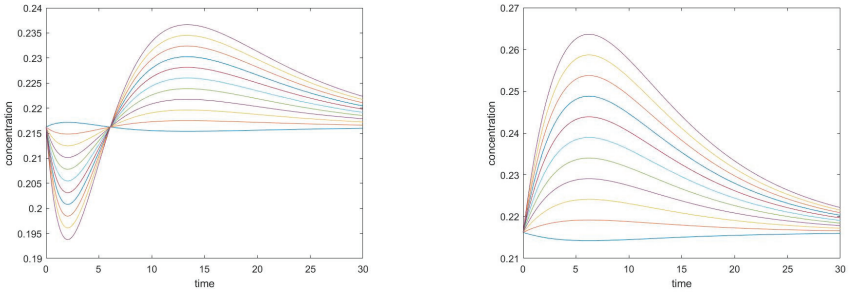

(**a**) (**b**)

Figure 16. (**a**) Small diagonal kinetic constant k_5^+, (**b**) large diagonal kinetic constant k_5^+.

4. Discussion

4.1. Comparing Structural Differences: Number of Species in Mechanism

Four-species mechanisms, in comparison with three-species mechanisms, demonstrate additional complex behavior (i.e., two extrema in concentration instead of one, and an inflexion point in concentration, which is an extremum in rate). Although the mechanisms in the current studies are all linear systems, a series of observable transient complexities can still be interesting to show further detailed information on the mechanism.

4.2. Evolution of Events: Effects of Kinetic Parameters on Complexity

Some complex behaviors only occur in parameter subdomains. Finding the boundary point between a lower and higher complexity (e.g., transition from one extremum to two) remains challenging because it entails the analysis of linear combinations of exponentials, which becomes complicated beyond three-species mechanisms. Overall, the importance of effects determined by kinetic parameters will be an important aspect in further studies of CPE experiments.

5. Conclusions and Future Applications of CPE

The conservatively perturbed equilibrium technique was studied for a given set of chemical mechanisms, featuring acyclic and cyclic mechanisms involving three or four species. Additional structures with different connectivities were also analyzed. The CPE approach allowed to find a link between the type of mechanism and properties of the system relaxation, contributing to decoding the behavior of dynamical systems and relating the observed phenomena to the underlying complexities.

When an unperturbed species is not connected directly with perturbed species, the initial rate is zero, and a rate extremum is unavoidable, which is an inflexion point of transient concentration.

Future applications of CPE could be in catalysis, in simulating isotope exchange reactions, or even more widely, in analyzing large biological systems.

Author Contributions: Conceptualization: G.S.Y.; Formal analysis: D.C.; Investigation: Y.X., D.C. and G.S.Y.; Methodology: G.S.Y.; Software: Y.X., X.L., D.C.; Supervision, G.S.Y. and D.C.; Validation: G.S.Y.; Visualization: Y.X. and X.L.; Writing (original draft): G.S.Y. and Y.X.; Writing (review and editing): D.C. All authors have read and agreed to the published version of the manuscript.

Funding: This research received no external funding.

Conflicts of Interest: The authors declare no conflict of interest.

Appendix A

Analysis of the three-species cyclic mechanism: we want to show that with the addition of k_3^+ (k_3^- which is dependent on k_3^+), the less negative eigenvalue of the cycle transition matrix is more negative than that of the acyclic transition matrix.

First, we can obtain the expression of the nonzero eigenvalues of the cyclic case:

$$\lambda_p \cdot \lambda_m = k_1^+ k_2^+ + k_1^+ k_3^+ + k_2^+ k_3^+ + k_1^+ k_2^- + k_3^+ k_1^- + k_2^+ k_3^- + k_1^- k_2^- + k_1^- k_3^- + k_2^- k_3^-$$

$$\lambda_p, \lambda_m = -\frac{1}{2}\left(k_1^+ + k_1^- + k_2^+ + k_2^- + k_3^+ + k_3^- \pm \sqrt{\left(k_1^+ + k_1^- + k_2^+ + k_2^- + k_3^+ + k_3^-\right)^2 - 4\left(\lambda_p \cdot \lambda_m\right)}\right)$$

Let $A = k_1^+ + k_1^- + k_2^+ + k_2^-$, $C = k_1^- k_2^- + k_1^+ k_2^- + k_1^+ k_2^+$, then

$$\lambda_p \cdot \lambda_m = C + k_1 k_3 + k_2 k_3 + k_3 k_1^- + k_2 k_3^- + k_1^- k_3^- + k_2^- k_3^-$$

Only terms related to k_3^+ and k_3^- are left in the expression, and, from the previous results regarding the expression for the three-species acyclic mechanism, its two nonzero eigenvalues are

$$\lambda_p, \lambda_m = -\frac{1}{2}(A \pm \sqrt{A^2 - 4C})$$

Since k_3^- can be expressed as $K \cdot k_3^+$, where K is a constant composed of only $k_1^+, k_1^-, k_2^+, k_2^-$, we can observe that the expression can be simplified as

$$\lambda_p, \lambda_m = -\frac{1}{2}(A + Bk_3^+ \pm \sqrt{\left(A + Bk_3^+\right)^2 - 4\left(C + Dk_3^+\right)})$$

where the A, B, C, D are constants that only consist of $k_1^+, k_1^-, k_2^+, k_2^-$, and are fixed in the comparison between acyclic and cyclic mechanisms.

We can now consider only the expression $A + Bx - \sqrt{(A + Bx)^2 - 4(C + Dx)}$ for the less negative eigenvalue.

Observe that

$$\lim_{x \to 0} A + Bx - \sqrt{(A + Bx)^2 - 4(C + Dx)} = A - \sqrt{A^2 - 4C}$$

The right-hand side of the equation is exactly the expression for the three species linear case. So, as k_3^+ and k_3^- converge to 0, the cyclic mechanism becomes the acyclic, which makes physical sense as well.

To show that the less negative eigenvalue of the cyclic transition matrix is more negative than that of the acyclic transition matrix, we need to show that

$$A + Bx - \sqrt{(A + Bx)^2 - 4(C + Dx)} > A - \sqrt{A^2 - 4C} \text{ for all } x > 0$$

First, since the eigenvalues of chemical systems are real,

$$(A + Bx)^2 - 4(C + Dx) > 0$$

The minimum of the left hand side is $-\frac{(2AB-4D)^2-4B^2\left(A^2-4C\right)}{4B^2}$ from the quadratic formula.

Thus $-\frac{(2AB-4D)^2-4B^2\left(A^2-4C\right)}{4B^2} > 0$, we simplify to get $ABD - B^2C - D^2 > 0$.

Secondly, we show that

$$\begin{gathered} A + Bx - \sqrt{(A + Bx)^2 - 4(C + Dx)} > A - \sqrt{A^2 - 4C} \\ \Leftrightarrow\ Bx + \sqrt{A^2 - 4C} > \sqrt{(A + Bx)^2 - 4(C + Dx)} \end{gathered}$$

Square both sides:

$$\begin{gathered} \Leftrightarrow (Bx)^2 + (A^2 - 4C) + 2Bx\sqrt{A^2 - 4C} > (A + Bx)^2 - 4(C + Dx) \\ \Leftrightarrow (Bx)^2 + (A^2 - 4C) + 2Bx\sqrt{A^2 - 4C} > (A + Bx)^2 - 4(C + Dx) \\ \Leftrightarrow Bx\sqrt{A^2 - 4C} > ABx - 2Dx \end{gathered}$$

Square both sides:

$$\begin{gathered} \Leftrightarrow\ Bx^2\left(A^2 - 4C\right) > (ABx)^2 + 4(Dx)^2 - 4ABDx^2 \\ \Leftrightarrow\ -4CBx^2 > 4D^2x^2 - 4ABDx^2 \\ \Leftrightarrow\ -CB > D^2 - ABD \end{gathered}$$

References

1. Yablonsky, G.S.; Branco, P.D.; Marin, G.B.; Constales, D. Conservatively Perturbed Equilibrium (CPE) in Chemical Kinetics. *Chem. Eng. Sci.* **2019**, *196*, 384–390. [CrossRef]
2. Yablonsky, G.S.; Branco, P.D.; Marin, G.B.; Constales, D. New Invariant Expressions in Chemical Kinetics. *Entropy* **2020**, *22*, 373. [CrossRef]
3. Yablonsky, G.S.; Constales, D.; Marin, G.B. Equilibrium relationships for non-equilibrium chemical dependencies. *Chem. Eng. Sci.* **2011**, *66*, 111–114. [CrossRef]
4. Yablonsky, G.S.; Gorban, A.N.; Constales, D.; Galvita, V.; Marin, G.B. Reciprocal Relations Between Kinetic Curves. *Europhys. Lett.* **2011**, *93*, 20004–20007. [CrossRef]
5. Yablonsky, G.S.; Constales, D.; Marin, G.B. New Types of Complexity in Chemical Kinetics: Intersections, Coincidences and Special Symmetric Relationships. *Adv. Chem. Phys.* **2014**, *157*, 69–73.
6. Branco Pinto, D.; Yablonsky, G.S.; Marin, G.B.; Constales, D. New Patterns in Steady-State Chemical Kinetics: Intersections, Coincidences, Map of Events (Two-Step Mechanism). *Entropy* **2015**, *17*, 6783–6800. [CrossRef]
7. Hankins, M.J.; Yablonsky, G.S.; Kiss, I.Z. Dual kinetic curves in reversible electrochemical systems. *PLoS ONE* **2017**, *12*, e0173786. [CrossRef] [PubMed]
8. Peng, B.; Yablonsky, G.S.; Constales, D.; Marin, G.B.; Muhler, M. Experimental confirmation of a new invariant for a non-linear chemical reaction. *Chem. Eng. Sci.* **2018**, *191*, 262–267. [CrossRef]
9. Yablonsky, G.S.; Constales, D.; Marin, G.B. Joint kinetics: A new paradigm for chemical kinetics and chemical engineering. *Curr. Opin. Chem. Eng.* **2020**, *29*, 83–88. [CrossRef]
10. Zeldovich, Y.B. Proof of the uniqueness of the solution of mass-action law equations. *Zh. Fiz. Khim.* **1938**, *11*, 685–687. (In Russian)
11. Zeldovich, Y.B. *Selected Works of Yakov Borisovich Zeldovich*; Volume I: Chemical and Hydrodynamics, Chapter "Proof of the Uniqueness of the Solution of the Equations of the Law of Mass Action"; Princeton University Press: Princeton, NJ, USA, 2014; pp. 144–147.
12. Shapiro, N.Z.; Shapley, L.S. Mass action laws and the Gibbs free energy function. *J. Soc. Ind. Appl. Math.* **1965**, *13*, 353–375. [CrossRef]
13. Aris, R. Prolegomena to the rational analysis of systems of chemical reactions. *Arch. Ration. Mech. Anal.* **1965**, *19*, 81–99. [CrossRef]
14. Aris, R. Prolegomena to the rational analysis of systems of chemical reactions II. Some addenda. *Arch. Ration. Mech. Anal.* **1968**, *27*, 356–364. [CrossRef]
15. Horn, F.; Jackson, R. General mass action kinetics. *Arch. Ration. Mech. Anal.* **1972**, *47*, 81–116. [CrossRef]
16. Vol'pert, A.I. Differential equations on graphs. *Math. USSR Sbornik.* **1972**, *17*, 571–582. [CrossRef]
17. Vol'pert, A.I.; Khudyaev, S.I. *Analysis in Classes of Discontinuous Functions and Equations of Mathematical Physics*; Martinus Nijhoff: Dordrecht, The Netherland, 1985; 704p.

18. Gorban, A.N. On the problem of boundary equilibrium points. *React. Kinet. Catal. Lett.* **1980**, *15*, 315–319.
19. Gorban, A.N.; Mirkes, E.M.; Yablonsky, G.S. Thermodynamics in the limit of irreversible reactions. *Phys. A Stat. Mech. Its Appl.* **2013**, *392*, 1318–1335. [CrossRef]
20. Gorban, A.N.; Yablonsky, G.S. Extended detailed balance for systems with irreversible reactions. *Chem. Eng. Sci.* **2011**, *63*, 5388–5399. [CrossRef]
21. Yablonskii, G.S.; Bykov, V.I.; Gorban, A.N.; Elokhin, V.I. Kinetic Models of Catalytic Reactions. In *Comprehensive Chemical Kinetics*; Compton, R.G., Ed.; Elsevier: Amsterdam, The Netherlands, 1991; Volume 32, 396p.
22. Marin, G.B.; Yablonsky, G.S.; Constales, D. *Kinetics of Chemical Reactions: Decoding Complexity*, 2nd ed.; John Wiley–VCH: Weinheim, Germany, 2019; p. 13.
23. Gorban, A.N.; Yablonsky, G.S. Three Waves of Chemical Dynamics. *Math. Model. Nat. Phenom.* **2015**, *10*, 1–5. [CrossRef]
24. Peng, B.; Zhu, X.; Constales, D.; Yablonsky, G.S. Experimental verification of conservatively perturbed equilibrium for a complex non-linear chemical reaction. *Chem. Eng. Sci.* **2020**, *229*, 116008. [CrossRef]
25. Eigen, M. Nobel Prize Lecture, "Immeasurably *Fast Reactions*". 11 December 1967. Available online: https://www.nobelprize.org/uploads/2018/06/eigen-lecture.pdf (accessed on 28 September 2020).
26. Bernasconi, C.F. *Relaxation Kinetics*; Academic Press: Cambridge, MA, USA, 1976; 288p.

entropy

MDPI

Article

Finite-Time Thermodynamics in Economics

Anatoly Tsirlin [1,*] and Larisa Gagarina [2]

[1] Ailamazyan Program Systems Institute of Russian Academy of Sciences, 152120 Rostov, Russia
[2] Institute of Systems and Program Engineering and Information Technologies, National Research University of Electronic Technology, 124482 Zelenograd, Russia; gagar@bk.ru
* Correspondence: tsirlin@sarc.botik.ru

Received: 15 July 2020; Accepted: 12 August 2020; Published: 13 August 2020

Abstract: In this paper, we consider optimal trading processes in economic systems. The analysis is based on accounting for irreversibility factors using the wealth function concept. The existence of the welfare function is proved, the concept of capital dissipation is introduced as a measure of the irreversibility of processes in the microeconomic system, and the economic balances are recorded, including capital dissipation. Problems in the form of kinetic equations leading to given conditions of minimal dissipation are considered.

Keywords: thermodynamics; economics; optimal processes; irreversibility

1. Introduction

Systems that include a large number individually unobservable and uncontrollable elements which interact with each other are called *macrosystems*. The behavior of a component in such a system can be stochastic and yet the behavior of the system on a macro level, when averaged processes are observed, is deterministic. Thermodynamic systems of various nature with a large number of molecules interacting with each other on a micro level are a classical example of a macrosystem.

When contact is established between inhomogeneous macrosystems the processes of stochastic interaction occur. In thermodynamics these are, e.g., heat exchange, diffusion, and chemical transformation processes. It is not possible to return the system, when stochastic interaction process occurred, into its initial state without changing the system's environment. This *irreversibility* of spontaneous processes of stochastic interactions is the key feature of macrosystems.

Microeconomics studies interaction of economic agents (EAs). An EA is a group of individual agents whose averaged characteristics determine the EAs' characteristics. Sometimes we will use an analogy between microeconomics and thermodynamics and refer to the economic system (ES), where all economic agents are subsystems. The interaction between EAs leads to exchange of resources between them and consumption and/or production of these resources by them. In the course of these interactions each agent strives to increase its utility by choosing which kind of resource to exchange with which other kind of resource and in which quantity. Economic systems can be *isolated* from the environment. In this case all the exchange takes place inside the system. Economic systems can be *open*. Then, exchange of all or some of the resources can also occur between the system and its environment.

The processes of stochastic interactions in economics are irreversible as they are in any macrosystem. However, they are quite different from irreversible processes in thermodynamics chiefly because each subsystem chooses to participate in an exchange if that does not lead to a "loss". Nevertheless, it is also possible to define an economic measure of irreversibility that attains maximum for an isolated system in equilibrium (like entropy in thermodynamics). It is also possible to define a non-negative function in economics similar to entropy production in thermodynamics and to formulate economic balances that include this function.

In the case when the duration of the processes is limited or the average intensity of the flows is fixed in the economy, the situation is very similar to finite-time thermodynamics (FTT).

In this paper a macrosystem approach to economic systems modeling is described. A number of economic problems that are similar to classical thermodynamic problems are solved.

2. Major Types of Economic Agents and Their Characteristics

The state of an economic agent is described by the vector of its stocks (amount of holdings) of resources $N = N_1, N_2, \ldots, N_k$ and capital (cash) M. We assume that capital is measured by all economic agents using a single common unit (e.g., gold or an international currency). N and M are extensive variables, that is, when homogeneous economic systems merge/split, the values of these variables change in the same proportion. An economic system is also described by a vector of intensive variables—the estimates of how valuable these resources are for it given by the prices $p = (p_1, ..., p_k)$ and the estimate of how valuable capital is for this system p_0. When economic systems merge, these variables equalize. *The new estimate p_i for the resource i (its internal equilibrium price) is equal to the minimal price, in units of capital, for which the economic agent is prepared to sell resource i and the maximal price at which it is prepared to buy it.*

When an economic agent is offering to buy and sell resources, it is described by its supply and demand functions. The demand function shows the quantity of the i-th resource it is prepared to purchase for the price c_i. The higher this price is, the lower, as a rule, is this demand. Finally, at some price $c_i = p_i$ the economic agent stops buying. This is similar to the dependence of the heat flux on the temperature of the source and the working fluid in a heat engine. If $c_i > p_i$, then it is prepared to sell the i-th resource, and the higher c_i is the larger quantity it is prepared to sell.

The unit of p_i is the unit of M divided by unit of N_i. These estimates are related to amounts of resources and capital of an economic agent in the same way intensive variable in thermodynamics are related to extensive ones. The units of c_i and p_i are the same, but c_i could be set manually by some intermediary agent. The estimate p_0 is the value of capital in units of some basic currency, for example, gold. More detailed discussion of the relationship between estimate of some resource and capital is given below.

In many cases demand and supply functions relate the price not to the quantity but to the flow of resource, $n_i(p_i, c_i)$. The function $n_i(p_i, c_i)$ determines the kinetics of resource exchange. If we define positive flow directed toward the economic agent then

$$\begin{gathered} \operatorname{sign} n_i(c_i, p_i) = \operatorname{sign}(p_i - c_i) \\ n_i(c_i, p_i) = 0 \text{ when } c_i = p_i \text{ and } \frac{\partial n_i}{\partial c_i} < 0. \end{gathered} \tag{1}$$

The dimension of the vector c is the unit of capital divided by the unit of resource.

We define three types of economic agents.

1. *Economic agents whose resource estimates p_i depend on the agent's state* (on its stocks of resources and capital). Usually, but not always, when the stock of a resource is decreasing its estimate is decreasing too, and when capital is increasing then the estimate is increasing. The economic agent can also exchange capital M with the environment. Here, the minimal price of selling (maximal price of buying) is the economic agent's estimate of capital. We denote it as $p_0(N, M)$. We shall call such systems *economic systems with finite capacity*.
2. *Economic agents with estimates p_i independent of stocks of the resource* are similar to thermodynamic systems with infinite capacity (reservoirs). We shall call them *economic reservoirs*. Economic markets where prices do not depend on the rate of trading are examples of economic reservoirs. The amount of resource that is sold/purchased here is so small in comparison with its stock that in practice it does not effect its estimate.

In the general case, a market's demand/supply function $n(c, p)$ depends on the prices of selling (buying) and on the estimates, and it obeys the conditions (1) for resource exchange kinetics. Such a market is called *monopolistic*. In the limit when for each flow n the difference between the price and estimate is infinitesimal (prices for any rate of flow n are equal to the market estimates), then the market is called a *market with perfect competition*. If this market is a reservoir then its prices do not depend on the demand but change over time under the influence of the external system factors.

3. *Intermediaries (firms) are active economic agents* which set the price or rate of resource selling (buying) independently of its stock in such a way that they extract maximum amount of capital. They are similar to a heat engine working fluid in thermodynamics. They can contact with a number of economic agents simultaneously setting different prices and flows for each of them. The intermediary's prices and its function that describes when to establish/break contact with an economic agent are controls.

   A firm can be a manufacturing firm which buys resources (raw materials, labor, or equipment) and sells its production, which is determined by its production function [1] and the price it sets. We denote the price for the i-th resource set by a firm as c_i.

2.1. Wealth Function and Capital Dissipation

Existence of a wealth function and its properties. During an exchange an economic agent sells and buys resources which alters its stocks of resources and capital. Let us introduce the function U by the differential

$$dU = dM + \sum_i p_i dN_i. \tag{2}$$

We shall call it *capitalization* of an economic agent because its variation takes into account changes of capital M as well as changes of *illiquid capital* (stocks) $F = \sum_i p_i N_i$. During equilibrium exchange when prices of selling/buying are infinitesimally close to the estimates p_i, U does not change, $dU = 0$, as $dM = -\sum_i p_i dN_i$. Such a process is reversible, because the economic agent can buy the same amount of resource as it sold using the capital from the selling and return to the original state without changing anything in its environment.

Suppose equilibrium exchange takes place between a firm and an economic agent when one resource is exchanged for another. Exchange is carried out reversibly and therefore the initial and the final states of the economic agent in the space with coordinates N_i coincide. If a firm can extract any capital as a result of this process, then it would be possible to extract an unlimited amount of capital using just one economic agent and not cause any changes in the environment. As this is not possible, it follows that for $p_0 = \text{const}$.

$$\oint \sum_i p_i(N, M)\, dN_i = 0. \tag{3}$$

From this condition it follows that a function $Z(N, p_0)$ exists such that its partial derivatives w.r.t. N_i are equal to p_i and its differential has the form,

$$dZ = \sum_i p_i\, dN_i + \frac{\partial Z}{\partial p_0}\, dp_0. \tag{4}$$

The condition (2) can be rewritten in the following form,

$$dU = dM + dZ - \frac{\partial Z}{\partial p_0}\, dp_0 = d(M + Z) - \frac{\partial Z}{\partial p_0}\, dp_0. \tag{5}$$

After denoting $M + Z = Y$ and $-\dfrac{\partial Z}{\partial p_0} = \gamma$ we get

$$dU = dY + \gamma\, dp_0. \tag{6}$$

Thus, this differential is a Pfaffian form with two variables which always has an integrating multiplier.

A *Pfaffian form* is a differential form of degree one, that is, the sum of the products of functions of some variables and the differentials of these variables,

$$dK = \sum_{i=1}^{n} F_i(x)\, dx_i. \tag{7}$$

If $n = 2$ and the functions F_i are differentiable, then it is always possible to a find multiplier $r(x)$ such that $dS = r(x)dK$ is a complete differential, that is, S depends on x and $\oint dS = 0$. We denote this multiplier for our system $p_0(N, M)$.

Thus, we proved that *there exists a function of state variables (extensive variables), $S(N, M)$, such that its differential has the form*

$$dS = p_0(N, M)dU = p_0(N, M)\left[dM + \sum_i p_i(N, M)dN_i\right]. \tag{8}$$

In a reversible cycle of resource exchange (that is, when the prices of resources coincide with their estimates) the function S does not change,

$$\oint dS = 0. \tag{9}$$

In cyclic processes the amounts of resources and capital are the same both for initial and final state. The condition (9) is satisfied if the price of some resource and its estimate are equal at each point of the cycle, so resource's flows are negligible.

The resource estimates can be expressed in terms of the function S as

$$p_0 = \frac{\partial S}{\partial M}, \qquad p_i = \frac{\partial S}{\partial N_i} \Big/ \frac{\partial S}{\partial M}, \quad i = 1, 2, ... \tag{10}$$

Here, the capital estimate $p_0 > 0$ for all economic agents, but p_i could be negative if the resource requires reprocessing or storage costs.

$S(N, M)$ is called the *wealth function*. The above-described proof of its existence is derived as the consequence of the impossibility to profit indefinitely from trading with one economic agent is an exact copy of the proof of the existence of entropy in thermodynamics. It was obtained by Rozonoer in Appendix of [2]. More general proof is given in [3].

In microeconomics the preferences of an economic agent are often described by its indifference curves (surfaces). Each such curve singles out the set of equally preferred states. If stocks of all resources of an economic agent except one remain constant and this one stock (which could be capital, the basic resource) is increased, then its state is transferred to the higher indifference curve. The existence of S was proven in [4] using the Ville axiom [5], which uses the notion of preferred states of an economic agent: *it is not possible to find a sequence of states $X_1, X_2, ..., X_m$ in the state space $X = (N, M)$ such that X_i is preferred to X_{i-1} for $i = 2, \ldots, m$, and the initial and final states coincide $X_1 = X_m$.*

During resource exchange between economic agents the *voluntary condition*, that the wealth functions S_ν of any participant cannot decrease, must be met (the only exception is exchange associated with charity). The voluntary condition precludes direct exchange of one resource unless its estimates for contacting agents are different. Such exchange becomes possible only if there is an intermediary.

If the wealth function is measured in units of local currency, then $p_0 > 0$ characterizes the value of foreign currency for an agent. Its unit is [unit of local currency/unit of foreign currency]. For currency exchange the estimate p_0 plays the same role as the estimate p for resource exchange.

The description of economic systems becomes similar to thermodynamic equations if we formally introduce an "economic temperature" as

$$T = \frac{1}{p_0} \tag{11}$$

as was done in [2,3].

When the properties of an economic agent do not change but its "scale" changes, its stocks of resources and capital are changed proportionally. It is natural to assume that the wealth function changes in the same way here, that is, that it is an extensive function just like N and M are. In this case, S is a uniform function of first degree and its derivatives on N and M are uniform functions of zero degree. From Euler's Theorem it follows that it can be written as

$$S(N, M) = p_0(M, N)\left(\sum_i p_i(M, N)N_i + M\right). \tag{12}$$

The dependence $p(N, M)$ can be found from experimental data.

If the existence of the wealth function S is postulated, then the estimates may be determined by solving the extremal problem

$$S(N, M) \to \max \Big/ \left(\sum_i p_i N_i + M\right) = V, \tag{13}$$

where V is fixed. In this case, the solution of the problem (13) and the values of p and p_0 are linked via

$$p_i(N, M) = \frac{\partial S}{\partial N_i} \Big/ \frac{\partial S}{\partial M}. \tag{14}$$

It is assumed that function S is continuously differentiable and strictly concave. Therefore, the solution of the problem (13) exists and is unique and each p_i decreases when N_i increases. Thus, an economic agent is similar to a finite capacity subsystem in thermodynamics. For an economic reservoir resource and capital estimates are constant and S is linear.

Despite the similarity of the welfare function to thermodynamic entropy, there are differences between them. In the general case the wealth function is not additive, and the sum of wealth functions for the subsystems is not equal to the wealth function of the entire system. Furthermore, the units of the wealth functions for different subsystems could be different. Unlike the wealth function, the capitalization, the capital, and invested capital have the same unit and are additive.

2.2. *Differential Links between Estimates—Economic Analogue of the Gibbs–Duhem Relation*

Let us write the differential of S

$$dS = p_0\left(dM + \sum_{i=1}^{n} p_i dN_i\right) = p_0 dU. \tag{15}$$

From (15) we get

$$dM = \frac{dS}{p_0} - \sum_{i=1}^{n} p_i dN_i. \tag{16}$$

From (12) it follows that

$$M = \frac{S}{p_0} - \sum_{i=1}^{n} p_i N_i \tag{17}$$

$$dM = \frac{dS}{p_0} + S\,d\left(\frac{1}{p_0}\right) - \sum_{i=1}^{n}(p_i dN_i + N_i dp_i). \tag{18}$$

The comparison of (18) and (16) yields the relation between capital estimate and resource estimate,

$$S\,d\left(\frac{1}{p_0}\right) - \sum_{i=1}^{n} N_i dp_i = 0. \tag{19}$$

Similarly, comparison of the differential of S found using (12) with the expression (15) yields

$$Mdp_0 + \sum_{i=1}^{n} N_i d(p_0 p_i) = 0. \tag{20}$$

The conditions (19) and (20) follow from the existence of the homogeneous function S. They are economic analogues of the Gibbs–Duhem equation in thermodynamics. One of their consequences when the state of the system is changed in such a way that the resource estimates are constant is that the capital estimate is also constant.

As the matrix of second derivatives for a twice differentiable function is symmetric, the sensitivity of the resource and capital estimates with respect to stock variations are linked by the following equations,

$$\frac{\partial(p_0 p_i)}{\partial N_j} = \frac{\partial(p_0 p_j)}{\partial N_i} = \frac{\partial^2 S}{\partial N_i \partial N_j} \tag{21}$$

$$\frac{\partial p_0}{\partial N_j} = \frac{\partial(p_0 p_j)}{\partial M} = \frac{\partial^2 S}{\partial M \partial N_j}. \tag{22}$$

It is easy to show using (21) and (22) that

$$\frac{\partial p_i}{\partial N_j} + p_i \frac{\partial p_j}{\partial M} = \frac{\partial p_j}{\partial N_i} + p_j \frac{\partial p_i}{\partial M}, \quad i, j = 1, ..., n. \tag{23}$$

The Equations (21) and (22) are economic analogs of the Maxwell relations.

2.3. Capital Dissipation

Let us again consider the cyclic process of interaction between one economic agent and one intermediary. We now require that the average rate of exchange is fixed. Then, the intermediary has to increase the price above the estimate p_i when it is buying and decrease it below estimates when selling. The economic agent's capitalization here increases because

$$\Delta U = \oint \sum (p_i(N, M) - c_i)\, dN_i > 0, \tag{24}$$

and the intermediary suffers losses of ΔU in comparison with the reversible process.

The change of capitalization is positive, as $p_0(N, M) > 0$.

The rate of the intermediary's losses due to irreversibility is non-negative,

$$\sigma(t) = \sum_i n_i(p_i, c_i)(p_i - c_i) \geq 0. \tag{25}$$

We shall call it the *capital dissipation* due to resource exchange irreversibility. It can be interpreted as trading costs.

The condition (24) of capitalization is non-decreasing (and therefore wealth is non-decreasing) during an economic exchange is analogy to the Clausius integral. The law that during a contact between two economic agents where a resource is transferred from the agent with lower estimate to the agent with higher estimate and that the net invested capital is not decreasing $(\Delta(F_1 + F_2) \geq 0)$

is the analogue of of the second law of thermodynamics. It allows us to construct an irreversible microeconomic theory similar to finite-time thermodynamics.

2.4. The Second Law of Microeconomics

The resource conservation laws in microeconomics are analogs of conservation of mass and energy in thermodynamics.

Let us consider the economic analogue of the other fundamental law of thermodynamics, the Second Law. Clausius' statement of the Second Law is "*Heat cannot of itself pass from a colder to a hotter body without some other change, connected herewith, occurring at the same time*." Leontovich's formulation is "*It is not possible to build a device which would produce positive work only by cooling one body without any other effects*."

In microeconomics these formulations correspond to the following statements. (i) *The flux of a scalar resource cannot flow from an economic agent with a higher estimate to an economic agent with a lower estimate without other changes taking place.* (ii) *It is not possible to produce profit by carrying out exchange with one economic agent without any other changes.*

Planck's statement says "*The entropy of an isolated thermodynamic system during an irreversible process can only increase and its exergy can only decrease. The equilibrium state of such a system has maximum entropy subject to imposed constraints*."

Similarly, *resource exchange processes in isolated microeconomic systems occur in such a direction that the net capitalization of the economic agents increases and attains a maximum subject to constraints imposed on the system, including the voluntary principle. At the same time, the potential ability to extract profit (profitability) decreases and attains a minimum under the same conditions.*

As the net amount of capital in an isolated system is constant ($dM = 0$), the maximum of capitalization corresponds to maximum of invested capital.

Table 1 shows major analogies between thermodynamic and economic systems. The following notations are used in Table 1. T_- and T are temperatures of the reservoir and contacting system, respectively; p_- is resource estimate on the perfect competition market; c is the resource price set by an intermediary; N is the stock of resources; U is internal energy; and q and n are the flows of heat and resource, respectively.

Table 1. Analogies between thermodynamic and economic systems.

Thermodynamic System		**Economic System**	
Name	**Notation**	**Name**	**Notation**
Temperature of a system with finite capacity	T	The reciprocal of capital estimate for EA	$1/p_0$
Reservoir (irreversible heat exchange)	$q = \alpha(T - T_-)$	Monopolistic market	$n = \alpha(p - p_-)$
Mass	N	Resource stock	N
Finite-capacity system, chemical potential	$\mu(N)$	Economic agent, resource estimate	$p(N)$
Temperature of the working fluid for heat engine	$T(t)$	Intermediary, price	$c(t)$
Free energy	A	Capital	M
Internal energy	E	Capitalization	U
Entropy	S	Wealth function	S
Entropy production	σ	Capital dissipation	σ

3. Economic Balances and Capital Dissipation

3.1. Open Systems

Consider an open economic system that exchanges resources and capital with an environment. The subscript i denotes the i-th resource and j denotes j-th subsystem. We assume that external flows entering the system are positive and leaving are negative. These flows can be divided into two group. First there are flows caused and effected by external factors. The flows from the second group depend on the prices set by external sellers and buyers and on the estimates of resources in the corresponding subsystem. Similarly to thermodynamics, we shall call the former flows convective and denote them by subscript k and the latter diffusive and denote them by subscript d. Note that a subsystem can produce some resources by using others.

The balance for the i-th resource is

$$\dot{N}_i = \sum_j \left(n_{ij}^k(t) + n_{ij}^d(p_j, c_j) + W_j(p_j)\alpha_{ij}\right), \quad i = 1, 2, \ldots \tag{26}$$

The sum here is over all subsystems, $W_j(p_j)$ is the production rate in the j-th subsystem, and the coefficients $\alpha_{ij} > 0$ if the i-th resource is produced in the j-th subsystem and $\alpha_{ij} < 0$ if it is consumed there. The α's determine the rate at which the i-th resource is produced (consumed); c_j is the price vector for the exchange between the j-th subsystem and its environment.

The balance on capital is

$$\dot{M} = \sum_j \left(m_j^k(t) - \sum_i c_{ij} n_{ij}^d(p_j, c_j)\right). \tag{27}$$

The balance on the invested capital is

$$\dot{U} = \dot{M} + \dot{F} = \dot{M} + \sum_{i,j} p_{ij}(N_j, M_j)(n_{ij}^k + n_{ij}^d(p_j, c_j)) + \sigma, \tag{28}$$

where the capital dissipation σ is

$$\sigma = \frac{1}{2}\sum_j \sum_\nu n_{j\nu}(p_j, p_\nu)(p_j - p_\nu) + \sum_j W_j(p_j) A_j. \tag{29}$$

Here p_j and p_ν are vectors of resource estimates for the j-th and ν-th subsystems with the components p_{ij} and $p_{i\nu}$. Correspondingly, $A_j = \sum_i \alpha_{ij} p_i$ and $n_{j\nu} = -n_{\nu j}$ is the vector-function of flow of resources.

The dissipation of capital, similar to the production of entropy in thermodynamics, is calculated as the product of the flow and the driving force, and it is always non-negative. It makes sense of capital losses associated with the creation of a flow of a given intensity. If $\Delta p_{j\nu} = p_j - p_\nu$ is small and the kinetic function $n_{j\nu}$ is differentiable, then σ is a positive-definite quadratic form.

Just as in the theory of FTT, in economics problems arise about the choice of exchange process parameters when we desire that a given average intensity of exchange flows with a minimum average capital dissipation.

The balance on capitalization is (28) with the capital dissipation σ defined by (29). Here, the first term is due to resource-exchange variation in the amount of illiquid capital and the second is due to production. For profitable production, the dependencies $W_i(p_i)$ are such that $W_i(p_i)\sum_j p_{ij}\alpha_{ij} = W_i(p_i)A_i(p_i, \alpha_i)$ are non-negative. p_j and p_ν are vectors of resource estimates for contacting subsystems with components p_{ji} and $p_{\nu i}$, and $n_{j\nu} = -n_{\nu j}$.

In a stationary regime the rhs of Equations (26)–(28) are equal to zero. In a cyclic regime when

$$N(0) = N(\tau), \quad M(0) = M(\tau), \quad U(0) = U(\tau), \tag{30}$$

the integrals of the rhs of these equations are equal zero.

3.2. Isolated Systems

Consider an isolated economic system with no external flows entering or leaving it. Then, the balance Equations (26)–(28) take the form

$$\dot{N}_i = \sum_j W_j(p_j)\alpha_{ij}, \quad N_i(0) = \sum_j N_{ij}(0) \tag{31}$$

$$\dot{M} = \sum_i \dot{M}_i = 0 \tag{32}$$

$$\dot{F} = \sum_j \dot{F}_j = \sigma \geq 0. \tag{33}$$

In equilibrium the invested capital is maximal and the flows n_{ij} and $W_j(p_j)$ are equal to zero. The distribution of capital M between the subsystems in equilibrium depends on the kinetics of resource exchange.

For each j-th subsystem of an isolated system

$$\dot{N}_{ji} = \sum_\nu n_{\nu ji}(p_j, p_\nu) + W_j(p_j)\alpha_{ij} \tag{34}$$

$$\dot{M}_j = \sum_{\nu,i} \tilde{n}_{\nu ji}(p_j, c_{j\nu})c_{j\nu i}, \quad i, j = 1, \ldots, n. \tag{35}$$

Here, $c_{j\nu}$ is the vector of intermediate prices with components $c_{j\nu i}$, which are to be found from the condition of flow continuity,

$$\tilde{n}_{\nu ji}(p_j, c_{j\nu}) = -\tilde{n}_{j\nu i}(c_{j\nu}, p_j) = n_{\nu ji}(p_j, p_\nu). \tag{36}$$

Thus, the price vector, and therefore the rhs of equation (35), depends on the forms of kinetic functions of supply and demand, $\tilde{n}_{\nu j}$. After expressing $c_{j\nu}$ from (36) and its substitution into $\tilde{n}_{j\nu}$ and $\tilde{n}_{\nu j}$ both these functions turn out to be equal to the kinetic function $n_{j\nu}(p_j, p_\nu)$ that was used in (29) and (34).

The equilibrium distribution of capital $\overline{M}$ is determined by the resource exchange kinetics, and $\overline{M}$ depends on equilibrium stocks $\overline{N}$ as they obey the condition

$$p_j(\overline{M}, \overline{N}) = p_\nu(\overline{M}, \overline{N}) = \lambda, \quad \forall j, \nu. \tag{37}$$

In some cases the object of interest is the set Q of the values of $\overline{M}$ that can be attained from the given initial state for different demand–supply functions $\tilde{n}(p, c)$.

For each j-th subsystem the minimal capital increase $\Delta M_j = \overline{M}_j - M_{j0}$ is achieved when the exchange with all the other subsystems is carried out using c_j arbitrarily close to p_j, that is, reversibly. Therefore, $\overline{M}_j^{min}$ can be found from the condition $S_j(\overline{M}_j, \overline{N}_j) = S_j(M_{j0}, N_{j0})$.

A maximal $\overline{M}_j^{max}$ corresponds to such an exchange for which it is possible to construct a range $\overline{M}_j^{min} \leq M_j \leq \overline{M}_j^{max}$ in the space of M_j. The intersection of this range with the plane

$$\sum_j \overline{M}_j = \sum_j M_{j0} \tag{38}$$

singles out the set Q of all feasible equilibrium distributions of capital.

As $\sigma(p) > 0$, the illiquid capital in the flows entering a non-homogeneous open system is always higher than in the flows leaving the system.

This condition $\sigma(p_1, p_2) \geq 0$ jointly with the balances (26)–(28) determine the boundary of the realizability area of irreversible process for an economic systems. The conditions imposed on the rates of various flows allow us to find the minimal capital dissipation, $\sigma_{\min} > 0$, achievable for these conditions. This reduces realizability area as the inequality $\sigma \geq 0$ is less restrictive than $\sigma \geq \sigma_{\min}$. This is analogous to the result that the realizability area for a heat engine in FTT is more restricted than if comparison is only made with an equilibrium system.

As the net amount of capital in an isolated system is constant ($dM = 0$), the maximum of capitalization corresponds to the maximum of invested capital.

As an example, we will calculate the capital dissipation σ for exchange between two economic agents with linear kinetics

$$n_1(p_1, c) = a_1(p_1 - c), \tag{39}$$

$$n_2(p_2, c) = a_2(p_2 - c). \tag{40}$$

From the condition $-n_1 = n_2 = n$ we get for $c(p_1, p_2)$

$$a_1(p_1 - c) + a_2(p_2 - c) = 0 \tag{41}$$

or

$$c = \frac{a_1 p_1 + a_2 p_2}{a_1 + a_2} \tag{42}$$

$$n(p_1, p_2) = -n_1(p_1, c(p_1, p_2)) = \overline{a}(p_2 - p_1), \tag{43}$$

where

$$\overline{a} = \frac{a_1 a_2}{a_1 + a_2}. \tag{44}$$

The dissipation is then

$$\sigma(p_1, p_2) = (p_2 - p_1)\overline{a}(p_2 - p_1) = \overline{a}(p_2 - p_1)^2 = \frac{n^2(p_1, p_2)}{\overline{a}}. \tag{45}$$

3.3. Maximum Profit Flow

A classical thermodynamic problem is finding the maximum power of a heat engine that receives heat from a source with temperature T_+ and gives part of it to a source with temperature T_-, taking into account the irreversibility of heat transfer (see in [6]). The economic analog of this is the problem of finding the maximum profit flow of a company buying an item on the market with an estimate p_1 and selling it on the market with rating $p_2 > p_1$.

The company must choose the optimal purchase and sales prices c_1 and c_2. Let the resource flow be

$$n = k_1(c_1 - p_1) = k_2(p_2 - c_2). \tag{46}$$

Then, after the optimal selection of purchase and sales prices, we get the maximum profit flow

$$m^* = \frac{(p_2 - p_1)^2}{2A}, \quad A = \left(1/k_1 + 1/k_2\right), \tag{47}$$

the optimal purchase sale flow

$$n^* = \frac{p_2 - p_1}{2A}, \tag{48}$$

and the corresponding optimal prices

$$c_1^* = p_1 + \frac{n^*}{K_1}, \quad c_2^* = p_2 - \frac{n^*}{K_2}. \tag{49}$$

4. Resource Exchange in Isolated Systems

In isolated economic systems the combined capital does not change ($\sum_j dM_j = 0$). Correspondingly, in isolated thermodynamic systems the total energy does not change. Meanwhile, the wealth function and capitalization of each subsystem increase during any resource exchange. This occurs due to increase of combined illiquid capital F, whose differential is

$$dF = \sum_j \sum_i p_{ji}(N_j, M_j) dN_{ji}. \tag{50}$$

We will demonstrate later in this paper that when a resource is exchanged for capital (sold) in an isolated system, the combined capitalization of the system,

$$dU \geq 0 \Rightarrow dF \geq 0 \tag{51}$$

increases. Equality here corresponds to reversible exchange. When one resource is exchanged into another without any exchange of capital (barter) and thus the capital distribution between subsystems is fixed, we have

$$dF > 0. \tag{52}$$

Therefore, barter is always irreversible (like heat exchange and diffusion processes in thermodynamics).

Resource/Capital Exchange in Economic Systems with Different Configurations

Selling. Suppose the system consists of two economic agents. At $t = 0$ the first economic agent has capital M_0 and the second holds resource N_0. At $t = 0$ the estimates obey $p_1 > p_2$, otherwise the trade would be blocked by the voluntary principle.

In equilibrium the balances

$$\overline{M_1} + \overline{M_2} = M_0 \tag{53}$$

$$\overline{N_1} + \overline{N_2} = N_0 \tag{54}$$

and the equality of estimates

$$p_1(\overline{N_1}, \overline{M_1}) = p_2(\overline{N_2}, \overline{M_2}) = \overline{p} \tag{55}$$

hold. The increase in capitalization of each of economic agents depends on what price is used during exchange. This price must obey the inequality

$$p_1 \geq c \geq p_2, \tag{56}$$

otherwise the voluntarity principle would be violated (as the price would be lower than the estimate when resource is sold to economic agent and higher when it is bough from him).

It is clear that

$$\frac{dM_1}{dN_1} = \frac{dM_2}{dN_2} = -c, \quad dN_2 = -dN_1, \tag{57}$$

$$M_1(0) = M_0, \quad M_2(N_0) = 0, \quad N_2(N_0) = 0. \tag{58}$$

For given $c(N_1)$ the conditions (57) allow us to express M_1, M_2, N_2 in terms of N_1. The change in capitalization can then be calculated as

$$\Delta U_1 = \int_0^{\overline{N_1}} (p_1(N) - c(N)) dN \tag{59}$$

$$\Delta U_2 = \int_0^{\overline{N_1}} (c(N) - p_2(N))dN. \tag{60}$$

For the whole system

$$\Delta U = \Delta U_1 + \Delta U_2 = \int_0^{\overline{N_1}} (p_1(N) - p_2(N))dN. \tag{61}$$

Because M_1, M_2 and N_2 are expressed in terms of N_1 and $c(N_1)$ in (57), p_1, p_2 in (59)–(61) depend not only on N_1.

The conditions (53)–(56) do not fully determine the state of equilibrium. They include three equations for four variables, $(\overline{M_1}, \overline{M_2}, \overline{N_1}, \overline{N_2})$. When $N_1 \to \overline{N_1}$, the price c tends to $\overline{p}$. If $c = p_2$, then $\Delta U_2 = 0$, and the increase of the system's capitalization is $\Delta U = \Delta U_1$. It can be found from Equation (61). If $c = p_1$ then $\Delta U = \Delta U_2$. The equilibrium states are different in these two cases.

The special case is when $c =$ const and equal to the equilibrium estimate $\overline{p}$. This the case of an *auction*. Here, the price is set in such a way that the amount of bough and sold resource are equal. In this case the condition

$$\overline{M_2} = (N_0 - \overline{N_2})\overline{p} \tag{62}$$

must be added to the conditions (53)–(55) to determine the final state.

It is not possible to transfer the system from one equilibrium state achieved by choosing some price c, which obeys inequalities (56), into another equilibrium state without reducing its capitalization and wealth function of one of its economic agents. Therefore, the set of equilibrium states is Pareto-optimal (i.e., consists of a set of compromises).

Suppose that the wealth functions have the same dimension. Let us find the state for which the sum $S_1(\overline{N_1}, \overline{M_1}) + S_2(\overline{N_2}, \overline{M_2})$ attains its maximum subject to constraints (53) and (54). The stationarity conditions of the Lagrange function on the state variables,

$$L = \sum_{i=1}^{2} S_i(\overline{N_i}, \overline{M_i}) + \lambda_1(\overline{N_1} + \overline{N_2}) + \lambda_2(\overline{M_1} + \overline{M_2}) \tag{63}$$

leads to the equations

$$\frac{\partial S_i}{\partial \overline{N_i}} = \lambda_1, \quad \frac{\partial S_i}{\partial \overline{M_i}} = \lambda_2, \quad i = 1, 2. \tag{64}$$

As

$$\frac{\partial S_i}{\partial \overline{M_i}} = p_{i0}(\overline{N_i}, \overline{M_i}) \tag{65}$$

and

$$\frac{\partial S_i}{\partial \overline{N_i}} = p_{i0}(\overline{N_i}, \overline{M_i}) p_i(\overline{N_i}, \overline{M_i}), \tag{66}$$

it follows that in equilibrium, which corresponds to the maximum of the wealth function, both resource estimates p_i (see (55)) and the capital estimates p_{i0} are the same for all subsystems. The latter condition makes the set (53)–(55) complete.

If resource estimates do not depend on the capital M, then capitalization U depends on M and N, and dU is a total differential. In this case, it is possible to construct level curves of the function $U(N, M)$ on the plane with coordinates M_1, N_1 and origin O_1. Along these lines, $dU_1 = 0$ and $\frac{dM_1}{dN_1} = -p_1(N_1)$. As the estimate increases when N_1 increases, the slope of these lines decreases and the curves are convex. The capital $M_1 \leq M^0$. The initial state of the economic agent corresponds to the point M^0 on the abscissa.

Similarly, let us draw the level curves for the capital M_2 and resource N_2 of the second economic agent (the origin here is O_2, the positive direction of the resource N_2 axis is down, and the capital M_2 axis is to the left). This figure is called an Edgeworth diagram (see Figure 1). The points where level curves of U_1 and U_2 touch obey the conditions of equilibria (55). The set of such points makes the set of equilibrium. The initial state of any system corresponds to the right lower corner of Edgeworth diagram and any of its points obey balances (53) and (54).

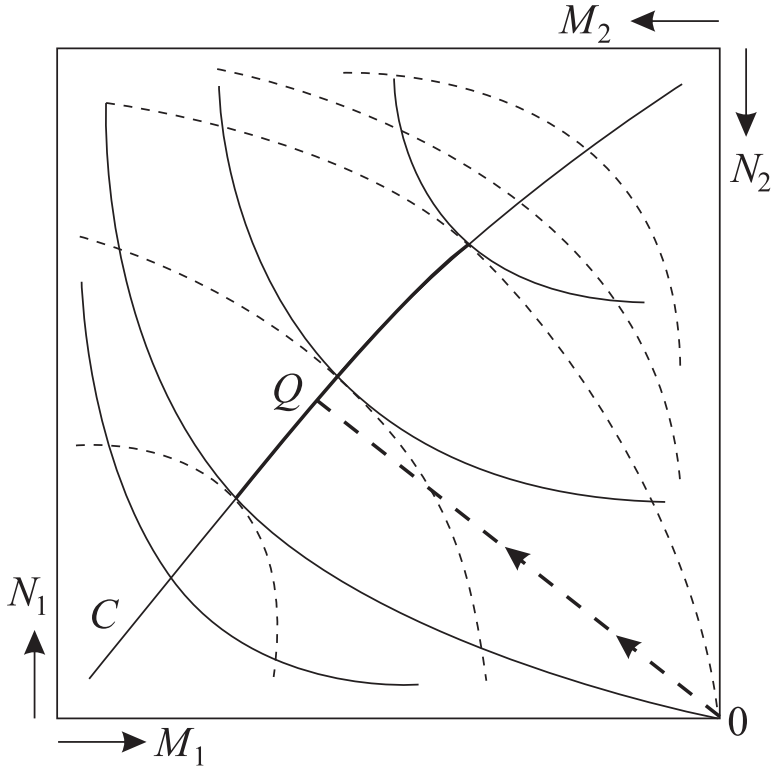

Figure 1. The Edgeworth diagram shows the possibilities of resource exchange in a closed system consisting of two economic agents. The dashed and solid lines show the level lines of the welfare functions of the first and second economic agents, respectively, and the arrows from the origin of the coordinate system in the upper right corner show the directions of growth of resource reserves and capital of each of them. The touch points of the level lines form an equilibrium curve. The section of this curve, highlighted by the bold line, is reachable from the initial state 0, as upon transition to this section the welfare functions of both economic agents increase. The point Q where the vector $0\vec{Q}$ is perpendicular to the bold line corresponds to barter exchange.

However, not all points on the equilibrium curve can be reached without violation of the voluntary condition. Points that can be reached are singled out by the inequality (56). They guarantee that no agent ends up with a lower capitalization. The reachable piece of the equilibrium curve Θ is denoted by the bold line in Figure 1. The point on it which corresponds to auction trading is given by the intersection of this curve with the straight line drawn from the initial state of the system orthogonally to Θ.

Consider exchange through the auction between n economic agents on m kinds of resources occurs. The conditions of equilibrium are

$$p_i^j(\overline{N}^i) = \lambda_j, \quad \begin{matrix} i = 1, ..., n \\ j = 1, ..., m. \end{matrix} \tag{67}$$

We again denote

$$\Delta N_{ij} = \overline{N_{ij}} - N_{ij}(0), \quad \begin{matrix} j = 1, ..., m \\ i = 1, ..., n. \end{matrix} \tag{68}$$

The balances on resources

$$\sum_{j=1}^{n} \Delta N_{ij} = 0, \quad j = 1, ..., m \tag{69}$$

and capital

$$\Delta M_j = -\sum_{i=1}^{m} \lambda_i \Delta N_{ij}, \quad j = 1, ..., n \tag{70}$$

need to be added to the conditions of equilibrium (67). The conditions (67)–(70) allow us to find states of all contacting economic agents and the increment of the system wealth function,

$$\Delta S = \sum_{j=1}^{n} (S_j(\overline{M_j}, \overline{N_j}) - S_j(0)). \tag{71}$$

It is always positive.

For the Cobb–Douglas wealth function,

$$S = M^{\gamma_0} \prod_{i=1}^{m} N_i^{\gamma_i}, \quad \gamma_i \geq 0, \quad \sum_{i=0}^{m} \gamma_i = 1, \tag{72}$$

$$p_i = \frac{\partial S / \partial N_i}{\partial S / \partial M} = \frac{\gamma_i M}{\gamma_0 N_i}, \quad i = 1, ..., m \tag{73}$$

the conditions, derived above, take the form

$$\overline{N_{ij}} = \frac{\gamma_{ij}}{\lambda_i} \frac{\overline{M_j}}{\gamma_{0j}}, \quad i = 1, ..., n, \quad j = 1, ..., m, \tag{74}$$

$$\overline{M_j} = U_{0j} - \sum_{i=1}^{m} \lambda_i \Delta N_{ij}, \tag{75}$$

$$\lambda_i = \frac{\sum\limits_{j=1}^{n} \overline{M_j} \dfrac{\gamma_{ij}}{\gamma_{0j}}}{\sum\limits_{j=1}^{n} N_{ij}(0)}, \tag{76}$$

where $U_{0j} = M_j(0) + \sum_{i=1}^{m} \lambda_i N_{ij}(0)$ is the capitalization of the j-th economic agent with respect to the equilibrium prices.

Exchange with reservoir. As a reservoir's estimates p^0 are constant, the lines $U = \text{const}$ in Figure 1 are straight. Maximal increase of an economic agent's ΔU corresponds to the exchange using prices p^0. Then in equilibrium the capital $\overline{M}$ and resource stocks $\overline{N}$ obey the conditions

$$p_i(\overline{M}, \overline{N}) = p_i^0, \quad i = 1, ..., m, \tag{77}$$

$$\overline{M} - M_0 = \sum_{i=1}^{m} p_i^0 (N_{i0} - \overline{N_i}), \tag{78}$$

$$\overline{M} \geq 0, \quad \overline{N_i} \geq 0, \quad i = 1, ..., m. \tag{79}$$

M_0 and N_0 are the initial values of M and N. If condition (79) holds, then the conditions (77) and (78) determine the equilibrium state of the system. Otherwise, some of the variables are set to zero which reduces the number of conditions ((77) and (78)) to be used to find the rest of the variables.

Let us calculate the economic agent's capitalization for $m = 1$.

$$\Delta U = \int_{N_0}^{\overline{N}} \frac{dU}{dN} dN = \int_{N_0}^{\overline{N}} \left(\frac{\partial U}{\partial M} \frac{dM}{dN} + \frac{\partial U}{\partial N} \right) dN. \tag{80}$$

As

$$\frac{dM}{dN} = -p^0, \quad \frac{\partial U}{\partial N} = p(M, N), \quad M = M_0 - p^0(N - N_0) \tag{81}$$

we find

$$\Delta U = \int_{N_0}^{\overline{N}} [p(M_0 - p^0(N - N_0), N) - p^0] dN. \tag{82}$$

If $p \geq p^0$ then $dN \geq 0$. Otherwise $dN \leq 0$ and ΔU is non-negative.

Next, we show that the increase of the economic agent's wealth function is maximal when market prices are used during the exchange. Indeed,

$$S(\overline{N}, \overline{M}) = S\left(\overline{N_1}, ..., \overline{N_m}, M(0) - \sum_{i=1}^{m} p_i^0 (\overline{N_i} - N_i(0)) \right) \to \max_{\overline{N}}. \tag{83}$$

The conditions of maximum $S(\overline{N})$,

$$\frac{\partial S}{\partial \overline{N_i}} = \frac{\partial S}{\partial \overline{M}} \frac{\partial \overline{M}}{\partial \overline{N_i}} + \frac{\partial S}{\partial \overline{N_i}} = p_0(p_i - p_i^0) = 0, \quad i = 1, ..., m \tag{84}$$

coincide with the conditions of equilibrium (77). Thus, the wealth function attains maximum at equilibrium.

Let us specify these equations for the particular case when the economic agent's wealth function has the Cobb–Douglas form (72). Then, the conditions of equilibrium (77) become the set of linear equations

$$\overline{N_i} c_i \left(1 + \frac{\gamma_0}{\gamma_i} \right) + \sum_{\nu=1, \nu \neq i}^{m} c_\nu \overline{N_\nu} = U_0 = M(0) + \sum_{\nu=1}^{m} c_\nu N_\nu(0), \quad i = 1, ..., m. \tag{85}$$

Here, U_0 is capitalization of the economic agent in its initial state using market prices. The solution of Equation (85) becomes

$$\overline{M} = U_0 \gamma_0, \quad \overline{N_i} = U_0 \frac{\gamma_i}{c_i}, \quad i = 1, ..., m. \tag{86}$$

The value of the wealth function in equilibrium with the market here is

$$\overline{S} = S(\overline{N}) = U_0 \gamma_0^{\gamma_0} \prod_{i=1}^{m} \left(\frac{\gamma_i}{c_i} \right)^{\gamma_i}. \tag{87}$$

Example 1. *Suppose*

$$S = (M, N_1, N_2) = M^{1/3} N_1^{1/2} N_2^{1/6}. \tag{88}$$

The initial stocks of resources and prices are

$$M(0) = 1, \quad N_1(0) = 2, \quad N_2(0) = 3, \quad c_1 = 10, \quad c_2 = 20. \tag{89}$$

The conditions of equilibrium and balance on capital take the form

$$\frac{\overline{M}}{\overline{N_1}} = \frac{20}{3}, \quad \frac{\overline{M}}{\overline{N_2}} = 40, \tag{90}$$

$$\overline{M} = 1 - 10(\overline{N_1} - 2) - 20(\overline{N_2} - 3). \tag{91}$$

From conditions (86) and (87) we obtain

$$U_0 = 81, \quad \overline{N_1} = 81/20 = 4.05, \quad \overline{N_2} = 81/120 = 0.675, \quad \overline{M} = 27. \tag{92}$$

$$\overline{S} = \overline{M}^{1/3}\,\overline{N_1}^{1/2}\,\overline{N_2}^{1/6} = 5.65, \quad S(0) = 1.69. \tag{93}$$

The increase of the economic agent's wealth function $\Delta S = S(\overline{N}) - S(0) = 3.96$.
For $m > 1$

$$\Delta U = \sum_{\nu=1}^{m} \int_{N_{0\nu}}^{\overline{N_\nu}} [p_\nu(M(N), N) - p_\nu^0] dN_\nu, \tag{94}$$

where

$$M(N) = M_0 + \sum_{\nu=1}^{m} p_\nu^0 (N_{0\nu} - N_\nu). \tag{95}$$

Barter. The condition that exchange is done voluntarily means that exchange of one kind of resource is possible only if this resource's estimates by the contacting subsystems have opposite signs. For example, production waste may have negative estimate for one subsystem and positive for the other which can process this waste into useful products. If all estimates have the same sign, then the exchange can only occur if not less than two kinds of resources are exchanged and when there is a counterflow of either capital or another kind of resource (barter). Here, any state for which the vector of resource estimates p for all subsystems are equal, and these resources cannot be used for exchange that would increase the wealth function of the ν-th subsystem,

$$S_\nu = p_{0\nu} \left(M_\nu + \sum_{i=1}^{n} p_i N_{i\nu} \right) = p_{0\nu} U_\nu \tag{96}$$

and further they would not reduce the wealth functions of other contacting subsystems, turn out to be equilibrium. Thus, in economics, unlike in thermodynamics, all Pareto-optimal states turn out to be in equilibrium. One of these states corresponds to an exchange via auction. Prices here are determined by the conditions of non-accumulation of resources during re-selling. At the end of the resource exchange, the capitalization U_ν of each subsystem ν based on equilibrium estimates is equal to the initial capitalization. This determines the distribution of capital.

If the functions S_ν have the same dimensionality (which is not always the case), then it is possible to find that state on the Pareto set which maximizes the combined wealth function. This means that none of the subsystems would benefit more from a transition to new new equilibrium state than the others would loose. As we demonstrated above, this state corresponds to equality of the capital estimates,

$$p_{0\nu} = p_0, \quad \nu = 1, ..., m, \tag{97}$$

which, jointly with conditions of equilibrium and conditions of non-accumulation, determine the distributions of all resources.

Consider a system that includes two economic agents that both have two types of resources and no capital. In the initial state the resource stocks and their estimates are given by

$$N_1^0 = (N_{11}^0, N_{12}^0), \quad N_2^0 = (N_{21}^0, N_{22}^0), \quad p_{1\nu}^0(N_\nu^0), \quad p_{2\nu}^0(N_2^0), \quad \nu = 1, 2. \tag{98}$$

The estimates here either do not depend on capital or the distribution of capital $\overline{M}$ is fixed.

If the initial stocks have such values that the solution of the conditions of equilibrium,

$$p_{11}(\overline{N_1}) = p_{21}(\overline{N_2}), \tag{99}$$

$$p_{12}(\overline{N_1}) = p_{22}(\overline{N_2}), \tag{100}$$

$$\overline{N_1} + \overline{N_{21}} = N_{11}^0 + N_{21}^0, \quad \overline{N_{12}} + \overline{N_{22}} = N_{12}^0 + N_{22}^0, \tag{101}$$

are positive, then these conditions completely determine the state of the system.

In the general case of barter exchange in which n economic agents take part, each of which holds m kinds of resources, the conditions of equilibrium take the form

$$\sum_{i=1}^{n} \overline{N_{i\nu}} = \sum_{i=1}^{n} N_{i\nu}^0 = N_\nu^0, \quad \nu = 1, ..., m, \tag{102}$$

$$p_{i\nu}(\overline{N_i}, \overline{M_i}) = \lambda_\nu, \quad i = 1, ..., n, \quad \nu = 1, ..., m. \tag{103}$$

For the non-degenerate case of convex (with respect to $\overline{N_i}$) functions $p_{i\nu}(\overline{N})$, the conditions (102) and (103) determine the equilibrium distribution of resources for fixed capital $\overline{M_i}$.

For isolated economic systems the following statement holds.

For each distribution of initial capital $\overline{M}$ between subsystems, resources are distributed in such a way that the net sum of invested capital attains its maximum conditional on the constraints imposed on the system:

$$F(\overline{M}) = \sum_i \sum_\nu p_{i\nu}(N_i, \overline{M_i}) N_i \to \max_{N_i} \tag{104}$$

subject to conditions (102). This maximum is

$$F^*(\overline{M}) = \sum_\nu \lambda_\nu(\overline{M}) N_\nu^0. \tag{105}$$

In its turn the distribution of capital $\overline{M}$ between subsystems obeys the conditions of capital balance, inequalities that follow from the voluntary nature of exchange. It also depends on the form of the kinetic functions.

5. Stationary State of an Open Economic System

Exchange between markets. Suppose the system consists of two markets. They exchange a vector of resources N whose estimates on the first and second market correspondingly are p_1 and p_2. From the economic balances it follows that capital dissipation here is

$$\sigma = \sum_i n_i(p_1, p_2)(p_{2i} - p_{1i}). \tag{106}$$

For flows proportional to the price difference, $n_i = a_{i12}(p_{2i} - p_{1i})$, analogous to simple flows in thermodynamics, we get

$$\sigma = \sum_i a_{i12}(p_{2i} - p_{1i})^2. \tag{107}$$

Stationary open system. A stationary regime in an open economic system where there is no convective flows is possible only if it includes at least two economic reservoirs. We denote flows

between the ν-th and j-th subsystems as $n_{\nu j}(p_\nu, p_j)$. For each ν-th economic agent, the vector balances of resources take the following form,

$$\sum_j n_{\nu j} + n_\nu^d + W_\nu \alpha_\nu = 0, \tag{108}$$

where j is the subscript denoting the j-th subsystem. In accordance with (29) capital dissipation becomes

$$\sigma = \frac{1}{2}\sum_{\nu,j} n_{\nu j}(p_\nu, p_j)(p_\nu - p_j) + \sum_\nu n_\nu^e(p_\nu, c_\nu)(p_\nu - c_\nu) + \sum_\nu W_\nu \alpha_\nu p_\nu. \tag{109}$$

In particular, if the system is near equilibrium and flows are proportional to the estimate differences, and the rates of production $W_{\nu j}\alpha_\nu$ are constant, then the dissipation takes the following form, similar to exchange between markets,

$$\sigma = \frac{1}{2}\sum_{\nu,j,i} a_{\nu j i}(p_{\nu i} - p_{j i})^2 + \sum_{i,\nu} p_{\nu i} W_{\nu i}\alpha_{\nu i} + \sum_\nu a_{\nu i}(p_{\nu i} - c_{\nu i})^2. \tag{110}$$

Here, ν, j are subsystem subscripts and i is the resource subscript.

6. Principle of Minimal Capital Dissipation

The factor that causes resource exchange flows to occur (the "driving force") is the difference between the resource estimates in two contacting subsystems or between the price and the estimate (for definiteness we will consider the latter). Near equilibrium this difference is small and flows can be assumed to depend linearly on the difference of price and estimate.

The driving force of resource exchange here is $\Delta = p - c$. We assume that the flow directed to the economic agent is positive, then

$$n_i = \sum_{\nu=1}^n a_{\nu i}\Delta_\nu = \sum_{\nu=1}^n a_{\nu i}(p_\nu - c_\nu), \quad i = 1, ..., n. \tag{111}$$

We shall call the matrix A with the elements $a_{i\nu}$ the matrix of kinetic coefficients of the economic agent. It determines exchange kinetics between the economic agent and its environment.

The resource exchange flow causes a counter flow of capital such that

$$\frac{dM}{dt} = -\sum_{i=1}^n c_i n_i. \tag{112}$$

The rate of change of the wealth function is

$$\begin{aligned}\frac{dS}{dt} = \frac{\partial S}{\partial N_0}\frac{dN_0}{dt} + \sum_{i=1}^n \frac{\partial S}{\partial N_i} g_i = -p_0 \sum_{i=1}^n c_i g_i + + p_0 \sum_{i=1}^n p_i g_i = \\ = p_0 \sum_{i=1}^n (p_i - c_i) g_i = p_0 \Delta^T A \Delta.\end{aligned} \tag{113}$$

Here, Δ is the vector of driving forces.

As capital estimate $p_0 > 0$ and since resource exchange is voluntary and therefore wealth function cannot decrease during an exchange, it follows that the matrix A is positive definite. Let us show that it is also symmetrical.

Indeed, if we extract Δ from (111), then for any infinitesimal time interval the expression (113) takes the form

$$\frac{dS}{p_0} = dN^T B dN, \tag{114}$$

where dN is the column vector of increments of stocks of resources and $B = A^{-1}$. The elements $b_{i\nu}$ of this matrix are

$$b_{i\nu} = \frac{\partial^2(\frac{S}{p_0})}{\partial N_i \partial N_\nu} = b_{\nu i}, \quad i, \nu = 1, ..., n. \tag{115}$$

Thus, B is positive definite and symmetric. Therefore, for small deviations from equilibrium, the inverse of the B matrix of supply and demand, $A = B^{-1}$ is symmetric and positive definite. Further, the following *reciprocity conditions* hold. The influence of the difference between the price and estimate of the ν-th resource on the flow of the i-th resource is the same as the influence of the difference of the price and estimate of the i-th resource on the flow of the ν-th resource.

After taking into account the symmetry of the kinetic coefficient matrix, the conditions of minimum σ (see (110)) with respect to $p_{\nu i}$ $(\nu = 1, ..., k)$ for each economic agent lead to the equations such that

$$\sum_j a_{\nu ji}(p_{\nu i} - p_{ji}) + W_{\nu i}\alpha_{\nu i} + a_{\nu i}(p_{\nu i} - c_{\nu i}) = 0 \quad \forall_i, \nu. \tag{116}$$

For linear flows this coincides with resource balance equations for each of the subsystems (108). As a consequence, the following statement is true. *Resources and capital are distributed in equilibrium in an open economic system with near linear laws of resource exchange in such a way that capital dissipation σ is minimal.* This is the analogue of the Prigogine principle in irreversible thermodynamics [7].

7. Conclusions

We have shown above that the mathematical descriptions of processes occurring between thermodynamic systems and between economic systems have much in common. The concept of irreversibility of economic transport phenomena is introduced, and the problem of minimum irreversibility for a limited duration, or a given average intensity, of economic processes similar to FTT are considered. These analogies are treated in a large number of studies (see [8–11] a.o.). As so may concepts are similar, here we rather emphasize the main difference between thermodynamic and economic systems.

In thermodynamics any consequences of energy or mass transport between the subsystems of an isolated system are accompanied by an increase in the total entropy. However, the entropy of one subsystem can decrease while the entropy of another one increases by at least the same amount.

In economics not only the total welfare function grows under similar conditions, but also the welfare function of each of the subsystems according to the condition of voluntarity. Moreover, each flow of resource transport is accompanied by a counter flow of capital transport.

Equations of thermodynamic balances correspond in economics to balance equations for capital, for each kind of resources, and for welfare. The role of dissipation is played by the growth rate of the welfare function (it is non-negative). The constraints must be accompanied by the requirements of non-negativity for the growth rate of the welfare function for each subsystem.

Author Contributions: Methodology, A.T. and L.G.; Supervision, A.T.; Validation, L.G.; Writing—original draft, A.T.; Writing—review & editing, L.G. All authors have read and agreed to the published version of the manuscript.

Funding: This research received no external funding.

Conflicts of Interest: The authors declare no conflicts of interest.

References

1. Petrov, A.A. *Economics, Models, Computational Experiment (Ekonomika, Modeli, Vychislitelnyj Eksperiment)*; Nauka: Moscow, Russia, 1966; p. 252. (In Russian)
2. Rozonoèr, L.I. A Generalized Thermodynamic Approach to Resource Exchange and Allocation. II, III. *Autom. Remote Control* **1973**, *34*, 915–927, 1272–1289.
3. Martinás, K. Irreversible microeconomics. In *Complex Systems in Natural and Economic Sciences*; Martinás, K., Moreau, M., Eds.; ELFT: Budapest, Hungary, 1995; p. 114.

4. Hurwicz, L.; Richter, M.K. An Integrability Condition with Applications to Utility Theory and Thermodynamics. *J. Math. Econ.* **1979**, *6*, 7–14. [CrossRef]
5. Ville, J.; Newman, P.K. The Existence-Conditions of a Total Utility Function. *Rev. Econ. Stud.* **1951**, *19*, 123–128. [CrossRef]
6. Curzon, F.L.; Ahlborn, B. Efficiency of a Carnot engine at maximum power output. *Am. J. Phys.* **1975**, *43*, 22–24. [CrossRef]
7. Nicolis, G.; Prigogine, I. *Self-Organization in Nonequlibrium Systems: From Dissipative Structures to Order through Fluctuations*; Wiley: Hoboken, NJ, USA, 1977; p. 512.
8. Lichnerowicz, M. Un modèle d'èchange èconomique (Èconomie et thermodynamique). *Annales de l'I.H.P. Probabilités et Statistiques* **1970**, *6*, 159–200.
9. Samuelson, P.A. Maximum Principle in Analytical Economics. *Am. Econ. Rev.* **1972**, *62*, 249–262.
10. Salamon, P.; Komlos, J.; Andresen, B.; Nulton, J.D. A Geometric View of Welfare Gains with Non-instantaneous Adjustment. *Math. Soc. Sci.* **1987**, *13*, 153–163. [CrossRef]
11. Samuelson, P.A. *Foundations of Economic Analysis*; Enlarged ed.; Harvard University Press: Cambridge, MA, USA, 1983; p. 604.

entropy

MDPI

Editorial

Future Perspectives of Finite-Time Thermodynamics

Bjarne Andresen [1,*] and Peter Salamon [2,*]

[1] Niels Bohr Institute, University of Copenhagen, Blegdamsvej 17, DK-2100 Copenhagen Ø, Denmark
[2] Department of Mathematics and Statistics, San Diego State University, 5500 Campanile Drive, San Diego, CA 92182-7720, USA
* Correspondence: andresen@nbi.ku.dk (B.A.); salamon@sdsu.edu (P.S.)

Finite-time thermodynamics was created 45 years ago as a slight modification of classical thermodynamics, by adding the constraint that the process in question goes to completion within a finite length of time. It was started using very simple models of real processes and has since then evolved into many new areas as clearly evidenced by the 20 quite diverse papers of this Special Issue "Finite-Time Thermodynamics" [1–20]. The philosophy has remained the same: add a time constraint for the processes involved and optimize for your desired quantity (power, efficiency, profit, population, whatever). But the types of processes considered and the accuracy of the modeling have expanded immensely from the original simple Curzon-Ahlborn engine.

While much work is still needed optimizing concrete and very important processes and machines in our daily lives, we would here like to raise our gaze to more distant horizons. Where could the field go next to expand our insight and modeling abilities?

Some of the most promising directions we are imagining are beyond what is traditionally considered thermodynamics. One direction which contains many astonishing concepts, and which has already been underway for many years, is quantum finite-time thermodynamics. Not only will one encounter the 'usual' quantum effects, some very untraditional ones also appear. Quantum resources like coherence and entanglement carry available work. It follows that Carnot engines working between heat reservoirs containing such "hidden" resources can appear to violate Carnot's bound [21]. Similarly, systems with bounded upper energy levels can exhibit negative temperatures. Such systems can turn a heat input into pure work without further flows. Recent "shortcuts to equilibrium" [22] can take a system from one equilibrium state to another equilibrium state within a short period of time as opposed to a usual adiabatic transformation which in principle would require an infinite length of time. In other words, we can generate reversible transformations in lossy systems taking place in a finite time by appropriate controls. As quantum computing using q-bits develop, such *quantum finite-time thermodynamic considerations in lossy environments* and related optimal solutions for design of the physical equipment will become very important to gain the full potential of quantum computing.

One area of particular concern in connection with quantum systems is that they are governed by Hamiltonian dynamics and thus in principle are lossless. By contrast, finite-time thermodynamics always involves losses. Its goal is to minimize these losses and calculate the optimal paths using available controls, not just natural free flows. Thus what we need to develop is a *general thermodynamic description of open quantum systems*, i.e., including the lossy interaction with external reservoirs [23,24]. The Lindblad superoperator has been extensively used for this purpose, but is it general enough for quantum computing, and how can we control the rate of transfers, the core component of finite-time thermodynamics, in the loss minimization optimization?

Quantum thermodynamics typically involves translating thermodynamics many orders of magnitude down from the human scale to the atomic scale where many concepts are different (e.g., temperature and pressure). What happens in the opposite direction, moving many orders of magnitude up from the human scale to the galactic scale? A scale typically

Citation: Andresen, B.; Salamon, P. Future Perspectives of Finite-Time Thermodynamics. *Entropy* **2022**, *24*, 690. https://doi.org/10.3390/e24050690

Received: 6 May 2022
Accepted: 7 May 2022
Published: 13 May 2022

involves both a spatial and a temporal dimension, often connected by the speed of light. The issue here is that any measurement can be split into 3 regions of accessibility. If we are talking about timescales, there will be a central region which we can observe properly. At times shorter than that, our instruments cannot tell events apart and thus establish "before" and "after" and causality. Processes on timescales longer than our window of observability are not detected since we see no change. Exploring this '*slow-time thermodynamics*' we have just scratched the surface [25] in an attempt to find out which thermodynamic concepts survive (e.g., mass), which ones either disappear or take on a new appearance (e.g., temperature and entropy), and which new ones may emerge. Entropy production, which is a crucial quantity for rate processes, surely will acquire new components from processes which we on human time and space scales can follow in detail but which on the grander scale become impossible to tell apart and thus appear statistical. Wind is such an example. This is a wide open field, not least identifying rate processes, their entropy production rates, and how possibly to control them.

Another virgin territory of finite-time thermodynamics may be found within biology, ranging from the chemical processes of sub-components of single cells (e.g., energy transfer processes in mitochondria) to ecological competition (e.g., corals vs. algae) to evolution. Many attempts have been made at using entropies in comparing the evolution and thus competition of species, ranging from the well established Shannon and Kullback-Leibler forms to home-cooked expressions. While the questions attacked are indeed of great importance for our understanding of biological systems, there is a serious need for a *precise thermodynamic formulation of the basic interactions and objectives of the biological system components* before one can hope for reliable dynamic (finite-time) conclusions. Attempts have been made to model evolutionary steps as phase transitions in the spin glass description of aging. Both are strongly out-of-equilibrium processes with memory and are conceptually similar.

After many years of dormancy, methods based on *thermodynamic geometry* have recently started bearing fruit. The connection between thermodynamic length and dissipation has been used to bound the operation of quantum heat engines for adiabatically driven closed systems [2]. Thermodynamic curvature measures interaction strength, and its use led to better equations of state and shed light on black hole thermodynamics [26]. We anticipate that these are just the beginning and there is much more insights to come from thermodynamic geometry.

Thermodynamics-like theories can be used in any area where optimizing behavior is central to the ruling paradigm. These include the disciplines of economics and biology. Optimizing behavior can infuse finite-time thermodynamic ideas and reasoning into such disciplines and leads to carry-over concepts such as dissipation in capital markets [17]. In economics, models assuming optimizing behavior abound with producer optimizing production, consumer optimizing utility, and government optimizing total welfare. These optimization problems give ample opportunity for mapping thermodynamic models into the situation along the lines of mapping mechanics problems into electronic circuits. Much of Georgescu-Roegen's classic work [27] exploits such mappings. But while it is clear that optimizing behavior is involved, such behaviors in economics and biology stem from the phenomena for which the actual objective function, operating on a given timescale in a given situation, is usually controversial. We expect finite-time thermodynamics to be a future guide to such efforts as a template and as a source of readily adapted models with large palettes of objective functions and associated optimizing behaviors.

Unlike biological or economic systems, computer systems have clear objective functions purely by engineering design. How to achieve optimizing behavior is the main issue here and simulated annealing has been its workhorse example [28]. Optimal cooling depends on the heat capacity and relaxation time of a fictitious physical system that is naturally associated with the optimization problem. Finding similar finite-time thermodynamics based *data mining techniques* to extract the most information with the least work

from a database is likely to be a fertile area. This connection to information engines has made great strides [29] and is poised for more.

Standard predictions for the future of engineering involve *designing for sustainability and easy recycling*. But surely the dominant design theme of the next few decades is designing for product intelligence. Since intelligent behavior entails solving some optimization problem under given constraints, our above stated criteria for thermodynamics-like models are fulfilled. Finite time is certainly one of these constraints, so we expect finite-time thermodynamics-like models to play an important role. Since we are approaching the "technological singularity" [30], this may even be the most important development that can benefit from finite-time thermodynamics-like models.

Author Contributions: Both authors contributed equally to the paper. All authors have read and agreed to the published version of the manuscript.

Funding: This research received no external funding.

Conflicts of Interest: The authors declare no conflict of interest.

References and Note

1. Berry, R.S.; Salamon, P.; Andresen, B. How It All Began. *Entropy* **2020**, *22*, 908. [CrossRef] [PubMed]
2. Abiuso, P.; Miller, H.J.D.; Perarnau-Llobet, M.; Scandi, M. Geometric Optimisation of Quantum Thermodynamic Processes. *Entropy* **2020**, *22*, 1076. [CrossRef] [PubMed]
3. Andresen, B.; Essex, C. Thermodynamics at Very Long Time and Space Scales. *Entropy* **2020**, *22*, 1090. [CrossRef] [PubMed]
4. Chen, L.; Ma, K.; Ge, Y.; Feng, H. Re-Optimization of Expansion Work of a Heated Working Fluid with Generalized Radiative Heat Transfer Law. *Entropy* **2020**, *22*, 720. [CrossRef]
5. Dann, R.; Kosloff, R.; Salamon, P. Quantum Finite-Time Thermodynamics: Insight from a Single Qubit Engine. *Entropy* **2020**, *22*, 1255. [CrossRef]
6. De Vos, A. Endoreversible Models for the Thermodynamics of Computing. *Entropy* **2020**, *22*, 660. [CrossRef]
7. Essex, C.; Das, I. Radiative Transfer and Generalized Wind. *Entropy* **2020**, *22*, 1153. [CrossRef]
8. Gonzalez-Ayala, J.; Mateos Roco, J.M.; Medina, A.; Calvo Hernández, A. Optimization, Stability, and Entropy in Endoreversible Heat Engines. *Entropy* **2020**, *22*, 1323. [CrossRef]
9. Insinga, A.R. The Quantum Friction and Optimal Finite-Time Performance of the Quantum Otto Cycle. *Entropy* **2020**, *22*, 1060. [CrossRef]
10. Masser, R.; Khodja, A.; Scheunert, M.; Schwalbe, K.; Fischer, A.; Paul, R.; Hoffmann, K.H. Optimized Piston Motion for an Alpha-Type Stirling Engine. *Entropy* **2020**, *22*, 700. [CrossRef]
11. Muschik, W.; Hoffmann, K.H. Modeling, Simulation, and Reconstruction of 2-Reservoir Heat-to-Power Processes in Finite-Time Thermodynamics. *Entropy* **2020**, *22*, 997. [CrossRef] [PubMed]
12. Roach, T.N.F. Use and Abuse of Entropy in Biology: A Case for Caliber. *Entropy* **2020**, *22*, 1335. [CrossRef] [PubMed]
13. Rogolino, P.; Cimmelli, V.A. Thermoelectric Efficiency of Silicon-Germanium Alloys in Finite-Time Thermodynamics. *Entropy* **2020**, *22*, 1116. [CrossRef] [PubMed]
14. Ruppeiner, G.; Seftas, A. Thermodynamic Curvature of the Binary van der Waals Fluid. *Entropy* **2020**, *22*, 1208. [CrossRef]
15. Schön, J.C. Optimal Control of Hydrogen Atom-Like Systems as Thermodynamic Engines in Finite Time. *Entropy* **2020**, *22*, 1066. [CrossRef]
16. Sun, M.; Xia, S.; Chen, L.; Wang, C.; Tang, C. Minimum Entropy Generation Rate and Maximum Yield Optimization of Sulfuric Acid Decomposition Process Using NSGA-II. *Entropy* **2020**, *22*, 1065. [CrossRef]
17. Tsirlin, A.; Gagarina, L. Finite-Time Thermodynamics in Economics. *Entropy* **2020**, *22*, 891. [CrossRef]
18. Tsirlin, A.; Sukin, I. Averaged Optimization and Finite-Time Thermodynamics. *Entropy* **2020**, *22*, 912. [CrossRef]
19. Xi, Y.; Liu, X.; Constales, D.; Yablonsky, G.S. Perturbed and Unperturbed: Analyzing the Conservatively Perturbed Equilibrium (Linear Case). *Entropy* **2020**, *22*, 1160. [CrossRef]
20. Zhang, Y.; Kowalski, G.J. Calorimetric Measurements of Biological Interactions and Their Relationships to Finite Time Thermodynamics Parameters. *Entropy* **2022**, *24*, 561. [CrossRef]
21. Allahverdyan, A.E.; Nieuwenhuizen, T.M. Extraction of work from a single thermal bath in the quantum regime. *Phys. Rev. Lett.* **2000**, *85*, 1799. [CrossRef] [PubMed]
22. Guéry-Odelin, D.; Ruschhaupt, A.; Kiely, A.; Torrontegui, E.; Martínez-Garaot, S.; Muga, J.G. Shortcuts to adiabaticity: Concepts, methods, and applications. *Rev. Mod. Phys.* **2019**, *91*, 045001. [CrossRef]
23. Breuer, H.-P.; Petruccione, F. *The Theory of Open Quantum Systems*; Oxford University Press on Demand: Oxford, UK, 2002.
24. Dann, R.; Kosloff, R. Quantum thermo-dynamical construction for driven open quantum systems. *Quantum* **2021**, *5*, 590. [CrossRef]
25. Essex, C.; Andresen, B. The Ideal Gas in Slow Time. *J. Non-Equilib. Thermodyn.* **2021**, *46*, 35–43. [CrossRef]
26. Special Issues of Entropy, Geometry in Thermodynamics (https://www.mdpi.com/journal/entropy/special_issues/geometry_in_thermodynamics, accessed on 30 June 2015) and Geometry in Thermodynamics II (https://www.mdpi.com/journal/entropy/special_issues/geometry_in_thermodynamics_II, (accessed on 28 February 2018).

27. Georgescu-Roegen, N. The entropy law and the economic process. In *The Entropy Law and the Economic Process*; Harvard University Press: Cambridge, MA, USA, 2013.
28. Salamon, P.; Sibani, P.; Frost, R. *Facts, Conjectures, and Improvements for Simulated Annealing*; SIAM: Philadelphia, PA, USA, 2002.
29. Deffner, S.; Jarzynski, C. Information Processing and the Second Law of Thermodynamics: An Inclusive, Hamiltonian Approach. *Phys. Rev. X* **2013**, *3*, 041003. [CrossRef]
30. Vinge, V. The coming technological singularity. *Whole Earth Rev.* **1993**, *81*, 88–95.

MDPI
St. Alban-Anlage 66
4052 Basel
Switzerland
Tel. +41 61 683 77 34
Fax +41 61 302 89 18
www.mdpi.com

Entropy Editorial Office
E-mail: entropy@mdpi.com
www.mdpi.com/journal/entropy

MDPI
St. Alban-Anlage 66
4052 Basel
Switzerland

Tel: +41 61 683 77 34

www.mdpi.com

ISBN 978-3-0365-4950-7